MICROSTRAIN PARTITIONING, TRIP KINETICS AND DAMAGE EVOLUTION IN THIRD GENERATION DUAL PHASE AND TRIP-ASSISTED ADVANCED HIGH STRENGTH STEELS

MICROSTRAIN PARTITIONING, TRIP KINETICS AND DAMAGE EVOLUTION IN THIRD GENERATION DUAL PHASE AND TRIP-ASSISTED ADVANCED HIGH STRENGTH STEELS

BY CONCETTA PELLIGRA, B.Eng

A Thesis

Submitted to the School of Graduate Studies

in Partial Fulfilment of the Requirements

for the Degree

Doctor of Philosophy

McMaster University

Doctor of Philosophy (2024) McMaster University

(Materials Science & Engineering) Hamilton, Ontario, Canada

TITLE:	Microstrain Partitioning, TRIP kinetics, and Damage Evolution in Third Generation Dual Phase and TRIP-assisted Advanced High Strength Steels
AUTHOR:	Concetta Pelligra, B.Eng (McMaster University)
SUPERVISOR:	Professor. David S. Wilkinson
NUMBER OF PAGES:	362

Lay Abstract

A lot of research up to now has been invested in the automotive industry to create steels that are lightweight, strong and show improved crashworthiness. The means by which this has been achieved is with the use of innovative processing routes to manufacture and implement Advanced High Strength Steels (AHSSs) in a vehicle's body-in-white. Nonetheless, the constant global pressure to reduce greenhouse gas emissions has eventually driven research to a third-generation class of ultrahigh strength, lightweight AHSSs. These steels retain the weight savings of their second-generation counterparts but are more cost-effective to manufacture and can be adapted to current industrial line capabilities. Considerable work has been done to enable the manufacturing of 3G steels, yet the steel characteristics which underpin fracture, thereby affecting the crashworthiness of these steels, continues to be weakly understood. As such, at a microscopic scale, this thesis uses three different promising 3G AHSSs candidates to evaluate the impact their unique steel characteristics has on the ability to resist damage evolution and fracture.

Abstract

Lightweighting demands have been achieved by third generation (3G) Advanced High Strength Steels (AHSSs) by a means of increased strength. The challenge faced in doing so, however, is in ensuring that ductility and crashworthiness is efficiently retained. Key methods in which automotive research has been invested to achieve this strength-ductility balance is by microalloying to promote grain refinement, the introduction of precipitates, and the effective use of plasticity enhancing mechanisms. Specifically, the ability to tailor the stability of retained austenite during deformation has been crucial in manipulating the strength-to-ductility ratio of 3G AHSSs using the Transformation Induced Plasticity (TRIP) effect. On the other hand, dual phase (DP) (i.e: non-TRIP-assisted steels) continue to be most significantly manufactured due to their robust thermomechanical processing but are also compromised by their poor damage tolerance. Hence, considerable reports are available regarding the damage tolerance of DP steels, but the ability for the volume expansion associated with the austenite-to-martensite transformation to suppress damage evolution and enhance a steel's local formability has not yet been thoroughly investigated.

Nonetheless, the damage processes that lead to fracture in 3G AHSSs are complex. A full understanding of the underlying phenomena requires a careful assessment of the strain partitioning amongst phases, how the microstructure evolves with strain and how damage, in the form of voids and micro-cracks, nucleates and grows. This can only be accomplished by applying a range of methodologies, including microscopic Digital Image Correlation (µDIC), X-ray Computed Microtomography (µXCT), Electron Backscattered Diffraction (EBSD) and X-ray Diffraction (XRD), all of which can be tracked as deformation proceeds.

This PhD thesis uses a novel post µDIC data processing technique to prove that a reduction in strain gradient, linked to the evolution Geometrically Necessary Dislocations (GNDs), at dissimilar phase interfaces is attainable with vanadium-microalloying and with use of the TRIP effect. A local strain gradient post µDIC data processing technique was developed and first applied on 3G DP steels to show that the microcompatibility between ferrite and martensite directly at the interface is considerably improved with vanadium-microalloying. This in turn microscopically explains this DP steel's increased local formability/damage tolerance with vanadium micro-

additions. Moreover, when applying this novel µDIC technique on two other 3G experimental steels of interest, an ultrahigh strength Quench & Partition (Q&P) steel and a continuous galvanizing line (CGL)-compatible Medium-Mn (med-Mn) steel, an even slower evolution of microstrain gradients at dissimilar phase interfaces was observed. This indicates that, although vanadium-microalloying can improve the damage tolerance of a DP steel, its ability to achieve the ultrahigh strengths is a direct result of the severe inhibition of dislocation motion at dissimilar phase boundaries. Eventually, at high strains, these local strain gradients cannot be maintained and results in premature damage nucleation. By comparison, at such high strains, distinct evidence of damage nucleation was not apparent in the 3G TRIP-assisted steels which is the result of a slow strain gradient evolution delayed by the effective use of TRIP.

This finding triggered a further investigation into isolating the impact the rate of TRIP exhaustion has on damage development. By intercritically annealing this prototype med-Mn steel (0.15C-5.8Mn-1.8Al-0.71Si) with a martensitic starting microstructure, within a narrow temperature interval (from 665 to 710°C), it was possible to make significant changes in the steel's rate of TRIP exhaustion without making considerable changes to its physical microstructure. This steel exhibits the largest true strain at fracture ($\varepsilon_f = 0.61$), meets U.S. Department of Energy (DoE) mechanical targets (28,809 MPa%), and shows sustained monotonic work hardening when intercritically annealed at an intermediate IA temperature of 685°C for 120s. In addition, this IA condition showed optimal damage tolerance properties as an abundance of voids nucleated during its tensile deformation, but their growth was suppressed by prolonging TRIP over a large strain range. There is reason to believe that the heterogeneous distribution of austenite and Mn throughout this 685°C IA condition compared to the other two enabled its suppressed TRIP kinetics and in turn improved damage tolerance.

The impact that changes in stress-state, from a stress triaxiality of 0.33-0.89, has on microstrain partitioning, TRIP kinetics and damage evolution was tested on this med-Mn at its 685°C IA condition. With the machining of notches on tensile specimens, it was seen that a high stress triaxiality (0.74-0.89) accelerated the rate of TRIP, whereas the introduction of shear, through a misaligned notched specimen design, delayed TRIP kinetics. The change in mean stress imposed by the notches was deemed to have played an active role in TRIP exhaustion during the material's

tensile deformation. A unique electropolishing micro-speckle patterning technique was applied to show that the amount of strain that can be accommodated by the steel’s the polygonal ferrite-tempered martensitic regions are considerably impacted by external modifications in stress-state. While damages studies using different such notched tensile geometries revealed that once a critical void size is reached in this med-Mn steel, coalescence proceeds at an increasing, exponential rate up to fracture. It continues to remain a challenge to quantify the effects microstrain partitioning, TRIP kinetics and damage evolution separately, opening new avenues for future experimental and modeling investigations.

Acknowledgements

I would like to thank my supervisor, Dr. David S. Wilkinson for his support and mentorship throughout my PhD journey. It has been a pleasure to work for the prestigious Dr. Wilkinson and I thank him for his technical advice, mentorship and for the opportunity to present at multiple conferences. I would also like to thank Dr. Joseph R. McDermid, Dr. Hatem Zurob, and Dr. Jidong Kang for providing me with technical advice as my supervisory committee members. I'd like to express my gratitude to Dr. Javad Samei, who continued to support my academic career and proofread my manuscripts even after his post-doctoral term. I have co-authored 4 papers to date with Dr. Samei. He has been an amazing mentor throughout this journey. As well, I thank my External Examiner, Dr. C. Cem Tasan, for providing his technical expertise during my thesis defense, and for his review of this thesis.

I would like to thank the International Zinc Association Galvanized Autobody Partnership (IZA-GAP) and the Natural Sciences and Engineering Research Council of Canada (NSERC), under grant CRDJ522309-17, for their funding of this Ph.D. project. As well, I thank CanmetMaterials, General Motors Global R&D Centre, and U.S. Steel Research for providing the sheet steels - an ultrahigh strength Dual Phase, Quench & Partition, and medium Mn (med-Mn) steel, respectively for this thesis.

I would also like to thank the following people:

- Dr. Joey Kish, Dr. Elizabeth McNally, Dr. Moisei Bruhis, and my colleagues at the Centre for Automotive Materials and Corrosion (CAMC) for helping me with my experiments and providing me with feedback during my CAMC presentations. I would especially like to thank Dr. Daniella Pallisco and Dr. Kazi Mahmudul Haque Bhadhon who helped me in the onboarding of the IZA-GAP project, and in providing me with technical advice on med-Mn steels whenever needed.

- My previous and current teammates in the Wilkinson Research group: Diyar Salehiyan, Ivar Smets, Youssef Salib, Nizia Mendes Fonseca, Cal Siemens, and Mahmoud Diab either for their help on conducting experiments, their assistance during my very tedious, long synchrotron experiments at the Argonne National Lab, as well as for their coding and ABAQUS guidance.

- Dr. Shahryar Asqardoust and Dr. Abhishek Sarmah, from McMaster's Mechanical Engineering Department, for initially training me on ABAQUS and for helping me with my finite element modelling difficulties.

- Raymond Fullerton and John Thomson (McMaster Steel Research Centre) for always performing the heat treatments of my med-Mn steel using the McMaster Galvanizing simulator within a timely manner

- Tim Schmidt from Trilion for providing Digital Image Correlation (DIC) training and for his help in co-ordinating the shipment of DIC equipment to the Argonne National Lab for synchrotron experiments.

- I thank the U. S. Department of Energy, Office of Science, Office of Basic Energy Sciences, under Contract No. DE-AC02-06CH11357 for being able to use the Argonne Photon Source (APS) 11-ID-C beamline, as well as beamline scientists for training and technical guidance - Dr. Andrey Andreevich Yackovenko and Dr. Tyra Chenice Douglas

- The staff of the Canadian Centre for Electron Microscopy (CCEM). I thank Chris Butcher and Jhoynner Martinez for SEM training, electropolishing training and for help with SEM issues even on weekends and evenings. I'd like to thank Travis Casagrande for providing me with FIB training. I would like to thank Sabaa Rashid and Dr. Xiang Wang for TEM preparation and analysis, as well as Andy Duft for repairing our in-situ SEM tensile jig when necessary. I am grateful to Dr. Samantha Stambula and Dr. Brian Langelier for giving me the opportunity to showcase microscale DIC techniques on their CCEM youtube channel.

- Doug Culley and Dr. Xiaogang Li for their help with my sample preparation in the Materials Science and Engineering (MSE) labs, as well as Ed McCaffery for helping me with any computer/software issues during my studies.

- Dr. Babak Shalchi Amirkhiz and Dr. Nafiseh Zafer from CanmetMaterials for their help in my TEM analysis.

- Dr. James Britten, and Vicky Jarvis for training me on x-ray diffraction and for their support in helping me analyze my data both from the McMaster Analytical X-ray (MAX) facility laboratory, and from Argonne National Lab.

- Dr. Louis G. Hector Jr., from General Motors Global R&D centre, who spent a significant amount of time proofreading our paper on an ultrahigh strength Q&P steel, and I thank him for his helpful feedback. As well I'd like to express my gratitude to Dr. Abu-Farha who answered many of my questions about his experimental set-up at APS' 11-ID-C beamline.

- Jim Cleaver for the machining of my specimens as well as his innovative designs and fabrications of our in-situ SEM jigs, microtensile polishing devices, microtensile specimen holders, etc. None of my in-situ SEM testing experiments would have been possible without his machining expertise.

During the last 6 months of my Ph.D. journey, I was given the opportunity to work as a Post-Doctoral Fellow in Dr. Nabil Bassim's group in collaboration with the CCEM under Dr. Brian Langelier and Fibics Inc, under Mike Phaneuf. I thank them for hiring me and for providing me with the opportunity to learn more about the advantages of advanced microscopy. During this time, I worked a lot with Mehdi Mosayebi, and Travis Casagrande who I thank in providing me with additional microscopy training, and technical support.

Most importantly, I give a never-ending thank you to my parents, Giuseppe and Corra and brother, Paolo Pelligra for always encouraging me during my academic pursuits. I wouldn't have completed this thesis without their encouragement, and I dedicate this thesis to them.

It has been an honour to go from an undergraduate student to a Post-Doctoral Fellow at McMaster's MSE department. This department has not only always fostered my learning but also my growth as an individual.

Table of Contents

List of Figures

List of Tables

List of Abbreviations and Symbols

$\mathbf{A_0}$	Initial Cross Sectional Area
$\mathbf{A_f}$	Minimum Area at Fracture
α_{RT}	Rice and Tracey Growth Rate Parameter
β	Shape factor of the Plastic Zone
$\boldsymbol{\varepsilon_1}$	Major Strain
$\boldsymbol{\varepsilon_2}$	Minor Strain
$\boldsymbol{\varepsilon_3}$	Thickness Strain
$\boldsymbol{\varepsilon'}$	Strain Gradient
$\boldsymbol{\varepsilon_{Avg}}$	Average von Mises Strain
$\boldsymbol{\varepsilon_{eff}}$	Effective Strain
$\boldsymbol{\varepsilon_f}$	True Strain at Fracture
$\boldsymbol{\varepsilon_{phase}}$	Average von Mises Phase Strain
$\boldsymbol{\varepsilon_{local}}$	Local von Mises Strain
$\boldsymbol{\varepsilon_u}$	True Uniform Strain
$\boldsymbol{\varepsilon_{loc}^{True}}$	Local True Strain
$\boldsymbol{\varepsilon'_M}$	Median Strain Gradient
ε_p	Plastic strain
$\mathbf{F_{Avg}}$	Average Force
$\mathbf{F_e}$	Epitaxial Ferrite
$\mathbf{F_{GS}}$	Ferrite Grain Size
$\mathbf{F_i}$	Intercritical Ferrite
$f_{martensite}$	Fraction of Martensite Transformed
$\mathbf{F_{Max}}$	Maximal/Buckling Force
$\mathbf{K_{1C}}$	Fracture Toughness
$\mathbf{l_0}$	Initial ligament length
$\mathbf{M_s}$	Martensite Start Temperature
$\mathbf{M_f}$	Martensite Finish Temperature
nXCT	X-ray nano-Tomography
$\boldsymbol{\sigma_m}$	Mean Hydrostatic Stress
$\boldsymbol{\sigma_{VM}}$	von Mises Equivalent Stress
$^{\sigma_m}/_{\sigma_{VM}}$	Stress Triaxiality
$\Delta G_{\gamma\rightarrow\alpha'}$	Free Energy of the austenite-to-martensite transformation
ΔRAVF	Change in local retained austenite fraction
$\boldsymbol{\sigma}$	Standard Deviation
$\boldsymbol{\mu}$	Median
µDIC	Micro-Digital Image Correlation
µXCT	X-ray Computed Microtomography
$\boldsymbol{\rho}$	Radius of curvature
$\mathbf{t_0}$	Initial thickness
$\mathbf{T_p}$	Partitioning Temperature
$\mathbf{t_p}$	Partitioning time
$\mathbf{T_q}$	Quench Temperature

γ	Austenite
γ-M	Initial Austenite-Transformed Martensite
W_e	Essential Work to Fracture
W_f	Total Work of Fracture
W_p	Non-essential (plastic) work
V_m	Martensite Volume fraction
w_f	specific essential work of fracture
w_p	specific plastic work
V(C,N)	Vanadium Carbonitrides
V_m	Martensite Volume fraction

1G,2G,3G	First, Second, Third Generation
2D, 3D	Two-,Three-dimensional

AFM	Atomic Force Microscopy
AHSS	Advanced High Strength Steel
APS	Argonne Photon Source
APT	Atom Probe Tomography
AUS	Austenitic Stainless Steel
Avg	Average

BCC	Body-Centred-Cubic
BCT	Body-Centered-Tetragonal
BE	Backscatter Electron
BEV	Battery Electric Vehicle
BF	Bright Field
BIW	Body-In-White

CAL	Continuous Annealing Line
CAMC	Centre for Automotive Materials and Corrosion
CCD	Charged-Coupled Device
CCEM	Canadian Centre for Electron Microscopy
CDF	Cumulative Distribution Function
CFB	Carbide-Free Bainitic
CGL	Continuous Galvanizing Line
CI	Confidence Interval
Co-XRD	Cobalt-sourced X-ray Diffraction
CP	Complex Phase
CPE	Constrained Paraequilibrium
CR	Cold-rolled
CT	Compact Tension
CVN	Charpy V-notch

DENT	Double-edge-notched-tensile
DF	Dark Field
DFT	Density Functional Theory
DIC	Digital Image Correlation
DoE	Department of Energy
DP	Dual Phase
e-beam	Electron beam
EBSD	Electron Backscatter Diffraction
EDS	Energy X-ray Dispersive Spectroscopy
ET	Everhart-Thornley
EWF	Essential Work to Fracture
F	Ferrite
FCC	Face-Centred-Cubic
FEM	Finite Element Model
FEG	Field Emission Gun
FESEM	Field Emission Scanning Electron Microscope
FG	Fine-Grained
F.I.	Formability Index
FIB	Focused Ion Beam
FLD	Forming Limit Diagram
F/M	Ferrite/Martensite Interface
FOV	Field of View
F-TM	Ferrite-Tempered Martensite
Ga	Gallium
GAP	Galvanizing Association Partnership
GDEOS	Glow-discharge Optical Emission Spectroscopy
GM	General Motors
GNDs	Geometrically Necessary Dislocations
HAADF	High-angle Annual Dark Field
HAZ	Heat-Affected Zone
HCP	Hexagonal-Close-Packed
HER	Hole Expansion Ratio
HET	Hole Expansion Test
HE-XRD	High Energy X-Ray Diffraction
HR	Hot-rolled
HSLA	High-Strength-Low Alloy
HSS	High Strength Steel
IA	Intercritical Annealing

IBT	Isothermal Bainitic Treatment
IC	Interfacial Cracking
ICCT	International Council on Clean Transportation
ICEV	Internal Combustion Engine Vehicle
ICP-OES	Plasma Optical Emission Spectroscopy
IF	Interstitial Free
IG	Intergranular Cracking
IFPZ	Inner Fracture Process Zone
IZA	International Zinc Association
M	Martensite
MAX	McMaster Analytical X-ray facility
MC	Martensite Cracking
med-Mn	Medium-Mn
MGS	McMaster Galvanizing Simulator
MS	Martensitic Steel
NSERC	Natural Sciences and Engineering Research Council of Canada
ND	Normal Direction
nXCT	X-ray nano-tomography
OPDZ	Outer Plastic Deformation Zone
PDF	Probability Distribution Function
PHS	Press-Hardened Steel
PMMA	Polymethyl-methacrylate
PSR	Phase Strength Ratio
PUE	Post-Uniform Elongation
PVD	Physical Vapour Deposition
Pxl	Pixel
Q&P	Quench and Partition
Q&T	Quench and Temper
RA	Retained Austenite
RA%	Reduction in Area
RD	Rolling Direction
RT	Rice and Tracey
RVE	Representative Volume Element
SAED	Selected Area Electron Diffraction
SE	Secondary Electron
SEM	Scanning Electron Microscope
SENT	Single-edge-notched-tensile

SFE	Stacking Fault Energy
SGP	Strain Gradient Plasticity
SPD	Severe Plastic Deformation
SPIR	Strain Partitioning Intensity Ratio
SSD	Statistically Stored Dislocation
SS	Stainless Steel
STEM	Scanning Transmission Electron Microscopy
TBF	Transformation Induced Plasticity-Bainitic-Ferritic
TE	Total Elongation
TEM	Transmission Electron Microscope
TG	Transgranular
TM	Tempered Martensite
TRIP	Transformation-Induced Plasticity
TWIP	Twinning-Induced Plasticity
U'	External Force
UE	Uniform Elongation
UFG	Ultra-fine Grain
U.S.	United States
UTS	Ultimate Tensile Strength
V-added	Vanadium-added
V-free	Vanadium-free
wEDM	Wire Electrical Discharge Machining
XCT	X-ray Computed Tomography
X-FEG	X-Field Emission Gun
XRD	X-ray Diffraction
YS	Yield Strength

Declaration of Academic Achievement

This thesis was prepared in partial fulfillment of the Doctor of Philosophy degree at McMaster University. The research was performed from September 2017 to April 2024 and examines the damage tolerance and Transformation Induced Plasticity (TRIP) kinetics of a series of prototype third generation (3G) advanced high strength steels (AHSSs). These steels are: an ultrafine grain (UFG) vanadium-microalloyed Dual Phase (DP) steel with a 1300 MPa strength, (DP1300), an ultrahigh strength austenitic-martensitic Quench & Partition (Q&P) steel with a 1500 MPa strength, (QP1500), and a prototype Medium-Mn (med-Mn) steel with continuous galvanizing line (CGL) industrial compatibility in which the strengths/elongations are tailorable based on intercritical annealing (IA) parameters. Investigations on these select ultrahigh strength steels and specifically, TRIP kinetics, was first motivated by the initial work of Samei et al. (2020) as reproduced in Chapter 3, in which X-ray microtomography (µXCT) was used to assess the evolution of damage during deformation of a range of AHSSs, from first generation (1G) to 3G steels. The author of this thesis is a co-author of this publication.

Overall, the damage tolerance of these steels, UFG DP1300, QP1500 and med-Mn, was examined in two-dimensions (2D) using in-situ Scanning Electron Microscope (SEM) tensile testing coupled with micro-digital image correlation (µDIC) and in three-dimensions (3D) using µXCT. TRIP kinetics of the appropriate steels was determined using synchrotron-sourced High Energy X-ray Diffraction (HE-XRD) with specimens subjected to uniaxial tension and again coupled with digital image correlation (DIC). The author performed the experiments, analyzed the results, and prepared all manuscripts under the supervision of Professor David S. Wilkinson.

The publication by Samei et al. (2020) motivating this detailed work on UFG DP1300, QP1500 and then this med-Mn steel is included in this thesis. Moreover, the major findings from this thesis, has been published in two peer-review journal publications specifically on the UFG DP1300 steel, in Chapter 4, and QP1500 steel, in Chapter 5. Two draft manuscripts have been prepared, which will be submitted to peer-review journals on this CGL compatible med-Mn steel.

It should be noted that Elsevier Ltd., the publisher of Materials Letters, the International Journal of Plasticity, and Materials Science and Engineering: A journals permits authors to reuse their published articles in their theses/dissertations. The publications featured in this thesis are as follows:

1. Samei, J., Pelligra, C., Amirmaleki, M., Wilkinson, D.S., 2020. Microstructural design for damage tolerance in high strength steels. Mater. Lett. 269. https://doi.org/10.1016/j.matlet.2020.127664

2. Pelligra, C., Samei, J., Kang, J., Wilkinson, D.S., 2022. The effect of vanadium on microstrain partitioning and localized damage during deformation of unnotched and notched DP1300 steels. Int. J. Plast. 158. https://doi.org/10.1016/j.ijplas.2022.103435

3. Pelligra, C., Samei, J., Shalchi Amirkhiz, B., Hector, L. G., & Wilkinson, D. S. (2024). Microstrain partitioning, transformation induced plasticity, and the evolution of damage during deformation of an austenitic-martensitic 1.5 GPa quench and partition steel. Materials Science and Engineering: A, 146181. https://doi.org/10.1016/j.msea.2024.146181

4. Pelligra, C., Samei, J., Amirkhiz, Zafer, N., Kang, J., Wilkinson, D.S., 2023. Microstrain Partitioning, Transformation Induced Plasticity, and Damage Evolution of a Third Generation Medium Mn Advanced High Strength Steel. In Draft form.

5. Pelligra, C., Wilkinson, D.S., 2023. Effect of Triaxiality on Microstrain Partitioning, Transformation Induced Plasticity, and the Evolution of Damage in a Third Generation Medium Mn Advanced High Strength Steel. In Draft form.

During this PhD, the author was able to collaborate on other publications on different materials. These publications (not included in this thesis) include:

6. Barella, S., Gruttadauria, A., Menezes, J.T.O., Castrodeza, E.M., Quaini, S.E., Pelligra, C., McNally, E.A., 2023. The Reliability of Single-Step and Double-Step Quench and Partitioning Heat Treatments on an AISI 420A Low Carbon Martensitic Stainless Steel. Metall. Mater. Trans. A. https://doi.org/10.1007/s11661-023-07145-2

7. Samei, J., Asgari, H., Pelligra, C., Sanjari, M., Salavati, S., Shahriari, A., Amirmaleki, M., Jahanbakht, M., Hadadzadeh, A., Amirkhiz, B. S., & Mohammadi, M. (2021). A hybrid additively manufactured martensitic-maraging stainless steel with superior strength and corrosion resistance for plastic injection molding dies. *Additive Manufacturing*, *45*. https://doi.org/10.1016/j.addma.2021.102068

1 Introduction and Overall Context

The oil crisis in 1975, although it lasted a short time, dramatically shifted the focus of automotive manufacturing to reducing vehicle weight for improved fuel economy and reduced green house gas emissions (Fonstein, 2015). As of May 2020, the km/litre targets shared by the International Council on Clean Transportation (ICCT) for passenger cars and light trucks in the US is to achieve ~15-21km/litre by 2026, and by the European Union is ~23km-35km/litre by 2030 ("International Council for Clean Transportation. Global comparison of passenger car and light commercial vehicle fuel economy/ghg emissions standards.," 2017). Currently, vehicles such as: the 2016 Chevrolet Malibu, and 2016 Honda Pilot are 136 kg less than their previous models (Hall, 2015).

Historically, the first member, and most manufactured Advanced High Strength Steels (AHSSs) to date are Dual Phase (DP) steels, with a ferritic matrix and dispersion of martensitic islands (Magee and Davies, 1971; Matlock and Speer, 2009; Tasan et al., 2015). At the time, these DP steels, which showed high strength and variable ductility, were commercialized to compete with full aluminum Body-in-White (BIW) car frames (Bouaziz et al., 2013; Fonstein, 2015). Since then, the increased usage of AHSSs in BIWs has been for crash critical components, specifically side impacts, roof crushes, and frontal impacts (Findley et al., n.d.). Up to now, there's been an emphasized use of DP steels in front-end applications and exterior panels (De Cooman et al., 2012).

Eventually, conventional thermal processing used in first generation (1G) AHSSs was tailored to further promote dislocation strengthening using the austenite (ɣ)-to-martensite transformation at room temperature (Pereloma and Edmonds, 2012) adding another contribution to strain hardening as opposed to only the interaction between hard and soft phases as is in DP steels (Jacques et al., 2007). A two-stage heat treatment was developed to create Transformation Induced Plasticity (TRIP) steels which entailed partially stabilizing ɣ to drive a strong phase transformation upon room temperature deformation (Jacques et al., 2001). TRIP steels, pioneered by Nippon steel (Fonstein, 2015), were designed to be used at servicing temperatures between the martensite start and martensite finish, M_s and M_f respectively, in which the ɣ is thermally stable, but unstable with respect to strain. This fact is even more pronounced when strain is being applied at a temperature very close to the M_s (Parker and Zackay, 1973).

The so-called banana diagram globally used in industry, as shown in Figure 1.1, characterizes AHSSs by its product of ultimate tensile strength (UTS), and total elongation (TE). 1G AHSSs achieved UTS x TE ≤ 20,000 MPa% (De Moor et al., 2010; Matlock and Speer, 2009). TRIP steels occupy the top of the 1G AHSSs band as a result of their enhanced ɣ strain hardening capacity at high strains (Matlock and Speer, 2009). Other AHSSs in the 1G family are complex phase (CP) steels, martensitic steels (MS), and Press-Hardened Steels (PHS).

With the retention of ɣ at ambient temperatures to enhance ductility, TRIP steels showed improved energy absorption capability (Fonstein, 2015). The true advantage with the use of TRIP steels and its high energy absorption capability is in mitigating passenger injury during side impact collisions or in the case of a vehicle roll over (De Cooman et al., 2012; Fonstein, 2015). Although not known at the time, the true ductility of these 1G TRIP steels is limited by the fractional cementite precipitation during the bainite transformation (Pereloma and Edmonds, 2012).

Eventually, a remarkable strength-to-ductility ratio was achieved in the development of second generation (2G) AHSSs by using Twinning Induced Plasticity (TWIP) and strain-induced transformation of Hexagonal-Close-Packed (HCP)-martensite effects. These steels opened the possibility of extending the usage of AHSSs to a wider range of automotive applications in which their mechanical target envelope was 50,000 ≤ UTS×TE ≤ 80,000 MPa%, as shown in Figure 1.1. Examples of steels that form part of the 2G AHSS family are Mn-rich TWIP steels, and AUSs. Nevertheless, challenges in manufacturing these low carbon sheet steels, the required heavy alloying, poor weldability, etc., limited its progress to commercialization (Fonstein, 2015).

Although production of 2G AHSSs is difficult and limited, the metallurgical lessons learned during their development have been invaluable to the advancement of current third generation (3G) AHSSs. Particularly, the behavior of retained ɣ and its tendency to TRIP, TWIP or remain stable during deformation has been crucial in manipulating the strength-to-ductility ratio of 3G AHSSs. The recent pressures of increasing oil costs, and governmental restrictions on greenhouse gas emission levels is ultimately driving the production of steel that is high strength, reasonably ductile, lightweight, and lean alloyed. To remain competitive with magnesium and aluminum alloys, the specific strength (strength-density ratio) of steel needs to be increased (McGarth and Van Aken, 2012). The major advantage of steels is the high elastic stiffness and strength, allowing thin steels to be produced, making mass reduction with steels efficient in comparison to lighter materials such as magnesium, aluminum or polymer composites in which a large thickness is needed to compensate for their low elastic stiffnesses (Matlock and Speer, 2006; McGarth and Van Aken, 2012). It is predicted that there's a potential of 30-40% in weight reduction with the use of 3G AHSSs which range from 1300-1500MPa in strength (De Cooman et al., 2012). Additional members of the 3G AHSSs family include TRIP-Bainitic-Ferritic (TBF) steels, Q&P steels, med-Mn steels (Liu et al., 2018), and nanoprecipitation steels (Raabe et al., 2009). The 3G mechanical specific targets of 1200MPa x 30%, and 1500MPa x 25% is set by the United States Department of Energy (U.S. DoE).(Matlock and Speer, 2009)A more modest 3G mechanical property target is UTS x TE ≥24000MPa% as suggested by Matlock et al. (2012) and suits the AutoSteel Partnership specific target of 1500MPa x 20%. The ultrafine grain (UFG) DP1300 steel, ultrahigh strength Quench & Partition (Q&P) steel, QP1500, and Medium-Mn (med-Mn) steel described in this thesis, Chapters 3-7, is plotted in Figure 1.1.

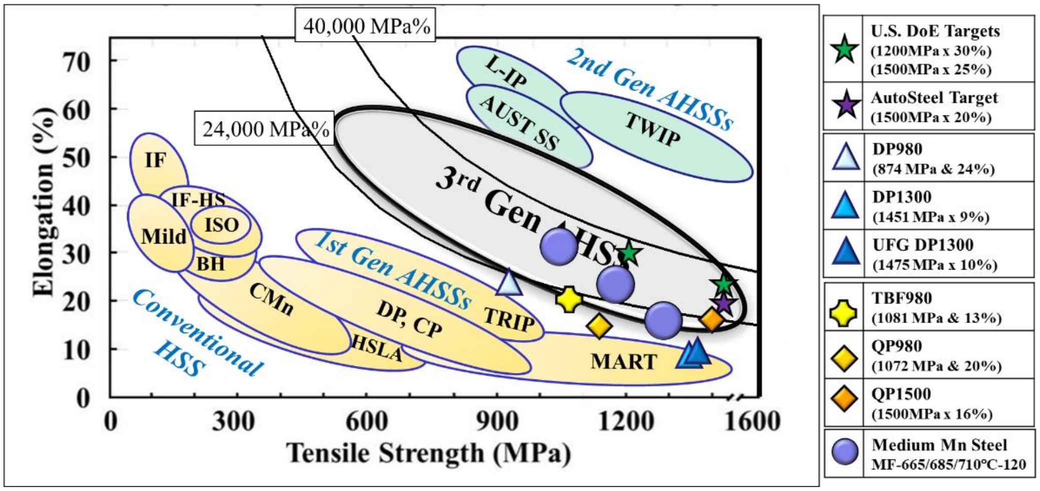

Figure 1.1 shows the iconic "banana diagram" illustrating the different steel grades as a function of strength and elongation, courtesy of World AutoSteel. In general, there is a trade-off between strength and tensile elongation. However, advanced processing of materials can be produced to achieve higher products of UTS x TE. Although these AHSSs are now being made to achieve 3G U.S. DoE targets, they still show poor bending performance (Larour et al., 2017).

Furthermore, what is currently starting to be more critically acknowledged by automakers is that the banana diagram offers limited information on the true capability of these steels to be formed into complex automotive components. Designating ductility by means of tensile elongation is only applicable to stretching operations involved in automotive manufacturing. However, many forming operations are not dominated by stretching, and rather by more complex strain states, including bending, stamping, drawing, etc. (Jacques et al., 2007; Lian et al., 2021). For example, in a car crash, B-pillars could be subjected to both crushing and bending-type loadings (Findley et al., n.d.). In reference to TRIP steels, the mechanical stability of the ɣ is affected by different strain states and can overall cause changes in the vehicle's crashworthiness (Lian et al., 2021). As well, the UTS x TE product obtainable from the banana diagram provides a *crude* approximation of toughness in which the actual energy required to produce fracture (i.e.,energy absorbed during post-uniform elongation) is not captured (Frómeta et al., 2019; Matlock and Speer, 2009). A common concern with increasing the strength of thin 3G AHSSs is in the loss of actual toughness, and adequate techniques of measuring toughness (Findley et al., n.d.). It is important to note that the steels plotted in Figure 1.1 are from uniaxial tensile tested with an ASTM E8/E8M – 21 (2021) sub-size specimen design, this is another parameter which effects elongation (%) (De Moor et al., 2010; Park et al., 2019), and therefore its placement on the graph in Figure 1.1. Datsko and Yang, (1960) were the first to recognize the reduction in area (RA%), or true strain at fracture (ε_f) obtained simply from a uniaxial tensile test, offers an alternative measure of ductility which can be related to various forming operations, such as bending and the hole expansion ratio (HER).

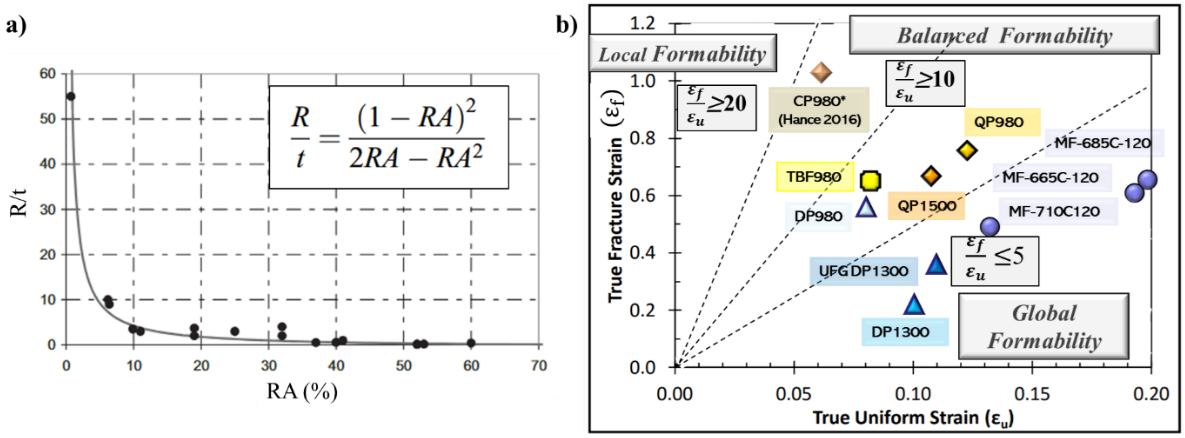

Figure 1.2: shows the relationship of bendability (R/t) to RA%, where R is the minimum bending radius and RA% is the reduction in area at fracture (Bouaziz et al., 2013; Datsko and Yang, 1960). The trendline in this diagram is strongly consistent with the data obtained from literature on a wide range of materials, including Mg, Al, brass, titanium, steel, cast irons and plastic bar stock (Datsko and Yang, 1960). This work has been critical in predicting the hemming ability estimation of aluminum (Iacono et al., 2010; Lin et al., 2009). Figure 1.2 (a) was adapted from Datsko and Yang (1960) as well as Bouaziz et al. (2013). Figure 1.2 (b) was adapted from Hance (2016).

As documented by Hance (2018, 2016), material formability can be classified into two categories: Global and Local formability. The global forming potential of a material is understood as its resistance to necking, important for stretching or deep drawing-type operations and can be described by various tensile properties, including the strain hardening exponent, the true uniform strain, and by Forming Limit Curves (FLCs) (Frómeta et al., 2021). However, the local forming potential of a material is understood by its resistance to fracture, also referred to as damage tolerance. This is important for understanding a steel's stretch flangeability, edge cracking sensitivity (Kardes Sever, 2022; Samei et al., 2019), and its crashworthiness. Most challenges associated with the application of ultrahigh strength AHSSs are related to fracture, in which these steels show limited cracking resistance, limited hole expandability, etc. (Frómeta et al., 2017; Mori et al., 2010). Thus far, there is no apparent relationship between these material's resistance to fracture and tensile strength/ductility.

Despite the advances that have been made to manufacture lean-alloyed AHSSs with the use of TRIP/TWIP deformation mechanisms, research is still being invested in improving the local formability of DP steels due to its robust thermo-mechanical processing (Pelligra et al., 2022; Scott et al., 2018, 2017; Tang et al., 2021; Tasan et al., 2015). On the other hand, research is also being invested in 3G TRIP-assisted steels, such as ultrahigh strength Q&P, and med-Mn steels. For instance, a lot of recent work to date has been done to modify steel manufacturing processes, such as developing 1-step vs. 2-step quench and partitioning routes (Barella et al., 2023; Kong et al., 2017; Speer et al., 2005) to promote manufacturing energy efficiency, and IA (Bhadhon, 2022; Pallisco and McDermid, 2020; Patel, 2019). Particular focus has been put on processing 3G steels such that they compatible with industry standard CGLs and continuous annealing lines (CALs) (Arlazarov et al., 2016; Bhadhon, 2022; Pallisco, 2021; Patel, 2019; Williams et al., 2022). However, the mechanisms which prompt fracture in TRIP-assisted steels, still requires critical investigation as information on the relationship between TRIP kinetics and damage has not yet been experimentally ventured in detail (Jacques et al., 2001; Samei et al., 2020).

Specifically, there's a ≈3% volume change associated with the ɣ-to-martensite transformation (Parker and Zackay, 1973) which is thought to hinder micro-void nucleation (Jacques et al., 2001; Samei et al., 2020). This is in tandem to the volume expansion associated with the transformation of monoclinic to a tetragonal phase in yttria stabilized (Withers, 2015).

Furthermore, microscopic defects/cracks cause a degradation in material performance during forming or can, when applied to an engineering structure, reduce its overall lifespan. The main issue with engineering applications is creating structure factors against failure which is realistic and reflective of the material's micro-damage evolution properties (Brünig et al., 2008). It is fundamentally known amongst material scientists, that the nucleation and coalescence of voids in ductile materials are the precursors to meso-sized cracks which eventually lead to fracture (Brünig et al., 2008). With this being said, the use of in-situ micromechanical studies, whether in two-dimensional (2D) using SEM-based imaging techniques or in three-dimensional (3D) using tomography, is done to understand the evolution of microstrain partitioning and damage for the development of such damage models. It is critical to note however, that there is an arising complexity tied to performing, for instance, in-situ SEM tensile testing coupled with DIC to map microstrain partitioning, as a result of the complicated microstructures in 3G TRIP-assisted steels. As a result, a lot of effort to date has been put towards developing micro-speckle patterning techniques which are compatible with Electron Backscatter Diffraction (EBSD) scanning (Dutta et al., 2019, 2018; Hoefnagels et al., 2019; Wang et al., 2017; Zhang et al., 2020).

Another issue addressed in this thesis is that most damage models are experimentally validated using uniaxial tensile testing, and hence, limited to predicting material response at different stress triaxialities (i.e. a material's performance when subjected to a concentrated load, such as in bending) (Brünig et al., 2008; Polatidis et al., 2020). This is more important as material ductility is reduced with increasing triaxiality of the stress-state (Brünig et al., 2008). The use of notched tensile specimens, with differing notched radii, is used most conveniently to describe material ductility under different stress triaxialities within the tension regime (Bao and Wierzbicki, 2004; Jacques et al., 2001).

That being said, most TRIP kinetic data available at different stress-states in the literature concerns austenitic stainless steels (AUSs), which generally possess a much narrower stacking fault energy (SFE) range in comparison to low-alloyed TRIP-assisted AHSSs. Limited work to date has been devoted to investigating the influence stress-state has on TRIP kinetics in 3G AHSSs (Park et al., 2019; Polatidis et al., 2020; Wu et al., 2018). Likewise, in general, most studies reporting damage evolution in 3D have been made on AUSs, TWIP steels, or low strength AHSSs (Fabrègue et al., 2015, 2013) and rare documentations are available on the influence that stress-state has on damage evolution in 3G AHSSs. With the use of µXCT, Lorthios et al. (2010) does report however the promotion of shear-type fracture and suppression of void growth with 'butterfly' style specimens on steels which exhibit significant amounts of TWIP that any deformation experienced by voids was dependent on its surrounding microstructure. To reiterate, the complex interplay that the austenite-to-martensite transformation and its associated $\approx$3% volume expansion has on mitigating void nucleation has been speculated by several (Jacques et al., 2001; Parker and Zackay, 1973; Samei et al., 2020), but only very recently ventured by few (Schoell et al., 2022; Toda et al., 2022). Schoell et al. (2022) and Toda et al. (2022) use sophisticated synchrotron-sourced tomography techniques to capture damage evolution and TRIP in stainless steels (SSs) and 1G TRIP steels. Yet, this thesis, specifically, Chapters 6 and 7 describe the first microtomographic investigations conducted on a CGL-compatible 3G med-Mn steels with promising commercialization potential.

1.1 Research Objectives

Considerable research has been invested in developing complex processing routes which can produce thin Advanced High Strength Steels (AHSSs) that meet the 3G U.S. Department of Energy (DoE) mechanical targets. Common techniques used amongst the automakers to achieve these targets are through the micro-addition of key elements, and through the metastabilization of austenite (ɣ) at room temperature. Although commercialized versions of micro-alloyed and TRIP-assisted steels do exist, little is known about the microstructural ways in which grain refinement and Transformation Induced Plasticity (TRIP) kinetics can delay damage evolution. The ability for the volume expansion associated with the ɣ-to-martensite transformation to suppress damage has been speculated by several (Jacques et al., 2001; Parker and Zackay, 1973; Samei et al., 2020), but not yet thoroughly investigated. Nonetheless, early on in this thesis work, journal article reproduced in Chapter 3, a comparative study conducted on the damage tolerance of first generation (1G) and third generation (3G) AHSSs showed that the rate of damage accumulation can be effectively reduced with significant microalloying, and with TRIP. This initial study triggered the further investigations carried out in this P.h.D thesis to understand how microstrain partitioning amongst phases, the evolution of microstructure with strain, and the accumulation of damage leads to fracture in 3G AHSSs. Of particular interest has been the role that TRIP plays in damage development of these steels, which is not only influenced by steel microstructure, but also by external factors, including the type of stress being applied.

With this being said, the main objective of this Ph.D. thesis has been to determine the influence that prominent 3G steel microstructural features, including grain refinement and TRIP kinetics, as well as modifications in stress-state has on the microstrain partitioning behavior leading to damage in AHSSs. An ultrafine grain Dual Phase (DP) steel, ultrahigh strength Quench & Partition (Q&P) steel, and prototype continuous galvanizing line (CGL)-compatible med-Mn steel was used for this investigation. The main objective of this Ph.D. thesis has been divided into three subobjectives as follows:

1) Determine the microstrain partitioning and strain gradient behavior with the use of micro-Digital Image Correlation (μDIC) post-processing techniques in 3G steels without TRIP (UFG DP1300) and with TRIP (QP1500).
2) Determine the intercritical annealing (IA) parameters that suppresses damage and maximizes ductility through the use of an optimal TRIP rate.
3) Determine the influence a high stress-triaxiality has on the microstrain partitioning, TRIP kinetics, and damage evolution of a 3G steel

A prototype med-Mn steel with a martensitic starting microstructure was predominantly used to achieve subobjectives 2) and 3). Subobjective 2) encompassed systematically modifying TRIP kinetics through minor adjustments in IA temperature and, hence, without imposing drastic changes to the steel's physical microstructure. This enabled the selection of an optimal IA condition which showed prolonged TRIP kinetics, and the most delay in damage evolution. Subobjective 3) was then carried out using this med-Mn steel at its optimal IA condition.

1.2 Thesis Layout

This sandwich thesis is outlined as follows:

- Chapter 2: Literature Review - This chapter is an overview of advances made in the industry to create 3G steels and attempts that have been made to evaluate their damage tolerance/local forming potentials. As well this chapter reinforces the fundamentals of TRIP and its application in 3G steels (including Q&P, and med-Mn steels). Some emphasis in this chapter has been devoted to documenting the developments that have been made to characterize multiphase AHSSs using µDIC combined with Electron Backscatter Diffraction (EBSD), and X-ray microtomography (µXCT). Lastly, the impact that variation in stress-state has on TRIP behavior and damage nucleation in AHSSs is also detailed.
- Chapter 3: Comparative study on the Damage tolerance of 1G and 3G AHSSs – This chapter is a reproduction of the journal article entitled "Microstructural design for damage tolerance in high strength steels" published in Materials Letters in 2020. The author of this thesis is a co-author of the following publication in which she contributed to the conceptualization and investigation of damage in these AHSSs. This is a paper which shows that grain refinement achieved through microalloying, and TRIP reduced the rate of damage evolution as a function of uniaxial strain in 1G and 3G AHSSs. Furthermore, this paper was the initial motivation for further work to be done on understanding the impact TRIP, and its associated volume expansion, has on damage evolution.
- Chapter 4: This chapter is a reproduction of the journal article entitled "The effect of vanadium on microstrain partitioning and localized damage during deformation of unnotched and notched DP1300 steels" published in the International Journal of Plasticity in 2022. This paper carefully analyzes the microstrain partitioning amongst phases which eventually led to void nucleation or microcracking. A novel 'local strain gradient'-µDIC-based technique was introduced in this paper and was used to estimate the pile-up of Geometrically Necessary Dislocations (GNDs) in unnotched and notched ultrahigh strength 3G DP steel specimens.
- Chapter 5: This chapter is a reproduction of the manuscript entitled "Microstrain Partitioning, Transformation Induced Plasticity, and Evolution of Damage during Deformation of an Austenitic-Martensitic 1.5GPa Quench & Partition Steel" accepted in the Materials Science and

Engineering: A journal. This paper does a thorough microscopic characterization of an ultrahigh strength Q&P steel in order to explain its high ε_f and superior toughness. The advantage of TRIP-assistance in 3G microstructures is deduced by conducting a comparison of this Q&P steel to the UFG DP steel featured in Chapter 5. Both steels show similar strengths and grain sizes. The μDIC-based computation technique introduced in Chapter 4 is used to show the evolution of GNDs increasing more slowly in the Q&P steel than that of the DP steel.

- Chapter 6: This chapter is a reproduction of the draft manuscript entitled "Microstrain Partitioning, Transformation Induced Plasticity, and Damage Evolution of a Third Generation Medium Mn Advanced High Strength Steel." This paper features an experimental, CGL-compatible med-Mn steel (0.15C-5.8Mn-1.8Al-0.71Si) with a martensitic starting microstructure. In this paper, this med-Mn steel intercritically annealed at 685°C for 120s reached 3G mechanical targets, and also showed a high ε_f. An abundance of voids nucleate during deformation at this 685°C IA condition but that their growth is suppressed by prolonged TRIP over a large strain range. A similar μDIC-based computation comparative studies detailed in Chapter 4 and 5, was also performed in this paper.
- Chapter 7: This chapter is a reproduction of the draft manuscript entitled "Effect of Triaxiality on Microstrain partitioning, Transformation Induced Plasticity, and the Evolution of Damage in a Third Generation Medium Mn Advanced High Strength Steel." This paper uses the experimental, CGL-compatible med-Mn steel from Chapter 6 subjected to its optimal IA condition at 685°C for 120s. In this paper, different notch geometries was introduced within the gauge section of tensile specimens to investigate the effect that changes in stress-state has on microstrain partitioning, TRIP kinetics and damage development.
- Chapter 8: Global Discussion
- Chapter 9: Concluding Statements

2 Literature Review

2.1 Approaches Made to Develop 3G AHSSs

2.1.1 Advances made to the 'Banana Diagram'

In the ever-tightening emission regulations to achieve carbon neutrality, steels continue to be a critical material of choice for its high elastic stiffness and strength without the need for thick sheets to be used. In the application of Advanced High Strength Steels (AHSSs) to meet these lightweighting/strength standards, the so called 'banana diagram' is used conventionally by the automotive industry. The banana diagram compares High Strength Steels (HSSs) and AHSSs based on their TE and UTS. It is important to note, however, that the TE in particular can vary substantially based on the specimen design, strain path, stress-state, etc… AHSSs on this diagram do show a greater potential of absorbing the kinetic energy (higher UTS x TE values) in comparison to steels of prior generations (Bouaziz et al., 2013), such as single-phase High Strength Low Alloy (HSLA) steels (Frómeta et al., 2021; Kardes Sever, 2022).

$$\mathrm{F_{avg}} = \mathrm{K}\sqrt{\mathrm{UTS}}\mathrm{t}^{2} \qquad \text{Equation 2.1}$$

$$\mathrm{F_{max}} = \mathrm{K}\sqrt{\mathrm{YS}}\mathrm{t}^{0.75} \qquad \text{Equation 2.2}$$

The energy absorbed during a vehicle crash is assessed by the average force (F_{avg}) experienced by the vehicle's 'crash box' during the crash, strongly dependent on the material's UTS, and the maximal force/buckling force (F_{max}) experienced by the vehicle's B-pillar, strongly dependent on the material's yield strength (YS) (Bouaziz et al., 2013). Therefore, in order to maintain crashworthiness with the use of thin steels, high F_{avg} and F_{max}, as well as the YS and UTS needs to be increased. As can be shown in Equation 2.1 versus Equation 2.2, the thickness has stronger dependence on the F_{avg}, energy absorption potential of the 'crash' box than the F_{max}, energy adsorption by the B-pillar.

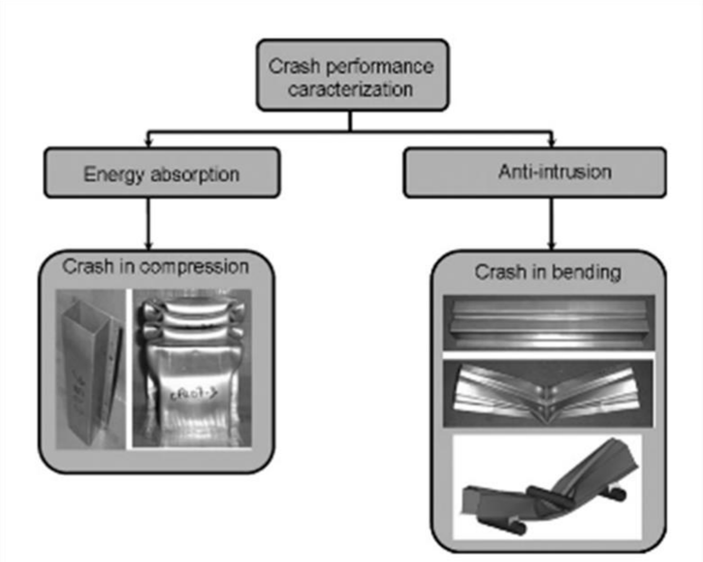

Figure 2.1: Lab-scale Crash Performance characterization. Adapted from Bouaziz et al. (2013).

As well, the automotive industry uses Forming Limit Diagrams (FLD) to understand a steel's behavior while being formed into complex components required in automotive structures (i.e. the amount of plastic strain a material can undergo before localized necking) (Bouaziz et al., 2013). FLDs are mainly created on the basis of the strain hardening potential of the steel (Bouaziz et al., 2013). The post-uniform elongations as well as the reduction in area (RA%) characterizing the damage tolerance/local forming potential of AHSSs is not captured on neither the banana diagram nor in FLDs. It is important to consider as well that AHSSs which feature considerable amount of TWIP as its being deformed, in general, produce slant-shear type fracture which cannot adequately described by the FLDs (Lorthios et al., 2010). Bending, on the other hand, is dependent not only on the material's strain hardening behavior but also on its reduction in area at fracture (Bouaziz et al., 2013), its resistance to crack formation (Suppan et al., 2018) and has been used previously to assess shear-slant-type fracture in AHSSs (Hudgins and Matlock, 2016). More than this however, there is a significant amount of stress triaxiality that is experienced by an automotive component when it's impacted, depending on its position on the vehicle and the equivalent plastic strain it experiences during the crash (Findley et al., n.d.). Multiphase microstructures and TRIP-assistance in AHSSs has been critical in achieving targeted U.S. DoE standards. Figure 2.2 shows that AHSSs with a greater retained austenite content (i.e. % in this instance) increases the UTSxTE. Frómeta et al. (2021) found that a TRIP steel with an UTS of

780MPa, TRIP780, and 1180MPa strengthened-3G steels, specifically, a DP and TBF steel, with retained austenite contents of 15-16% showed the highest UTSxTE, whereas the lowest UTSxTE was associated with a DP steel, with an UTS of 780MPa, DP780 steel which exhibited the lowest retained austenite content. However, it should be clearly seen in Figure 2.2 that there is little to no dependence of the retained austenite content on the ε_f and essential work to fracture (W_e) (Frómeta et al., 2021).

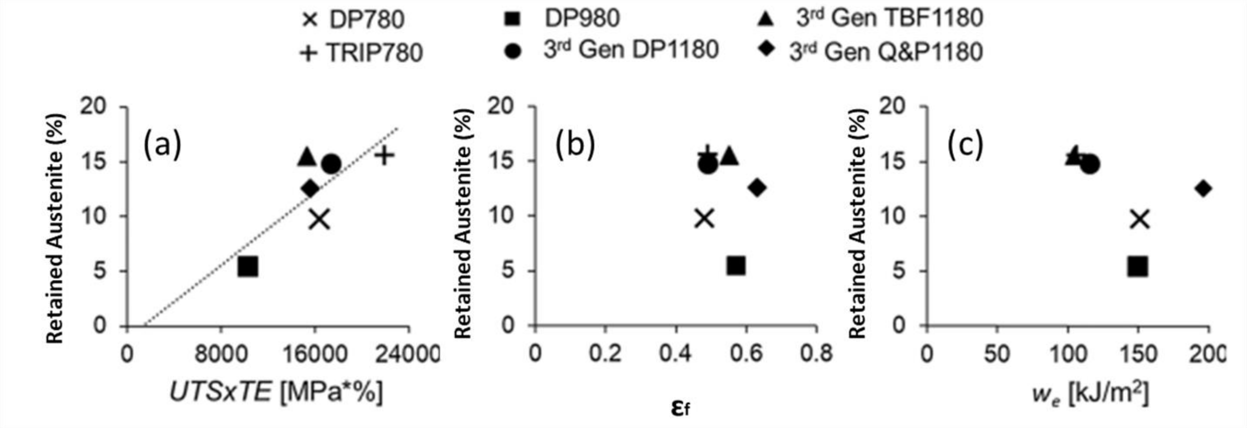

Figure 2.2: Relationship between retained austenite content (%) and UTSxTE (a) ε_f (b) and essential work of fracture (w_e)(c). Adapted from Frómeta et al. (2021)

As a result of the complicated role retained austenite plays in the fracture behavior of AHSSs, several attempts have been made in the literature to understand the local forming potential/damage tolerance by means of calculating the fracture strain and the fracture toughness of AHSSs. Larour et al. (2017) use the local thickness fracture strain to assess the edge crack sensitivity (i.e.i.e. local forming potential of AHSSs) inspired by previous investigations which published a correlation between the ISO16630 hole expansion testing (HET) standards and the tensile thickness strain (i.e. otherwise known as the ε_f), for cold and hot-rolled, CR and HR, respectively, AHSSs (Denks et al., 2019). The HER, for example, is a key industrial indicator of stretch flanging performance and edge cracking tendency (i.e.i.e. damage tolerance/local forming potential) in sheet steels (Chen et al., 2014; Hasegawa et al., 2004; Scott et al., 2017; Yoon et al., 2016). Yet, the risk of edge cracking is greater for AHSSs, and therefore the inconsistencies with HER measurements (punched vs. milled vs. laser jet holes) is more dominant. Other inconsistencies degrading the reliability of HER testing of AHSSs include tooling condition, hole surface/edge quality, crack detection method, the blanking-to-stamping time gap, aging of the metal, etc.…) (Frómeta et al., 2019; Hance et al., 2013; Karelova et al., 2009; Larour et al., 2017; Lin et al., 2023; Ramisetti and Fan, 2018).

Mild steels, for instance, do not show predominant edge cracking tendency and therefore, any inconsistencies with HERs testing methods is less significant (Casellas et al., 2017). These authors note however that research is lacking to further understand the connection between the ε_f and bendability. They advise that a new tensile testing standard needs to be developed to evaluate the fracture of AHSSs and that determine the fracture strain from plane strain notched tensile samples could be more suitable for bending and crash predictions (Larour et al., 2017). As well, it should be considered, from Figure 2.2, that although w_e and ε_f aim to understand a resistance to fracture, the two are not interchangeable parameters.

An additional, common concern among steel and automakers is in the measurement of fracture toughness of sheet steels, as fracture toughness, K_{IC}, is only constant and reliably measurable for thick specimens. The conventional method used to determine such fracture parameters is using a Charpy V-notch (CVN) Impact energy test. This test is not suitable for thin sheet steels, as it would result in buckling and misalignment (Findley et al., n.d.). To bypass this issue, General Motors (GM) pioneered the “stacked Charpy” specimen design, in which several sheets of steel were riveted together, in order to estimate the ductile-to-brittle transition temperature of PHSs (Enloe et al., 2017), however (Findley et al.,n.d.) note that there is significantly less triaxiality in such a Charpy Impact specimen design compared to testing with the classical, thick Charpy Impact specimen. The stress-strain fields at the crack tip in sheet materials (i.e. plane stress) do not translate to predicting the stress-strain field of a crack-tip in a 3D, thick structure under plain strain conditions (Pardoen et al., 2002).

Another approach that has been ventured by several to calculate the fracture toughness/cracking resistance of sheet steels under plane stress is by using the Essential Work of Fracture (EWF) methodology first proposed by Cotterell and Reddel (1977). For ductile materials, the EWF methodology divides the nonelastic crack tip zone into two: the inner fracture process zone (IFPZ), and the outer plastic deformation zone (OPDZ). Mathematically, the total work of fracture (W_f), is the summation of the work needed to create a new surface/cause damage, representing toughness, in the IFPZ as defined by the W_e, and the work performed in the OPDZ to accommodate the large strains in the vicinity of the crack tip (i.e. necking in ductile materials) defined as the non-essential (plastic) work (W_p). EWF testing is conducted on Double-Edge-Notched-Tension (DENT) specimens in which it is required that the ligament length (l_0) be >5 times the thickness (t_0) of the specimen, but not larger than the plastic zone (Cotterell and Reddel, 1977). Equation 2.3 shows how the W_e is proportional to the specific essential work of fracture (w_e) and ligament's cross section (l_0t_0), the initial ligament length and material thickness, respectively, whereas W_p is proportional to the specific plastic work (w_p) per unit volume (${l_0}^2t_0$) and a shape factor of the plastic zone (β).

$$\mathrm{W_f} = \mathrm{W_e} + \mathrm{W_p} = \mathrm{w_e} l_0 t_0 + \mathrm{w_p} l_0^2 t_0 \qquad \text{Equation 2.3}$$

If normalized by l_0t_0, a linear regression between the specific work of fracture (w_f) to the w_e and w_p can be computed for different l_0 lengths.

$$\mathrm{w}_f = \frac{\mathrm{W_f}}{\mathrm{l_0 t_0}} = \mathrm{w_e} + \mathrm{w_p}\beta l_0 \qquad \text{Equation 2.4}$$

Equation 2.4 can be used to determine the slope (w_p), where β is equivalent to $\pi/4$ for a circular plastic zone. The w_p depends on the plate thickness and therefore is not an intrinsic parameter (Pardoen et al., 2002). Figure 2.3 shows the w_f for a series of AHSSs.

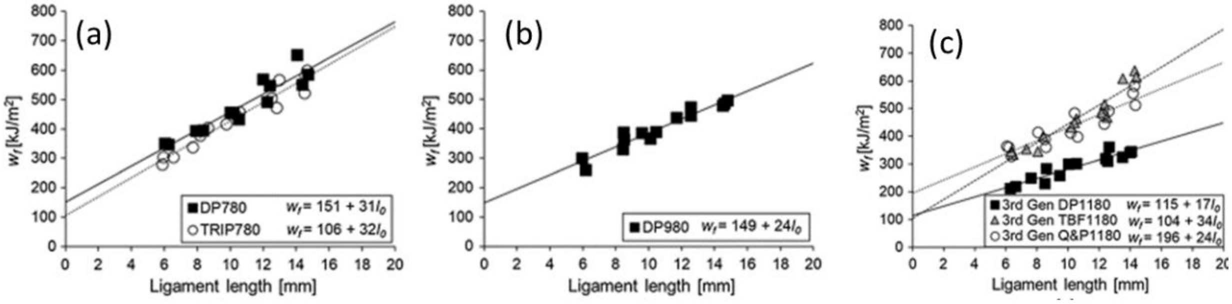

Figure 2.3: W_f as a function of ligament length [mm] for AHSSs of varying strength levels, 780MPa (a) 980MPa (b) and 1180 (c). Adapted from Frómeta et al. (2021).

In Figure 2.3 a) and c), the TRIP780, and 3G Steels: TBF1180 and DP1180, show similar and low w_e, despite having the largest amount of retained austenite. Whereas, in Figure 2.3 the Q&P1180

3G steel, and 1G DP steels – DP780 and DP980, with variable retained austenite content, 6-13%, have ~0.55-0.7x of an increase in w_e. This emphasizes that fact that fracture resistance is not solely only controlled by the retained austenite content but on the steel's matrix factors such as; tempered martensite (TM) grain size and distribution (de Diego-Calderón et al., 2016; Frómeta et al., 2021). Also, this correlates well with the fact that the QP1180 steel a homogeneous distribution of TM throughout its microstructure and attained the highest $w_{e,}$ as shown in Figure 2.3. A decent correlation between the we and HER ($R^2 = 0.79$) was observed by Frómeta et al. (2021), which means that the w_e is an effective technique for assessing the local formability of AHSSs.

2.1.2 Advances made to DP steels

DP steels, containing a soft ferritic matrix with a dispersion of hard martensite islands, continue to be the most widely used AHSS due to their robust thermomechanical processing, lean alloying, balanced mechanical properties and high strain hardening (Ashby, 1966; Speich and Miller, 1979; Tasan et al., 2015). The use of an abundance of carbides, as opposed to martensite, to contrast the ferrite matrix requires a substantial increase in carbon but can result in a deterioration in toughness and poor weldability (Azizi et al., 2022). Martensite and ferrite DP structured steels are created by full annealing (in the austenitic regime) or IA (in the ferritic-austenitic regime) of a CR steel, with fine ferrite-carbide/pearlite constituents, which is then followed by quenching and holding the steel at a temperature just below the M_s. Intercritical annealing enables more control of the final volume fraction of martensite and can be adjusted just by changing the IA temperature. Rapid cooling promotes the general transformation of austenite-to-martensite while leaving the ferrite unaffected (Dai et al., 2021).

In general, DP steels contain 0.06-0.15 wt% C (provides strengthening by stabilizing austenite and martensite), 1.5-3 wt%Mn (provides austenite stabilization, solid-solution strengthening in ferrite and mitigates grain growth during intercritical annealing(Liu et al., 2023)), Cr (to retard bainite formation), Mo (to retard bainite transformation and aid in precipitation strengthening (Chen et al., 2020)), Si (to be solid solution strengthener and promote ferrite transformation) and V/Nb (for precipitation strengthening and grain refinement (Tasan et al., 2015)). Grain refined DP steel either maintains or improves its toughness in comparison to its coarse-grained DP counterpart (Azizi et al., 2022; Tasan et al., 2015).

In DP steels, there are two key micro-mechanisms of damage: martensite cracking and ferrite/martensite (F/M) interfacial decohesion, again highly dependent on the local microstructure. He et al. (1984) said that martensite cracking is more prominent in coarse DP structures and brittle fracture (Liu et al., 2023) whereas F/M decohesion is more observed in finer microstructures. Tasan et al. (2015) attempted to correlate DP characteristics, such as; ferrite grain size and martensite volume fraction (V_m), with different micro-mechanisms of damage: martensite cracking, F/M decohesion or both. Figure 2.4 shows that as the V_m is increased, the likelihood of martensite continuity is increased, and martensite cracking is prevalent. Whereas in the case of fine ferrite grains at a low V_m, both martensite cracking and F/M decohesion are equally likely and increasing the V_m with a fine ferrite grain DP steel, can increase the probability of martensite cracking. Contrarily and more simply, Tang et al. (2021) observed that with an increase in V_m in DP steels the dominant mechanism of damage nucleation goes from ferrite/ferrite interfacial decohesion, to F/M interfacial decohesion, then to martensite cracking.

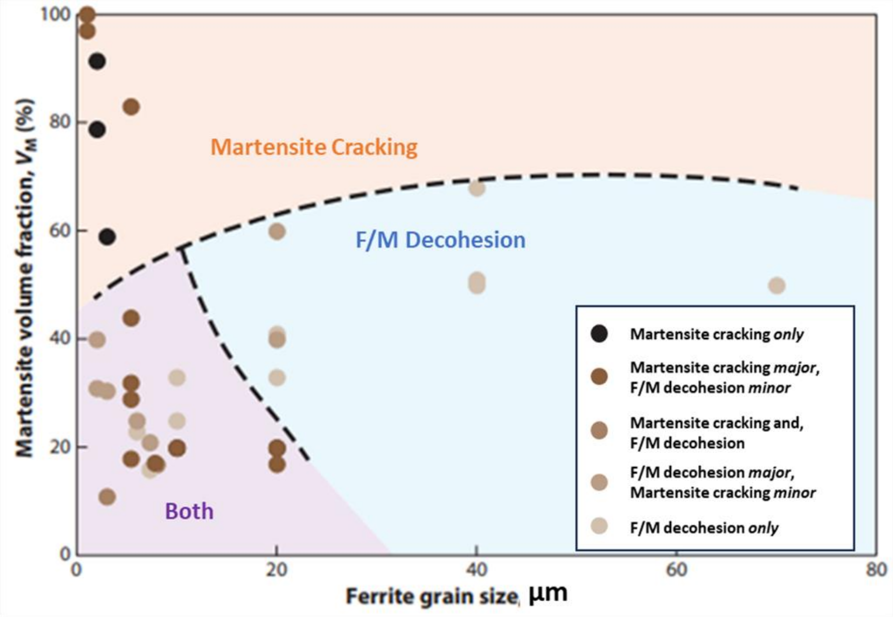

Figure 2.4: Micro-mechanisms of damage in DP steels (F/M decohesion and martensite cracking) as a function of ferrite grain size and $V_{m.}$ Adapted from Tasan et al. (2015).

Several avenues have been ventured to promote the grain refinement of DP thin steels and enable them to achieve ultrahigh strengths. Such avenues include: equal-channel angular pressing (i.e. severe plastic deformation) (Park et al., 2005; Park et al., 2004; Zhao et al., 2021), cold rolling (Tsipouridis et al., 2006), cyclic heating (Park et al., 2020), along with vanadium-microalloying (Scott et al., 2018, 2017) and medium Mn alloying (Liu et al., 2023) etc… The challenge in mechanically refining grains with the use of severe plastic deformation techniques is in scaling it up for mass production(Park et al., 2020; Zhao et al., 2021). To mitigate such a limitation, Liuet al. (2023) utilize the combined effect of vanadium-microalloying and medium Mn alloying to develop UFG DP steels with a ~1470MPa strength level. It is agreed by many that the need for a Vm > 50% is required in the development of ultrahigh strength DP steels (Liu et al., 2023; Scott et al., 2017). Other approaches such as the incorporation of TRIP kinetics, a topic detailed in the following Thesis' chapters 5-7, has been incorporated into DP microstructures to achieve ultrahigh strength levels (>1000MPa)(Dai et al., 2021).

With a reduction in grain size, the area fraction of F/M boundaries is increased, and this results in high strain hardening at low strains due to GND evolution (Suppan et al., 2018). At higher strains however, strain hardening is governed by martensite deformation and the formation of Statistically Stored Dislocations (SSDs) which is independent of grain size (Jiang et al., 1995). Moreover, some have noted that grain refinement in DP steels promote ductile fracture mechanisms (Calcagnotto et al., 2012; Liu et al., 2023). Yet, it is critical to note that in grain refined DP steels, the stress-strain partitioning is more heterogeneous, and the size/dispersion of martensite islands (i.e. local configuration) is more critical.

That being said, stress triaxiality is traditionally mapped at the global not local scale (Cheloee Darabi et al., 2020; Park et al., 2015; Wang et al., 2016), which has less of an importance to predicting the stress-strain behavior of UFG steels in which the stress-strain response is heterogeneous and dependent on the configuration of martensite islands surrounding the ferrite. Paul (2013) performed representative volume element (RVE) simulations at the grain level to understand the local deforming capacity of ferrite in the vicinity of martensite islands. Modelling the local triaxiality within a UFG DP microstructure was also carried out by Williams et al. (2022) in which they found that a high stress triaxiality (~1.4) was observed in ferrite between two large martensite islands within close proximity. This correlates well with speculations made by Tasan et al. (2015) in which well dispersed martensite islands enables ferrite strain accommodation whereas martensite islands confining ferrite enables early strain localization.

In performing Energy X-ray Dispersive Spectroscopy (EDS) on an DP steel vanadium-microalloyed, Williams et al. (2022) observed that the ferrite, with overall more vanadium carbonitride (V (C,N)) precipitates than the martensite, has a densely packed V(C,N)/weak Mn hard core and softer outer core as a result of less V (C,N)/more Mn. They differentiate the inner core as intercritical ferrite (F_i) and outer core as epitaxial ferrite (F_e) in their publication (Williams et al., 2022). Particularly, they found that the local triaxiality of the DP microstructure modelled as a 3-Phase (martensite, F_i and F_e) versus a 2-phase (martensite and ferrite) microstructure resulted in strain localization being distinctly apparent. Ultimately, the purpose of vanadium microalloying in DP steels is to increase the ferrite phase strength overall. This is done with the purpose of globally reducing the strain incompatibility between ferrite and martensite, thereby reducing the likelihood of F/M decohesion and improving the steel's post-uniform elongation (Samei et al., 2019b; Scott et al., 2018, 2017). However, Williams et al. (2022), similar to Liu et al. (2023), found that variation in Mn within ferrite in such steels can also play a role in extending its post-uniform elongation. They found a ~20% improvement in HER with only a <100MPa decrease in tensile strength in the V-microalloyed DP steels intercritically annealed at temperatures 810°C versus those intercritically annealed at 710°C. It is well known that the diffusion of Mn at these temperatures is significantly enabled.

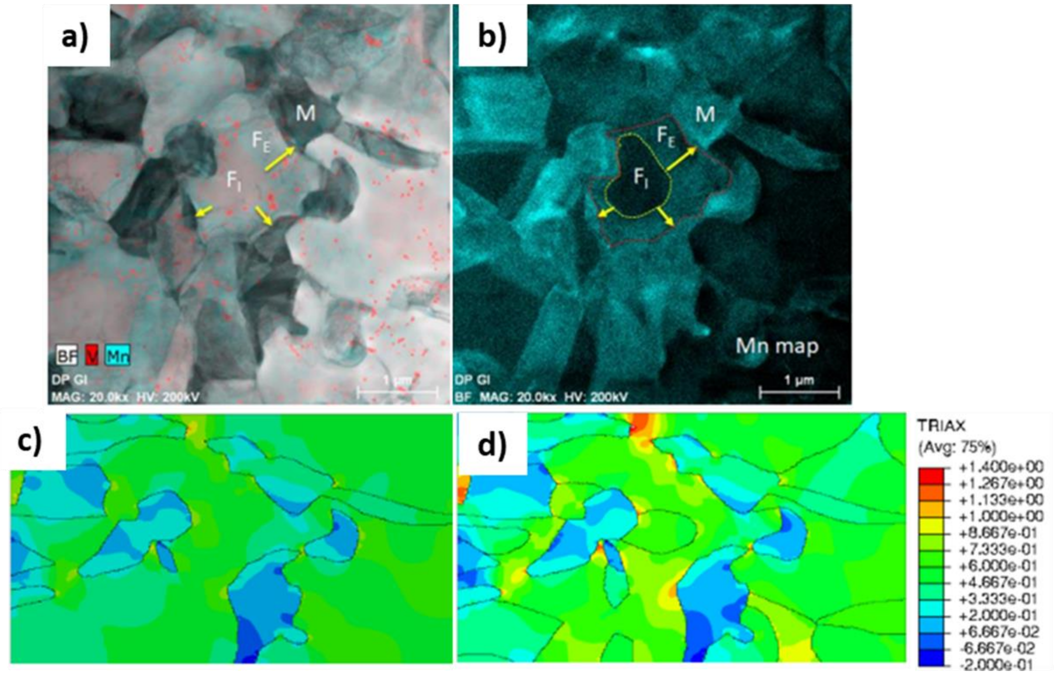

Figure 2.5: Scanning Transmission Electron Microscopy (STEM) bright-field highlighting martensite, F_i, and F_e with superimposed EDS maps of V (a) and Mn (b) Finite Element Model (FEM) of triaxiality at an effective strain of 0.33 considering only two phases (martensite,ferrite) (c) and considering three phases (martensite, F_i, and F_e) (d). Adapted from Williams et al. (2022)

Yet, current research ventures are being made to more thoroughly understand the micromechanisms of damage in these DP steels, particularly where good stretch flangeability (i.e. good HER) and bendability is required (Suppan et al., 2018). The large strain incompatibility between the ferrite and martensite results in interfacial cracking which is a more potent micromechanism of damage for untempered DP steels (Kang et al., 2007). In ideal scenarios, microcracking in DP steels is blunted by the localized deformation and hardening with the ferrite enabling ductile as opposed to brittle fracture (Tasan et al., 2015). Nonetheless, various researchers have used different methods to quantify the strength differential between phases causing the large strain incompatibility resulting in interfacial cracking. Scott et al. (2018) introduced the concept of determining a ferrite:martensite Phase Strength Ratio (PSR) with the use of nanoindentation to gauge its HER performance. The authors found that the addition of vanadium-microalloying (from 0.003 to 0.14 wt%V) of an ultrahigh strength DP steel led to a mean reduction of 32% in PSR and a HER improvement of 15%. However, these authors advise that the HER relationship with PSR is not linear and impacted by microstructural parameters such as: the local configuration of the martensite surrounding the soft ferrite. The ultimate benefit of vanadium-microalloying investigated through this ultrahigh strength DP steel is the fact that it selectively strengths the ferrite, therefore, reducing this steel's potency to interfacial cracking (i.e. improving its post-uniform elongation) while simultaneously maintaining its strength (Pushkareva et al., 2013; Samei et al., 2019b; Scott et al., 2018, 2017). Pushkareva et al. (2013) and Scott et al. (2018) note however, that the PSR can be reduced more efficiently by tempering and provides a substantial improvement to damage tolerance compared to vanadium microalloying. This is because tempering kinetics are fastest for the martensite islands containing the most carbon (i.e. the hardest martensite) (Williams et al., 2022), therefore reducing the strain differential at F/M interfaces where damage is most likely to happen.

2.1.3 Use of The TRIP Effect in AHSSs

Conventional TRIP steels are a mixture of allotriomorphic ferrite (50-55vol%), austenite (7-15vol%), and bainite (30-35vol%) with a high Si content to limit cementite precipitation during the growth of upper bainite (Bhadeshia, 2002; Kuziak et al., 2008). As a result, this carbon partitions into the retained austenite and stabilizes it (Bhadeshia, 2002; Kuziak et al., 2008; Soleimani et al., 2020). In general, TRIP steels have higher amounts of carbon, silicon and/or aluminum than DP steel grades. However, >0.5wt% Si can lead to challenges in casting, surface quality and galvanizing as a result of oxide film formation. Moreover, it is suggested that a partial substitution of aluminum enables an improvement in strength/ductility balance whereas a complete substitution with aluminum deteriorates it (De Meyer et al., 2000; Oliver et al., 2007).

This concept of utilizing unique thermomechanical processing to retain austenite at room temperature and develop TRIP steels was first enforced by Parker and Zackay, 1973). These steels follow a 2-step heat treatment, in which the steel is first intercritically annealed above Ac_1, followed by an Isothermal Bainitic Treatment (IBT) at the upper bainite range (~350-400°C) (Soleimani et al., 2020). The IBT (or slow cooling) stage retains austenite in the microstructure by enabling carbon enrichment and reduces its local M_s temperature to below zero (Oliver et al., 2007).

TRIP steels have the ability to show a high fracture toughness as a result of the stress- or strain induced transformation from metastable austenite-to-martensite (Parker and Zackay, 1973). The main difference in strengthening between DP and TRIP steels is that strain hardening is not only affected by the interaction between hard and soft phases but also by the mechanically induced transformation from austenite-to-martensite (Jacques et al., 2007). As a result, however, TRIP steels show better stretch flanging performance to DP steels while maintaining a high TE (Suppan et al., 2018).

When austenite transforms to martensite, there is an increase in volume of about 3%, corresponding to 1% linear increase in each principal direction. This volume expansion is said to cancel a portion of the triaxial stress near the 'notch' (i.e. the notch induced during necking of ductile materials), resulting in a reduced stress intensity and inhibiting brittle type fracture (Parker and Zackay, 1973; Withers, 2015). According to Christian (1982) and then later Bhadeshia (2002), when 15% of the austenite is transformed into martensite, there's a 2.25% increase in tensile elongation as a result of the phase transformation. From this, Dutta et al. (2018) estimated in testing a med-Mn steel, that with 40% of reverted austenite transformed into martensite at fracture, the TRIP effect contributes <3% to the steel's TE. Overall, in theory, the work used up to by a phase transformation, triggered ahead of a stress-concentrated crack tip, can improve steel toughness, as the rate of cracking is reduced (Courtney, 2005; Withers, 2015). In sheet steels, the stress state near the crack tip is said to be plane strain which inevitably is expected to drive TRIP most (Hill, 1952; Jacques et al., 2007). However, the stress required to drive the martensitic transformation decreases as the grain size increases, which is because the matrix phases has less of a 'shielding effect' to suppress the transformation from occurring (Courtney, 2005). Experimentally, it has been seen the TRIP can either improve or be detrimental to a material's damage tolerance as the martensite transformed is very brittle (Frómeta et al., 2021; Samei et al., 2020). Though it is implied that the amount of GNDs formed during the transformation to martensite to delay the onset on necking is greater in AHSSs with higher volume fractions of austenite (Frómeta et al., 2021).

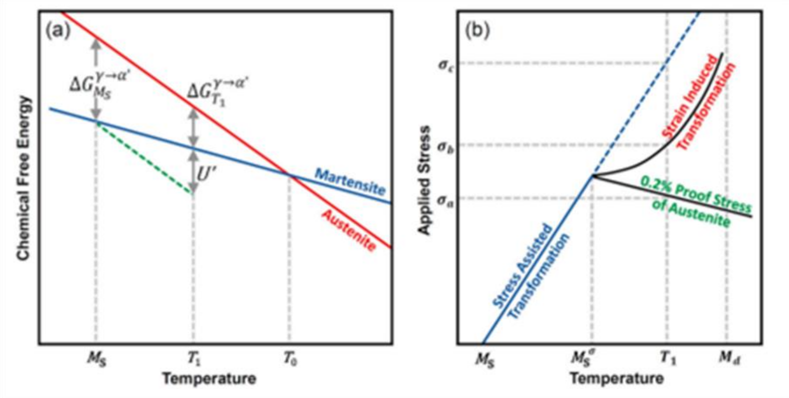

Figure 2.6: Chemical Free energies of austenite and martensite versus temperatures (a) The transition from Stress-Assisted to Strain-Induced Transformation from the applied stress versus temperature adapted from Soleimani et al. (2020) and Tamura (1982)

Fundamentally, the martensite start temperature (M_s) is the critical temperature which gives the system the free energy for the austenite to martensite transformation ($\Delta G_{\gamma\to\alpha'}$)(Tamura, 1982). When the system is undercooled to just below M_s, enough free energy is available to start the martensitic transformation. On the other hand, given that martensite transformation is dominated by a shear co-operative movement of atoms, the application of an external force, U', can be used to activate martensite nucleation in steel at temperatures > M_s, say at T_1 (Pereloma and Edmonds, 2012). This lowers the $\Delta G_{\gamma\to\alpha'}$ to make the stress-assisted austenite to martensite transformation favourable (Patel and Cohen, 1953). At an even higher temperature, say at T_0, there is no thermodynamic driving force for a phase transformation because austenite and martensite are equally stable (Pereloma and Edmonds, 2012). Alloying with C, Mn, Si, Cr, Ni, and/or Nb lowers the M_s temperature therefore increasing austenite stability and modifying its SFE (Patel and Cohen, 1953; Sugimoto and Mukherjee, 2017; Talonen and Hänninen, 2007). As a result of not being a structure in equilibrium, stacking faults in austenite increases the total energy of the lattice (Dieter, 1961).

In a stress-assisted austenite-to-martensite transformation situation, although the stress applied may be considerably less than the yield stress of austenite, pre-existing stress concentrators (such as defects on the local scale of the austenite) can assist in the nucleation of martensite. Yet, if the stress applied is greater than the yield stress of austenite, austenite plastically deforms and introduces new defects for martensite nucleation. Examples of strain induced regions favourable for martensite nucleation are stacking faults, in-grain shear bands, dislocation intersections, and microbands (Pereloma et al., 2016). McDermid et al. (2011) was able to successfully establish a simple relationship between TRIP and the normalized flow stress in conventional high Al, low Si TRIP steels. It was found that this relationship was independent of heat treatment applied, retained austenite volume fraction, and local retained austenite chemistry, whereas a more distinct influence of the afore mentioned parameters is indeed noted in the classical strain-based model proposed by Olson and Cohen (1975). Alternatively, Samek et al. (2006) suggests that the strain-induced transformation is overall responsible in enhancing the steel's strength-ductility balance.

The tendency of austenite to TRIP during deformation, i.e. transform from austenite-to-martensite under an applied load, or to exhibit Twinning-Induced Plasticity (TWIP) has been crucial in manipulation the strength-elongation ratio (Qin and Bhadeshia, 2007) of second generation (2G) AHSSs and third generation (3G) AHSSs thereafter (Qin and Bhadeshia, 2007; Soleimani et al., 2020). De Moor et al. (2010) hypothetically varied combinations of ferrite/martensite and austenite/martensite in steel microstructures to model mechanical properties. As shown in Figure 2.7 (a) 1G steel mechanical properties are modelled adequately using dual ferrite/martensite mixtures, whereas 3G steel mechanical properties are modelled adequately using dual austenite/martensite mixtures. In this instance, however, they did not consider the ability for unstable austenite to transform to martensite with applied stresses/strains. As a result, De Moor et al. (2010) extended their study to predict the ideal TRIP rate which achieves 3G mechanical property targets by varying austenite stability in four different scenarios (conditions A-D) of austenite/ferrite microstructures. In Figure 2.7 (b), condition D shows TRIP being exhausted at low strains, and resulting in only achieving 1G mechanical properties, whereas 3G mechanical properties are attainable with prolonged TRIP kinetics as featured in conditions A-C. Each data point in Figure 2.7 (c) refers to the initial austenite fraction ranging from 0% to 85%. Condition A, with a significant amount of stable austenite which does not TRIP, can attain 2G AHSSs properties. On the other hand, a complex microstructure with ~40% austenite and gradual TRIP kinetics, enabling structured usage of strain hardening associated with TRIP, can reach mechanical targets within the general 3G AHSSs envelope.

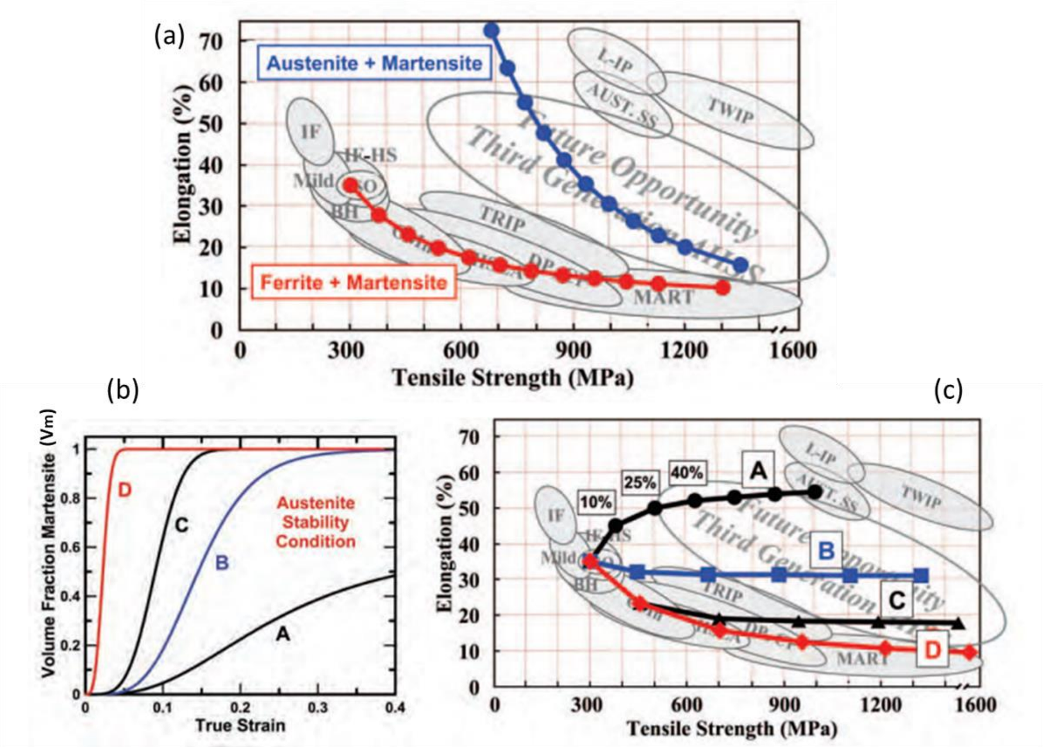

Figure 2.7: Hypothetical ferrite/martensite and austenite/martensite mixtures superimposed on top of the Banana Diagram (a) Variations in TRIP kinetics (b) and their placement on the banana diagram (c). Adapted from De Moor et al. (2010).

Furthermore, the intrinsic SFE of the retained austenite strongly influences the way in which the material accommodates strain, whether through dislocation glide, TRIP or TWIP, and again can be modified with increased alloying. In general, a 10 mJ/m^2 $\leq$ SFE $\leq$ 20 mJ/m^2 favours strain-induced martensitic transformations, whereas an intermediate SFE range, 20 mJ/m^2 $\leq$ SFE $\leq$ 50 mJ/m^2 favours twinning, and a high SFE, SFE $\geq$ 50 mJ/m^2 favours dislocation glide (Lu et al., 2016; Noh et al., 2019; Saeed-Akbari et al., 2009; Wong et al., 2016). When separation distance between the partial dislocations is narrow, such that cross slip is easily done, it is more energetically favourable to twin (i.e. TWIP) instead of transform (i.e. TRIP) (Dieter, 1961). TWIP in steels is a way to produce a ‘dynamic Hall Petch’ effect, in which the mean dislocation path is reduced, enabling increased local work hardening which in turn delays necking (Lu et al., 2016). An intermediate transformation to ε-martensite (with an HCP crystallographic structure) can sometimes occur during the austenite-to-Body-Centred-Tetragonal (BCT) martensite. Less active slip systems are present in brittle, ε-martensite (with a HCP structure) in comparison to Face-Centred-Cubic (FCC)-austenite islands which can reduce overall steel formability. Moreover, the SFE which activates the transition of TRIP-to-TWIP-to-dislocation glide is strongly dependent on the material's chemical composition and temperature. Ultimately, there is less of a tendency for TWIP to occur at the high or low SFE extremes which means that once TWIP is exhausted, TRIP can be activated (Wong et al., 2016). With that being said, Mn content can be used to tailor the behavior of austenite during deformation by changing its SFE. A high Mn (15-30%) content favours an intermediate transformation to ε-martensite (HCP structure), while a medium Mn (5-12%) content favours a direct transformation to α ′-martensite (BCT structure)(Wong et al., 2016).

The austenite grain size also has an effect on its SFE (David K. Matlock and Speer, 2009; Soleimani et al., 2020) in addition to temperature (Lee et al., 2016), and stress state (Blondé et al., 2014; Jacques et al., 2007; Yu et al., 2006). In theory, decreasing the austenite grain size lowers its local Ms temperature, therefore rendering the austenite more stable, yet this relationship has been found to be non- monotonic (Soleimani et al., 2020). For example, a reduction in grain size, from 18 to 1.5µm, of a 204Cu stainless steel (SS) resulted in TRIP being suppressed, whereas, in the case of UFG steels (~0.5µm) a faster rate of ɣ-to-martensite transformation was observed (Soleimani et al., 2020). It is important to note that controlling the austenite to maximize a materials uniform elongation, may also lead to a significant decrease in post-uniform elongation (Frommeyer and Brüx, 2006; Jacques et al., 2007). Other factors besides composition, temperature and grain size that affect the SFE include: the number of inclusions, residual stresses, and the concentration of interstitials (i.e. C and N)(Lu et al., 2016). Overall, quenching and partitioning as well as IA are two methods the automotive industry has used to develop 3G lean alloyed AHSSs with significant amounts of austenite with tailored SFEs.

2.2 Quench and Partition (Q&P) steels

In conventional TRIP steels, the supersaturation of carbon in ferrite is relieved by partitioning to austenite, and carbide precipitation. The key differences between 1G and 3G steels is the higher retained austenite volume fraction, the Mn content ranging from 3-12 wt% (Wu et al., 2018), and the greater presence of martensite, as opposed to bainite as in TRIP steels, enabling very high strength levels to be achieved (De Cooman and Speer, 2006). Q&P steels are suitable for anti-intrusion automotive components protecting the passengers from side impact collisions, such as;

B-pillar reinforcements, sills, bumper reinforcements, cross members and longitudinal beams (De Cooman and Speer, 2006; Wang and Speer, 2013).

In the Q&P process, with a typical ~3wt%Mn content (Wu et al., 2018), the diffusion of carbon from martensite to austenite is optimized by suppressing carbide precipitation with Si alloying. The Q&P process was first proposed by Speer et al. (2015) assuming a Constrained Paraequilibrium (CPE) condition in which long range diffusion of substitutional atoms is absent and only carbon can diffuse beyond unit cell dimensions at low temperatures. As well, the CPE condition assumes that martensite/austenite interfaces are essentially immobile, and that their respective volume fractions are constrained (Speer, 2012). This is used to calculate the endpoint of carbon partitioning (i.e. maximum amount of carbon which can enrich austenite) between stationary martensite and untransformed austenite in the absence of competing mechanisms such as carbide formation, carbon trapping at dislocations, or bainite formation (De Cooman and Speer, 2006; Speer, 2012). In general, carbon is the main form of interstitial strengthening provided in Q&P steels, a small amount of carbon in martensite produces a tetragonal distortion which in turn, produces a shear stress component that attracts edge, screw and mixed dislocations. The introduction of carbon within the lattice not only expands and contracts its volume isotopically, producing symmetrical distortions, but is also producing shear strain, i.e. a non-symmetrical distortion.

In 2012, Baosteel was the first company to commercialize a Q&P steel with a UTS of 980MPa (QP980). Q&P steels yield an excellent tensile strength to elongation ratio, with similar chemical compositions, but fewer alloying elements than conventional TRIP steels (Findley et al., 2017). More specifically, higher strength Q&P steels contain limited amounts of ferrite in order to maximize carbon partitioning into austenite and as a result can exceed 1100MPa in strength (Toji et al., 2014). These steels are first either fully austenitized (above the Ac_3), as shown in Figure 2.8, or intercritically annealed, to attain controlled volume fractions of ferrite and austenite, and then subjected to an intermediate quench at T_q between the M_s and M_f temperatures for a time period (t_q) as shown in Figure 2.8 (David K. Matlock and Speer, 2009). Quenching at a pre-determined temperature between the M_s and M_f enables a controlled volume fraction of martensite to be introduced into the microstructure. These steels are then subjected to ‘partitioning’ in which they are held at a temperature (T_p) which can also be the T_q (for 1-step Q&P) or above the T_q (for 2-step Q&P) for a time period (t_p). During this partitioning stage, the carbon from the martensite diffuses into the austenite. For reference, traditional Quench and Temper (Q&T) processes are used to improve the toughness by promoting carbide formation and retained austenite decomposition, whereas the retained austenite is intentionally stabilized in Q&P processes to improve toughness.

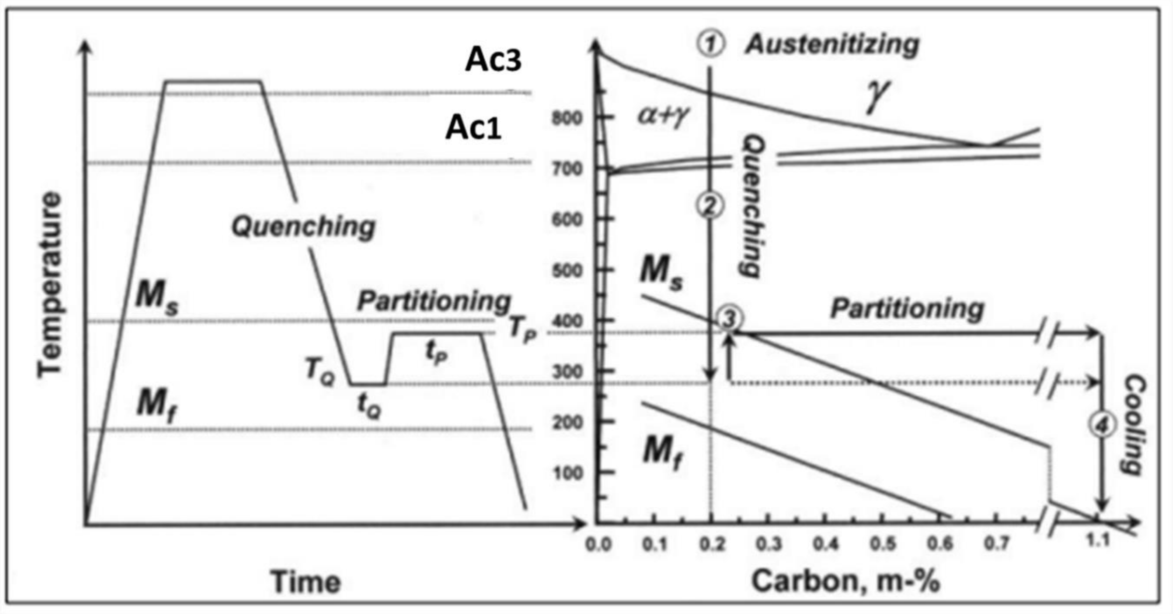

Figure 2.8: 2-step Q&P Processing. Adapted from De Cooman and Speer (2006)

The Koistinen and Marburger relationship, as shown in Equation 2.5, is used to define the T_q below the M_s temperature in which the fraction of martensite transformed is maximized. Equation 2.5 shows that the amount of martensite transformed is directly related to T_q and is not dependent on time since the martensitic transformation is diffusionless.

$$f_{\text{martensite}} = 1 - e^{-1.1\text{x}10^{-2}(M_s - T_q)} \qquad \text{Equation 2.5}$$

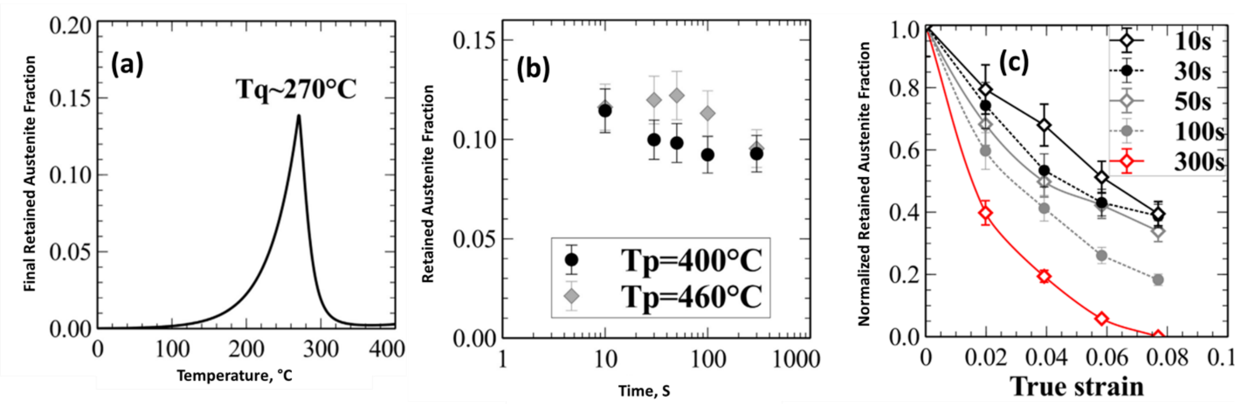

Figure 2.9: Maximum retained austenite attainable at the optimal T_q of a 0.2C-2.2Mn-1.4Si-0.2Cr (wt%) Q&P processed steel (a) variation in retained austenite when partitioned at 400°C versus 460°C held at various partitioning times 10s-300s (b) and the TRIP kinetics of the 460°C partitioned samples (c). Adapted from Arlazarov et al. (2016)

As shown in Figure 2.9 (a), for a 0.2C-2.2Mn-1.4Si-0.2Cr (wt%) Q&P steel studied by Arlazarov et al. (2016), quenching at temperatures above this optimal T_q, increases the amount of retained austenite available in the microstructure, but can lead to insufficient carbon enrichment and weak austenite stabilization, hence promoting martensite formation during the final quench. On the other hand, quenching at temperatures below this optimal T_q retains a low volume fraction of austenite, and any carbon which partitions into thus austenite over-stabilizes it, inhibiting any efficient use of TRIP to delay the onset of necking. To a similar extent, the choice of partitioning temperature and time should also be optimized to avoid the precipitation of carbides, thus reducing the carbon available to stabilize austenite. In Arlazarov et al. (2016), partitioning conditions of 400°C and 460°C varied from 10-300s were chosen such that they are compatible with industry standard CGLs and CALs. In this instance, T_p had a more profound effect on mechanical properties and retained austenite volume fraction than t_p as shown in Figure 2.9 (b). Yet, it is critical to note that t_p did have a significant impact on the higher temperature partitioned (460°C) samples, as shown in Figure 2.9 (c). Increasing the t_p from 100s to 300s when partitioning at 460°C, as detailed in Figure 2.9 (c), completely exhausts TRIP at 8% true strain, whereas partitioning for only 100s retains ~20% of the austenite content at a true strain of 8%. Although advancements have been made to apply Q&P processing with CGL or CAL compatibility, annealing above the AC_3 temperature in a Q&P process results in a thick layer of oxides that impacts reactive wetting.

2.3 Medium Mn (med-Mn) steels

The goal with 3G med-Mn steels in reference to 2G steels is to reduce the amount of Mn used but continuing to delay the diffusion-controlled pearlite and bainite formation while retaining a significant proportion of austenite at room temperature (McGarth and Van Aken, 2012). Med-Mn steels are particularly attractive due to their easily customizable high UTSxTE (30-70 GPa) (Hu et al., 2017; Suh and Kim, 2017; Yang et al., 2021) dependent on the 3G steel's starting microstructure, chemistry and IA parameters. As well, the ability to tailor their thermomechanical processing routes to be compatible with industry CGLs and CALs (Bhadhon et al., 2023; De Moor et al., 2011; Lee et al., 2011; Pallisco and McDermid, 2023) makes these 3G steels promising for commercialization. For instance, recently, microalloying med-Mn steels with Sn has been shown to improve reactive wetting during the galvanizing of med-Mn steels (Pourmajidian and McDermid, 2019). Yet, close control of the temperature variation during continuous annealing is needed for uniformity in microstructure and mechanical properties, making the overall industrial productions of these steels difficult (Du et al., 2019; Yi et al., 2018). In general, these steels are intercritically annealed to achieve a high (20-50vol%) austenite content and an ultrafine ferrite grain size (Dai et al., 2021). The strong impact that austenite content has on mechanical properties has been illustrated by Dai et al. (2021), as shown in Figure 2.10 (a) and (b).

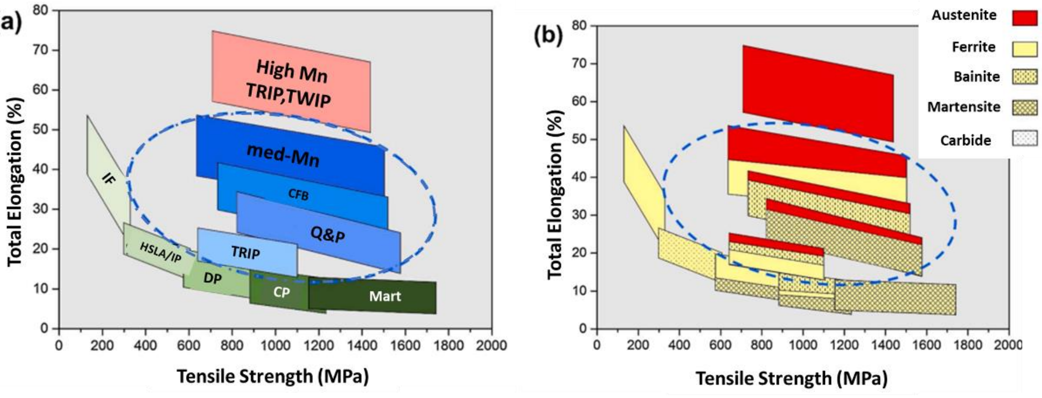

Figure 2.10: The iconic banana diagram highlighting the placement of various AHSSs (a). The iconic banana highlighting the placement of AHSSs with different volume fractions of austenite (b). Adapted from (Dai et al., 2021)

It is critical to note in Figure 2.10 (b) that only considers med-Mn steels with a austenitic-ferritic microstructure. A more reasonable, thorough comparison of 3G steels can be conducted by those with increasing austenite fractions and all martensitic-based matrices. Despite this, the key message from Figure 2.10 (b) is that increasing the amount of metastable austenite into AHSSs' structures improves its energy absorption capability as a result of the TRIP effect.

2.3.1 Alloy Design in med-Mn steels

Intercritical annealing is a thermomechanical processing technique applied to med-Mn steels to revert and stabilize, through carbon and Mn diffusion, significant amounts of austenite, generally more than that of using the Q&P method. In general, the rate of carbon and Mn partitioning during IA governs the chemical stability of austenite, while the mechanical stability of austenite is dictated by its morphology. It is important to note that a high carbon content can deteriorate weldability, which can be problematic during the joining of automotive components (Gibbs et al., 2011). Aside from being an austenite stabilizer, Mn plays a critical role in solid solution strengthening, as detailed in section 2.1.2 and further in section 2.4, and in increasing the product of UTSxTE (Fonstein, 2015). In addition, Si, Al, and P additions can increase the Ac_1 and Ac_3 temperature, and therefore, can offer improved austenite reversion kinetics at high IA temperatures (Hofmann et al., 2006; Suh et al., 2010). This in turn enables processing robustness (Sun et al., 2019). Additions of Al enables the IA to be expanded (Gibbs et al., 2011; Suh et al., 2010; Sun et al., 2018), hence the temperature sensitivity experienced by Med-Mn steels during IA can be reduced (Bai et al., 2020; Sun et al., 2019). As well, an increase in IA temperature can be attained to increase the diffusion rate of Mn and carbon and increase the overall amount of reverted austenite. Aside from being a carbide suppressor, Si acts as a solid solution strengthener. Al also has the ability to supress carbide formation and reduce the density of both FCC and BCC phases but is less effective as a solid solution strengthener compared to Si (Bellhouse, 2010; Bellhouse and McDermid, 2011). Moreover, Al and Si alloying has less of an effect on retained austenite volume fraction and stability compared to Mn and C. Frommeyer et al. (2003) in investigating a Fe-xMn-3Si-3Al steel found that increasing Mn content from 15 to 20 then to 25wt%, changes the steel's mode of deformation from pure TRIP, to combined TRIP-TWIP, then to TWIP. Dumay et al. (2008) then Saeed-Akbari et al. (2009) have developed models to calculate the SFE of Mn-rich TRIP steels, but little has done yet to understand the impact of alloying on SFE in med-Mn steels.

2.3.2 Reverted Austenite Kinetics in med-Mn Steels

Significant work has been done proving that the starting microstructure (i.e. whether tempered martensitic/CR or martensitic before IA), in addition to IA parameters, affects a med-Mn steel's austenite reversion kinetics (He et al., 2019). Up to now, it has been proven repeatedly that a martensitic starting microstructure offers fast austenite reversion kinetics because of the abundance of available sites for austenite nucleation (Bhadhon et al., 2022; Cao et al., 2011; Pallisco and McDermid, 2020). Ultimately, this means that austenite reverted from a martensitic starting microstructure is attainable at lower and shorter IA temperatures/times than compared to a tempered martensitic starting microstructure. As well, Steineder et al. (2018) noted that predominantly lath-type microstructure achieved through a martensitic starting microstructure is compatible with industrial CALs. A lath-type austenite structure versus a globular austenite structure, generally promoted by a CR starting microstructure, is said to be more mechanically stable due to the surrounding plastic constraints imposed by the martensitic matrix (Bhadhon et al., 2022), and more chemically stable due to the higher C and Mn diffusing at a shorter distance (Luo and Dong, 2015; McDermid et al., 2011). Several have noted that a globular austenitic structure is less stable than a lath-type structure whereas others have observed that the partial transformation to martensite of a single coarse austenite block can also prolong the steel's overall TRIP kinetics (Salehiyan et al., 2018; Zhang et al., 2021). This fact is reinforced with the work by Toda et al. (2022) on a C-Mn-Si multiphase steel in which they also noted a more gradual transformation of retained austenite grains$\geq$ 2.5μm in diameter, with approximately 2x more strain required to fully transform a coarse versus a fine retained austenite grain. On the contrary, Xiong et al. (2013) argue that the phases surrounding the metastable austenite, whether coarse or fine, low or high carbon, have a greater impact on the steel's ability to accommodate the volume expansion associated with TRIP. For instance, retained austenite has been observed to be more stable within large ferrite grains (Tirumalasetty et al., 2012), or surrounded by bainite (Timokhina et al., 2004; Zhang and Findley, 2013).

As for IA treatments applied to med-Mn steels, excessive holding times during IA results in an over-saturation of Mn and carbon, rendering the austenite too stable to transform upon straining to provide additional strength. As well, too long an IA results in a reduction in dislocation density, and in turn a low work hardening rate (Soleimani et al., 2020). However, Furukawa et al. (1994) found early on that an increase in annealing time (i.e. 5 min to 1h) resulted in 'peak' properties being attainable at lower temperatures. More practically, the IA holding time needs to be shortened to fit CGL-processes, however this too can lead to austenite being insufficiently chemically stabilized. Ideally, the stability of austenite should be tailored such that TRIP occurs continuously throughout the straining processes and heterogeneities within the microstructure can help to ensure this occurs (i.e. difference in local carbon enrichments of austenite) (Jacques et al., 2007).

2.3.3 Mechanical Properties of med-Mn steels

Discontinuous yielding accompanied by Ludering is an unfavourable feature of med-Mn steels that can impact the steel's formability due to severe localized thinning and can result in a rough surface during stamping (Steineder et al., 2018; Wang et al., 2017; Yi et al., 2018). Traditionally, Ludering is the result of interstitials (i.e. carbon in reference to a Cottrell atmosphere) pinning dislocation motion. Sites for carbon pinning include at the interface of retained austenite and ferrite with martensite, and at dislocations within a phase (which can be beneficial in inhibiting its grain growth during intercritical annealing (Gao et al., 2020)), but also promotes discontinuous yielding (Ma et al., 2020). Hence, discontinuous yielding is highly dependent on the local microstructure, such as phase distribution, morphology, etc… (Yin et al., 2023). During deformation, slight incremental increases in stress are required to unpin these dislocations, resulting in heterogeneous dislocation motion (Steineder et al., 2018). It has been proposed that martensite embryo can also act as dislocation pinning sites (Sun et al., 2017). Some view discontinuous yielding in med-Mn steels as problematic as it increases the chance of premature failure (Wang et al., 2017), yet others argue that martensitic transformation during Ludering provides the necessary, gradual strain hardening to delay material necking (Ryu et al., 2013). In general, discontinuous yielding has been observed in intercritically annealed CR med-Mn steels with an UFG microstructure (Abu-Farha et al., 2018; Luo et al., 2015), but this has not been the case in Dutta et al.'s (2018) med-Mn steel investigations. Moreover, Gibbs et al. (2014) advise that IA at temperatures ≥ 600°C leads the ferrite recrystallization and contributes to yield point elongation.

Continuous yielding, on the other hand, has been found achievable through the introduction of a bimodal grain size distribution in med-Mn steels with ≥ 3 wt% in Al and/or Si promoting the formation of δ-ferrite (Choi et al., 2017; Sarkar et al., 2017). In principle, the coarse δ-ferrite grains enables a higher work hardening rate to be achieved than what is usually obtainable in fine-grained (FG), single phase materials (Wang et al., 2002; Wu and Zhu, 2017). Abu-Farha et al. (2018) then Salehiyan (2018) has found rather than continuous yielding is mostly featured in Q&P microstructures, whilst testing a QP980 steel. This continuous yielding enabled the QP980 steel to feature smooth and continuous TRIP kinetics, as was not the case in testing steels which featured Ludering (Abu-Farha et al., 2018).

2.4 Strengthening Mechanisms in 3G AHSSs

An abundance of strengthening mechanisms are employed in the successful manufacturing and application of 3G AHSSs. Among all 3G AHSSs common strengthening mechanisms include: solution strengthening, (i.e. through Si and Mn alloying (Girault et al., 2001)); precipitation strengthening, as a result of carbides within the microstructure (i.e. V or Nb carbides or epsilon carbides in TM (Celada-Casero et al., 2022; Pushkareva et al., 2020; Scott et al., 2017)); grain refinement; interstitial strengthening (through carbon/nitrogen) and dislocation strengthening. First and foremost, carbon in martensite produces a tetragonal distortion, a shear strain, non-symmetrical distortion to which its relative contribution to strengthening is high ($3G$), where G is the shear modulus. In comparison, the symmetrical distortion imposed by substitutional solute strengthening is low ($G/10$) (Courtney, 2005).

The production of UFG DP steels with >1GPa in strength has been conveniently achieved through V-microalloying resulting in precipitation strengthening, and medium Mn alloying resulting in solid solution strengthening (Liu et al., 2023; Scott et al., 2018, 2017). Compared to mild steels, as performed by Spenger et al. (2008), DP and TRIP AHSSs have additional dislocation density evolution. Increases in work hardening of mild steels is associated with SSDs (i.e. the statistical trapping of dislocations during plastic slip). DP and TRIP steels however produce GNDs alongside SSDs to accommodate the strain gradients which arise from local crystallographic misorientations and the interaction of contrasting phases (i.e. martensite and ferrite in DP steels) during straining. The larger the difference in contrasting phase strengths, the greater the strain gradient produced during straining, and as a result the more GNDs are required to maintain the steel's plastic flow(Krizan et al., 2018). Moreover, as pointed out by Samei et al. (2019) in finer steel microstructures (i.e. in 3G steels) the strain gradient cannot fully develop.

To enhance strengthening further, TRIP-assisted steels have an additional dislocation-based strengthening term which arises from the mobile partial dislocations produced as a result of the volume expansion from the austenite-to-martensite transformation (~18%) (Hatem and Zikry, 2011; Sandvik and Wayman, 1983; Wang et al., 2023). These mobile partials move most freely in a ferritic matrix as opposed to a martensitic- or bainitic-based matrix. More importantly a high work hardening rate is achieved by TRIP steels with moderate TRIP kinetics. The high interfacial strength associated with the moving phase boundary during the transformation also promotes ductility (Liu et al., 2017). Jacques (2004) was able to successfully capture the propagation of dislocations in ferrite resulting from a martensitic transformation via TEM, as shown in Figure 2.11 (a). However, Jacques (2004) does note that the increase in strength provided by conventional TRIP-assisted steels, is not solely attributed to TRIP but also due to the dynamic composite, multiphase nature of their microstructures, in which there is a large chemical and mechanical variability amongst phases. That being said, with the use of neutron diffraction to determine the stress partitioning amongst phases, the rule of mixtures can be applied to predict the macro stress-strain response of the steel. As shown in Figure 2.11 (b), Jacques used the rule of mixtures to predict the flow curve of the TRIP-assisted steel without considering martensite (only ferrite, bainite and austenite), and as a result was able to provide an estimate of the additional hardening provided by TRIP. Jacques et al. (2007) was able to extend upon this work by not only defining stress partitioning amongst phases with the use of neutron diffraction, but also strain partitioning amongst phases via µDIC.

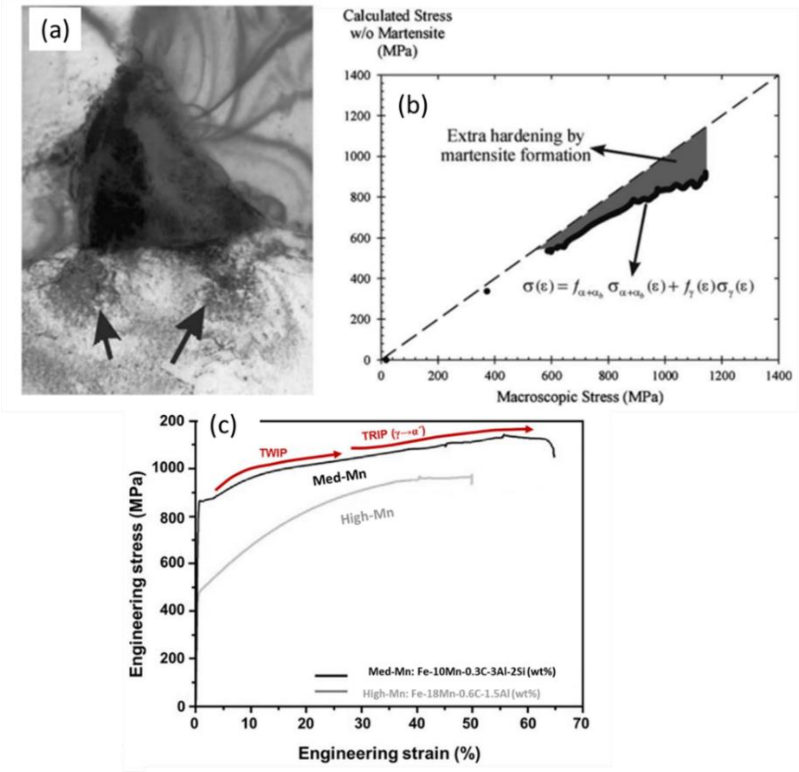

Figure 2.11: Bright-Field Transmission Electron Microscopy (TEM) image showing the propagation of GNDs in ferrite surrounding a newly strain-induced martensite island (a) The stress-strain curve predicted for a conventional TRIP steel using the rule of mixtures, such that the contribution of martensite to strengthening is excluded in order to determine the hardening provided by TRIP (b) The combined advantage of TRIP and TWIP in med-Mn steels (c). Figure 2.11 (a) and (b) is adapted from Jacques (2004) while Figure 2.11 (c) is adapted from Bleck et al. (2019)

Furthermore, there are 3G AHSSs that utilize a combination of TRIP and TWIP effects, in which TWIP has a "dynamic Hall Petch effect" such that twin boundaries divide grains into smaller parts decreasing the dislocation mean free path. In comparing a 3G med-Mn steel to a Mn-rich steel, as shown in Figure 2.11 (c), the med-Mn steel shows improved strength and elongation with the combined use of TRIP and TWIP strengthening mechanisms (Bleck et al., 2019). Bleck et al. (2019) presumed that the most efficient occurrence of martensite nucleation was at the intersection of mechanically induced twins. They do, however, miscount the effect that Si additions have on strengthening in TRIP steels, which also impacts the increase in strengthening seen in Figure 2.11 (c).

2.5 Deformation and Micromechanism of Damage Determination Techniques

Nowadays, one of the most common methods to map strain in 3G AHSSs is with DIC, in which the field of view (FOV) and imaging system can be tailored such that strain is mapped at various length scales. Direct mapping of strain distribution using interferometric techniques was one of the first techniques used to measure strain partitioning from the difference in phase of a scattered light wave before and after deformation. Interferometric techniques offer point-wise measurements with high resolution, whereas DIC have the benefit of offering a full-field strain measurement with resolution dependent on the imaging system being used. Two-dimensional (2D) DIC uses a single fixed camera to solely capture in-plane deformation of a planar object while 3D DIC is applied when out-of-plane strain of the test object (i.e. curved surfaces, severe out-of-plane distortions) cannot be neglected. Figure 2.12 shows the general set-up of a 2D DIC test conducted at the macroscale with the use of a Charged-Coupled Device (CCD) camera in (a) and the microscale with the use of an SEM in (b). Figure 2.12 (c) exemplifies the microstrain partitioning maps processed with DIC which can be achieved with the use of an in-situ SEM tensile testing set-up (Zhou, 2018). This set-up is used in Chapters 4-7 to investigate microstrain partitioning in the DP1300 steels, QP1500 steel, and med-Mn steels, respectively, of interest in this thesis.

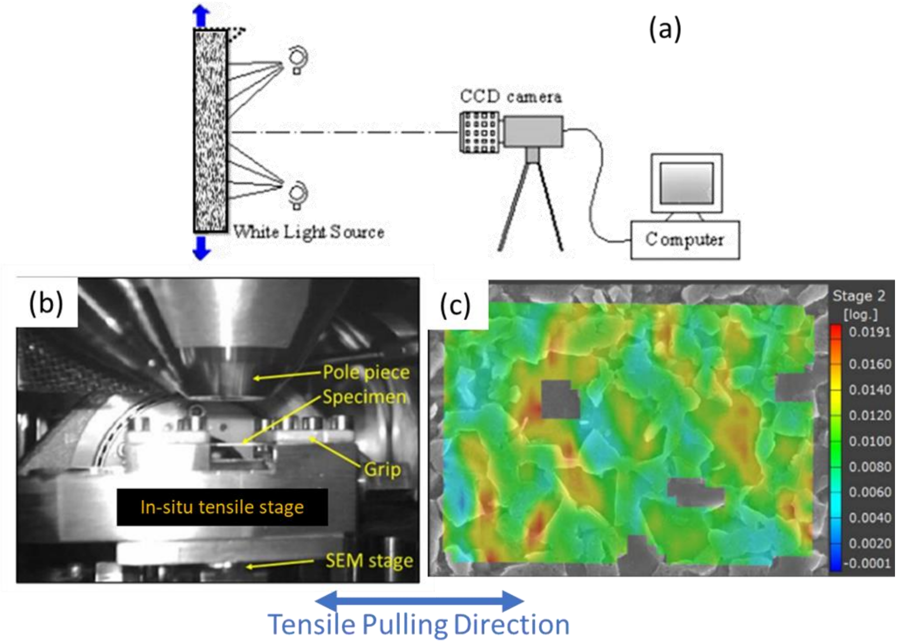

Figure 2.12: General macroscale set-up of a 2D DIC test conducted using a CCD camera (a) set-up of a µDIC test conducted using a in-situ tensile stage and SEM (b) an example of the microstrain mapping

possible with the use of a in-situ tensile stage and SEM (c). Figure 2.12 (a) is adapted from Pan et al. (2009) and Figure 2.12 (b) and (c) is adapted from Zhou (2018).

The steps for performing 2D DIC are as follows: (1) apply a random speckle pattern, as shown in Figure 2.12a – the specimen surface must have a random grey scale intensity distribution which deforms compatibly with the specimen, (2) acquire a series of images of the planar specimen's surface before and sequences after the specimen is loaded, (3) process the acquired images using a computer program to obtain strain information (Pan et al., 2009). Ultimately, there are two key assumptions made when applying 2D DIC to obtain localized strain measurements (Pan et al., 2009). Firstly, it is assumed that the specimen remains parallel to the CCD sensor during deformation and any out-of-plane motion is negligible - an increase in an in-plane displacement can be the result of large out-of-plane motion. Secondly, it is assumed that the imaging system used does not suffer geometric distortion such that the non-linear correspondence between the physical point and the imaged point during deformation is minimal. This is more pronounced in high-resolution imaging systems (i.e. SEM, Atomic Force Microscopy (AFM), etc…). Despite the fact that this geometric distortion is greater with high-resolution DIC or otherwise termed as µDIC, it is important that strains are resolved at length scales smaller than the average constituents to achieve the 'in-grain' strain. This is of more importance if the goal is to formulate "high-fidelity models of damage and failure" (Rajan et al., 2012). In order to successfully achieve the in-grain strain for µDIC computation, however, the speckle patterning method or DIC parameters chosen for post-processing needs to first be optimized. There are three key DIC parameters that will be varied in order to find an optimal combination:

1. Facet Size - dimension in pixels that the user sets to compute the average strain. The larger the facet size, the greater the measurement accuracy, however the lower the strain resolution. It is recommended to avoid edges of a uniform intensity (grey level), and that a stochastic pattern incorporating several gray level variations enables the best computation. With a micro-to-nano FOV, the effects of drifting using high-resolution imaging systems (i.e. SEMs) is more susceptible to producing a systematic error. Di Gioacchino and Quinta da Fonseca (2013) has found that this drift becomes less prominent with the use of large facets.

2. Facet Step - distance between facet centres in pixels, also adjustable by the user; a decrease in facet step results in an increase in spatial density. Noise in the computation

accumulates when the strain gauge (facet step) is short in comparison to the surface roughness (Schmidt, 2012). As proven by Carter et al. (2015) and shown in Figure 2.13, the choice in facet step has a greater impact than facet size on strain resolution.

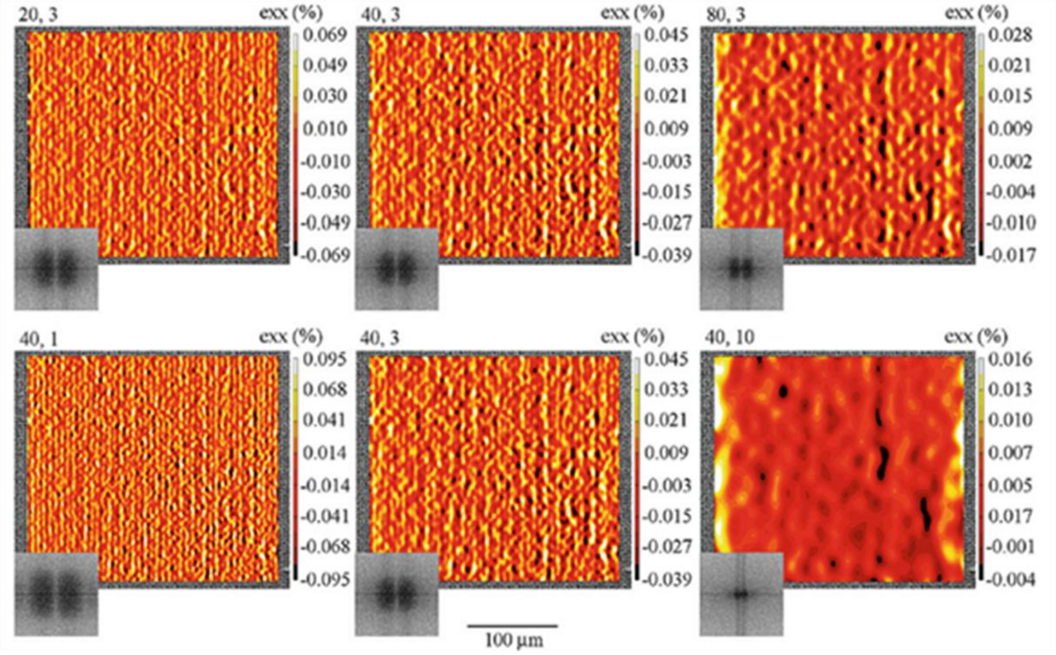

Figure 2.13: The impact of varying facet size (from 20-80 pixels) to varying facet step (from 1-10 pixels) on the resolution of DIC computation. Adapted from Carter et al. (2015).

3. Strain Tensor Neighbourhood - is the number of facet centres used for strain computation. The default setting of the Strain Tensor Neighbourhood to 3 which means that three facet centres/two facet steps are used for a single strain computation (Schmidt, 2012). Figure 2.14a is a schematic illustrating the difference between a Strain Tensor Neighbourhood of 3 (default) versus that of 5, in which five facet centres/four facet steps are used for strain computation. In Chapters 4-7, a strain tensor neighbourhood of 3 is used such that a 3x3 matrix series of facets were approximately equal to the average grain size of the matrix phases as shown in the schematic, Figure 2.14 b.

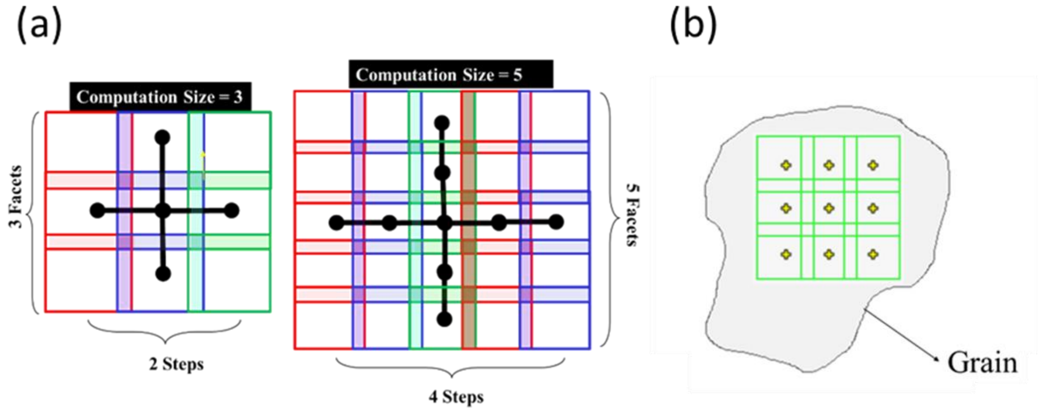

Figure 2.14: Comparison of a Strain Tensor Neighbourhood computation 3 versus 5 (a) The adjustment of facet size/step needed to produce a Strain Tensor Neighbourhood 3 to achieve the average 'in-grain' strain (b).

2.5.1 Micro-Digital Image Correlation (µDIC)

For DIC performed on a millimetre-scale or larger FOV, spraying white and black dots using a spray bottle or an airbrush is conventionally used. Although speckle patterning via spray painting or airbrushing is inexpensive, and easy-to-use, the powder size used, liquid viscosity, spray distance, and air pressure needs to be predetermined (Dong and Pan, 2017). Ultimately, the spatial resolution of strain measured increases with increasing the density of features, and the smaller these features, the smaller the facets that can be used for effective DIC computation (Di Gioacchino and Quinta da Fonseca, 2013). To resolve strains in a micro-to nano- FOV an abundance of other micro-speckle patterning techniques have been explored and can be segregated into two categories: *microstructure-dependent or microstructure-independent*.

Microstructure-dependent micro-to-nano speckle patterning are used most often, and are strictly related to the scale of a material's microstructural features, including inclusions, grain boundaries, additives, second phases, etc. The technique of processing a set of SEM images obtained at a focused location as a function of increasing strain with DIC was first applied in 2005 on an Al alloy strip cast material. The variation in grey level intensities from the development in-grain slip lines at small strains, and evolution of surface topography at the onset of necking was sufficient for DIC correlation (Kang et al., 2005). Then the etching technique was applied in 2007 to evaluate strain partitioning between phases on a low strength DP steel with and without TM (Kang et al., 2007). Moreover, after loading an etched, ultrahigh strength Q&P steel in tension, Arlazarov et al. (2016) as well as Krizan et al. (2018) noted a critical visible change in martensite-austenite islands within the microstructure. When undeformed, this Q&P steel featured smooth grey-centred islands with white edges, which they classified as martensite-austenite islands, to islands with considerable roughness after being strained as shown in Figure 2.15. However, due to this abrupt change in microstructure the following authors would not have been able to use their images for µDIC mapping.

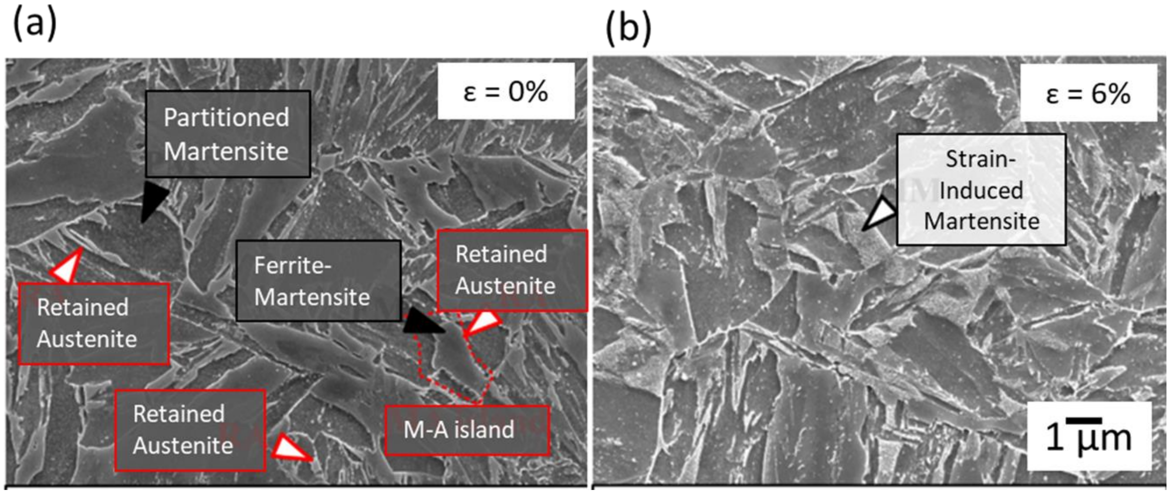

Figure 2.15: SEM micrographs of a ultrahigh strength Q&P microstructure, quenched at 270°C and partitioned at 460C for 100s in its undeformed state (a) and deformed to an engineering strain of 6% (b). In (a), Arlazarov et al., (2016) attribute rough grey features as Partitioned Martensite, bright-whiter regions are Retained Austenite, and smooth grey centred-islands with white edges as martensite-austenite islands. In (b), bright, light grey island featuring roughness were considered the Strain-Induced Martensite. Adapted from Arlazarov et al. (2016).

It is also important to keep in mind that 'grain grooving' and 'feature-free' grains post-etching can result in strain errors, including, stress-intensification or reduced DIC mapping coverage. However, due to cost, time efficiency, and equipment availability the most widely used approach of surface patterning for µ-DIC is indeed etching of the microstructure (Yan et al., 2015).

Two common, *microstructure-independent* methods is using lithography techniques as well as Focused Ion Beam (FIB) milling/(or) deposition. Although both can be costly speckle patterning options and limited to the applicability to non-flat substrates, they are easily reproducible. Lithography has been applied several times to study the micro-deformation of materials achieving ~300nm speckles on an Al-alloy (Zhang et al., 2014), 45nm speckles on an Al-Mg alloy (Zhang et al., 2014), and has been combined/contrasted with a material's etched microstructure for tracking (Ososkov et al., 2007). In Ososkov et al. (2007), the gold grid of cross hairs was advantageous for micro-strain measurements at high strains where damage initiated and resulted in poor DIC correlation with an etched microstructure. However, processing an etched microstructure with DIC improved the accuracy of the micro-strain measurements at low strains because the resolution could be fitted to the grain size of the material (Ososkov et al., 2007). In short, lithography involves a spin-coated polymer resist of polymethyl-methacrylate (PMMA) to be put on the sample followed by a mask (or desired pattern) being irradiated via electron/ultra-violet exposure on the surface. Then, in order to see the pattern printed, the sample is submerged in a developing solution in which (for positive resists) features irradiated gets dissolved. This is followed by depositing a metal deposition, typically gold which is a high atomic number and contrast to most material substrates (Di Gioacchino and Quinta da Fonseca, 2013). An issue with high atomic number deposits is the fact that they can heavily scatter electron beams, limiting their sample penetration depth, as well as obscuring any microstructural strain information below the speckle (Yan et al., 2015). Some researchers enforce the need for a dramatic contrast between the matrix and micro-speckle whereas others have enforced the need for a ratio of 50:50 between light and dark, to avoid the possibility of a facet containing pixels of the same greyscale. On the other hand, FIB micro-to-nano-speckle patterning through milling requires a high ion current to obtain high quality edges whereas FIB micro-to-nano-speckle patterning via deposition requires gas precursors such as W or Pt (Dong and Pan, 2017). The critical issues underlying the use of FIB for nano-to-micro speckle pattern is the introduction of residual stresses from surface milling and ion implantation.

The colloidal silica drop casting technique, physical vapour deposition (PVD) of a low-temperature solder alloy (i.e. using InSn (Hoefnagels et al., 2019)), as well as electropolishing speckling techniques are other examples of microstructural independent, inexpensive speckling methods which, however, require ample parameter optimization. A challenge with the colloidal silica speckling method is mitigating the silica particles' sensitivity to clustering (Hoefnagels et al., 2019); but on the other hand, it is an advantageous technique due to their low atomic number and, in being amorphous, they enable weak beam scattering (i.e. minimizing diffraction contrast), good adherence to the surface and compatible deformation with the substrate. The colloidal silica micro-speckle patterning technique has been applied more frequently on in-situ tensile tests in which EBSD of 3G steel microstructures was necessary (Dutta et al., 2019; Wang et al., 2017; Yan et al., 2015). However, none of these researchers note the issue of removing the hydrocarbon film developed post-EBSD scanning which can reduce the contrast between particles, and background, and introduce drift during SE imaging, causing errors in the μDIC computation. The most proposed solution is with the use of plasma cleaning, however, depending on the hydrocarbon layer thickness and the degree of colloidal silica film adherence, this also presents another parameter-optimization challenge (Zhang et al., 2020). Moreover, Hoefnagels et al. (2019) suggest that their PVD one-step deposition method is tunable to the DIC application at hand with the pressure and temperature used being the ultimate factors governing the speckle size. Although they successfully deposit a wide range of speckle sized patterns on multiple materials, their highest average local von Mises strain published was 5%. As well, there's the challenge of correlating the local strains to the underlying microstructure. Hoefnagels et al. (2019) did propose that an (electro-)chemical etching can be used to remove the InSn for EBSD scanning, however this must be done after the material has been strained.

With that being said, the combined use of EBSD and DIC at the same local region is highly informative in correlating microstrains to microstructural evolution (i.e. grain orientations, misorientations, phase transformations, etc.), but is very challenging to successfully achieve. In an attempt to solve this, Zhang et al. (2020) proposed a 2-step electropolishing methodology which is both a *microstructure-dependent and -independent* speckle patterning technique. In electropolishing, the atoms are pulled off the substrate from the applied voltage to attain a smoothened, slightly etched surface (microstructure-dependent), however applying too high of a voltage can result in an exponential rate of deep etching, and pitting (micro-structure independent). Zhang et al. (2020) electropolish their material until they achieve a smooth surface for EBSD mapping, then re-electropolish their material at a high voltage to enable 'pitting decoration' as shown in Figure 2.16. Zhang et al. (2020) do note however, that during the re-electropolishing step, if conducted at too high voltage the result can be catastrophic, especially if the electrolyte stirring rate, time, temperature, etc. is not optimized beforehand. For instance, electropolishing of multiphase materials is difficult as the dissolution phases are incompatible, resulting in the removal of one phase more than another (Chatterjee, 2015), and too much topography from electropolishing can result in deteriorated EBSD signal quality.

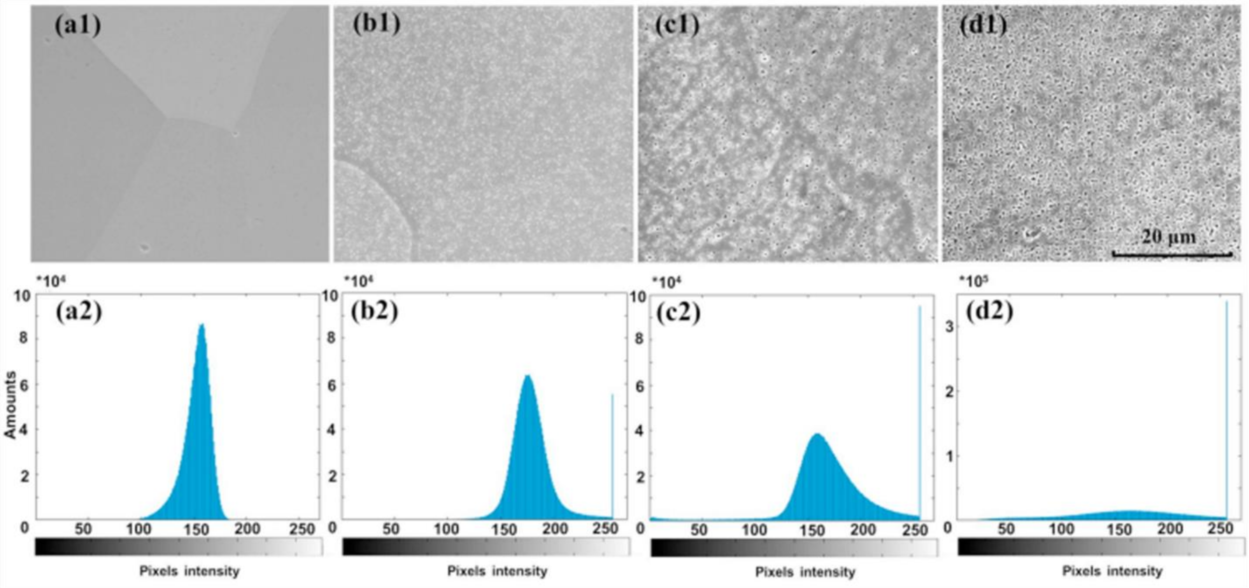

Figure 2.16: Speckle patterning using electropolishing to enable EBSD and μDIC. Figure 2.16 (a_1) and (d_1) refers to the smooth electropolished surface required for successful EBSD and its corresponding tight grey scale variation, respectively. Figure 2.16 (b_1-d_1) refers to the second electropolishing step to enable pitting decoration at various voltages (from 25-45V). The corresponding variation in grey scale is featured in Figure 2.16 (b_2-d_2). A wide greyscale is required for successful μDIC computation. The stir rate and electropolishing duration was fixed at 1000rpm and 30s in all cases, respectively. Adapted from Zhang et al. (2020).

Another important factor that needs to be considered for accurate μDIC computation with the use of SEM acquired images, are the imaging parameters and the type of detector being used. Due to the traditional angled placement of an Everhart-Thornley (ET) SEM detector, shadowing arises from the surface topography which can result in poor DIC mapping coverage at high strain or can result in artificially increased local strains being computed. This means that even though a *microstructure-independent* patterning technique (such as FIB milling/deposition, or colloidal silica) may be used for successful μDIC computation, microstructural dependence as a result of using the ET detector's angled placement can influence the μDIC computation. To mitigate this issue, Yan et al. (2015) suggested decreasing the aperture size (therefore, reducing the beam current) and voltage, to minimize any backscatter electron (BE) signal/diffraction contrast from the microstructure, and improve the depth of focus. The following authors mapped out the effect of increasing or decreasing the aperture size, voltage and current with respect to an ET (Conventional) detector or In-lens detector as shown in Figure 2.17.

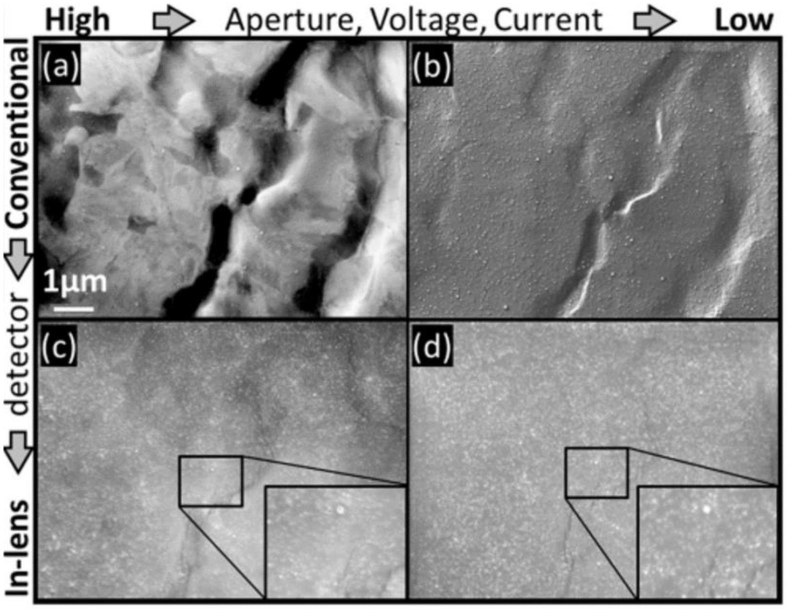

Figure 2.17: Microstructure-independent pattern imaging effects from aperature size, voltage and current while using an ET (Conventional) detector (a), (b) and an In-lens Detector (c), (d). Adapted from Yan et al. (2015).

However, for small apertures, and since the depth of focus-to-working distance relationship is inversely proportional, in order to obtain an image that is completely in focus a short working distance is required. This is problematic with the use of commercially available in-situ mechanical testing devices in which large working distances are generally needed to accommodate the device's height. On the other hand, secondary electron (SE) imaging with an in-lens detector, being placed directly above the imaging plane, minimizes the topographical and diffraction contrast from the sample especially at small apertures, and voltages, as shown in Figure 2.17d. In contrast to Yan et al. (2015), Jin et al. (2008) then Di Gioacchino and Quinta da Fonseca, (2013) suggested enhancing the BE signal with the use of a short working distance and a high voltage to essentially by-pass any arising surface topography visible in an SE image during deformation. In addition to an ET SEM detector causing shadowing and affecting the accuracy of local, in-plane measurements with the use DIC, surface roughening with increasing strain, as a result of slip steps, grain rotations, and damage nucleation (Dutta et al., 2018; Raabe et al., 2003), also deteriorates the accuracy of in-plane DIC measurements. Oh et al. (2021) suggests either measuring the out-of-plane deformation and incorporating it into the strain measurement to dictate the accuracy of the in-plane strain measurement with the use of both SEMs and AFMs or eliminating any arising surface-roughening completely by re-polishing of globally, pre-strained specimens then subjecting them to in-situ SEM tensile testing. The specimens globally pre-strained to high strains (i.e. 20%. 40%) were evidently less ductile when subjected to in-situ SEM tensile testing and led to poor DIC mapping coverage early on in the straining process. However, these results were combined with the µDIC results from in-situ tensile testing of specimen globally pre-strained at lower strains (i.e. 5%,10%).

2.5.1.1 µDIC to study deformation and damage in 3G AHSSs

Gaining in popularity is understanding the microstrain partitioning in UFG 3G AHSSs those with and without TRIP assistance with the coupling of in situ SEM tensile testing with DIC. Such studies aid in the microstructural design of damage tolerant 3G AHSSs. Ruggles et al. (2016)has already successfully determined the that local strains surrounding the hard phases were 5x greater in the DP than its somewhat equivalent TRIP-assisted steel at fracture with the use of µDIC. As well, they stated qualitatively that DP steels show a patchwork-microstrain-type pattern, while TRIP-assisted steels show pronounced microshear suggesting plastic compatibility between phases. Chapters 5 and 6 do the same sort of comparison as Ruggles et al. (2016) but for ultrahigh strength DP and TRIP steels, and with DIC performed at a much higher resolution. As noted in section 2.1.2, high-resolution investigations are critical in UFG steels as the stress-strain response is heterogeneous and dependent on the configuration of phases.

EBSD mapping, has also been deemed a critical tool, in determining the underlying complex microstructure in multiphase TRIP steels before acquiring SEM images at various strain levels for µDIC computation. In general, the dislocation activity of a material with an intermediate grain size from 1µm to 10nm is weakly understood (El-Naaman et al., 2016; Meyers et al., 2006). In ultrahigh strength DP steels, Tang et al. (2021) determined the mesoscopic, 2µm x 2µm resolution, origin of damage in a DP980 steel using the traditional etching microspeckle patterning technique for DIC. Pelligra et al. (2022), publication in Chapter 4, built upon Tang et al. (2021) study of micromechanisms of deformation and damage with the use of DIC of an etched microstructure but at a much finer resolution than the grain size of their UFG DP steel of study,

~0.3µm x 0.3µm resolution. Despite their differences in resolution with regards to DIC computation, the two agree that the strain gradient produced at the F/M interfaces of DP steels drives interfacial cracking. The concept of Strain Gradient Plasticity (SGP), related to the pile up of GNDs at an interface to enable compatible deformation as introduced by Ashby (1970), has been deemed instrumental in modulating the ductility of FG materials (Fleck et al., 1994; Huang et al., 2018; Li et al., 2020; Mazzoni-Leduc et al., 2010). Tang et al. (2021), approximated the shear stress as a result of dislocation pile up at the F/M interface of DP steels is ~10GPa at 1nm away from the boundary. They made this speculation based on the experiments conducted by Guo et al. (2014). Tang et al. (2021) emphasized that this high stress is the contribution of shear stresses acting on dislocations as the hydrostatic stress has no impact on dislocation movement. Most researchers use the von Mises strain to capture the evolution of GNDs and, when necessary, the shape-changes associated with TRIP during straining (Dutta et al., 2018; Tang et al., 2021).

Wang et al. (2017) focused on the martensite size impact on damage rather than the impact of different austenite characteristics or TRIP in a 3G Q&P steel. They observed, in performing µDIC of a colloidal silica speckle patterned surface, that damage initiated at TM/coarse martensite boundaries (Wang et al., 2017). The following authors were able to determine the different martensitic regions within the microstructure by performing EBSD on the undeformed material. Overall, they found that catastrophic damage accumulation in the form of bands was found in coarse martensite islands while damage was overall delayed in lath martensitic regions in the form of homogeneously distributed strain localization spots.

Recently, Yin et al. (2023) used µDIC to analyze the Ludering and localized damage initiation in an UFG (41600MPa%) 0.15C – 5.9Mn med-Mn steel. The following authors speckle pattern their steel using gold remodelling of a 5nm film using the procedure laid out by Luo et al. (2005). They found that strain concentrates in austenite, activating TRIP, and in channels of ferrite at low strains, promoting microshearing which led to the steel’s Ludering. Contrarily, at high strains they reported a shift in strain localization happening most dominantly in the ferrite. This led to pronounced strain partitioning at prior austenite/ferrite interfaces. In terms of damage, they found that once TRIP was exhausted, in area of the microstructure were there was no ferrite, void nucleation occurred at the triple junction along the loading direction. Wang et al. (2017) and Tan et al. (2019) advise that a homogeneous distribution of retained austenite will improve ductility in med-Mn steels, and the presence of ferrite in these UFG materials is needed to resist crack initiation and propagation.

To drive this point further, in investigating med-Mn steels without ferrite, Dutta et al. (2018) compared microstrain partitioning of a HR and CR med-Mn steel with differing grain sizes by using µDIC combined with EBSD mapping. These authors used the colloidal silica dispersion technique to produce a fine speckle pattern for µDIC. In the HR samples, lath-type retained austenite formed at lath boundaries organized within prior austenite grain packets and maintained the crystallographic orientation of the prior austenite. Contrarily, in the CR samples, the retained austenite had a combination of ellipsoidal and globular morphology and showed variable crystallographic orientation throughout its microstructure. For the HR samples, lath-type retained austenite are agglomerated within prior austenite grains, and those oriented at 45° to the tensile direction, sheared preferentially as a single unit, resulting in a considerable proportion of the steel transforming into martensite quickly. Whereas, in the CR steel condition, straining of the retained austenite islands occurred homogeneously as a result of their wide variation in crystallographic orientations.

2.5.2 X-ray Microtomography (µXCT)

Two-dimensional (2D) observations of void nucleation, growth and coalesce are easy to implement, however the information may not be fully representative of the damage events occurring within the bulk of the material. For example, voids that may not have coalesced at the surface may have coalesced within the bulk of the sample as suggested by Buffière et al. (1999). There are several methods used to correlate 2D visualized voids with 3D analysis, including, serial sectioning, fractography, freeze fractography, ultrasound, and densitometry as listed by several authors (Mummery et al., 1993; Weck, 2007; Zhou, 2018). However, all of these methods are destructive thus introducing artefacts to the analysis, can be time-consuming, do not provide any information on the deformation history leading to damage events, and do not provide any localized information (Buffière et al., 1999; Lorthios et al., 2010; Mummery et al., 1993; Weck, 2007). Figure 2.18 compares the number of cracked particles seen at the surface (2D) versus the bulk (3D) (Buffière et al., 1999). Despite this, however, Buffière et al. (1999) found that qualitatively the same damage mechanisms at the surface and the bulk, but quantitatively that damage growth was larger inside the bulk. As well, they found that although the probability of a particle cracking is higher within the bulk than the surface, the ratio of their probabilities is constant at higher plastic strains (~3%), as shown in Figure 2.18. At low plastic strains rather (<1%), they have found that it is possible to quantify the same fraction of broken particles within the bulk and at the surface, as shown in Figure 2.18.

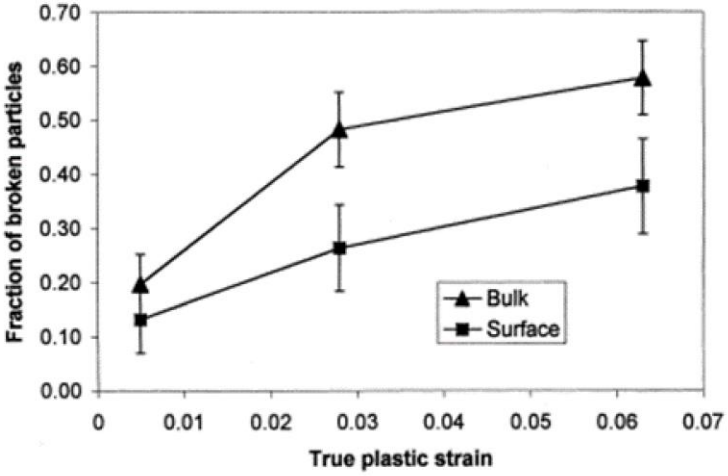

Figure 2.18: Fraction of cracked particles observed at the surface versus those quantified within the bulk as a function of true plastic strain. Adapted from Buffière et al. (1999)

There are various reasons why researchers believe there is a drastic difference of damage seen in 2D versus 3D such as; the linking of particles/phases, voids et... and its distribution is only truly representative from a 3D analysis, polishing can eliminate or add surface artefacts, and the stress-state within the bulk of the material is not that same as that observed in 2D. Researchers have suggested that a greater fraction of cracked particles should be expected at the surface because they are partially relaxed from the compressive stresses that these same particles experience within the bulk (Salvo et al., 2003; Weck, 2007). However, Mummery and Derby (1994) suggested that it’s the change in plane stress (at the surface) to plane strain (in the bulk) that causes the difference in cracked particles observed in 3D versus 2D. Ultimately, the assumption made when using 2D imaging techniques to obtain a material’s properties is that there’s homogeneity/uniformity throughout its thickness, and/or the property of interest is insensitive to the material’s possible heterogeneities (i.e. the elastic modulus) (Zhang and Wang, 2018).

That being said, X-ray tomography is a one of the most convenient, non-destructive, and most informative 3D mesoscopic techniques to track damage. Particularly, x-ray tomography is advantageous in detecting voids, because of its significantly different attenuation coefficients in comparison to the material itself, this is termed as 'absorption contrast tomography'. This contrast of intensities can be observed from the radiographs obtained at different angles by the detector. Ultimately, the use of µXCT to observe damage evolution in materials enables the separation of void nucleation from void growth. Void growth can be understood by analyzing a proportion of the largest voids (i.e. 20 or 50) which mostly contribute to total fracture of the material (Fabrègue et al., 2015; Samei et al., 2018). Damage evolution parameters, such as void density, void area fraction, and average void size are described in section 2.5.2.1.

Furthermore, during the set-up of an X-ray Computed Tomography (XCT) geometric-based scan, it is important to keep in mind that an increase in the FOV results in a decreased resolution (Weck, 2007) yet, in general, laboratory scale geometric-based XCT systems have routinely been successful in characterizing materials at the microscale (Zhang and Wang, 2018). At the end of the scan, the finite number of radiographs obtained at different angles of rotation are post-processed in a 3D reconstruction software (Weck, 2007). Buffière et al. (1999) conducted in-situ tensile testing using high-resolution synchrotron x-ray tomography for improved microstructural 3D characterization of an Al-SiC composite. A synchrotron accelerates electrons to almost the speed of light to create a highly coherent X-ray beam that can provide the highest resolution of crack initiation locations. The difference between a laboratory-based XCT system and x-rays generated via synchrotron radiation is it improvement in brilliance and monochromaticity (Zhang and Wang, 2018). In Buffière et al.'s (1999) work, given that the attenuation coefficients of Al and Si are close, the synchrotron improved the contrast between phases during 3D reconstruction of the radiographs post-scanning. The ability for a synchrotron to differentiate between small variations in refractive index is termed as 'Phase Contrast tomography'. In addition to being able to differentiate between phases, phase-contrast imaging has also been used to detect small features of damage (Lorthios et al., 2010).

2.5.2.1 µXCT to study damage in 3G AHSSs

Minimal work to date has been devoted to using tomography to understand damage in 3G AHSSs. Most work to date on 3G steels with regards to tomography has been performed on the atomic scale to capture elemental segregation. For example, correlative TEM (i.e. to target a specific grain boundaries) and Atom Probe Tomography (APT) (i.e. to define elemental partitioning at the grain boundary) analysis has been conducted by Toji et al. (2014) on a 2-step Q&P steel and by several on med-Mn steels in the literature (Guo et al., 2022; Patra et al., 2021; Sun et al., 2019). The first report using tomography at the microscale to compare damage evolution on a series of 1G and 3G AHSSs was published by Samei et al. (2020), and also featured in Chapter 3. Med-Mn steels however were not included in this publication. Through the use of µXCT, Samei et al. (2020) was able to conclude that grain refinement achieved through microalloying, and TRIP kinetics can reduce the rate of damage accumulation. As well, using µXCT, Samei et al. (2019) were able to understand precisely the impact of vanadium microalloying on post-uniform elongation in 3G DP steels. The authors found that void volume fraction of the largest 50 voids was reduced by 43%, and the mean void diameter was reduced by ~1.1x with a ~47x increase in vanadium content within the 3G DP steel. Overall, they were able to conclude that the smaller mean void size in the vanadium-microalloyed 3G DP steel played a positive role on suppressing fracture, as larger voids in its 3G steel counterpart imposed greater stress/strain localizations and led to faster fracture. Most µXCT studies have been conducted using the absorption contrast mode, as detailed in section 2.5.2, (Azizi et al., 2022; Pelligra et al., 2022; Salehiyan et al., 2020; Samei et al., 2019b; Samei et al., 2019; Samei et al., 2020; Weck et al., 2008, 2007). Some, however, with the benefit of high energy synchrotron-sourced tomography were able to perform ultrahigh-resolution absorption contrast tomography (Schoell et al., 2022) and phase-contrast tomography (Toda et al., 2022, 2017). These different tomography modes are discussed in detail in section 2.5.2.

Recently, Toda et al. (2022) have been the first to use a combination of contrast-enhanced X-ray nano-tomography (nXCT) (at 20-30keV high energy, with a spatial resolution of 160nm) and pencil-beam diffraction tomography at synchrotron facility, Spring-8, to investigate TRIP in a 0.1C-5Mn-1Si steel. Figure 2.19 (a) to (c) shows a cross sectional slice observed by nXCT at several strains. In Figure 2.19 (a) to (c), the contrast between the retained austenite (bright regions) and ferrite/martensite (dark regions) was obtained, however, due to their very small differences in density, ferrite and martensite could not be segmented. In following the yellow arrows in Figure 2.19 (a) to (c) the gradual transformation of coarse retained austenite island can be understood.

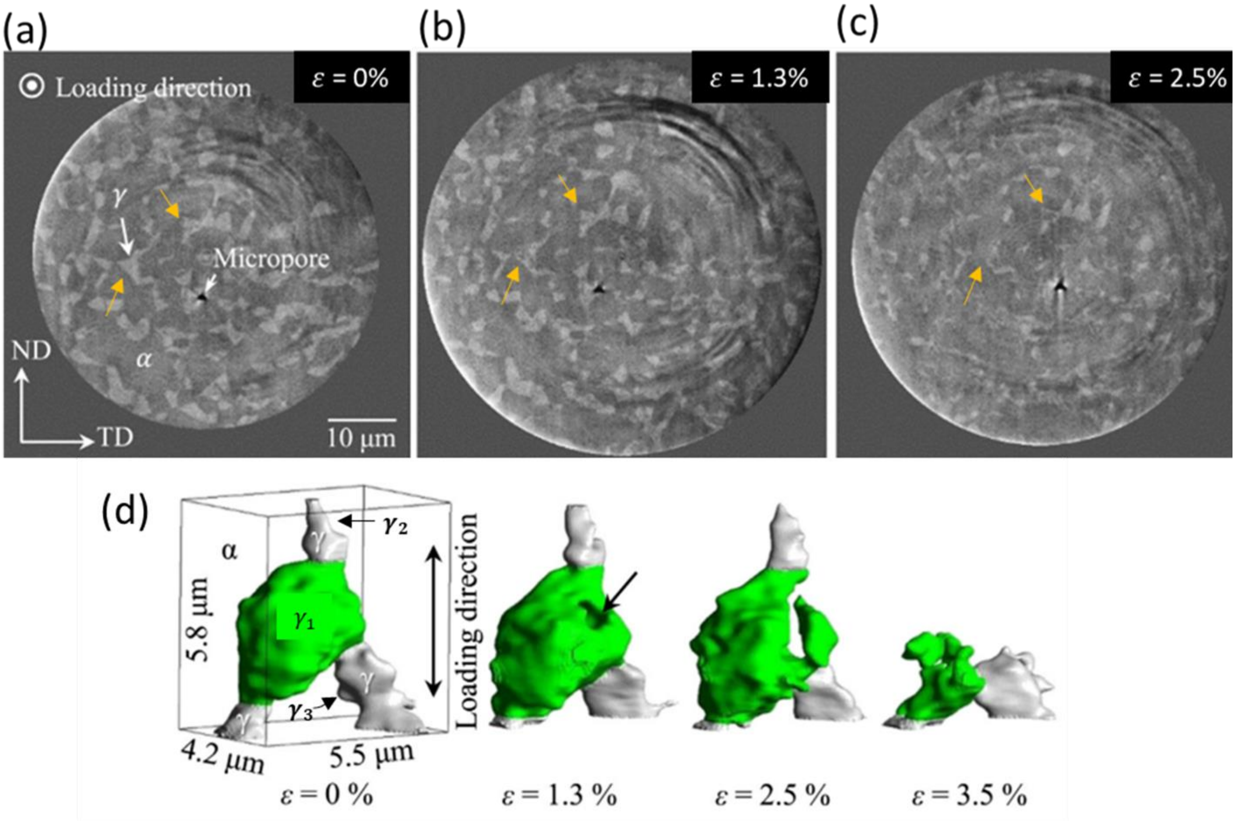

Figure 2.19: Transverse nXCT projections of a 0.1C-5Mn-1Si TRIP steel at different strains, ε = 0% (a), ε = 1.3% (b) and ε = 2.5% (c). The bright regions are the retained austenite and the darker regions are the ferrite/martensite. Figure 2.19 (d) is the 3D reconstruction of a local ferrite/martensite and austenite aggregate from ε = 0% to ε = 3.5%. Adapted from Toda et al. (2022).

Figure 2.19d shows a reconstructed section of the microstructure, in which the coarse green grain (ɣ1) shows a gradual transformation whereas finer retained austenite grains (ɣ2) and (ɣ3) shows a complete transformation at a strain 2.5% <ε<3.5% or retains completely untransformed at ε≥3.5%, respectively. With the pencil beam X-ray Diffraction (XRD) data, Toda et al. (2022) was able to determine the local TRIP kinetics of retained austenite islands at different crystallographic orientations. Similarly, synchrotron-based tomography coupled with XRD and fatigue testing of single-edge notched austenitic stainless-steel specimens was carried out by Schoell et al. (2022). The following authors hypothesized that TRIP acted as a retardation mechanism, due to the fact that only martensite was present in the vicinity of the cracked single edge notch.

In cross-sectioning of two intercritically annealed (700°C and 750°C) med-Mn tensile specimens pulled to fracture, Sun et al. (2019) looked at the voids close to the fracture surface. Both IA conditions enabled the med-Mn steel to fracture in a ductile manner, despite showing complete TRIP exhaustion very close to the fracture surface. This observation is in accordance with Schoell et al. (2022) tomography studies. They reported damage in this med-Mn steel to occur, most prominently, via void nucleation at F/M interfaces, and less prominently via martensite cracking similar to classical DP steels(Landron et al., 2010; Tasan et al., 2015) as shown in Figure 2.20 (a) to (d). Similar to the damage parameters evaluated by several with the use of µXCT (Fabrègue et al., 2015, 2013; Samei et al., 2019b; Samei et al., 2020; Zhou, 2018), Sun et al. (2019) compared the void density, average void size and void area fraction of the different IA conditions as shown in Figure 2.20e, f, and g respectively. The void density is defined as the number of voids per area of interest, whereas the void area fraction is the total area of voids per area of interest (Zhou, 2018).

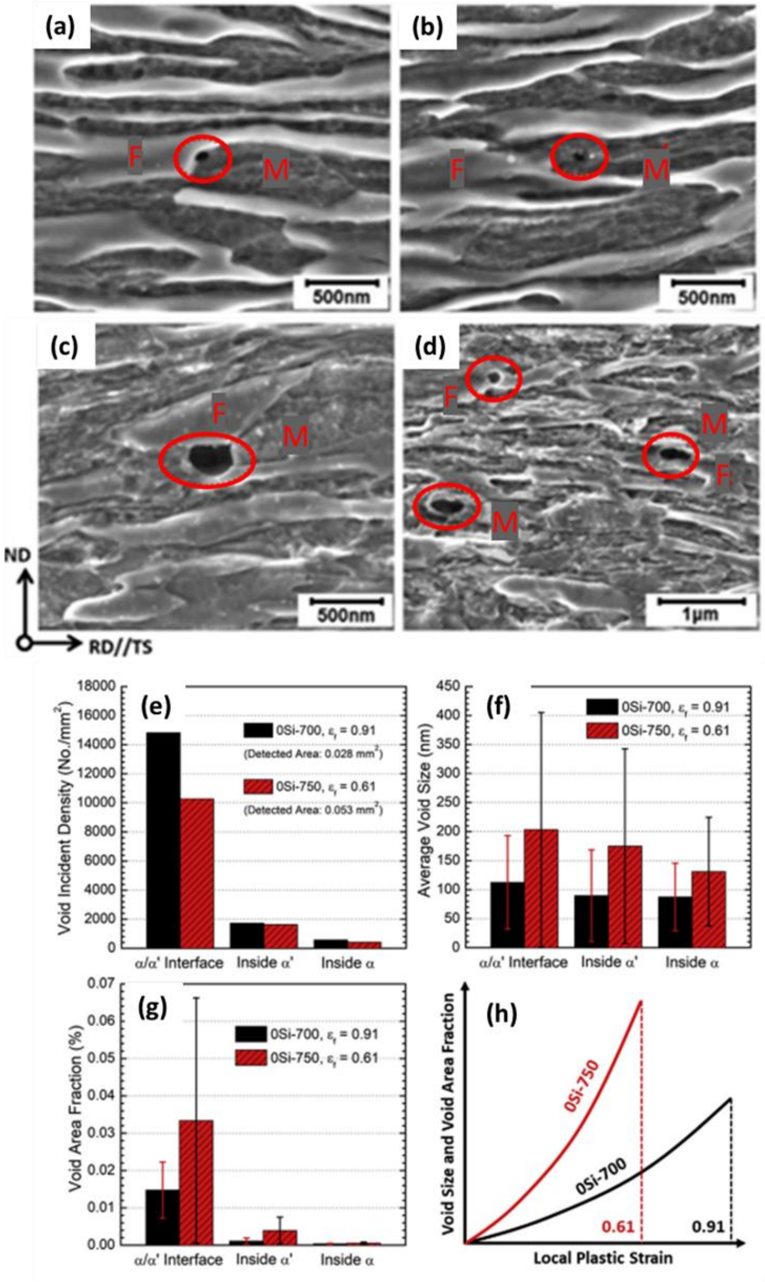

Figure 2.20: SEM images near the fracture surface showing void formation in samples intercritically annealed at 700°C (a), (b), and 750°C (c), (d). Figure 2.20 shows the void density (e), average void size (f), and void area fraction (g) of the intercitically annealed samples at 700°C and 750°C. Figure 2.20 (h) is a schematic *predicting* the evolution of void size and area fraction as a function of plastic strain. Adapted from Sun et al. (2019).

Despite the differences whilst comparing the evolution of voids in 2D versus 3D, as detailed in section 2.5.2, cross-sectioning of fractured tensile samples enables voids to be categorized into their respective micromechanism of damage, as shown in Figure 2.20 (e) to (g). In reference to Figure 2.20 (f) to (g) , Sun et al. (2019) found that IA at 700°C resulted in on average a 2x decrease in void area fraction and void size versus the 750°C condition, yet interestingly the void density is higher in the 700°C IA condition, as shown in Figure 2.20e. The authors proposed that austenite would be more slowly consumed during necking when intercritically annealing this steel at 700°C, allowing the volume expansion associated with the martensitic transformation to impede void growth/coalescence and thus delay its damage evolution rate as speculated in Figure 2.20h. Of course, the damage evolution curves featured in Figure 2.20h is based on a hypothesis made by Sun et al. (2019), such 3D local information on the deformation history leading to damage events cannot be determined through 2D examinations, also noted in section 2.5.2 (Buffière et al., 1999; Fabrègue et al., 2015; Mummery et al., 1993; Weck, 2007). Ultimately, besides the work previously conducted by our group on 3G steels (Azizi et al., 2022; Pelligra et al., 2022; Salehiyan et al., 2020; Samei et al., 2019a, 2019b; Samei et al., 2019; Samei et al., 2020), to our knowledge, Chapters 6 and 7 are the first reports using XCT to understand damage evolution using XCT on med-Mn steels.

2.6 Stress-state impact on TRIP kinetics in AHSSs

Along with chemical composition, grain size, and strain rate, deformation mode/stress-state has a prominent impact on the rate of TRIP exhaustion in steels (Yu et al., 2006). Magee and Davies (1971) found that there's a selection of martensite variants favourably oriented with respect to the stress/strain state. The martensite transformation, which is a shear and dilatational displacement, parallel and normal, respectively, to the habit plane dictates the contributions of the normal/hydrostatic and shear/deviatoric components from the applied stress (Jacques et al., 2007; Patel and Cohen, 1953).

An easily, accessible method of quantifying TRIP kinetics has been in performing lab-based XRD scans on the though-thickness of cross-sectioned tensile specimens strained to varying degrees (Bhadhon et al., 2022; Pallisco and McDermid, 2020; Patel, 2019). However, this methodology is limiting in terms of specimen penetration, and it can only provide a few points to speculate the steel's TRIP kinetics. HE-XRD has been used by a few researchers to obtain highly resolved, volumetric information on the retained austenite behavior during tensile testing which is needed for realistic automotive damage modelling (Hu et al., 2017; Park et al., 2019). The retained austenite volume fraction within the ultrahigh strength Q&P steel of study in Chapter 5 as well as the med-Mn steel in Chapter 6 has been quantified using the Co-sourced (Co-XRD) method outlined by (Bhadhon et al., 2022; Pallisco and McDermid, 2020; Patel, 2019), and the HE-XRD synchrotron-sourced method initially developed by Abu-Farha et al. (2018). The combined use of in situ DIC and HE-XRD as a 3G AHSSs is being strained has been performed in Q&P steels (QP980, and QP1500) by Park et al. (2019), and on a med-10wt% Mn steel by (Abu-Farha et al., 2018; Wu et al., 2018b). Abu-Farha et al. (2018) investigated the two TRIP-assisted steels: a QP980 steel which deformed homogeneously and a med-10wt% Mn steel which deformed via propagative instabilities (i.e. Ludering). A simple, continuous decrease in the retained austenite volume fraction was featured in the QP980 steel, in which they suggest that traditional approaches of determining TRIP kinetics (i.e. quantifying strain with a strain gauge), rather than the more instrumentation-intensive DIC-coupled-synchrotron approach, would suffice. On the other hand, the med-10wt% Mn steel featured a more complex stepped-type decrease in retained austenite exhaustion in which they attribute is a result of this steel's propagative instabilities. They found that there was a greater difference in TRIP kinetics when strain was measured conventionally (via a strain gauge) versus via DIC on this med-10wt% Mn steel. DIC-based local measurements offered fewer data points because the decrease in retained austenite was only detected when Ludering was captured within the DIC FOV (Abu-Farha et al., 2018). At the time, only the TRIP kinetics of *straight-gauged* tensile specimens were investigated.

That being said, an abundance of analyses to date understanding TRIP kinetics as a function of stress-state has been performed on AUSs (Jacques et al., 2007), which is limiting to understanding TRIP kinetics as a function of stress-state for multiphase, low-alloyed TRIP-assisted steels. For instance, due to the fact that the number of alloying elements differ in type and quantity in AUSs versus multiphase TRIP-assisted steels means that AUSs exhibit a narrower SFE range, and as a result this affects its TRIP kinetics. Alloying with Ni and Cr increases the SFE in Fe-Mn alloys but decreases it in carbon-containing steels (Lu et al., 2016; Qi-Xun et al., 2002). Therefore, the role that TRIP has in composite-type strengthening has a more critical impact on low-alloyed TRIP steels than AUSs (Jacques et al., 2007). Moreover, martensite is said to typically nucleate at stacking fault intersections in AUSs (Spencer et al., 2004), which is not always the case in multiphase low-alloyed TRIP-assisted steels.

In testing Fe-Ni alloys, Patel and Cohen (1953) found that the M_s temperature was lowered (i.e. supressed TRIP) when subjected to hydrostatic pressure but increased (i.e. promoted TRIP) for tension and compression. They suggested that shear stress component overpowered the normal stress component's ability to suppress TRIP when under compression, whereas both the shear and normal stress components are proportioned to aid in the promotion of TRIP under uniaxial tension. Precisely, Jacques et al. (2007) state that the mechanical driving force for the austenite-to-martensite transformation is not necessarily lower in a shear test versus a uniaxial test but is critically dependent on the shear component. Whereas the largest driving force for a transformation from austenite-to-martensite is expected to be in the plain strain condition. The stress triaxiality ($^{\sigma_m}/_{\sigma_{VM}}$), which is the ratio of hydrostatic stress (σ_m) to the von Mises equivalent stress (σ_{VM}), is a measure that most researchers use to understand the relationship between TRIP subjected to different modes of deformation.

Jacques et al. (2007) found, in using neutron diffraction, that, in general, with increasing stress triaxiality, from shear ($^{\sigma_m}/_{\sigma_{VM}}$ ~ 0) to plain strain-DENT specimens ($^{\sigma_m}/_{\sigma_{VM}}$ = 0.6), there is a increase in the TRIP rate, as shown in Figure 2.21 (a). The fastest TRIP rates experienced were those of the plane stress-notched ($^{\sigma_m}/_{\sigma_{VM}}$= 0.52), and DENT specimens. However, in the case of the biaxially loaded specimens, the Marciniak ($^{\sigma_m}/_{\sigma_{VM}}$ = 0.42), and equiaxial ($^{\sigma_m}/_{\sigma_{VM}}$ = 0.66) specimens, a delayed TRIP rate was featured in the equiaxial specimens in comparison to the Marciniak ones, as shown in Figure 2.21 a.

Furthermore, it can be noted from Jacques et al. 's (2007) work, Figure 2.21a, that significantly different TRIP rates is exhibited by the equibiaxial and DENT specimens despite having a similar triaxialities ($^{\sigma_m}/_{\sigma_{VM}}$ = 0.6 – 0.66). The authors attribute this difference to their different deformation mode ratios, the ratio of the major (ε_2) to minor (ε_1) strain, R_1 = $^{\varepsilon_2}/_{\varepsilon_1}$. A R_1 = -0.5 is for uniaxial tension, R_1 =0 is for plane strain, and R_1 =1 is for balanced biaxial tension (Zanjani et al., 2014). Jacques et al. (2007) defined R_1 of the DENT specimens as ~0, and defined R_1 as -0.36

and 1 for the Marciniak and equibiaxial specimens, respectively. However, contradicting this, from neutron diffraction studies on an ultrahigh strength Q&P/TBF steel using cruciform-shaped samples subjected to different biaxial loading conditions, Polatidis et al. (2020) showed their equibiaxial tension ($^{\sigma_m}/_{\sigma_{VM}}$ = 0.66) and uniaxial tension ($^{\sigma_m}/_{\sigma_{VM}}$ = 0.33) specimens featured similar TRIP kinetics. As a result, their work rather suggests that the deformation mode does not impact the rate of TRIP exhaustion during straining.

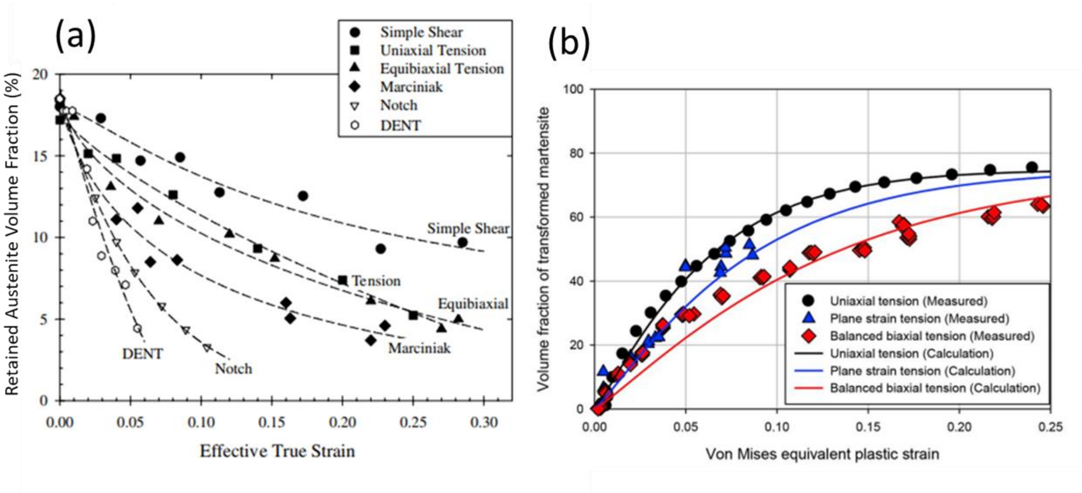

Figure 2.21: Retained austenite volume fraction, determined via neutron diffraction, as a function of effective true strain for a 0.3C-1.42Mn-1.4Si TRIP steel (a). Adapted from Jacques et al. (2007). Figure 2.21 (b) shows the volume fraction of transformed martensite (i.e. at 0% means no strain-induced martensite is present in the microstructure) as a function of von Mises equivalent strain for a QP980 steel. Adapted from Park et al. (2019).

Park et al. (2019), Wu et al. (2018), and Polatidis et al. (2020) are among the few authors who published the impact of stress-state on TRIP kinetics in >1GPa AHSSs with the use of combined synchrotron-sourced XRD and DIC. The details of the experimental procedures carried out by Abu-Farha et al. (2018), Hu et al. (2017) and Park et al. (2019) have been also applied with slight modifications to this thesis and are detailed in Chapters 5-7. In general, similar to Abu-Farha et al. (2018), Park et al. (2019) note that TRIP exhaustion in the Q&P steels has a smooth profile in the absence of Ludering, as shown in Figure 2.21a. Only in their ultrahigh strength QP1500 steel did they note a serrated TRIP exhaustion profile even though this steel deformed homogeneously. We contradict this observation in Chapter 5, in performing a similar experiment on thus QP1500 steel. We note that the TRIP exhaustion of this QP1500 steel has a smooth profile when subjected to a slow tensile strain rate. The serrated flow featured by Park et al. (2019) could be a result of adiabatic specimen heating when subjected to a high strain rate of testing (Nanda et al., 2021). As well, Park et al. (2019) studied the effect different stress states (uniaxial tension, plain strain tension, and balanced biaxial tension) has on TRIP kinetics in Q&P steels, as shown in Figure 2.21b. Contrary to Jacques et al. (2007), who speculated that the largest driving force for the austenite-to-martensite transformation is expected for the plain strain condition, which are the DENT specimens in Figure 2.21a, Park et al. (2019) found an intermediate rate of TRIP exhaustion is featured when the QP980 steel was subjected to plane strain tension ($^{\sigma_m}/_{\sigma_{VM}}$ = 0.62) and slow TRIP kinetics under the balanced biaxial tension ($^{\sigma_m}/_{\sigma_{VM}}$ = 0.67) as shown in Figure 2.21b.

Wu et al. (2018) address the change in local retained austenite volume fraction ($\Delta RAVF$) from different deformation modes and complex loadings/strain paths by stamping a med-10wt% Mn steel into a T-panel. This shape was used to emulate a portion of an anti-intrusion, stamped component in vehicles. Three dimensional DIC was applied to map the ε_2 and ε_1 strains and, as a result, enable the determination the local complex loading (linear versus bi-linear) and deformation mode experienced by med-10wt%Mn steel during the stamping process. After stamping, the T-panel was sectioned into small specimens for HE-XRD scanning based on its deformation mode. Again in contrast to Jacques et al. (2007), the least austenite transformed was featured by the plain strain condition ($\Delta RAVF$ = 11%), and most austenite transformed was featured by the uniaxial tension condition ($\Delta RAVF$ = 53%), both following a linear strain path, as shown in Figure 2.22a and b. The following authors suggest that rather the effective strain (ε_{eff}) governs the TRIP kinetics – overall, they documented that the higher the ε_{eff}, the less stable the austenite against TRIP. The ε_{eff} was calculated using Equation 2.6, and is shown as the dotted lines in Figure 2.22b. The greatest ($\Delta RAVF$ = 59%) was featured by section 8 which exhibited biaxial tension and a bilinear strain path (i.e. an eventual faster increase in ε_2 versus ε_1).

$$\varepsilon_{eff} = \frac{\sqrt{2}}{3}\left((\varepsilon_1 - \varepsilon_2)^2 + (\varepsilon_1 - \varepsilon_3)^2 + (\varepsilon_2 - \varepsilon_3)^2\right)^{1/2} \qquad \text{Equation 2.6}$$

where ε_3 is the thickness strain measured with the assumption volume by $\varepsilon_3 = -(\varepsilon_1 + \varepsilon_2)$

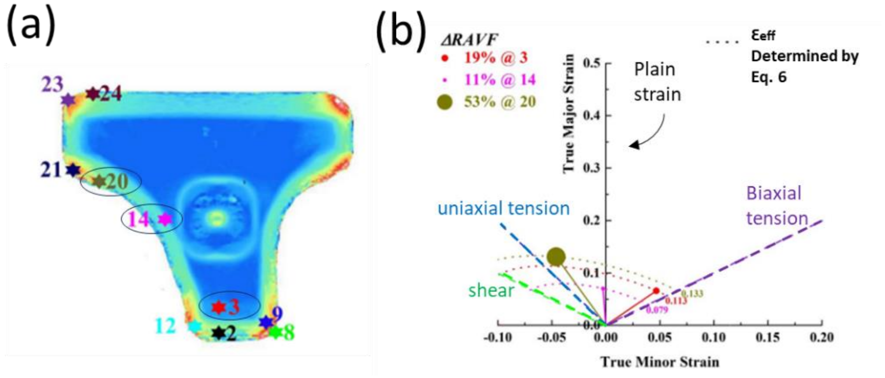

Figure 2.22: Major Strain DIC map of T-Shape panel with regions sectioned for HE-XRD scanning (a) FLD of sections 3, 14 and 20 subjected to different deformation modes all under a linear strain path - biaxial tension, plain strain tension and uniaxial tension, respectively (b)

Nonetheless, TRIP kinetics of a med-Mn steel subjected to different stress-states has been scarcely reported to date in the literature.

2.7 Stress-state impact on Damage in AHSSs

In addition to TRIP kinetics, Bao and Wierzbicki (2004) found early on that tailoring the notch geometry of a sheet metal produces differences in its final mode of fracture as a result of the different stress triaxialities being experienced by the specimens during straining. The notch radius, itself, can be varied to impart different degrees of stress triaxiality (Findley et al., n.d.). Experiments of notched specimens enable one's ability simulate the effect of a stress concentration in a component, e.g. drilled hole, on fracture resistance. (Findley et al., n.d.). For AHSSs the fracture mode is classically ductile, such that fracture is the result of micro-void nucleation and coalescence.

Fabrègue et al. (2015) found that in testing uniaxially, an Interstitial Free (IF), a Mn-rich TWIP and a AUS 316L, that there is a difference in their evolution of triaxiality with increased deformation, and this in turn affected each steel's void growth kinetics (Huang, 1991; Rice and Tracey, 1969). During the uniaxial tensile test, they reported that the triaxiality of specimens for the TWIP steel remains somewhat constant, whereas the IF and AUSs 316L steel specimens featured considerable necking (i.e. increasing triaxiality). As a result, these steels showed an exponential increase in void growth rate, as shown in Figure 2.23. Such study enabled Fabrègue et al. (2015)

to conclude that the rate of void nucleation is high in the Mn-rich TWIP steels, as a result of twins being sufficient void nucleation sites, and any minor growth of such voids can lead to rapid void coalescence and immediate fracture of the steel. Interestingly however, although the AUSs also feature twinning upon being strained, its ability to exhibit a significant proportion of dislocation glide, more than that of the Mn-rich TWIP steel, enables the steel to accommodate a similar void density and ε_f as the IF steel. The IF steel only features dislocation glide upon deformation, and, in theory, its predominant void nucleation site is at grain boundaries (Fabrègue et al., 2015).

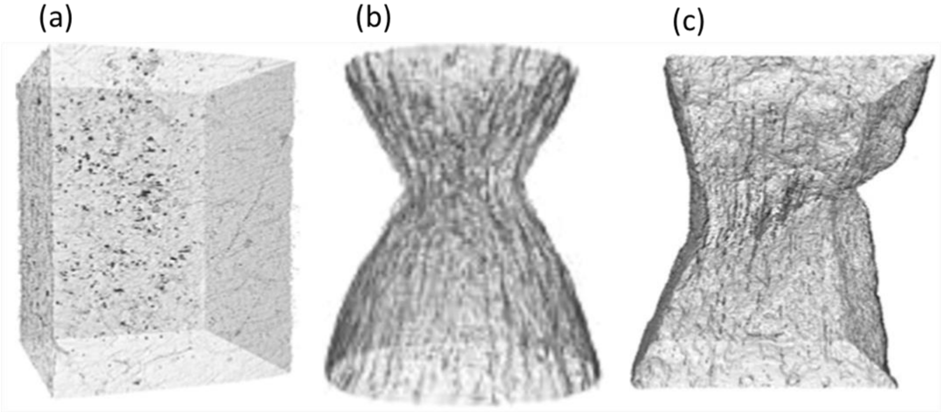

Figure 2.23: Microtomography 3D reconstructions of a Mn-rich TWIP steel (a) an IF steel (b) and a 316L AUSs (c). Adapted from Fabrègue et al. (2015).

More specifically, Scavino et al. (2010) and Lorthios et al. (2010) found that slant-type fracture occurs at whatever the stress-state in steels whose predominate mode of plastic deformation is TWIP. Yet, to guarantee slant-type fracture while pulling TWIP steels in tension, Lorthios et al. (2010) analyzed the damage evolution of a fracture 'butterfly' style specimens, adapted from (Brünig et al., 2008). 'Butterfly' style specimens were used in this scenario to purposefully activate a low stress triaxiality and shear fracture as shown in Figure 2.24a. The sample sectioned at fracture in their work is featured in Figure 2.24b. Similar to (Fabrègue et al., 2015; Huang, 1991; Rice and Tracey, 1969; Samei et al., 2019b), Lorthios et al. (2010) observed using XCT that the low stress triaxiality induced by the butterfly gauge section of the specimen limited the growth rate of voids, and they speculated that any deformation experienced by voids was determined by the surrounding material. The maximum triaxiality their butterfly specimens experienced during straining was only 0.33, which is the initial triaxiality used for conventional testing of uniaxial tensile specimens. Strain localization within the gauge through FEM modelling of these butterfly specimens is shown in Figure 2.24c. Specifically, it was documented that there's scare but significant void growth well below the slant-type fracture surface as a result of the linking of void strings (>10μm) with a preferential elongation along the rolling direction as shown in Figure 2.24d. As a result, these elongated voids did not contribute directly to the fracture surface, and rather microvoids of ~0.5 μm in size were featured on the fracture surface (Lorthios et al., 2010).

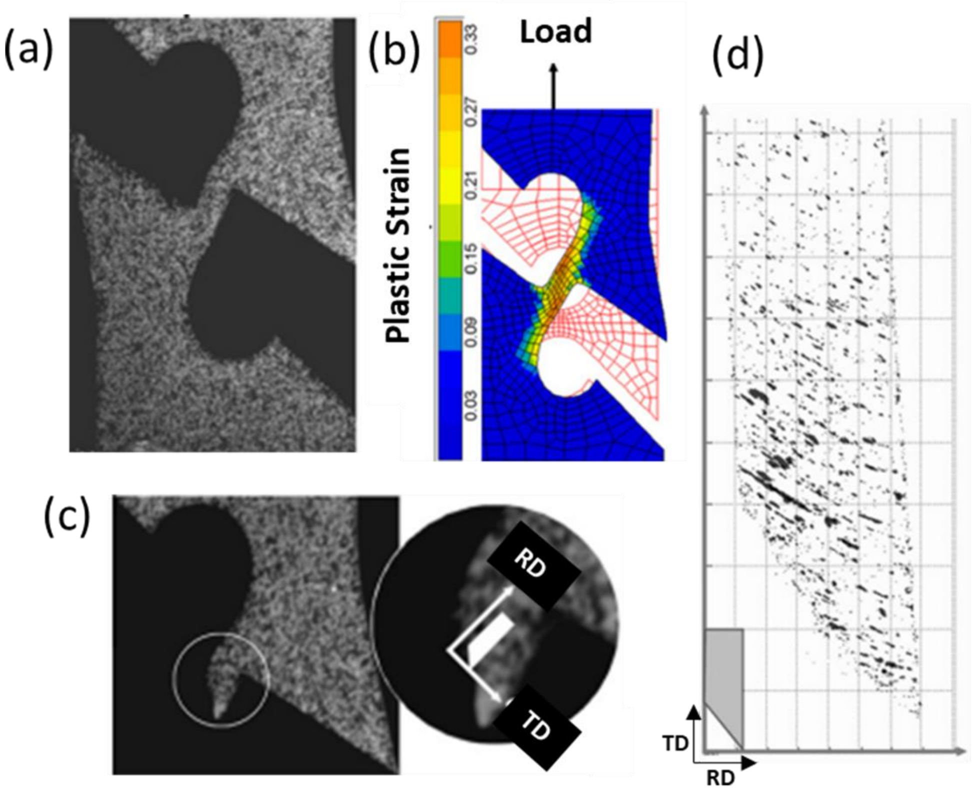

Figure 2.24: Geometry of the 'butterfly' specimen (a), the finite element model of the butterfly specimen being loaded (b), the region sectioned for tomography of the fractured specimen (c) and the 3D reconstruction of voids in this section (d). Adapted from Lorthios et al. (2010).

Similar to the conclusion made in section 2.6, little to no work to date has been devoted to investigating damage in med-Mn steels under different states of stress. To our knowledge, Chapter 7 is the first report of the influence that stress triaxiality has on TRIP kinetics and damage in med-Mn steels.

2.8 References

Abu-Farha, F., Hu, X., Sun, X., Ren, Y., Hector, L.G., Thomas, G., Brown, T.W., 2018. In Situ Local Measurement of Austenite Mechanical Stability and Transformation Behavior in Third-Generation Advanced High-Strength Steels. Metall Mater Trans A Phys Metall Mater Sci 49, 2583–2596. https://doi.org/10.1007/s11661-018-4660-x

Arlazarov, A., Ollat, M., Masse, J.P., Bouzat, M., 2016. Influence of partitioning on mechanical behavior of Q&P steels. Materials Science and Engineering: A 661, 79–86. https://doi.org/10.1016/j.msea.2016.02.071

Ashby, M.F., 1966. Work hardening of dispersion-hardened crystals. Philosophical Magazine 14, 1157–1178. https://doi.org/10.1080/14786436608224282

Azizi, H., Samei, J., Zurob, H.S., Wilkinson, D.S., Embury, D., 2022. A novel approach to producing architectured ultra-high strength dual phase steels. Materials Science and Engineering: A 833. https://doi.org/10.1016/j.msea.2021.142582

Bai, M., Yang, D., Wang, G., Ryu, J., Lee, K., Yi, H., 2020. Enhancing the robustness and efficiency in the production of medium Mn steels by Al addition. Metals (Basel) 10, 1–19. https://doi.org/10.3390/met10111432

Bao, Y., Wierzbicki, T., 2004. On fracture locus in the equivalent strain and stress triaxiality space. Int J Mech Sci 46, 81–98. https://doi.org/10.1016/j.ijmecsci.2004.02.006

Barella, S., Gruttadauria, A., Menezes, J.T.O., Castrodeza, E.M., Quaini, S.E., Pelligra, C., McNally, E.A., 2023. The Reliability of Single-Step and Double-Step Quench and Partitioning Heat Treatments on an AISI 420A Low Carbon Martensitic Stainless Steel. Metallurgical and Materials Transactions A. https://doi.org/10.1007/s11661-023-07145-2

Bellhouse, E.M., 2010. Galvanizing of Al-Si TRIP-Assisted Steels. McMaster University.

Bellhouse, E.M., McDermid, J.R., 2011. Selective Oxidation and Reactive Wetting during Galvanizing of a CMnAl TRIP-Assisted Steel. Metallurgical and Materials Transactions A 42, 2753–2768. https://doi.org/10.1007/s11661-011-0685-0

Bhadeshia, H.K.D.H., 2002. TRIP-Assisted Steels? ISIJ International 42, 1059–1060.

Bhadhon, K., 2022. Mechanical Properties and Galvanizing of Medium-Mn Steel (Doctor of Philosophy). McMaster University, Hamilton.

Bhadhon, K.M.H., Pallisco, D.M., McDermid, J.R., 2023. Continuous Hot-Dip Galvanizing of Medium-Manganese Third-Generation Advanced High-Strength Steels. Steel Res Int. https://doi.org/10.1002/srin.202200898

Bhadhon, K.M.H., Wang, X., McDermid, J.R., 2022. Effects of CGL-compatible thermal processing, starting microstructure, and Sn micro-alloying on the mechanical properties of a medium-Mn third generation advanced high strength steel. Materials Science and Engineering A 833. https://doi.org/10.1016/j.msea.2021.142563

Bleck, W., Brühl, F., Ma, Y., Sasse, C., 2019. Materials and Processes for the Third-generation Advanced High-strength Steels. BHM Berg- und Hüttenmännische Monatshefte 164, 466–474. https://doi.org/10.1007/s00501-019-00904-y

Blondé, R., Jimenez-Melero, E., Zhao, L., Schell, N., Brück, E., van der Zwaag, S., van Dijk, N.H., 2014. The mechanical stability of retained austenite in low-alloyed TRIP steel under shear loading. Materials Science and Engineering: A 594, 125–134. https://doi.org/https://doi.org/10.1016/j.msea.2013.11.001

Bouaziz, Olivier, Zurob, H., Huang, M., 2013. Driving force and logic of development of advanced high strength steels for automotive applications. Steel Res Int 84, 937–947. https://doi.org/10.1002/srin.201200288

Bouaziz, O., Zurob, H., Huang, M., 2013. Driving Force and Logic of Development of Advanced High Strength Steels for Automotive Applications. Steel Res Int 84, 937–947.

Brünig, M., Chyra, O., Albrecht, D., Driemeier, L., Alves, M., 2008a. A ductile damage criterion at various stress triaxialities. Int J Plast 24, 1731–1755. https://doi.org/10.1016/j.ijplas.2007.12.001

Buffière, J.-Y., Maire, E., Cloetens, P., Lormand, G., Fougères, R., 1999. Characterization of internal damage in a MMCp using X-ray synchrotron phase contrast microtomography. Acta Mater 47, 1613–1625. https://doi.org/10.1016/S1359-6454(99)00024-5

Calcagnotto, M., Ponge, D., Raabe, D., 2012. On the Effect of Manganese on Grain Size Stability and Hardenability in Ultrafine-Grained Ferrite/Martensite Dual-Phase Steels. Metallurgical and Materials Transactions A 43, 37–46. https://doi.org/10.1007/s11661-011-0828-3

Cao, W.Q., Wang, C., Shi, J., Wang, M.Q., Hui, W.J., Dong, H., 2011. Microstructure and mechanical properties of Fe-0.2C-5Mn steel processed by ART-annealing. Materials Science and Engineering A 528, 6661–6666. https://doi.org/10.1016/j.msea.2011.05.039

Carter, J.L.W., Uchic, M.D., Mills, M.J., 2015. Impact of Speckle Pattern Parameters on DIC Strain Resolution Calculated from In-situ SEM Experiments. Conference Proceedings of the Society for Experimental Mechanics Series 66, 119–126. https://doi.org/10.1007/978-3-319-06977-7_16

Casellas, D., Lara, A., Frómeta, D., Gutiérrez, D., Molas, S., Pérez, L., Rehrl, J., Suppan, C., 2017. Fracture Toughness to Understand Stretch-Flangeability and Edge Cracking Resistance in AHSS. Metall Mater Trans A Phys Metall Mater Sci 48, 86–94. https://doi.org/10.1007/s11661-016-3815-x

Celada-Casero, C., Vercruysse, F., Linke, B., Smith, A., Kok, P., Sietsma, J., Santofimia, M.J., 2022. Analysis of work hardening mechanisms in Quenching and Partitioning steels combining experiments with a 3D micro-mechanical model. Materials Science and Engineering: A 846, 143301. https://doi.org/10.1016/j.msea.2022.143301

Chatterjee, B., 2015. Science and Industry of Electropolishing. Galvanotechnik 71, 71–93.

Cheloee Darabi, A., Guski, V., Butz, A., Kadkhodapour, J., Schmauder, S., 2020. A comparative study on mechanical behavior and damage scenario of DP600 and DP980 steels. Mechanics of Materials 143, 103339. https://doi.org/https://doi.org/10.1016/j.mechmat.2020.103339

Chen, C.Y., Chiang, L.J., Chen, C.C., Liao, M.H., Kuo, J.S., Chou, Y.H., 2020. Exploring How (Ti + Mo)/C and Ti/Mo Influence the Precipitation Behaviors within Microalloyed Steels: Experimental Evidence and Related Patents Investigation. J Mater Eng Perform 29, 1882–1891. https://doi.org/10.1007/S11665-020-04608-0/FIGURES/10

Chen, X., Jiang, H., Cui, Z., Lian, C., Lu, C., 2014. Hole expansion characteristics of ultra high strength steels. Procedia Eng 81, 718–723. https://doi.org/10.1016/j.proeng.2014.10.066

Choi, H., Lee, S., Lee, J., Barlat, F., De Cooman, B.C., 2017. Characterization of fracture in medium Mn steel. Materials Science and Engineering: A 687, 200–210. https://doi.org/10.1016/j.msea.2017.01.055

Christian, J.W., 1982. Deformation By Moving Interfaces. Metallurgical transactions. A, Physical metallurgy and materials science 13 A, 509–538. https://doi.org/10.1007/BF02644415

Cotterell, B., Reddel, J.K., 1977. The essential work of plane stress ductile fracture. Int J Fract 13, 267–277. https://doi.org/10.1007/BF00040143

Courtney, T.H., 2005. Mechanical Behavior of Materials, 2nd ed. Waveland Press, Inc., Long Grove, Illinois.

Dai, Z., Chen, H., Ding, R., Lu, Q., Zhang, C., Yang, Z., van der Zwaag, S., 2021. Fundamentals and application of solid-state phase transformations for advanced high strength steels containing metastable retained austenite. Materials Science and Engineering: R: Reports 143, 100590. https://doi.org/10.1016/j.mser.2020.100590

Datsko, J., Yang, C.T., 1960. Correlation of Bendability of Materials With Their Tensile Properties. Journal of Engineering for Industry 309–313.

De Cooman, B., Kwon, O., Chin, K., 2012. State-of-the-knowledge on TWIP steel. Materials Science and Technology 28, 513–527. https://doi.org/10.1179/1743284711Y.0000000095

De Cooman, B.C., Speer, J.G., 2006. Quench and Partitioning Steel: A New AHSS Concept for Automotive Anti-Intrusion Applications. Steel Res Int 77, 634–640. https://doi.org/10.1002/srin.200606441 de Diego-Calderón, I., Sabirov, I., Molina-Aldareguia, J.M., Föjer, C., Thiessen, R., Petrov, R.H., 2016. Microstructural design in quenched and partitioned (Q&P) steels to improve their fracture properties. Materials Science and Engineering: A 657, 136–146. https://doi.org/10.1016/j.msea.2016.01.011

De Meyer, M., Vanderschueren, D., De Cooman, B., 2000. The Influence of Al on the Properties of Cold Rolled C-Mn-Si TRIP Steels. IRON AND STEELMAKER 27, 55–63.

De Moor, Emmanuel, Gibbs, P., Speer, J.G., Matlock, D., Schroth, J.G., 2010. Strategies for third-generation advanced high-strength steel development. Iron and Steel Technology 7, 133–144.

De Moor, E., Matlock, D.K., Speer, J.G., Merwin, M.J., 2011. Austenite stabilization through manganese enrichment. Scr Mater 64, 185–188. https://doi.org/10.1016/j.scriptamat.2010.09.040

Denks, I.A., Schneider, M., Westhäuser, S., Lesch, C., 2019. On the Correlation between Suitable Material Parameters for the Prediction of Local Formability of Advanced High Strength Steels. Steel Res Int 90. https://doi.org/10.1002/srin.201800460

Di Gioacchino, F., Quinta da Fonseca, J., 2013. Plastic Strain Mapping with Sub-micron Resolution Using Digital Image Correlation. Exp Mech 53, 743–754. https://doi.org/10.1007/s11340-012-9685-2

Dieter, G.E.Jr., 1961. Metallurgy and Metallurgical Engineering Series. McGraw Hill Book Company, New York.

Dong, Y.L., Pan, B., 2017. A Review of Speckle Pattern Fabrication and Assessment for Digital Image Correlation. Exp Mech 57, 1161–1181. https://doi.org/10.1007/s11340-017-0283-1

Du, P.J., Yang, D.P., Bai, M.K., Xiong, X.C., Wu, D., Wang, G.D., Yi, H.L., 2019. Austenite stabilisation by two step partitioning of manganese and carbon in a Mn-TRIP steel. Materials Science and Technology (United Kingdom) 35, 2084–2091. https://doi.org/10.1080/02670836.2019.1572316

Dumay, A., Chateau, J.-P., Allain, S., Migot, S., Bouaziz, O., 2008. Influence of addition elements on the stacking-fault energy and mechanical properties of an austenitic Fe–Mn–C steel. Materials Science and Engineering: A 483–484, 184–187. https://doi.org/10.1016/j.msea.2006.12.170

Dutta, A., Ponge, D., Sandlöbes, S., Raabe, D., 2019. Strain partitioning and strain localization in medium manganese steels measured by in situ microscopic digital image correlation. Materialia (Oxf) 5. https://doi.org/10.1016/j.mtla.2019.100252

Dutta, A., Ponge, D., Sandlöbes, S., Raabe, D., 2018. Understanding Hot vs. Cold Rolled Medium Manganese Steel Deformation Behavior Using In Situ Microscopic Digital Image Correlation. Materials Science Forum 941, 198–205. https://doi.org/10.4028/WWW.SCIENTIFIC.NET/MSF.941.198

Enloe, C.M., Coryell, J., Wang, J., 2017. Retained Austenite Stability and Impact Performance of Advanced High Strength Steel at Reduced Temperatures. SAE International Journal of Materials and Manufacturing 10, 2017-01–1707. https://doi.org/10.4271/2017-01-1707

Fabrègue, D., Landron, C., Bouaziz, O., Maire, E., 2015. Comparison of Damage Evolution in Different Steels by Means of 3D X Ray Tomography. Steel Res Int 86, 1197–1203. https://doi.org/10.1002/srin.201500072

Fabrègue, D., Landron, C., Bouaziz, O., Maire, E., 2013. Damage evolution in TWIP and standard austenitic steel by means of 3D X ray tomography. Materials Science and Engineering: A 579, 92–98. https://doi.org/10.1016/J.MSEA.2013.05.013

Findley, K.O., Golem, L.L., Cho, L., Clarke, K.D., n.d. Evaluating crash relevant properties of advanced high strength steels.

Findley, K.O., Hidalgo, J., Huizenga, R.M., Santofimia, M.J., 2017. Controlling the work hardening of martensite to increase the strength/ductility balance in quenched and partitioned steels. Mater Des 117, 248–256. https://doi.org/10.1016/j.matdes.2016.12.065

Fonstein, N., 2015. Advanced high strength sheet steels: Physical metallurgy, design, processing, and properties, 1st ed, Advanced High Strength Sheet Steels: Physical Metallurgy, Design, Processing, and Properties. Springer. https://doi.org/10.1007/978-3-319-19165-2

Frómeta, D., Lara, A., Grifé, L., Dieudonné, T., Dietsch, P., Rehrl, J., Suppan, C., Casellas, D., Calvo, J., 2021. Fracture Resistance of Advanced High-Strength Steel Sheets for Automotive Applications. Metall Mater Trans A Phys Metall Mater Sci 52, 840–856. https://doi.org/10.1007/s11661-020-06119-y

Frómeta, D., Lara, A., Parareda, S., Casellas, D., 2019. Evaluation of edge formability in high strength sheets through a fracture mechanics approach, in: AIP Conference Proceedings. https://doi.org/10.1063/1.5112704

Frómeta, D., Tedesco, M., Calvo, J., Lara, A., Molas, S., Casellas, D., 2017. Assessing edge cracking resistance in AHSS automotive parts by the Essential Work of Fracture methodology. J Phys Conf Ser 896, 012102. https://doi.org/10.1088/1742-6596/896/1/012102

Frommeyer, G., Brüx, U., 2006. Microstructures and mechanical properties of high-strength Fe-Mn-Al-C light-weight TRIPLEX steels. Steel Res Int 77, 627–633. https://doi.org/10.1002/srin.200606440

Frommeyer, G., Brüx, U., Neumann, P., 2003. Supra-Ductile and High-Strength Manganese-TRIP/TWIP Steels for High Energy Absorption Purposes. ISIJ International 43, 438–446. https://doi.org/10.2355/isijinternational.43.438

Furukawa, T., Huang, H., Matsumura, O., 1994. Effects of carbon content on mechanical properties of 5%Mn steels exhibiting transformation induced plasticity. Materials Science and Technology 10, 964–970. https://doi.org/10.1179/mst.1994.10.11.964

Gao, B., Lai, Q., Cao, Y., Hu, R., Xiao, L., Pan, Z., Liang, N., Li, Y., Sha, G., Liu, M., Zhou, H., Wu, X., Zhu, Y., 2020. Ultrastrong low-carbon nanosteel produced by heterostructure and interstitial mediated warm rolling. Sci Adv 6. https://doi.org/10.1126/sciadv.aba8169

Gibbs, P.J., De Cooman, B.C., Brown, D.W., Clausen, B., Schroth, J.G., Merwin, M.J., Matlock, D.K., 2014. Strain partitioning in ultra-fine grained medium-manganese transformation induced plasticity steel. Materials Science and Engineering: A 609, 323–333. https://doi.org/10.1016/j.msea.2014.03.120

Gibbs, P.J., De Moor, E., Merwin, M.J., Clausen, B., Speer, J.G., Matlock, D.K., 2011. Austenite Stability Effects on Tensile Behavior of Manganese-Enriched-Austenite Transformation-Induced Plasticity Steel. Metallurgical and Materials Transactions A 42, 3691–3702. https://doi.org/10.1007/s11661-011-0687-y

Girault, E., Mertens, A., Jacques, P., Houbaert, Y., Verlinden, B., Van Humbeeck, J., 2001. Comparison of the Effects of Silicon and Aluminium on the Tensile Behaviour of Multiphase Trip-Assisted Steels. Scr Mater 44, 885–892.

Guo, Q., Yen, H.-W., Luo, H., Ringer, S.P., 2022. On the mechanism of Mn partitioning during intercritical annealing in medium Mn steels. Acta Mater 225, 117601. https://doi.org/10.1016/j.actamat.2021.117601

Guo, Y., Britton, T.B., Wilkinson, A.J., 2014. Slip band–grain boundary interactions in commercial-purity titanium. Acta Mater 76, 1–12. https://doi.org/10.1016/j.actamat.2014.05.015

Hall, J., 2015. The impact of new steel technology on automotive lightweighting. CAR MBS.

Hance, B., 2018. Advanced High-Strength Steel (AHSS) Performance Level Definitions and Targets, in: SAE International Journal of Materials and Manufacturing. pp. 2018-01–0629. https://doi.org/10.4271/2018-01-0629

Hance, B., 2016. Advanced high strength steel: Deciphering local and global formability. International Automotive Body Congress, IABC 2016 DEARBORN - Papers.

Hance, B.M., Comstock, R.J., Scherrer, D.K., 2013. The influence of edge preparation method on the hole expansion performance of automotive sheet steels. SAE Technical Papers 2. https://doi.org/10.4271/2013-01-1167

Hasegawa, K., Kawamura, K., Urabe, T., Hosoya, Y., 2004. Effects of microstructure on stretch-flange-formability of 980 MPa grade cold-rolled ultra high strength steel sheets. ISIJ International 44, 603–609. https://doi.org/10.2355/isijinternational.44.603

Hatem, T.M., Zikry, M.A., 2011. A model for determining initial dislocation-densities associated with martensitic transformations. Materials Science and Technology 27, 1570–1573. https://doi.org/10.1179/1743284711Y.0000000079

He, B.B., Wang, M., Huang, M.X., 2019. Resetting the Austenite Stability in a Medium Mn Steel via Dislocation Engineering. Metallurgical and Materials Transactions A 50, 2971–2977. https://doi.org/10.1007/s11661-019-05222-z

He, X.J., Terao, N., Berghezan, A., 1984. Influence of martensite morphology and its dispersion on mechanical properties and fracture mechanisms of Fe-Mn-C dual phase steels. Metal Science 18, 367–373. https://doi.org/10.1179/030634584790419953

Hill, R., 1952. On discontinuous plastic states, with special reference to localized necking in thin sheets. J Mech Phys Solids 1, 19–30. https://doi.org/10.1016/0022-5096(52)90003-3

Hoefnagels, J.P.M., van Maris, M.P.F.H.L., Vermeij, T., 2019. One-step deposition of nano-to-micron-scalable, high-quality digital image correlation patterns for high-strain in-situ multi-microscopy testing. Strain 55. https://doi.org/10.1111/str.12330

Hofmann, H., Mattissen, D., Schaumann, T.W., 2006. Advanced cold rolled steels for automotive applications. Materwiss Werksttech 37, 716–723. https://doi.org/10.1002/mawe.200600057

Hu, B., Luo, H., Yang, F., Dong, H., 2017. Recent progress in medium-Mn steels made with new designing strategies, a review. J Mater Sci Technol 33, 1457–1464. https://doi.org/10.1016/j.jmst.2017.06.017

Hu, X.H., Sun, X., Hector, L.G., Ren, Y., 2017a. Individual phase constitutive properties of a TRIP-assisted QP980 steel from a combined synchrotron X-ray diffraction and crystal plasticity approach. Acta Mater 132, 230–244. https://doi.org/10.1016/J.ACTAMAT.2017.04.028

Huang, Y., 1991. Accurate Dilatation Rates for Spherical Voids in Triaxial Stress Fields. J Appl Mech 58, 1084–1086.

Hudgins, A.W., Matlock, D.K., 2016. The effects of property differences in multiphase sheet steels on local formability. Materials Science and Engineering: A 654, 169–176. https://doi.org/10.1016/j.msea.2015.12.035

Iacono, C., Sinke, J., Benedictus, R., 2010. Prediction of minimum bending ratio of aluminum sheets from tensile material properties. J Manuf Sci Eng 132, 0210011–0210019. https://doi.org/10.1115/1.4000960

International Council for Clean Transportation. Global comparison of passenger car and light commercial vehicle fuel economy/ghg emissions standards. [WWW Document], 2017. The International Council on Clean Transportation (ICCT).

Jacques, P., Furnemount, Q., Pardoen, T., Delannay, F., 2001. On the Role of Martensitic Transformation on Damage and Cracking Resistance in Trip-assisted multiphase steels. Acta Mater 49, 139–152. https://doi.org/10.1016/S1359-6454(00)00215-9

Jacques, P.J., 2004. Transformation-induced plasticity for high strength formable steels. Curr Opin Solid State Mater Sci 8, 259–265. https://doi.org/10.1016/j.cossms.2004.09.006

Jacques, P.J., Delannay, F., Ladrière, J., 2001. On the influence of interactions between phases on the mechanical stability of retained austenite in transformation-induced plasticity multiphase steels. Metall Mater Trans A Phys Metall Mater Sci 32, 2759–2768. https://doi.org/10.1007/s11661-001-1027-4

Jacques, P.J., Furnémont, Q., Lani, F., Pardoen, T., Delannay, F., 2007. Multiscale mechanics of TRIP-assisted multiphase steels: I. Characterization and mechanical testing. https://doi.org/10.1016/j.actamat.2007.02.029

Jiang, Z., Guan, Z., Lian, J., 1995. Effects of microstructural variables on the deformation behaviour of dual-phase steel. Materials Science and Engineering: A 190, 55–64. https://doi.org/https://doi.org/10.1016/0921-5093(94)09594-M

Jin, H., Lu, W.-Y., Korellis, J., 2008. Micro-scale deformation measurement using the digital image correlation technique and scanning electron microscope imaging. J Strain Anal Eng Des 43, 719–728. https://doi.org/10.1243/03093247JSA412

Kang, J., Ososkov, Y., Embury, D.J., Wilkinson, D.S., 2007. Digital image correlation studies for microscopic strain distribution and damage in dual phase steels. Scr Mater 56, 999–1002. https://doi.org/10.1016/j.scriptamat.2007.01.031

Kang, J., Wilkinson, D.S., Embury, J.D., Jain, M., 2005. Microscopic Strain Mapping Using Scanning Electron Microscopy Topography Image Correlation at Large Strain. J Strain Anal Eng Des 40, 559–570. https://doi.org/10.1243/030932405X16151

Kardes Sever, N., 2022. Material characterisation for strength and formability limits of DP 1180 sheet. Canadian Metallurgical Quarterly 61, 282–291. https://doi.org/10.1080/00084433.2022.2044687

Karelova, A., Krempaszky, C., Werner, E., Tsipouridis, P., Hebesberger, T., Pichler, A., 2009. Hole expansion of dual-phase and complex-phase AHS steels - Effect of edge conditions. Steel Res Int 80. https://doi.org/10.2374/SRI08SP110

Kong, H., Chao, Q., Cai, M.H., Pavlina, E.J., Rolfe, B., Hodgson, P.D., Beladi, H., 2017. One-step quenching and partitioning treatment of a commercial low silicon boron steel. Materials Science and Engineering A 707, 538–547. https://doi.org/10.1016/j.msea.2017.09.038

Krizan, D., Steineder, K., Kaar-Schickinger, S., Hebesberger, T., 2018. DEVELOPMENT OF THIRD GENERATION ADVANCED HIGH STRENGTH STEELS FOR AUTOMOTIVE APPLICATIONS.

Kuziak, R., Kawalla, R., Waengler, S., 2008. Advanced high strength steels for automotive industry. Archives of Civil and Mechanical Engineering 8, 103–117. https://doi.org/10.1016/S1644-9665(12)60197-6

Landron, C., Bouaziz, O., Maire, E., Adrien, J., 2010. Characterization and modeling of void nucleation by interface decohesion in dual phase steels. Scr Mater 63, 973–976. https://doi.org/10.1016/j.scriptamat.2010.07.021

Larour, P., Freudenthaler, J., Weissböck, T., 2017. Reduction of cross section area at fracture in tensile test: Measurement and applications for flat sheet steels. J Phys Conf Ser 896. https://doi.org/10.1088/1742-6596/896/1/012073

Lee, S., Lee, S.-J., De Cooman, B.C., 2011. Austenite stability of ultrafine-grained transformation-induced plasticity steel with Mn partitioning. Scr Mater 65, 225–228. https://doi.org/10.1016/j.scriptamat.2011.04.010

Lee, Y.-K., Lee, S.-J., Han, J., 2016. Critical assessment 19: stacking fault energies of austenitic steels. Materials Science and Technology 32, 1–8. https://doi.org/10.1080/02670836.2015.1114252

Lian, C., Zhang, H., Lin, J., Wang, L., 2021. Deformation mechanism and microstructure evolution of medium-Mn AHSS under various loading conditions. Int J Mech Sci 212. https://doi.org/10.1016/j.ijmecsci.2021.106812

Lin, B., Fan, D.P., Liu, S., 2023. The Influence of Testing Parameters on Hole Expansion of a 980 MPa Steel. International Symposium on New Developments in Advanced High-Strength Sheet Steels.

Lin, G., Jack Hu, S., Cai, W., 2009. Evaluation of formability in bending/hemming of aluminum alloys using plane-strain tensile tests. J Manuf Sci Eng 131, 0510091–0510099. https://doi.org/10.1115/1.3123316

Liu, J., Chen, C., Feng, Q., Fang, X., Wang, H., Liu, F., Lu, J., Raabe, D., 2017. Dislocation activities at the martensite phase transformation interface in metastable austenitic stainless steel: An in-situ TEM study, Materials Science and Engineering A. https://doi.org/10.1016/j.msea.2017.06.107

Liu, L., He, B., Huang, M., 2018. The Role of Transformation-Induced Plasticity in the Development of Advanced High Strength Steels. Adv Eng Mater 20. https://doi.org/10.1002/adem.201701083

Liu, L., Li, L., Liang, Z., Huang, M., Peng, Z., Gao, J., Luo, Z., 2023. Towards ultra-high strength dual-phase steel with excellent damage tolerance: The effect of martensite volume fraction. Int J Plast 170, 103778. https://doi.org/10.1016/j.ijplas.2023.103778

Lorthios, J., Nguyen, F., Gourgues, A.-F., Morgeneyer, T.F., Cugy, P., 2010. Damage observation in a high-manganese austenitic TWIP steel by synchrotron radiation computed tomography. Scr Mater 63, 1220–1223. https://doi.org/10.1016/j.scriptamat.2010.08.042

Lu, J., Hultman, L., Holmström, E., Antonsson, K.H., Grehk, M., Li, W., Vitos, L., Golpayegani, A., 2016. Stacking fault energies in austenitic stainless steels. Acta Mater 111, 39–46. https://doi.org/10.1016/j.actamat.2016.03.042

Luo, H., Dong, H., 2015. New ultrahigh-strength Mn-alloyed TRIP steels with improved formability manufactured by intercritical annealing. Materials Science and Engineering: A 626, 207–212. https://doi.org/10.1016/j.msea.2014.12.049

Luo, H., Dong, H., Huang, M., 2015. Effect of intercritical annealing on the Lüders strains of medium Mn transformation-induced plasticity steels. Mater Des 83, 42–48. https://doi.org/10.1016/j.matdes.2015.05.085

Luo, Y., Ruff, J., Ray, R., Gu, Y., Ploehn, H., Scrivens, W., 2005. Vapor-Assisted Remodeling of Thin Gold Films. Chemistry of Materials 17. https://doi.org/10.1021/cm051127w

Ma, Y., Sun, B., Schökel, A., Song, W., Ponge, D., Raabe, D., Bleck, W., 2020. Phase boundary segregation-induced strengthening and discontinuous yielding in ultrafine-grained duplex medium-Mn steels. Acta Mater 200, 389–403. https://doi.org/10.1016/j.actamat.2020.09.007

Magee, C.L., Davies, R.G., 1971. The structure, deformation and strength of ferrous martensites. Acta Metallurgica 19, 345–354. https://doi.org/10.1016/0001-6160(71)90102-7

Matlock, D., Speer, J.G., 2006. Design considerations for the next generation of advanced high strength sheet steels. Proceedings of the Third International Conference on Advanced Structural Steels 774–781.

Matlock, D.K., Speer, J.G., 2009. Microstructure and Texture in Steels. Springer London, London. https://doi.org/10.1007/978-1-84882-454-6

Matlock, David K., Speer, J.G., 2009. Third Generation of AHSS: Microstructure Design Concepts, in: Microstructure and Texture in Steels. Springer London, London, pp. 185–205. https://doi.org/10.1007/978-1-84882-454-6_11

Matlock, D.K., Speer, J.G., Moor, E. De, Gibbs, P.J., 2012. Recent developments in advanced high strength sheet steels for automotive applications: An overview. International Iron and Steel Symposium.

McDermid, J.R., Zurob, H.S., Bian, Y., 2011. Stability of Retained Austenite in High-Al, Low-Si TRIP-Assisted Steels Processed via Continuous Galvanizing Heat Treatments. Metallurgical and Materials Transactions A 42, 3627–3637. https://doi.org/10.1007/s11661-011-0678-z

McGarth, M.C., Van Aken, D., 2012. Development of Third Generation Advanced High Strength Steels (ProQuest Dissertations & Theses Global). Missouri University of Science and Technology.

Mori, K., Abe, Y., Suzui, Y., 2010. Improvement of stretch flangeability of ultra high strength steel sheet by smoothing of sheared edge. J Mater Process Technol 210, 653–659. https://doi.org/10.1016/j.jmatprotec.2009.11.014

Mummery, P.M., Anderson, P., Davis, G.R., Derby, B., Elliott, J.C., 1993. Damage assessment in particle-reinforced metal matrix composites using x-ray microtomography. Scripta Metallurgica et Materiala 29, 1457–1462.

Mummery, P.M., Derby, B., 1994. In situ scanning electron microscope studies of fracture in particulate-reinforced metal-matrix composites. J Mater Sci 29, 5615–5624. https://doi.org/10.1007/BF00349956

Nanda, T., Singh, V., Singh, G., Singh, M., Kumar, B.R., 2021. Processing routes, resulting microstructures, and strain rate dependent deformation behaviour of advanced high strength steels for automotive applications. Archives of Civil and Mechanical Engineering 21. https://doi.org/10.1007/s43452-020-00149-4

Noh, H.-S., Kang, J.-H., Kim, K.-M., Kim, S.-J., 2019. Different Effects of Ni and Mn on Thermodynamic and Mechanical Stabilities in Cr-Ni-Mn Austenitic Steels. Metallurgical and Materials Transactions A 50, 616–624. https://doi.org/10.1007/s11661-018-5042-0

Oh, H.S., Biggs, K., Güvenç, O., Ghassemi-Armaki, H., Pottore, N., Tasan, C.C., 2021. In-situ investigation of strain partitioning and microstructural strain path development up to and beyond necking. Acta Mater 215. https://doi.org/10.1016/j.actamat.2021.117023

Oliver, S., Jones, T.B., Fourlaris, G., 2007. Dual phase versus TRIP strip steels: Microstructural changes as a consequence of quasi-static and dynamic tensile testing. Mater Charact 58, 390–400. https://doi.org/10.1016/j.matchar.2006.07.004

Olson, G.B., Cohen, M., 1975. Kinetics of strain-induced martensitic nucleation. Metallurgical Transactions A 6, 791–795. https://doi.org/10.1007/BF02672301

Ososkov, Y., Wilkinson, D.S., Jain, M., Simpson, T., 2007. In - situ measurement of local strain partitioning in a commercial dual - phase steel. Int. J. Mat. Res. 98, 664–673. https://doi.org/10.3139/146.101526

Pallisco, D.M., 2021. Galvanizing of Medium-Mn Advanced High Strength Steel (PhD Thesis). McMaster University , Hamilton.

Pallisco, D.M., McDermid, J.R., 2023. On the Selective Oxidation of a 0.15C-6Mn-2Al-1Si Third-Generation Advanced High Strength Steel During Two-Stage Annealing Treatments. Metall Mater Trans A Phys Metall Mater Sci. https://doi.org/10.1007/s11661-023-06985-2

Pallisco, D.M., McDermid, J.R., 2020. Mechanical property development of a 0.15C–6Mn–2Al–1Si third-generation advanced high strength steel using continuous galvanizing heat treatments. Materials Science and Engineering A 778, 139111. https://doi.org/10.1016/j.msea.2020.139111

Pan, B., Qian, K., Xie, H., Asundi, A., 2009. Two-dimensional digital image correlation for in-plane displacement and strain measurement: A review. Meas Sci Technol 20. https://doi.org/10.1088/0957-0233/20/6/062001

Pardoen, T., Marchal, Y., Delannay, F., 2002. Essential work of fracture compared to fracture mechanics—towards a thickness independent plane stress toughness. Eng Fract Mech 69, 617–631. https://doi.org/10.1016/S0013-7944(01)00099-6

Park, K.-T., Han, S.Y., Ahn, B.D., Shin, D.H., Lee, Y.K., Um, K.K., 2004. Ultrafine grained dual phase steel fabricated by equal channel angular pressing and subsequent intercritical annealing. Scr Mater 51, 909–913. https://doi.org/https://doi.org/10.1016/j.scriptamat.2004.06.017

Park, K.-T., Lee, Y., Shin, D., 2005. Fabrication of Ultrafine Grained Ferrite/Martensite Dual Phase Steel by Severe Plastic Deformation. Isij International - ISIJ INT 45, 750–755. https://doi.org/10.2355/isijinternational.45.750

Park, M.H., Shibata, A., Tsuji, N., 2020. Challenging Ultra Grain Refinement of Ferrite in Low-C Steel Only by Heat Treatment. Front Mater 7, 604792. https://doi.org/10.3389/FMATS.2020.604792/BIBTEX

Park, N., Huh, H., Nam, J.B., Jung, C.G., 2015. Anisotropy effect on the fracture model of DP980 sheets considering the loading path. International Journal of Automotive Technology 16, 73–81. https://doi.org/10.1007/s12239-015-0008-3

Park, T., Hector Jr., L.G., Hu, X., Abu-Farha, F., Fellinger, M.R., Kim, H., Esmaeilpour, R., Pourboghrat, F., 2019. Crystal plasticity modeling of 3rd generation multi-phase AHSS with martensitic transformation. International Journal of Plasticity 120, 1–46.

Parker, E.R., Zackay, V.F., 1973. Enhancement of Fracture Toughness in High Strength Steel By Microstructural Control. Engineering Fract Mechanics 5, 147–165.

Patel, J R, Cohen, M., 1953. Criterion for the action of applied stress in the martensitic transformation. Acta Metallurgica 1, 531–538. https://doi.org/https://doi.org/10.1016/0001-6160(53)90083-2

Patel, J.R., Cohen, M., 1953. Criterion for the action of applied stress in the martensitic transformation. Acta Metallurgica 1, 531–538. https://doi.org/10.1016/0001-6160(53)90083-2

Patel, V., 2019. Microstructure and Mechanical Properties of Medium Mn steel (Master of Science). McMaster University, Hamilton.

Patra, A.K., Athreya, C.N., Mandal, S., Hari Kumar, K.C., Subramanya Sarma, V., 2021. High strength-high ductility medium Mn steel obtained through CALPHAD based alloy design and thermomechanical processing. Materials Science and Engineering: A 810, 140756. https://doi.org/10.1016/j.msea.2021.140756

Paul, S.K., 2013. Effect of martensite volume fraction on stress triaxiality and deformation behavior of dual phase steel. Mater Des 50, 782–789. https://doi.org/10.1016/J.MATDES.2013.03.096

Pelligra, C., Samei, J., Kang, J., Wilkinson, D.S., 2022. The effect of vanadium on microstrain partitioning and localized damage during deformation of unnotched and notched DP1300 steels. Int J Plast 158. https://doi.org/10.1016/j.ijplas.2022.103435

Pereloma, Elena., Edmonds, D. V., 2012. Diffusionless transformations, high strength steels, modelling and advanced analytical techniques. Woodhead Pub.

Pereloma, E. V., Gazder, A.A., Timokhina, I.B., 2016. Retained austenite: transformation-induced plasticity. University of Wollongong Australia.

Polatidis, E., Haidemenopoulos, G.N., Krizan, D., Aravas, N., Panzner, T., Smíd, M.ˇ, Papadioti, I., Casati, N., Van Petegem, S., Van Swygenhoven, H., 2020. The effect of stress triaxiality on the phase transformation in transformation induced plasticity steels: Experimental investigation and modelling the transformation kinetics. https://doi.org/10.1016/j.msea.2020.140321

Pourmajidian, M., McDermid, J.R., 2019. On the reactive wetting of a medium-Mn advanced high-strength steel during continuous galvanizing. Surf Coat Technol 357, 418–426. https://doi.org/10.1016/j.surfcoat.2018.10.028

Pushkareva, I., Scott, C., Goune, M., Valle, N., 2013. Distribution of Carbon in Martensite During Quenching and Tempering Dual Phase Steels and Consequences for Damage Properties. ISIJ International 53, 1215–1223.

Pushkareva, I., Shalchi-Amirkhiz, B., Allain, S.Y.P., Geandier, G., Fazeli, F., Sztanko, M., Scott, C., 2020. The influence of vanadium additions on isothermally formed bainite microstructures in medium carbon steels containing retained austenite. Metals (Basel) 10. https://doi.org/10.3390/met10030392

Qin, B., Bhadeshia, H.K.D.H., 2007. Crystallography of TWIP Steel. Graduate Institute of Ferrous Technology. Pohang University of Science and Technology. https://doi.org/10.1002/bmb.15

Qi-Xun, D., Xiao-Nong, W.A.-D.C., Xin-Min, L., 2002. Stacking fault energy of cryogenic austenitic steels. Chinese Physics 11, 315. https://doi.org/10.1088/1009-1963/11/6/315

Raabe, D., Ponge, D., Dmitrieva, O., Sander, B., 2009. Nanoprecipitate-hardened 1.5 GPa steels with unexpected high ductility. Scr Mater 60, 1141–1144. https://doi.org/10.1016/j.scriptamat.2009.02.062

Raabe, D., Sachtleber, M., Weiland, H., Scheele, G., Zhao, Z., 2003. Grain-scale micromechanics of polycrystal surfaces during plastic straining. Acta Mater 51, 1539–1560. https://doi.org/10.1016/S1359-6454(02)00557-8

Rajan, V.P., Rossol, M.N., Zok, F.W., 2012. Optimization of Digital Image Correlation for High-Resolution Strain Mapping of Ceramic Composites. Exp Mech 1407–1421.

Ramisetti, N., Fan, D., 2018. The impact of diffusible hydrogen on the formability of Galvannealed DP980 steel.

Rice, J.R., Tracey, D.M., 1969. On the ductile enlargement of voids in triaxial stress fields*. J Mech Phys Solids 17, 201–217. https://doi.org/10.1016/0022-5096(69)90033-7

Ruggles, T., Cluff, S., Miles, M., Fullwood, D., Daniels, C., Avila, A., Chen, M., 2016. Ductility of Advanced High-Strength Steel in the Presence of a Sheared Edge. JOM 68, 1839–1849. https://doi.org/10.1007/s11837-016-1927-9

Ryu, J.H., Kim, J.I., Kim, H.S., Oh, C.-S., Bhadeshia, H.K.D.H., Suh, D.-W., 2013. Austenite stability and heterogeneous deformation in fine-grained transformation-induced plasticity-assisted steel. Scr Mater 68, 933–936. https://doi.org/10.1016/j.scriptamat.2013.02.026

Saeed-Akbari, A., Imlau, J., Prahl, U., Bleck, W., 2009. Derivation and Variation in Composition-Dependent Stacking Fault Energy Maps Based on Subregular Solution Model in High-Manganese Steels. Metallurgical and Materials Transactions A 40, 3076–3090. https://doi.org/10.1007/s11661-009-0050-8

Salehiyan, D., 2018. Microstrain Partitioning and Damage in a QP980 Steel (Master of Applied Science). McMaster University , Hamilton.

Salehiyan, D., Samei, J., Amirkhiz, B.S., Hector, L.G., Wilkinson, D.S., 2020. Microstructural Evolution During Deformation of a QP980 Steel. Metall Mater Trans A Phys Metall Mater Sci 51, 4524–4539. https://doi.org/10.1007/s11661-020-05882-2

Salehiyan, D., Samei, J., Wilkinson, D.S., 2018. In-situ characterization of microstructural damage in QP980 steel, in: Minerals, Metals and Materials Series. pp. 443–450. https://doi.org/10.1007/978-3-319-72526-0_42

Salvo, L., Cloetens, P., Maire, E., Zabler, S., Blandin, J.J., Buffière, J.Y., Ludwig, W., Boller, E., Bellet, D., Josserond, C., 2003. X-ray micro-tomography an attractive characterisation technique in materials science. Nucl Instrum Methods Phys Res B 200, 273–286. https://doi.org/10.1016/S0168-583X(02)01689-0

Samei, J., Pelligra, C., Amirmaleki, M., Wilkinson, D.S., 2020. Microstructural design for damage tolerance in high strength steels. Mater Lett 269. https://doi.org/10.1016/j.matlet.2020.127664

Samei, Javad, Pelligra, C., Amirmaleki, M., Zhou, L., Salehiyan, D., Kang, J., Wilkinson, D.S., 2019a. On the Influence of Grain Refinement and Transformation Induced Plasticity on Damage and Ductility in High Strength Steels. Scr Mater.

Samei, J., Salib, Y., Amirmaleki, M., Wilkinson, D.S., 2019. The role of microstructure on edge cracks in dual phase and quench and partitioning steels subject to severe cold rolling. Scr Mater 173, 86–90. https://doi.org/10.1016/J.SCRIPTAMAT.2019.08.012

Samei, Javad, Zhou, L., Kang, J., Wilkinson, D.S., 2019b. Microstructural analysis of ductility and fracture in fine-grained and ultrafine-grained vanadium-added DP1300 steels. Int J Plast 117, 58–70. https://doi.org/10.1016/j.ijplas.2017.12.009

Samei, J., Zhou, L., Kang, J., Wilkinson, D.S., 2018. Microstructural analysis of ductility and fracture in fine-grained and ultrafine-grained vanadium-added DP1300 steels. Int J Plast 117, 58–70. https://doi.org/10.1016/j.ijplas.2017.12.009

Samek, L., De Moor, E., Penning, J., De Cooman, B.C., 2006. Influence of alloying elements on the kinetics of strain-induced martensitic nucleation in low-alloy, multiphase high-strength steels. Metallurgical and Materials Transactions A 37, 109–124. https://doi.org/10.1007/s11661-006-0157-0

Sandvik, B.P.J., Wayman, C.M., 1983. CHARACTERISTICS OF LATH MARTENSITE: PART I. CRYSTALLOGRAPHIC AND SUBSTRUCTURAL FEATURES. Metallurgical transactions. A, Physical metallurgy and materials science 14 A, 809 – 822. https://doi.org/10.1007/bf02644284

Sarkar, A., Sanyal, S., Bandyopadhyay, T.K., Mandal, S., 2017. Enhanced strength-ductility relationship in a medium Mn high Al-alloyed multicomponent steel through thermomechanical processing. Materials Science and Engineering: A 703, 205–213. https://doi.org/10.1016/j.msea.2017.07.045

Scavino, G., D'Aiuto, F., Matteis, P., Russo Spena, P., Firrao, D., 2010. Plastic Localization Phenomena in a Mn-Alloyed Austenitic Steel. Metallurgical and Materials Transactions A 41, 1493–1501. https://doi.org/10.1007/s11661-010-0191-9

Schmidt, T., 2012. 3D ARAMIS Sensitivity, Accuracy and Data Validity Considerations.

Schoell, R., Xi, L., West, H., Hosemann, P., Park, J.-S., Kenesei, P., Almer, J., Shayer, Z., Kaoumi, D., 2022. Investigation of the fatigue crack behavior of 304 stainless steels using synchrotron X-ray tomography and diffraction: Influence of the martensite fraction and role of inclusions. Mater Charact 188, 111903. https://doi.org/10.1016/j.matchar.2022.111903

Scott, C.P., Fazeli, F., Shalchi Amirkhiz, B., Pushkareva, I., Allain, S.Y.P., 2017. Structure-properties relationship of ultra-fine grained V-microalloyed dual phase steels. Materials Science and Engineering A 703, 293–303. https://doi.org/10.1016/j.msea.2017.07.051

Scott, C.P., Shalchi Amirkhiz, B., Pushkareva, I., Fazeli, F., Allain, S.Y.P., Azizi, H., 2018. New insights into martensite strength and the damage behaviour of dual phase steels. Acta Mater 159, 112–122. https://doi.org/10.1016/j.actamat.2018.08.010

Soleimani, M., Kalhor, A., Mirzadeh, H., 2020. Transformation-induced plasticity (TRIP) in advanced steels: A review. Materials Science and Engineering A 795. https://doi.org/10.1016/j.msea.2020.140023

Speer, J.G., 2012. Phase transformations in quenched and partitioned steels, in: Phase Transformations in Steels. Elsevier, pp. 247–270. https://doi.org/10.1533/9780857096111.2.247

Speer, J.G., De Moor, E., Clarke, A.J., 2015. Critical Assessment 7: Quench and partitioning. Materials Science and Technology 31, 3–9. https://doi.org/10.1179/1743284714Y.0000000628

Speer, J.G., Rizzo Assuncao, F.C., Matlock, D.K., Edmonds, D. V., 2005. The “quenching and partitioning” process: nackground and recent progress. Ibero-american Journal of Materials 8.

Speich, G.R., Miller, R.L., 1979. Mechanical Properties of Ferrite-Martensite Steels. IEEE Conference Record of Annual Pulp and Paper Industry Technical Conference 145–182.

Spencer, K., Embury, J.D., Conlon, K.T., Véron, M., Bréchet, Y., 2004. Strengthening via the formation of strain-induced martensite in stainless steels. Materials Science and Engineering: A 387–389, 873–881. https://doi.org/10.1016/j.msea.2003.11.084

Spenger, F., Hebesberger, T., Pichler, A., Krempaszky, C., Werner, E.A., 2008. AHS Steel Grades: Strain Hardening and Damage as Material Design Criteria.

Steineder, K., Krizan, D., Schneider, R., Béal, C., Sommitsch, C., 2018. On the Damage Behavior of a 0.1C6Mn Medium-Mn Steel. Steel Res Int 89. https://doi.org/10.1002/srin.201700378

Sugimoto, K., Mukherjee, M., 2017. TRIP aided and complex phase steels, in: Automotive Steels. Elsevier, pp. 217–257. https://doi.org/10.1016/B978-0-08-100638-2.00008-0

Suh, D.W., Kim, S.J., 2017. Medium Mn transformation-induced plasticity steels: Recent progress and challenges. Scr Mater 126, 63–67. https://doi.org/10.1016/j.scriptamat.2016.07.013

Suh, D.-W., Park, S.-J., Lee, T.-H., Oh, C.-S., Kim, S.-J., 2010. Influence of Al on the Microstructural Evolution and Mechanical Behavior of Low-Carbon, Manganese Transformation-Induced-Plasticity Steel. Metallurgical and Materials Transactions A 41, 397–408. https://doi.org/10.1007/s11661-009-0124-7

Suh, D.W., Park, S.J., Lee, T.H., Oh, C.S., Kim, S.J., 2010. Influence of Al on the microstructural evolution and mechanical behavior of low-carbon, manganese transformation-induced-plasticity steel. Metall Mater Trans A Phys Metall Mater Sci 41, 397–408. https://doi.org/10.1007/s11661-009-0124-7

Sun, B., Fazeli, F., Scott, C., Brodusch, N., Gauvin, R., Yue, S., 2018. The influence of silicon additions on the deformation behavior of austenite-ferrite duplex medium manganese steels. Acta Mater 148, 249–262. https://doi.org/10.1016/j.actamat.2018.02.005

Sun, B., Palanisamy, D., Ponge, D., Gault, B., Fazeli, F., Scott, C., Yue, S., Raabe, D., 2019. Revealing fracture mechanisms of medium manganese steels with and without delta-ferrite. Acta Mater 164, 683–696. https://doi.org/10.1016/j.actamat.2018.11.029

Sun, B., Vanderesse, N., Fazeli, F., Scott, C., Chen, J., Bocher, P., Jahazi, M., Yue, S., 2017. Discontinuous strain-induced martensite transformation related to the Portevin-Le Chatelier effect in a medium manganese steel. Scr Mater 133, 9–13. https://doi.org/10.1016/j.scriptamat.2017.01.022

Suppan, C., Hebesberger, T., Pichler, A., Rehrl, J., Kolednik, O., 2018. On the microstructure control of the bendability of advanced high strength steels. Materials Science and Engineering A 735, 89–98. https://doi.org/10.1016/j.msea.2018.07.080

Talonen, J., Hänninen, H., 2007. Formation of shear bands and strain-induced martensite during plastic deformation of metastable austenitic stainless steels. Acta Mater 55, 6108–6118. https://doi.org/https://doi.org/10.1016/j.actamat.2007.07.015

Tamura, I., 1982. Deformation-induced martensitic transformation and transformation-induced plasticity in steels. Metal Science 16, 245–253. https://doi.org/10.1179/030634582790427316

Tan, X., Ponge, D., Lu, W., Xu, Y., Yang, X., Rao, X., Wu, D., Raabe, D., 2019. Carbon and strain partitioning in a quenched and partitioned steel containing ferrite. Acta Mater 165, 561–576. https://doi.org/10.1016/j.actamat.2018.12.019

Tang, A., Liu, H., Chen, R., Liu, G., Lai, Q., Zhong, Y., Wang, L., Wang, J., Lu, Q., Shen, Y., 2021. Mesoscopic origin of damage nucleation in dual-phase steels. Int J Plast 137. https://doi.org/10.1016/j.ijplas.2020.102920

Tasan, C.C., Bechtold, M., Schemmann, L., Tsuzaki, K., Raabe, D., Diehl, M., Zheng, C., Koyama, M., Roters, F., Ponge, D., Peranio, N., Yan, D., 2015. An Overview of Dual-Phase Steels: Advances in Microstructure-Oriented Processing and Micromechanically Guided Design. Annu Rev Mater Res 45, 391–431. https://doi.org/10.1146/annurev-matsci-070214-021103

Tasan, C C, Diehl, M., Yan, D., Bechtold, M., Roters, F., Schemmann, L., Zheng, C., Peranio, N., Ponge, D., Koyama, M., Tsuzaki, K., Raabe, D., 2015. An Overview of Dual-Phase Steels: Advances in Microstructure-Oriented Processing and Micromechanically Guided Design. https://doi.org/10.1146/annurev-matsci-070214-021103

Timokhina, I.B., Hodgson, P.D., Pereloma, E. V, 2004. Effect of microstructure on the stability of retained austenite in transformation-induced-plasticity steels. Metallurgical and Materials Transactions A 35, 2331–2341. https://doi.org/10.1007/s11661-006-0213-9

Tirumalasetty, G.K., van Huis, M.A., Kwakernaak, C., Sietsma, J., Sloof, W.G., Zandbergen, H.W., 2012. Deformation-induced austenite grain rotation and transformation in TRIP-assisted steel. Acta Mater 60, 1311–1321. https://doi.org/10.1016/j.actamat.2011.11.026

Toda, H., Hirayama, K., Okamura, K., Suzuki, T., Takeuchi, A., Uesugi, M., Fujihara, H., 2022. Multimodal assessment of mechanically induced transformation in metastable multi-phase steel using X-ray nano-tomography and pencil-beam diffraction tomography. Acta Mater 234, 117956. https://doi.org/10.1016/j.actamat.2022.117956

Toda, H., Takijiri, A., Azuma, M., Yabu, S., Hayashi, K., Seo, D., Kobayashi, M., Hirayama, K., Takeuchi, A., Uesugi, K., 2017. Damage micromechanisms in dual-phase steel investigated with combined phase- and absorption-contrast tomography. Acta Mater 126, 401–412. https://doi.org/10.1016/j.actamat.2017.01.010

Toji, Y., Matsuda, H., Herbig, M., Choi, P.P., Raabe, D., 2014. Atomic-scale analysis of carbon partitioning between martensite and austenite by atom probe tomography and correlative transmission electron microscopy. Acta Mater 65, 215–228. https://doi.org/10.1016/j.actamat.2013.10.064

Tsipouridis, P., Werner, E., Krempaszky, C., Tragl, E., 2006. Formability of High Strength Dual-phase Steels. Steel Res Int 77, 654–667. https://doi.org/10.1002/srin.200606444

Wang, H., Yan, Y., Jia, F., Han, F., 2016. Investigations of fracture on DP980 steel sheet in roll forming process. J Manuf Process 22, 177–184. https://doi.org/https://doi.org/10.1016/j.jmapro.2016.03.008

Wang, L., Speer, J.G., 2013. Quenching and Partitioning Steel Heat Treatment. Metallography, Microstructure, and Analysis 2, 268–281. https://doi.org/10.1007/s13632-013-0082-8

Wang, M.-M., Hell, J.-C., Tasan, C.C., 2017. Martensite size effects on damage in quenching and partitioning steels. Scr Mater 138, 1–5. https://doi.org/10.1016/j.scriptamat.2017.05.021

Wang, W., Liu, Y., Zhang, Z., Yang, M., Zhou, L., Wang, J., Jiang, P., Yuan, F., Wu, X., 2023. Deformation mechanisms for a new medium-Mn steel with 1.1 GPa yield strength and 50% uniform elongation. J Mater Sci Technol 132, 110–118. https://doi.org/10.1016/j.jmst.2022.05.048

Wang, X. G., Wang, L., Huang, M.X., 2017. Kinematic and thermal characteristics of Lüders and Portevin-Le Châtelier bands in a medium Mn transformation-induced plasticity steel. Acta Mater 124, 17–29. https://doi.org/10.1016/j.actamat.2016.10.069

Wang, X.G., Wang, L., Huang, M.X., 2017. Kinematic and thermal characteristics of Lüders and Portevin-Le Châtelier bands in a medium Mn transformation-induced plasticity steel. Acta Mater 124, 17–29. https://doi.org/10.1016/j.actamat.2016.10.069

Wang, Y., Chen, M., Zhou, F., Ma, E., 2002. High tensile ductility in a nanostructured metal. Nature 419, 912–915. https://doi.org/10.1038/nature01133

Weck, A., Segurado, J., Llorca, J., Wilkinson, D., Böhm, H., 2007. Numerical simulations of void linkage in model materials using a nonlocal ductile damage approximation. Int J Fract 148, 205–219. https://doi.org/10.1007/s10704-008-9195-5

Weck, A., Wilkinson, D.S., Maire, E., Toda, H., 2008. Visualization by X-ray tomography of void growth and coalescence leading to fracture in model materials. Acta Mater 56, 2919–2928. https://doi.org/10.1016/j.actamat.2008.02.027

Weck, A.G., 2007. The Role of Coalescence on Ductile Fracture (PhD Thesis). McMaster University , Hamilton.

Williams, B., Abu-Samk, K., Xue, J., Shalchi Amirkhiz, B., Scott, C., 2022. Microstructure Modelling of the HEC Behaviour of a Novel Vanadium DP980 Cold Rolled Alloy. Minerals, Metals and Materials Series 909–920. https://doi.org/10.1007/978-3-031-06212-4_82

Withers, P.J., 2015. Fracture mechanics by three-dimensional crack-tip synchrotron X-ray microscopy. Philosophical Transactions of the Royal Society A: Mathematical, Physical and Engineering Sciences 373. https://doi.org/10.1098/RSTA.2013.0157

Wong, S.L., Madivala, M., Prahl, U., Roters, F., Raabe, D., 2016. A crystal plasticity model for twinning- and transformation-induced plasticity. Acta Mater. https://doi.org/10.1016/j.actamat.2016.07.032

Wu, W., Wang, Y.-W., Makrygiannis, P., Zhu, F., Thomas, G.A., Hector, L.G., Hu, X., Sun, X., Ren, Y., 2018. Deformation mode and strain path dependence of martensite phase transformation in a medium manganese TRIP steel. Materials Science and Engineering: A 711, 611–623. https://doi.org/10.1016/J.MSEA.2017.11.008

Wu, X., Zhu, Y., 2017. Heterogeneous materials: a new class of materials with unprecedented mechanical properties. Mater Res Lett 5, 527–532. https://doi.org/10.1080/21663831.2017.1343208

Xiong, X.C., Chen, B., Huang, M.X., Wang, J.F., Wang, L., 2013. The effect of morphology on the stability of retained austenite in a quenched and partitioned steel. Scr Mater 68, 321–324. https://doi.org/10.1016/J.SCRIPTAMAT.2012.11.003

Yan, D., Tasan, C.C., Raabe, D., 2015. High resolution in situ mapping of microstrain and microstructure evolution reveals damage resistance criteria in dual phase steels. Acta Mater 96, 399–409. https://doi.org/10.1016/j.actamat.2015.05.038

Yang, Y., Mu, W., Sun, B., Jiang, H., Mi, Z., 2021. New insights to understand the strain-state-dependent austenite stability in a medium Mn steel: An experimental and theoretical investigation. Materials Science and Engineering: A 809. https://doi.org/10.1016/j.msea.2021.140993

Yi, H.L., Sun, L., Xiong, X.C., 2018. Challenges in the formability of the next generation of automotive steel sheets. Materials Science and Technology (United Kingdom) 34, 1112–1117. https://doi.org/10.1080/02670836.2018.1424383

Yin, W., Briffod, F., Hu, H., Yamazaki, K., Shiraiwa, T., Enoki, M., 2023. Quantitative investigation of strain partitioning and failure mechanism in ultrafine grained medium Mn steel through high resolution digital image correlation. Scr Mater 229, 115386. https://doi.org/10.1016/j.scriptamat.2023.115386

Yoon, J.I., Jung, J., Lee, H.H., Kim, G.S., Kim, H.S., 2016. Factors governing hole expansion ratio of steel sheets with smooth sheared edge. Metals and Materials International 22, 1009–1014. https://doi.org/10.1007/s12540-016-6346-5

Yu, H.Y., Kai, G.Y., De Jian, M., 2006. Transformation behavior of retained austenite under different deformation modes for low alloyed TRIP-assisted steels. Materials Science and Engineering: A 441, 331–335. https://doi.org/https://doi.org/10.1016/j.msea.2006.08.061

Zanjani, N.A., Dervaric, A., Kalyanasundaram, S., 2014. A Novel Buckling Indicator using the Correlation Between in-Plane and out-of-Plane Displacements. International Journal of Engineering Research & Technology (IJERT) 3.

Zhang, L., Wang, S., 2018. Correlation of Materials Property and Performance with Internal Structures Evolvement Revealed by Laboratory X-ray Tomography. Materials 11, 1795. https://doi.org/10.3390/ma11101795

Zhang, S., Findley, K.O., 2013. Quantitative assessment of the effects of microstructure on the stability of retained austenite in TRIP steels. Acta Mater 61, 1895–1903. https://doi.org/10.1016/j.actamat.2012.12.010

Zhang, S., Godfrey, A., Zhang, C., Liu, W., Juul Jensen, D., 2020. Surface patterning for combined digital image correlation and electron backscatter diffraction in-situ deformation experiments. Mater Charact 164. https://doi.org/10.1016/j.matchar.2020.110332

Zhang, X., Yan, J., Liu, T., Liu, H., Shi, Y., Zhou, Q., Zhao, L., Lv, Z., 2021. Microstructural evolution and mechanical behavior of a novel heterogeneous medium Mn cold-rolled steel. Materials Science and Engineering: A 800, 140344. https://doi.org/10.1016/j.msea.2020.140344

Zhang, Y., Topping, T.D., Lavernia, E.J., Nutt, S.R., 2014. Dynamic Micro-Strain Analysis of Ultrafine-Grained Aluminum Magnesium Alloy Using Digital Image Correlation. Metallurgical and Materials Transactions A 45, 47–54. https://doi.org/10.1007/s11661-013-1805-9

Zhao, L., Speer, J.G., Hodgson, P., Tsuji, N., 2021. Editorial: New Developments and Challenges in Advanced High-Strength Steels. Front Mater 8. https://doi.org/10.3389/fmats.2021.786932

Zhou, L., 2018. Effect of Vanadium on Fracture of DP1300 Steels (Master of Science). McMaster University.

3 Microstructural design for damage tolerance in high strength steels

Javad Samei[1], Concetta Pelligra[1], Maedeh Amirmaleki[2], David S. Wilkinson[1]

[1]Department of Materials Science and Engineering, McMaster University, Hamilton, Canada

[2]Department of Mechanical and Industrial Engineering, University of Toronto, 5 King's College Road, Toronto, Canada

Materials Letters 269 (2020) 127664

3.1 Abstract

We have investigated the capabilities of first and third generation high strength steels for sustainable accommodation of microstructural damage before fracture occurs. Steels have been subjected to tensile tests followed by X-ray computed tomography to record the evolution of microstructural damage during deformation. Damage growth is correlated with the Rice-Tracey model. Results show that both grain refinement and transformation induced plasticity of retained austenite to martensite lead to enhanced damage tolerance, leading to the suppression of fracture and improved ductility.

3.2 Introduction

Damage tolerance is a materials property which accounts for the ability to sustain defects in the form of voids and microcracks without failure. In materials with low damage tolerance after initiation of the first internal damage, failure and fracture occurs rapidly. Utilization of those materials in structures and engineering components is limited since quality inspections such as nondestructive testing cannot predict the time of failure sufficiently well in advance. Recently, grain refinement (Kadkhodapour et al., 2011; Samei et al., 2019b) and the quench and partitioning heat treatment (Tan et al., 2019; Wang and Speer, 2013) have been found to provide effective methods for further enhancing the mechanical properties of so-called third generation (3G) advanced high strength steels. While a great deal of attention has been paid to the processing and microstructure of these materials, there is relatively little known about the micromechanical processes that control damage tolerance and ductile fracture in these multi-phase steels. X-ray computed tomography (XCT) has proven to be an appropriate technique for quantitative characterization of the evolution of microstructural damage in steels (Landron et al., 2012; Maire et al., 2008). The goals of this study are to quantitatively determine the evolution of damage in first and third generation dual phase (DP), TRIP, and quench and partition (Q&P) steels, and to determine the influence of microstructural features on damage tolerance.

3.3 Experimental Work

The characteristics of the 1 mm thick steel sheets investigated in this study are presented in Table 3.1, where TE is the total elongation, UTS is the engineering ultimate tensile strength, F_{GS} is the ferrite grain size, and F, M, and RA vol% are the volume percentages of ferrite, martensite and retained austenite, respectively. QP1500 has the finest microstructure, mainly consisting of martensite in the forms of islands and laths. The average size of the islands is 0.45mm while the laths are in nano-scale scale, typically under 100nm. Interrupted tensile tests were carried out using a in-house test stage on sub-size tensile test specimens as described elsewhere (Samei et al., 2019a). A Bruker Skyscan 1172 XCT system was used to scan the gauge volume at 100 kV using an Al/Cu filter with a pixel dimension of 0.65mm. Quantitative analysis was performed using Bruker's commercial CTAn software and 3D models were made using the CTvol software. The DP1300 specimen was scanned at 6, while the other materials were each scanned at 7 different strains before fracture occurred. Retained austenite was measured close to the fracture surface in QP steels by X-ray diffraction (XRD) analysis with a 0.3mm beam size and 80min exposure time.

Table 3.1: Characteristics of the steels.

	TE (%)	UTS (MPa)	F_{GS} (µm)	F vol%	M vol%	RA vol%	C wt%	Si wt%	Mn wt%	V wt%
TRIP780	33	805	5.3	79	12	9	0.15	0.13	1.58	0.04
DP780	24	874	4.9	77	23	-	0.13	0.03	2.01	-
DP1300	9	1451	4.6	50	50	-	0.23	0.19	1.59	-
DP1300 (UFG)	10	1475	1.3	50	50	-	0.21	0.19	1.65	0.14
QP980	20	1072	4.9	38	54	8	0.21	1.47	1.96	-
QP1500	16	1544	-	-	83	17	0.20	1.60	3.40	-

3.4 Results and Discussion

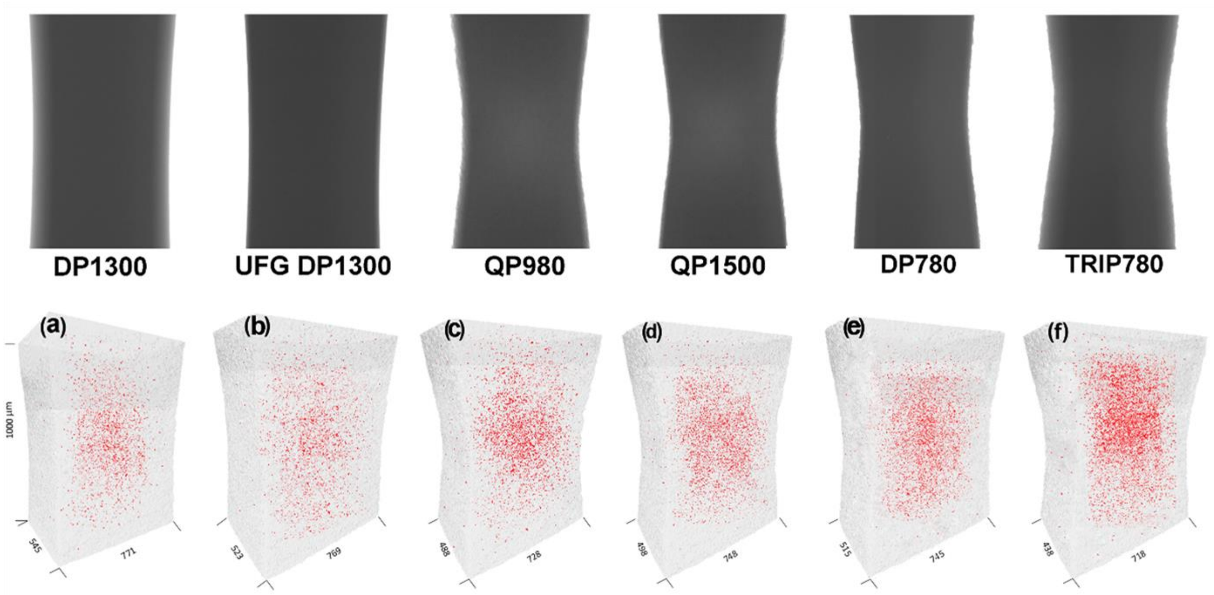

Figure 3.1: Evolution of damage (a) void volume fraction, (b) void density, mean void size for the largest 500 voids in (c) high-strength, and (d) ultrahigh-strength steels. Dashed lines in (c) and (d) represent the modified RT model prediction of void growth.

Figure 3.1 shows the images of the gauge section at the last step prior to fracture. The X-ray radiographs (top) demonstrate that macroscopic localization of deformation is greater in TRIP780 compared to DP780, and in the QP steels compared to both DP1300 steels. The 3D XCT models (bottom) illustrate the extent and distribution of internal microscopic damage. For better visualization, only voids larger than 2.2mm^3 are shown on the models; however, all detected voids are considered in quantitative analysis. As can be seen, damage is concentrated in the centre of the specimens which results in the final fracture process being initiated in the centre and then progressing towards the surface, as is typical of cup-cone type ductile fracture.

A quantitative analysis of microstructural damage during plastic deformation is presented in Figure 3.2. All steels show an exponential type increase in void volume fraction with true strain. Of the 6 steels in this study, damage evolution is fastest (per unit of strain) in DP1300; this material also shows the least amount of damage at fracture. The slower evolution of damage in the UFG DP1300 steel can be associated with a finer microstructure which leads to the nucleation of much smaller voids. Since void growth is a strain dependent phenomenon, it takes further plastic strain for the voids in the UFG DP1300 steel to grow and reach the critical void fraction for damage linkage and fracture. Although QP980 has a coarser microstructure, damage evolution is significantly slower than in UFG DP1300. This is likely because of TRIP-assisted deformation in QP steels. The transformation of FCC austenite to BCC martensite in low carbon steels is accompanied by a volume increase. This adds a local compression strain to the transformed area and also leads to local work hardening through the production of geometrically necessary dislocations. This may serve to decrease the rate of void growth locally, although further investigation is required to prove this conjecture. XRD analysis shows that undeformed QP980 and QP1500 have 8 and 17 vol% austenite, respectively. The austenite level is then reduced to near 0 vol% at fracture. The slowest rate of damage growth is observed in QP1500 which has the finest microstructure and experiences the greatest amount of TRIP. The effect of TRIP can also be seen by comparing damage evolution in DP780 and TRIP780, which exhibit similar grain size and strength. Both the rate of damage nucleation and growth are significantly slower in TRIP780 specifically after a true strain 0.3. Moreover, TRIP780 can accommodate approximately twice as much damage prior to fracture compared to DP780. Similar to the QP steels the volume fraction of austenite is reduced considerably during deformation, in this case from a starting level of 9 vol% to 1.3 vol% at fracture.

Figure 3.2b shows that the void density, defined as the number of voids per unit volume, increases continuously, indicating the continuous nucleation of voids. Very little nucleation is observed at low strain, up to about 0.1, as the material undergoes sufficient deformation to create the high local stresses needed to fracture hard particles or decohere interfaces. Once necking commences void nucleation tends to accelerate (Goods and Brown, 1979; Samei et al., 2016). Void density rises most rapidly in DP780, due to cracking within martensite bands at low strains (Samei et al., 2014; Samei et al., 2014). The slowest nucleation rate is seen in QP1500. However, it is important to recognize that nano-scale voids could not be detected because of the XCT pixel resolution of 0.65mm; and so, due to its extremely fine microstructure, there may be many unidentified voids. Therefore, Figure 3.2b should be interpreted as showing the evolution of void density in each steel, rather than the absolute density of voids.

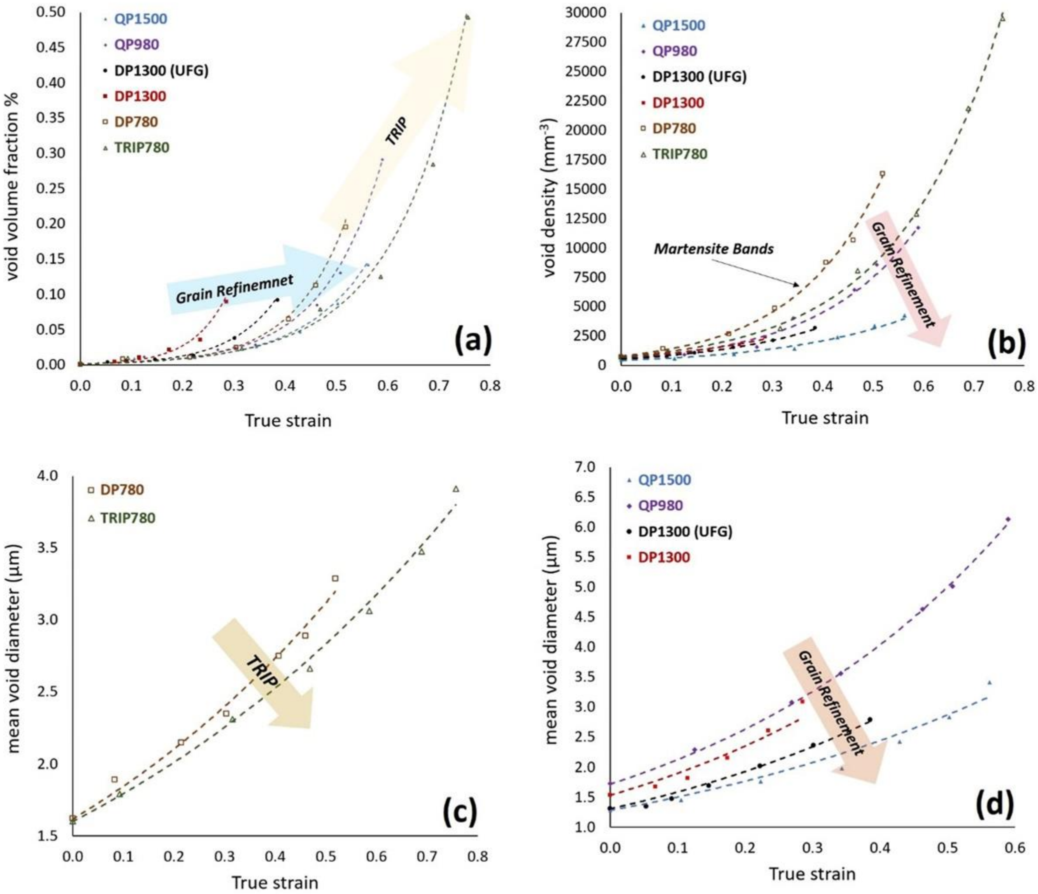

Figure 3.2: Evolution of damage (a) void volume fraction, (b) void density, mean void size for the largest 500 voids in (c) high-strength, and (d) ultrahigh-strength steels. Dashed lines in (c) and (d) represent the modified RT model prediction of void growth.

Final fracture is driven by the coalescence of large voids in the structure. Although sub-micron recently nucleated voids may increase void volume fraction somewhat, they have little influence on the final fracture process as indicated by Maire et al. (2008). We therefore focus on the evolution of the largest voids in the material. Thus, Figure 3.2c and d show the mean void diameter of the largest 500 voids in these steels. If we assume that the largest voids maintain their size ranking during deformation, this data can be compared with the Rice and Tracey (RT) (Rice and Tracey, 1969) void growth model using:

$$\frac{dR}{R} = \alpha_{RT} \exp\left(\frac{3}{2}\, T\right) d\varepsilon \qquad \text{Equation 3.1}$$

where α_{RT} is a growth rate parameter and T is stress triaxiality. As described elsewhere (Landron et al., 2011), we have determined evolutions of T using finite element modeling from onset of plastic deformation and during post-uniform deformation and the α_{RT} was calculated by curve fitting. The obtained RT models are shown on the Figure 3.2 c and d for the steels. Figure 3.3 shows the optimum value of α_{RT} derived from this analysis. Both the rate of damage evolution and α_{RT} show a descending trend:

i) from DP1300 to UFG DP1300 due to grain refinement

ii) from QP980 to QP1500, due to both grain refinement and an increase in amount of TRIP (from 7 to 17 vol%)

iii) from DP780 to TRIP780 due to TRIP, accompanied by an acceleration of damage due to cracking of martensite bands early in the deformation.

iv) from UFG DP1300 to QP1500, due primarily to TRIP.

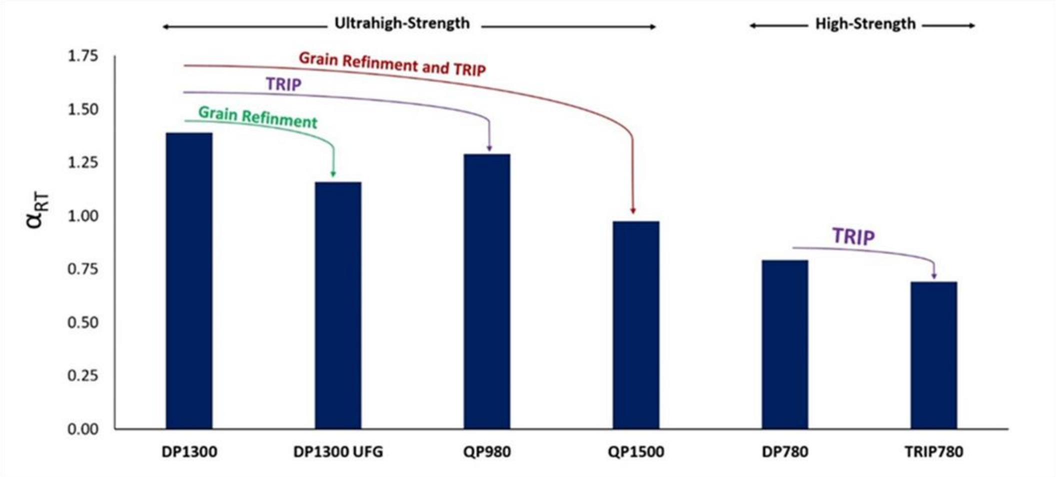

Figure 3.3: Modified α_{RT} for each steel.

3.5 Conclusion

In summary, DP780, TRIP780, DP1300, UFG DP1300, QP980, and QP1500 steels have been subjected to tensile tests coupled with XCT. Quantitative analysis demonstrates that grain refinement and TRIP reduce the rate of damage development during plastic deformation; and therefore, enhanced damage tolerance. Both mechanisms can be utilized to develop optimized microstructures that will enhance the ductility of advanced high strength steels.

3.6 Acknowledgements

We are grateful to CanmetMATERIALS (Dr. Colin Scott) for providing the DP1300 steels and to General Motors (Dr. Lou Hector) for providing QP980 and QP1500 steels.

3.7 References

Goods, S.H., Brown, L.M., 1979. Overview No. 1: The nucleation of cavities by plastic deformation. Acta Metallurgica 27, 1–15. https://doi.org/10.1016/0001-6160(79)90051-8

Kadkhodapour, J., Butz, A., Ziaei Rad, S., 2011. Mechanisms of void formation during tensile testing in a commercial, dual-phase steel. Acta Mater 59, 2575–2588. https://doi.org/10.1016/j.actamat.2010.12.039

Landron, C., Maire, E., Adrien, J., Bouaziz, O., 2011. Damage characterization in Dual-Phase steels using X-ray tomography, in: Proulx, T. (Ed.), Optical Measurements, Modeling, and Metrology, Volume 5. Springer New York, New York, NY, pp. 11–18.

Landron, C., Maire, E., Adrien, J., Suhonen, H., Cloetens, P., Bouaziz, O., 2012. Non-destructive 3-D reconstruction of the martensitic phase in a dual-phase steel using synchrotron holotomography. Scr Mater 66, 1077–1080. https://doi.org/10.1016/J.SCRIPTAMAT.2012.03.003

Maire, E., Bouaziz, O., Di Michiel, M., Verdu, C., 2008. Initiation and growth of damage in a dual-phase steel observed by X-ray microtomography. Acta Mater 56, 4954–4964. https://doi.org/10.1016/j.actamat.2008.06.015

Rice, J.R., Tracey, D.M., 1969. On the ductile enlargement of voids in triaxial stress fields*. J Mech Phys Solids 17, 201–217. https://doi.org/10.1016/0022-5096(69)90033-7

Samei, Green, D.E., Golovashchenko, S., 2014. Metallurgical Investigations on Hyperplasticity in Dual Phase Steel Sheets. J Manuf Sci Eng 136. https://doi.org/10.1115/1.4027492

Samei, J., Amirmaleki, M., Shirinzadeh Dastgiri, M., Marinelli, C., Green, D.E., 2019a. In-situ X-ray tomography analysis of the evolution of pores during deformation of AlSi10Mg fabricated by selective laser melting. Mater Lett 255, 126512. https://doi.org/10.1016/j.matlet.2019.126512

Samei, J., Green, D., Golovashchenko, S., 2014. Analysis of Failure in Dual Phase Steel Sheets Subject to Electrohydraulic Forming. J Manuf Sci Eng 136, 051010. https://doi.org/10.1115/1.4027940

Samei, J., Green, D.E., Cheng, J., de Carvalho Lima, M.S., 2016. Influence of strain path on nucleation and growth of voids in dual phase steel sheets. Mater Des 92. https://doi.org/10.1016/j.matdes.2015.12.103

Samei, J., Zhou, L., Kang, J., Wilkinson, D.S., 2019b. Microstructural analysis of ductility and fracture in fine-grained and ultrafine-grained vanadium-added DP1300 steels. Int J Plast 117, 58–70. https://doi.org/10.1016/j.ijplas.2017.12.009

Tan, X., Ponge, D., Lu, W., Xu, Y., Yang, X., Rao, X., Wu, D., Raabe, D., 2019. Carbon and strain partitioning in a quenched and partitioned steel containing ferrite. Acta Mater 165, 561–576. https://doi.org/10.1016/j.actamat.2018.12.019

Wang, L., Speer, J.G., 2013. Quenching and Partitioning Steel Heat Treatment. Metallography, Microstructure, and Analysis 2, 268–281. https://doi.org/10.1007/s13632-013-0082-8

4 The Effect of Vanadium on Microstrain Partitioning and Localized Damage during Deformation of Unnotched and Notched DP1300 Steel Specimen

Concetta Pelligra[1], Javad Samei[1], Jidong Kang[2], David S. Wilkinson[1]

[1]Department of Materials Science and Engineering, McMaster University, Hamilton, ON, L8S 4L7, Canada

[2]CanmetMATERIALS, Natural Resources Canada, Hamilton, Ontario, L8P 0A5, Canada

International Journal of Plasticity 158 (2022) 103435

4.1 Abstract

The use of vanadium-microalloying in ultrahigh strength dual phase (DP) steels has been shown to yield a fine dispersion of nano-scale vanadium carbonitrides (V(C,N)) in ferrite along with a pronounced grain refinement, leading to enhanced micromechanical compatibility and increased local ductility. Here we present data on microstrain partitioning and the evolution of damage in vanadium-free (V-free) Fine-Grained (FG) and vanadium-added (V-added) Ultra Fine-Grained (UFG) DP steels, each with a UTS of about 1300MPa (DP1300), using quasi in-situ tensile tests coupled with scanning electron microscopy, followed by microscopic Digital Image Correlation (μDIC). Quantitative analysis shows that the homogenization of microstrain between ferrite and martensite is locally enhanced and the strain gradients at the ferrite/martensite (F/M) interfaces reduced in the V-added steel. This trend was also evident in the V-added steel exhibiting different states of stress obtained with unique notched microtensile specimen designs. Three different μDIC-based computational techniques were used to quantify the extent of microstrain partitioning, in order to determine the mechanistic basis for the increase in true strain to fracture with vanadium-microalloying. This work was supplemented with damage evolution studies in both V-free and V-added materials using high resolution, field emission scanning electron microscope (FESEM) imaging, and X-ray computed microtomography (μXCT). These corroborate the microscopic analyses and confirm that both vanadium-microalloying and stress-state impacts the local strain gradient at ferrite/martensite (F/M) interfaces, and thereby changes the way damage is initiated and grows within the material.

4.2 Introduction

The use of thin sheets made from Advanced High Strength Steels (AHSSs) has been widely adopted by the automotive industry to promote fuel efficiency and thereby reduce greenhouse gas emissions in vehicle design. Dual Phase (DP) steels were the first of the AHSS family to offer an enhanced strength-ductility combination and they remain the most widely used due to their robust thermo-mechanical processing and attractive mechanical properties (Tasan et al., 2015). Moreover, some argue that AHSSs with Transformation Induced Plasticity (TRIP) capability (e.g. Quench & Partition steels) only improves the global formability of the steel, while its local forming potential is either comparable to that of a DP steel of a similar strength level (Tang et al., 2021) or worse with the local activation of TRIP in highly stress-concentrated areas, such as; at a crack tip (Frómeta et al., 2021). Hance (2016) accentuates the difference between the global formability (i.e. a material's response to a uniformly applied load) and local formability (i.e. a material's response to a concentrated applied load) by plotting the true strain at fracture versus the true uniform strain (Hance, 2016).

On an industrial scale, expanded utilisation of high strength DP steels is being compromised by their limited local formability and therefore, poor damage tolerance (Casellas et al., 2017; Frómeta et al., 2021, 2019; Ghadbeigi et al., 2010; Samei et al., 2020; Tang et al., 2021) during forming operations requiring sufficient bendability and stretch-flangeability performance (Li et al., 2020; Min et al., 2017) or during rolling where edge cracking is susceptible (Samei et al., 2019). Precisely, Tang et al. (2021) attributes the heightened likeliness of damage nucleation and poor local formability to the significant increase in martensite content required to achieve ultrahigh strength.

The Hole Expansion Ratio (HER), for example, is a key industrial indicator of stretch flanging performance and edge cracking tendency in sheet steels (Chen et al., 2014; Hasegawa et al., 2004; Scott et al., 2017; Yoon et al., 2016). Chen et al. (2014) show two distinct trends of HER to tensile strength relationship in AHSSs - a linear decrease in HER with increasing tensile strength for relatively low strength AHSSs, and for AHSSs with tensile strengths greater than 840MPa, the HER tends to a constant value (30-40%). This plateau of HER at ultrahigh tensile strength levels suggests that, despite the increase in the amount of brittle phases needed to achieve higher levels of strength, complex forming operations are not significantly compromised.

Specifically, in evaluating the HER of two ultrahigh strength DP steels with comparable tensile strengths and martensite volume fractions, Scott et al. (2018) documented that increases in vanadium-microalloying led to a reduction in the mean ferrite:martensite Phase Strength Ratio (PSR) by 32% and HER improvement of 15%. These authors claim that HER can be improved with decreased PSR in ultrahigh strength DP steel, but this is not a proportional relationship and is impacted by other microstructural parameters which have a significant influence on damage behaviour, such as the local configuration of the martensite surrounding the soft ferrite. Although, these two papers present somewhat contradictory results, it is agreed that the HER-tensile strength relationship is not linear in DP steels and that there is a critical damage sensitivity locally at the F/M interface (Chen et al., 2014; Hasegawa et al., 2004; Scott et al., 2017). These inconsistencies in HERs of AHSSs can also however be a result of poor experimental reliability inherently associated with the test (i.e. hole surface and edge quality, tooling conditions, crack detection method, etc…) (Frómeta et al., 2019; Hance et al., 2013; Karelova et al., 2009; Larour et al., 2017).

Microscopic heterogeneity, due to the large strength differential between ferrite and martensite in DP steels, results in significant microstrain partitioning (Kang et al., 2007; Landron et al., 2010; Samei et al., 2013; Tang et al., 2021) which can ultimately lead to premature failure as a result of reduced post-uniform elongation. The poor true ductility of Ultra Fine-Grained (UFG), strong materials is due to the limited space for dislocation interaction, multiplication and motion (El-Naaman et al., 2016; Khan and Liu, 2016; Li et al., 2020) while the dislocation activity of a material with an intermediate grain size from 1μm to 10nm is weakly understood(El-Naaman et al., 2016; Meyers et al., 2006). The concept of Strain Gradient Plasticity (SGP), motivated by the pile up of Geometrically Necessary Dislocations (GNDs) at an interface to enable compatible deformation and accommodate large strain gradients of multi-phase materials, was first presented by Ashby (1970) and Fleck et al. (1994) and deemed instrumental in modulating the ductility of Fine-Grained (FG) materials (Fleck et al., 1994; Huang et al., 2018; Li et al., 2020; Mazzoni-Leduc et al., 2010). One of the challenges continuum modellers have is capturing the complex behavior of dislocation motion - an idealistic smoothened GND field is typically used (El-Naaman et al., 2016; Van Beers et al., 2013). This suggests the need for further work to be done at the experimental level to statistically capture detailed behavior of GNDs at a phase boundary or interface. Alternatively, one can use microstrain measurements near interfaces to measure strain gradients at the continuum scale, and model strain localization using classical theories (i.e. crystal plasticity and J2 flow theory) as has been done previously on DP steels (Yalçinkaya et al., 2019).

Recently it has been proven that introducing a fine distribution of vanadium carbonitride (V(C,N)) nanoprecipitates selectively strengthens the ferrite phase and improves the post-uniform elongation without a reduction in strength (Samei et al., 2019; Scott et al., 2017). Scott et al. (2017) hypothesized, given that interface decohesion is the most common mechanism of damage in FG, cold rolled and annealed microstructures driven by strain incompatibilities, when this strain incompatibility is reduced, interfacial decohesion is reduced and the dominant damage mechanism to be seen in the V-added steel is decohesion at ferrite/nanoprecipitate interfaces. The effect of enhanced dislocation multiplication, and therefore supressed strain partitioning improved by V(C,N) precipitation in ferrite was speculated previously by Kamikawa et al. (2015) Kamikawa et al. (2015) with conventional uniaxial tensile testing. In addition, the use of vanadium- microalloying in steels has been proven to be beneficial in increasing the strength and toughness of forging steels(Wang et al., 2020) by decreasing the bainite transformation temperature (Pushkareva et al., 2020) and increasing the yield strength of high C steels (Gwon et al., 2017).

The large impact of vanadium-microalloying on mechanical properties has enabled the investigation of its role in suppressing damage through grain refinement and mechanical homogenization (Samei et al., 2019; Scott et al., 2017). Nanoindentation testing carried out by Samei et al. (2019) and Scott et al. (2018) on ultrahigh strength DP steel deduced that the increased vanadium content improved mechanical compatibility between ferrite and martensite and is the reason for improvement in true strain to fracture. Scott et al. (2018) used cumulative distribution plots to convey that the V-free material showed an overall greater and wider variation in martensite island nanohardness.

To date, modelling the severity of F/M decohesion does not reflect recent experimental findings on the effect of redistributing carbon through vanadium-microalloying. Rather the computation work by Ramazani et al. (2016) using Density Functional Theory (DFT) atomistic modelling, showed that the local strain required to initiate F/M decohesion increases with increasing local carbon content of martensite, thereby making martensite cracking the predominant source of damage initiation. Our paper experimentally focuses on the local strains required for F/M decohesion in ultrahigh strength DP steels whilst still capturing the local strains initiating M cracking.

Triaxiality is the ratio of mean stress to the von Mises equivalent stress. The true strain to fracture has a complex dependence on triaxiality. At low stress triaxialities the highest true strain to fracture that can be achieved is 0.45, but once the triaxiality exceeds about 0.4, the fracture strain falls off parabolically (Bao and Wierzbicki, 2004; Pineau et al., 2016). The Lode parameter (L), which describes the directionality of the stress-state, ranging from -1 to 1, also plays a significant role in ductile fracture, particularly at low triaxialities (Barsoum et al., 2012; Danas and Ponte Castañeda, 2012; Kiran and Khandelwal, 2014). Most of the factors that contribute to ductile fracture in AHSSs are intrinsic to steel microstructure such as large particle sizes, high aspect ratios, high volume fraction, and high matrix strength. Extrinsic factors, such as the specimen geometry, which can alter the strain distribution of a material even under simple uniaxial tension are important to consider in ductile fracture. However, these have been predominately studied on soft model materials (Lou et al., 2012; Weck et al., 2008; Weck, 2007) or lower strength DP steels (Landron et al., 2010). Moreover, damage evolution models are usually validated with experimental data from uniaxial tensile testing. However, such parameters are questionable to understanding damage evolution of materials subjected to multiaxial stress states with different stress triaxialities (Brünig et al., 2008). Up to now, the effect of stress-state on the evolution of damage has not been experimentally examined in detail on AHSSs at the microscopic scale. The experimental investigation of fracture as a function of different stress states using DIC is currently gaining significant popularity in materials in which their pertinency to multiple applications is being hindered such as in low strength commercially-available DP steels (Cheloee Darabi et al., 2020), anisotropic magnesium alloys (Habib et al., 2019), aluminum alloys (Brünig et al., 2021), and polycrystalline alpha-titanium alloys (Skripnyak et al., 2020).

At the grain level, Representative Volume Element (RVE) simulations showed the effect of martensite volume fraction on the local triaxiality in a DP steel. It was concluded through this study that the local deforming capacity of ferrite is ultimately governed by the vicinity of martensitic particles (Paul, 2013). Although martensite volume fraction does show a strong impact on triaxial stress development during straining of DP steels, this model does not take into account steel chemistry and intercritical annealing temperatures which initially dictates the mechanical properties of ferrite and martensite in DP steels (Paul, 2013). In some modelling ventures, the most dominant damage nucleation site in DP steels, especially those containing high volume fractions of martensite (Tasan et al., 2014), F/M decohesion is ignored as it is on a much smaller (atomic) scale in relation to the modeled RVE (Rana et al., 2018).

The influences of strain rate and path (Ha et al., 2017; Samei et al., 2016), microstructural constituents (Amirmaleki et al., 2016), secondary phases (Ismail et al., 2019), and deformation temperature (Li et al., 2019) on the micromechanics, plasticity, and fracture of high-strength DP steels has been investigated. Also, the microstructural responses of high-strength DP steels has been studied using quasi in-situ mechanical testing coupled with microscopy. For instance, Tasan et al. (2014) used the μDIC technique for characterization of localized strain and damage in DP600 and DP800 steels and Tang et al. (2021) presented a mesoscale map with a resolution of 2μm x 2μm for a DP980 steel deformed under uniaxial tension. Matsuno et al. (2015) obtained the damage patterns in the microstructure of a DP steel using a laser microscope. However, there are limited studies on micromechanical characterization of *ultra*high strength DP steels where the ultimate tensile strength reaches 1.5GPa.

In this paper, we present detailed data on microstrain partitioning and the evolution of localized damage in the microstructure of a FG and an UFG V-added DP steel with ultrahigh strength (DP1300) to determine the effect of modifications in chemistry and microstructural refinement on the F/M decohesion behaviour. A Field emission Scanning Electron Microscope (FESEM) was used during quasi in-situ tensile testing to obtain nano-scale resolution strain maps and to determine the development of microstrain inside sub-micron microstructural features using

Digital Image Correlation (DIC) (Kang et al., 2005). Three different approaches are used to study strain partitioning of ferrite and martensite. A novel approach to document the nature of the strain gradient across a large number of F/M interfaces and how it is linked to the evolution of microstructural damage under different states of stress is also introduced in this paper. Ultimately, it is seen that an increase in vanadium-microalloying produces a lower, less variable local strain gradient at the F/M interface. Damage evolution as a function of increasing strain of ultrahigh strength DP steel specimens both in unnotched and notched states are reported using high resolution SEM imaging and X-ray computed microtomography (µXCT). Muhammad et al. (2021) have already shown that with DIC and XCT data, a machine learning framework can be developed to predict the strain distribution and fracture of an AlSi10Mg alloy. DIC point strain measurements captured by Muhammad et al. (2021) are of a larger resolution (~50µm between points) than of those presented in this paper (~0.2µm between points), defining the forming potential of the material at a more global scale. Most recently, Zhang et al. (2022) have been able to apply machine learning to predict local strain incompatibility and damage nucleation at grain boundaries of simulated 3D magnesium microstructures with different textures.

Overall, the objective with this paper is to characterize the role that vanadium-microalloying plays on improving the local forming properties of ultrahigh strength DP steels under different states of stress. We do this by quantifying the microstrain partitioning between ferrite and martensite and therefore, F/M decohesion potency, using µDIC-based computational techniques that target strain partitioning at different length scales. Supplementary data on damage evolution and microvoid growth captured using high resolution SEM imaging and µXCT opens avenues for robust modelling and the potential for industrial utilisation of ultrahigh strength DP steels.

4.3 Experimental and numerical procedures

4.4 Materials

The characteristics of the FG and UFG DP1300 steels investigated in this work are summarized in Table 4.1. Martensite volume fraction has a significant influence on the plastic behavior of DP steels (Lai et al., 2016; Paul, 2013). To negate this effect, the heat treatment of the two steels were modified slightly so as to reach approximately the same amount of martensite in both steels as described elsewhere (Scott et al., 2017). In Table 4.1, the increase in vanadium content (from

0.003wt% to 0.14wt%) is the major compositional difference between the steels. The DP steel which contains only 0.003wt% vanadium is classified as V-free while the steel which contains 0.14wt% V is classified as V-added in this paper. The differences in chemical composition (wt%) and microstructure (Martensite Volume% and Grain Size), along with the mechanical property differences in Engineering ultimate tensile strength (Eng. σ_{UTS}) and total elongation (Eng. ε_{total}) of both steels tested parallel to the rolling direction is also shown in Table 4.1.

Table 4.1: Characteristics of the DP1300 steels

	Martensite Volume (vol%)	Grain Size (µm)	Eng. σ_{UTS} (MPa)	Eng. ε_{total}	Chemical Composition (wt%)					
					C	Mn	Si	V	Cr	Al
V-free	40.5±5.4	4.8±0.4	1451±45	0.182±0.035	0.23	1.59	0.19	0.003	0.027	0.011
V-added	40.2±2.8	1.6±0.1	1475±33	0.353±0.016	0.21	1.65	0.19	0.14	0.032	0.019

4.5 Tensile testing coupled with Digital Image Correlation (DIC)

To investigate the influences of vanadium and stress-state on deformation, hourglass geometry specimens, as shown in Figure 4.1, were prepared using fine wire Electrical Discharge Machining (wEDM), in both unnotched and notched (root radii of 1.00 or 0.20mm) configurations. As previously described in Salehiyan et al. (2020), the hourglass geometry is essential to localize the deformation at the centre of the specimen for microscopic investigations during testing. The notched specimens with radii of 1.00 and 0.20mm are referred to as R1 and R0.2, respectively.

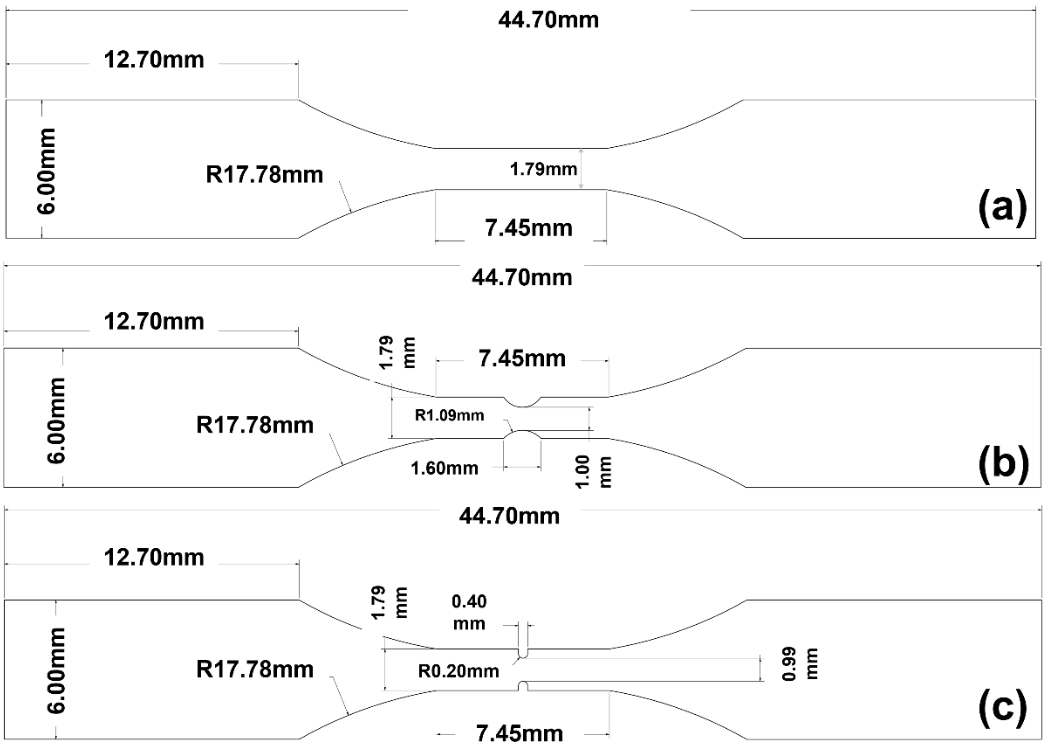

Figure 4.1 Microtensile specimen designs (a) unnotched, (b) notched R1, and (c) notched R0.2

Although there is hydrostatic component variation as a function of distance away from the notch, therefore varying triaxiality within the necked region of notched microtensile specimen, microstrain mapping was conducted within the centre of the specimen to make a fair comparison to the microtensile hourglass specimen. Finite Element Modelling (FEM) using ABAQUS/CAE 6.14 was performed to reasonably approximate the global triaxiality within the centre of the notch location. An implicit model was chosen for the 3D simulation. Isotropic hardening with elastic constants of steel, E = 210GPa and v = 0.3, was used. The true stress-plastic strain past yielding inputs were taken from experimental uniaxial tensile test DIC data of unnotched and notched specimen and fitted to a Voce-Linear hardening model using the Curve Fitting App in MATLAB until an R^2 value of 0.99 was achieved. The equation and curve fitting parameters obtained from MATLAB are detailed in Appendix A, Figure A 4.1. Mesh sizing was set to be greater than the grain size of the V-free (approximated at 5μm) and V-added (approximated at 1μm) materials to obtain a broadened 'past grain-level' indication of triaxiality. Eight-node, linear brick, continuum elements (C3D8R) were used with reduced integration and hourglass control. Global triaxiality outputs were taken from the centre of the specimen, whereas the local triaxiality outputs were obtained from centroids of the imaging locations detailed in Figure 4.2. The global triaxiality and local triaxiality graphs and average values are shown in Appendix A Figure A4.2. ABAQUS simulations of the microtensile hourglass specimen used in this study were previously performed by which shows a uniform strain distribution up to necking within the narrowest region of the specimen, and no strain concentration. The specimen design of Figure 4.1a has an L value of -1 indicating an axisymmetric uniaxial tension stress-state, while the specimen shown in Figure 1c has a L value of 0 indicating a plain strain stress-state. For the Figure 4.1b specimen the L value is in between -1 and 0, in which the stress-state experienced by this specimen design is a combination of axisymmetric uniaxial and plain strain (Barsoum et al., 2012). The effect of Lode parameter on void deformation (i.e. void dilation or elongation) and coalescence leading to fracture of 3G AHSSs will be detailed in a subsequent publication, as has been investigated previously (Danas and Ponte Castañeda, 2012; Kiran and Khandelwal, 2014).

4.5.1 Macro-Digital Image Correlation

One set of specimens was used for macroscopic uniaxial tensile tests coupled with digital image correlation (DIC). Before tensile testing, specimens were ground with #400 SiC paper to remove a possible oxide layer, and a stochastic speckle pattern was sprayed onto the gauge section. Specimens were pulled using a 100kN tensile frame (MTS) at a nominal strain rate of $6 \times 10^{-4}/s$. A 2D DIC system (with a single 1 Megapixel camera) was used to acquire images during tensile testing at 1 frame per second. The true strain at fracture was calculated according to $\varepsilon_{\mathrm{f}} = \ln \frac{\mathrm{A}_0}{\mathrm{A}_{\mathrm{f}}}$, where A_0 is the initial cross-sectional area before deformation and A_f is the minimum area at fracture. A_f was calculated taking into account the left, right and centre thickness of the fractured surface ("ASTM E8M-Standard Test Methods for Tension Testing of Metallic Materials," 2021; Casellas et al., 2017; Hance, 2016). As presented in Table 4.2, the notches reduce the true strains at fracture, particularly for the R0.2 geometry in the V-free steel. The increase in toughness with vanadium-microalloying of notched specimens, using the area integral trapezoid method on true stress-strain curves of notched specimens, has also been approximated in Table 4.2. The true stress-strain curves of unnotched and notched V-free and V-added specimens are shown in the Appendix A Figure A 4.1.

Table 4.2 True fracture strains and toughness (MJ/m^3) approximations

	V-free	V-free R1	V-free R0.2	V-added	V-added R1	V-added R0.2
True Fracture Strain	0.18	0.14	0.04	0.35	0.23	0.13
Toughness	276	84	19	409	155	99

It is important to note that as the notch gets sharper with increasing strain, the true fracture strain becomes less meaningful, yet the fracture strains reported in Table 4.2 indicates that there is a reduction in overall ductility introduced by the notch. As well, it is possible that any abrupt changes in strain were not captured due to the limited resolution of performing DIC within a notched area (Tardif and Kyriakides, 2012).

4.5.2 Micro-Digital Image Correlation

For SEM tensile testing, specimens were polished to a 50% 0.04μm colloidal silica suspension-50% ethylene glycol finish for 1.5 minutes to remove any machining effects. The specimens were etched with 2% Nital for 10 sec at room temperature (Zhou, 2018). The specimens were subject to quasi in-situ interrupted tensile tests using an in-house test stage coupled with field emission scanning electron microscopy, JEOL JSM-7000F. As a result of the factor of three decrease in grain size from the V-added steel (1.6±0.1µm) to its V-free counterpart (4.8±0.4µm), the magnification for SEM imaging was increased by a similar amount, from 2700-3000× to 9000× so that the micromechanisms of damage in the two steels can be visually comparable during testing. As well, SEM imaging magnifications were selected carefully such that sufficient sites, with variable grey scale, were available for correlation during Digital Image Correlation (DIC) computation, as described in the following. Imaging was obtained within the centre of the specimen, ~400-500µm from the notches. This is done purposefully to avoid any potential (~25µm deep) Heat Affected Zone (HAZ) that may have developed during wEDM (Choudhary et al., 2010). In this work, we have quantified triaxiality at a more globalized scale; however, the local arrangement of martensite islands within the ferrite matrix affects the stress-state of the material. Figure 4.2 shows the specific imaging locations of notched V-free and V-added specimen.

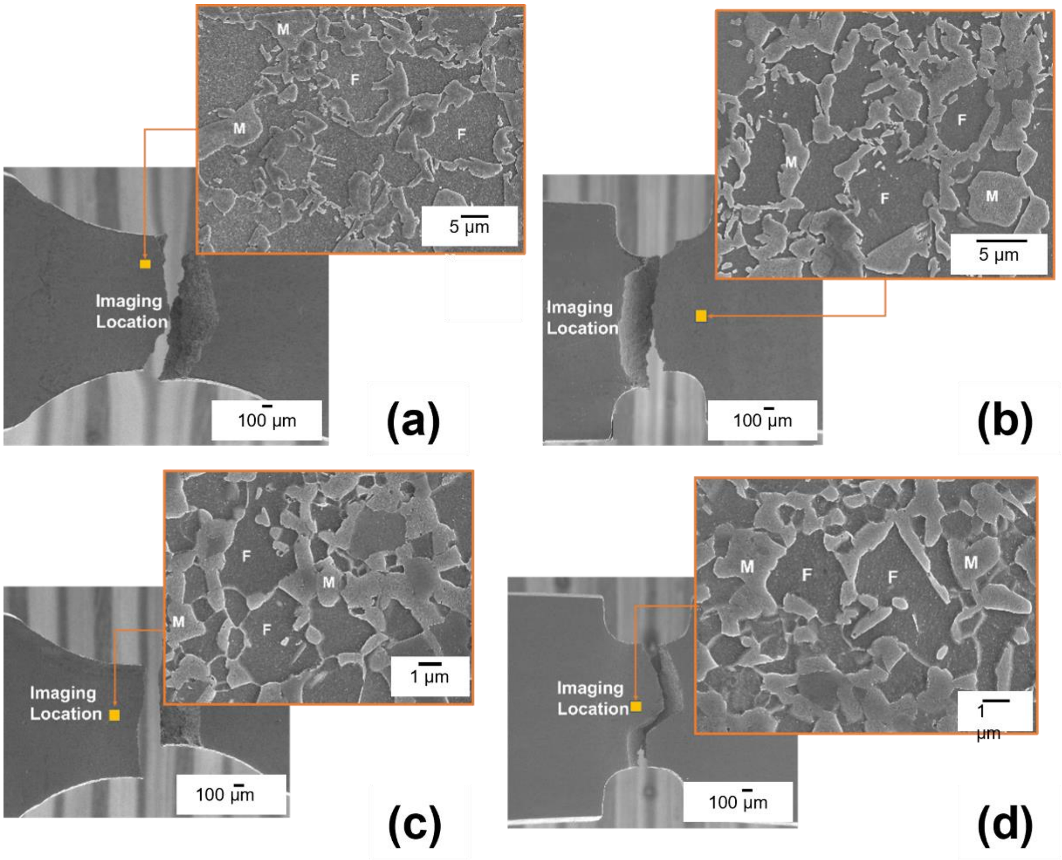

Figure 4.2 SEM imaging locations on microtensile specimens (a) V-free R1.0 (b) V-free R0.2 (c) V-added R1.0, and (d) V-added R0.2. SEM Imaging locations are those used for local triaxiality determinations in Appendix A Figure A4.2b.

4.5.3 Microstrain computation procedure

To obtain microstrain maps, the microscopic Digital Image Correlation (μDIC) method, first developed by Kang et al. (2005), was performed using the GOM Correlate Professional ARAMIS software package in which the von Mises equivalent strain is computed, assuming that deformation takes place at constant volume. Mapping using the von Mises equivalent strain is said to be correlative to the density of GNDs (Dutta et al., 2019). The software calculates the strain through facets and the local strain is considered uniform within one facet. The facet size selection can have a significant influence on data processing and should be optimized to obtain the best compromise between adequate strain computation and spatial resolution, as illustrated in Figure 4.3. When the strain tensor neighbourhood (termed as computation size, in previous ARAMIS versions) is set to 3, the virtual gauge length corresponds to two times the step size. To obtain the local strain at the grain level, the virtual gauge length should be smaller than the average grain size, as shown in Figure 4.3. In other words, the step size was chosen such that on average, a minimum of three points for local strain computation lie within an average-sized martensitic island. The step sizes in four groups of data are set to be similar (0.22 and 0.23µm) so that the strain value is comparable between the V-free and V-added steels, as indicated in Table 4.3. A median filter degree of 1 was applied in order to smooth strain mapping of strain hot spot artefacts.

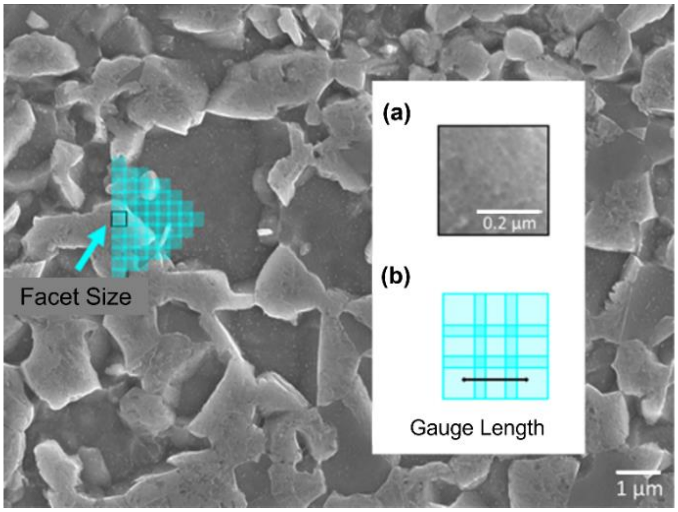

Figure 4.3 SEM image of the V-added steel from the µDIC experiment (a) enlarged images of the local field (within martensite) with a size of one facet, and (b) schematic drawing of 3×3 facets. The black line indicates the gauge length used in the calculation.

Table 4.3 Parameters of the microstrain calculations in GOM Correlate

	V-free	V-free R1	V-free R0.2	V-added	V-added R1	V-added R0.2
Represented Area (µm^2)	34×27	44×35	34×27	15×11	13×11	13×11
Resolution (µm/pixel)	0.013	0.017	0.013	0.006	0.005	0.005
Facet × Step size (pixel)	23×17	19×13	23×17	51×39	61×43	61×43
Facet × Step size (µm×µm)	0.31×0.23	0.32×0.22	0.31×0.22	0.31×0.23	0.31×0.22	0.31×0.22

4.5.4 Microstrain data post-processing

Strain partitioning at the microscopic level is determined using three different methods. These are described in the following and summarized in Table 4.4.

Table 4.4 DIC Method summary of quantifying strain partitioning in DP1300 steels

Method No.	DIC methodology	DIC number scans/image	Number of F/M interface intersections	DIC scanning orientation	Computed von Mises strain type
1	Area	1	--	---	Average
2	Section	5	6	Horizontal	Local
3	Line	195	204	Varied	Local

Method 1 – Average Phase Strain: The average phase strain refers to the average von Mises strain computed from the martensitic islands or ferrite patches within a given viewing area. This method provides an indication of strain partitioning between ferrite and martensite by collecting strain maps and quantifying the average von Mises strain (ε_{Avg}) over an area imaged.

Method 2 – Local Phase Strain: A series of horizontal sections is used to quantify the local von Mises strain (ε_{Local}) as a function of the section scan distance. This method enables us to map the difference in strain partitioning between ferrite and martensite between the two steels.

Method 3 – Local Strain Gradient: Short line scans are drawn across many individual F/M interfaces quantifying the local von Mises strain (ε_{Local}) at a sub-micron scale. This is used to quantify the strain gradient across each interface. As noted in Table 4.4, many interfacial line scans can be obtained from each image, thus providing statistically significant data using line scans considerably smaller in length than the sections in Method 2. The use of short line scans in this method also enables microstrain evolution at the F/M interface to be computed at multiple orientations.

4.5.5 Strain gradient

We use Method 3 to determine the "strain gradient" at the F/M interface, where the von Mises strain as a function of distance is computed. As shown in Figure 4.4a, short line scans in random orientations were drawn at F/M interfaces and the von Mises strains were recorded along the lines as presented in Figure 4.4b for three sample line scans. Using Origin2020 the strain variation along each line scan was fitted to the Boltzmann sigmoidal function, shown as Equation 4.1 below; line scans which did not have an adequate fit to the function were eliminated from the analysis.

$$\mathrm{\varepsilon} = \frac{\mathrm{\varepsilon_{min}} - \mathrm{\varepsilon_{max}}}{\mathrm{A} + \mathrm{e}^{(\mathrm{x}-\mathrm{x_0})/\mathrm{dx}}} + \mathrm{\varepsilon_{max}} \qquad \text{Equation 4.1}$$

$$\varepsilon' = \frac{(\varepsilon_{max} - \varepsilon_{min})}{4dx} \qquad \text{Equation 4.2}$$

where ε’ in Equation 4.2 is the strain gradient at the F/M interface. The derivation of Equation 4.1 to Equation 4.2 is detailed in the Appendix B. The Boltzmann sigmoidal function is used to describe transition phenomena in which the inflection point corresponds to a critical stage in which there is a transition from one steady state to another. The strain gradients computed using the Method 3 methodology is summarized using Weibull cumulative distribution function (CDF) plots and histograms, achieved with Minitab 2019. As shown in Equation 4.1 and illustrated in Figure 4.4c, the von Mises strain (ε) is exported as a function of position (x). ε_{min} and ε_{max} in this case describe the local strain in the ferrite and martensite respectively before approaching the F/M interface. x_0 is the inflection point, or the nominal position of the F/M interface while dx is the width of the transition zone (i.e the line scan length in this analysis). The *A* constant adjusts the position of the inflection point with respect to the geometric location and is set to 1, thereby positioning the transition point precisely at the F/M interface.

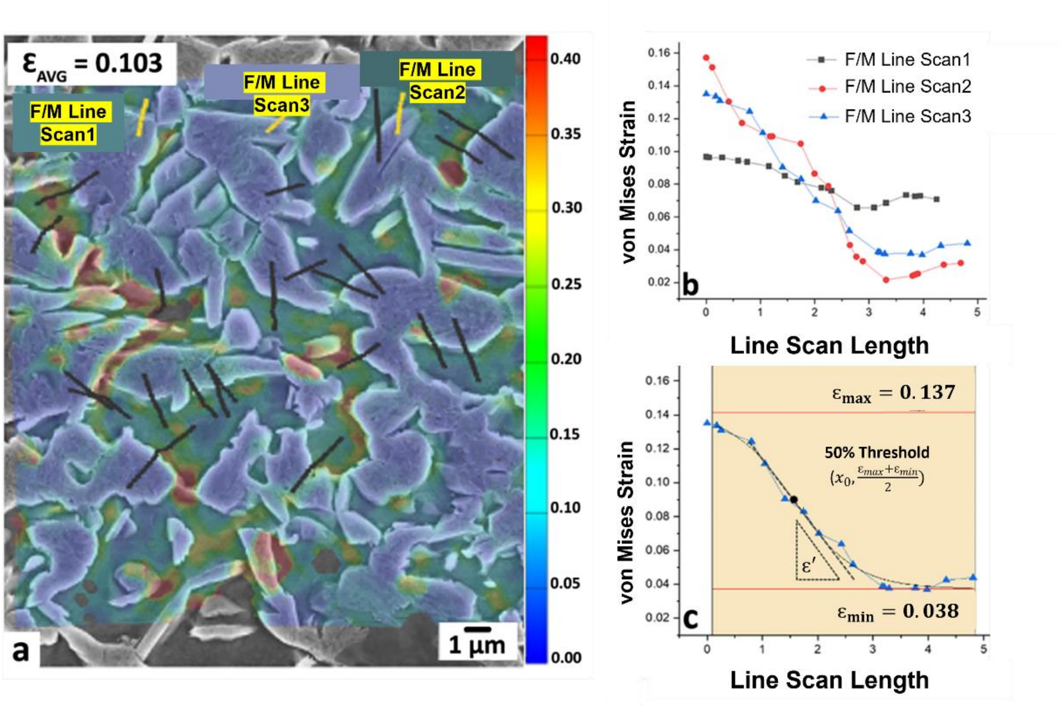

Figure 4.4 Data post-processing to determine the "strain gradient" in Method 3 (a) random lines at the F/M interface, (b) variation of microstrain along the 3 sample lines in (a), and (c) determination of the transition point

4.6 Results and Discussion

4.6.1 Influences of vanadium on the micromechanical compatibility of ferrite and martensite

Nanoindentation tests show that the difference between the hardness of ferrite and martensite in DP1300 is reduced in the V-added steel (Samei et al., 2019). Here, we use a modeling approach presented in Equation 4.3, to estimate the plastic behaviour of each phase in the V-free and V-added steels based on the Rodriguez and Guttierez method (Rodriguez and Gutierrez, 2003) shown in Equation 4.4-Equation 4.7, used previously on different grades of DP steels (Ch.Darabi et al., 2017; Rana et al., 2018). The ferrite in the V-added steel is strengthened by V(C,N) nanoprecipitates. The effect is considered based on the Ashby strengthening model (Ashby, 1966) presented in Equation 4.8.

$$\sigma_{flow} = \sigma_o + \sigma_c + \sigma_\varepsilon + \sigma_{V(C,N)}$$

σ_o: *solid solution hardening*

σ_c: *strengthening due to interstitial carbon atoms*

σ_ε: *dislocation-based work hardening*

$\sigma_{V(C,N)}$: *second − phase work hardening (precipitation strengthening)*

Equation 4.3

$$\sigma_0 = 77 + 80\%Mn + 60\%Si + 80\%Cr + 11\%Mo + 5000\%N_{ss}$$ Equation 4.4

$$ferrite: \sigma_c^f = 5000 \times (\%C_{ss}^f)$$ Equation 4.5

$$martensite: \sigma_c^m = 3065 \times (\%C_{ss}^m) - 161$$ Equation 4.6

$$\sigma_{\varepsilon_p} = \alpha M \mu \sqrt{b} \sqrt{\frac{1 - e^{-Mk_r\varepsilon_p}}{k_r L}}$$ Equation 4.7

M: Taylor Factor; *μ*: Shear Modulus [MPa]; *b*: Burger's vector [m]; *α*: constant;

K_r: Recovery Rate; *L*: dislocation mean free path [m]

Equation 4.8

$$Ferrite\ in\ the\ V - added\ Steel: \sigma_{V(C,N)} = 2KG\sqrt{\frac{2bf\varepsilon_p}{d_p}}$$

The values of each parameter are presented in Table 4.5. $\%N_{ss}$, $\%C_{ss}^f$, and $\%C_{ss}^m$ are determined using Thermo-Calc simulations and a TCFE7 database. As detailed originally by Rodriguez and Gutierrez (2003) and subsequently in Amirmaleki et al. (2016), the strengthening effect of carbon is different in ferrite and martensite, $\%C_{ss}^f$, and $\%C_{ss}^m$ in wt% respectively, and therefore these contributions have been calculated separately, σ_c^f and σ_c^m in MPa respectively. The derivation of values and parameters in Equation 4.7 for DP steels are presented in Amirmaleki et al. (2016) Moreover, Equation 4.8 accounts for additional Orowan strengthening provided by nitrogen, $\%N_{ss}$ in wt%, as it is almost fully consumed to form V(C,N) in the V-added steel. Only Orowan strengthening of V(C,N) nanoprecipitates in ferrite was considered, V(C,N) precipitation in martensite is scarce and therefore, negligible in the V-added material (Samei et al., 2019; Scott et al., 2017). No tangible increase in strength to martensite is expected as a result of minor V(C,N) nanoprecipitates. K, material constant, G, rigidity modulus, and d_p, carbide diameter [nm], in

Equation 8 are obtained from Kosaka and Funakawa (2016), and f, volume fraction of carbides, for the V-added DP1300 is reported by Scott et al. (2017). Equation 4.8 considers the Orowan strengthening from V(C,N) nanoprecipitates in relation to plastic strain (ε_p).

Table 4.5 The values of the parameters used in the modeling

	C_{ss}^{f}	C_{ss}^{m}	N_{ss}^{f}	N_{ss}^{m}	K	d_p (nm)	f
V-free	0.0092	0.3828	0.002	0.004	-	-	-
V-added	0.0081	0.3216	0.000	0.000	0.24	3.7	0.0026

Figure 4.5a shows the calculated true stress-strain curves for ferrite and martensite in the V-free and V-added DP1300 steels. Martensite is stronger in V-free steel due to its higher carbon content; however, in the V-added steel, a fraction of carbon is used to form V(C,N) and this leads to a softer martensite. Ferrite is stronger in the V-added steel due to its finer grainer size and smaller dislocation mean free path (L) and V(C,N) nanoprecipitate work hardening is more pronounced at higher strain levels. The relationship between L and ferrite grain size is outlined in Amirmaleki et al. (2016). As a result, as presented in Figure 4.5b, the difference between the ferrite and martensite strength is lower in the V-added steel. This is in good agreement with nanoindentation test results (Samei et al., 2019). Figure 4.5b shows that there is a greater decrease in microstrain between ferrite and martensite in the V-added steel than V-free steel with increasing true plastic strain. This correlates well with the SGP theory which states that GND pile up at the F/M interface produces back stress strengthening in the soft ferrite phase to a similar strength of the hard martensite phase (Li et al., 2020).

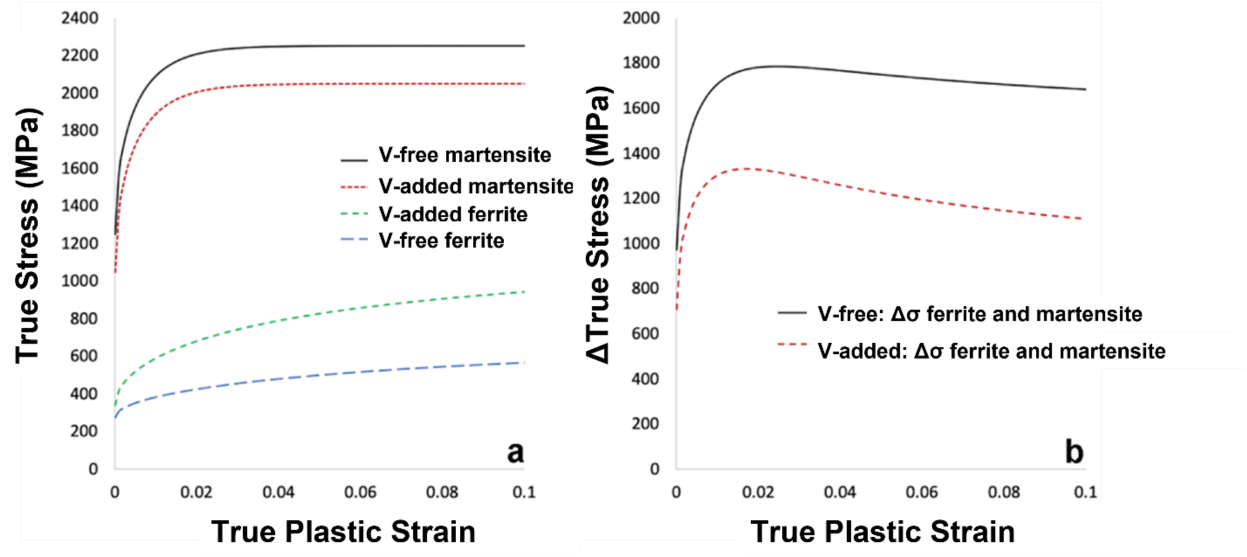

Figure 4.5 Numerical modeling: (a) true stress-strain relationship in ferrite and martensite, and (b) flow stress difference between ferrite and martensite in V-free and V-added DP1300 steels

4.7 Microstrain partitioning at F/M Interfaces

In this section we outline three methods for determining the degree of strain partitioning between ferrite and martensite. The first two methods are already in common use while the third presents a novel approach to determining the precise gradient in plastic strain at the interface between the hard and soft phases.

4.7.1 Method 1 - Average Phase Strain

Average overall and individual phase strains collected from µDIC imaged areas shows strain partitioning between ferrite and martensite is more pronounced in the V-free steel, as shown in Figure 4.6. This result was obvious, as the strength mismatch has been significantly reduced as a result of vanadium additions. Similar conclusions both from in-situ SEM tensile testing and nanoindentation have been documented elsewhere (Samei et al., 2019).

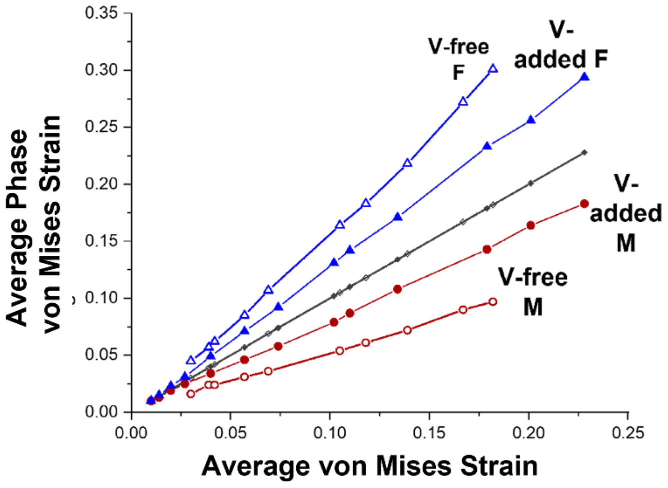

Figure 4.6 Average phase vs Average von Mises strain comparison between unnotched V-free and V-added DP1300 steels. Note: Average von Mises strain refers to the average strain computed over the imaged area.

The strain incompatibility increases linearly with strain for both steels, such that at ε_{Avg}=0.18, the difference between ferrite and martensite average phase strains is 20% in the V-free steel but only 10% in the V-added material. Imaging at multiple strain increments for the notched specimens was much more complex and as a result insufficient average strains were computed to report its trend.

4.7.2 Method 2 - Local Phase Strain

Figure 4.7 shows the variations of strain along 5 parallel lines in both steels and for all three test geometries. Each horizontal section shows the variation in local strain at multiple (between 4 and 8) F/M interfaces. Accumulating the local strain data from all 5 sections on each sample, peaks and troughs per section were segregated to determine the average of local maximum and minimum strains as shown in Table 4.6. An average local maximum 'peak' strain is situated either within the deformable ferrite phase, F/M interface or at a martensite damage initiation site, whereas an average local minimum 'trough' strain is situated most predominately solely within the harder martensitic phase.

Table 4.6 Average local maximum ‘peak’ & minimum ‘trough’ strain computation comparison between unnotched V-free and V-added DP1300 steels

ε_{Avg}	0.09±0.03					
Specimen	V-free	V-free R1	V-free R0.2	V-added	V-added R1	V-added R0.2
$\varepsilon_{\text{Peak,Avg local}}$	0.14±0.1	0.12±0.10	0.11±0.09	0.16±0.07	0.14±0.06	0.06±0.02
$\varepsilon_{\text{Trough,Avg local}}$	0.05±0.05	0.06±0.06	0.03±0.02	0.05±0.03	0.05±0.03	0.03±0.01

At ε_{Avg}=0.09±0.03, well past yielding for both DP1300 steels, the reduced variability/standard deviation in average local ‘peak’ to ‘trough' strain in the V-added material for both unnotched and notched specimens suggests that strain partitioning at the F/M interface is weakened with vanadium-microalloying.

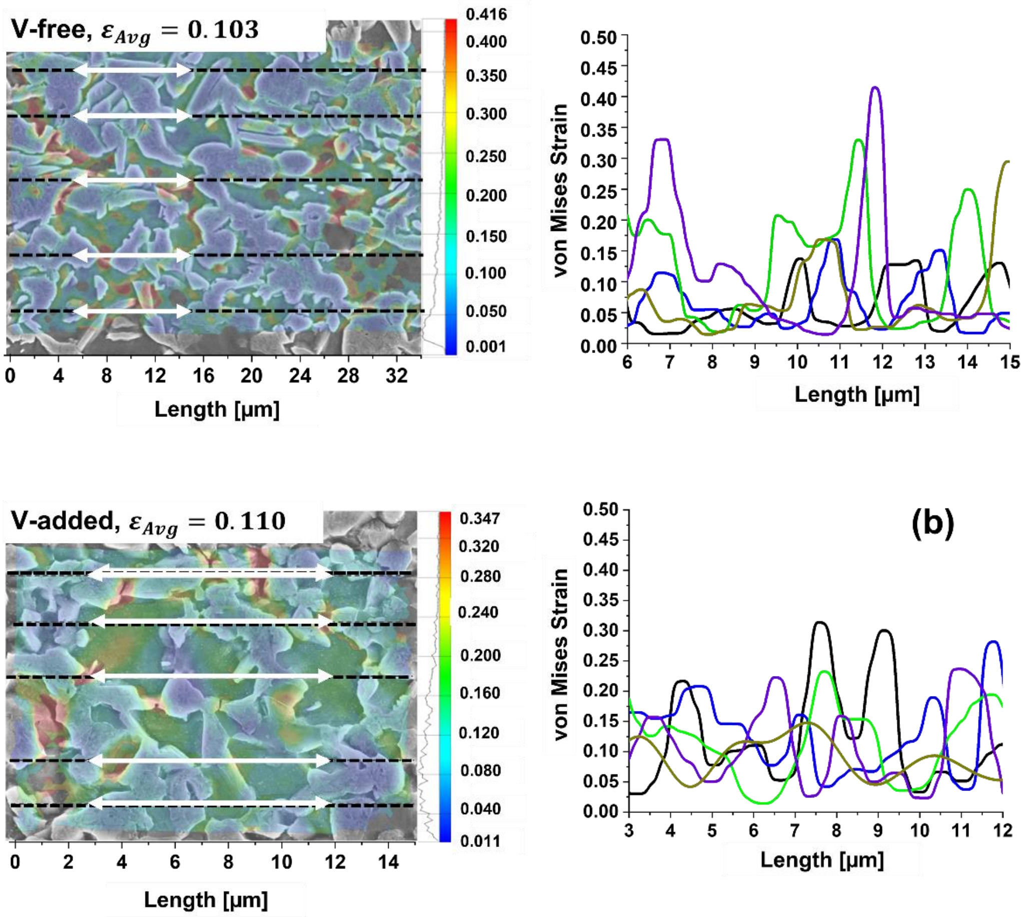

Figure 4.7 Local strain variations on 5 sample lines in the unnotched (a) V-free and (b) V-added Specimen

A series of horizontal, single-oriented DIC computed line sections gives some evidence that strain compatibility is improved locally at the F/M interface in the V-added steel as can be qualitatively observed in Figure 4.7 with less fluctuation in local strain in the V-added material. Additional data for the notched specimen geometries are contained in Appendix C Figure C4.1 which further substantiates this conclusion. The horizontal line section data suggests macroscopically that ductility is improved with vanadium-microalloying additions, but damage, and hence the local forming potential, of these ultrahigh strength DP steels is highly sensitive to the individual martensitic island condition such as surface continuities, necking morphology, etc., and cannot be explained by horizontal sections alone. Rather, more detailed data from individual F/M interfaces is required. The fact that there is still 'room to reveal' damage nucleation sites in DP steels, despite these being the first AHSS developed, with the use of strain gradient computations, is also supported by Tang et al. (2021).

4.7.3 Method 3 - Local Strain Gradient

Approximately 200 line scans were made across individual F/M interfaces for each test configuration and the strain gradient was calculated in each case according to the approach outlined in Figure 4.4. The µDIC-based computational technique of line scanning at multiple orientations across phase boundaries has also been applied to a limited degree by other researchers (Dutta et al., 2019; Wang et al., 2017). Weibull Probability Density Functions (PDFs) and Cumulative Distribution Functions (CDFs) are used in Method 3 to summarize the strain gradient from these line scans. The two types of plots convey comparable information, as shown in Table 4.7. The PDF, $\mathrm{g(x)}$, is the derivative of $\mathrm{f(x)}$, the CDF, normalized by the scale factor in a two-parameter Weibull distribution. The CDF plots are graphed as increasing, stepwise functions, while PDF plots are histograms. The two-parameter Weibull distribution used accounts for only positive values of strain gradient – the strain gradient is always computed from F to M. Weibull PDFs and CDFs have been used recently by Voyiadjis et al. (2021) to capture the heterogeneous plastic flow in a copper alloy subjected to cylindrical nanoindentation. The shape (Weibull slope, β) describes how the data is distributed; $\beta\approx3$ approximates a normal distribution whereas a $\beta\approx1$ gives a right-skewed distribution. The scale factor, η is approximately at the 63rd percentile of the data. Considering a constant β, variation in η either compresses (η decreased) or stretches (η

increased) this distribution (Forbes et al., 2010; Weibull, 1951). The two-parameter Weibull distribution equation used to fit the probability distribution functions of V-free and V-added strain gradients using Minitab software is shown in Table 4.7.

Table 4.7 Weibull Distribution Functions

Cumulative Distribution Function	Probability Density Function
$\mathrm{f(x)} = 1 - \mathrm{e}^{\mathrm{x}^{\beta}}$	$\mathrm{g(x)} = \frac{\beta}{\eta}\left(\frac{\mathrm{x}}{\eta}\right)^{\beta-1} \mathrm{e}^{-(\frac{\mathrm{x}}{\eta})^{\beta}}$
$\beta<0$ range is $x \geq 0$	$\beta<0$, $\eta<0$, range is $0 \leq x < \infty$

The CDF plot shows that for $\varepsilon_{Avg}\approx0.06$ the F/M interface strain gradient is significantly less in the unnotched V-added than in the V-free specimen. Ninety percent of strain gradients calculated at the F/M interface in Figure 4.8a$_1$ are smaller in the V-added than V-free specimen ($\varepsilon'\approx0.06$ vs. $\varepsilon'\approx0.2$, respectively). At $\varepsilon_{Avg}\approx0.10$, well past the point of yielding of both DP1300 steels, when strain partitioning is further pronounced between ferrite and martensite as well as damage now introduced, the strain gradient continues to be significantly less in the unnotched V-added than V-free specimen with 90% of strain gradients calculated in Figure 4.8b$_1$ being smaller in the V-added than V-free specimen ($\varepsilon'\approx0.1$ vs. $\varepsilon'\approx0.3$, respectively). This directly indicates that strain compatibility at the F/M is improved in the V-added steel even at higher strains in which damage is evident. The PDF plots show a significantly narrower deviation from the 'mean' (63rd percentile) of strain gradient in the V-added specimen. Even with an increase in average strain from $\varepsilon_{Avg}\approx0.06$ to $\varepsilon_{Avg}\approx0.1$, the trend of the V-added material deviating much less from the 'mean' strain gradient continues to be prevalent as shown in Figure 4.8a$_2$ and b$_2$. This is also reflected quantitatively in the β and η parameters, at both average strains $\varepsilon_{Avg}\approx0.06$ and $\varepsilon_{Avg}\approx0.1$ in Figure 4.8. The V-added material has a steeper/larger β, and reduced η. This implies that the strain gradients between ferrite and martensite in the V-added material are overall lower and there's a narrower distribution of these strain gradients in comparison to the V-free material.

With the addition of a slight notch (R1) to the specimen design, vanadium-microalloying continues to be significant in reducing the strain gradient at the F/M interface. At $\varepsilon_{Avg}\approx0.1$, within the post-uniform elongation regime, leading to full fracture, of both ultrahigh strength notched

R1 steels, the CDF plot again shows that the majority of strain gradients calculated, as shown in Appendix C Figure C4.2a_1 is still less in the V-added than in the V-free R1 specimen ($\varepsilon^{'}\approx0.1$ vs. $\varepsilon^{'}\approx0.8$, respectively). The PDF plot in Appendix C Figure C4.2(a_2), continues to show a tight spread from the 'mean' strain gradient in the V-added material, steeper/larger β, and smaller *η*, even with an added notch to the specimen design. There is approximately double an increase in scale (η) in strain gradient when comparing to the unnotched V-free (η≈0.1-0.2 in Figure 4.8$a_{2,}b_2$), and V-free R1 ($\eta\approx0.4$ in Appendix C Figure C4.2a_2) specimen at an $\varepsilon_{Avg}\approx0.11$. It was expected that at a higher stress-state from the applied notches, there would be a decrease in deviation from a 'mean' strain gradient. However, there could be stress localized influences from the martensite island arrangement in the specific images used for microstrain mapping as suggested by multiple sources (Amirmaleki et al., 2016; Hasegawa et al., 2004; He et al., 1984; Scott et al., 2018).

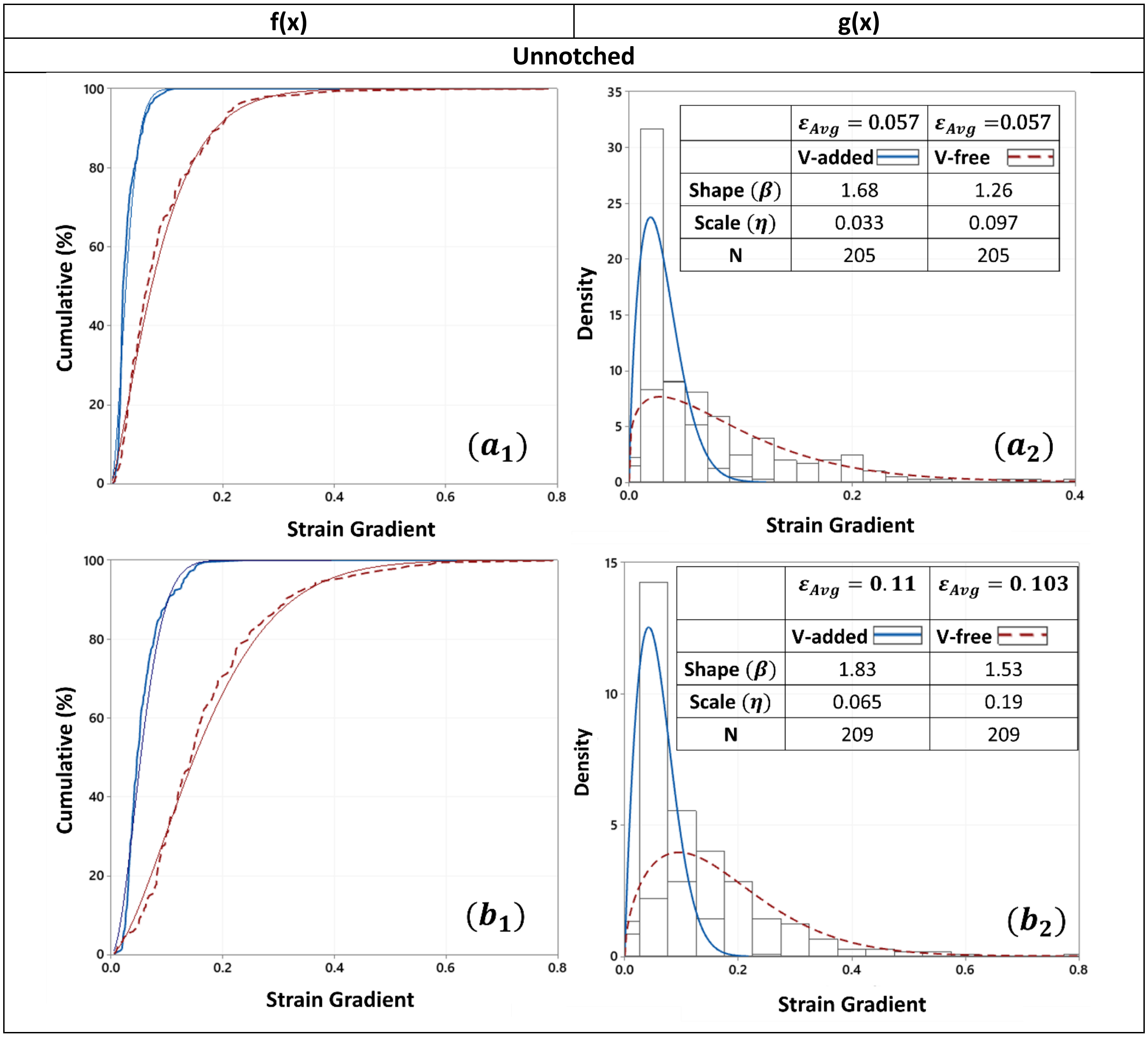

	$\varepsilon_{Avg} = 0.057$	$\varepsilon_{Avg} = 0.057$
	V-added	V-free
Shape (β)	1.68	1.26
Scale (η)	0.033	0.097
N	205	205

	$\varepsilon_{Avg} = 0.11$	$\varepsilon_{Avg} = 0.103$
	V-added	V-free
Shape (β)	1.83	1.53
Scale (η)	0.065	0.19
N	209	209

Figure 4.8 Boltzmann-Sigmodial fitted Weibull distribution plots (Cumulative, left plots f(x); Probability Density, right plots g(x)) comparing unnotched V-free, V-added specimens at ε_{Avg}≈0.06 ($a_{1,2}$), and at ε_{Avg}≈0.10 ($b_{1,2}$)

With a severe notch (R0.2), vanadium-microalloying continues to play a significant role in reducing the strain gradient locally at the F/M interface. At ε_{Avg}≈0.06, close to full fracture of the V-free R0.2 specimen and within the post-uniform regime of the V-added R0.2 specimen, the CDF plot in Appendix C Figure C4.2 b_1 shows that the strain gradient is significantly less in the V-added than V-free R0.2 specimen, with the majority strain gradients being ε'≈0.05 and ε'≈0.4, respectively. The PDF plot Appendix C Figure C4.2 b_2 again shows a narrow spread from the ‘mean’ strain gradient in the V-added material and this is also captured from the steeper/larger β, and smaller η than V-free material at the higher triaxial state.

The greater variability in strain gradients observed at the F/M interface is the most probable reason for earlier fracture in the unnotched V-free microtensile specimen, considering F/M decohesion is the dominant mechanism of damage in DP steels (Matsuno et al., 2015; Samei et al., 2014; Tasan et al., 2014). This was seen using Method 3 that the local von Mises strain computed from numerous, randomly oriented lines projected across F/M regions. This novel approach to defining the strain gradient experimentally and with statistical significance using DIC enables a connection between the UFG scale local strain distribution with the atomic strain distribution (Ghadbeigi et al., 2010), as well as inferring information about dislocation interactions upon straining at the sub-micron level on a series of DP and Interstitial-Free (IF) steels was modelled by Carvalho Resende et al. (2013). The application of in-situ tensile testing under a Transmission Electron Microscope (TEM) to observe the motion of dislocations has been done by previous researchers, on DP (Chen et al., 2020), TRIP (Liu et al., 2017), and pipeline steels (Zhong et al., 2006). The coupling of dislocation-based modelling proposed by Carvalho Resende et al. (2013) and in-situ TEM tensile testing performed by Chen et al. (2020) on DP steels could enable the modelling of severe strain gradients (i.e. a strain differential captured along a nanoscale distance) to be adequately modelled.

Although a reduced strain gradient at the F/M interface in a V-added DP steel makes interfacial decohesion less likely, as shown with Method 3, the V-added material still exhibits classical DP steel micromechanisms of damage, including: martensite cracking mode I and II. Some may also argue that nanoindentation may provide similar results; however, as mentioned by Rodriguez and Gutierrez (2003) nanoindentation is a surface sensitive technique in which the interfacial surface roughness between two grains/phases does not allow for correct interpretation of the data. This is more critical with UFG sizes such as in V-added DP1300 steels. This novel strain gradient µDIC-computational technique provides a means to capture the differences in strain partitioning directly at the F/M interface.

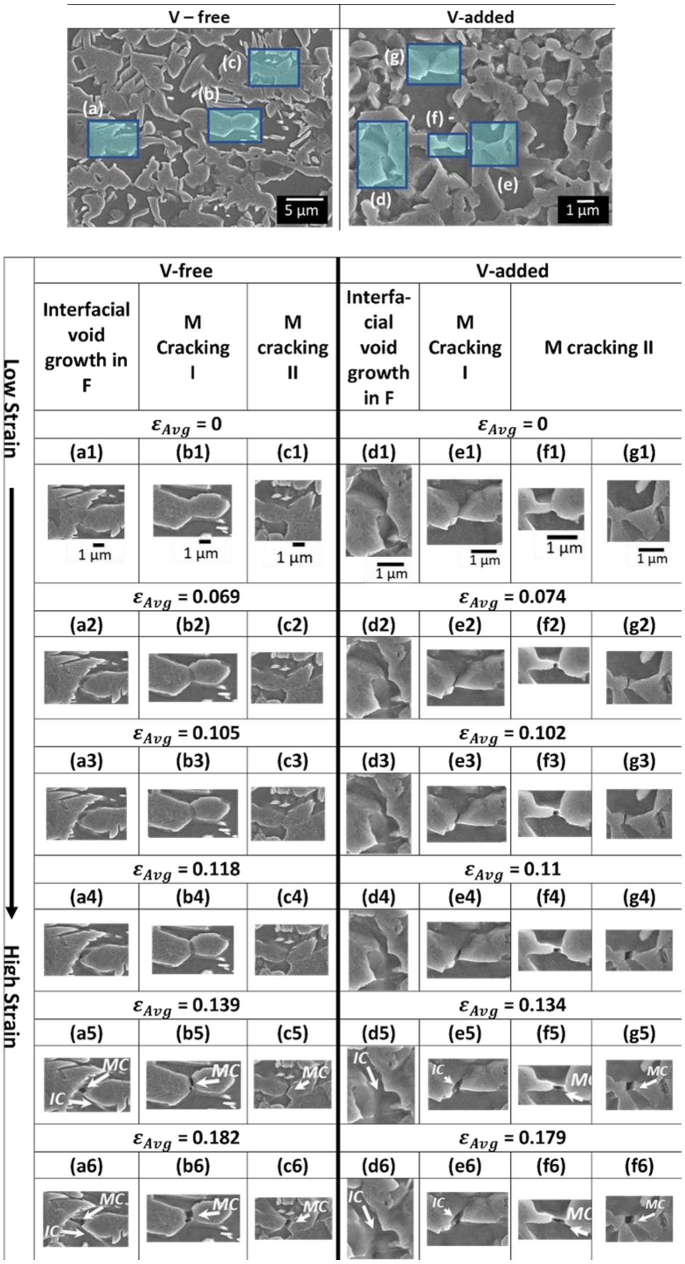

Figure 4.9: Micromechanisms of damage in unnotched V-free and V-added specimen (Top) selected locations for tracking evolutions of damage, and (Below) SEM images revealing micro-event development.

(MC refers to Martensite Cracking ; IC refers to Interfacial Cracking)

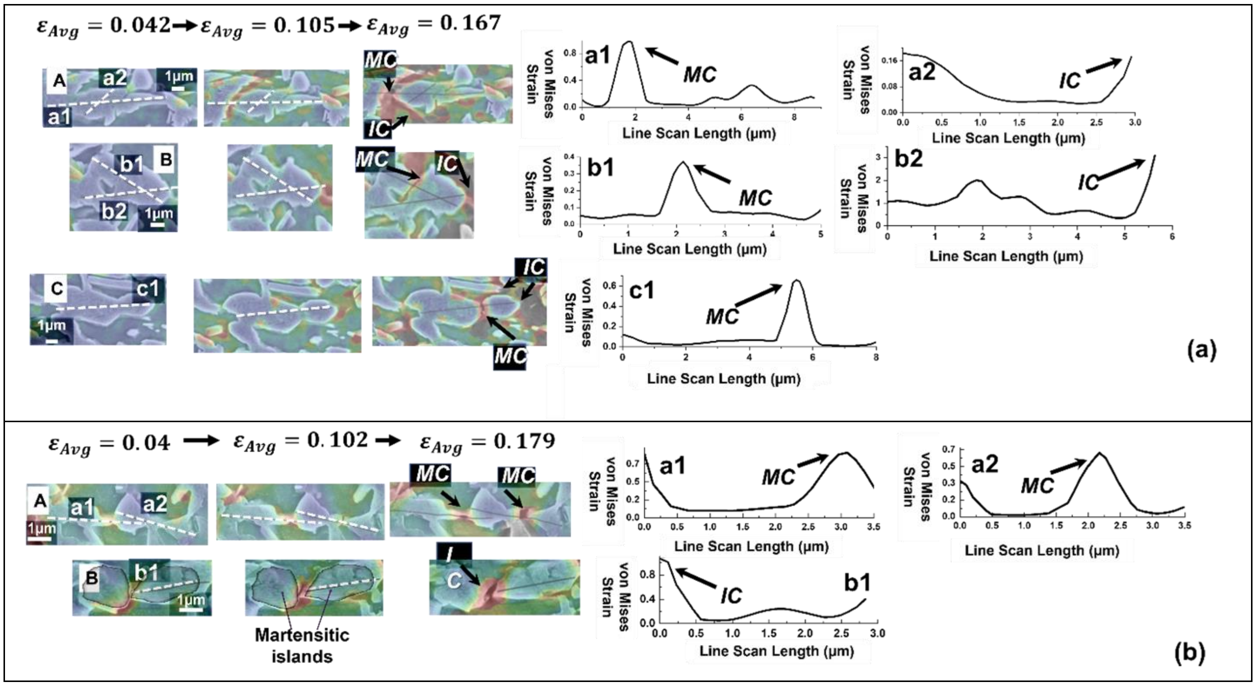

Figure 4.10: Development of local damage in the microstructure of unnotched (a) V-free, (b) V-added specimens

(MC refers to Martensite Cracking; IC refers to Interfacial Cracking)

4.8 Microstructural damage

4.8.1 Evolution of localized damage

The development of local damage events involving martensite cracking and F/M interfacial cracking was captured qualitatively through FESEM imaging and quantitatively with the use of DIC line scanning in the for unnotched and notched V-free and V-added R1 specimens. Figure 4.9 shows the nucleation and growth of microstructural damage through FESEM imaging while Figure 4.10 details the evolution of local von Mises strain just before martensite or interfacial cracking of the unnotched V-free and V-added specimens. Microstructural damage and the evolution of local von Mises strain just before martensite or interfacial cracking of the notched V-free and V-added R1 specimen is shown in Appendix D Figure D4.1 and Appendix E Figure E 4.1, respectively. As indicated in Table 4.2, the true strain at fracture in the R0.2 specimens was too low to capture the evolution of damage before fracture occurred.

There are three types of damage development processes that are observed during the quasi in-situ tensile tests: martensite cracking occurring transverse to the loading direction (modes I), or at some angle to the loading direction induced by shear localization (mode II), and F/M interfacial void growth within ferrite due to the decohesion (Landron et al., 2010; Samei et al., 2014). Each is observed in both steels. In Figure 4.9, V-free, at site a ($a_{1\text{-}6}$), martensite cracking occurs gradually in shear (mode II) then grows in the adjacent ferrite while propagating along the F/M interface. In Figure 4.9, V-free, at site b ($b_{1\text{-}6}$), martensite cracking occurs perpendicular to the tensile pulling direction (mode I). Figure 4.9, V-free, at site c ($c_{1\text{-}6}$), is another example of martensite cracking in shear (mode II). Figure 4.9, V-added, at sites d ($d_{1\text{-}6}$) and e ($e_{1\text{-}6}$), F/M decohesion occurs between two martensite islands of close proximity. Examples of ductile and brittle martensite cracking (mode I) is shown in Figure 4.9, V-added, at site f ($f_{1\text{-}6}$) and at site g ($g_{1\text{-}6}$) of one martensitic island, respectively.

The types of damage development processes observed in the unnotched V-free and V-added specimen were also observed during in-situ tensile testing of notched R1 specimen. Consistent with the observations seen in Figure 4.9 V-added at site d ($d_{1\text{-}6}$), Appendix D Figure D4.1, V-free R1 at site a ($a_{1\text{-}5}$) shows F/M decohesion between two martensite islands. However, instead of damage expanding laterally in ferrite with increasing ε_{Avg} (as seen in the void behaviour of Figure 4.9 V-added at site d ($d_{1\text{-}6}$)) damage propagates in shear within the ferrite with increasing ε_{Avg} and not along the F/M interface, the typical mode of damage propagation in DP steels. Appendix D Figure D4.1, V-free R1, at site b ($b_{1\text{-}5}$) is another instance in which F/M interfacial decohesion occurred, and damage continues to propagate through martensitic islands. By way of contrast, in Appendix D Figure D4.1, V-free R1 at site c ($c_{1\text{-}5}$) we observe martensite shearing (mode II). Appendix D Figure D4.1, V-added R1, at site d ($d_{1\text{-}5}$) shows decohesion along the V(C,N) nanoprecipitate/F interface. This is the desired micromechanism of damage alternative to F/M decohesion as described in Scott et al. (2017) as a result of enhanced vanadium-microalloying. Appendix D Figure D4.1, V-added R1 at site e ($e_{1\text{-}5}$) reveals martensite cracking (mode I) at the surface discontinuity “hole” in the martensitic island. Similarly, Appendix D Figure D4.1, V-added R1 at site f ($f_{1\text{-}5}$) shows substantial deformation in the tail end of a small martensitic island eventually followed by martensite cracking in shear (mode II).

Local von Mises strains were captured from a series of line scans at multiple orientations on various martensitic islands showing full strain mapping coverage just before damage developed, i.e. region of uncorrelation within the area of interest. This analysis was performed on several locations from unnotched specimens in Figure 4.10 and notched R1 specimens in Appendix E Figure E 4.1 which showed sufficient correlation at high strains. The line scans with different orientations, shown in Figure 4.10aA and Figure 4.10aB, show examples of two different micromechanisms of damage. In Figure 4.10aA, also referenced in Figure 4.9 site a (a_{1-6}), the a1 line scan shows severe martensite cracking at a $\varepsilon_{Local} \geq 0.9$, whereas in a different orientation, the a2 line scan shows F/M decohesion at a $\varepsilon_{Local} \geq 0.2$. In Figure 4.10aB, the b1 line scan shows martensite cracking in shear at 45° to the tensile direction, at the surface discontinuity/stress concentrator, and the b2 line scan shows F/M interface decohesion at a $\varepsilon_{Local} \geq 0.3$. Figure 4.10aC, also referenced in Figure 4.9 site b(b_{1-6}), shows a martensitic island cracking perpendicular to the loading direction indicating brittle fracture at $\varepsilon_{Local} \geq 0.6$ with the c1 line scan.

In the unnotched V-added material, Figure 4.10bA, both ductile (a1 line scan) and brittle (a2 line scan) martensite cracking characteristics are observed in one martensitic island. This is the same location referenced in Figure 4.9 site f (f_{1-6}) and site g (g_{1-6}). The a1 line scan shows significant necking with ductile-like micro-fracture at $\varepsilon_{Local} \geq 0.85$, while the a2 line scan shows brittle-type micro-fracture at $\varepsilon_{Local} \geq 0.7$, both occurring in the thinnest portions of the one martensitic island. Rather in Figure 4.10bB , also referenced in Figure 4.9 site e (e_{1-6}); shear fracture of a martensitic island is seemingly shown; however, this is an instance of F/M decohesion between two martensite islands (the separation of both martensitic islands is outlined in black in Figure 4.10bB) situated within a few nanometers of each other. This is a similar instance to what was observed in Figure 4.9 site d (d_{1-6}); yet, Figure 4.10bB shows two martensite islands much closer together, and may have once been a single martensite island prior to the steel finishing processes, or as a result of 'quenching flaws' (He et al., 1984). This could suggest that there is a threshold in spacing between martensite islands in which void growth in ferrite can be accommodated.

In Appendix E Figure E 4.1aA, the notched V-free R1 specimen, ductile martensite cracking was observed. The a1 line scan shows gradual micro-necking of the thinnest portion within a martensitic island, with complete cracking of this island occurring at a $\varepsilon_{Local} \geq 0.9$. In Appendix E Figure E 4.1aB, also referenced in Appendix D Figure D4.1 site b (b_{1-5}), the b1 line scan shows severe interfacial cracking between ferrite and martensite. A significant difference in greyscale contrast due to the interfacial crack was observed from ε_{Avg}=0.108 to ε_{Avg}=0.167 which in turn resulted in poor DIC strain correlation/mapping coverage at an ε_{Avg}=0.167 directly in the F/M interfacial cracked location. Therefore, damage will have had nucleated in this region at a $\varepsilon_{Local}\geq 0.45$. In Appendix E Figure E 4.1aC, similar to Figure 4.10bB, shows the separation of two martensitic islands within nanometers of each other. Kadkhodapour et al. (2011) and Cheloee Darabi et al. (2020) also pointed out the deformation localization of ferrite between two martensite islands in lower strength DP steels (800-980MPa) than presented in this paper. They specifically attribute the eventual void formation in the ferrite between martensite islands due to the local high stress triaxiality (Cheloee Darabi et al., 2020; Kadkhodapour et al., 2011; Rana et al., 2018).

In the case of the notched V-added R1 notched specimen, Appendix E Figure E 4.1bA shows martensite cracking seemingly out of plane having been promoted by a surface discontinuity "hole" in the martensite island similar to what was observed in Figure 4.10aB. Damage nucleated readily during uniaxial tensile straining at $\varepsilon_{Avg}\geq 0.083$ and $\varepsilon_{Local}\geq 0.14$ at this particular site. Appendix E Figure E 4.1bB indicates a martensitic island which shows zero to little local deformation at a high strain of ε_{Avg}=0.182, the smooth curvature of the martensite island is presumed to be the reason for its suppressed local deformation. Rather, interfacial cracking of either side of this martensitic island was observed at an $\varepsilon_{Local}\geq 0.28$. Appendix E Figure E 4.1bC, brittle-like martensite cracking occurs at $\varepsilon_{Local}\geq 0.1$.

4.8.2 X-ray computed tomography analysis of damage

Once damage is introduced at high strains, strain correlation is less likely to be captured via DIC computation. This 2D investigation of damage is supplemented with 3D characterization of damage evolution using µXCT. Examining voids at the surface of the material is not fully indicative of void nucleation and coalescence within the bulk, for reasons detailed by Salvo et al. (2003). Figure 4.11 shows the radiographs and µXCT models of the fractured V-free and V-added specimens. The red pixels on the µXCT models present microstructural damage including martensite cracking, interfacial voids, and micro-cracks. The fracture surfaces consist of local ductile and shear type fractures, the specific influence of vanadium on fracture surfaces of these steels was discussed elsewhere (Samei et al., 2019). Ductile fracture is based on void nucleation and growth which eventually form micro-cracks due to void coalescence and leads to fracture. Shear fractures occur due to development of micro-shear bands. As well, the Rice and Tracey model (Rice and Tracey, 1969) with an isolated void analysis, using a non-hardening material, developed a relationship between void growth and stress triaxiality. They incorporate a multiplication factor, D, to account for the dilation of voids, which they make proportional to triaxiality. The dilation of voids presented a greater impact on ductile damage than any changes in void shape at higher stress triaxialities, or at a high mean stress. The growth rate of voids as a function of triaxiality has also been modelled of thus steels previously (Samei et al., 2020). It was found that vanadium-microalloying reduced the rate of damage evolution and void growth.

There are noticeable amounts of voids in the unnotched specimens up to 0.2mm below the fracture surfaces; however, in the notched specimens, most of the damage exists below the fracture surface. It can be concluded that fracture occurred in the notched specimens as soon as damage accumulated at the center due to the higher stress-state and therefore, significantly reduced the damage tolerance of the steels. This further explains the decrease in true strain at fracture of the notched specimen reported in Table 4.2.

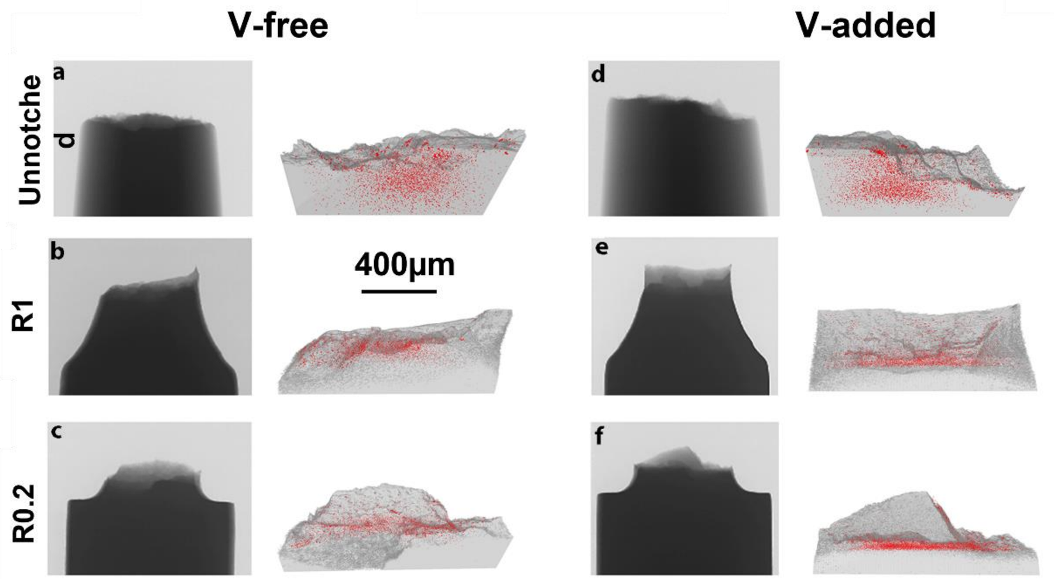

Figure 4.11 Radiographs and μXCT models of the V-free and V-added fractured specimens: the red pixels in the 3D models represents the microstructural damage such as voids and micro-cracks

We have previously used µXCT to quantify microstructural damage evolution as a function of true strain in a wide range of alloys (Nemcko et al., 2016; Samei et al., 2020, 2019); however, in the current work, due to the short gauge lengths and existence of the notches, we could not accurately determine the macroscopic true strain along the gauge area. Nevertheless, as presented in Figure 4.12, we have quantified the distribution of void size up to about 400μm below the top of the fracture surfaces. If the first local peaks at 1.0-1.2μm are ignored (which are at the resolution limit and prone to noise), we can say that the size histograms follow a normal distribution. The first peak at the left side can be associated with the F/M interfacial voids which nucleate due to severe decohesion during post-uniform elongation. As fracture occurs soon after initiation of those voids, they have not had the chance to grow (void growth is a strain-dependent phenomenon); and therefore, lead to the local peaks.

Note that the average void size in the V-free steels are higher than the V-added steels due to larger grain size. Also, the average void size is reduced from the unnotched to R1 and R0.2 specimen as these specimens fractured at lower strains levels.

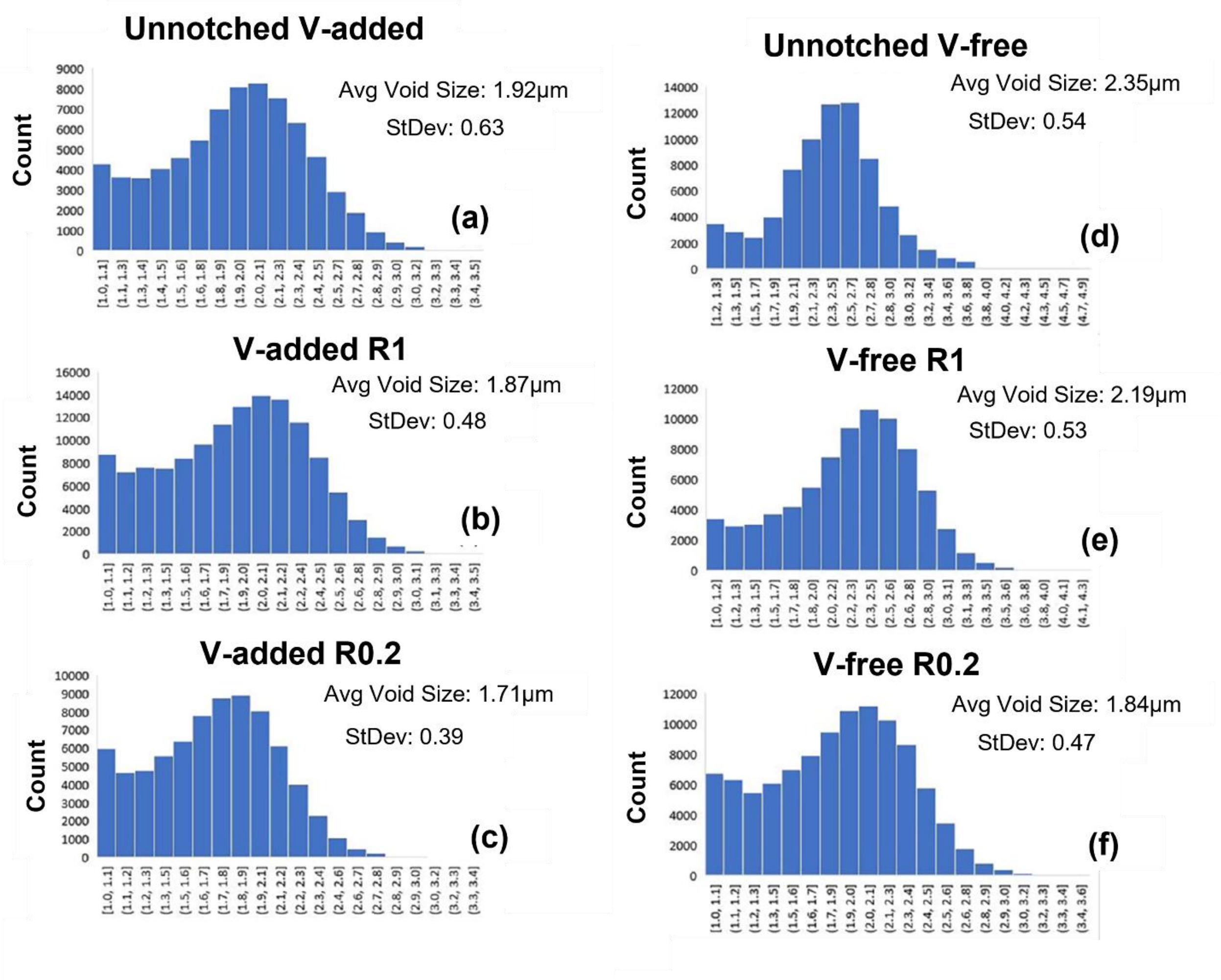

Figure 4.12 Void size distribution in V-added (a) unnotched, (b) R1, (c) R0.2, and V-free (d) unnotched, (e) R1, (f) R0.2 Specimens

4.9 Conclusions

Three different µDIC-based computational techniques were used to define microstrain partitioning between ferrite and martensite. Method 1 is the conventional method of defining strain partitioning based on the average von Mises strain, and average phase strains of ferrite and martensite within the imaged area are quantified. Method 2 is another conventional µDIC-based computational technique, which uses a series of section scans to determine the local strain as a function of section scan length. Although Method 2 does provide multiple opportunities for local strain quantification at the F/M interface, the sections made are typically of one orientation, as is in accordance with conventional DIC computational procedures. It was seen that making focused, multi-oriented line scans on one martensite island can lead to different results in terms of strain partitioning and the micromechanism of damage it experiences. Method 3 quantifies a new parameter called the "strain gradient" in which the change in strain from ferrite to martensite at the interface is calculated using the Boltzmann-Sigmoidal function. This approach confirms that vanadium-microalloying plays a significant role by improving the micromechanical compatibility between ferrite and martensite directly at the interface. This work was repeated on specimen with either a shallow 1mm (R1) notch radius or a severe 0.2mm (R0.2) notch radius. Regardless of this imposed increase in stress-state through specimen design, the strain gradient at the F/M interface in the V-added steel continued to show a more homogenized strain distribution, most importantly at the F/M interface, in the V-added material. Method 3 offers a novel approach to quantifying microstrain partitioning between ferrite and martensite in DP steels, thereby determining the local forming potential of the microstructure with statistical confidence. In other words, Methods 1 and 2 are preferred approaches to defining microstrain partitioning when the global ductility of the material is of importance, i.e. deforming a large portion of a material simultaneously, rather than local ductility, i.e. subjecting the material to a concentrated load. Furthermore, Method 3 provides the opportunity for adequate modelling of F/M decohesion severity in DP steels.

To complete the understanding that vanadium-microalloying reduces the strain gradient at the F/M interface, and therefore suppresses damage to achieve high true strains to fracture, the micromechanisms of damage were tracked using high resolution SEM imaging and 3D characterization of damage evolution was achieved with µXCT. We found that fracture occurs based on void nucleation and growth which begins at the center of the specimens. Extensive damage was found at up to 0.2mm below the fracture surfaces in the unnotched specimens; however, µXCT captured the majority of voids just below the fracture surface which indicates that earlier fracture occurred in the notched specimens as soon as small amounts of microstructural damage accumulated in the center. This was quantitatively confirmed in the void size histograms. The average void size was smaller in R1 compared to the unnotched specimens, and the smallest in the R0.2 specimens due to reduction of the true strain at fracture strain since void growth is a strain-dependant phenomenon.

4.10 Acknowledgements

The authors would like to thank Colin P. Scott at CanmetMATERIALS, Hamilton, ON, Canada, for providing the DP1300 steels. The authors would also like to thank Linfeng Zhou for her contribution to acquiring SEM images during in-situ tensile testing.

4.11 References

Amirmaleki, M., Samei, J., Green, D.E., van Riemsdijk, I., Stewart, L., 2016. 3D micromechanical modeling of dual phase steels using the representative volume element method. Mechanics of Materials 101. https://doi.org/10.1016/j.mechmat.2016.07.011

Ashby, M.F., 1970. The deformation of plastically non-homogeneous materials. Philosophical Magazine 21, 399–424. https://doi.org/10.1080/14786437008238426

Ashby, M.F., 1966. Work hardening of dispersion-hardened crystals. Philosophical Magazine 14, 1157–1178. https://doi.org/10.1080/14786436608224282

ASTM E8M-Standard Test Methods for Tension Testing of Metallic Materials, 2021.

Bao, Y., Wierzbicki, T., 2004. On fracture locus in the equivalent strain and stress triaxiality space. Int J Mech Sci 46, 81–98. https://doi.org/10.1016/j.ijmecsci.2004.02.006

Barsoum, I., Faleskog, J., Pingle, S., 2012. The effect of stress state on ductility in the moderate stress triaxiality regime of medium and high strength steels. Int J Mech Sci 65, 203–212. https://doi.org/10.1016/j.ijmecsci.2012.10.003

Brünig, M., Chyra, O., Albrecht, D., Driemeier, L., Alves, M., 2008. A ductile damage criterion at various stress triaxialities. Int J Plast 24, 1731–1755. https://doi.org/10.1016/j.ijplas.2007.12.001

Brünig, M., Gerke, S., Koirala, S., 2021. Biaxial experiments and numerical analysis on stress-state-dependent damage and failure behavior of the anisotropic aluminum alloy en aw-2017a. Metals (Basel) 11. https://doi.org/10.3390/met11081214

Carvalho Resende, T., Bouvier, S., Abed-Meraim, F., Balan, T., Sablin, S.S., 2013. Dislocation-based model for the prediction of the behavior of b.c.c. materials - Grain size and strain path effects. Int J Plast 47, 29–48. https://doi.org/10.1016/j.ijplas.2013.01.003

Casellas, D., Lara, A., Frómeta, D., Gutiérrez, D., Molas, S., Pérez, L., Rehrl, J., Suppan, C., 2017. Fracture Toughness to Understand Stretch-Flangeability and Edge Cracking Resistance in AHSS. Metall Mater Trans A Phys Metall Mater Sci 48, 86–94. https://doi.org/10.1007/s11661-016-3815-x

Ch.Darabi, A., Chamani, H.R., Kadkhodapour, J., Anaraki, A.P., Alaie, A., Ayatollahi, M.R., 2017. Micromechanical analysis of two heat-treated dual phase steels: DP800 and DP980. Mechanics of Materials 110, 68–83. https://doi.org/10.1016/j.mechmat.2017.04.009

Cheloee Darabi, A., Guski, V., Butz, A., Kadkhodapour, J., Schmauder, S., 2020. A comparative study on mechanical behavior and damage scenario of DP600 and DP980 steels. Mechanics of Materials 143, 103339. https://doi.org/https://doi.org/10.1016/j.mechmat.2020.103339

Chen, B., Lu, T., Yin, K., Sun, B., Dong, Q., Wang, X., 2020. In-situ observation of microcrack evolution in a dual-phase steel during tensile straining. Materials Science and Technology (United Kingdom) 36, 674–680. https://doi.org/10.1080/02670836.2020.1729499

Chen, C.Y., Chiang, L.J., Chen, C.C., Liao, M.H., Kuo, J.S., Chou, Y.H., 2020. Exploring How (Ti + Mo)/C and Ti/Mo Influence the Precipitation Behaviors within Microalloyed Steels: Experimental Evidence and Related Patents Investigation. J Mater Eng Perform 29, 1882–1891. https://doi.org/10.1007/S11665-020-04608-0/FIGURES/10

Chen, X., Jiang, H., Cui, Z., Lian, C., Lu, C., 2014. Hole expansion characteristics of ultra high strength steels. Procedia Eng 81, 718–723. https://doi.org/10.1016/j.proeng.2014.10.066

Choudhary, R., Kumar, H., Garg, R.K., 2010. Analysis and evaluation of heat affected zones in electric discharge machining of EN-31 die steel. Indian Journal of Engineering and Materials Sciences 17, 91–98.

Danas, K., Ponte Castañeda, P., 2012. Influence of the Lode parameter and the stress triaxiality on the failure of elasto-plastic porous materials. Int J Solids Struct 49, 1325–1342. https://doi.org/10.1016/j.ijsolstr.2012.02.006

Denys, K., Coppieters, S., Seefeldt, M., Debruyne, D., 2016. Multi-DIC setup for the identification of a 3D anisotropic yield surface of thick high strength steel using a double perforated specimen. Mechanics of Materials 100, 96–108. https://doi.org/10.1016/j.mechmat.2016.06.011

Dutta, A., Ponge, D., Sandlöbes, S., Raabe, D., 2019. Strain partitioning and strain localization in medium manganese steels measured by in situ microscopic digital image correlation. Materialia (Oxf) 5. https://doi.org/10.1016/j.mtla.2019.100252

El-Naaman, S.A., Nielsen, K.L., Niordson, C.F., 2016. On modeling micro-structural evolution using a higher order strain gradient continuum theory. Int J Plast 76, 285–298. https://doi.org/10.1016/j.ijplas.2015.08.008

Fleck, N.A., Muller, G.M., Ashby, M.F., Hutchinson, J.W., 1994. Strain gradient plasticity: Theory and experiment. Acta Metallurgica Et Materialia 42, 475–487. https://doi.org/10.1016/0956-7151(94)90502-9

Forbes, C., Evans, M., Hastings, N., Peacock, B., 2010. Weibull Distribution. Statistical Distributions 193–201. https://doi.org/10.1002/9780470627242.ch46

Frómeta, D., Lara, A., Grifé, L., Dieudonné, T., Dietsch, P., Rehrl, J., Suppan, C., Casellas, D., Calvo, J., 2021. Fracture Resistance of Advanced High-Strength Steel Sheets for Automotive Applications. Metall Mater Trans A Phys Metall Mater Sci 52, 840–856. https://doi.org/10.1007/s11661-020-06119-y

Frómeta, D., Lara, A., Parareda, S., Casellas, D., 2019. Evaluation of edge formability in high strength sheets through a fracture mechanics approach, in: AIP Conference Proceedings. https://doi.org/10.1063/1.5112704

Ghadbeigi, H., Pinna, C., Celotto, S., Yates, J.R., 2010. Local plastic strain evolution in a high strength dual-phase steel. Materials Science and Engineering A 527, 5026–5032. https://doi.org/10.1016/j.msea.2010.04.052

Gwon, H., Kim, J.K., Shin, S., Cho, L., De Cooman, B.C., 2017. The effect of vanadium micro-alloying on the microstructure and the tensile behavior of TWIP steel. Materials Science and Engineering A 696, 416–428. https://doi.org/10.1016/j.msea.2017.04.083

Ha, J., Lee, J., Kim, J.H., Lee, M.G., Barlat, F., 2017. Investigation of plastic strain rate under strain path changes in dual-phase steel using microstructure-based modeling. Int J Plast 93, 89–111. https://doi.org/10.1016/j.ijplas.2017.02.005

Habib, S.A., Lloyd, J.T., Meredith, C.S., Khan, A.S., Schoenfeld, S.E., 2019. Fracture of an anisotropic rare-earth-containing magnesium alloy (ZEK100) at different stress states and strain rates: Experiments and modeling. Int J Plast 122, 285–318. https://doi.org/10.1016/j.ijplas.2019.07.011

Hance, B., 2016. Advanced high strength steel: Deciphering local and global formability. International Automotive Body Congress, IABC 2016 DEARBORN - Papers.

Hance, B.M., Comstock, R.J., Scherrer, D.K., 2013. The influence of edge preparation method on the hole expansion performance of automotive sheet steels. SAE Technical Papers 2. https://doi.org/10.4271/2013-01-1167

Hasegawa, K., Kawamura, K., Urabe, T., Hosoya, Y., 2004. Effects of microstructure on stretch-flange-formability of 980 MPa grade cold-rolled ultra high strength steel sheets. ISIJ International 44, 603–609. https://doi.org/10.2355/isijinternational.44.603

He, X.J., Terao, N., Berghezan, A., 1984. Influence of martensite morphology and its dispersion on mechanical properties and fracture mechanisms of Fe-Mn-C dual phase steels. Metal Science 18, 367–373. https://doi.org/10.1179/030634584790419953

Huang, C.X., Wang, Y.F., Ma, X.L., Yin, S., Höppel, H.W., Göken, M., Wu, X.L., Gao, H.J., Zhu, Y.T., 2018. Interface affected zone for optimal strength and ductility in heterogeneous laminate. Materials Today 21, 713–719. https://doi.org/10.1016/j.mattod.2018.03.006

Ismail, K., Perlade, A., Jacques, P.J., Pardoen, T., Brassart, L., 2019. Impact of second phase morphology and orientation on the plastic behavior of dual-phase steels. Int J Plast 118, 130–146. https://doi.org/10.1016/j.ijplas.2019.02.005

Kadkhodapour, J., Butz, A., Ziaei Rad, S., 2011. Mechanisms of void formation during tensile testing in a commercial, dual-phase steel. Acta Mater 59, 2575–2588. https://doi.org/10.1016/j.actamat.2010.12.039

Kamikawa, N., Hirohashi, M., Sato, Y., Chandiran, E., Miyamoto, G., Furuhara, T., 2015. Tensile behavior of ferrite-martensite dual phase steels with nano-precipitation of vanadium carbides. ISIJ International 55, 1781–1790. https://doi.org/10.2355/isijinternational.ISIJINT-2015-106

Kang, J., Ososkov, Y., Embury, D.J., Wilkinson, D.S., 2007. Digital image correlation studies for microscopic strain distribution and damage in dual phase steels. Scr Mater 56, 999–1002. https://doi.org/10.1016/j.scriptamat.2007.01.031

Kang, J., Wilkinson, D.S., Embury, J.D., Jain, M., 2005. Microscopic Strain Mapping Using Scanning Electron Microscopy Topography Image Correlation at Large Strain. J Strain Anal Eng Des 40, 559–570. https://doi.org/10.1243/030932405X16151

Karelova, A., Krempaszky, C., Werner, E., Tsipouridis, P., Hebesberger, T., Pichler, A., 2009. Hole expansion of dual-phase and complex-phase AHS steels - Effect of edge conditions. Steel Res Int 80. https://doi.org/10.2374/SRI08SP110

Khan, A.S., Liu, J., 2016. A deformation mechanism based crystal plasticity model of ultrafine-grained/nanocrystalline FCC polycrystals. Int J Plast 86, 56–69. https://doi.org/10.1016/j.ijplas.2016.08.001

Kiran, R., Khandelwal, K., 2014. A triaxiality and Lode parameter dependent ductile fracture criterion. Eng Fract Mech 128, 121–138. https://doi.org/10.1016/j.engfracmech.2014.07.010

Kosaka, N., Funakawa, Y., 2016. Work hardening in ferritic steel containing ultra-fine carbides. ISIJ International 56, 311–318. https://doi.org/10.2355/isijinternational.ISIJINT-2015-218

Lai, Q., Brassart, L., Bouaziz, O., Gouné, M., Verdier, M., Parry, G., Perlade, A., Bréchet, Y., Pardoen, T., 2016. Influence of martensite volume fraction and hardness on the plastic behavior of dual-phase steels: Experiments and micromechanical modeling. Int J Plast 80, 187–203. https://doi.org/10.1016/j.ijplas.2015.09.006

Landron, C., Bouaziz, O., Maire, E., Adrien, J., 2010. Characterization and modeling of void nucleation by interface decohesion in dual phase steels. Scr Mater 63, 973–976. https://doi.org/10.1016/j.scriptamat.2010.07.021

Larour, P., Freudenthaler, J., Weissböck, T., 2017. Reduction of cross section area at fracture in tensile test: Measurement and applications for flat sheet steels. J Phys Conf Ser 896. https://doi.org/10.1088/1742-6596/896/1/012073

Li, J., Lu, W., Chen, S., Liu, C., 2020. Revealing extra strengthening and strain hardening in heterogeneous two-phase nanostructures. Int J Plast 126. https://doi.org/10.1016/j.ijplas.2019.11.005

Li, X., Roth, C.C., Mohr, D., 2019. Machine-learning based temperature- and rate-dependent plasticity model: Application to analysis of fracture experiments on DP steel. Int J Plast 118, 320–344. https://doi.org/10.1016/j.ijplas.2019.02.012

Liu, J., Chen, C., Feng, Q., Fang, X., Wang, H., Liu, F., Lu, J., Raabe, D., 2017. Dislocation activities at the martensite phase transformation interface in metastable austenitic stainless steel: An in-situ TEM study. Materials Science and Engineering: A 703, 236–243. https://doi.org/https://doi.org/10.1016/j.msea.2017.06.107

Lou, Y., Huh, H., Lim, S., Pack, K., 2012. New ductile fracture criterion for prediction of fracture forming limit diagrams of sheet metals. Int J Solids Struct 49, 3605–3615. https://doi.org/10.1016/j.ijsolstr.2012.02.016

Lou, Y., Zhang, S., Yoon, J.W., 2020. Strength modeling of sheet metals from shear to plane strain tension. Int J Plast 134. https://doi.org/10.1016/j.ijplas.2020.102813

Matsuno, T., Teodosiu, C., Maeda, D., Uenishi, A., 2015. Mesoscale simulation of the early evolution of ductile fracture in dual-phase steels. Int J Plast 74, 17–34. https://doi.org/10.1016/j.ijplas.2015.06.004

Mazzoni-Leduc, L., Pardoen, T., Massart, T.J., 2010. Analysis of size effects associated to the transformation strain in TRIP steels with strain gradient plasticity. European Journal of Mechanics, A/Solids 29, 132–142. https://doi.org/10.1016/j.euromechsol.2009.08.001

Meyers, M.A., Mishra, A., Benson, D.J., 2006. Mechanical properties of nanocrystalline materials. Prog Mater Sci 51, 427–556. https://doi.org/10.1016/j.pmatsci.2005.08.003

Min, J., Stoughton, T.B., Carsley, J.E., Carlson, B.E., Lin, J., Gao, X., 2017. Accurate characterization of biaxial stress-strain response of sheet metal from bulge testing. Int J Plast 94, 192–213. https://doi.org/10.1016/j.ijplas.2016.02.005

Muhammad, W., Brahme, A.P., Ibragimova, O., Kang, J., Inal, K., 2021. A machine learning framework to predict local strain distribution and the evolution of plastic anisotropy & fracture in additively manufactured alloys. Int J Plast 136. https://doi.org/10.1016/j.ijplas.2020.102867

Nemcko, M.J., Qiao, H., Wu, P., Wilkinson, D.S., 2016. Effects of void fraction on void growth and linkage in commercially pure magnesium. Acta Mater 113, 68–80. https://doi.org/10.1016/j.actamat.2016.04.008

Paul, S.K., 2013. Effect of martensite volume fraction on stress triaxiality and deformation behavior of dual phase steel. Mater Des 50, 782–789. https://doi.org/10.1016/J.MATDES.2013.03.096

Pineau, Andre, Pineau, A, Benzerga, A.A., Pardoen, T., 2016. Overview article Failure of Metals I – Brittle and Ductile Fracture Overview article Failure of Metals I – Brittle and Ductile Fracture. Acta Mater 107, 424–483. https://doi.org/10.1016/j.actamat.2015.12.034

Pushkareva, I., Shalchi-Amirkhiz, B., Allain, S.Y.P., Geandier, G., Fazeli, F., Sztanko, M., Scott, C., 2020. The influence of vanadium additions on isothermally formed bainite microstructures in medium carbon steels containing retained austenite. Metals (Basel) 10. https://doi.org/10.3390/met10030392

Ramazani, A., Kazemiabnavi, S., Larson, R., 2016. Quantification of ferrite-martensite interface in dual phase steels: A first-principles study. Acta Mater 116, 231–237. https://doi.org/10.1016/J.ACTAMAT.2016.06.047

Rana, A.K., Paul, S.K., Dey, P.P., 2018. Effect of Martensite Volume Fraction on Strain Partitioning Behavior of Dual Phase Steel. Physical Mesomechanics 21, 333–340. https://doi.org/10.1134/S1029959917040070

Rice, J.R., Tracey, D.M., 1969. On the ductile enlargement of voids in triaxial stress fields*. J Mech Phys Solids 17, 201–217. https://doi.org/10.1016/0022-5096(69)90033-7

Rodriguez, R., Gutierrez, I., 2003. Unified Formulation to Predict the Tensile Curves of Steels with Different Microstructures. Materials Science Forum 426–432, 4525–4530.

Salehiyan, D., Samei, J., Amirkhiz, B.S., Hector, L.G., Wilkinson, D.S., 2020. Microstructural Evolution During Deformation of a QP980 Steel. Metall Mater Trans A Phys Metall Mater Sci 51, 4524–4539. https://doi.org/10.1007/s11661-020-05882-2

Salvo, L., Cloetens, P., Maire, E., Zabler, S., Blandin, J.J., Buffière, J.Y., Ludwig, W., Boller, E., Bellet, D., Josserond, C., 2003. X-ray micro-tomography an attractive characterisation technique in materials science. Nucl Instrum Methods Phys Res B 200, 273–286. https://doi.org/10.1016/S0168-583X(02)01689-0

Samei, Green, D.E., Golovashchenko, S., 2014. Metallurgical Investigations on Hyperplasticity in Dual Phase Steel Sheets. J Manuf Sci Eng 136. https://doi.org/10.1115/1.4027492

Samei, J., Green, D., Golovashchenko, S., 2014. Analysis of Failure in Dual Phase Steel Sheets Subject to Electrohydraulic Forming. J Manuf Sci Eng 136, 051010. https://doi.org/10.1115/1.4027940

Samei, J., Green, D.E., Cheng, J., de Carvalho Lima, M.S., 2016. Influence of strain path on nucleation and growth of voids in dual phase steel sheets. Mater Des 92. https://doi.org/10.1016/j.matdes.2015.12.103

Samei, J., Green, D.E., Golovashchenko, S., Hassannejadasl, A., 2013. Quantitative microstructural analysis of formability enhancement in dual phase steels subject to electrohydraulic forming. J Mater Eng Perform 22. https://doi.org/10.1007/s11665-012-0438-2

Samei, J., Pelligra, C., Amirmaleki, M., Wilkinson, D.S., 2020. Microstructural design for damage tolerance in high strength steels. Mater Lett 269. https://doi.org/10.1016/j.matlet.2020.127664

Samei, J., Zhou, L., Kang, J., Wilkinson, D.S., 2019. Microstructural analysis of ductility and fracture in fine-grained and ultrafine-grained vanadium-added DP1300 steels. Int J Plast 117, 58–70. https://doi.org/10.1016/j.ijplas.2017.12.009

Scott, C.P., Fazeli, F., Shalchi Amirkhiz, B., Pushkareva, I., Allain, S.Y.P., 2017. Structure-properties relationship of ultra-fine grained V-microalloyed dual phase steels. Materials Science and Engineering A 703, 293–303. https://doi.org/10.1016/j.msea.2017.07.051

Scott, C.P., Shalchi Amirkhiz, B., Pushkareva, I., Fazeli, F., Allain, S.Y.P., Azizi, H., 2018. New insights into martensite strength and the damage behaviour of dual phase steels. Acta Mater 159, 112–122. https://doi.org/10.1016/j.actamat.2018.08.010

Skripnyak, V. V., Skripnyak, E.G., Skripnyak, V.A., 2020. Fracture of titanium alloys at high strain rates and under stress triaxiality. Metals (Basel) 10. https://doi.org/10.3390/met10030305

Tang, A., Liu, H., Chen, R., Liu, G., Lai, Q., Zhong, Y., Wang, L., Wang, J., Lu, Q., Shen, Y., 2021. Mesoscopic origin of damage nucleation in dual-phase steels. Int J Plast 137. https://doi.org/10.1016/j.ijplas.2020.102920

Tardif, N., Kyriakides, S., 2012. Determination of anisotropy and material hardening for aluminum sheet metal. Int J Solids Struct 49, 3496–3506. https://doi.org/10.1016/j.ijsolstr.2012.01.011

Tasan, C.C., Bechtold, M., Schemmann, L., Tsuzaki, K., Raabe, D., Diehl, M., Zheng, C., Koyama, M., Roters, F., Ponge, D., Peranio, N., Yan, D., 2015. An Overview of Dual-Phase Steels: Advances in Microstructure-Oriented Processing and Micromechanically Guided Design. Annu Rev Mater Res 45, 391–431. https://doi.org/10.1146/annurev-matsci-070214-021103

Tasan, C.C., Hoefnagels, J.P.M., Diehl, M., Yan, D., Roters, F., Raabe, D., 2014. Strain localization and damage in dual phase steels investigated by coupled in-situ deformation experiments and crystal plasticity simulations. Int J Plast 63, 198–210. https://doi.org/10.1016/j.ijplas.2014.06.004

Van Beers, P.R.M., McShane, G.J., Kouznetsova, V.G., Geers, M.G.D., 2013. Grain boundary interface mechanics in strain gradient crystal plasticity. J Mech Phys Solids 61, 2659–2679. https://doi.org/10.1016/j.jmps.2013.08.011

Voyiadjis, G.Z., Jeong, J., Kysar, J.W., 2021. Grain size dependence of polycrystalline plasticity modeling in cylindrical indentation. Comput Mech 68, 499–543. https://doi.org/10.1007/s00466-020-01940-z

Wang, L., Li, M., Tan, H., Feng, Y., Xi, Y., 2020. Enhanced Mechanical Properties of a Gradient Nanostructured Medium Manganese Steel and Its Grain Refinement Mechanism. J Mater Eng Perform 29, 3812–3823. https://doi.org/10.1007/s11665-020-04903-w

Wang, X.G., Wang, L., Huang, M.X., 2017. Kinematic and thermal characteristics of Lüders and Portevin-Le Châtelier bands in a medium Mn transformation-induced plasticity steel. Acta Mater 124, 17–29. https://doi.org/10.1016/j.actamat.2016.10.069

Weck, A., Wilkinson, D.S., Maire, E., 2008. Observation of void nucleation, growth and coalescence in a model metal matrix composite using X-ray tomography. Materials Science and Engineering A 488, 435–445. https://doi.org/10.1016/j.msea.2007.11.050

Weck, A.G., 2007. The Role of Coalescence on Ductile Fracture. PhD-thesis Ph.D., 291.

Weibull, W., 1951. Wide applicability. J Appl Mech 103, 293–297.

Yalçinkaya, T., Güngör, G.Ö., Çakmak, S.O., Tekoğlu, C., 2019. A Micromechanics Based Numerical Investigation of Dual Phase Steels. Procedia Structural Integrity 21, 61–72. https://doi.org/10.1016/j.prostr.2019.12.087

Yoon, J.I., Jung, J., Lee, H.H., Kim, G.S., Kim, H.S., 2016. Factors governing hole expansion ratio of steel sheets with smooth sheared edge. Metals and Materials International 22, 1009–1014. https://doi.org/10.1007/s12540-016-6346-5

Zhang, H., Coppieters, S., Jiménez-Peña, C., Debruyne, D., 2019. Inverse identification of the post-necking work hardening behaviour of thick HSS through full-field strain measurements during diffuse necking. Mechanics of Materials 129, 361–374. https://doi.org/10.1016/j.mechmat.2018.12.014

Zhang, S., Wang, L., Zhu, G., Diehl, M., Maldar, A., Shang, X., Zeng, X., 2022. Predicting grain boundary damage by machine learning. Int J Plast 150. https://doi.org/10.1016/j.ijplas.2021.103186

Zhong, Y., Xiao, F., Zhang, J., Shan, Y., Wang, W., Yang, K., 2006. In situ TEM study of the effect of M/A films at grain boundaries on crack propagation in an ultra-fine acicular ferrite pipeline steel. Acta Mater 54, 435–443. https://doi.org/10.1016/j.actamat.2005.09.015

Zhou, L., 2018. Effect of Vanadium on Fracture of DP1300 Steels (Master of Science). McMaster University.

4.12 Appendices

4.12.1 Appendix A: Finite Element Estimation of Stress Triaxiality in Notched Tensile Specimen

Based on the approach outlined in Section 4.3, Figure A 4.1 shows the approximated true stress versus true plastic strain data extrapolated to a plastic strain past each specimen's true strain at fracture using the Voce-Linear hardening model. For this work, we focus predominately on microscopic deformation and therefore smoothening of the experimental macro-DIC-acquired, directly at the center of specimen notches, has been applied to reduce any dramatic fluctuations seen in stress-strain behavior. This was done in order to simplify the analysis and merely highlight the significant differences in flow between the unnotched and notched specimen. The virtual extensometer drawn for the DIC computation of notched specimen was placed in the centre of the notches and did not extend past 0.5mm for each of the notched R1 and R0.2 specimen tested. It is worth noting that, in general, computing the stress-strain curves of notched specimen is not reliable due to the non-uniform deformation in both the x and y axis.

$$\sigma = \sigma_y + q * \left(1 - e^{-b*\varepsilon_{pl}}\right) + h * \varepsilon_{pl} \qquad \text{Equation A 4.1}$$

(a)

	σ_y	q	b	h
V-free R0.2	1300.53	147.30	556	1891
V-free R1	779.27	511.70	75	917
V-added R0.2	687.70	889.20	122	1240
V-added R1	759.99	673.50	104	1385

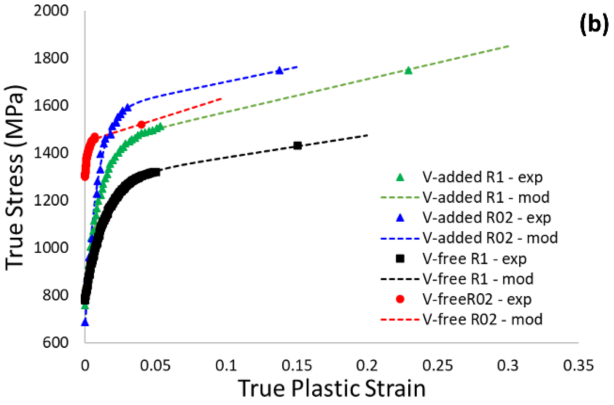

Figure A 4.1: In ABAQUS simulations, the true stress-strain curves were extrapolated past the true strain at fracture for each notched specimen. MATLAB fitted parameters to Equation A 4.1(a). True stress-plastic strain inputs of V-free and V-added notched specimen (b).

*(*exp *refers to experimentally determined uniaxial tensile testing data;* mod *refers to modelled data from MATLAB)*

A finite element model was developed using eight-node, linear brick, continuum elements (C3D8R) with reduced integration and hourglass control. Global triaxiality outputs were obtained from the centre of the specimen, whereas the local triaxiality outputs were obtained from centroids of the imaging locations detailed in Figure 4.2. To obtain the local triaxiality of the area images the centroid of 4 joined elements were averaged, sampling a volume of $5\text{x}10^{-4}\ \text{mm}^3$. The intent of this work is to capture microstrain gradients and the micromechanisms of damage in V-free and V-added unnotched and notched specimen, rather than their differences in plastic behavior. Advanced methods to identify the strain hardening behaviors of non-uniformly deforming specimen will be implemented in a future study, such as those employed elsewhere (Denys et al., 2016; Lou et al., 2020; Tardif and Kyriakides, 2012; Zhang et al., 2019).

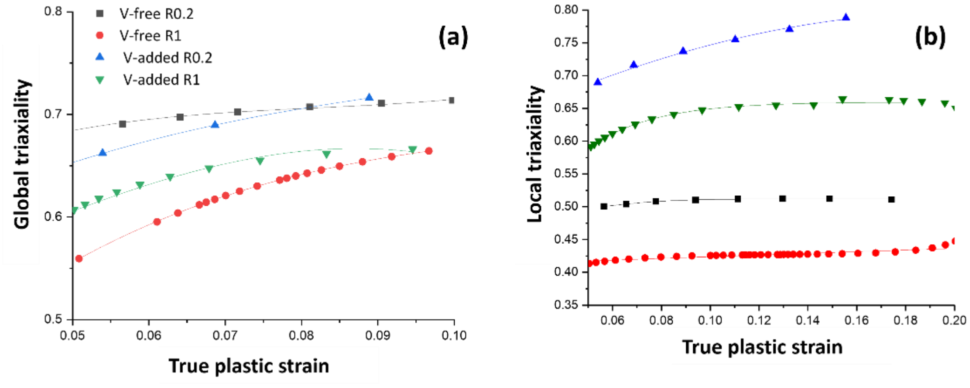

	V-free R1	V-free R0.2	V-added R1	V-added R0.2
Average Global Triaxiality	0.65	0.70	0.65	0.70
Average Local Triaxiality	0.42	0.48	0.60	0.62

(c)

Figure A4.2 Global triaxiality (a) and local triaxiality (b) as a function of plastic strain. The quantified average Global and Local triaxiality of notched V-free and V-added specimen (c)

4.12.2 Appendix B: Determination of Strain Gradient Parameters

$$\varepsilon = \frac{\varepsilon_{\min} - \varepsilon_{\max}}{A + e^{(x-x_0)/dx}} + \varepsilon_{\max}$$ Equation B4.1

We now assign $\beta = \varepsilon_{min} - \varepsilon_{max}$ and substituting A= 1, we can determine the strain gradient ε':

$$\varepsilon' = \frac{-\beta(^{-1}/_{dx})e^{(x-x_0)/dx}}{(e^{(x-x_0)/dx})^2}$$ Equation B4.2

$$\varepsilon' = \frac{-\beta\left(^{-1}/_{dx}\right)e^{(x-x_0)/dx}}{\left(1+2e^{(x-x_0)/dx}+\left(e^{(x-x_0)/dx}\right)^2\right)} \qquad \text{Equation B4.3}$$

As x approaches x_0 we find that $e^{(x-x_0)/dx} \sim e^0 \sim 1$ and so

$$\varepsilon' = \frac{-\beta\left(^{-1}/_{dx}\right)}{(1+2+(1)^2)} = \frac{\beta\left(^{1}/_{dx}\right)}{(4)} = \frac{\varepsilon_{min}-\varepsilon_{max}}{(4\,dx)} \qquad \text{Equation B4.4}$$

Therefore,

$$\varepsilon' = \frac{\varepsilon_{min}-\varepsilon_{max}}{4\,dx} \qquad \text{Equation B4.5}$$

4.12.3 Appendix C: Assessment of Strain Variation Using Methods 2 and 3

The table below contains additional line scans based on method 2 for the two notched geometries.

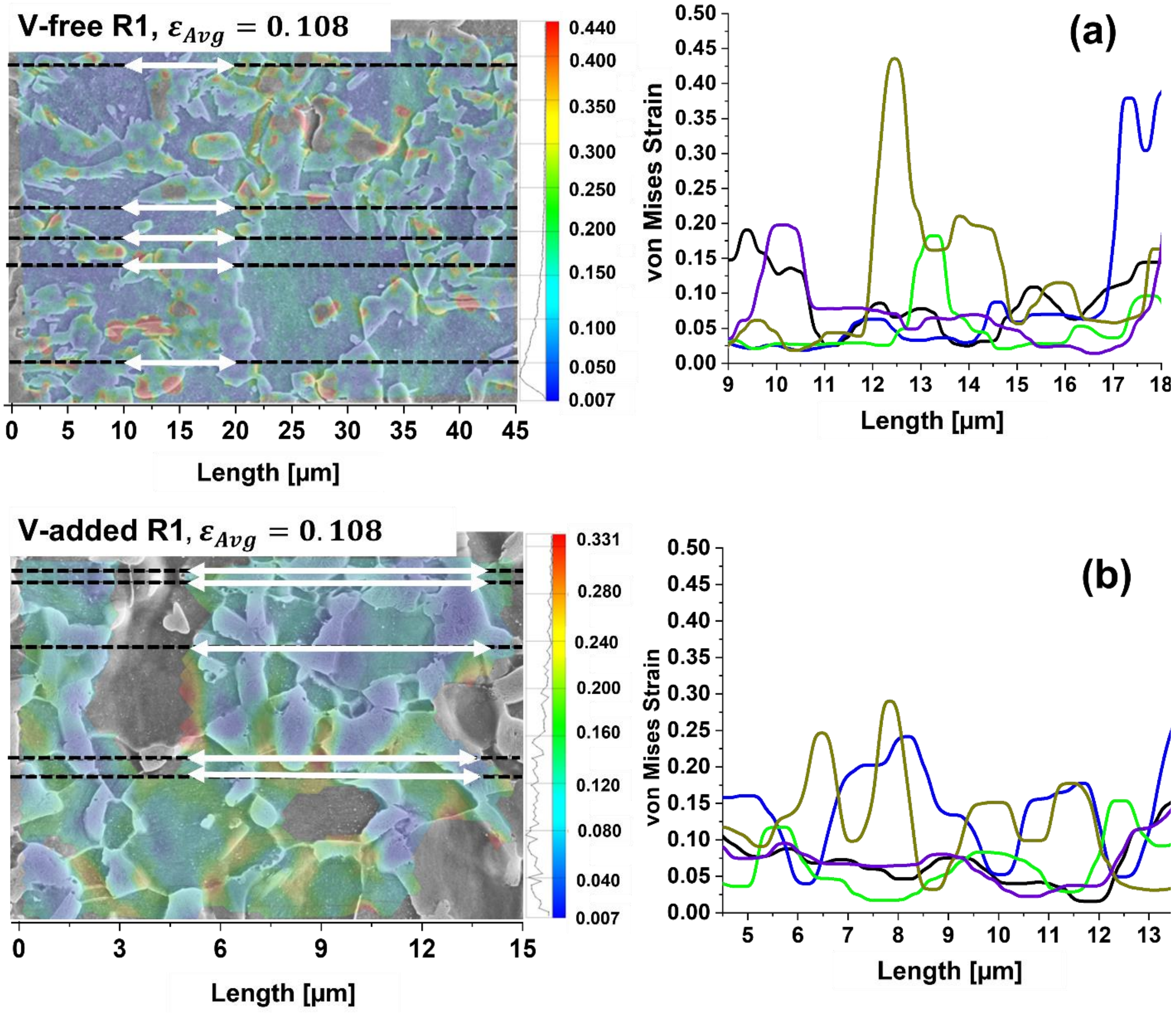

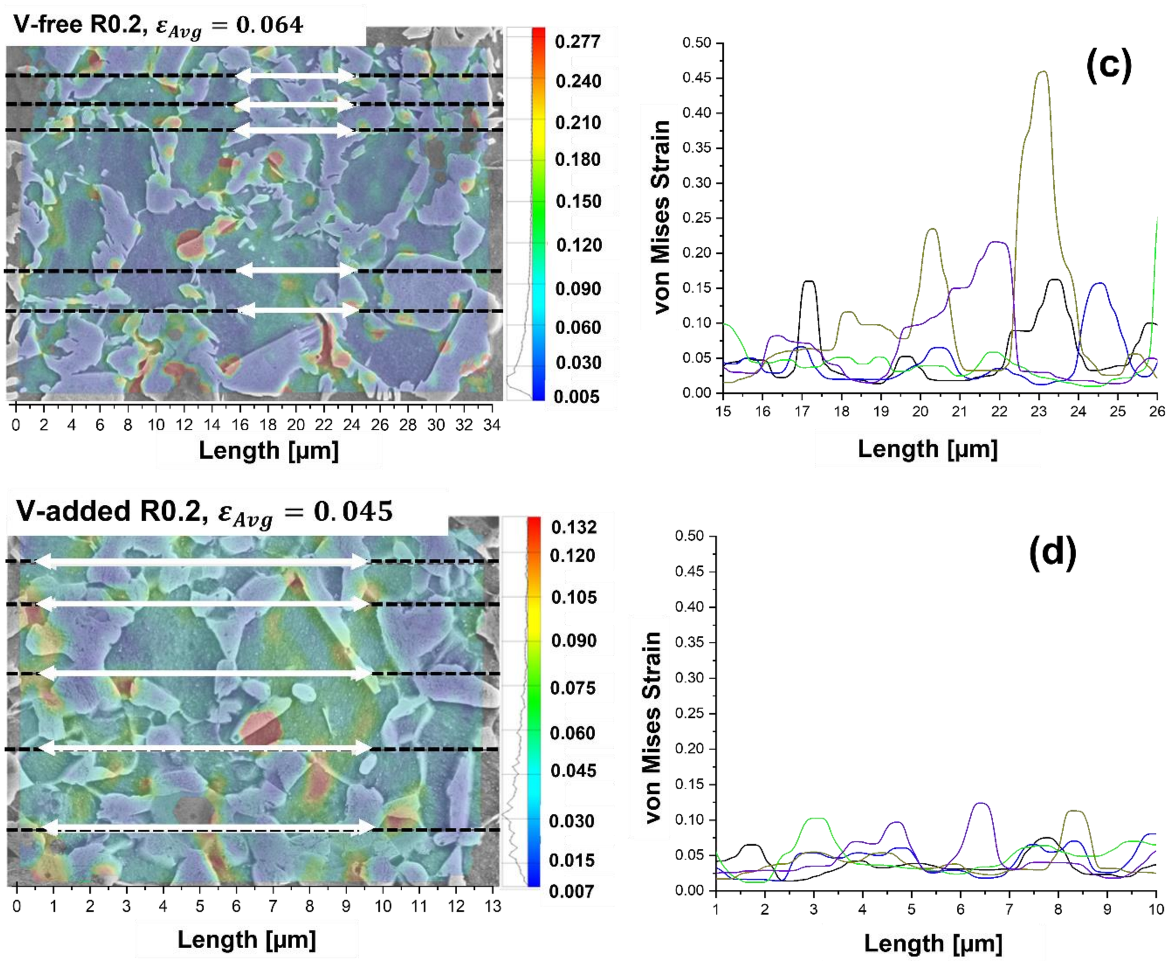

Figure C4.1 Local strain variations on 5 sample lines for the notched (a) V-free, (b) V-added R1 and (c) V-free, (d) V-added R0.2 specimens

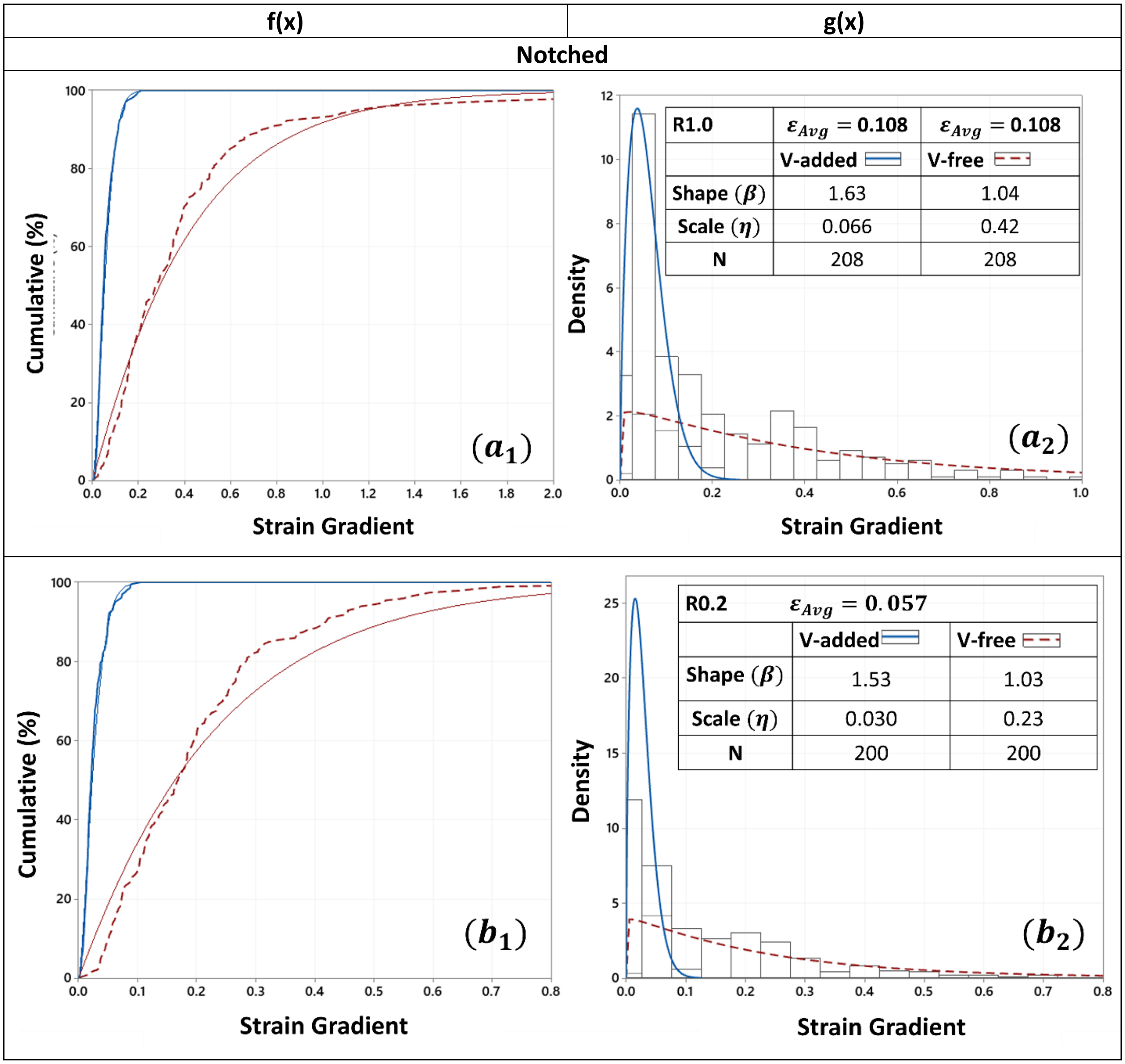

R1.0	$\varepsilon_{Avg} = 0.108$	$\varepsilon_{Avg} = 0.108$
	V-added	V-free
Shape (β)	1.63	1.04
Scale (η)	0.066	0.42
N	208	208

R0.2	$\varepsilon_{Avg} = 0.057$	
	V-added	V-free
Shape (β)	1.53	1.03
Scale (η)	0.030	0.23
N	200	200

Figure C4.2 Boltzmann-Sigmodial fitted Weibull distribution plots (Cumulative, left plots; Probability Density, right plots g(x)) comparing notched V-free and V-added specimens at R1 ($a_{1,2}$) and at R0.2 ($b_{1,2}$)

4.12.4 Appendix D: Evolution of local von Mises strain in notched specimens

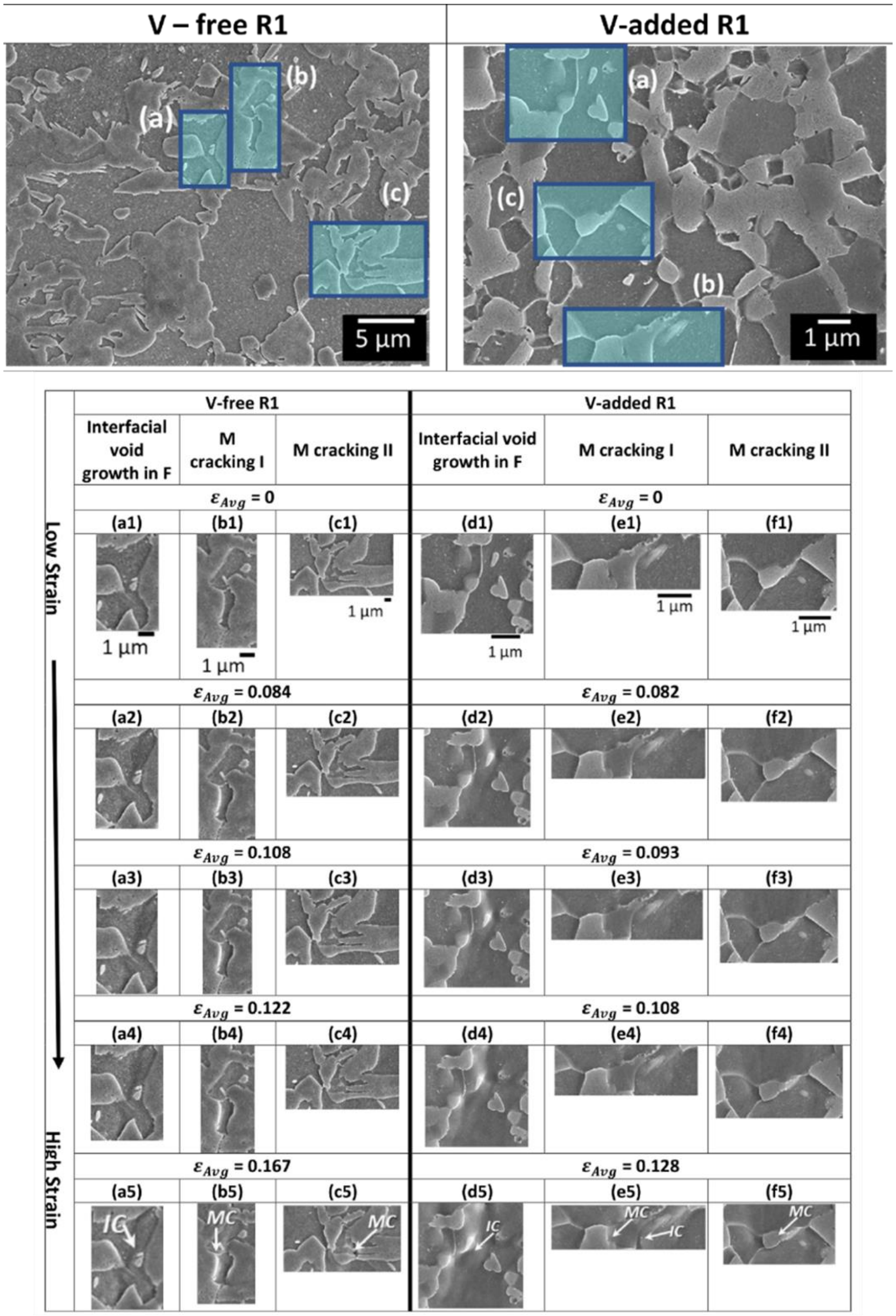

Figure D4.1: Micromechanisms of damage in notched V-free and V-added R1 specimen (Top) selected locations for tracking evolutions of damage, and (Below) SEM images revealing micro-event development

(MC refers to Martensite Cracking; IC refers to Interfacial Cracking)

4.12.5 Appendix E: Evolution of Localized Damage in Notched Specimens

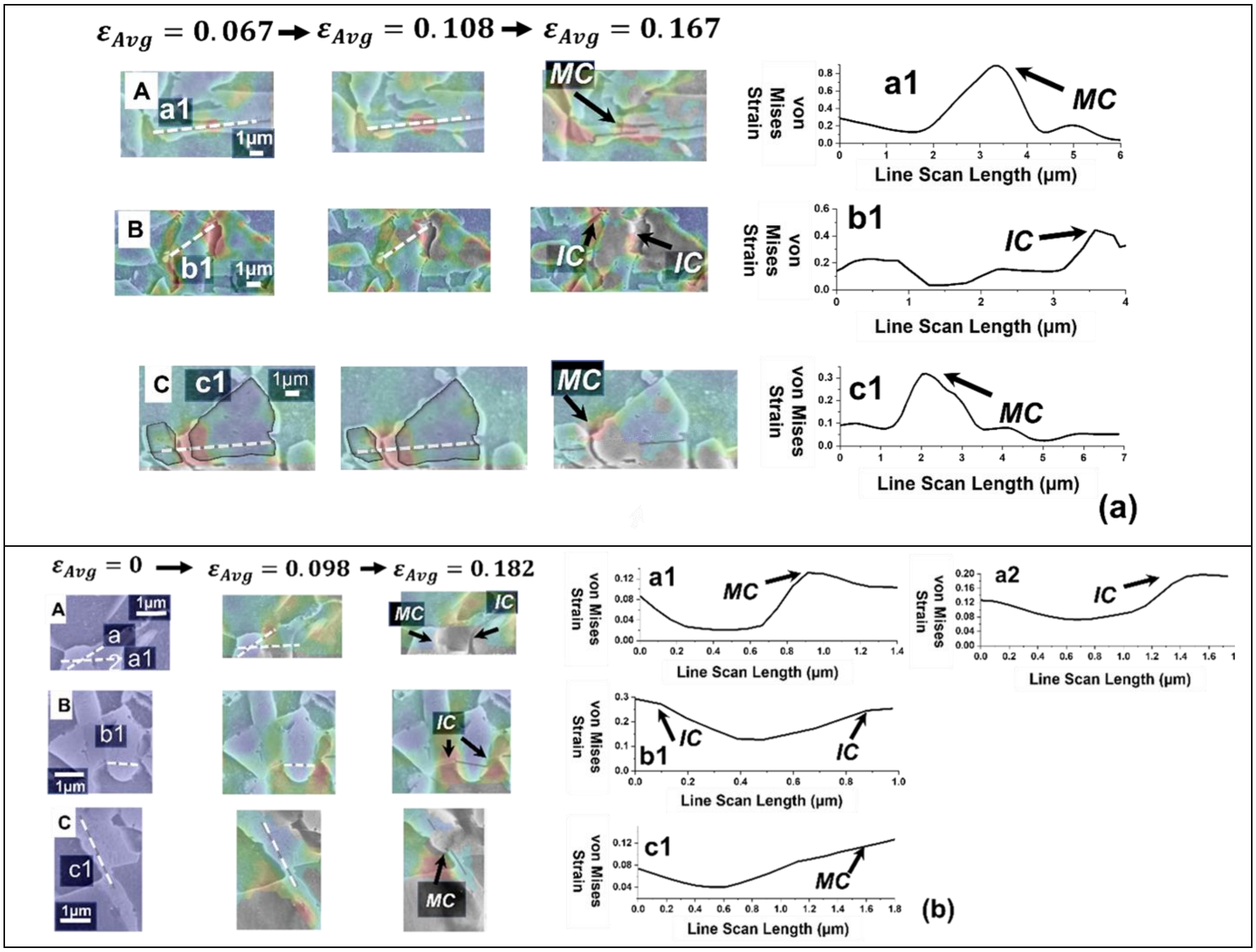

Figure E 4.1: Development of local damage in the microstructures of notched (a) V-free R1, and (b) V-added R1.

5 Microstrain Partitioning, Transformation Induced Plasticity, and the Evolution of Damage during Deformation of an Austenitic-Martensitic 1.5GPa Quench and Partition Steel

Concetta Pelligra[1], Javad Samei[1], Babak Shalchi Amirkhiz[2], Louis G. Hector Jr.[3], David S. Wilkinson[1]

[1]Department of Materials Science and Engineering, McMaster University, Hamilton, ON, L8S 4L7, Canada

[2]CanmetMATERIALS, Natural Resources Canada, Hamilton, Ontario L8P 0A5, Canada

[3]General Motors R&D Centre, Warren, MI, 48090 United States of America

Materials Science and Engineering: A 895 (2024) 146181

5.1 Abstract

The coupling of multiple advanced characterization techniques performed on a Fe-0.2C-3.4Mn-1.6Si, austenitic-martensitic, Quench and Partition steel (Q&P) with ultrahigh strength (~1.5 GPa) microscopically explains its high true strain at fracture (ε_f) and superior toughness. The benefits of Transformation Induced Plasticity assistance in Third Generation (3G) steel microstructures have been deduced by comparing the behavior of this Q&P steel to that of a Dual Phase (DP) steel of similar strength and grain size. More precisely, by using a novel Digital Image Correlation (DIC)-based computation technique, introduced by Pelligra et al. (2022), we have shown that the local strain gradient at dissimilar phase interfaces, linked to the evolution of Geometrically Necessary Dislocations, increases more slowly in the Q&P steel than in the DP steel, and as a result enables the steel to achieve a high ε_f. Detailed studies of the micromechanical compatibility between phases and dynamic evolution of damage in this Q&P steel have been obtained through quasi in-situ tensile tests conducted under a Field Emission Scanning Electron Microscope coupled with Digital Image Correlation at the microscopic scale. Additionally, void evolution with strain was evaluated using X-ray Computed microtomography while the TRIP kinetics were determined via High Energy X-ray Diffraction. This ultrahigh strength Q&P steel shows an improvement in the micromechanical compatibility, as co-deformation and micro-shearing of dissimilar phases were observed. Despite advances made in the literature to improve the formability of 3G DP steels, these critical microstructural properties render the application of Q&P processes to 3G steels a more suitable manufacturing route in the development of future anti-intrusion and impact resistance components in vehicle body structures.

5.2 Introduction

The development of thin, strong automotive steel sheets for improved fuel economy and reduced green house gas emissions was initially motivated by the oil crisis in 1974. Dual Phase (DP) steels were the first of the Advanced High Strength steel (AHSS) family to be commercialized and compete with Body-in-White (BIW) frames constructed fully from light weight aluminum (Fonstein, 2015). Up to today, the critical limitation of DP steels arises from their poor damage tolerance properties (e.g. poor stretch flangeability, as indicated by weak Hole Expansion Ratios (HERs)). This is the result of a strong microstrain differential between ferrite and martensite. Multiple researchers have shown that the HER of DP steels is inferior to every other AHSS microstructure (Casellas et al., 2017; Chen et al., 2014; Hance et al., 2013; Scott et al., 2018). Despite this, research investigations are still being made to improve the damage tolerance and expand the usage of DP steels as a result of their robust thermomechanical processing (Scott et al., 2017; Tasan et al., 2015). Without reducing steel strength, Scott et al. (2017) documented a 15 % increase in HER with vanadium-microalloying in a 3G DP steel. They attribute this improvement in damage tolerance to a 32 % reduction in the ferrite: martensite Phase Strength Ratio (PSR), which decreases the frequency of ferrite/martensite (F/M) decohesion at high strains. At the micro-level, Samei et al. (2019), then Pelligra et al. (2022) found that increasing the content of vanadium in an Ultra-Fine Grained DP steel, with an ultimate tensile strength (UTS) of 1300 MPa, (UFG DP1300), resulted in microstructural homogenization, reduced microstrain partitioning between phases, and delayed fracture. On the other hand, a more significant amount of research has been devoted to developing Transformation-Induced Plasticity (TRIP) steels that promote dynamic dislocation strengthening using the retained austenite (ɣ)-to-martensite transformation at room temperature. These materials show the potential to improve passenger safety with their high toughness (Celada-Casero et al., 2022; Fonstein, 2015; Jacques et al., 2001; Soleimani et al., 2020). TRIP-assisted steels are advantageous to DP steels because of their improved work hardening (Celada-Casero et al., 2022; Soleimani et al., 2020) and inherent micromechanical compatibility between phases (Dong et al., 2022). Liu et al. (2017) Liu et al. (2017) observed, through in-situ Transmission Electron Microscope (TEM) tensile testing, that the local damage accumulation in a TRIP steel is reduced because of strain being accommodated by the gliding of partial dislocations on two independent slip planes during the transformation. Moreover, the tendency of ɣ to undergo TRIP during deformation, i.e. transform from ɣ-to-martensite under an applied load, or to exhibit Twinning-Induced Plasticity (TWIP), has been crucial in manipulating the Stacking Fault Energy (SFE), and hence the strength-elongation ratio of second generation (2G) AHSSs and third generation (3G) AHSSs thereafter (Qin and Bhadeshia, 2007; Soleimani et al., 2020). In contrast to the phase transformation associated with TRIP, TWIP refers to the development of a mechanically induced domain crystal inside a parent ɣ particle, which shares the same lattice points but in mirrored symmetry (Wang and Zhang, 2016). More importantly, 3G TRIP-assisted steels generally have fewer alloying elements than conventional TRIP steels (Findley et al., 2017) making them more likely to being commercialized. Quench and Partition (Q&P) steels are an example of 3G TRIP-assisted AHSSs which utilize a heat treatment to partially stabilize ɣ through the use of carbon partitioning combined with a considerable amount of Si to inhibit cementite precipitation (Ghosh et al., 2022). The use of quenching and partitioning was first introduced by Speer et al. (2003). This complex manufacturing technique was proposed on the basis that only carbon can diffuse sufficiently rapidly beyond unit cell dimensions below the intercritical annealing regime, termed Constrained Para-Equilibrium (CPE) (Speer et al., 2005). Ultimately, Q&P steels allow cold forming of automotive components which is not possible with conventional high strength steels of comparable strength levels (De et al., 2003). Steels prepared with the quenching and partitioning approach to retain austenite result in refined microstructures with elevated strengths (Speer et al., 2005) and improved elongations, compared to their Quench & Temper (Q&T) counterparts (Barella et al., 2023; Tobata et al., 2012). These steels are first either fully austenitized or intercritically annealed, then subjected to an intermediate quench between the martensite start (M_s) and martensite finish (M_f) temperatures and held at such temperature (for 1-step Q&P) or above the M_s temperature (for 2-step Q&P) (Barella et al., 2023; Kong et al., 2017). In general, the commercialization of 3G TRIP-assisted steels is promising for future anti-intrusion (De Moor et al., 2010) and hot stamping applications (Savic et al., 2020) while meeting the increasing demands for vehicle mass reduction. Comparatively, DP steels used to date are for front-end applications and exterior panels (De Moor et al., 2010). Ultimately, it is predicted that there's a potential of 30–40 % in weight reduction with the use of 3G AHSSs which range from

1300 to 1500 MPa in strength (De Cooman et al., 2012). Savic et al. (2020) compared baseline mechanical properties (Yield Strength (YS), Uniform Elongation (UE), UTS and Total Elongation (TE)) of several >1 GPa, specifically 1180 MPa, AHSSs, one of which was a Q&P steel. The benefits in applying Q&P processes to AHSSs can be noted from Savic et al.'s (2020) work, in which their Q&P steel of interest approaches 3G mechanical targets (~26,000 MPa%) with the least strain rate dependence, whilst also maintaining an ultrahigh YS (~1120 MPa). A high YS is advantageous for anti-intrusion applications, especially compared to the other 3G Carbide-Free bainitic (CFB) TRIP steels featured in their study. This is in tandem to the Q&P steel grade featured in this paper, further discussed in sections 5.3.2 and 5.8.1, in which 3G mechanical properties are approached, and a high YS is maintained. That being said, Q&P processes have been recently applied to improve the ductility of press hardenable steels (PHS)(Liu et al., 2011; Lobbe et al., 2016), martensitic stainless steels (Samei et al., 2021), ductile cast irons (Nishikawa et al., 2019) and Medium Mn (med-Mn) steels (Hidalgo et al., 2019; Seo et al., 2017). The dynamic assessment of microstrain partitioning and damage through in-situ Scanning Electron Microscope (SEM) tensile testing coupled with Digital Image Correlation (DIC), now referred to a µDIC, was first introduced by Kang et al. (2005)and applied to an abundance of automotive steels at lower strengths than this ultrahigh strength Q&P steel of the present study (Ruggles et al., 2016; Tang et al., 2021; Tasan et al., 2014; Yan et al., 2015). The differences in strain partitioning between phases, and damage evolution of a DP and TRIP-assisted Bainitic-Ferritic (TBF) steel of the same strength (980 MPa) were compared by Ruggles et al. (2016). Microstrain maps processed by DIC of this DP steel showed a patchwork type strain pattern, while the TBF steel showed pronounced shear banding suggesting plastic compatibility between phases and therefore, enhanced ductility. Quantitatively, the local strains surrounding the hard phases were 5x higher in the DP than the TBF steel at failure (Ruggles et al., 2016). The present paper offers the same sort of comparison to Ref. (Ruggles et al., 2016) in which differences in microstrain partitioning are evaluated; however, at a higher DIC computation resolution than of that published elsewhere (Kang et al., 2007, 2005; Pelligra et al., 2022; Ruggles et al., 2016; Tang et al., 2021). Furthermore, it was suggested through in-situ tensile testing coupled with Electron Backscatter Diffraction (EBSD) of a commercial Q&P steel, with an ultimate tensile strength (UTS) of 980MPa, (QP980), that there is a critical blocky ɣ size in which compatible deformation with ferrite was possible (Salehiyan, 2018). Blocky ɣ greater than such a threshold size would crack, but its low volume fraction within the steel did not seem to cause detrimental effects to overall composite flow (Samei et al., 2019). This was proven with the use of X-ray computed microtomography (µXCT), in which this QP980 steel, with a ferrite grain size of 4.9µm, showed significantly slower damage evolution compared to an UFG DP1300 steel. The authors attributed this slower damage evolution to the possibility of TRIP-assisted deformation in Q&P steels (Samei et al., 2020). Wang et al. (2017) assessed the impact of martensite morphology on damage evolution while experimenting on a predominately martensitic, TRIP-assisted steel, of similar strength to the Q&P steel detailed in the present paper. They observed, using µDIC on post-processed EBSD maps acquired at different levels of strain, that damage initiated, in the form of micro-cracking at tempered martensite (TM)/coarse martensite phase boundaries. Strain localization in a band-form due to rectangular shaped, high angled, and coarse martensitic islands was observed as more severe than strain localization in the form of dispersed spots throughout the microstructure. With the coupling of Atom Probe Tomography (APT) and TEM, Toji et al. (2014) noted that increasing partitioning time would increase Mn to partition into ɣ and impact the overall macroscopic mechanical behavior of a high strength Q&P steel. Overall, a lot of research to date has been focused on manipulating the Q&P process such as varying Si or Mn content (Ghosh et al., 2022; Qin and Bhadeshia, 2007), microalloying (Findley et al., 2017) or applying cyclic Q&P treatments to attain desired microstructural properties with high ɣ volume fraction for continuous work hardening (Hidalgo et al., 2019). However, the micromechanisms of damage that prompts fracture in these ultrahigh strength TRIP-assisted steels has yet to be explored in significant detail. More importantly, the ≈ 3 % volume change associated with TRIP (Parker and Zackay, 1973) is thought to hinder micro-void nucleation (Jacques et al., 2001; Samei et al., 2020), but this has not been thoroughly investigated. Edge cracking resistance, sometimes described as a material's local formability or damage tolerance (Frómeta et al., 2021, 2019b; Hance, 2016; Larour et al., 2017), has been observed to be poor in first generation (1G) and 3G Q&P steels relative to DP steels. Samei et al. (2020) speculated that this is likely due to the lower carbon content in martensite, otherwise known as the TM, within Q&P steels.

Alternatively, Frómeta et al. (2021), in testing Double-Edge-Notched-Tensile (DENT) specimens of a series of 1G and 3G steels, speculated that the carbon-depleted martensite (or TM) increases the steel's cracking resistance while TRIP reduces cracking resistance in a 3G Q&P steel. Moreover, Samei et al. (2020) showed an improvement of damage tolerance in a TRIP-assisted microstructure by comparing a 1G DP steel to a TRIP steel of similar strength and grain size. They found that, along with a lower damage evolution rate, the TRIP-assisted microstructure also tolerated ~2x more damage at fracture in comparison to the 1G DP steel. Although these sources are contradictory, globally amongst steel researchers it is understood that optimized microstructural design will delay fracture, and it is therefore, necessary to incorporate microstructural features, including microstrain partitioning amongst phases, in fracture modelling (Celada-Casero et al., 2022; Maire et al., 2012). The objective of the present study is to determine the extent to which improved microstructural strain accommodation amongst phases, as a result of the TRIP effect, acts to suppress damage and delay localized fracture in an ultrahigh strength (1.5 GPa) austenitic-martensitic Q&P steel. We first accomplish this with a detailed microstructural characterization of this ultrahigh strength Q&P steel, followed by a thorough comparison of this steel to a DP counterpart of similar strength and grain size. This comparative study has been done to further our understanding of the benefits that TRIP-assistance has in 3G steel microstructures. Quasi in-situ FESEM tensile testing coupled with DIC, as well as µXCT were used to evaluate the microstrain partitioning amongst phases and to capture damage evolution, respectively. A more detailed investigation of the evolution of Geometrically Necessary Dislocations (GNDs) with increasing applied strain was undertaken with the use of a novel µDIC-based computational technique (Pelligra et al., 2022). TRIP kinetics of this ultrahigh strength Q&P steel were determined using High Energy X-ray Diffraction (HE-XRD) as the steel was quasi-statically strained. Ultimately, this paper provides microstructural reasoning as to why this ultrahigh strength Q&P steel can be a suitable candidate for automotive components which require supreme crashworthiness.

5.3 Materials and Methods

5.3.1 Material

The subject material is a two-phase, 16 ± 3 vol% austenitic-balance martensitic Q&P sheet steel, having an UTS of 1500 MPa, (QP1500) and total elongation (TE) of 14 %. This ultrahigh strength Q&P steel was homogenized after casting at 1250°C, then hot rolled from a start temperature of 1250 ◦C to a finishing temperature of 900°C to achieve a final thickness of 4 mm. The steel was then coiled at 650°C, pickled at 85°C and cold rolled to a final thickness of 1 mm. After cold rolling the Q&P process was performed on the steel during which it was austenitized at 820°C (above the Ac_3), then quenched to 180°C, and partitioned at 400°C for 100s. This steel is similar to that used by Park et al. (2019) in the development of crystal plasticity models in which this Q&P steel was produced in lab heats to the recommendations of Refs. (De Moor et al., 2011; Thomas et al., 2015). Discrepancies of the ɣ content as a result of differences in lab heats used or analysis methods have also been noted previously in a QP980 steel (Abu-Farha et al., 2018). During partitioning, the initially quenched martensite was tempered while some of the ɣ, and those which exhibited weak Mn enrichment decomposed to ferrite or, more likely, in the case of ultrahigh strength steels, to bainite (Ding et al., 2023). Using the M_s equation developed by Barbier (2014), the global M_s temperature of the ultrahigh strength Q&P steel is 314°C. The M_s equation proposed by Barbier not only considers the effect of Mn, Si, and C on the M_s, but it also accounts for the effect on Cu, and Ti (>0.5 wt%) in decreasing the M_s temperature (Barbier, 2014). The chemical composition of the subject QP1500 steel, from Glow-Discharge Optical Emission Spectroscopy (GDOES), is detailed in Table 5.1. A significant Si content is typical in Q&P steels, whilst a moderate alloying of Mn in AHSSs is more compatible with industrial practices (Ding et al., 2023).

Table 5.1 QP1500 Chemical Composition (wt%)

C	Mn	Si	Cu	Ti	Ni	P	S	Fe
0.19	3.4	1.6	0.01	0.01	0.008	0.005	0.002	Balance

5.3.2 Mechanical Properties

Mechanical properties were determined following the ASTM E8/ E8M − 15a standard. Sub-size tensile specimens were prepared by wire Electrical Discharge Machining (wEDM) parallel to the rolling direction (RD). Each specimen was ground with 600 grit paper to remove surface oxides and to avoid potential stress concentrators that may result in premature facture. Uniaxial tensile tests were conducted on a 100 kN Instron tensile frame at room temperature using a 1 mm/min crosshead speed. A 25 mm extensometer was used for elongation measurements. The true strain at fracture (ε_f) was calculated using $\varepsilon_f = \ln\left(\frac{A_0}{A_f}\right)$, where A_0 is the initial cross-sectional area before deformation and A_f is the minimum area at fracture. A_f was measured taking into account the left, right and centre thickness of the fractured surface ("ASTM E8M-Standard Test Methods for Tension Testing of Metallic Materials," 2021; Casellas et al., 2017; Hance, 2016). The ASTM subsize tensile specimens' mechanical properties of the subject QP1500 steel are detailed in Table 5.2. The UTS, signifies the Ultimate tensile strength in MPa, UE, Uniform Elongation in %, TE, Total Elongation in %, YS, Yield Strength in MPa, and ε_f, represents the true strain at fracture. A 95 % Confidence Interval (CI) was calculated based on triplicate measurements.

Table 5.2 Mechanical Tensile Properties of QP1500.

	UTS (MPa)	UE (%)	TE (%)	YS (MPa)	ε_f
RD	1540±83	10±1	14±2	1290±120	0.6 ±0.1

5.4 Microstructural Characterization

Before microstructural characterization was carried out, except for the TEM analysis, specimens were polished using standard metallographic polishing procedures, as documented by Salehiyan, (2018). After polishing, Cobalt-Sourced X-ray Diffraction (Co-XRD) was performed on undeformed specimens to verify that the polishing procedure used did not transform a significant amount (≤ 3 vol%) of ɣ to martensite. This ɣ content was compared to the Q&P material used by Park et al. (2019) in which the authors detected 17.5 vol% of ɣ using High Energy X-ray Diffraction (HE-XRD). Details of the Co-XRD procedure used are discussed in section 5.4.4.

5.4.1 Optical and SEM imaging

A Keyence Digital Microscope VHX-5000 was used to observe the steel subjected to Behara's Tint etching (100 mL of distilled water, 0.5 mL hydrochloric acid, and 1g potassium metabisulfite). This etchant tints the TM and bainite, while leaving the carbon-saturated retained austenite and/or transformed martensite (ɣ-M) unetched/white (De et al., 2003; Jeong et al., 1993). In an attempt to observe the distribution of ɣ at a macroscopic level, specimens were tempered at 240°C. This method had previously been used by Bellhouse (2010) on low strength TRIP steels, adapted from Girault et al. (1998), to precipitate ε-carbides in the martensite and allow some differentiation between martensite and ɣ (Soleimani et al., 2020). High-resolution images of the steel after a 1 % Nital etch were acquired with a Field Emission Scanning Electron Microscope (FESEM) of both the heat-treated and as-received Q&P steel. These heat-treated specimens were only used for optical/SEM imaging characterization detailed in section 5.8.2. All other microstructural characterization or mechanical experiments conducted on this steel were performed on its as-received microstructure. Blocky islands observed in the microstructure refer to the retained austenite and/or transformed martensite and are termed as ɣ-M throughout the remainder of this paper.

5.4.2 Electron Backscatter Diffraction

EBSD mapping employed a JSM-7000 Field Emission Scanning Electron Microscope (FESEM) equipped with Aztec indexing software of the cross-sectioned, through-thickness, polished specimen. Maps were collected at a 70◦ tilt at an accelerating voltage of 20 kV, and probe current of 15 mA. The total grain size was measured to be submicron using EBSD for both the Body-Centred-Cubic (BCC) and Face-Centred-Cubic (FCC) phases. In-situ tensile testing coupled with EBSD was also performed to validate the occurrence of gradual TRIP in blocky ɣ islands and the accumulation of GNDs in the TM BCC versus ɣ FCC phase with increased tensile deformation. This procedure is adapted from Salehiyan et al. (2020).

5.4.3 Transmission Electron Microscopy

A Tecnai Osiris TEM with an X-Field Emission Gun (X-FEG), operating at an acceleration voltage of 200 kV was employed with conventional bright field and dark field imaging modes. As well, Scanning Transmission Electron Microscopy (STEM) was performed using a combination of bright field and High-Angle Annular Dark Field (HAADF) detectors. For elemental mapping of the microstructure, Energy X-ray Dispersive Spectroscopy (EDS) was used in STEM mode. To prepare the TEM specimens, 3 mm disks were punched from manually ground 80 µm thick foils. Subsequently, electropolishing was carried out on these disks at 16 V in a twin jet electropolisher

(Struers) using an electrolyte of 10 % perchloric acid in methanol held at − 40 ◦C until perforation was achieved.

5.4.4 X-ray Diffraction

The ɣ content was determined using a Bruker D8 DISCOVER with a DAVINCI design diffractometer equipped with a Vantec 500 (MiKroGap TM technology) area detector and Cobalt Sealed Tube Source. The specimen surface was ground with a fine grit to remove the decarburization layer that may have developed on the specimen, preventing an accurate quantification of ɣ. The X-ray beam size and exposure time used to measure the ɣ content were 0.5 mm and 40 min/measurement, respectively. Specimens were scanned over a 2θ range from 45° to 127° and penetrated ~20µm below the steel's surface (i.e. 2 % of this 1 mm thick steel). The collected two-dimensional (2D) frames were then integrated with the aid of DIFFRAC.EVA Version 4.0 software and the percentage of ɣ was calculated with the Topas software version 4.2 (Salehiyan, 2018). It was presumed that only martensite or TM, without ferrite, was contained in this Q&P steel microstructure, which has been deemed a reasonable assumption considering this steel's exceptional strength (Findley et al., 2017; Toji et al., 2014; Yang et al., 2021). As well, a Hexagonal Closed Packed (HCP)-martensite, otherwise known as epsilon martensite, peak identifier was added during post-processing of XRD scans to validate its absence.

5.5 TRIP Kinetics

The ɣ volume fraction and its mechanical stability as a function of uniaxial strain was determined through HE-XRD. Other researchers have measured TRIP kinetics in 3G steels using cross-sectioned, through-thickness interrupted tensile specimens with the use of Cobalt-sourced X-ray Diffraction (Co-XRD) (Bhadhon, 2022; Pallisco and McDermid, 2020; Patel, 2019). However, this methodology is limiting in terms of specimen penetration, and can only provide a few points to delineate the steel's TRIP kinetics. HE-XRD provides highly resolved, representative information on the ɣ behavior during tensile testing which is needed for realistic automotive damage modelling (Hu et al., 2017; Park et al., 2019). In-situ uniaxial tensile testing, equipped with a 13 kN load frame, was performed at room temperature inside the synchrotron X-ray beam chamber of beamline 11-ID-C at the Argonne Photon Source (APS). Voltage and wavelength used were 105 keV and 0.1173 Å, respectively. The PerkinElmer aSi flat panel area detector was placed at 1.9 m from the specimen to collect high angle ɣ measurements, and a 0.5 × 0.5 mm beam impingement area was used. The HE-XRD beam impingement area was aligned in x and y to determine the precise centre of the specimen for ɣ acquisition. A CeO2 standard was used to calibrate the specimen-to-detector distance of 1.9 m, beam position and tilt. Tensile testing was performed at a strain rate of 0.15 mm/min. A preload <100N was applied to the specimen before commencing each test. A fine white and black speckle pattern was applied on the wEDM dog-bone specimens using an Iwata airbrush for high-resolution 2D DIC. The customized dog-bone dimensions and novel HE-XRD experimentation are detailed in Figure 5.1. The 50 mm DIC camera lens (2448x2048 pixels resolution) with 165 mm of extension tubes was fixed at 180 mm and ~15◦ from the specimen, enabling an 8 mm field of view. Light adjustments were made to maximize speckle patterning contrast whilst avoiding pixel over-saturation. DIC was used to precisely define the localized von Mises strain within the region of 0.5 × 0.5 mm HE-XRD acquisition. HE-XRD measurements of the undeformed specimen were also acquired at multiple rotation degrees to ensure that ɣ measurements were independent of the beam's impingement angle. This experimental procedure was adapted from the original work performed by Abu-Farha et al. (2018).

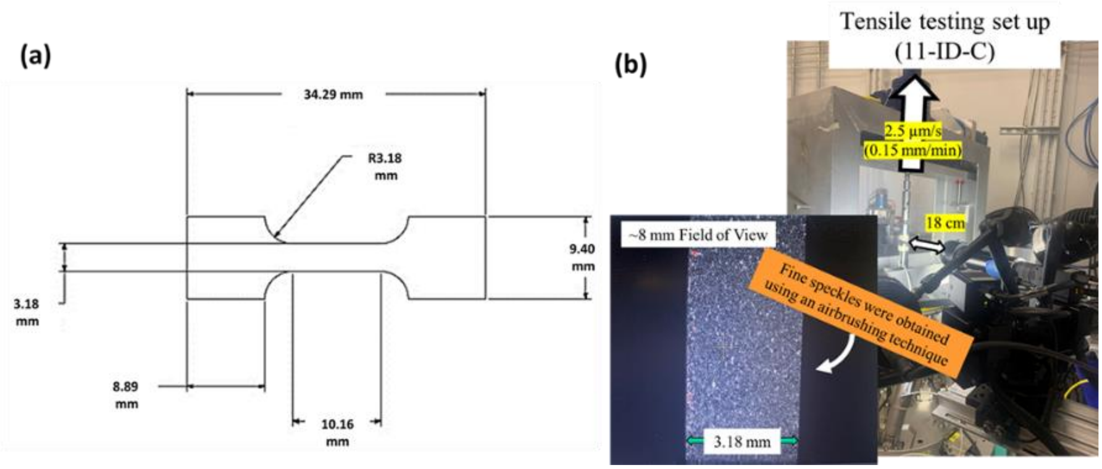

Figure 5.1 Customized dog-bone geometry for the load frame at Argonne APS beamline 11-ID-C. (a) HE-XRD acquisition combined with DIC and uniaxial tensile testing (b) at the Argonne APS Beamline 11-ID-C.

5.6 Microstrain Partitioning

A careful assessment of the microstrain partitioning amongst ɣ-M and TM phases as well as the dynamic evolution of damage in this ultrahigh strength Q&P steel was carried out using quasi in-situ FESEM tensile testing. An hourglass microtensile specimen geometry was used to centralize deformation and damage, as has been applied elsewhere (Kang et al., 2023, 2005; Samei et al., 2019). The use of a manual in-house built tensile stage allowed the working distance to be decreased (10 mm) for improved resolution. The accelerating voltage was kept low (10 kV) to prevent excessive heating, charging, and damage of the specimen during imaging. Imaging was acquired within the centre of the specimen to purposefully avoid any Heat Affected Zone (HAZ) that may have developed during the wEDM specimen preparation (Choudhary et al., 2010). The acquired images at a focused location as a function of tensile strain were coupled with DIC to obtain high-resolution microstrain maps of the microstructure (Kang et al., 2007, 2005). Microstrain partitioning was visualized and quantified from FESEM images processed using the ARAMIS DIC software, GOM Correlate 2018 (gom, 2016). The microstructural features revealed prior etching with 1 % Nital for 10s enabled sufficient µDIC correlation at high average von Mises strains, ε_{Avg} >0.26 as detailed in section 5.8.4. The software assigns facets with a set of unique grayscale intensities from a reference image and tracks the displacement of said facets in the deformed states to compute strain (Schreier et al., 2009). A facet comprising of a unique variation of greyscale-levelled pixels (pxls) rather than a pxl with one grey level is used for convenient tracking in subsequent images. The facet size and point distance (distance between facet centres) were optimized to resolve this steel's average 'in-grain' strain and provide sufficient mapping coverage particularly at high strains. The smaller the point distance applied, the better the spatial resolution of the microstrain map at the cost of longer computational time (gom, 2016). However, to develop reliable damage and failure models, strain needs to be obtained on a scale smaller than the microstructural constituents (Rajan et al., 2012). As well, it is important to note that noise in the strain computation can accumulate if the degree of facet overlap is short in comparison to the surface roughness (Dong and Pan, 2017; Kant and Losic, 2013). To compensate for this, a median filter of 3 was applied to the analysis. At the minimum strain tensor neighbourhood/computation size of 3, the Virtual Strain Gauge length corresponds to two times the point distance (Pelligra et al., 2022). Figure 5.2a and b shows several facets overlapping within a blocky ɣ-M island and outlines an example of 3x3 square of facets used for the µDIC computation. The facet size and point distance used for the µDIC analysis of this QP1500 steel is described in Table 5.4. A facet size of 29pxl x 29pxl and point distance of 11pxl was chosen, resulting in a ~20 % overlap of the facets. The result is a 3x3 facet square height and width which is less than the average grain size of the steel and therefore resolves the average 'in-grain' strain of the Q&P microstructure. An exact 1:1 correlation is not always possible due to the large variation in grain size (i.e. Figure 5.5c shows a ∓ 0.6μm standard deviation in ɣ grain size) in 3G steel microstructures (Dutta, 2019). The microstrain maps were computed using the von Mises equivalent strain with the assumption that deformation takes place at constant volume. The average von Mises strain is calculated within the imaged area during quasi in-situ FESEM tensile testing and is termed as ε_{Avg} throughout this paper. Details of using the ε_{Avg} from an imaged area compared to other μDIC-based computational techniques have been described elsewhere (Pelligra et al., 2022). Microstrain mapping with the von Mises Strain is said to directly correlate to the density of GNDs (Dutta et al., 2019). The local strain gradient (ε') was calculated at dissimilar phase interfaces. Specifically, the ε' was calculated at the retained austenite-transformed martensite/tempered martensite (ɣ-M/TM) interface in the QP1500 steel or at the F/M interface in the UFG DP1300 steel. This procedure was introduced previously by Pelligra et al. (2022).

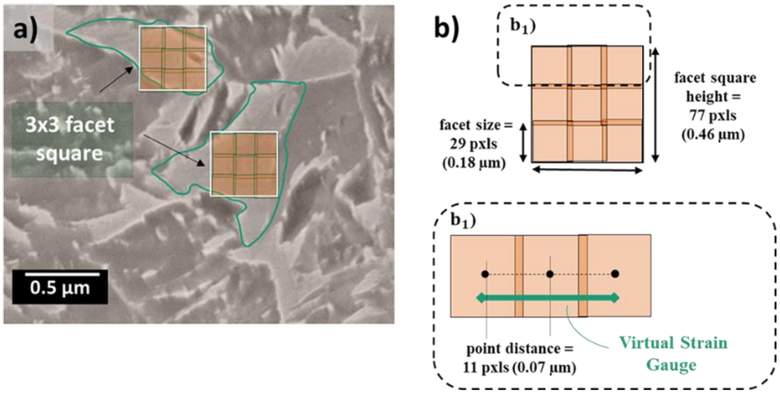

Figure 5.2: DIC computational methodology (a) 3x3 facet square sizes to calculate the in-grain strain (b,b1) schematic of choice in facet size (29pxl x 29pxl) and point distance (11pxl) to obtain a virtual Strain Gauge of 22pxls (0.14µm). The conversion of pxls to microns takes into account the FESEM imaging resolution which is detailed in Table 5.4.

5.7 Damage

Interrupted uniaxial tensile tests coupled with µXCT were carried out to quantify the development of microstructural damage. The hourglass microtensile specimen geometry used for quasi in-situ FESEM tensile testing described in section 5.4 was also used for interrupted µXCT tensile testing. A Bruker Skyscan1172 XCT equipped with a 100 kV X-ray source and an Al/Cu filter was used. Scans were performed at incremental strains and after fracture. The specimen was placed on a rotating stage closest to the source to achieve the highest resolution possible (0.72µm/pixel or 0.37µm^3/voxel). The specimen was rotated 360◦ with a 2D projection obtained every 0.4° rotation to collect a total of 900 images. The commercial Skyscan 1172 software packages, NRecon, CTan and CTVol, were used to reconstruct the 2D projections into a three-dimensional (3D) model to observe as well as quantify internal voids and dimples (voids at the surface).

5.8 Results

5.8.1 Mechanical Properties

Table 5.2 shows that this ultrahigh strength Q&P steel has properties approaching the modest 3G mechanical property envelope (UTS x TE ≥ 24,000 MPa%) as suggested by De Moor et al. (2010) on the basis of the United States Department of Energy's (U.S. DoE) wider 3G mechanical targets (36,000 MPa% ≤ UTS x TE ≥ 40,000MPa%) (Matlock and Speer, 2009) at 21,560MPa%. A representative true stress-strain curve up to the point of necking is illustrated in Figure 5.3. The work hardening curve shown in Figure 5.3 was obtained by taking the derivative of the steel's representative true stress-true plastic strain curve. The work hardening of this steel shows continuous yielding which is associated with a high martensite fraction, a high mobile dislocation density and the generation of dislocations from the ɣ-to-martensite transformation (Bhadeshia and Honeycombe, 2006; Eckner et al., 2019; Gerbase et al., 1979; Wendler et al., 2017). This Q&P steel maintains the classical continuous yielding featured in DP steels (Fonstein, 2015) and other high strength Q&P steels (Celada-Casero et al., 2022; Findley et al., 2017; Savic et al., 2020). The work hardening and true stress-strain curves of this ultrahigh strength Q&P steel are compared to that of a DP steel in the Appendix A, Figure A 5.1. As noted by Liu et al. (2017), a pre-existing high dislocation density, such as that accumulated during continuous yielding, does not suppress the cooperative atomic displacements associated with the deformation-induced transformation to martensite.

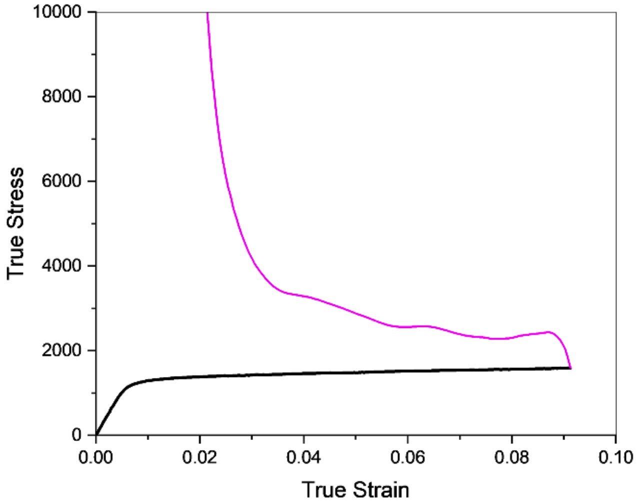

Figure 5.3 True Stress-Strain and Work Hardening Curves of QP1500

5.8.2 Microstructural Characterization

Figure 5.4a shows a discontinuous network of ɣ-M in the centre of the as-received steel sheet, revealed using a Behara tint etching solution. In previous comparisons made by Avramovic-Cingara et al. (2009) and Ramazani et al. (2014) of failure initiation in a centreline banded (i.e. a continuous martensite network) versus unbanded (i.e. a discontinuous martensite network) DP steel, with 600 MPa strength, (DP600), failure took place at a higher plastic strain in the equiaxed microstructure than in the banded microstructure. Similarly, in a TRIP steel, with 780 MPa strength, (TRIP780), investigated by Samei et al. (2020), coarse ɣ particles in a banded-type network was also seen; however, this steel achieved the highest ε_f relative to other AHSSs despite this 'microstructural anomaly'. Microstructural heterogeneity was thoroughly studied by Tasan et al. (2014) using techniques similar to those used here. They concluded that regions with a lower volume fraction of heterogeneously distributed, blocky martensite accommodated more strain relative to regions of uniformly distributed martensite in high volume fractions. Since delamination cracking at the centre thickness was not observed in the as-received Q&P steel microstructure, this centralized network of ɣ-M shown in Figure 5.4a and b does not meaningfully affect the steel's ductility.

FESEM imaging of heat-treated QP1500 steel specimens, using the procedure outline in section 5.4.1, did not show any sort of martensitic tempering or ɣ decomposition, as shown in Figure 5.4c. This indicates that the ɣ in this Q&P steel is significantly more chemically stable against heat treatment than the lower strength TRIP steels investigated by Bellhouse (2010) and Girault et al. (2001). Martensite tempering and ɣ decomposition was eventually observed when this steel was heat-treated at 450°C for 30 min, as applied to another Q&P steel (Findley et al., 2017). Figure 5.4d shows the as-received steel in which the microstructure is mainly lamellar-like with a scarce presence of blocky ɣ-M islands reaching a maximum size of 1.5µm in diameter. Examples of prior austenite grain packets consisting of blocks with embedded laths of differing orientations are highlighted in orange in Figure 5.4d (Toji et al., 2014). The matrix microstructure of this steel is predominately TM, with some instances of bainite.

Scanning Transmission Electron Microscopy (STEM), performed on this as-received Q&P steel show dislocated, lath-like structure within the grains, as can be seen in Figure 5.4e and f. The presence of this high dislocation density explains this Q&P steel's continuous work hardening, featured in Figure 5.3. The lath widths shown in Figure 5.4e range from 60 to 150nm in size. Instances of TiC precipitation and Mn solute segregation in ɣ-M regions is evident, as shown in the superimposed EDS map on HAADF images of Figure 5.4e$_1$, e$_2$ and f$_1$ respectively. The Mn solute segregation, as observed in blocky ɣ-M regions in Figure 5.4f$_1$ within the microstructure, could explain the significant amount (16 ± 3 vol%) of austenite retained in this steel. Long-range diffusion of Mn is not kinetically possible during the partitioning process, so this solute segregation is a result of the austenitic annealing performed early on in the Q&P processing. As well, this gradient in Mn heterogeneity between different phases in the microstructure is thought to effectively suppress TRIP (Ding et al., 2023).

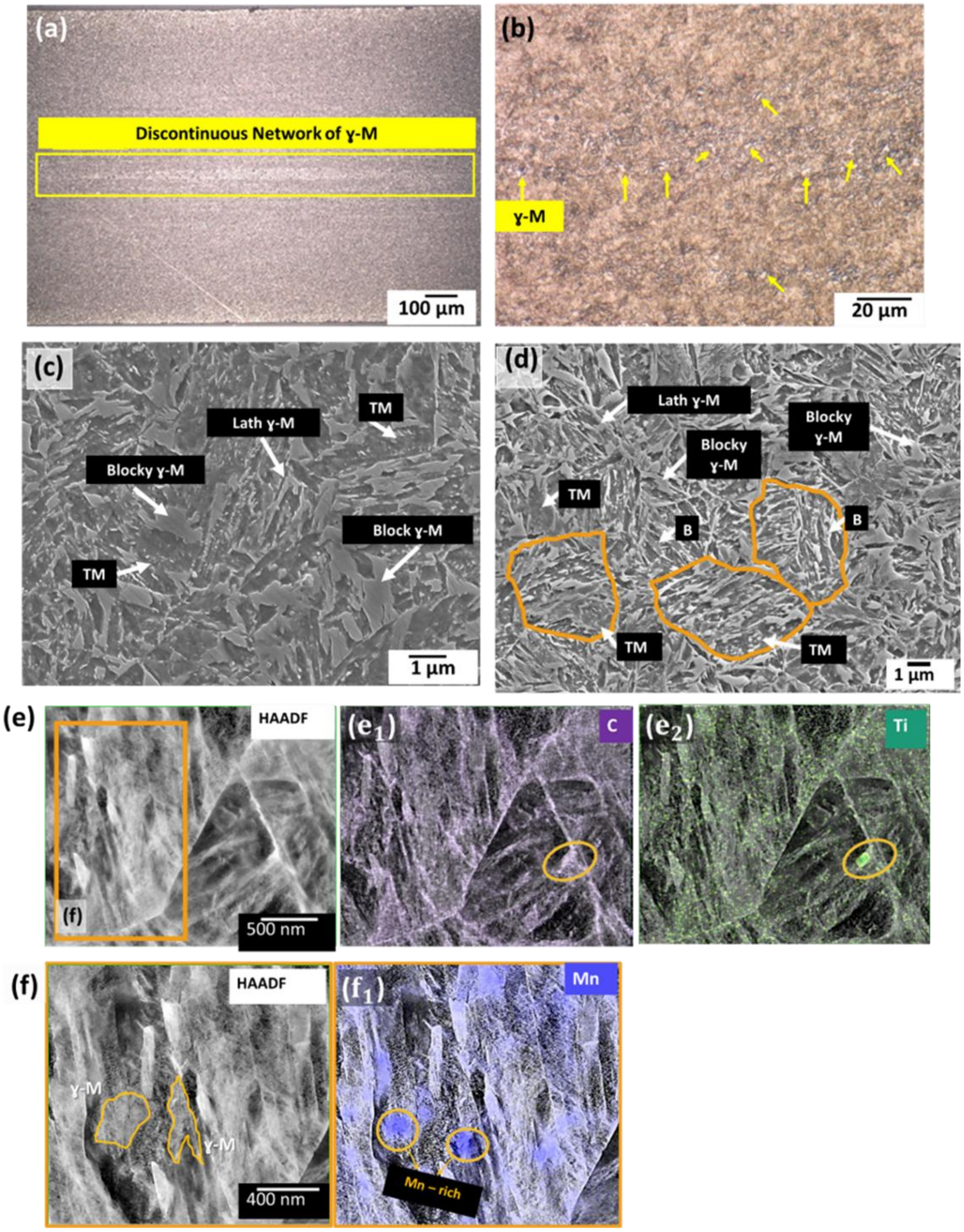

Figure 5.4 Digital Microscope Images using Behara's etchant of QP1500 heat-treated for 2h at 240°C, ɣ-M islands are etched white (a) Centralized network of ɣ-M (b) ɣ-M islands at high magnification within the centre thickness of the steel. FESEM imaging of QP1500 heat-treated for 2h at 240°C (c) and as-received (d). STEM-HAADF image of highly dislocated, lath-like structure (e) superimposed with EDS maps of carbon (e_1) and Ti (e_2). STEM-HAADF image outlining ɣ-M islands (f) superimposed with an EDS map of Mn (f_1)

Several EBSD maps were acquired on an undeformed, cross-sectioned, through-thickness specimen polished to a mirror finish. Each EBSD map captured on average an area of 1500µm^2

and a total of 990 ɣ islands. A considerable variation in ɣ grain size was determined in which a standard deviation of ±0.6µm was achieved. A representative EBSD map is shown in Figure 5.5a and b. In Figure 5.5c, the highest frequency of ɣ island diameter is from 0.39 to 0.45µm. A bin size of 0.06µm was used. Overall, the distribution of ɣ sizes is right-skewed, with the ɣ on average being smaller than the martensite islands also shown in Figure 5.5c. A similar right-skewed trend in ɣ grain size was also seen in Park et al. (2019)when investigating this QP1500 steel.

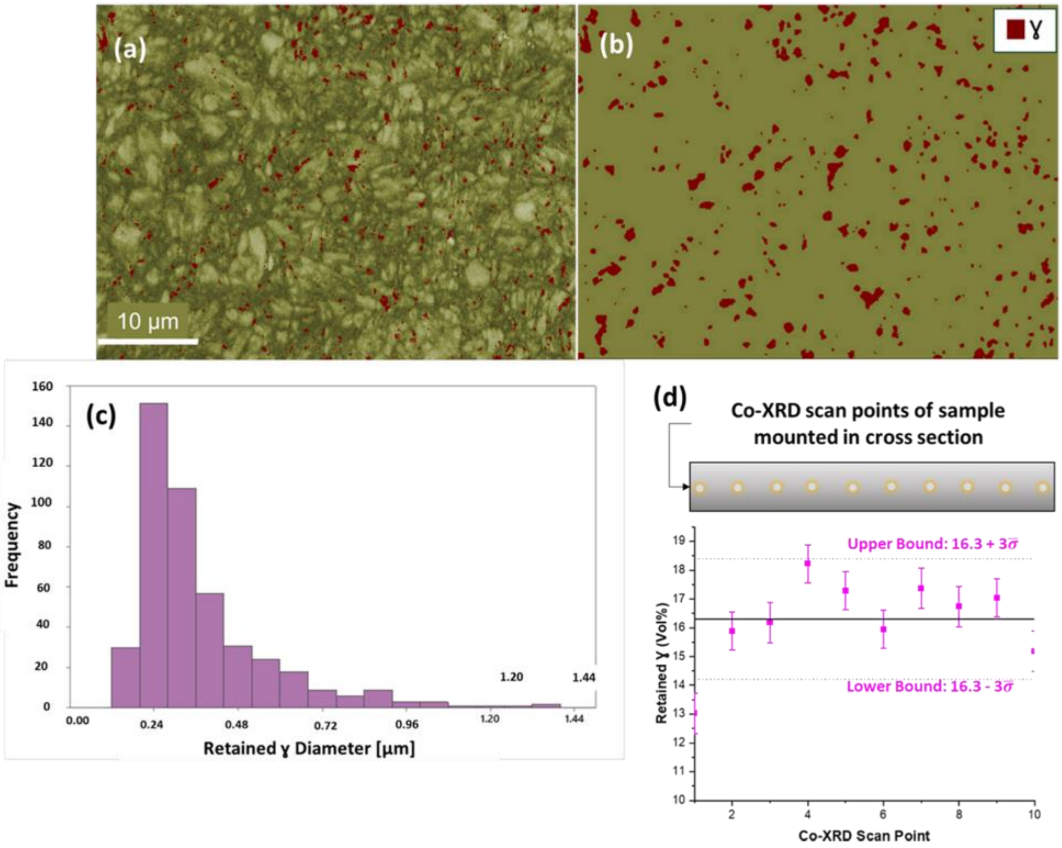

Figure 5.5 EBSD map of QP1500 on an undeformed cross section, through-thickness of the steel with the superimposed Band Contrast map (a) and without the superimposed Band Contrast map (b), showing 5.2 vol% ɣ in red, (c) distribution of ɣ size (d). In (d), the ɣ in the undeformed QP1500 steel in cross section, through-thickness was measured using Co-XRD. The upper and lower bounds is plotted to 3x the standard deviation of all ten of the ɣ measurement (±3σ).

A reliable quantification of ɣ was done using Co-XRD, while ɣ quantified using optical microscopy, EBSD and image analysis tends to be underestimated due to its limited resolution (De et al., 2003;

Ding et al., 2023; Jacques et al., 2001; Kickinger et al., 2021; Zhao et al., 2014). Co-XRD was used as opposed to Copper (Cu) -sourced XRD, ($\lambda_{Co,Avg}$ = 1.79Å versus $\lambda_{Co,Avg}$ = 1.54Å), to avoid Fe fluorescence. Co-XRD scanning was performed on 10 points across the cross-sectioned, through-thickness of the steel, as shown in Figure 5.5d. An average ɣ content of 16.3 vol% was detected, with points 1 & 10 showing the lowest ɣ content, likely due to X-ray beam spillage at the specimen's edges. Similar results were also achieved from XRD scanning of the polished surface (normal direction, ND) of this steel. This is the plane imaged during in-situ SEM tensile testing. The ɣ carbon content was calculated from the ɣ lattice parameter (a (Å)) using the combined equations of Dyson and Holmes (1970) and Ruhl and Cohen (1969) in Equation 5.1. The ɣ carbon content was calculated to be 0.97 wt%C. A high carbon content within austenite is typical of Q&P processed steels (Devaraj et al., 2018; Hu et al., 2023).

$$a\ (\text{Å}) = 3.572 + 0.0012\ (\text{wt\% Mn}) - 0.00157\ (\text{wt\% Si}) + 0.056\ (\text{wt\% Al}) + 0.033\ (\text{wt\% C}) \quad \text{Equation 5.1}$$

The vol% quantified by EBSD mapping (3.9–6.5 vol%) was significantly less than the average ɣ measured via Co-XRD (16.3 vol%) (Salehiyan et al., 2020). This indicates that there is a large portion of ɣ tied up as interlath films which can only be detected via XRD and are undetectable via EBSD scanning or FESEM imaging.

5.8.3 High Energy X-ray Diffraction (HE-XRD)

As shown in Figure 5.6, measurements obtained using HE-XRD show that the ɣ content is reduced to below 4 vol% by the time the specimen reaches its UTS. The coarser, low carbon ɣ grains are most likely completely or partially transformed near the beginning of straining, while the smallest ɣ grains, with a locally lower M_s temperature and higher carbon content, remain untransformed even at high strains past necking (Liu et al., 2018; Salehiyan et al., 2020; Turteltaub and Suiker, 2006). On the contrary, Xiong et al. (2013) argue that the phases surrounding the metastable ɣ, whether coarse or fine, low or high carbon, have a greater impact on the steel's ability to accommodate the volume expansion associated with the martensitic transformation. However, the gradual transformation (i.e. break up) of coarser ɣ grains with small changes in displacement were observed. These are circled in yellow in Appendix C, Figure C 5.1. Figure 5.6a shows the location of localized von Mises strain (ε_{local}) DIC measurements computed within the region of HE-

XRD acquisition. The discrepancy in DIC strain measured using the centralized portion of the specimen's gauge (5.1mm × 3.18mm), ε_{Avg}, versus the DIC strain measured accounting only for the HE-XRD beam impingement area (0.5 mm × 0.5 mm), εlocal has been noted previously (Abu-Farha et al., 2018). The facet size X point distance used for this DIC analysis is 0.1 × 0.03mm, theoretically encompassing ~100 grains within a single facet. Any shifts in the HE-XRD beam impingement area on the specimen during tensile testing was adjusted for in the DIC strain computation. Synchronizing HE-XRD ɣ acquisition directly within the specimen's neck without precise knowledge of the necking location in a straight-gauged specimen before starting the tensile test can result in lower strain measurements (Abu-Farha et al., 2018). For this reason, Figure 5.6b shows the ɣ transformed up to a ε_{local} of ≈ 0.2. Furthermore, it is important to note that the elongations exhibited by the smaller tensile specimen size from these HE-XRD experiments, as shown in Figure 5.1a, are approximately 2x larger than those calculated with ASTM sub-size tensile specimens, as documented in Table 5.2. The UE and TE were calculated to be 19 ± 3 % and 27 ± 8 % respectively, for these smaller customized dog-bone specimen used in the HE-XRD experimentation. These measurements are taken from three specimens, and error bars are calculated using a 95 % CI.

The TRIP kinetics show a sigmoidal trend, with TRIP being most pronounced past the UTS of the steel. As shown in Figure 5.6b, ≈ 73 % of ɣ is transformed up to a ε_{local} of ≈ 0.2, leaving ≥ 27 % of ɣ to be transformed during post-uniform elongation. These customized dog-bone specimens fractured at a ε_f of ≈ 0.6 similar to the microtensile specimen used in sections 5.6 and 0 for quasi in-situ FESEM tensile testing and µXCT investigations, respectively.

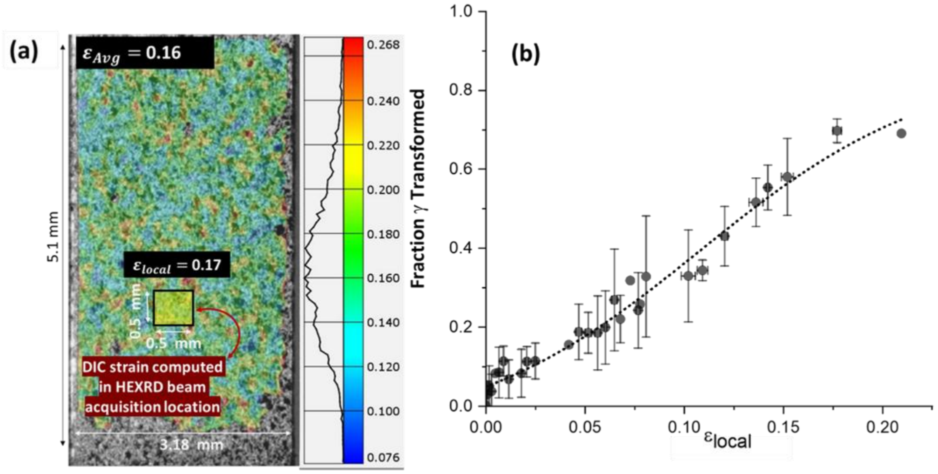

Figure 5.6 The DIC local von Mises (ε_{local}) measurements computed within the region of HE-XRD acquisition compared to ε_{Avg} from the imaged area (i.e. dog-bone gauge) (a). The ɣ- to-martensite transformation as a function of ε_{local} (b). HE-XRD was performed simultaneously during tensile testing. The error bars are to one standard deviation to the fraction of ɣ and $\varepsilon_{local,}$ measurements of three specimens.

The reported TRIP kinetics of this ultrahigh strength Q&P steel are different from that observed by Park et al. (2019) due to the different strain rates of tensile testing used during the HE-XRD acquisition. An extension rate of 0.15 mm/min was used in this paper while an extension rate of 1.8 mm/min was used by Park et al. (2019). Figure 5.6b exhibits a slower, more sigmodal trend in TRIP kinetics, and does not show the serrated flow of this steel published in Park et al. (2019). A comparison between the two is shown in Appendix B, Figure B 5.1. A sigmoidal trend is typical of TRIP steels as speculated first by Santacreu et al. (2006) and then again by Ref. (Beese and Mohr, 2011).

5.8.4 Microstrain Partitioning

A combination of quasi in-situ FESEM tensile testing of etched microtensile specimens, as well as microstrain mapping using DIC enabled the investigation of microstrain partitioning and 2D damage evolution in this ultrahigh strength Q&P steel. Figure 5.7a–c shows microstrain maps at an ε_{Avg} of 0.23, 0.27 and 0.28. This SEM imaging site was closest to the point of fracture and experienced the highest ε_{Avg} in the material just before fracture, therefore showing the most severe microstrain partitioning amongst phases. In Figure 5.7c$_1$, the micro-shearing observed in Figure 5.7a–c (dotted black line) was interrupted as a result of the damage which initiated at the weakest point/thinnest portion of a blocky ɣ-M island (blue arrows). It is important to note that the ε_{Avg} in Figure 5.7c$_1$ is lower than that of Figure 5.7c (ε_{Avg} of 0.28 versus 0.26) due to the loss in correlation/microstrain mapping coverage in Figure 5.7c$_2$. Alternatively, the map in Figure 5.7c$_2$ also shows a significant loss in correlation due to extensive TM plastic deformation. However, the strain localization that was mapped (i.e. red region in Figure 5.7c$_2$) increased the ε_{Avg} in Figure 5.7c$_1$ compared to that of Figure 5.7c (ε_{Avg} of 0.30 versus 0.28).

Microstrain mapping with the use of DIC shows strain partitioning between phases, and micro-shear banding in this Q&P steel. This is said to be a result of the small microstrain contrast between phases (Ruggles et al., 2016). Mico-shearing in 3G TRIP-assisted steels can suppress void growth, as shown in the identification of micromechanisms of damage seen in this ultrahigh strength Q&P steel in Appendix D, Figure D 5.1.

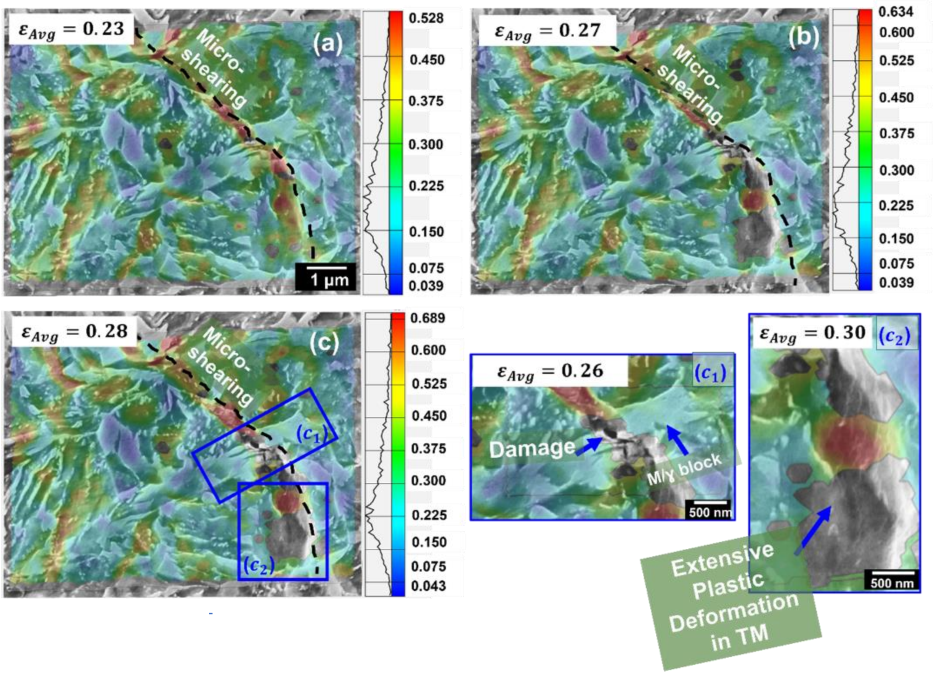

Figure 5.7 Microstrain maps in the post-uniform elongation regime of QP1500 at an ε_{Avg} of 0.23 (a) 0.27 (b) and 0.28 (c). The black dashed curve in (a,b,c) shows evidence of micro-shearing in the steel until a blocky ɣ-M like is reached and damage initiated (c$_1$) followed by extensive plastic deformation in the TM region (c$_2$)

5.8.5 Damage Evolution and Fracture

Figure 5.8 shows this steel's localized neck and the evolution of damage (red pixels) in 3D from two different perspectives, termed as the Front View and Top View. The Front View 3D reconstructions are taken parallel to the width of the specimen, while the Top View reconstructions are taken perpendicular to the specimen's width. Here, damage is most prominent within the final 5 % local true strain ($\varepsilon_{\mathrm{loc}}^{\mathrm{True}}$) before fracture, and negligible void formation is seen before the onset of necking. The εTrue loc using µXCT 3D reconstructions, as shown in Figure 5.8, was calculated using the reduction in area, taking into account the change in width and thickness of the sheets at fracture. The equation used is described in a previous publication (Samei et al., 2019). At higher strains, just before fracture (from $\varepsilon_{\mathrm{loc}}^{\mathrm{True}}$ = 0.62 to 0.66), damage localizes within micro-shear bands within the neck.

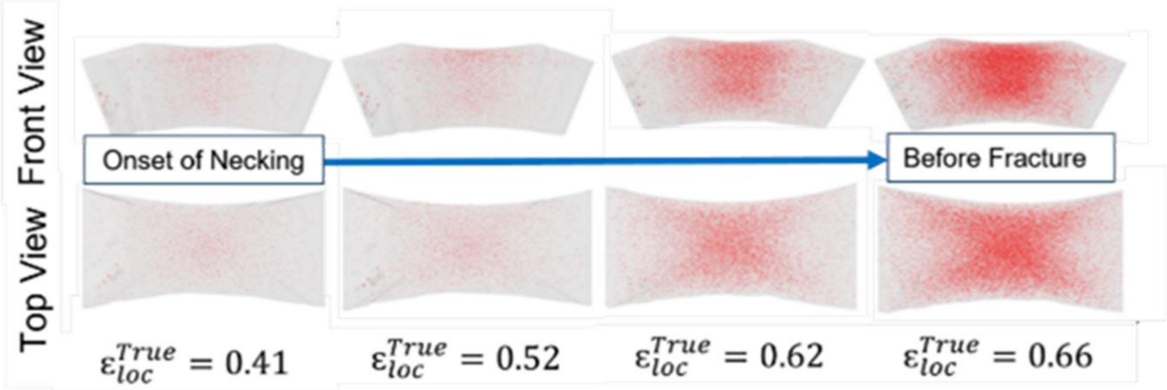

Figure 5.8 3D reconstructions of a QP1500 fracture surface during post-uniform elongation (red represents internal voids in the material)

The void volume fraction, void density, and size of the largest voids were quantified to understand microstructural damage as a function of increasing true strain in Figure 5.9a, b and c, respectively. Figure 5.9a and b indicate that the void number density and void volume fraction grow gradually up to a $\varepsilon_{\mathrm{loc}}^{\mathrm{True}}$ of about 0.4, i.e. at the onset of necking. This is followed by a rapid acceleration of damage, as measured by both parameters. This is due to progressive nucleation and growth of voids after necking at higher stress triaxialities as described elsewhere (Liu et al., 2018; Pelligra et al., 2022; Turteltaub and Suiker, 2006). Figure 5.9c shows the 50, 500, and 5000 largest voids. These were tracked up to fracture as the largest voids are those that contribute most to fracture. Moreover, counting only the largest voids eliminates effects due to void nucleation and the growth of small voids above the XCT counting threshold. The average diameter of the 50 largest voids just before fracture is 5.6µm; however, that of the 5000 largest voids is 3.3µm. This is in good agreement with previous findings for an ultrahigh strength DP steel (Samei et al., 2019) in which the largest 50 voids play an influential role in development of ductile fracture. It is critical to recognize that the void density, as shown in Figure 5.9a, which refers to the nucleation rate of voids (Samei et al., 2020), is seemingly negligible up to an $\varepsilon_{\mathrm{loc}}^{\mathrm{True}}$ of 0.12. Due to the limited µXCT pixel resolution of 0.72µm, and the fine Q&P microstructure, many of the nano-scaled voids remained unidentified. However, we have captured the presence of these nano-scaled voids in section 5.6 and Figure 5.7 using quasi in-situ FESEM tensile testing. Figure 5.7c and c_1 show void diameters ranging from 0.07 to 0.012µm. Moreover, in Samei et al.'s (2020) comparison of damage evolution on a range of AHSSs, they found that QP1500 fractures at a $\varepsilon_{\mathrm{loc}}^{\mathrm{True}}$ of 0.56 with a 0.14 void volume fraction, while UFG DP1300 fractures at a $\varepsilon_{\mathrm{loc}}^{\mathrm{True}}$ 0.39 with a 0.09 void volume fraction. QP1500 and DP1300 being both ultrahigh strength and UFG steels, show the work hardening benefits that come from dislocation pile ups at dissimilar phase boundaries, but QP1500 also has TRIP-assistance which enables its delayed fracture.

It should be noted that, along with different specimen sizes, the method of quantifying strain in µXCT experiments differs from that of quantifying strain using DIC during quasi in-situ FESEM tensile testing and HE-XRD experiments. As well, issues in strain computation with DIC can result in poor mapping coverage at high strains. This makes the coupling of 2D and 3D experimental datasets complex.

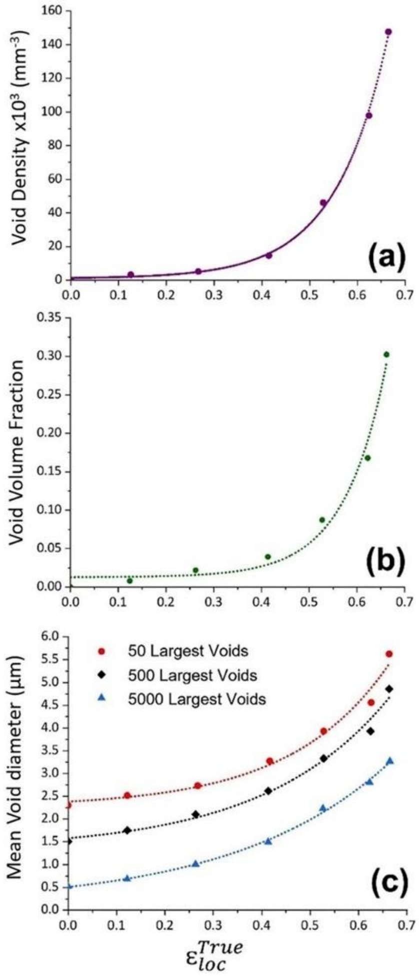

Figure 5.9 Quantitative analysis of void evolution during uniaxial deformation of QP1500 (a) density, (b) volume fraction, and mean diameter of the largest voids (c).

As observed in Figure 5.10a, the overall fracture mode is ductile with a prominent macroscopic cup-and-cone morphology. This is typical of multiphase steels with interlath thin ɣ films (Kokosza and Pacyna, 2008). Fractography shows high local deformation located within the centre of the fracture surface as the dimple sizes range from the micro-to nano-scale. The largest dimples are located at the centre and the smallest along the edges of the fracture surface. This was also seen in the fracture surface analysis of QP980 (Ruhl and Cohen, 1969) and may be a characteristic feature of fracture in Q&P steels. Moreover, we can see shear fracture regions located along the edges of the fracture surface. Previous work suggests that martensitic clusters with high dislocation densities can hinder crack propagation with shearing (Eckner et al., 2019). This corroborates well with the µDIC analysis conducted on this steel, in which we highlighted instances where suppressed void growth/crack propagation by micro-shearing was observed

(Eckner et al., 2019; Javad Samei et al., 2019). Fractography of the fracture surface qualitatively correlates well with the 3D reconstruction obtained in µXCT scanning in which a high void concentration is featured in the centre of the fracture surface.

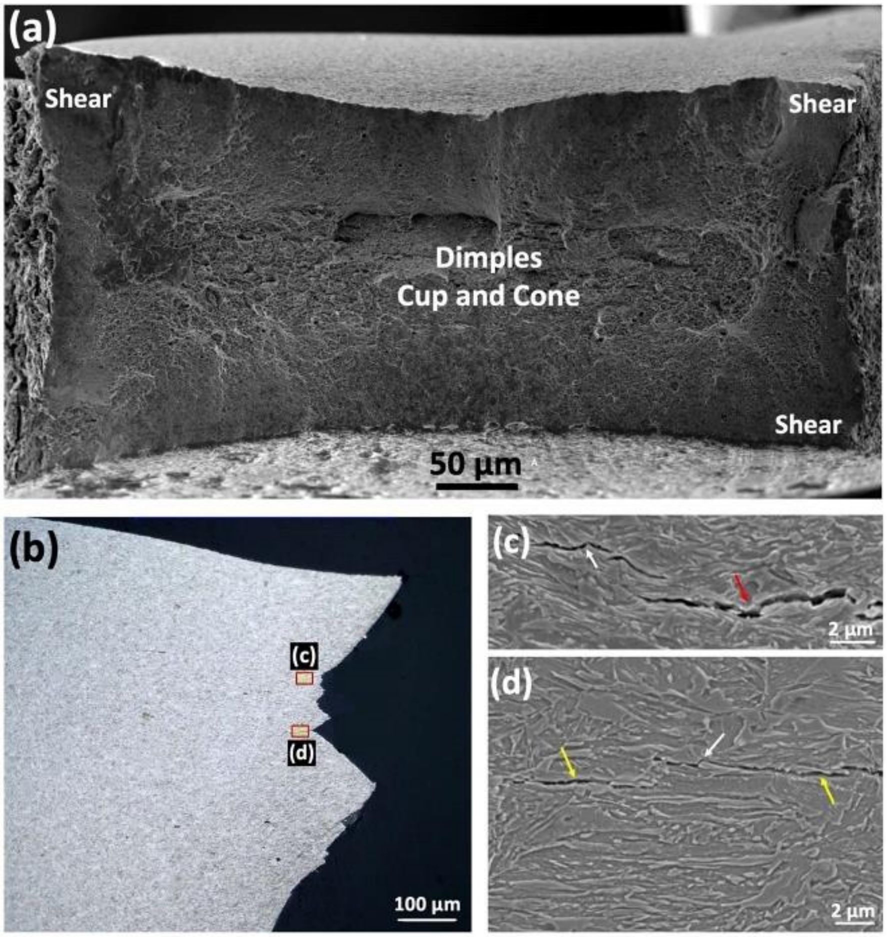

Figure 5.10 FESEM imaging of the Fracture surface: ductile cup-cone fracture with shear lip (a), fracture cross section (b), white and yellow arrows show IG and interfacial micro-cracks, respectively (c,d).

Figure 5.10b shows the tensile specimen at fracture in cross section in which we see shear lips further enforcing its ductile fracture. Micro-cracking refers to cracks which do not directly propagate to the fracture surface. All regions imaged in Figure 5.10c and d show evidence of transgranular (TG) and interfacial micro-cracking. Some evidence of MnS stingers was detected with EDS but these were in low quantities, irregularly dispersed far from the fracture surface, and therefore do not contribute significantly to the steel's overall fracture. Figure 5.10c shows regions of extensive lath elongation parallel to the tensile direction. This may suggest that these are not highly carbon-concentrated ɣ-M islands and as a result, show extreme ductility. Although the fine grain size is expected to hinder crack initiation, coarser microstructures can delay crack propagation more effectively (Xie et al., 2011). Severe edge cracking during rolling of the subject QP1500 was investigated by Samei et al. (2019). They observed wide, vertical crack opening displacement suggesting extensive local plastic flow growing towards the strip's centreline and the initiation of oblique cracks through martensite or along phase boundaries. This is similar to the intergranular cracking (IG) along ɣ/M boundaries shown in Figure 5.10c and d. TG is most likely due to the co-deforming capability of ɣ-M islands and TM regions such that there is not a preference of void nucleation to occur at the ɣ-M island ("hard"), TM region ("soft") interface.

5.9 Discussion

Table 5.3 compares various mechanical properties of this QP1500 and an UFG DP1300 steel. The chemical and microstructural details of this vanadium-microalloyed UFG DP steel are given elsewhere (Samei et al., 2019; Scott et al., 2018, 2017). Microstructurally, the QP1500 steel contains ≈80 vol% of martensitic phases (fresh and transformed martensite) and ≈20 vol% ɣ while the UFG DP1300 steel contains ≈50 vol% martensite and ≈50 vol% (Park et al., 2019; Scott et al., 2017). Although both the QP1500 and UFG DP1300 have comparable UTS values, the TRIP-assistance in QP1500 provides a ≈1.5 times increase in US DoE parameter, UTSxTE, and a ≈3 times increase in toughness. The toughness values featured in Table 5.3 were measured using the area integral trapezoid method under the true stress-strain curves. The UTSxTE product provides a crude toughness approximation; and underestimates the actual energy required to produce fracture because the energy absorbed during post-uniform elongation is not captured (Frómeta et al., 2019a). An attempt to address this disparity was introduced by Hance (2016), who suggested two methods of classifying and rating the formability of AHSSs. The first involves computing the local versus global Strain Ratio ($\frac{\varepsilon_f}{\varepsilon_u}$), i.e. the true strain at fracture over the true uniform strain. steels with a high value of this ratio (>20) exhibit better local formability while those with a low value (<5) exhibit better global formability. Intermediate values are indicative of balanced formability. A second approach involves the Formability Index (F.I.), which is the geometric mean of ε_u and ε_f. As shown in Table 5.3, this QP1500 steel can be classified as having 'Balanced/Global Formability', whereas the UFG DP1300 steel can be classified as having better 'Global formability' and rated as having overall 'Fair' formability (Hance, 2016). There is one difficulty with the Hance approach. By plotting the ductility data for a range of alloys on a ε_u vs. ε_f plot with lines of fixed ($\frac{\varepsilon_f}{\varepsilon_u}$) ratios used to suggest different formability regions, it can be inferred that there is a trade-off between local and global formability (Hance, 2016). However, this is not always the case. For example, a first generation (1G) TRIP780 steel can attain a high ε_f (≈0.7) and TE (33 %) while also being able to tolerate the greatest amount of voids before fracture in comparison to various other AHSSs tested in that study (Samei et al., 2020).

Table 5.3 Mechanical Property comparison between QP1500 and DP1300 steels

	UTSxTE (MPa%)	Toughness ($\mathrm{MJ/m^3}$)	True Uniform Strain (ε_u)	True Strain at Fracture (ε_f)	$\frac{\varepsilon_f}{\varepsilon_u}$	F.I. $\sqrt{\varepsilon_u * \varepsilon_f}$
UFG DP1300	14750	409	0.08	0.28	3.5	0.15
QP1500	21560	1323	0.11	0.60	5.5	0.26

In comparing microstrain partitioning of the two steels in Table 5.3 with the use of quasi in-situ FESEM tensile testing coupled with DIC, it was seen that microstrain partitioning between phases is significantly less severe in the QP1500 than in the UFG DP1300 steel. To make the microstrain maps obtained comparable and to compensate for the difference in representative area (i.e. differences in magnification) captured between both steels, the facet and step sizes were tailored such that they exhibited the same sizes in microns as shown in Table 5.4. This same methodology was used previously (Pelligra et al., 2022). The FESEM images acquired for this analysis are those from Pelligra et al., (2022); however, the µDIC analysis (i.e. with different facet size X point distance used) was redone for this comparison. The ε_{Avg} is compared to the local average phase strain, ε_{phase}, (i.e. the average von Mises strain of different phases within the area imaged).

Table 5.4: Parameters used in the microstrain of Figure 5.11 and Figure 5.12

	QP1500	DP1300
Represented Area (μm^2)	8.0x6.4	15.4x12.3
Resolution (μm/pixel)	0.006	0.006
Facet × Step size (pixel)	29×11	31×11
Facet × Step size (μm×μm)	0.18×0.07	0.18×0.07

It is important to recall that the ferrite in this UFG DP1300 contains an abundance of nanoscale vanadium carbonitrides which provide improved particle-strengthening as described by the Orowan mechanism (Scott et al., 2018, 2017). As shown in Figure 5.11, there is ≈2x increase in the ɣ-M phase strain ($\varepsilon_{\gamma\text{-M,phase}}$) in the QP1500 steel versus the martensitic phase strain ($\varepsilon_{\text{M,phase}}$) in the UFG DP1300 steel throughout all ε_{Avg} values examined. For example, at an $\varepsilon_{\text{Avg}} \approx 0.20$, the QP1500 steel exhibits a $\varepsilon_{\gamma\text{-M,phase}} = 0.15$ whereas the UFG DP1300 steel exhibits a $\varepsilon_{\text{M,phase}} = 0.08$. Similarly, a ≈1.5x decrease in phase strain is seen when comparing the softer phases of both steels, the $\varepsilon_{\text{TM,phase}}$ in the QP1500 steel to the $\varepsilon_{\text{F,phase}}$ in the UFG DP1300 steel, at all ε_{Avg} strains examined. This indicates that there is enhanced balanced formability of the QP1500 steel, as further interfacial energy is required to nucleate a void at the interfaces of its harder/softer phases. Although, the purpose of vanadium-microalloying is meant to soften martensite and therefore, reduce the degree of microstrain partitioning between phases in this UFG DP1300 steel, the partitioning heat treatment performed on the QP1500 steel has a greater impact in reducing the microstrain partitioning between phases.

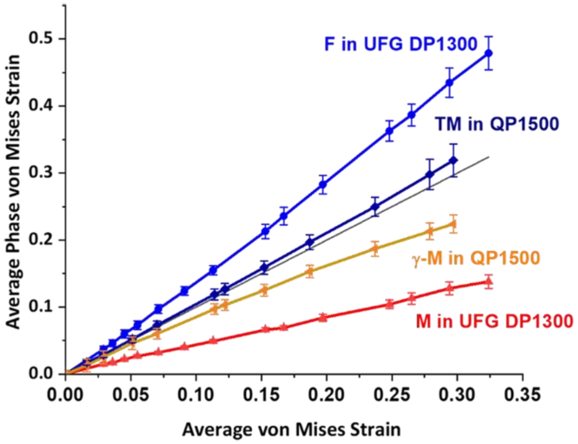

Figure 5.11 Microstrain partitioning between different phases in QP1500 and DP1300 (F, TM,ɣ-M, M)

These results corroborate well with the in-situ tensile testing coupled with EBSD experiment conducted on QP1500, shown in Appendix C, Figure C 5.1, Figure C5.2 and Figure C5.3. The evolution of GNDs at all three of the displacements featured in Appendix C, Figure C 5.1, Figure C5.2 and Figure C5.3,are greater in the TM (BCC) regions versus those of the ɣ (FCC) regions. This suggests that a sufficient amount of carbon partitioned and therefore chemically stabilized the ɣ from exhibiting early TRIP. Similar to the microstrain partitioning analysis conducted by Kang et al., (2023), any sparse presence of lower bainite (i.e. ferrite embedded with carbides oriented at ~60° (Hesamodin Talebi et al., 2017)) was grouped with the dense presence of TM (i.e. ferrite embedded with randomly distributed carbides) for the quantitative microstrain partition analyses presented in Figure 5.11 and Figure 5.12.

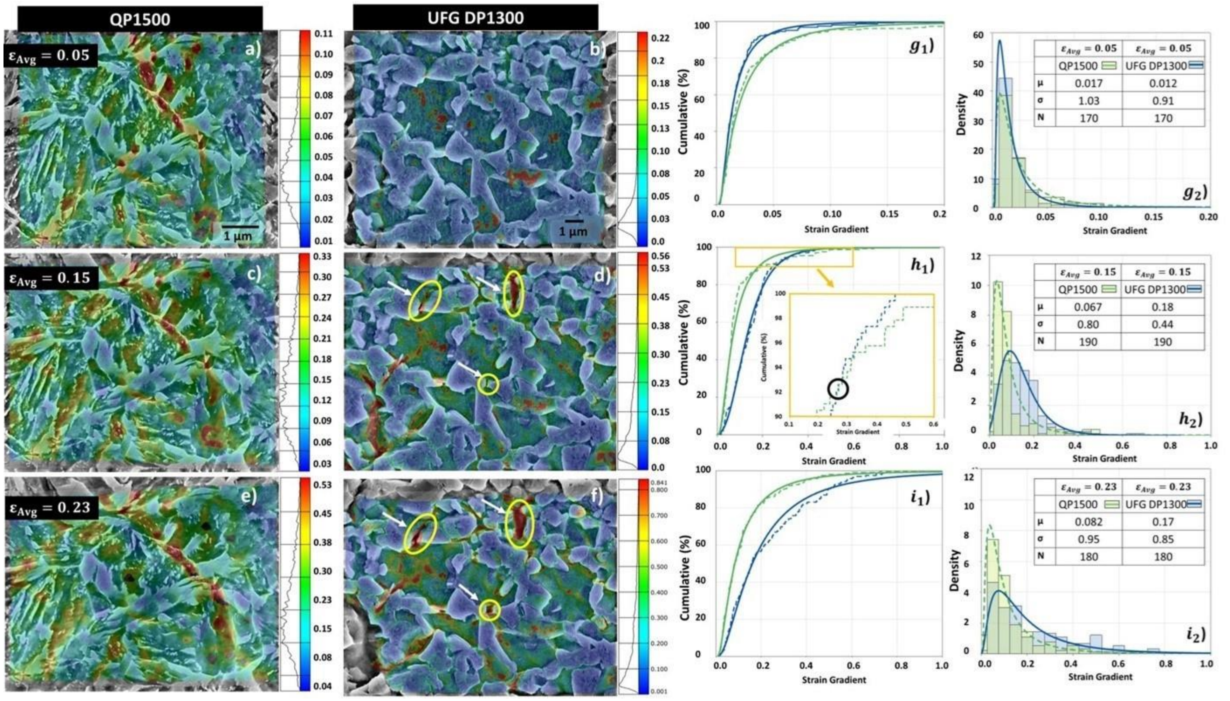

Figure 5.12 Microstrain maps of QP1500 and DP1300 steels at an ε_{Avg} of 0.05 (a,b), 0.15 (c,d), and 0.23 (e,f), respectively. CDF and PDF plots of local von Mises strain in microstrain partitioning amongst phases in QP1500 and UFG DP1300 at ε_{Avg} of 0.05 ($g_{1,2}$), 0.15 ($h_{1,2}$), and 0.23 ($i_{1,2}$)

Interfacial local strain gradient (ε’) measurements have been compared between the QP1500 and DP1300 steels at an ε_{Avg} of 0.05, 0.15 and 0.23. This novel μDIC-based computational technique (Pelligra et al., 2022) was used to understand the accumulation of GNDs at dissimilar phase interfaces. As well, this μDIC-based computational technique is being used as an alternative means to determining phase strengths without the use of nanoindentation. Nanoindentation is a surface sensitive technique in which surface roughness (Rodriguez and Gutierrez, 2003) as well as the submicron grain size of AHSSs weakens the reliability of its results (Li et al., 2020; Srivastava et al., 2015). Greater than 150 line scans for each ε’ measurement at dissimilar phase interfaces were collected and summarized using a Cumulative Distribution Function and Probability Distribution Function, a CDF and PDF, respectively, as shown in Figure 5.12. A lognormal distribution was used to fit the right-skewed data in the CDF and PDF plots using the Minitab software. In reference to Figure 5.12g_2,h_2, and i_2, the two parameters presented in the lognormal distribution, which are fitted to only positive values, represent the median (μ), otherwise known as the exponential of the ‘location’, $e^{location}$, and scale/standard deviation (σ). It is important to keep in mind that the mention of ε’ here refers to a collection of ε’ measurements at dissimilar phase interfaces for the two steels. The CDF plot shows that for an ε_{Avg} ≈0.05, the majority of F/M strain gradients in the UFG DP1300 steel is less severe than the ɣ-M/TM strain gradients in the QP1500 steel. Specifically, 90 % of ε′ at F/M interfaces in the DP1300 are lower than those calculated at the ɣ-M/TM interfaces in the QP1500 steel, as shown in Figure 5.12g_1 and g_2 (ε′ ≈0.03 vs. ε′ ≈0.07, respectively). This is consistent with the fact that, in DP steels, the YS increases with increasing martensite content, and, at the micro-level, the F/M interfaces can act as sources of dislocation generation even at low strains (Davies, 1979; Fonstein, 2015; Scott et al., 2017). At an ε_{Avg} ≈0.15, strain partitioning between dissimilar phases is overall more pronounced in both steels and damage is evidently introduced in the UFG DP1300 steel, as highlighted in Figure 5.12d and f with the white arrows. In the CDF plots, Figure 5.12h_1 and h_2, 90 % of ε′ are lower in the QP1500 steel versus that of the UFG DP1300 steel (ε′ ≈0.19 vs. ε′ ≈0.24, respectively). On the other hand, from 99 % of ε′ computed, the QP1500 steel exhibits a higher ε′ than the UFG DP1300 steel (ε′ ≈0.49 vs. ε′ ≈0.43, respectively). In Figure 5.12i_1 and i_2 at an ε_{Avg} ≈0.23, when damage is more severe in the UFG DP1300 steel, 90 % of ε′ at dissimilar phase interfaces in the QP1500 steel is ~ 1.6x lower than that of the UFG DP1300 steel (ε′ ≈0.3 vs. ε′ ≈0.49, respectively). As shown in Figure 5.12h_2 and i_2, the μ (i.e. measure of central tendency), shows that the ε′ are lower in the QP1500 than the UFG DP1300 steel at high strains (ε_{Avg} = 0.15 and 0.23), whereas this trend is reversed at low strains (ε_{Avg} = 0.05). The σ, on the other hand, is wider in the QP1500 than the UFG DP1300 steel in all three ε_{Avg} strains examined. To attain a high strength, the ductility of the UFG DP1300 steel is compromised by the more severe inhibition of dislocation motion at dissimilar phase boundaries. This inevitably results in premature damage nucleation, as shown in Figure 5.12d and f. This damage nucleation however is not observed in the QP1500 steel, as shown in Figure 5.12c and e at the same ε_{Avg} of 0.23, meaning that dislocation motion is not as severely inhibited across dissimilar phase boundaries (Hu et al., 2023).

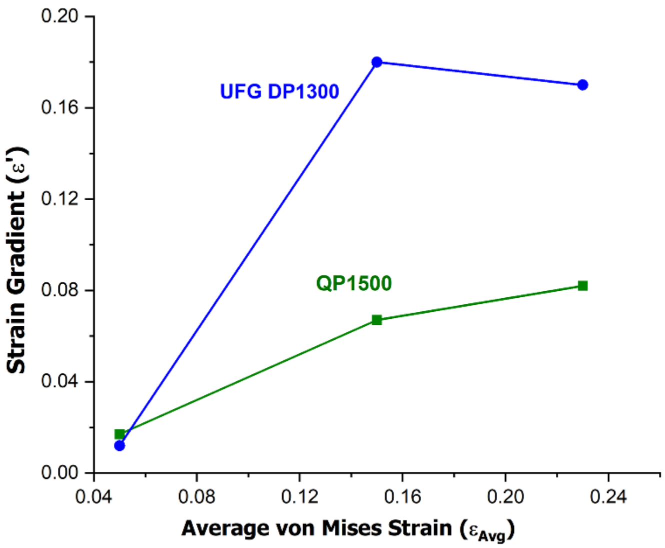

Figure 5.13: The evolution of strain gradient (ε') with increasing average von Mises strain (ε_{Avg}) for QP1500 and UFG DP1300.

Overall, it can be deduced that the evolution of ε' at the dissimilar phase interfaces is slower in the QP1500 versus the DP1300 with increasing ε_{Avg}. The graph in Figure 5.13 plots the µ of ε' as a function of the ε_{Avg} featured in Figure 5.12 to show this phenomenon.

5.10 Summary Remarks and Conclusions

This paper thoroughly documents the micromechanisms of damage that lead to fracture in an ultrahigh strength Q&P steel and explains the advantages that the TRIP effect provides to 3G steel microstructures by comparing this steel to a DP steel of similar strength and grain size. Microstructural damage of this Q&P steel was detailed through the use of quasi in-situ FESEM tensile testing coupled with µDIC and µXCT, whereas TRIP kinetics of this steel were determined through HE-XRD. The following main contributions can be drawn from the Q&P characterization:

- This ultrahigh strength Q&P steel shows remarkable strength (1.5GPa), sufficient elongation (TE =14%), and high toughness (1323 MJ/m^3) as a result of its large post-uniform elongation potential (i.e. a high ε_f of 0.6).
- This steel exhibits continuous yielding (similar to that seen in DP steels) associated with the accumulation of GNDs at dissimilar phase interfaces, and the generation of mobile dislocations at these interfaces. A non-smooth work hardening curve with peaks in work hardening can be attributed to bursts of TRIP in the steel.

- A classical sigmodial trend in TRIP kinetics was observed in this QP1500 steel with ≥ 27 % of the ɣ remaining untransformed up to the start of the post-uniform deformation period. This steel features a dependence of strain rate on TRIP exhaustion, in which a higher strain rate promoted faster TRIP kinetics. However, differences in tensile strain rate still resulted in ≥ 27 % (4 vol%) of ɣ untransformed just before post-uniform deformation.
- The ability for this steel to retard TRIP to high strains can be explained by the high average carbon content within the ɣ (0.97 wt% C), the micro-segregation of Mn lowering the local Ms temperatures for select ɣ particles, and the large, as well as variable, amount of interlath film ɣ, representing 2–10 vol% in the steel microstructure.

By comparing this Q&P steel to a DP counterpart to further understand the benefits of TRIP-assistance in 3G steel microstructures, the following conclusions can be made:

- This QP1500 steel shows superior crash-resistant properties to the UFG DP1300 steel with a ≈1.5x increase in U.S. DoE parameter and ≈3x increase in toughness, despite containing a ≈ 30 vol% increase in martensitic (TM and M) phases.
- Voids in this QP1500 steel are submicron in size, whether they are pre-existing or nucleate during deformation and, in some instances, these voids are suppressed from further growth by micro-shearing as the steel is strained. Specifically, there is ≅ 1.5-2x increase and decrease of the hard and soft phase strains, ɣ-M and TM, respectively, when comparing the QP1500 to an UFG DP1300 steel.
- The evolution of ε’ (i.e. accumulation of GNDs) at dissimilar phase interfaces is slower in the QP1500 versus the DP1300 with increasing ε_{Avg}. The ε’ at the dissimilar phase interfaces are smaller and grow more slowly in the QP1500 than in the UFG DP1300 steel.

Although, from uniaxial tension tests, this ultrahigh strength Q&P steel shows exceptional crash-resistant properties, future work needs to be devoted to understanding the behavior of 3G TRIP-assisted steels when subjected to other modes of deformation/strain paths (i.e. shear, plane-strain tension, balanced-biaxial tension, etc.). The coupling of advanced characterization techniques presented in this paper to qualitatively as well as quantitatively understand the role of TRIP exhaustion on damage evolution can be extended to TRIP-assisted steels under more complex straining conditions.

5.11 Acknowledgements

The authors would like to thank Nizia Mendes-Fonseca and Cal Siemens (from McMaster University) for their assistance at the APS Beamline. The authors would also like to thank Dr. Xiang Wang for TEM sample electropolishing preparation and Dr. Douglas Ivey for conducting the TEM analysis. Use of the Advanced Photon Source was supported by the U. S. Department of Energy, Office of Science, Office of Basic Energy Sciences, under Contract No. DE-AC02-06CH11357. The support of APS beamline scientists, Dr. Andrey Andreevich Yackovenko and Dr. Tyra Chenice Douglas, is gratefully acknowledged. We also thank NSERC for the funding received under the Discovery Grant Program.

5.12 References

Abu-Farha, F., Hu, X., Sun, X., Ren, Y., Hector, L.G., Thomas, G., Brown, T.W., 2018. In Situ Local Measurement of Austenite Mechanical Stability and Transformation Behavior in Third-Generation Advanced High-Strength Steels. Metall Mater Trans A Phys Metall Mater Sci 49, 2583–2596. https://doi.org/10.1007/s11661-018-4660-x

ASTM E8M-Standard Test Methods for Tension Testing of Metallic Materials, 2021.

Avramovic-Cingara, G., Ososkov, Y., Jain, M.K., Wilkinson, D.S., 2009. Effect of martensite distribution on damage behaviour in DP600 dual phase steels. Materials Science and Engineering A 516, 7–16. https://doi.org/10.1016/j.msea.2009.03.055

Barbier, D., 2014. Extension of the martensite transformation temperature relation to larger alloying elements and contents. Adv Eng Mater 16, 122–127. https://doi.org/10.1002/adem.201300116

Barella, S., Gruttadauria, A., Menezes, J.T.O., Castrodeza, E.M., Quaini, S.E., Pelligra, C., McNally, E.A., 2023. The Reliability of Single-Step and Double-Step Quench and Partitioning Heat Treatments on an AISI 420A Low Carbon Martensitic Stainless Steel. Metallurgical and Materials Transactions A. https://doi.org/10.1007/s11661-023-07145-2

Beese, A.M., Mohr, D., 2011. Effect of stress triaxiality and Lode angle on the kinetics of strain-induced austenite-to-martensite transformation. Acta Mater 59, 2589–2600. https://doi.org/10.1016/j.actamat.2010.12.040

Bellhouse, E.M., 2010. GALVANIZING OF AL-SI TRIP-ASSISTED STEELS. McMaster University.

Bhadeshia, H.K.D.H., Honeycombe, S.R., 2006. Steels: Microstructure and Properties, Steels: Microstructure and Properties. https://doi.org/10.1016/B978-0-7506-8084-4.X5000-6

Bhadhon, K.M.H., Wang, X., McDermid, J.R., 2022. Effects of CGL-compatible thermal processing, starting microstructure, and Sn micro-alloying on the mechanical properties of a medium-Mn third generation advanced high strength steel. Materials Science and Engineering A 833. https://doi.org/10.1016/j.msea.2021.142563

Casellas, D., Lara, A., Frómeta, D., Gutiérrez, D., Molas, S., Pérez, L., Rehrl, J., Suppan, C., 2017. Fracture Toughness to Understand Stretch-Flangeability and Edge Cracking Resistance in AHSS. Metall Mater Trans A Phys Metall Mater Sci 48, 86–94. https://doi.org/10.1007/s11661-016-3815-x

Celada-Casero, C., Vercruysse, F., Linke, B., Smith, A., Kok, P., Sietsma, J., Santofimia, M.J., 2022. Analysis of work hardening mechanisms in Quenching and Partitioning steels combining experiments with a 3D micro-mechanical model. Materials Science and Engineering: A 846, 143301. https://doi.org/10.1016/j.msea.2022.143301

Chen, X., Jiang, H., Cui, Z., Lian, C., Lu, C., 2014. Hole expansion characteristics of ultra high strength steels. Procedia Eng 81, 718–723. https://doi.org/10.1016/j.proeng.2014.10.066

Choi, I.D., Bruce, D.M., Kim, S.J., Lee, C.G., Park, S.H., Matlock, D.K., Speer, J.G., 2002. Deformation behavior of low carbon TRIP sheet steels at high strain rates. ISIJ International 42, 1483–1489. https://doi.org/10.2355/isijinternational.42.1483

Choi, J.Y., Jin, W., 1997. Strain induced martensite formation and its effect on strain hardening behavior in the cold drawn 304 austenitic stainless steels. Scr Mater 36, 99–104. https://doi.org/10.1016/S1359-6462(96)00338-7

Choudhary, R., Kumar, H., Garg, R.K., 2010. Analysis and evaluation of heat affected zones in electric discharge machining of EN-31 die steel. Indian Journal of Engineering and Materials Sciences 17, 91–98.

Davies, R.G., 1979. Early stages of yielding and strain aging of a vanadium-containing dual-phase steel. Metallurgical Transactions A 10, 1549–1555. https://doi.org/10.1007/BF02812021

De, A.K., Speer, J.G., Matlock, D., 2003. Color tint-etching for multiphase steels. Advanced Materials and Processes 161, 27–30.

De Cooman, B., Kwon, O., Chin, K., 2012. State-of-the-knowledge on TWIP steel. Materials Science and Technology 28, 513–527. https://doi.org/10.1179/1743284711Y.0000000095

De Moor, E., Gibbs, P.J., Speer, J.G., Matlock, D.K., 2010. Strategies for Third-Generation Advanced High Strength Steel Development. Iron and Steel Technology 7, 133–144.

De Moor, E., Speer, J.G., Matlock, D.K., Kwak, J.H., Lee, S.B., 2011. Effect of carbon and manganese on the quenching and partitioning response of CMnSi steels. ISIJ International 51, 137–144. https://doi.org/10.2355/isijinternational.51.137

Devaraj, A., Xu, Z., Abu-Farha, F., Sun, X., Hector, L.G., 2018. Nanoscale Solute Partitioning and Carbide Precipitation in a Multiphase TRIP Steel Analyzed by Atom Probe Tomography. Jom 70, 1752–1757. https://doi.org/10.1007/s11837-018-2974-1

Ding, R., Zhang, Chaofan, Wang, Y., Liu, C., Yao, Y., Zhang, J., Yang, Z., Zhang, Chi, Liu, Y., Chen, H., 2023. Mechanistic role of Mn heterogeneity in austenite decomposition and stabilization in a commercial quenching and partitioning steel. Acta Mater 250. https://doi.org/10.1016/j.actamat.2023.118869

Dong, X.X., Shen, Y.F., Jia, N., Zhu, Y.T., 2022. Improving mechanical properties and retained-austenite stability of a medium carbon Q&P steel by adjusting phase ratio. Materials Science and Engineering A 833. https://doi.org/10.1016/j.msea.2021.142580

Dong, Y.L., Pan, B., 2017. A Review of Speckle Pattern Fabrication and Assessment for Digital Image Correlation. Exp Mech 57, 1161–1181. https://doi.org/10.1007/s11340-017-0283-1

Dutta, A., 2019. Deformation behaviour and texture memory effect of multiphase nano-laminate medium manganese steels".

Dutta, A., Ponge, D., Sandlöbes, S., Raabe, D., 2019. Strain partitioning and strain localization in medium manganese steels measured by in situ microscopic digital image correlation. Materialia (Oxf) 5. https://doi.org/10.1016/j.mtla.2019.100252

DYSON DJ, HOLMES B, 1970. Effect of Alloying Additions on the Lattice Parameter of Austenite. J Iron Steel Inst (London) 208, 469–474.

Eckner, R., Kruger, L., Ullrich, C., Wendler, M., Volkova, O., 2019. Fracture toughness of high-alloy austenitic-martensitic TRIP steels after Q&P processing. Int J Fract 215, 139–151. https://doi.org/https://doi.org/10.1007/s10704-018-0332-

Findley, K.O., Hidalgo, J., Huizenga, R.M., Santofimia, M.J., 2017. Controlling the work hardening of martensite to increase the strength/ductility balance in quenched and partitioned steels. Mater Des 117, 248–256. https://doi.org/10.1016/j.matdes.2016.12.065

Fonstein, N., 2015. Advanced high strength sheet steels: Physical metallurgy, design, processing, and properties, 1st ed, Advanced High Strength Sheet Steels: Physical Metallurgy, Design, Processing, and Properties. Springer. https://doi.org/10.1007/978-3-319-19165-2

Frómeta, D., Lara, A., Grifé, L., Dieudonné, T., Dietsch, P., Rehrl, J., Suppan, C., Casellas, D., Calvo, J., 2021. Fracture Resistance of Advanced High-Strength Steel Sheets for Automotive Applications. Metall Mater Trans A Phys Metall Mater Sci 52, 840–856. https://doi.org/10.1007/s11661-020-06119-y

Frómeta, D., Lara, A., Molas, S., Casellas, D., Rehrl, J., Suppan, C., Larour, P., Calvo, J., 2019a. On the correlation between fracture toughness and crash resistance of advanced high strength steels. Eng Fract Mech 205, 319–332. https://doi.org/10.1016/j.engfracmech.2018.10.005

Frómeta, D., Lara, A., Parareda, S., Casellas, D., 2019b. Evaluation of edge formability in high strength sheets through a fracture mechanics approach, in: AIP Conference Proceedings. https://doi.org/10.1063/1.5112704

Gerbase, J., Embury, J.D., Hobbs, R.M., 1979. Mechanical Behavior of Some Dual Phase Steels - With Emphasis on the Initial Work Hardening Rate., IEEE Conference Record of Annual Pulp and Paper Industry Technical Conference.

Ghosh, S., Kaikkonen, P., Javaheri, V., Kaijalainen, A., Miettunen, I., Somani, M., Kömi, J., Pallaspuro, S., 2022. Design of tough, ductile direct quenched and partitioned advanced high-strength steel with tailored silicon content. Journal of Materials Research and Technology 17, 1390–1407. https://doi.org/10.1016/j.jmrt.2022.01.073

Girault, E., Jacques, P., Harlet, P., Mols, K., Van Humbeeck, J., Aernoudt, E., Delannay, F., 1998. Metallographic Methods for Revealing the Multiphase Microstructure of TRIP-Assisted Steels. Mater Charact 40, 111–118. https://doi.org/10.1016/s1044-5803(97)00154-x

gom, 2016. GOM Correlate. Gom.Com.

Hance, B., 2016. Advanced high strength steel: Deciphering local and global formability. International Automotive Body Congress, IABC 2016 DEARBORN - Papers.

Hance, B.M., Comstock, R.J., Scherrer, D.K., 2013. The influence of edge preparation method on the hole expansion performance of automotive sheet steels. SAE Technical Papers 2. https://doi.org/10.4271/2013-01-1167

Hesamodin Talebi, S., Ghasemi-Nanesa, H., Jahazi, M., Melkonyan, H., 2017. In situ study of phase transformations during non-isothermal tempering of bainitic and martensitic microstructures. Metals (Basel) 7. https://doi.org/10.3390/met7090346

Hidalgo, J., Celada-Casero, C., Santofimia, M.J., 2019. Fracture mechanisms and microstructure in a medium Mn quenching and partitioning steel exhibiting macrosegregation. Materials Science and Engineering A 754, 766–777. https://doi.org/10.1016/j.msea.2019.03.055

Hu, C., Huang, C.P., Liu, Y.X., Perlade, A., Zhu, K.Y., Huang, M.X., 2023. The dual role of TRIP effect on ductility and toughness of a medium Mn steel. Acta Mater 245. https://doi.org/10.1016/j.actamat.2022.118629

Hu, X.H., Sun, X., Hector, L.G., Ren, Y., 2017. Individual phase constitutive properties of a TRIP-assisted QP980 steel from a combined synchrotron X-ray diffraction and crystal plasticity approach. Acta Mater 132, 230–244. https://doi.org/10.1016/J.ACTAMAT.2017.04.028

Jacques, P., Furnemount, Q., Pardoen, T., Delannay, F., 2001. On the Role of Martensitic Transformation on Damage and Cracking Resistance in Trip-assisted multiphase steels. Acta Mater 49, 139–152. https://doi.org/10.1016/S1359-6454(00)00215-9

Jacques, P.J., Allain, S., Bouaziz, O., De, A., Gourgues, A.-F., Hance, B.M., Houbaert, Y., Huang, J., Iza-Mendia, A., Kruger, S.E., Radu, M., Samek, L., Speer, J., Zhao, L., van der Zwaag, S., 2009. On measurement of retained austenite in multiphase TRIP steels — results of blind round robin test involving six different techniques. Materials Science and Technology 25, 567–574. https://doi.org/10.1179/174328408X353723

Jeong, W.C., Matlock, D.K., Krauss, G., 1993. Effects of tensile-testing temperature on deformation and transformation behavior of retained austenite in a 0.14C-1.2Si-1.5Mn steel with ferrite-bainite-austenite structure. Materials Science and Engineering A 165, 9–18. https://doi.org/10.1016/0921-5093(93)90621-K

Kang, J., Ososkov, Y., Embury, D.J., Wilkinson, D.S., 2007. Digital image correlation studies for microscopic strain distribution and damage in dual phase steels. Scr Mater 56, 999–1002. https://doi.org/10.1016/j.scriptamat.2007.01.031

Kang, J., Pottore, N.S., Zhu, H., Tasan, C.C., 2023. An in situ investigation of neighborhood effects in a ferrite-containing quenching and partitioning steel: Mechanical stability, strain partitioning, and damage. Acta Mater 254. https://doi.org/10.1016/j.actamat.2023.118985

Kang, J., Wilkinson, D.S., Embury, J.D., Jain, M., 2005. Microscopic Strain Mapping Using Scanning Electron Microscopy Topography Image Correlation at Large Strain. J Strain Anal Eng Des 40, 559–570. https://doi.org/10.1243/030932405X16151

Kant, K., Losic, D., 2013. FIB Nanostructures. Springer International Publishing. https://doi.org/10.1007/978-3-319-02874-3

Kickinger, C., Suppan, C., Hebesberger, T., Schnitzer, R., Hofer, C., 2021. Microstructure and mechanical properties of partially ferritic Q&P steels. Materials Science and Engineering A 815. https://doi.org/10.1016/j.msea.2021.141296

Kokosza, A., Pacyna, J., 2008. Effect of retained austenite on the fracture toughness of tempered tool steel, Archives of Materials Science and Engineering.

Kong, H., Chao, Q., Cai, M.H., Pavlina, E.J., Rolfe, B., Hodgson, P.D., Beladi, H., 2017. One-step quenching and partitioning treatment of a commercial low silicon boron steel. Materials Science and Engineering A 707, 538–547. https://doi.org/10.1016/j.msea.2017.09.038

Lagneborg, R., Siwecki, T., Zajac, S., Hutchinson, B., 1999. Role of vanadium in microalloyed steels. Scandinavian Journal of Metallurgy 28, 186–241.

Larour, P., Freudenthaler, J., Weissböck, T., 2017. Reduction of cross section area at fracture in tensile test: Measurement and applications for flat sheet steels. J Phys Conf Ser 896. https://doi.org/10.1088/1742-6596/896/1/012073

Li, Z., Kiran, R., Hu, J., Hector, L.G., Bower, A.F., 2020. Analysis and design of a three-phase TRIP steel microstructure for enhanced fracture resistance. Int J Fract 221, 53–85. https://doi.org/10.1007/s10704-019-00405-6

Liu, H., Lu, X., Jin, X., Dong, H., Shi, J., 2011. Enhanced mechanical properties of a hot stamped advanced high-strength steel treated by quenching and partitioning process. Scr Mater 64, 749–752. https://doi.org/10.1016/J.SCRIPTAMAT.2010.12.037

Liu, J., Chen, C., Feng, Q., Fang, X., Wang, H., Liu, F., Lu, J., Raabe, D., 2017. Dislocation activities at the martensite phase transformation interface in metastable austenitic stainless steel: An in-situ TEM study. Materials Science and Engineering: A 703, 236–243. https://doi.org/https://doi.org/10.1016/j.msea.2017.06.107

Liu, L., He, B., Huang, M., 2018. The Role of Transformation-Induced Plasticity in the Development of Advanced High Strength Steels. Adv Eng Mater 20. https://doi.org/10.1002/adem.201701083

Lobbe, C., Hering, O., Hiegemann, L., Tekkaya, E.A., 2016. Setting Mechanical Properties of High Strength Steels for Rapid Hot Forming Processes. MDPI 9.

Maire, E., Morgeneyer, T., Landron, C., Adrien, J., Helfen, L., 2012. Bulk evaluation of ductile damage development using high resolution tomography and laminography. Elsevier 328–336.

Matlock, D.K., Speer, J.G., 2009. Microstructure and Texture in Steels. Springer London, London. https://doi.org/10.1007/978-1-84882-454-6

Nanda, T., Singh, V., Singh, G., Singh, M., Kumar, B.R., 2021. Processing routes, resulting microstructures, and strain rate dependent deformation behaviour of advanced high strength steels for automotive applications. Archives of Civil and Mechanical Engineering 21. https://doi.org/10.1007/s43452-020-00149-4

Nishikawa, A.S., Miyamoto, G., Furuhara, T., Tschiptschin, A.P., Goldenstein, H., 2019. Phase transformation mechanisms during Quenching and Partitioning of a ductile cast iron. Acta Mater 179, 1–16. https://doi.org/10.1016/j.actamat.2019.08.001

Pallisco, D.M., McDermid, J.R., 2020. Mechanical property development of a 0.15C–6Mn–2Al–1Si third-generation advanced high strength steel using continuous galvanizing heat treatments. Materials Science and Engineering A 778, 139111. https://doi.org/10.1016/j.msea.2020.139111

Park, T., Hector Jr., L.G., Hu, X., Abu-Farha, F., Fellinger, M.R., Kim, H., Esmaeilpour, R., Pourboghrat, F., 2019. Crystal plasticity modeling of 3rd generation multi-phase AHSS with martensitic transformation. International Journal of Plasticity 120, 1–46.

Parker, E.R., Zackay, V.F., 1973. ENHANCEMENT OF FRACTURE TOUGHNESS IN HIGH STRENGTH STEEL BY MICROSTRUCTURAL CONTROL. Engineering Fract Mechanics 5, 147–165.

Patel, V., 2019. Microstructure and Mechanical Properties of Medium Mn steel. McMaster University.

Pelligra, C., Samei, J., Kang, J., Wilkinson, D.S., 2022. The effect of vanadium on microstrain partitioning and localized damage during deformation of unnotched and notched DP1300 steels. Int J Plast 158. https://doi.org/10.1016/j.ijplas.2022.103435

Pushkareva, I., Shalchi-Amirkhiz, B., Allain, S.Y.P., Geandier, G., Fazeli, F., Sztanko, M., Scott, C., 2020. The influence of vanadium additions on isothermally formed bainite microstructures in medium carbon steels containing retained austenite. Metals (Basel) 10. https://doi.org/10.3390/met10030392

Qin, B., Bhadeshia, H.K.D.H., 2007. Crystallography of TWIP Steel. Graduate Institute of Ferrous Technology. Pohang University of Science and Technology. https://doi.org/10.1002/bmb.15

Rajan, V.P., Rossol, M.N., Zok, F.W., 2012. Optimization of Digital Image Correlation for High-Resolution Strain Mapping of Ceramic Composites. Exp Mech 1407–1421.

Ramazani, A., Ebrahimi, Z., Prahl, U., 2014. Study the effect of martensite banding on the failure initiation in dual-phase steel. Comput Mater Sci 87, 241–247. https://doi.org/10.1016/j.commatsci.2014.01.051

Rodríguez, R., Gutierrez, I., 2003. Correlation between nanoindentation and tensile properties influence of the indentation size effect. Materials Science and Engineering A 361, 377–384. https://doi.org/10.1016/S0921-5093(03)00563-X

Ruggles, T., Cluff, S., Miles, M., Fullwood, D., Daniels, C., Avila, A., Chen, M., 2016. Ductility of Advanced High-Strength Steel in the Presence of a Sheared Edge. JOM 68, 1839–1849. https://doi.org/10.1007/s11837-016-1927-9

Ruhl, R., Cohen, M., 1969. Splat Quenching of Iron-Carbon Alloys. Transactions of The Metallurgical Society of AIME 245, 241.

Salehiyan, D., 2018. Microstrain Partitioning and Damage in a QP980 Steel (Master of Applied Science). McMaster University , Hamilton.

Salehiyan, D., Samei, J., Amirkhiz, B.S., Hector, L.G., Wilkinson, D.S., 2020. Microstructural Evolution During Deformation of a QP980 Steel. Metall Mater Trans A Phys Metall Mater Sci 51, 4524–4539. https://doi.org/10.1007/s11661-020-05882-2

Samei, J., Asgari, H., Pelligra, C., Sanjari, M., Salavati, S., Shahriari, A., Amirmaleki, M., Jahanbakht, M., Hadadzadeh, A., Amirkhiz, B.S., Mohammadi, M., 2021. A hybrid additively manufactured martensitic-maraging stainless steel with superior strength and corrosion resistance for plastic injection molding dies. Addit Manuf 45. https://doi.org/10.1016/j.addma.2021.102068

Samei, J., Pelligra, C., Amirmaleki, M., Wilkinson, D.S., 2020. Microstructural design for damage tolerance in high strength steels. Mater Lett 269. https://doi.org/10.1016/j.matlet.2020.127664

Samei, J., Salib, Y., Amirmaleki, M., Wilkinson, D.S., 2019. The role of microstructure on edge cracks in dual phase and quench and partitioning steels subject to severe cold rolling. Scr Mater 173, 86–90. https://doi.org/10.1016/J.SCRIPTAMAT.2019.08.012

Samei, Javad, Zhou, L., Kang, J., Wilkinson, D.S., 2019. Microstructural analysis of ductility and fracture in fine-grained and ultrafine-grained vanadium-added DP1300 steels. Int J Plast 117, 58–70. https://doi.org/10.1016/j.ijplas.2017.12.009

Santacreu, P.-O., Glez, J.-C., Chinouilh, G., Fröhlich, T., 2006. Behaviour Model of Austenitic Stainless Steels for Automotive Structural Parts. Steel Res Int 77, 686–691. https://doi.org/https://doi.org/10.1002/srin.200606448

Savic, V., Hector, L., Alturk, R., Enloe, C., 2020. High Strain Rate Tensile Behavior of 1180MPa Grade Advanced High Strength Steels. SAE Int J Adv Curr Pract Mobil 2, 2020-01–0754. https://doi.org/10.4271/2020-01-0754

Schreier, H., Orteu, J.J., Sutton, M.A., 2009. Image correlation for shape, motion and deformation measurements: Basic concepts, theory and applications. Image Correlation for Shape, Motion and Deformation Measurements: Basic Concepts,Theory and Applications 1–321. https://doi.org/10.1007/978-0-387-78747-3/COVER

Scott, C.P., Fazeli, F., Shalchi Amirkhiz, B., Pushkareva, I., Allain, S.Y.P., 2017. Structure-properties relationship of ultra-fine grained V-microalloyed dual phase steels. Materials Science and Engineering A 703, 293–303. https://doi.org/10.1016/j.msea.2017.07.051

Scott, C.P., Shalchi Amirkhiz, B., Pushkareva, I., Fazeli, F., Allain, S.Y.P., Azizi, H., 2018. New insights into martensite strength and the damage behaviour of dual phase steels. Acta Mater 159, 112–122. https://doi.org/10.1016/j.actamat.2018.08.010

Seo, E.J., Cho, L., De Cooman, B.C., 2015. Application of Quenching and Partitioning Processing to Medium Mn Steel. Metall Mater Trans A Phys Metall Mater Sci 46, 27–31. https://doi.org/10.1007/s11661-014-2657-7

Soleimani, M., Kalhor, A., Mirzadeh, H., 2020. Transformation-induced plasticity (TRIP) in advanced steels: A review. Materials Science and Engineering A 795. https://doi.org/10.1016/j.msea.2020.140023

Speer, J., Matlock, D.K., De Cooman, B.C., Schroth, J.G., 2003. Carbon partitioning into austenite after martensite transformation. Acta Mater 2611–2622.

Speer, J.G., Rizzo Assuncao, F.C., Matlock, D.K., Edmonds, D. V., 2005. The “quenching and partitioning” process: nackground and recent progress. Ibero-american Journal of Materials 8.

Srivastava, A., Ghassemi-Armaki, H., Sung, H., Chen, P., Kumar, S., Bower, A.F., 2015. Micromechanics of plastic deformation and phase transformation in a three-phase TRIP-assisted advanced high strength steel: Experiments and modeling. J Mech Phys Solids 78, 46–69. https://doi.org/10.1016/J.JMPS.2015.01.014

Tang, A., Liu, H., Chen, R., Liu, G., Lai, Q., Zhong, Y., Wang, L., Wang, J., Lu, Q., Shen, Y., 2021. Mesoscopic origin of damage nucleation in dual-phase steels. Int J Plast 137. https://doi.org/10.1016/j.ijplas.2020.102920

Tasan, C.C., Bechtold, M., Schemmann, L., Tsuzaki, K., Raabe, D., Diehl, M., Zheng, C., Koyama, M., Roters, F., Ponge, D., Peranio, N., Yan, D., 2015. An Overview of Dual-Phase Steels: Advances in Microstructure-Oriented Processing and Micromechanically Guided Design. Annu Rev Mater Res 45, 391–431. https://doi.org/10.1146/annurev-matsci-070214-021103

Tasan, C.C., Hoefnagels, J.P.M., Diehl, M., Yan, D., Roters, F., Raabe, D., 2014. Strain localization and damage in dual phase steels investigated by coupled in-situ deformation experiments and crystal plasticity simulations. Int J Plast 63, 198–210. https://doi.org/10.1016/j.ijplas.2014.06.004

Thomas, G., Matlock, D.K., Rana, R., Hector Jr, L.G., Abu-Farha, F., 2015. Integrated Computational Materials Engineering Lab Heat Results Supporting DOE Targets. Great Designs in STEEL.

Tobata, J., Ngo-Huynh, K.-L., Nakada, N., Tsuchiyama, T., Takaki, S., 2012. Role of Silicon in Quenching and Partitioning Treatment of Low-carbon Martensitic Stainless Steel. ISIJ International 52, 1377–1382. https://doi.org/10.2355/isijinternational.52.1377

Toji, Y., Matsuda, H., Herbig, M., Choi, P.P., Raabe, D., 2014. Atomic-scale analysis of carbon partitioning between martensite and austenite by atom probe tomography and correlative transmission electron microscopy. Acta Mater 65, 215–228. https://doi.org/10.1016/j.actamat.2013.10.064

Turteltaub, S., Suiker, A.S.J., 2006. Grain size effects in multiphase steels assisted by transformation-induced plasticity. Int J Solids Struct 43, 7322–7336. https://doi.org/10.1016/j.ijsolstr.2006.06.017

Wang, J., Zhang, X., 2016. Twinning effects on strength and plasticity of metallic materials. MRS Bull 41, 274–281. https://doi.org/10.1557/mrs.2016.67

Wang, M.-M., Hell, J.-C., Tasan, C.C., 2017. Martensite size effects on damage in quenching and partitioning steels. Scr Mater 138, 1–5. https://doi.org/10.1016/j.scriptamat.2017.05.021

Wendler, M., Ullrich, C., Hauser, M., Krüger, L., Volkova, O., Weiß, A., Mola, J., 2017. Quenching and partitioning (Q&P) processing of fully austenitic stainless steels. Acta Mater 133, 346–355. https://doi.org/10.1016/j.actamat.2017.05.049

Wu, W., Wang, Y.-W., Makrygiannis, P., Zhu, F., Thomas, G.A., Hector, L.G., Hu, X., Sun, X., Ren, Y., 2018. Deformation mode and strain path dependence of martensite phase transformation in a medium manganese TRIP steel. Materials Science and Engineering: A 711, 611–623. https://doi.org/10.1016/J.MSEA.2017.11.008

Xie, H., Jiang, Z., Yuen, W.Y.D., 2011. Analysis of microstructure effects on edge crack of thin strip during cold rolling. Metallurgical and Materials Transactions B: Process Metallurgy and Materials Processing Science 42, 1244–1252. https://doi.org/10.1007/s11663-011-9540-3

Xiong, X.C., Chen, B., Huang, M.X., Wang, J.F., Wang, L., 2013. The effect of morphology on the stability of retained austenite in a quenched and partitioned steel. Scr Mater 68, 321–324. https://doi.org/10.1016/J.SCRIPTAMAT.2012.11.003

Yan, D., Tasan, C.C., Raabe, D., 2015. High resolution in situ mapping of microstrain and microstructure evolution reveals damage resistance criteria in dual phase steels. Acta Mater 96, 399–409. https://doi.org/10.1016/j.actamat.2015.05.038

Yang, H., Wang, H., Yang, Z., Huang, Y., Li, D., Peng, Y., Wu, P., 2021. In situ neutron diffraction and crystal plasticity analysis on Q&P1180 steel during plastic deformation. Materials Science and Engineering A 802. https://doi.org/10.1016/j.msea.2020.140425

Zhao, H.S., Zhu, X., Li, W., Jin, X.J., Wang, L., Jiao, H., Jiang, D.M., 2014. Austenite stability for quenching and partitioning treated steel revealed by colour tint-etching method. Materials Science and Technology (United Kingdom) 30, 1008–1013. https://doi.org/10.1179/1743284714Y.0000000517

Zhou, L., 2018. Effect of Vanadium on Fracture of DP1300 Steels (Master of Science). McMaster University.

5.13 Appendices

5.13.1 Appendix A: Work hardening comparison between 3G TRIP-assisted steels

Figure A 5.1 features the continuous yielding and work hardening curves of both the QP1500 and UFG DP1300 steels. The work hardening curves in Figure A 5.1 were computed using the procedure outlined section 5.3.2. Both the QP1500 and UFG DP1300 steel were subjected to a tensile strain rate of $6x10^{-4}$ /s (Zhou, 2018). The continuous yielding of both steels is associated with their high martensite fraction, and mobile dislocation density which are generated at dissimilar phase interfaces. Initially, the UFG DP1300 steel has a higher work hardening rate than the QP1500 steel. This is likely related to gliding of partial dislocations on two independent slip planes during the ɣ-to-martensite transformation in TRIP-assisted steels. It should be noted that the local strain gradients (ε’) shown in Figure 5.12 and Figure 5.13 of the UFG DP1300 and QP1500 steels only accounts for the dislocations piling up at dissimilar phase interfaces, directly contributing to the ε’. However, at low strains, the ε’ in Figure 5.13 is slight larger in the QP1500 steel versus that of the UFG DP1300 steel. On the other hand, the work hardening rate in the UFG DP1300 is higher than the QP1500 steel as shown in Figure A 5.1. This suggests that there are other modes of dislocation motion inhibition that strongly influence the hardening of the UFG DP1300 steel, i.e. the pile up of dislocations at vanadium carbonitrides (Lagneborg et al., 1999; Pelligra et al., 2022; Pushkareva et al., 2020; Scott et al., 2018, 2017).

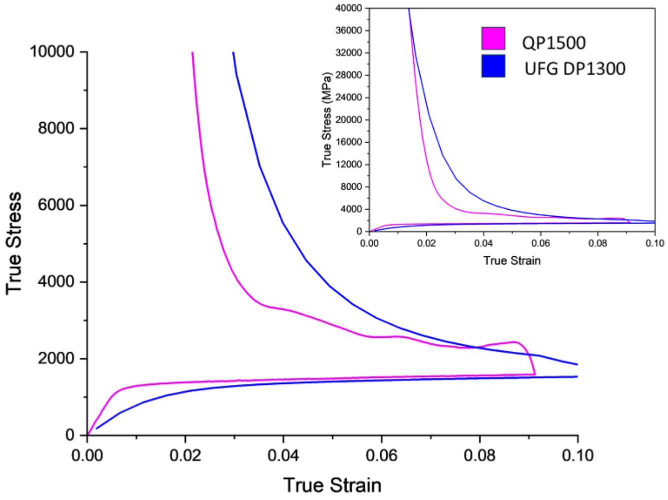

Figure A 5.1:Work hardening Rates of QP1500 and UFG DP1300 steel. Tensile data of UFG DP1300 steel is from Zhou (2018).

5.13.2 Appendix B: TRIP kinetics of QP1500

Figure B 5.1 compares the TRIP kinetics of this ultrahigh strength Q&P steel tested at the APS synchrotron X-ray beam chamber 11-ID-C at two different tensile strain rates (corresponding to extension rates of 0.15 mm/min in this paper versus 1.8 mm/min in Park et al. (2019)). All other conditions to which testing was performed in both instances are the same (i.e. voltage of 105 keV, wavelength of 0.1173 Å, detector-to-specimen distance of 1.9 m, etc.). In the present paper as well as in Park et al. (2019),~17.5-18 vol% of ɣ was captured before starting the tensile test. The quantification of strain using DIC, however, in both instances may differ. In the experiments conducted by Park et al. (2019), faster TRIP kinetics at a higher strain rate of the QP1500 steel is featured. Changes in the strain rate can affect the mechanical stability of austenite as a result of the adiabatic heating affect (Choi and Jin, 1997; Wu et al., 2018). Nanda et al. (2021) note that the adiabatic heating of specimens subjected to high strain rate testing resulted in suppressed TRIP kinetics. This point is, however, contradicted by experimental investigations conducted not only in this paper, as shown in Figure B 5.1, but also by Choi et al. (2002) and Savic et al. (2020) who reported an increase in ɣ-to-martensite transformation rate with an increase in strain rate (from 10^{-3}/s to 2.5x10^{2}/s). Savic et al. (2020) rather suggested that at high strain rates, TRIP exhaustion occurs faster in order to maintain a high strain hardening rate to prevent necking, and in turn, early failure. The data collected by Park et al. (2019) was fitted using a least squares algorithm to the rate form, Equation B 5.1, developed by Santacreu et al. (2006) then applied by Ref. (Beese and Mohr, 2011). Interestingly, despite differences in tensile strain rate, both instances show ≥ 27 % (4 vol%) of the ɣ untransformed at the start of its post-uniform elongation period.

$$\dot{f}_{\alpha'} = (f_{\alpha'}^{max} - f_{\alpha'})nD(D\bar{\varepsilon})^{n-1}\dot{\bar{\varepsilon}} \qquad \text{Equation B 5.1}$$

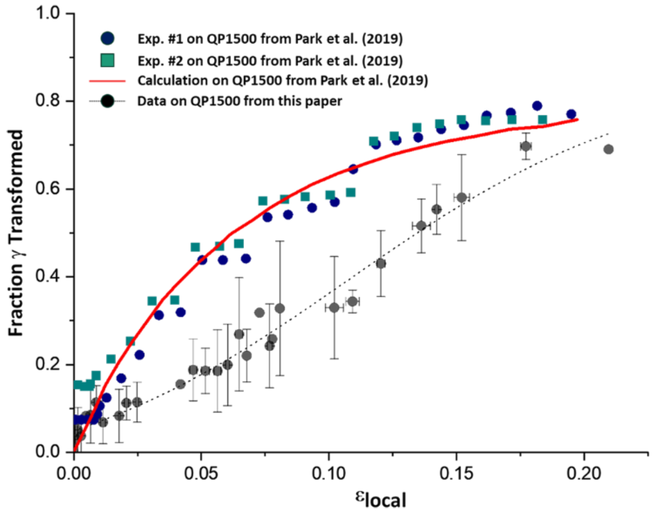

Figure B 5.1: TRIP Kinetics of QP1500 at 0.15mm/min and 1.8mm/min strain rates

Figure B 5.1 features the TRIP kinetics obtained from QP1500 steel in this paper at a strain rate of 0.15mm/min contrasted to the work of Park et al. (2019) at an extension rate of 1.8mm/min. In Park et al. (2019) they determined the TRIP kinetics of QP1500 experimentally (Exp #1 in blue dots, Exp #2 in green squares) and fitted their acquired data to Figure B 5.1, shown in red.

5.13.3 Appendix C: In-situ tensile testing coupled with EBSD

Interrupted tensile tests coupled with EBSD were carried out using microtensile specimens to investigate the occurrence of TRIP and to capture GND evolution in the material. Figure C 5.1, Figure C5.2, and Figure C5.3 show the strained microstructure of the subject QP1500 steel at different levels of displacement, 0, 0.07, and 0.23 mm, respectively. Figure C 5.1, Figure C5.2, and Figure C5.3 shows EBSD phase maps (a_1, b_1, c_1, d_1), quality maps (a_2, b_2, c_2, d_2), and the GND evolution maps in BCC (a_3, b_3, c_3, d_3), and FCC (a_4,b_4,c_4,d_4) obtained using the Aztec Crystal Software. Zero solutions were cleaned up from the analysis. The EBSD scanning parameters were maintained consistent to the procedure outlined in section 5.4.2. This investigation methodology was adapted from a previous study (Salehiyan et al., 2020). Progressive TRIP (i.e. the break up of ɣ) in initial blocky ɣ islands is highlighted with a yellow circle in Figure C 5.1a_1, Figure C5.2b_1, and Figure C5.3c_1 with increasing specimen displacement.

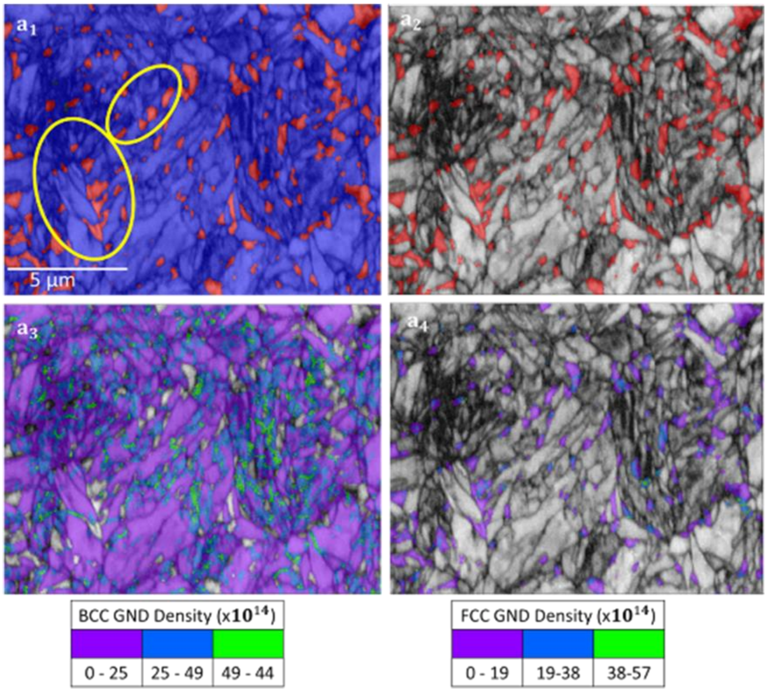

Figure C 5.1: Specimen with 0 mm displacement. EBSD Phase Map with ɣ (FCC) coloured red and TM (BCC) coloured blue (a_1); ɣ superimposed on EBSD Quality Map (a_2); Distribution of GNDs within the TM regions (a_3); Distribution of GNDs within the ɣ regions (a_4)

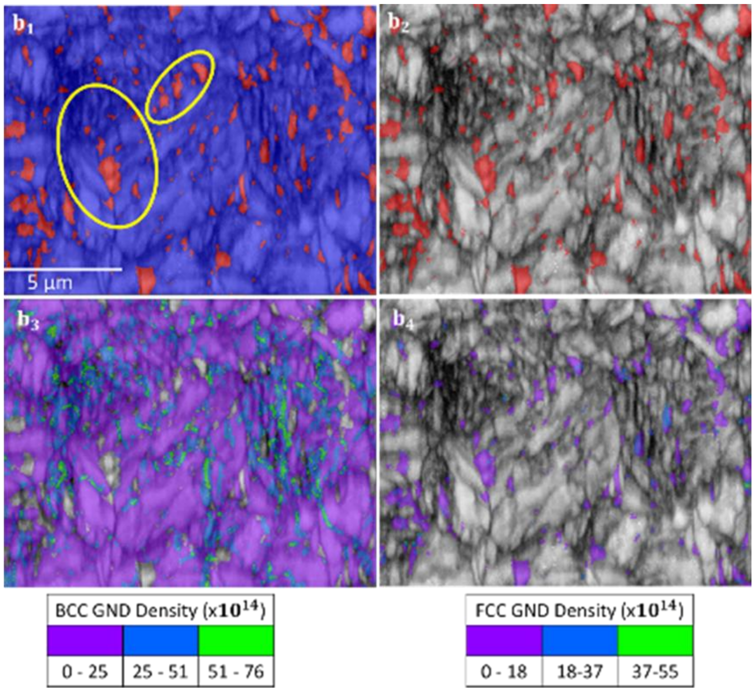

Figure C5.2: Specimen with 0.07 mm displacement. EBSD Phase Map with ɣ (FCC) coloured red and TM (BCC) coloured blue (b_1); ɣ superimposed on EBSD Quality Map (b_2); Distribution of GNDs within the TM regions (b_3); Distribution of GNDs within the ɣ regions (b_4)

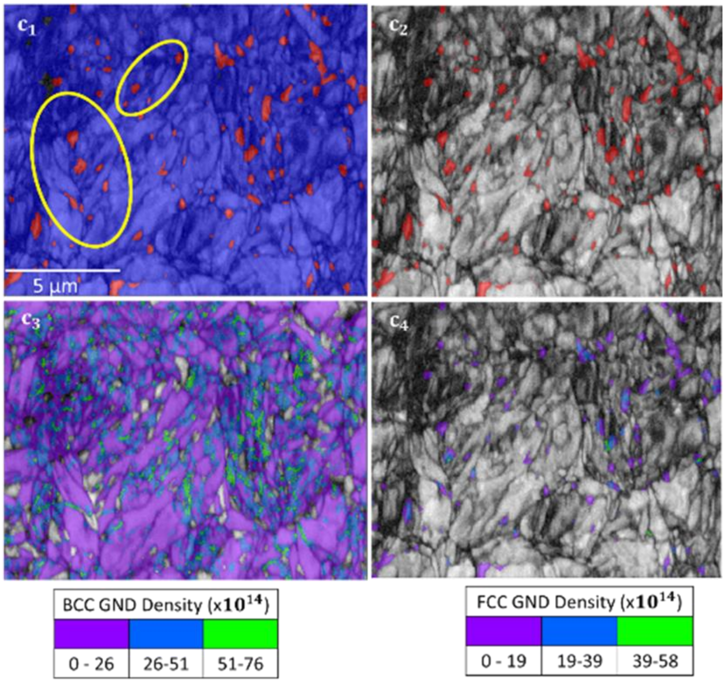

Figure C5.3: Specimen with 0.23 mm displacement. EBSD Phase Map with ɣ (FCC) coloured red and TM (BCC) coloured blue (c_1); ɣ superimposed on EBSD Quality Map (c_2); Distribution of GNDs within the TM regions (c_3); Distribution of GNDs within the ɣ regions (c_4)

5.13.4 Appendix D: Micromechanisms of Damage in QP1500

Microstrain mapping shows co-deformation of ɣ-M islands and TM. It is typical in low strength DP steels to see micro-cracking of martensite, void formation within ferrite, or interfacial cracking, but the two phases do not typically co-deform. Yet, recently it has been observed that vanadium nitrocarbides in ultrahigh strength DP steels selectively precipitate in ferrite, and scarcely in martensite, thereby enabling improved deformation of martensite. In Figure D 5.1, Site A (the same region shown in Figure 5.7 and Figure 5.12) experiences the highest ε_{Avg} in the material just before fracture, and therefore showed more severe microstrain partitioning amongst phases than Site B.

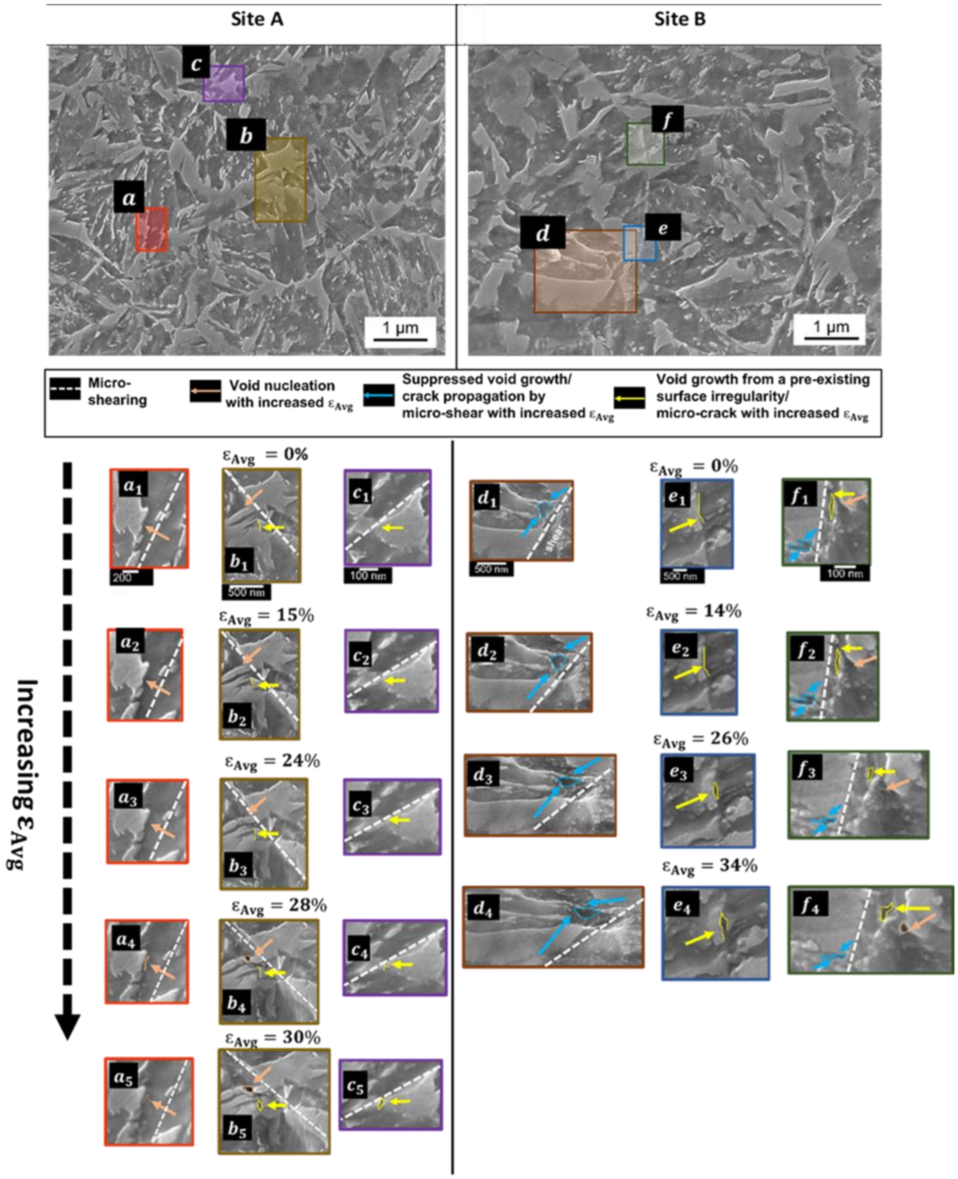

Figure D 5.1: Micromechanisms of Damage in QP1500

The arrows in Figure D 5.1 highlight the different micro-damage events which develop in the microstructure with increasing ε_{Avg}. Significant micro-shearing in the microstructure was observed during quasi in-situ FESEM tensile testing, this is detailed by the dotted white lines shown in Figure D 5.1. The peach arrows in Figure D 5.1 highlight voids which nucleate with increasing ε_{Avg}, blue arrows highlight voids or micro-cracks which eventually are suppressed by micro-shearing, and the yellow arrows highlight voids which grow from surface irregularities or develop from a micro-crack. In Site A (a_{1-5}), interfacial void nucleation is seen, but its growth in the TM patch is inhibited due to micro-shearing (the peach arrow points towards a peach ligament which decreases in length from $\varepsilon_{Avg} = 0.28$

to 0.30, shown in Site A ($a_{4,5}$)). Site A ($b_{1\text{-}5}$) shows micro-cracking at a narrow portion within the ɣ-M island initiating at an $\varepsilon_{Avg} = 0.28$, and then showing growth and distortion via micro-shearing at an $\varepsilon_{Avg} = 0.30$ (peach arrow). As well, Site A ($b_{1\text{-}5}$) shows micro-cracking to have nucleated at a surface irregularity/grain boundary then developing into an oval-type shape at an $\varepsilon_{Avg} = 0.30$ (yellow arrow). Another instance of oval-type void growth motivated by micro-shearing is seen in Site A ($c_{1\text{-}5}$) in which the void nucleated on a pre-existing surface irregularity. Site B ($d_{1\text{-}4}$) shows micro-shearing suppressing the growth and distorting the shape of a pre-existing void (indicated by the blue arrow). At Site B ($e_{1\text{-}4}$), micro-cracking is seen to have nucleated at a surface irregularity/grain boundary, this micro-crack expands parallel to the tensile direction, but does not grow or propagate (yellow arrow). In Site B ($f_{1\text{-}4}$), a pre-existing void in a blocky ɣ-M island is compressed from further growth via shear (blue arrow), as well as there are instances nearby of interfacial void nucleation (yellow arrow), and nucleation of a void at the ɣ-M and TM boundary (peach arrow at f_4). Many instances of micro-shearing and minimal instances of interfacial cracking were observed, further proving that there is considerable mechanical compatibility between phases in this material.

6 Microstrain Partitioning,Transformation Induced Plasticity, and Damage Evolution of a Third Generation Medium Mn Advanced High Strength Steel

Concetta Pelligra[1], Babak Shalchi Amirkhiz[2], Nafiseh Zafer[2], Jidong Kang[2], David S. Wilkinson[1]

[1]Department of Materials Science and Engineering, McMaster University, Hamilton, ON, L8S 4L7, Canada

[2]CanmetMATERIALS, Natural Resources Canada, Hamilton, Ontario L8P 0A5, Canada

6.1 Abstract

An experimental Medium Mn (med-Mn) steel (0.15C-5.8Mn-1.8Al-0.71Si) with a martensitic starting microstructure, intercritically annealed at 685°C for 120s, was discovered to have a large true strain at fracture ($\varepsilon_f = 0.61$) while also meeting established (strength x elongation) targets (28,809 MPa%), sustained monotonic work hardening and prolonged Transformation Induced Plasticity (TRIP) kinetics. This was found by varying the intercritical annealing (IA) temperature within a narrow temperature interval in order to isolate its impact on TRIP kinetics and damage development on such med-Mn steel. A comprehensive understanding of the microstructural damage processes leading to fracture is presented using quasi in-situ Scanning Electron Microscope tensile testing as well as X-ray Computed Microtomography. In addition, we precisely evaluated the TRIP kinetics of this steel using a combined Digital Image Correlation (DIC) and synchrotron-sourced High Energy X-ray Diffraction technique. With these methods, we demonstrate that an abundance of voids nucleate during deformation, but their growth can be suppressed by prolonging TRIP over a large strain range. Moreover, novel post- processing techniques to assess DIC acquired data at the microscopic scale have been used to gauge the severity of strain partitioning amongst phases and strain gradient evolution across dissimilar phase interfaces, in comparison with two 3G TRIP-assisted steels to one ultrafine grained Dual Phase steel. Overall, it has been found that, in addition to carefully moderating TRIP kinetics, the introduction of polygonal ferrite, as is conventional in med-Mn steels, enhances the local forming properties and damage tolerance in 3G TRIP-assisted microstructures.

6.2 Introduction

The production of thin, strong and cost-effective ultrahigh strength automotive sheet steels is being driven by emission regulations needed to achieve carbon neutrality. It is reported that a 10% reduction in vehicle mass can increase its fuel efficiency of Internal Combustion Engine vehicles (ICEVs) by 6-8% resulting in a 70% decrease in lifetime emissions (AutoSteel, 2011). For Battery Electric Vehicles (BEVs), the impact of battery weight makes lightweighting even more important, as this can increase the range of BEVs. An effective means of achieving weight reduction, while enhancing vehicle crash worthiness, involves the use of Advanced High Strength steels (AHSSs) in the construction of a vehicle's Body-in-White (BIW). Thus, 3G AHSSs can be used to make cost-effective modern vehicles that comply with passenger driving and general safety standards. These steels show an overall improved ultimate tensile strength (UTS) and total elongation (TE) in comparison to first generation (1G) AHSSs, while reducing costs compared to highly alloyed second generation (2G) AHSSs. Multiphase 3G AHSSs utilize the Transformation Induced Plasticity (TRIP) effect (i.e. the transformation from metastable austenite (ɣ)-to-martensite) to effectively tailor 3G steel strengths and elongations. Ultimately, the use of TRIP in AHSSs improves energy absorption potential, hence improving passenger safety in the event of a car collision, while also providing enhanced steel formability (Fonstein, 2015; Horvath et al., 2017).

Conventionally, 3G steels, are modestlydefined as those with UTS x TE $\geq$24000MPa% as suggested by Matlock et al. (2012). It is critical to note however, that the use of UTS, TE and their product offers limited information on the true sheet forming capability of these steels for complex automotive components (e.g. the strain hardening potential of 3G steels is not captured). Furthermore, while tensile elongation is a useful measure of ductility when applied to stretching operations, is does not predict the limits for most complex forming operations, including flanging, tight-radius bending, edge stretching, etc. (Hance, 2016, 2018). The true strain at fracture (ε_f), as measured from the reduction in area in a uniaxial tensile test, offers an alternative measure of ductility that can be correlated with forming operations that involve bending (Datsko & Yang, 1960). In analyzing a series of AHSSs, Hance (2016, 2018) proposed an alternative means of defining AHSS ductility. He suggested that the steel's performance should be classified by its ability to deform under a concentrated load (local forming potential) versus that of a uniform load (global forming potential). Alternatively, Frómeta et al. (2021), similar to Datsko & Yang (1960), directly acknowledge the weak correlation between the (UTS x TE) and the reduction in area.

Medium Mn (med-Mn) steels, with 4-10 wt%Mn, undergo a significant amount of ɣ reversion during intercritical annealing (IA) at temperatures ranging from ≈675°C to ≈700°C, whereas Quench and Partition (Q&P) steels retain ɣ through low temperature partitioning (≈400°C) relying on short-range carbon diffusion. Furthermore, recent publications show the potential of reducing the energy to manufacture 3G steels with 1-step Q&P processes (Barella et al., 2023; Mola & De Cooman, 2013). Some suggest that fully exhausting the TRIP effect at low strains or at high strains would be detrimental to mechanical properties (He et al., 2019). Therefore, optimal TRIP kinetics needs to be determined such that there is a balance in mechanical properties and minimized damage. In comparison to Q&P steels, med-Mn steels show greater Continuous Galvanizing Line (CGL) compatibility, and it has been proven that U.S. DoE targets can be achieved with industrially capable short annealing times (Bhadhon et al., 2017; Pallisco & McDermid, 2020).

Microstructural characteristics, such as grain size and elemental partitioning, of med-Mn steels is dependent on its IA parameters and starting microstructure (Pallisco & McDermid, 2020; Patel, 2019). With a martensitic starting microstructure, Cao et al. (2011) was able to achieve variable UTS x TE values within a broadened 3G mechanical property envelope (24,000-40,000 MPa%) (Matlock and Speer, 2009). This work resulted in significant changes in TE of 25-40% while keeping a common UTS ≈ 960MPa. Luo & Dong (2015) then Pallisco & McDermid (2020), compared cold-rolled and martensitic starting microstructures of med-Mn steels at one IA temperature of interest. Both noted an increase in the TE with a martensitic starting microstructure. During the IA treatment, lath-type ɣ nucleates at lath boundaries in a martensitic starting microstructure, while equiaxed grains nucleate at recrystallized ferrite boundaries in a cold-rolled starting microstructure. An abundance of martensite lath boundaries in a martensitic starting microstructure enables the nucleation of ultra-fine ɣ with a locally reduced M start temperature (M_s), which enhances its mechanical stability against TRIP (Lee et al., 2012).

TRIP is heavily dependent on a steel's Mn content, in which 5-12 wt% Mn content favours a direct transformation to martensite (Body-Centred-Tetragonal (BCT) structure) (Wong et al., 2016). Moreover, the ɣ stacking fault energy (SFE) indicates the mechanism by which the ɣ accommodates strain (i.e. via the activation of TRIP, Twinning-Induced Plasticity (TWIP) or dislocation glide). In general, a low SFE (<20 mJ/m^2) activates the TRIP effect, a medium SFE (20-40 mJ/m^2) activates twinning, and a high SFE (>45 mJ/m^2) favours dislocation glide. The local elemental partitioning during the IA treatment, and the steel's grain size are additional factors to defining the SFE of ɣ in these complex steels (Lee & Choi, 2000; Pallisco, 2021)

In general, multiphase materials do not plastically deform in the same manner because the number of slip systems for dislocation motion is not equal in each phase. Geometrically necessary dislocations (GNDs), essential to accommodate the strain gradient between hard and soft phases during deformation, sustains the deformation of the material without it resorting to immediate damage nucleation. As a result, the work hardening of the multiphase material is improved. Moreover, the strain gradient can be correlated to a material's 'back stress' or 'kinematic hardening', i.e. the piling up of dislocations at a boundary resulting in more stress required for new dislocation emission or further motion (Courtney, 2005; Li et al., 2020). The evolution of back stress/kinematic hardening of med-Mn steel has been estimated by Bhadhon et al. (2022) and Pallisco & McDermid (2020) using a load-unload-reload testing methodology initially applied to Dual Phase (DP) steels by Westphal et al. (2010). The localized strengthening in TRIP steels is a result of GND propagation in surrounding phases during the metastable ɣ-to-martensite transformation (Jacques, 2004). Intercritically annealing a med-Mn steel with a martensitic starting microstructure at 665°C resulted in an eventual plateau of the back stress with increasing true strain. This suggests that a significant amount of ɣ is stable against transformation, and therefore acts as an obstacle to dislocation motion (Pallisco & McDermid, 2020).

At a microscopic level, through in-situ Transmission Electron Microscopy (TEM) tensile testing, Liu et al. (2017) observed that local damage accumulation in a TRIP steel is reduced by means of improved strain compatibility resulting from partial dislocations travelling on two independent slip planes during the transformation. Examinations at the microscopic scale show that the macro formability of TRIP steels is improved because of the enhanced micromechanical compatibility between phases. This is consistent with the speculation made by Jacques et al. (2001) in which the volume expansion associated with the transformation of metastable ɣ-to-martensite can be used to suppress damage. However, only a few investigations have attempted to validate this concept.

The accumulation of GNDs at phase interfaces has been estimated experimentally by several researchers with the use of Digital Image Correlation at the microscopic scale (μDIC) on a heterogeneous micron-grained Cu/nanograined bronze laminate (Huang et al., 2018),ultrahigh strength DP steels (Pelligra et al., 2022), Q&P steels (Pelligra et al., 2024), as well as high entropy alloys (Siemens et al., 2023). Pelligra et al. (2022) use in-situ SEM tensile testing coupled with DIC, a technique first applied by Kang et al. (2005, 2007), to statistically quantify the strain gradient across dissimilar phase interfaces. Most microstructural evolution models made to date tend to show a much smoother GND field, than observed in reality (El-Naaman et al., 2016; Van Beers et al., 2013; Yalçinkaya et al., 2019). Several researchers to date have focussed on identifying the micromechanisms of damage through in-situ SEM tensile testing on 3G steels, but scarce reports have been made on the microstrains causing damage and then leading to fracture of med-Mn steels (Dutta et al., 2019).

Voids in multiphase materials are known to form by particle fracture, particle-matrix debonding, or form within the matrix near particles. These voids grow with increasing plastic strain and eventually coalesce (Thomason, 1968). Two-dimensional (2D) observations of damage in relation to the material's microstructure, i.e. via post-mortem fractography (Avramovic-Cingara et al., 2009; Samei, Zhou, et al., 2019) or in-situ tensile testing (Kang et al., 2023; Oh et al., 2024; Pelligra et al., 2022; Samei et al., 2018; Wang et al., 2017; Yan et al., 2015), is helpful, however, may not be fully representative of damage evolution within the bulk of the material. Buffière et al. (1999) suggested, for example, that voids that may not have coalesced at the surface may have coalesced within the bulk of the sample. They note a difference in the cracked particles at the surface versus those in the bulk. Some authors suggest that a greater fraction of cracked particles are to be expected at the surface as they are relaxed from compressive stresses as compared to the bulk (Kozłowska et al., 2019; Weck, 2007). Other issues with a 2D analysis of damage includes the potential for sample preparation to eliminate porosity, the full distribution of voids is limited through 2D sectioning, and, ultimately, the connectivity of voids is a three-dimensional (3D) parameter (Salvo et al., 2003). Analysing damage with the use of tomography in 3G steels having a >1GPa strength has so far been limited (Pelligra et al., 2022; Samei et al., 2020; Samei, Pelligra, et al., 2019), scarcely reported for TRIP steels, and no such reports have been made for med-Mn steels.

The damage events leading to fracture are affected by several factors both intrinsic to the microstructure (e.g. particle size (Nan & Clarke, 1996), particle aspect ratios, etc.), and extrinsic to the microstructure (e.g. specimen triaxiality (Bao & Wierzbicki, 2004; Toda et al., 2014)). In 3G steels, another intrinsic factor affecting void nucleation, grown and the overall rate at which damage evolves is TRIP kinetics (Samei et al., 2020; Sun et al., 2019). Sun et al. (2019) observed that intercritically annealing an ultra-fine grained (UFG) martensitic, low Al-Si med-Mn steel at 700°C and 750°C resulted in dramatic differences in terms of their void size/area fraction. They found that intercritically annealing at 700°C resulted in a higher (≈2x increase) volume fraction of ɣ at necking, smaller void size and void area fraction versus the 750°C condition. The authors proposed that ɣ would be more slowly consumed during necking when intercritically annealing this steel at 700°C, allowing the volume expansion associated with the martensitic transformation to oppose void nucleation and growth. The creation of localized compressive stresses associated with this positive change in volume, decreases the level of stress triaxiality at a damage initiation site, resulting in a reduced void growth rate and higher true strain to fracture (Hornbogen, 1978). Another way to look at this is to note that the energy required to initiate damage in martensite is smaller due to its lower ductility (Hornbogen, 1978). For both IA conditions, however, the micromechanisms of damage are the same (Sun et al., 2019). This suggests that TRIP has an influence on the local triaxiality, but not to a point in which the mechanism of fracture changes, as seen in Bao & Wierzbicki (2004) with different triaxial stress-states imposed using different specimen designs.

In this paper, we first present the IA temperature for this med-Mn steel, with a martensitic starting microstructure, which achieves the 3G mechanical targets and also shows optimal damage tolerance qualities. This is demonstrated through mechanical property testing, along with extensive microstructural characterization. As well, we present an in-depth analysis of this steel's microstrain gradient evolution and identify micromechanisms leading to fracture of this med-Mn at its optimal IA condition in comparison with other 3G steels, with and without TRIP-assistance. This has been accomplished using a novel μDIC computational techniques proposed by Pelligra et al. (2022) and Siemens et al. (2023).

6.3 Material and Methods

The as-received material is a prototype 3G med-Mn steel sheet with a 1.2 mm thickness. The thermomechanical processing route is detailed elsewhere (Mehrabi et al., 2023; Pallisco & McDermid, 2020). The chemical composition of this steel is given in Table 6.1 as determined by plasma optical emission spectroscopy (ICP-OES) and combustion analysis.

Table 6.1: Chemical Composition (wt%)

C	Mn	Al	Si	Cr	S
0.15	5.78	1.77	0.71	0.04	0.003

6.3.1 Heat Treatments

A predominantly martensitic (80% martensite-20% ferrite) starting microstructure, as determined using ThermoCalc, was obtained by heating the as-received material to 890°C for 600s, followed by quenching at -20°C/s to room temperature. A martensitic starting microstructure was chosen for detailed mechanical investigations based on previous work done by Pallisco & McDermid (2020) on a comparable med-Mn steel with a slightly higher Si content. By comparison, the increased Si level resulted in a ≈75°C drop in the AC_3 as determined with ThermoCalc. This can also impact SFE and hence, result in different TRIP kinetics (Dumay et al., 2008). Panels (120 x 200 mm) were heat treated using the McMaster Galvanizing Simulator (MGS), set to a dew point of -30°C, in order to mimic annealing and coating trials performed on similar prototype CGL-compatible med-Mn steels (Bhadhon et al., 2022; Mehrabi et al., 2023; Pallisco & McDermid, 2020; Patel, 2019). The panel temperature was monitored by a ype K thermocouple (0.5 mm, ∓3°C) welded to the surface. Specimens for microstructural analysis or tensile testing were extracted from the uniformly heat-treated zones as described elsewhere (Bellhouse, 2010; Patel, 2019). Pallisco & McDermid (2020) had shown that IA at 665°C for 120s of a martensitic starting microstructure resulted in significant reversion of ɣ which was stabilized up to high strains during tensile testing. As a result, IA was performed within a tight temperature interval from 665°C to 710°C at three different IA temperature conditions (665°C, 685°C, and 710°C). An IA holding time of 120s was chosen to be compatible with industrial galvanizing capabilities. An overaging treatment at 460^{0}C for 30s was also incorporated in these heat treatments to mimic the resulting effects on microstructure and mechanical properties during dipping in the Zn(Al,Fe) bath (Patel, 2019).

6.3.2 Mechanical Properties

Mechanical properties were determined at room temperature through uniaxial tensile testing of ASTM E8/E8M − 15a standard, sub-size tensile specimens, made by wire Electrical Discharge Machining (wEDM), and tested parallel to the rolling direction (RD). A 100kN Instron tensile frame was used with a 1mm/min crosshead speed. The true strain at fracture (ε_f) was calculated using $\varepsilon_{\mathrm{f}} = \ln\frac{\mathrm{A}_0}{\mathrm{A}_{\mathrm{f}}}$, where A_0 is the initial cross-sectional area and A_{f} is the minimum area at fracture, taking into account thickness variations throughout the fractured surface (ASTM E8M-Standard Test Methods for Tension Testing of Metallic Materials, 2021; Frómeta et al., 2017; Hance et al., 2013)

6.3.3 SEM Imaging and EBSD Mapping

To initially characterize the steel, a Field Emission Scanning Electron Microscope (FESEM) was used to acquire high-resolution images of the steel's surface after a 2% Nital etch for 15s. To differentiate between the Body-Centred-Cubic (BCC) and Face-Centred-Cubic (FCC) phases in the steel, Electron Back-scattered Diffraction (EBSD) mapping was conducted using a JSM-7000 FESEM equipped with Aztec indexing software. Mapping was performed with the specimen inclined to a 70° tilt and scanned at 20kV, with a probe current of 18mA and step size of 50nm. EBSD analysis revealed that the ɣ average grain size to be 0.31µm with a 3:1 aspect ratio which does not significantly change with each tested condition. Islands within the microstructure of this med-Mn steel are referred to as ɣ-M throughout this paper, in which ɣ could have transformed to martensite during the final quench of this steel or with increased deformation. The matrix phases rather are referred to as polygonal ferrite-tempered martensite (F-TM), with a grain size of 0.61µm, in this paper.

6.3.4 TEM Analysis

The Focused Ion Beam (FIB) lift-out technique was used to extract 0.2-0.3µm thick lamellae of undeformed and strained (0.15 engineering strain) specimens for TEM analysis. Strained specimens were used to observe GNDs and to provide evidence of TRIP. A Tecnai Osiris TEM with an X-Field Emission Gun (X-FEG), operating at an acceleration voltage of 200kV was employed with conventional bright field (BF) and dark field (DF) imaging modes. As well, Scanning Transmission Electron Microscopy (STEM) was performed using a combination of BF and High-Angle Annular Dark Field (HAADF) detectors. For elemental mapping of the microstructure, Energy X-ray Dispersive Spectroscopy (EDS) was used in STEM mode, in which enriched Mn islands were considered either reverted ɣ or martensite By coupling Selected Area Electron Diffraction (SAED) with high resolution EDS mapping, one can identify martensite as the regions exhibiting a BCC pattern, along with a high Mn concentration and presence of nano-twins.

6.3.4.1 Carbide Extraction Replicas

Carbon replica films with extracted second phases and carbides were obtained from freshly polished and etched undeformed specimen after immersion in a 4% Nital solution. The replicas were examined in a Talos L120C TEM operating at 120KeV. The carbide area fraction was determined using ImageJ.

6.3.5 XRD

Tensile tests were interrupted at intervals of 0.05 true strain to determine the TRIP kinetics of this intercritically annealed med-Mn steel. The gauge section of ASTM-E8 subsize tensile specimens were cross sectioned, mounted, and ground with a fine grit to remove the any decarburization preventing accurate ɣ quantification. The ɣ content was determined using a Bruker D8 DISCOVER diffractometer with a DAVINCI design equipped with Vantec 500 (MiKroGap TM technology) area detector and Cobalt Sealed Tube Source. The X-ray beam size and exposure time used to measure the ɣ content is 0.5 mm and 40 min/measurement, respectively. Specimenss were scanned over a 2θ range of 45° to 127°. The collected 2D frames were then integrated with the aid of DIFFRAC.EVA Version 4.0 software and the percentage of ɣ was calculated with Topas Version 4.2 as done by Salehiyan (2018) in accordance to the ASTM E975-13 standard, using the (111), (200), and (220) ɣ peaks (ASTM, 2009).

6.3.6 Tensile Testing and HE-XRD

A more statistically representative, volumetric quantification of ɣ as a function of uniaxial strain was determined through synchrotron-sourced High Energy X-Ray Diffraction (HE-XRD). These experiments provide an assessment of the impact IA treatments have on TRIP kinetics in this steel, while also helping to validate the initial TRIP kinetic assessments made using Cobalt sourced-X-ray Diffraction (Co-XRD) which only penetrated ~20µm below the steel's surface (Pelligra et al., 2024). Not only does HE-XRD provide through thickness measurements, we can also obtain many more data points over the course of the tensile test.

In-situ tensile testing, using a 13kN load frame, was performed at room temperature in the synchrotron X-ray beam chamber of the Argonne Photon Source (APS) 11-ID-C beamline using the parameters outlined by Abu-Farha et al. (2018). Tensile testing was performed at a strain rate of 0.15mm/min with an applied preload of <100N before commencing each test. A fine white and black speckle pattern was applied on the customized dog-bone specimens using an Iwata airbrush for high resolution 2D DIC acquisition. Details ofthe DIC camera parameters used at 11-ID-C has been presented previously (Pelligra et al., 2024). DIC was used to precisely define the localized strain within the region of HE-XRD acquisition. HE-XRD measurements were also acquired on undeformed, customized dog-bone specimen to ensure that ɣ measurements were independent from slight adjustments to the beam's impingement angle. The HE-XRD experiments conducted here use the conventional straight-gauged, customized dog-bone specimen design, applied first by others (Abu-Farha et al., 2018; Li et al., 2020; Park et al., 2019).

6.3.7 In-situ FESEM Tensile Testing

Microstrain partitioning amongst ɣ-M and F-TM phases as well as the dynamic evolution of damage in this med-Mn steel in its 685°C IA condition was carried out using quasi static in-situ FESEM tensile testing. Hourglass microtensile specimens were used to centralize deformation and damage (Salehiyan, 2018; Salehiyan et al., 2020; Zhou, 2018). A manual in-house built tensile stage was utilized for in-situ FESEM tensile testing, while etched images were acquired at a focused location as a function of increasing tensile strain to obtain high-resolution µDIC maps (Kang et al., 2005, 2007). Microstrain partitioning amongst ɣ-M and F-TM phases as well as the strain gradient across dissimilar phase interfaces is visualized and quantified from FESEM images processed using GOM Correlate 2018 software (gom, 2016). The facet size and point distance (distance between facet centres) in the GOM software was chosen to provide sufficient micro-detail and mapping coverage particularly at high average von Mises strains (ε_{Avg}). Microstrain mapping with von Mises Strain is said to directly correlate to the density of GNDs (Dutta et al., 2019). Further information on optimizing the facet size and point distance to achieve the average in-grain strain resolution in AHSSs was previously described (Pelligra et al., 2022).

6.3.8 µXCT

A Bruker Skyscan1172 X-ray Computed microtomography (µXCT) system equipped with a 100kV X-ray source and an Al/Cu filter was used to quantify damage by void nucleation and growth in the 665°C, 685°C, and 710°C IA conditions. µXCT scans was performed on fractured hourglass microtensile specimens with the same geometry of those used for in-situ FESEM tensile testing, as described above. With XCT systems that reply completely on geometric magnification, the specimen needs to be placed on a rotating stage close to the source to achieve a high resolution of 0.9µm/pixel or 0.73μm^3/voxel. Specimens were rotated 360° with a 2D projection obtained every 0.25° rotation to collect a total of 1440 images. The commercial Skyscan 1172 software packages, NRecon, CTan and CTVol, were used to reconstruct the 2D projections into a 3D model to observe and quantify internal voids and dimples (voids at the surface).

6.4 Results

6.4.1 Mechanical Properties

At all IA temperatures tested, the tensile strength is above 1GPa as shown in the mechanical properties chart, Table 6.2. Only modest changes in mechanical properties were observed when increasing the IA temperature by 20°C from 665°C to 685°C, except for the post-uniform elongation (PUE) which essentially doubles. Both conditions successfully achieve 3G generalized UTS x TE mechanical targets of 25,392 and 28,809MPa% respectively. The sensitivity of the mechanical properties of med-Mn steels to IA temperature has been noted by several researchers (Arlazarov et al., 2012; Bhadhon et al., 2017, 2022; Pallisco, 2021; Pallisco et al., 2017; Patel, 2019). Increasing the IA temperature further to 710°C results in significant changes to the mechanical properties. For example, UTS x TE is reduced to 21,104 MPa%, similar to that of an ultrahigh strength Q&P steel recently investigated (Pelligra et al., 2024). Yet, Pallisco & McDermid

(2020) found that the highest UTS x TE was achieved when their med-Mn steel with a martensitic starting microstructure was subjected to an IA treatment of 710°C for 120s (27,800MPa%). This fact further enforces the vital role alloying elements (such as; Si) play in the manipulating the Ms, and hence the stability of reverted ɣ, on the mechanical properties of 3G steels (Hofmann et al., 2006).

Table 6.2 Mechanical Tensile Properties

IA Temperature	**665°C**	**685°C**	**710°C**
Ultimate Tensile Strength (UTS) in MPa	1184 ± 132	1067 ± 87	1319 ± 150
Yield Strength (YS) in MPa	862 ± 59	862 ± 64	653 ± 303
Total Elongation (TE)	0.23 ± 0.01	0.27 ± 0.05	0.16 ± 0.03
Uniform Elongation (UE)	0.22 ± 0.01	0.23 ± 0.05	0.14 ± 0.05
Post-Uniform Elongation (PUE)	0.018 ± 0.01	0.043 ± 0.003	0.012 ± 0.02
True Strain at Fracture (ε_f)	0.57 ± 0.07	0.61 ± 0.03	0.40 ± 0.03
UTS x TE (MPa x %)	25,392	28,809	21,104

A 95% Confidence Interval (CI) was calculated based on triplicate measurements.

Engineering stress-strain curves (Figure 6.1a) provide a clearer sense of the impact of IA temperature on tensile behaviour. One clearly sees that there is a peak in the ductility at the intermediate IA temperature of 685°C. Sharp increases in the work hardening rate can be noted in Figure 6.1b. These are linked to the activation of plasticity enhancing mechanisms such as the TRIP and/or TWIP effects at a true strain of ≤ 0.05, close to the yield point elongation as shown in the stress-strain curves of Figure 6.1a. The 665°C and 710°C conditions follow a parabolic trend in work hardening whereas work hardening trend in the 685°C condition is monotonic/linear up to the UTS.

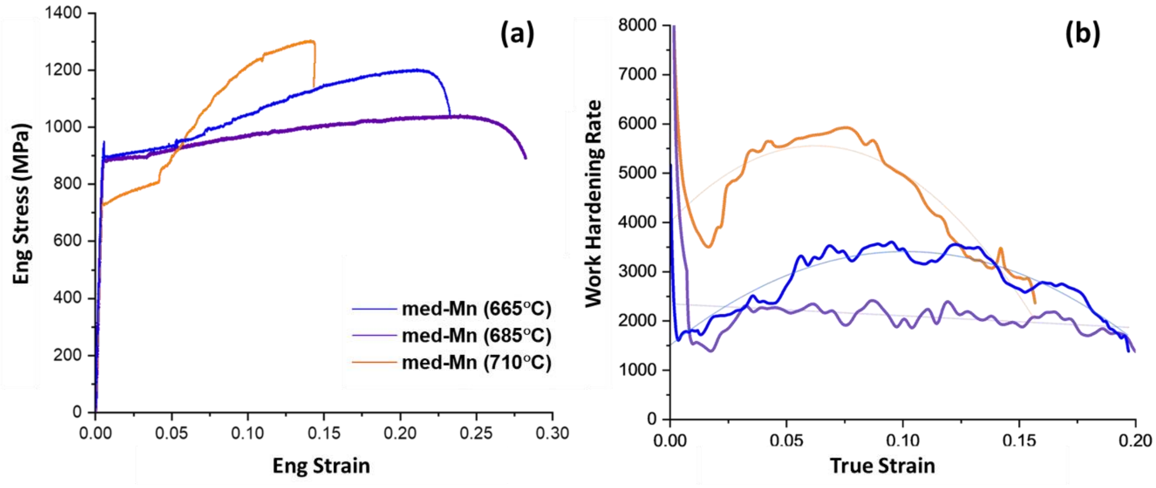

Figure 6.1:Engineering Stress-Strain (a) and Work hardening (b) Curves of the three IA conditions of interest in this paper – 665°C,685°C, and 710°C.

6.4.2 Microstructural Characterization

The undeformed microstructure of this steel consists of polygonal ferrite as well as both blocky- and lath-type ɣ-M. Packets of blocky- and lath-type ɣ-M are seen in Figure 6.2a and b. Globular carbides inside blocky-type ɣ-M are a result of tempering and ɣ decomposition (Talebi et al., 2018). This general microstructure as a function of starting microstructure is consistent with the observations of other researchers (Arlazarov et al., 2012; Luo & Dong, 2015; Shi et al., 2010) and did not change drastically with the modest changes in the IA treatment featured in this paper. This finding was critical in order to isolate the impact that IA has on TRIP kinetics and its role on damage development in med-Mn steels.

Examples of prior ɣ packets consisting of blocks with embedded lath-type ɣ-M of differing orientations are outlined in orange (Toji et al., 2014) in Figure 6.2a and b. Examples of polygonal ferrite are also labelled throughout Figure 6.2. Carbon depletion is clearly evident in the microstructure as shown in Figure 6.2c$_2$ of lath-type ɣ-M regions whereas a C-enriched blocky-type ɣ-M region is shown in Figure 6.2c$_{1,2}$, consistent with Xiong et al. (2013). They argued that a local C-enrichment within ɣ does not have a notable effect on supressing TRIP. Rather they found that the phases surrounding the metastable ɣ, whether coarse or fine, low or high in carbon, have a greater impact on the steel's ability to accommodate the volume expansion associated with the martensitic transformation (Xiong et al., 2013). Mn solute segregation, either complete or partial, within the microstructure could explain the significant amount of reverted ɣ (≈30 vol%) in this steel. Complete Mn segregation is more likely a result of the martensitic annealing step whereas partial Mn segregation is likely a result of the subsequent IA treatments. This gradient in Mn heterogeneity amongst phases is thought to effectively suppress TRIP (Ding et al., 2023) as a result of differing local M_s temperatures of the ɣ. STEM mode imaging coupled with EDS has been used to demonstrate the micro-segregation of Mn within the structure, as shown in Figure 6.2c_3. Here regions with a high Mn content are considered block- or lath-type ɣ-M whereas low Mn packet-sized regions are considered ferrite within the microstructure. The SAED patterns and corresponding dark field (DF) images presented in Figure 6.3c, dB as well as in Appendix A. Figure A 6.1 (eB-C,fB-C) and Figure A 6.2 (c-dA, c-dB), validate the presence of ferrite, ɣ and martensite in low Mn and high Mn rich regions, respectively. Dislocations in the polygonal ferrite were observed and likely due to the final quenching process, as shown in Figure 6.2$d_{2\text{-}4}$. TiC precipitates, seen in Figure 6.2c_4,d_4, act as pinning sites for these dislocations, providing a micro-strengthening mechanism.

Mehrabi et al. (2023) determined, using ThermoCalc, the cementite dissolution temperature of a med-Mn steel containing 1.1 wt%Si to be ≈650°C. They found that a martensitic starting microstructure resulted in very few carbide particles which suggests that the carbon remains supersaturated within the martensite. A significant number of carbides were present after an IA treatment at 665°C of this med-Mn steel with a martensitic starting microstructure. On the other hand, in the 685°C IA condition, these carbides quickly dissolved. The same goes for the 710°C IA condition. The area fraction of carbides decreases by ≈5x, from 0.001 to 0.0002, with a 20°C increase in IA temperature, from 665°C to 685°C. The remaining particles at these higher IA temperatures are nanoscale and enriched in Ti. The dissolution of these particles is much slower as they are formed at high temperatures, and their dissolution rate is controlled by Ti rather than carbon diffusion.

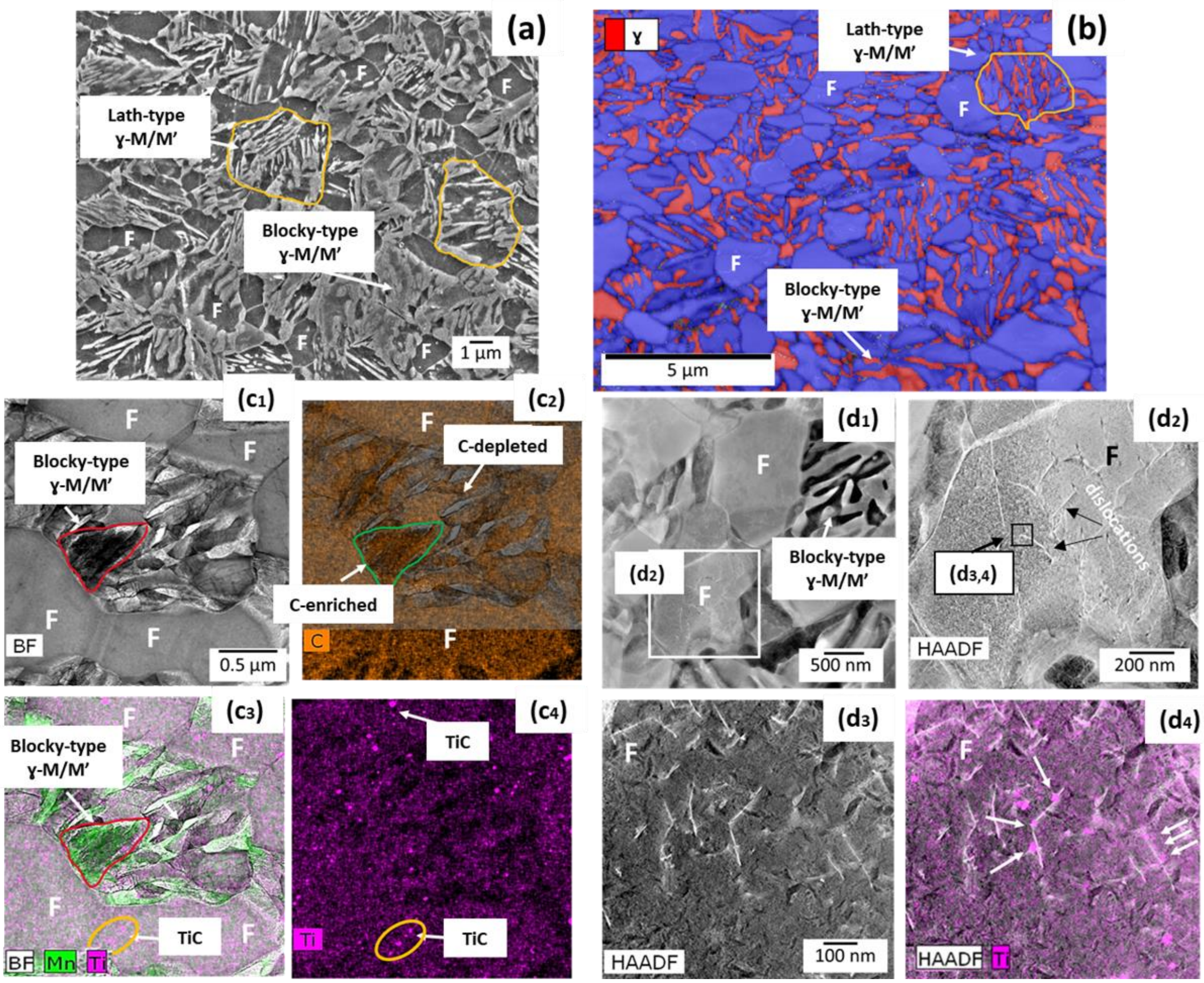

Figure 6.2: Representative SEM image of the undeformed med-Mn steel microstructure with a martensitic starting microstructure subjected to an IA treatment 685°C held for 120s (a). Packets consisting of blocky- and lath-type ɣ-M are outlined in the SEM image (a) and EBSD map (b). High magnification STEM images coupled with EDS of a blocky- and lath-type ɣ-M packet ($c_{1\text{-}4}$). High magnification STEM images coupled with EDS of polygonal ferrite grains ($d_{1\text{-}3}$). Dislocations within a ferrite grain are shown in ($d_{2\text{-}4}$).

Although the presence of polygonal ferrite as well as both blocky- and lath-type ɣ-M did not significantly differ with modest IA temperature changes, EDS mapping in representative regions of these TEM foils showed differences in local Mn content with changes in IA treatment.

SAED indexing was performed to visualize the ultra-fine (≈70nm) lath-type ɣ, ɣ-M and martensite in this steel. Figure 6.3 shows SAED indexed patterns performed on the 685°C IA condition. The results for the other conditions are shown in Appendix A. Before SAED indexing, EDS was used to preliminarily target lath-type ɣ or ɣ-M (Mn-enriched) versus polygonal ferrite (Mn-weak) areas.

Only with SAED indexing coupled with EDS mapping was it then possible to distinguish between martensite and ɣ within the steel. The reverted ɣ shows an FCC diffraction pattern while the martensite shows a BCT pattern with SAED indexing. Figure 6.3b offers a higher magnification BF TEM image of the red-squared-area in Figure 6.3a. The SAED pattern, obtained from the green encircled region in the BF image of Figure 6.3b shows the [0 1 1]ɣ zone axis in Figure 6.3c. The DF image from spot A which belongs to the $(1\bar{1}1)$ FCC reflection shows elongated ɣ grains, in Figure 6.3dA. The DF image from spot B corresponding to the to the $(1\ 1\ 0)$ BCC reflection, is not part of the major diffraction pattern indexed by zone axis [0 1 1]ɣ. As a result, this DF image shows an elongated ɣ grain with some partial transformation to martensite (ɣ-M), in Figure 6.3dB. Therefore, this justifies that Mn enrichment serves as an indicator to the ɣ or martensite phase. On the other hand, the region low in Mn, is polygonal ferrite, in Figure 6.3dB. Moreover, the DF image, specifically streaks in region C, shows evidence of planar defects (i.e. nano-twins) within the ɣ, in Figure 6.3dc. High resolution evidence, as opposed to a bulk GND estimation traditionally done with lattice distortions from EBSD (Ruggles & Fullwood, 2013) of strain contours is shown in Figure 6.3e and f respectively.

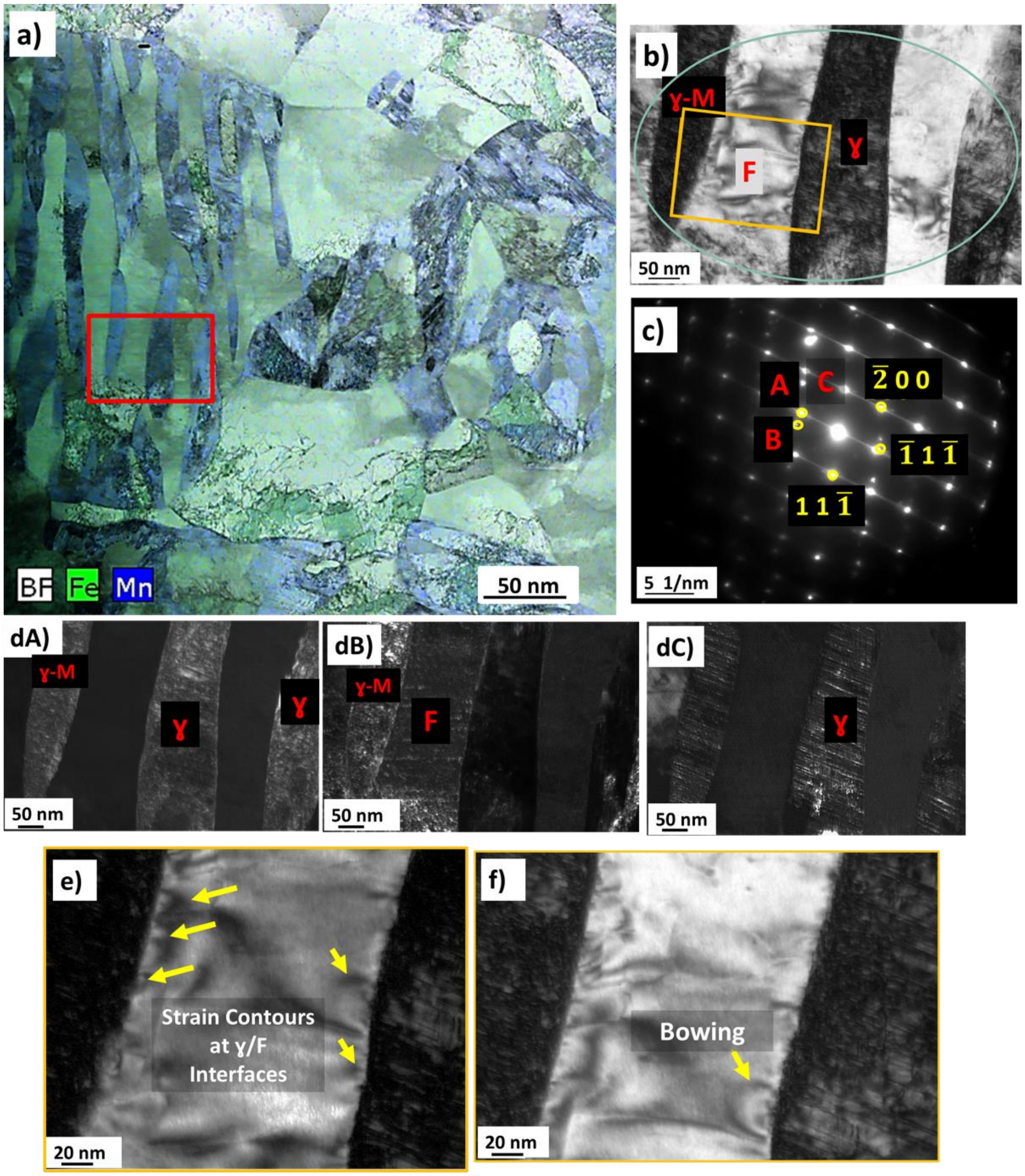

Figure 6.3: Representative EDS map of the undeformed martensitic annealed med-Mn steel microstructure subjected to an IA treatment 685°C held for 120s to target Mn-enriched and -weak regions (a). BF image (b) of the red-squared region from the EDS map in (a). SAED pattern (c) from green encircled region of BF image in (b), is indexed by the [0 1 1]ɣ zone axis. Dark field images from spots A, B and streak C, are labelled as dA, dB, dC respectively. Strain Contours representing the evolution of GNDs are in (e) and (f) which are also high magnification images from yellow-squared region in (b).

6.4.2.1 Characterization of the Reverted ɣ

A primary, reliable quantification of ɣ and an understanding of TRIP kinetics as a function of IA treatment was done using Co-XRD on cross-sectioned, intermittently strained tensile specimens, as shown in Figure 6.4. When ɣ is quantified using either optical microscopy or EBSD, it tends to be underestimated due to limited resolution (De et al., 2003; Ding et al., 2023; Jacques et al., 2009; Kickinger et al., 2021; Zhao et al., 2014). Thus, the difference between the ɣ detected by XRD and that detected by EBSD represents the amount of the reverted ɣ tied up as thin films. We have measured ɣ for all three IA conditions using EBSD (14-26%) and Co-XRD (29-38%), as shown in Figure 6.4. This indicates that ≈10-15% of the reverted ɣ is in the form of thin interlath films.

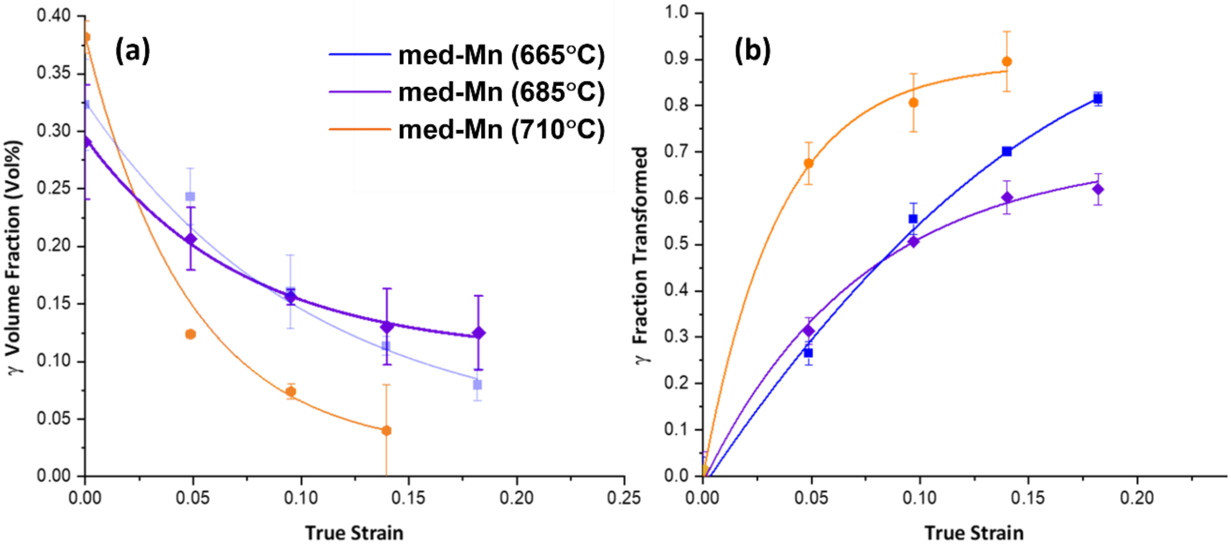

Figure 6.4: ɣ Volume Fraction and the faction ɣ that has transformed, as a function of True Strain, detected using Co-XRD.

The ɣ Fraction Transformed was calculated as was done by Pallisco & McDermid (2020).

6.4.2.2 TRIP Kinetics

Consistent with the Co-XRD results described in Figure 6.4, data from the HE-XRD experiments show that the 685°C IA condition results in the slowest transformation kinetics. The initial ɣ from the HE-XRD data is 32±1, 36±3, and 38±2 vol% of the 665°C, 685°C and 710°C IA conditions, respectively. This is comparable to the initial ɣ measured using Co-XRD as shown in Figure 6.4a, with the 685°C IA condition showing the most variability between the two techniques – ≈29 versus ≈36vol%. This indicates that there is a heightened heterogeneous distribution of ɣ through the thickness of the 685°C IA condition. Zhang et al. (2021) also found improved peak mechanical properties in a med-Mn steel intercritically annealed at an intermediate temperature. They attributed the increase in heterogeneity within the microstructure at such IA temperature to the increase high back stress strengthening (i.e. the accommodation of strain gradients via GNDs causing long-range back stresses (Wu et al., 2015)). Figure 6.5a and b shows the ɣ fraction transformed as a function of von Mises equivalent strain quantified within the precise location

(0.5 x 0.5 mm^2) of the HE-XRD data acquisition. Figure 6.5b contains shaded regions to signify the 95% confidence limits on the amount of ɣ fraction transformed. Appendix B contains a more in-depth analysis of this data which shows the mechanical stability of ɣ described by a decay factor k. For this med-Mn steel intercritically annealed at 665°C, 685°C and 710°C, the k-values are 4.9, 3.7, and 5.3, respectively. The most stable ɣ (i.e. lowest k-value) was attained in the 685°C IA condition.

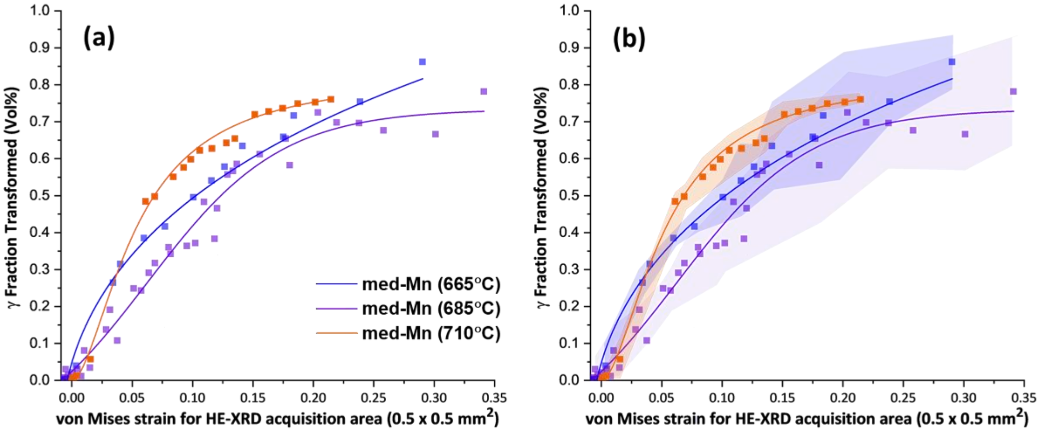

Figure 6.5:The TRIP kinetics of this med-Mn steel subjected to IA treatments of 665°C, 685°C,710°Cand held for 120s (a). Figure 6.5b is the same as that of (a) with the addition of shaded regions showing the 95% CI span of ɣ variability of every tested IA treatment with increasing von Mises strain.

The carbon content of ɣ was calculated from the austenite lattice parameter using the combined equations of Ruhl & Cohen (1969) and Dyson & Holmes (1970). This was determined to be 0.62-0.58wt%C using HE-XRD. Since the 685°C IA condition features the greatest variability in initial ɣ content and in TRIP kinetics (as indicated by the 95% CI error in Figure 6.5b), the carbon content within the ɣ is also expected to have the highest variability for this condition.

6.4.3 Damage Evolution and Fracture in 3D

Once damage is introduced at high strains, microstrain correlation is less likely to be captured via DIC. As a result, this 2D investigation of damage has been supplemented with 3D damage evolution characterization using µXCT. A µXCT-generated 3D reconstruction of a fractured sample is shown in Figure 6.6a. The analysis of fractured specimens using µXCT enables damage evolution to be quantified as a function of local true strain (Samei et al., 2018; Zhou, 2018). The void area fraction data shown in Figure 6.6b indicates that samples tested in the 665°C and 710°C IA conditions sustain the highest fraction of closed voids up to fracture. (Note that closed voids are those which are not connected with the surface and are therefore fully enclosed in the material). In contrast, specimens tested at the 685°C IA condition achieve the highest local true strain and accumulate the least amount of closed voids up to fracture. For all three steel conditions tested the void area fraction increases exponentially with strain. It is important to note, however, that due to the µXCT pixel resolution of 0.9µm, and this steel's fine microstructure, many nano-scaled voids remained unidentified until a local true strain of ≈0.6. We have captured the presence of these nano-scaled voids using quasi in-situ FESEM tensile testing, as detailed in section 6.4.3.1, where voids with diameters of ≈0.02-0.6 µm in size were identified. The *closed* void area fraction in Figure 6.6b was used to understand the steel's ability to accumulate voids (i.e. characterizing its damage tolerance) before fracturing. This is based on a per cross-section slice analysis – which analyzes void nucleation and growth as a 2D parameter considering the total area of one cross-sectional slice. The void density, on the other hand, is another 2D parameter which accounts for the number of voids per area of slice cross-section. For the 685°C IA condition, at a local true strain ≈0.4, we see an increase in the void density despite the constant void area fraction, as shown in Figure 6.6b and c, respectively. This suggests that void nucleation (i.e. increase in void density) is happening at a much faster rate than void coalescence. This inflection-type increase in void density was also seen in a microalloyed 3G DP steel (Zhou, 2018). Additionally, this provides evidence of voids being suppressed from further growth, therefore not increasing in void area fraction, as a result of the local compressive stresses imposed by the transformation from ɣ-to-martensite. This is consistent with the speculation made by Sun et al. (2019) in which at lower IA temperatures (700°C versus 750°C), the delay in ɣ transformation during necking opposes void growth and coalescence. The 685°C IA condition contains the highest void density, and lowest void area fraction at fracture, indicating that, although the most damage is to be observed in the 685°C IA condition, these voids coalesce at the slowest rate, and therefore allows this condition to attain the highest local true strain at fracture.

It is helpful to examine the largest 100 voids, those which contribute most to fracture. All three treatments achieve the same mean in volume equivalent void diameter, but there is a 6x increase in void diameter size variation (from ±0.1 to ±0.6µm) in the 685°C IA condition. This further reinforces the fact that void growth/coalescence is slow and/or supressed in this condition, and that a large portion of these voids remain small at fracture.

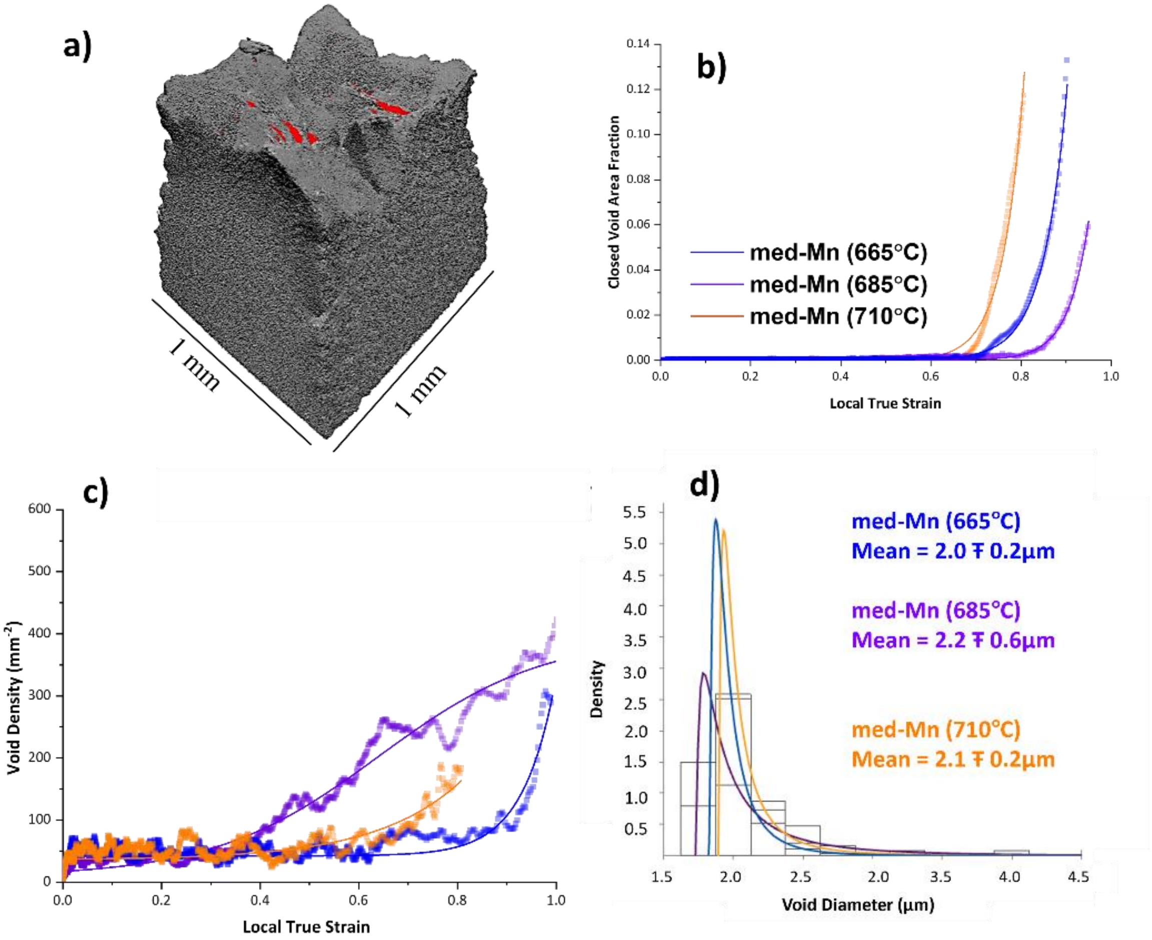

Figure 6.6: A 3D reconstruction produced from multiple cross-sectional slices in a µXCT scan (a) Void Area Fraction as a function of local true strain (b) Void Density as a function of local true strain (c) Cumulative Distribution Plot (CDF) of Void Diameter of the largest 100 voids (d) of the 665C, 685C and 710°C IA conditions.

Moreover, it is important to note that the specimens used in these tests have the same hourglass geometry of those used for quasi in-situ SEM tensile tests, therefore enabling high local true fracture strains to occur.

6.4.3.1 µDIC

Microstrain mapping coverage with the use of in-situ SEM tensile testing of etched microtensile samples is limited once strains are high. Nonetheless, this technique can be used to examine the micromechanisms of damage in 2D. Figure 6.7 shows the damage evolution of the steel in relation to the microstructure up to fracture. The SEM imaging location used for Figure 6.7 was captured within the neck of the steel and is very close to the point of facture. This site achieved the highest ε_{Avg} and exhibited the most severe strain localization of the steel.

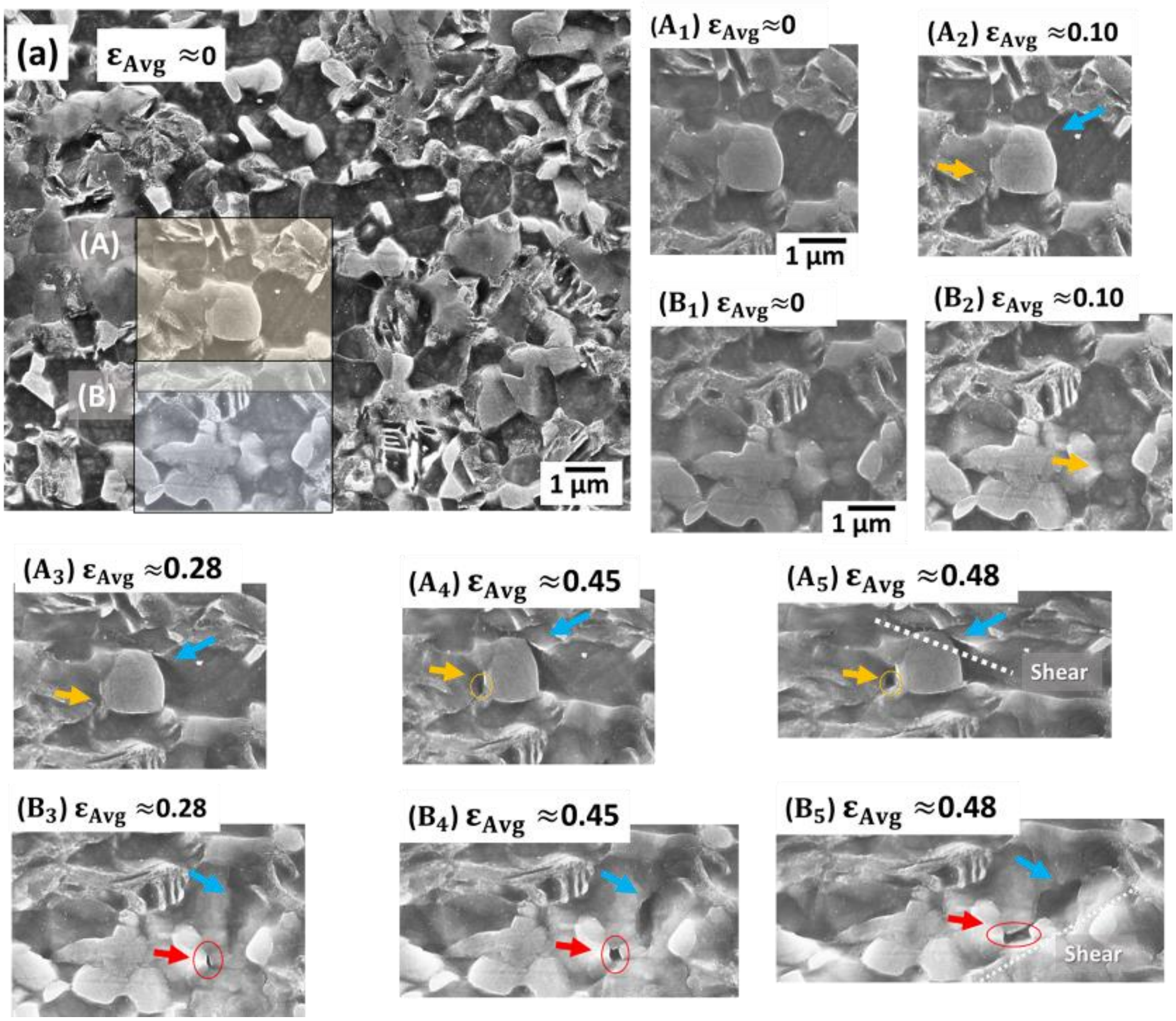

Figure 6.7: Micromechanisms of Damage of the 685°C IA condition. Blue arrows represent void nucleation + growth in ferrite, red arrows represent ɣ-M cracking and yellow arrows represents interfacial cracking.

Damage for the 685°C IA condition does not become evident until an average strain of about 0.28, as shown in Figure 6.7 (A_3 and B_3). Two instances of ɣ-M/ferrite interfacial decohesion are shown in Figure 6.7$A_{1\text{-}5}$, each of which initiates at $\varepsilon_{Avg} \approx 0.28$. After nucleating, these voids propagate in shear within the ferrite with increasing strain and not directly along the ɣ-M/ferrite interface, as shown in Figure 6.7$A_{3\text{-}5}$. We also see martensite island cracking transverse to the loading direction as shown in Figure 6.7$B_{1\text{-}5}$ for a ɣ-M island. This is similar to the observations made in a vanadium microalloyed ultrahigh strength DP steel (Pelligra et al., 2022), although in that work martensite cracking initiates at a considerably lower strain of about $\varepsilon_{Avg} \approx 0.11$. In Figure 6.7$B_{3-4}$, at $\varepsilon_{Avg} \leq 0.28$, a void nucleates and grows initially perpendicular within ferrite, but eventually becomes engulfed by micro-shearing of the overall microstructure, as shown in Figure 6.7B_5. The ɣ-M crack, which nucleated at $\varepsilon_{Avg} \approx 0.28$, (Figure 6.7$B_3$), also becomes engulfed by micro-shearing as shown in Figure 6.7B_5. Micro-shear banding in TRIP-assisted steels can be explained by the relatively small mechanical strength difference between phases (Ruggles et al., 2016).

6.4.3.2 Fractured Specimens and EDS analysis

Macroscopically, this med-Mn steel shows cup-cone type ductile fracture with delamination cracks, parallel to the loading direction, ranging from microns (≈400µm in Figure 6.8aB) to millimetres in length (≈1.28mm in Figure 6.8a and aA). This was consistent for all three IA conditions tested. The appearance of this fracture surface is comparable to what was seen in a med-Mn steel with a similar ε_f by Sun et al. (2019). Choi et al. (2017) found that specimens with an increased PUE also resulted in increased in delamination crack lengths, and were, as a result, not deemed harmful to ductility. A significant number of dimples were observed surrounding or arresting delamination cracks (Liu et al., 2018) as shown in Figure 6.8aC. Inclusions, that were present in fracture cross-sections for all three conditions, were analysed using EDS. Figure 6.8b shows the EDS analysis conducted for the 685°C IA condition at various locations, showing that these are primarily MnS inclusions. That for the other conditions are provided in the Appendix C.

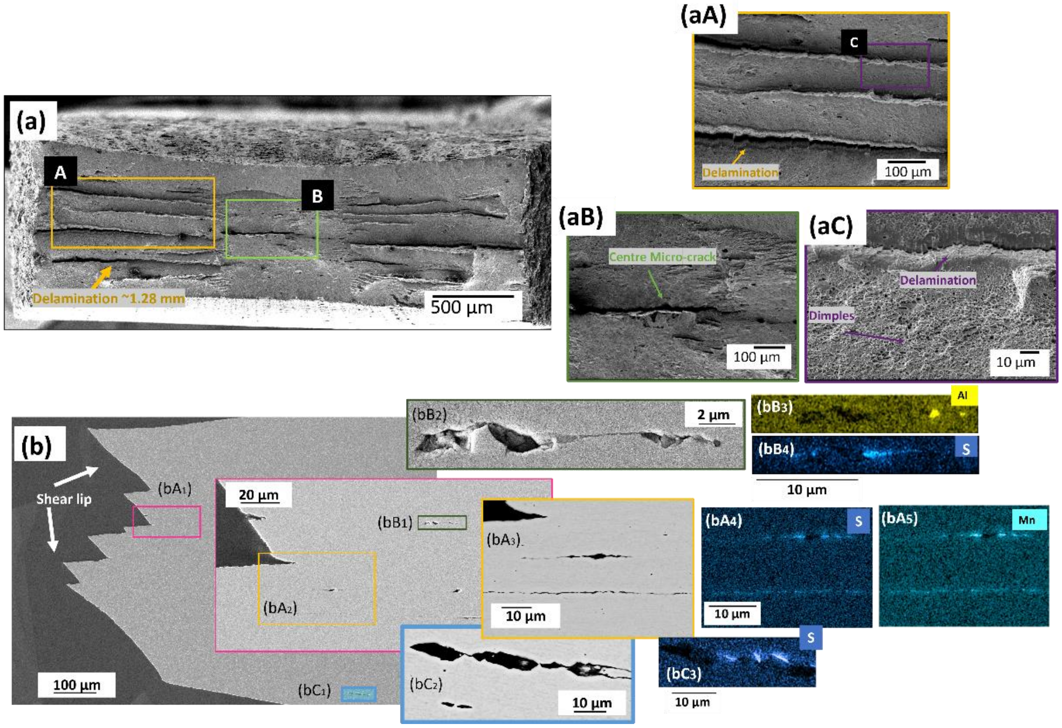

Figure 6.8: Ductile Cup-Cone fracture surface of this med-Mn steel at its 685°C IA condition (a). Evidence of delamination cracks (aA) centreline microcracks (aB) and fine dimples surrounding delamination cracks (aC) of this fracture surface. Cross-section of the fracture surface (b) provides evidence of stringers/inclusions closest to the centre of the fracture Figure 6.8bA$_{1-3}$ and is further detailed using EDS (bA$_{4-5}$). Stringers/inclusions embedded particles Figure 6.8 (bB$_{1-2}$, and bC$_{1-2}$) and EDS mapping of these regions Figure 6.8 (bA$_{4-5}$, and bC$_{3}$).

These inclusions most likely formed during desulfurization or deoxidation in the steelmaking process (Fruehan, 1978). Typically, inclusions are thought to act as void nucleation sites in ductile fracture. Although in most instances this is true, it is key to note the morphology of the inclusion. Figure 6.8bB$_{1,2-4}$ which shows a S-containing inclusion elongated into stingers during rolling. It has embedded Al-containing inclusions with rounded edges within it (Figure 6.8bB$_{3}$). Even though some decohesion of the inclusion/steel interface can be seen in Figure 6.8bB$_{2-3}$ these voids do not seem to affect material ductility, as this decohesion does not propagate to the fracture surface. If these inclusions were cuboid in nature, as shown in the Appendix C, Figure C 6.1 (aA$_{1-5}$), the decohesion and propagation of microcracks is more likely. It is probable that inclusion/steel interface decohesion can initiate at low strains (Choi et al., 2017) but grows very little with increasing strain. The MnS stingers in Figure 6.8b do not contribute directly to fracture but can explain why the steel in the 685°C IA condition has a large void density and low void area fraction long before fracture occurs, as noted in section 6.4.3. Figure 6.8bC$_1$ shows another instance of a S-containing stinger with embedded particles.

6.5 Discussion

For the first time, our study shows that, by carefully managing TRIP kinetics through modest adjustments of IA of med-Mn steels, it is possible to utilize the ɣ-to-martensite volume expansion to suppress damage. This is critical for improving the local forming potential of med-Mn steels with their ability to delay necking through TRIP. The key highlights from the extensive characterization conducted on this med-Mn steel is summarized in section 6.5.1, whereas in section 6.5.2 and 6.5.3 this med-Mn at its deemed optimal IA condition is compared to other 3G steels with and without TRIP-assistance currently under critical investigation. This was done to evaluate the severity of microstrain partitioning of this med-Mn condition and its ability to maintain large strain gradients which is a necessary requirement for local forming.

6.5.1 Summary of an intercritically annealed med-Mn steel

We have shown that the mechanical properties of a med-Mn steel can vary considerably as one modifies the IA conditions over a modest range of temperature from 665°C to 710°C. This occurs without significant variation in microstructure as noted in section 6.4.2. Within this range, an intermediate IA temperature of 685°C provides the optimal condition in that it achieves the highest UTS x TE (28,809MPa%), PUE (0.04)/ε_f (0.61) and extends TRIP to high strains, which in turn, explains this condition's sustained monotonic work hardening. With the use of µXCT, our work shows that this med-Mn steel at its 685°C IA condition showed the largest void density, but the lowest void area fraction at fracture. This ultimately proves that void nucleation is promoted at this condition, but that growth, as a result of the local compressive stresses imposed by the transformation from ɣ-to-martensite, is suppressed even more so than the other two IA temperatures considered. Sources of void nucleation at the 685°C IA condition were ɣ-M cracking, which initiate at ultrahigh strains (i.e. $\varepsilon_{Avg} \approx 0.48$ in Figure 6.6B$_5$), and within ferrite. Furthermore, micro-shearing, featured in microstructures with plastic phase compatibility, engulfed void nucleation within the ferrite. For such reasons, this med-Mn intercritically annealed at 685°C was chosen to compare to other 3G steels, in sections 6.5.2 and 6.5.3.

Moreover, it is important to note that through this research we have experimentally proven that the temperature of optimal TRIP behavior is influenced by the Si content in med-Mn steels. The peakUTS x TE of this med-Mn steel was achieved after IA at 685°C which is 25°C lower than the temperature of which peakUTS x TE properties achieved by Pallisco & McDermid (2020) on a very similar med-Mn steel with only a ~0.3wt% increase in Si. This provides evidence that further work needs to be devoted to understanding the role that Si has on retained austenite stability in med-Mn steels.

6.5.2 Med-Mn steel compared to other 3G Steels

In this section we compare the results on the current med-Mn steel intercritically annealed at 685°C for 120s with another TRIP-assisted, ultrahigh strength 3G steel, in this case QP1500, and with a 3G DP steel without TRIP-assistance, an ultrafine-grained (UFG) DP1300 steel. All three steels have a fine grain size, on average, ≤ 1µm. The chemical and microstructural details of the QP1500 and UFG DP1300 steels have been thoroughly investigated and are reported elsewhere (Pelligra et al., 2022; Samei et al., 2020; Samei, Pelligra, et al., 2019; Zhou, 2018). Table 6.3 compares various mechanical properties of these 3G steels.

Table 6.3: Mechanical Property Comparison between med-Mn, QP1500 and UFG DP1300

	UTS (MPa)	**TE**	**UTSxTE (MPa%)**	**Toughness ($\mathrm{MJ/m^3}$)**	**True Uniform Strain (ε_u)**	**True Strain at Fracture (ε_f)**	$\frac{\varepsilon_f}{\varepsilon_u}$	**F.I.** $\sqrt{\varepsilon_u * \varepsilon_f}$
med-Mn	1067	0.27	28,809	893	0.21	0.61	2.9	0.36
UFG DP1300	1475	0.10	14,750	409	0.08	0.28	3.5	0.15
QP1500	1540	0.14	21,560	1323	0.11	0.60	5.5	0.26

Of these steels only the med-Mn steel closely achieves the proposed 3G mechanical target property envelope (AutoSteel, 2011; Matlock & Speer, 2009). This med-Mn steel shows a ≈3x increase in elongation in comparison to the UFG DP1300 and QP1500 steels compensated by a 400-500 MPa decrease in strength. Despite having significantly different microstructures, the QP1500 and UFG DP1300 steels have similar strengths and true uniform elongations (ε_u), ≈1500MPa and ≈0.1 respectively. They do differ, however, in terms of ε_f and toughness, as detailed elsewhere (Pelligra et al., 2024). The toughness values quoted in Table 6.3 refer to the total area under the true stress-strain curves, as measured using the integral trapezoid method. The UTS x TE product also provides a rough approximation to the toughness; however, it underestimates the actual energy required to produce fracture because the energy absorbed during PUE is significant (Frómeta et al., 2019). The QP1500 steel achieves the highest toughness, while the UFG DP1300 achieves the lowest, and the med-Mn steel shows a toughness ≈2x greater than that of the UFG DP1300 steel. Interestingly, the med-Mn steel has a similar ε_f to that of the QP1500 steel, yet there is a ≈2x increase in ε_u, i.e. a two-fold delay in the onset of necking, of the med-Mn steel in comparison to the QP1500 steel, 0.21 vs 0.11. As shown inAppendix B , Figure B 6.1, these steels show similar TRIP kinetics, however the amount of ɣ in the med-Mn steel is increased by about ~2x compared to the QP1500 steel. Moreover, the shape changes associated with the transformation of ɣ-to-martensite are more easily accommodated by the surrounding polygonal ferrite in the med-Mn steel. The easy identification of GNDs in ferrite as shown in Figure 6.3 supports this. Ultimately, this difference in ε_u explains the variation in their ε_f /ε_u formability ratios and formability indices (F.I.).

The ε_f / ε_u strain ratio is used to predict whether an AHSS is more suited for local forming (i.e. forming instances in which large strain gradients are imposed, such as in bending) or global forming operations (i.e. forming instances in which a large portion of the material is deformed to similar strains, such as deep drawing). The F.I., on the other hand, is an intermediate value between the ε_u and ε_f which *rates* the overall formability, considering both local and global potential of AHSSs (Hance et al., 2013). The ε_f / ε_u strain ratio is less than 5 for the med-Mn steel suggesting that this material performs better in global versus local forming operations. The UFG DP1300 steel is also better suited to global forming operations, whereas the QP1500 steel shows marginally better local formability than the other two steels. Despite the fact that the med-Mn steel has a lower ε_f / ε_u strain ratio, it achieves the best F.I. rating of 'Very Good' whereas the QP1500 and UFG DP1300 steels achieve only 'Good' and 'Fair' F.I. ratings respectively.

6.5.2.1 Microstrain Partitioning

The severity of microstrain partitioning of this med-Mn condition can be evaluated by comparing it to QP1500 and UFG DP1300 steels. To compensate for the different sizes captured during SEM imaging for microstrain mapping, the square facet and step sizes were adjusted such that they exhibited the same sizes in microns, as shown in Table 6.4 for these three steels,. This same methodology was used previously (Pelligra et al., 2024).. The ε_{Avg} is compared to the local average phase strains for each component, ε_{phase}, (i.e. the average von Mises strain of different phases within the area imaged).

Table 6.4 Parameters of the microstrain calculations in GOM Correlate

	med-Mn	**UFG DP1300**	**QP1500**
Represented Area (µm^2)	8.1x6.4	15.4x12.3	8.0x6.4
Resolution (µm/pixel)	0.008	0.006	0.006
Facet × Step size (pixel)	29×9	31×11	29×11
Facet × Step size (µm×µm)	0.2x0.07	0.2×0.07	0.2×0.07

The choice in facet size (0.2µm x 0.2µm) and point distance (0.07µm) was made to obtain a virtual strain gauge of 0.14µm. This enabled the average in-grain strain to be resolved. A set of 3x3 facet squares, 0.46 µm x 0.46µm, is less than the average ferrite grain size (0.61µm) of this med-Mn steel. This DIC post-processing methodology is described in detail by Pelligra et al. (2022, 2024).

In Figure 6.9a, we compare the microstrain partitioning between the hard and the soft phases in each of the three steels. In the case of the two 3G TRIP-assisted steels of interest, this involves the island (ɣ-M) and matrix ferritic and/or TM phases. Both the med-Mn steel and QP1500 steel show improved microstrain (i.e. reduced) partitioning behavior compared to the UFG DP1300 steel because of the improved plastic compatibility between island and matrix phases. With increasing deformation, the strain that can be accommodated by the ɣ-M constituents in the med-Mn steel and QP1500 steels are similar. This is likely related to the fact that both steels show similar rates of TRIP exhaustion, as described in Appendix B, Figure B 6.1. As is expected, the polygonal ferrite-tempered martensite (F-TM) in the med-Mn steel is slightly more deformable than the TM in the QP1500 steel. Out of the two 3G TRIP-assisted steels, only in the med-Mn steel is the impact of ferrite apparent. For example, at an ε_{Avg} = 0.3, the $\varepsilon_{TM,phase}$ = 0.32, while the $\varepsilon_{F\text{-}TM,phase}$ = 0.36. It is important to note that although the strain partitioning between contrasting phases in the med-Mn steel is greater than that of the QP1500 steel, both achieve the same fracture strain.

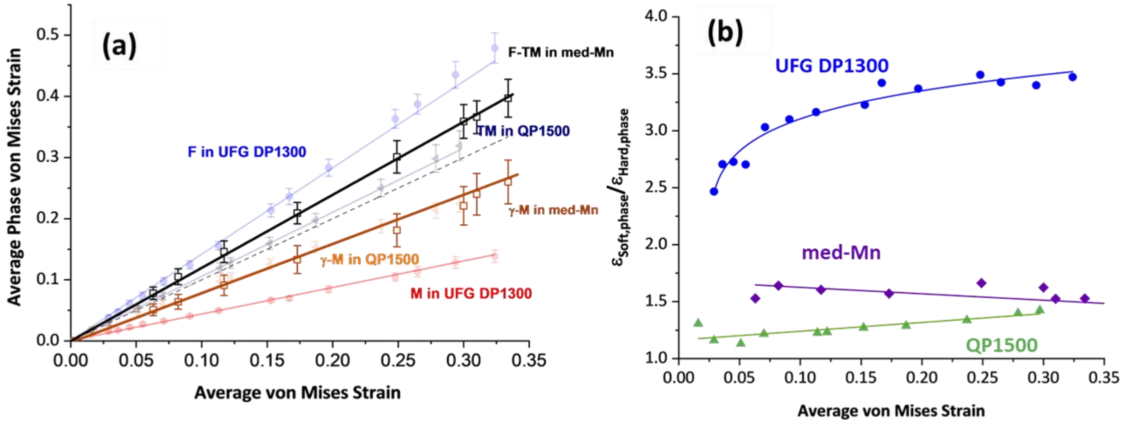

Figure 6.9: The microstrain partitioning between 3G steels by evaluating the Average von Mises strain versus the Average Phase von Mises strain in (a) and the SPIR in (b)

Another method to quantify the degree of microstrain partitioning uses the strain partitioning intensity ratio (SPIR), as shown in Equation 6.1, originally developed by Siemens et al. (2023),and shown in Figure 6.9b.

$$\mathrm{SPIR} = \frac{\varepsilon_{\mathrm{matrix,phase}}}{\varepsilon_{\mathrm{island,phase}}}$$

Equation 6.1: The Strain Partitioning Intensity Ratio (SPIR) formula

For these steels, SPIR is based on the strain ratio between the matrix phase and the island phase. An SPIR value of one suggests that these phases co-deform equally, whereas a SPIR$>$ 1 suggests that the matrix phase accommodates more strain than the island phase. In this instance, the med-Mn steel and QP1500 steel, both have a SPIR $\approx$ 1-1.75. As deformation proceeds, the SPIR decreases in the med-Mn steel at a similar rate to the increase in SPIR of the QP1500 steel. This suggests that the matrix phases (i.e. F-TM) gradually accommodates more or less strain than the island phase(s) (i.e. ɣ-M) with increasing deformation in the QP1500 and med-Mn steel, respectively. Yet, in both instances, the steels exhibit a significant amount of co-deformation. The UFG DP1300 steel shows a roughly two-fold increase in SPIR compared to the med-Mn and QP1500 steel, indicating that the matrix (i.e. ferrite) accommodates most of the strain in this alloy with limited deformation of the island phase (i.e. martensite). The increase in SPIR of this steel can be fitted to a power law with an eventual flattening out of the SPIR at higher strains. Ultimately, an intermediate degree of microstrain partitioning between the matrix and island phase(s) is shown in the med-Mn steel compared to the QP1500 and UFG DP1300 steels.

6.5.2.2 Local Strain Gradients

Similar to our previous work, Pelligra et al. (2024), the local strain gradients (ε’) across interphase boundaries were fitted to a 2-parameter lognormal distribution, in which only positive values are used. Figure 6.10a shows these distributions along with their medians (μ) and standard deviations (σ). It is important to recall that the mention of ε’ here refers to a *collection* of ε’ measurements at dissimilar phase interfaces for these steels.

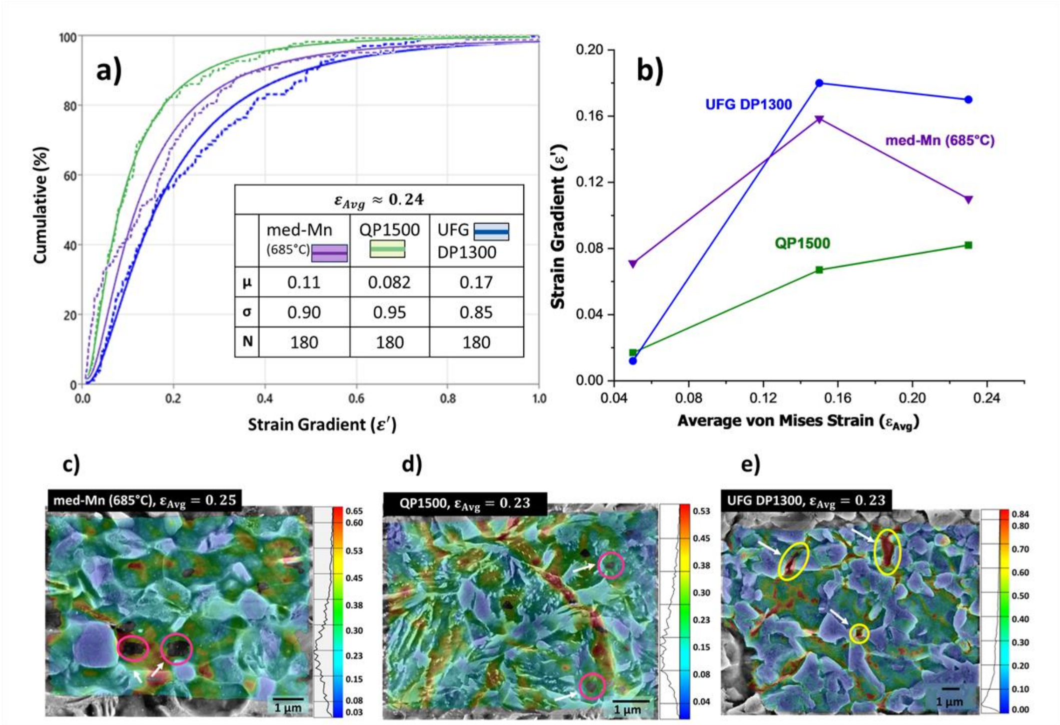

$\varepsilon_{Avg} \approx 0.24$			
	med-Mn (685°C) ▬	QP1500 ▬	UFG DP1300 ▬
μ	0.11	0.082	0.17
σ	0.90	0.95	0.85
N	180	180	180

Figure 6.10: Strain Gradient Comparison between 3G steels, fitted to lognormal distributions (a). The median of the cumulative ε’ values from (a) are plotted as a function of ε_{Avg} in (b). Microstrain maps of the med-Mn, QP1500 and UFG DP1300 steels at an $\varepsilon_{Avg} \approx 0.24$ (c-e). Pink encircled areas in the med-Mn and QP1500 steel in Figure 6.10c and d, signify microstructural evolution which caused poor DIC coverage. On the other hand, yellow encircled areas in the UFG DP1300 steel, in Figure 6.10e, shows instances of damage.

The evolution of the median strain gradient (ε'_M) with increasing ε_{Avg} is greater in the UFG DP1300 than the QP1500 steel. The med-Mn steel, on the other hand, shows an intermediate rate of ε'_M evolution with increasing ε_{Avg} as shown in Figure 6.10 b. This is likely due to the fact that the med-Mn steel has more phases than the QP1500, and therefore more variability in its local strain gradient. Interestingly, despite both being 3G TRIP-assisted steels with similar TRIP kinetics, the ε'_M of the med-Mn steel peaks at a $\varepsilon_{Avg} \approx 0.24$ and then drops, whereas for the QP1500 steel the

ε'_M continues to increase. Multiple studies have indicated that martensite formed via displacive shear can induce a high proportion of screw dislocations (~18%) (Hatem & Zikry, 2011; He et al., 2017; Sandvik & Wayman, 1983). These dislocations are able to move easily through the polygonal ferrite in the med-Mn steel, whereas they are more likely to be pinned by carbides in the TM of the QP1500 steel therefore, increasing dislocation accumulation.

Figure 6.10 (c-e) compares the microstrain maps of the respective steels at an $\varepsilon_{Avg} \approx 0.24$. At this point, damage in the form of martensite cracking (mode I), martensite shearing (mode II) and interfacial cracking is seen in the UFG DP1300 steel (Pelligra et al., 2022). This is due to the fact that the UFG DP1300 steel inhibits dislocation motion *(i.e. the increasing strain gradient cannot be maintained)* even more than the two 3G TRIP assisted steels, eventually resulting in damage nucleation, as shown in Figure 6.10e.

The 3G TRIP-assisted steels, on the other hand, show a significant amount of strain variation in their microstrain maps without any evidence of damage at this high $\varepsilon_{Avg} \approx 0.24$. In this instance, dislocation motion is not being as severely inhibited in the 3G TRIP-assisted steels *(i.e. the ε' are lowered and can be maintained)*. Additionally, it is important to note that there are instances that show uncorrelated regions in their microstrain maps. Aside from damage nucleation, this could be a result of surface topography evolution, slip steps, grain rotations, phase transformations, etc., which cause a large difference in grey scale value, leading to poor DIC correlation in those spots (Oh et al., 2021). The med-Mn steel shows more uncorrelated regions than in the QP1500 steel, as shown in Figure 6.10c and d, respectively. This is consistent with the fact that the F-TM in the med-Mn steel is overall more deformable than the TM in the QP1500 steel, as graphed in Figure 6.9.

6.5.3 Summary of this med-Mn steel compared to other 3G steels

The benefits in TRIP-assistance, as well as the severity of microstrain partitioning in the med-Mn steel has been evaluated by comparing it to another 3G TRIP-assisted steel, QP1500 and 3G non-TRIP-assisted steel, an UFG DP1300 steel. The following conclusions can be made from this comparative study:

- Despite achieving neither the largest strength nor toughness, the significant concentration (30 vol%) of ɣ and the presence of polygonal ferrite in the med-Mn steel enables it to achieve the highest ε_u, and the best F.I. rating, while also being the only one of these steels that sits within the generalized 3G UTS x TEmechanical target envelope.
- Both the med-Mn steel and QP1500 steel achieve the same ε_f, even though the severity of strain partitioning between dissimilar phases is greater in the med-Mn steel. This is due to the presence of polygonal ferrite within the med-Mn steel microstructure, which is more deformable than the TM within the QP1500 steel.
- The med-Mn steel shows an intermediate rate of ε'_M evolution with increasing $\varepsilon_{Avg.}$ At high strains, the UFG DP1300 steel microstructure shows martensite cracking/shearing and interfacial cracking as a result of not being able to maintain the high strain gradient. On the other hand, at this high strain, there is still a significant amount of strain variation in both TRIP-assisted steels. For these steels, the ε' are not as high and dislocation motion is more easily accommodated than in the DP steel. More uncorrelated regions are present in the med-Mn steel versus the QP1500 steel, further suggesting that the polygonal ferrite in the med-Mn steel is deforming to a greater extent than the TM in the QP1500 steel. Furthermore, the decrease in ε'_M at a $\varepsilon_{Avg} > 0.18$ of the med-Mn steel, highlights the ability for dislocations to move easily through the ferrite, whereas their path of motion is hindered by the TM carbides of the QP1500 steel.

6.6 Concluding Remarks and Future Considerations

To conclude, in this paper we have demonstrated that significant variations in mechanical properties can be obtained when intercritically annealing a med-Mn steel (0.15C-5.8Mn-1.8Al-0.71Si) with a martensitic starting microstructure over a tight temperature range of 665°C to 710°C. The novelty of this work arises from the narrow temperature interval we have chosen to vary our IA experiments in the attempt to isolate the impact that IA temperature has on TRIP kinetics and its role on damage development in med-Mn steels. We have demonstrated that an intermediate IA 685°C condition held for 120s, led to a large true strain at fracture ($\varepsilon_f = 0.61$) while also meeting 3G mechanical targets (28,809 MPa%) and sustained monotonic work hardening as a result of its prolonged TRIP during straining. We have also demonstrated that, despite void nucleation being promoted at this IA 685°C condition, its growth is most effectively suppressed by the local compression resulting from the continuous ɣ-to-martensite transformation during straining. Ultimately, this provides evidence that in slowing down TRIP, the rate of damage accumulation is reduced, which enhances the local formability of such 3G steels.

In addition, we have provided a thorough comparison between two TRIP-assisted steels and a non-TRIP-assisted steel (UFG DP1300) to deduce the contribution of TRIP to 3G microstructures, with ferrite (med-Mn steel) and without (QP1500 steel). With the use of a new post µDIC data processing technique, we have been able to show that TRIP provides an advantage in 3G steels by exhibiting on average lower strain gradients at dissimilar phase interfaces with increasing average strain. Furthermore, the dislocation motion arising from the local strain gradient evolving at dissimilar phase interfaces is more easily accommodated in the med-Mn steel as a result of it containing polygonal ferrite, whereas the TM carbides within the QP1500 steel impede dislocation motion. This explains the heightened macro local forming capacity of this med-Mn steel compared to the QP1500 steel.

Although we have extensively documented the ability for TRIP, when carefully managed, to suppress damage in 3G med-Mn steel microstructures, the rate of TRIP can vary substantially with more complex straining conditions. Extensive studies have been performed to understand TRIP kinetics as a function of strain rate, deformation mode, etc. on austenitic stainless steels (AUSs), but no studies have been similarly conducted on 3G TRIP-assisted steels. Moreover, the concepts learned in studying the effect that complex straining has on TRIP in AUSs is not completely transferrable to 3G TRIP steels as they can possess much wider stacking fault range. We therefore suggest future research be devoted to understanding the local forming behavior of 3G TRIP-assisted steels when subjected to more complex straining conditions, such as shear, plane-strain tension, balanced-biaxial tension, etc. The microscopic techniques we have presented here to investigate microstrain partitioning amongst phases, strain gradient evolution and damage development can also be applied to evaluating the effect that TRIP has on damage in 3G steels deformed at comparable complex conditions to automotive forming applications.

6.7 Acknowledgements

The authors would like to acknowledge the financial support of NSERC (grant CRDJ522309-17) and International Zinc Association (IZA)-Galvanizing Association Partnership (GAP) members. US steel R&D is gratefully acknowledged for their in-kind fabrication of this prototype med-Mn steel. We acknowledge the many fruitful discussions with Dr. Joseph R. McDermid concerning this project. The authors would like to thank Ivar Smets for the EDS analysis of cross-sectioned fracture surfaces. The authors would also like to acknowledge the Canadian Centre for Electron Microscopy's (CCEM) Xiang Wang for TEM sample electropolishing preparation as well as carbide extraction replica results and Sabaa Rashid for FIB TEM lift-outs. The authors would also like to acknowledge Advanced Photon Source (APS) beamline scientists, Dr. Andrey Andreevich Yackovenko and Dr. Tyra Chenice Douglas as well as Nizia Mendes Fonseca and Cal Siemens (McMaster University) for their technical support. Use of the APS was supported by the U. S. DoE, Office of Science, Office of Basic Energy Sciences, under Contract No. DE-AC02-06CH11357.

6.8 References

Abu-Farha, F., Hu, X., Sun, X., Ren, Y., Hector, L. G., Thomas, G., & Brown, T. W. (2018). In Situ Local Measurement of Austenite Mechanical Stability and Transformation Behavior in Third-Generation Advanced High-Strength Steels. *Metallurgical and Materials Transactions A: Physical Metallurgy and Materials Science*, *49*(7), 2583–2596. https://doi.org/10.1007/s11661-018-4660-x

Arlazarov, A., Gouné, M., Bouaziz, O., Hazotte, A., Petitgand, G., & Barges, P. (2012). Evolution of microstructure and mechanical properties of medium Mn steels during double annealing. *Materials Science and Engineering A*, *542*, 31–39. https://doi.org/10.1016/j.msea.2012.02.024

ASTM E8M-Standard Test Methods for Tension Testing of Metallic Materials. (2021). Asm International.

AutoSteel, W. (2011). *Future Steel Vehicle overview report 2011*. www.autosteel.org

Avramovic-Cingara, G., Saleh, C. A. R., Jain, M. K., & Wilkinson, D. S. (2009). Void nucleation and growth in dual-phase steel 600 during uniaxial tensile testing. *Metallurgical and Materials Transactions A: Physical Metallurgy and Materials Science*, *40*(13), 3117–3127. https://doi.org/10.1007/s11661-009-0030-z

Bai, M., Yang, D., Wang, G., Ryu, J., Lee, K., & Yi, H. (2020). Enhancing the robustness and efficiency in the production of medium Mn steels by Al addition. *Metals*, *10*(11), 1–19. https://doi.org/10.3390/met10111432

Bao, Y., & Wierzbicki, T. (2004). On fracture locus in the equivalent strain and stress triaxiality space. *International Journal of Mechanical Sciences*, *46*(1), 81–98. https://doi.org/10.1016/j.ijmecsci.2004.02.006

Barella, S., Gruttadauria, A., Menezes, J. T. O., Castrodeza, E. M., Quaini, S. E., Pelligra, C., & McNally, E. A. (2023). The Reliability of Single-Step and Double-Step Quench and Partitioning Heat Treatments on an AISI 420A Low Carbon Martensitic Stainless Steel. *Metallurgical and Materials Transactions A*. https://doi.org/10.1007/s11661-023-07145-2

Bellhouse, E. M. (2010). *GALVANIZING OF AL-SI TRIP-ASSISTED STEELS*. McMaster University.

Bhadhon, K. M. H., McDermid, J. R., Wang, X., McNally, E. A., & Goodwin, F. E. (2017). Fine-Scale Microstructure Characterization And Mechanical Properties Of CGL-Compatible Heat Treated Medium-Mn TRIP Steel. *Proceedings of Galvatech 2017*, 493–500.

Bhadhon, K. M. H., Wang, X., & McDermid, J. R. (2022). Effects of CGL-compatible thermal processing, starting microstructure, and Sn micro-alloying on the mechanical properties of a medium-Mn third generation advanced high strength steel. *Materials Science and Engineering A*, *833*. https://doi.org/10.1016/j.msea.2021.142563

Buffière, J.-Y., Maire, E., Cloetens, P., Lormand, G., & Fougères, R. (1999). Characterization of internal damage in a MMCp using X-ray synchrotron phase contrast microtomography. *Acta Materialia*, *47*(5), 1613–1625. https://doi.org/10.1016/S1359-6454(99)00024-5

Cao, W. Q., Wang, C., Shi, J., Wang, M. Q., Hui, W. J., & Dong, H. (2011). Microstructure and mechanical properties of Fe-0.2C-5Mn steel processed by ART-annealing. *Materials Science and Engineering A*, *528*(22–23), 6661–6666. https://doi.org/10.1016/j.msea.2011.05.039

Choi, H., Lee, S., Lee, J., Barlat, F., & De Cooman, B. C. (2017). Characterization of fracture in medium Mn steel. *Materials Science and Engineering: A*, *687*, 200–210. https://doi.org/10.1016/j.msea.2017.01.055

Courtney, T. H. (2005). *Mechanical Behavior of Materials* (2nd ed.). Waveland Press, Inc.

Datsko, J., & Yang, C. T. (1960). Correlation of Bendability of Materials With Their Tensile Properties. *Journal of Engineering for Industry*, 309–313.

De, A. K., Speer, J. G., & Matlock, D. K. (2003). Color tint-etching for multiphase steels. *Advanced Materials and Processes*, *161*(2), 27–30.

De Moor, E., Gibbs, P. J., Speer, J. G., & Matlock, D. K. (2010). Strategies for Third-Generation Advanced High Strength Steel Development. *Iron and Steel Technology*, *7*(11), 133–144.

Ding, R., Zhang, C., Wang, Y., Liu, C., Yao, Y., Zhang, J., Yang, Z., Zhang, C., Liu, Y., & Chen, H. (2023). Mechanistic role of Mn heterogeneity in austenite decomposition and stabilization in a commercial quenching and partitioning steel. *Acta Materialia*, *250*. https://doi.org/10.1016/j.actamat.2023.118869

Dumay, A., Chateau, J. P., Allain, S., Migot, S., & Bouaziz, O. (2008). Influence of addition elements on the stacking-fault energy and mechanical properties of an austenitic Fe-Mn-C steel. *Materials Science and Engineering: A*, *483–484*(1-2 C), 184–187. https://doi.org/10.1016/j.msea.2006.12.170

Dutta, A., Ponge, D., Sandlöbes, S., & Raabe, D. (2019). Strain partitioning and strain localization in medium manganese steels measured by in situ microscopic digital image correlation. *Materialia*, *5*. https://doi.org/10.1016/j.mtla.2019.100252

DYSON DJ, & HOLMES B. (1970). Effect of Alloying Additions on the Lattice Parameter of Austenite. *J Iron Steel Inst (London)*, *208*(pt 5), 469–474.

El-Naaman, S. A., Nielsen, K. L., & Niordson, C. F. (2016). On modeling micro-structural evolution using a higher order strain gradient continuum theory. *International Journal of Plasticity*, *76*, 285–298. https://doi.org/10.1016/j.ijplas.2015.08.008

Fonstein, N. (2015). Advanced high strength sheet steels: Physical metallurgy, design, processing, and properties. In *Advanced High Strength Sheet Steels: Physical Metallurgy, Design, Processing, and Properties* (1st ed.). Springer. https://doi.org/10.1007/978-3-319-19165-2

Frómeta, D., Lara, A., Grifé, L., Dieudonné, T., Dietsch, P., Rehrl, J., Suppan, C., Casellas, D., & Calvo, J. (2021). Fracture Resistance of Advanced High-Strength Steel Sheets for Automotive Applications. *Metallurgical and Materials Transactions A: Physical Metallurgy and Materials Science*, *52*(2), 840–856. https://doi.org/10.1007/s11661-020-06119-y

Frómeta, D., Lara, A., Molas, S., Casellas, D., Rehrl, J., Suppan, C., Larour, P., & Calvo, J. (2019). On the correlation between fracture toughness and crash resistance of advanced high strength steels. *Engineering Fracture Mechanics*, *205*, 319–332. https://doi.org/10.1016/j.engfracmech.2018.10.005

Frómeta, D., Tedesco, M., Calvo, J., Lara, A., Molas, S., & Casellas, D. (2017). Assessing edge cracking resistance in AHSS automotive parts by the Essential Work of Fracture methodology. *Journal of Physics: Conference Series*, *896*, 012102. https://doi.org/10.1088/1742-6596/896/1/012102

Fruehan, R. J. (1978). Desulfurization of liquid steel containing aluminum or silicon with lime. *Metallurgical Transactions B*, *9*(2), 287–292. https://doi.org/10.1007/BF02653694

gom. (2016). GOM Correlate. In *Gom.Com*. http://www.gom.com/3d-software/gom-correlate.html

Hance, B. (2016). Advanced high strength steel: Deciphering local and global formability. *International Automotive Body Congress, IABC 2016 DEARBORN - Papers*.

Hance, B. (2018). Advanced High-Strength Steel (AHSS) Performance Level Definitions and Targets. *SAE International Journal of Materials and Manufacturing*, *11*(4), 2018-01–0629. https://doi.org/10.4271/2018-01-0629

Hance, B. M., Comstock, R. J., & Scherrer, D. K. (2013). The influence of edge preparation method on the hole expansion performance of automotive sheet steels. *SAE Technical Papers*, *2*. https://doi.org/10.4271/2013-01-1167

Hatem, T. M., & Zikry, M. A. (2011). A model for determining initial dislocation-densities associated with martensitic transformations. *Materials Science and Technology*, *27*(10), 1570–1573. https://doi.org/10.1179/1743284711Y.0000000079

He, B. B., Hu, B., Yen, H. W., Cheng, G. J., Wang, Z. K., Luo, H. W., & Huang, M. X. (2017). High dislocation density–induced large ductility in deformed and partitioned steels. *Science*, *357*(6355), 1029–1032. https://doi.org/10.1126/science.aan0177

He, B. B., Wang, M., & Huang, M. X. (2019). Resetting the Austenite Stability in a Medium Mn Steel via Dislocation Engineering. *Metallurgical and Materials Transactions A*, *50*(6), 2971–2977. https://doi.org/10.1007/s11661-019-05222-z

Hofmann, H., Mattissen, D., & Schaumann, T. W. (2006). Advanced cold rolled steels for automotive applications. *Materialwissenschaft Und Werkstofftechnik*, *37*(9), 716–723. https://doi.org/10.1002/mawe.200600057

Hornbogen, E. (1978). Martensitic transformation at a propagating crack. *Acta Metallurgica*, *26*(1), 147–152. https://doi.org/10.1016/0001-6160(78)90211-0

Horvath, C. D., Enloe, C. M., Singh, J. P., & Coryell, J. J. (2017). Persistent challenges to advanced high-strength steel implementation. *International Symposium on New Developments in Advanced High-Strength Sheet Steels*, 1–10.

Huang, C. X., Wang, Y. F., Ma, X. L., Yin, S., Höppel, H. W., Göken, M., Wu, X. L., Gao, H. J., & Zhu, Y. T. (2018). Interface affected zone for optimal strength and ductility in heterogeneous laminate. *Materials Today*, *21*(7), 713–719. https://doi.org/10.1016/j.mattod.2018.03.006

Hutten, E., Liang, S., Bellhouse, E., Sarkar, S., Lu, Y., Langelier, B., & Zurob, H. S. (2021). Mechanical properties and precipitation behavior of high strength hot-rolled ferritic steel containing Nb and V. *Journal of Materials Research and Technology*, *14*, 2061–2070. https://doi.org/10.1016/j.jmrt.2021.07.107

Jacques, P., Furnemount, Q., Pardoen, T., & Delannay, F. (2001). On the Role of Martensitic Transformation on Damage and Cracking Resistance in Trip-assisted multiphase steels. *Acta Materialia*, *49*(1), 139–152. https://doi.org/10.1016/S1359-6454(00)00215-9

Jacques, P. J. (2004). Transformation-induced plasticity for high strength formable steels. *Current Opinion in Solid State and Materials Science*, *8*(3–4), 259–265. https://doi.org/10.1016/j.cossms.2004.09.006

Jacques, P. J., Allain, S., Bouaziz, O., De, A., Gourgues, A.-F., Hance, B. M., Houbaert, Y., Huang, J., Iza-Mendia, A., Kruger, S. E., Radu, M., Samek, L., Speer, J., Zhao, L., & van der Zwaag, S. (2009). On measurement of retained austenite in multiphase TRIP steels — results of blind round robin test involving six different techniques. *Materials Science and Technology*, *25*(5), 567–574. https://doi.org/10.1179/174328408X353723

Kang, J., Ososkov, Y., Embury, J. D., & Wilkinson, D. S. (2007). Digital image correlation studies for microscopic strain distribution and damage in dual phase steels. *Scripta Materialia*, *56*(11), 999–1002. https://doi.org/10.1016/J.SCRIPTAMAT.2007.01.031

Kang, J., Pottore, N. S., Zhu, H., & Tasan, C. C. (2023). An in situ investigation of neighborhood effects in a ferrite-containing quenching and partitioning steel: Mechanical stability, strain partitioning, and damage. *Acta Materialia*, *254*. https://doi.org/10.1016/j.actamat.2023.118985

Kang, J., Wilkinson, D. S., Embury, J. D., & Jain, M. (2005). Microscopic Strain Mapping Using Scanning Electron Microscopy Topography Image Correlation at Large Strain. *The Journal of Strain Analysis for Engineering Design*, *40*(6), 559–570. https://doi.org/10.1243/030932405X16151

Kickinger, C., Suppan, C., Hebesberger, T., Schnitzer, R., & Hofer, C. (2021). Microstructure and mechanical properties of partially ferritic Q&P steels. *Materials Science and Engineering A*, *815*. https://doi.org/10.1016/j.msea.2021.141296

Kozłowska, A., Janik, A., Radwański, K., & Grajcar, A. (2019). Microstructure Evolution and Mechanical Stability of Retained Austenite in Medium-Mn Steel Deformed at Different Temperatures. *Materials*, *12*(18), 3042. https://doi.org/10.3390/ma12183042

Lee, S., Lee, S. J., & De Cooman, B. C. (2012). Reply to comments on "Austenite stability of ultrafine-grained transformation-induced plasticity steel with Mn partitioning." *Scripta Materialia*, *66*(10), 832–833. https://doi.org/10.1016/J.SCRIPTAMAT.2012.02.018

Lee, Y. K., & Choi, C. S. (2000). Driving force for γ → ε martensitic transformation and stacking fault energy of γ in Fe-Mn binary system. *Metallurgical and Materials Transactions A: Physical Metallurgy and Materials Science*, *31*(2), 355–360. https://doi.org/10.1007/s11661-000-0271-3

Li, J., Lu, W., Chen, S., & Liu, C. (2020). Revealing extra strengthening and strain hardening in heterogeneous two-phase nanostructures. *International Journal of Plasticity*, *126*. https://doi.org/10.1016/j.ijplas.2019.11.005

Li, Z., Kiran, R., Hu, J., Hector, L. G., & Bower, A. F. (2020). Analysis and design of a three-phase TRIP steel microstructure for enhanced fracture resistance. *International Journal of Fracture*, *221*(1), 53–85. https://doi.org/10.1007/S10704-019-00405-6/FIGURES/15

Liu, C., Peng, Q., Xue, Z., Wang, S., & Yang, C. (2018). *Microstructure and Mechanical Properties of Hot-Rolled and Cold-Rolled Medium-Mn TRIP Steels*. https://doi.org/10.3390/ma11112242

Liu, J., Chen, C., Feng, Q., Fang, X., Wang, H., Liu, F., Lu, J., & Raabe, D. (2017). Dislocation activities at the martensite phase transformation interface in metastable austenitic stainless steel: An in-situ TEM study. In *Materials Science and Engineering A* (Vol. 703). https://doi.org/10.1016/j.msea.2017.06.107

Luo, H., & Dong, H. (2015). New ultrahigh-strength Mn-alloyed TRIP steels with improved formability manufactured by intercritical annealing. *Materials Science and Engineering: A*, *626*, 207–212. https://doi.org/10.1016/j.msea.2014.12.049

Matlock, D. K., & Speer, J. G. (2009). Third Generation of AHSS: Microstructure Design Concepts. In *Microstructure and Texture in Steels* (pp. 185–205). Springer London. https://doi.org/10.1007/978-1-84882-454-6_11

Mehrabi, A., McDermid, J. R., Wang, X., & Zurob, H. (2023). Austenite Nucleation and Growth as a Function of Starting Microstructure for a Fe–0.15C–5.56Mn–1.1Si–1.89Al Medium-Mn Steel. *Steel Research International*. https://doi.org/10.1002/srin.202200952

Mola, J., & De Cooman, B. C. (2013). Quenching and partitioning (Q&P) processing of martensitic stainless steels. *Metallurgical and Materials Transactions A: Physical Metallurgy and Materials Science*, *44*(2), 946–967. https://doi.org/10.1007/s11661-012-1420-1

Nan, C.-W., & Clarke, D. R. (1996). The Influence of Particle Size and Particle Fracture on the Elastic/Plastic Deformation of Metal Matrix Composites. *Acta Materialia*, *44*(9), 3801–3811.

Oh, H. S., Biggs, K., Güvenç, O., Ghassemi-Armaki, H., Pottore, N., & Tasan, C. C. (2021). In-situ investigation of strain partitioning and microstructural strain path development up to and beyond necking. *Acta Materialia*, *215*. https://doi.org/10.1016/j.actamat.2021.117023

Oh, H. S., Kang, J., Jiang, M., & Tasan, C. C. (2024). Role of the nanoscale austenite in micro-strain heterogeneity in PH17-4 martensitic stainless steels. *Materials Science and Engineering: A*, *895*, 146122. https://doi.org/10.1016/j.msea.2024.146122

Pallisco, D. M. (2021). *Galvanizing of Medium-Mn Advanced High Strength Steel*.

Pallisco, D. M., & McDermid, J. R. (2020). Mechanical property development of a 0.15C–6Mn–2Al–1Si third-generation advanced high strength steel using continuous galvanizing heat treatments. *Materials Science and Engineering A*, *778*, 139111. https://doi.org/10.1016/j.msea.2020.139111

Pallisco, D. M., McDermid, J. R., McNally, E. A., & Goodwin Frank E. (2017). Effect of Starting Microstructure and Intercritical Annealing Parameters on the Mechanical Property Development of a Medium-Mn Third-Generation Advanced High Strength Steel. *Galvatech*, 782–789. https://www.researchgate.net/publication/321097802

Park, T., Hector Jr., L. G., Hu, X., Abu-Farha, F., Fellinger, M. R., Kim, H., Esmaeilpour, R., & Pourboghrat, F. (2019). Crystal plasticity modeling of 3rd generation multi-phase AHSS with martensitic transformation. *International Journal of Plasticity* , *120*, 1–46.

Patel, V. (2019). *Microstructure and Mechanical Properties of Medium Mn steel*. McMaster University.

Pelligra, C., Samei, J., Kang, J., & Wilkinson, D. S. (2022). The effect of vanadium on microstrain partitioning and localized damage during deformation of unnotched and notched DP1300 steels. *International Journal of Plasticity*, *158*. https://doi.org/10.1016/j.ijplas.2022.103435

Pelligra, C., Samei, J., Shalchi Amirkhiz, B., Hector, L. G., & Wilkinson, D. S. (2024). Microstrain partitioning, transformation induced plasticity, and the evolution of damage during deformation of an austenitic-martensitic 1.5 GPa quench and partition steel. *Materials Science and Engineering: A*, 146181. https://doi.org/10.1016/j.msea.2024.146181

Ruggles, T., Cluff, S., Miles, M., Fullwood, D., Daniels, C., Avila, A., & Chen, M. (2016). Ductility of Advanced High-Strength Steel in the Presence of a Sheared Edge. *JOM*, *68*(7), 1839–1849. https://doi.org/10.1007/s11837-016-1927-9

Ruggles, T. J., & Fullwood, D. T. (2013). Estimations of bulk geometrically necessary dislocation density using high resolution EBSD. *Ultramicroscopy*, *133*, 8–15. https://doi.org/10.1016/j.ultramic.2013.04.011

Ruhl, R., & Cohen, M. (1969). Splat Quenching of Iron-Carbon Alloys. *Transactions of The Metallurgical Society of AIME*, *245*, 241.

Salehiyan, D. (2018). *Microstrain Partitioning and Damage in a QP980 Steel* [Master of Science]. McMaster University.

Salehiyan, D., Samei, J., Amirkhiz, B. S., Hector, L. G., & Wilkinson, D. S. (2020). Microstructural Evolution During Deformation of a QP980 Steel. *Metallurgical and Materials Transactions A: Physical Metallurgy and Materials Science*, *51*(9), 4524–4539. https://doi.org/10.1007/s11661-020-05882-2

Salvo, L., Cloetens, P., Maire, E., Zabler, S., Blandin, J. J., Buffière, J. Y., Ludwig, W., Boller, E., Bellet, D., & Josserond, C. (2003). X-ray micro-tomography an attractive characterisation technique in materials science. *Nuclear Instruments and Methods in Physics Research Section B: Beam Interactions with Materials and Atoms*, *200*, 273–286. https://doi.org/10.1016/S0168-583X(02)01689-0

Samei, J., Pelligra, C., Amirmaleki, M., & Wilkinson, D. S. (2020). Microstructural design for damage tolerance in high strength steels. *Materials Letters*, *269*. https://doi.org/10.1016/j.matlet.2020.127664

Samei, J., Pelligra, C., Amirmaleki, M., Zhou, L., Salehiyan, D., Kang, J., & Wilkinson, D. S. (2019). On the Influence of Grain Refinement and Transformation Induced Plasticity on Damage and Ductility in High Strength Steels. *Scripta Materialia*.

Samei, J., Zhou, L., Kang, J., & Wilkinson, D. S. (2018). Microstructural analysis of ductility and fracture in fine-grained and ultrafine-grained vanadium-added DP1300 steels. *International Journal of Plasticity*, *117*(November 2017), 58–70. https://doi.org/10.1016/j.ijplas.2017.12.009

Samei, J., Zhou, L., Kang, J., & Wilkinson, D. S. (2019). Microstructural analysis of ductility and fracture in fine-grained and ultrafine-grained vanadium-added DP1300 steels. *International Journal of Plasticity*, *117*, 58–70. https://doi.org/10.1016/j.ijplas.2017.12.009

Sandvik, B. P. J., & Wayman, C. M. (1983). CHARACTERISTICS OF LATH MARTENSITE: PART I. CRYSTALLOGRAPHIC AND SUBSTRUCTURAL FEATURES. *Metallurgical Transactions. A, Physical Metallurgy and Materials Science*, *14 A*(4), 809 – 822. https://doi.org/10.1007/bf02644284

Shi, J., Sun, X., Wang, M., Hui, W., Dong, H., & Cao, W. (2010). Enhanced work-hardening behavior and mechanical properties in ultrafine-grained steels with large-fractioned metastable austenite. *Scripta Materialia*, *63*(8), 815–818. https://doi.org/10.1016/j.scriptamat.2010.06.023

Siemens, C., Kang, J., & Wilkinson, D. S. (2023). In-situ investigation of damage mechanisms in duplex AlCoCrFeNi2.1 high entropy alloy. *Materials Science and Engineering: A*, *884*. https://doi.org/10.1016/j.msea.2023.145532

Sugimoto, K. I., Kobayashi, M., & Hashimoto, S. I. (1992). Ductility and strain-induced transformation in a high-strength transformation-induced plasticity-aided dual-phase steel. *Metallurgical Transactions. A, Physical Metallurgy and Materials Science*, *23 A*(11), 3085–3091. https://doi.org/10.1007/BF02646127

Sun, B., Palanisamy, D., Ponge, D., Gault, B., Fazeli, F., Scott, C., Yue, S., & Raabe, D. (2019). Revealing fracture mechanisms of medium manganese steels with and without delta-ferrite. *Acta Materialia*, *164*, 683–696. https://doi.org/10.1016/J.ACTAMAT.2018.11.029

Talebi, S. H., Jahazi, M., & Melkonyan, H. (2018). Retained austenite decomposition and carbide precipitation during isothermal tempering of a medium-carbon low-alloy bainitic steel. *Materials*, *11*(8). https://doi.org/10.3390/ma11081441

THOMASON P. F. (1968). A Theory for Ductile Fracture by Internal Necking of Cavities. *J. Inst. Met.*, *96*, 360–365. https://cir.nii.ac.jp/crid/1570291224538224640.bib?lang=en

Toda, H., Tsuruta, H., Horikawa, K., Uesugi, K., Takeuchi, A., Suzuki, Y., & Kobayash, M. (2014). Effects of stress triaxiality on damage evolution from pre-existing hydrogen pores in aluminum alloy. *Materials Transactions*, *55*(2), 383–386. https://doi.org/10.2320/matertrans.L-M2013841

Toji, Y., Matsuda, H., Herbig, M., Choi, P. P., & Raabe, D. (2014). Atomic-scale analysis of carbon partitioning between martensite and austenite by atom probe tomography and correlative transmission electron microscopy. *Acta Materialia*, *65*(65), 215–228. https://doi.org/10.1016/j.actamat.2013.10.064

Van Beers, P. R. M., McShane, G. J., Kouznetsova, V. G., & Geers, M. G. D. (2013). Grain boundary interface mechanics in strain gradient crystal plasticity. *Journal of the Mechanics and Physics of Solids*, *61*(12), 2659–2679. https://doi.org/10.1016/j.jmps.2013.08.011

Wang, M.-M., Hell, J.-C., & Tasan, C. C. (2017). Martensite size effects on damage in quenching and partitioning steels. *Scripta Materialia*, *138*, 1–5. https://doi.org/10.1016/j.scriptamat.2017.05.021

Weck, A. G. (2007). The Role of Coalescence on Ductile Fracture. *PhD-Thesis*, *Ph.D.*(March), 291. http://search.proquest.com/docview/304819833?accountid=14701

Westphal, M., McDermid, J. R., Boyd, J. D., & Embury, J. D. (2010). Novel thermal processing of dual phase steels: II - Work hardening and fracture mechanisms. *Canadian Metallurgical Quarterly*, *49*(1), 91–98. https://doi.org/10.1179/cmq.2010.49.1.91

Wong, S. L., Madivala, M., Prahl, U., Roters, F., & Raabe, D. (2016). A crystal plasticity model for twinning- and transformation-induced plasticity. *Acta Materialia*. https://doi.org/10.1016/j.actamat.2016.07.032

Wu, X., Yang, M., Yuan, F., Wu, G., Wei, Y., Huang, X., & Zhu, Y. (2015). Heterogeneous lamella structure unites ultrafine-grain strength with coarse-grain ductility. *Proceedings of the National Academy of Sciences*, *112*(47), 14501–14505. https://doi.org/10.1073/pnas.1517193112

Xiong, X. C., Chen, B., Huang, M. X., Wang, J. F., & Wang, L. (2013). The effect of morphology on the stability of retained austenite in a quenched and partitioned steel. *Scripta Materialia*, *68*(5), 321–324. https://doi.org/10.1016/J.SCRIPTAMAT.2012.11.003

Yalçinkaya, T., Güngör, G. Ö., Çakmak, S. O., & Tekoğlu, C. (2019). A Micromechanics Based Numerical Investigation of Dual Phase Steels. *Procedia Structural Integrity*, *21*, 61–72. https://doi.org/10.1016/j.prostr.2019.12.087

Yan, D., Tasan, C. C., & Raabe, D. (2015). High resolution in situ mapping of microstrain and microstructure evolution reveals damage resistance criteria in dual phase steels. *Acta Materialia*, *96*, 399–409. https://doi.org/10.1016/j.actamat.2015.05.038

Zhang, X., Yan, J., Liu, T., Liu, H., Shi, Y., Zhou, Q., Zhao, L., & Lv, Z. (2021). Microstructural evolution and mechanical behavior of a novel heterogeneous medium Mn cold-rolled steel. *Materials Science and Engineering: A*, *800*, 140344. https://doi.org/10.1016/j.msea.2020.140344

Zhao, H. S., Zhu, X., Li, W., Jin, X. J., Wang, L., Jiao, H., & Jiang, D. M. (2014). Austenite stability for quenching and partitioning treated steel revealed by colour tint-etching method. *Materials Science and Technology (United Kingdom)*, *30*(9), 1008–1013. https://doi.org/10.1179/1743284714Y.0000000517

Zhou, L. (2018). *Effect of Vanadium on Fracture of DP1300 Steels* [Master of Science]. McMaster University.

6.9 Appendices

6.9.1 Appendix A: TEM Analysis of med-Mn in its 665°C and 710°C IA conditions

Similar to the TEM analysis performed in section 6.4.2.1, before SAED indexing, EDS was used to preliminarily target lath-type ɣ or ɣ-M (Mn-enriched) versus polygonal ferrite (Mn-weak) areas. Figure A 6.1 refers to the TEM analysis performed on this 665°C IA condition. The EDS map in Figure A 6.1a is a representative area of the med-Mn 665°C IA condition's microstructure. Grains A-C labelled in Figure A 6.1a were chosen for further SAED indexing and DF imaging.

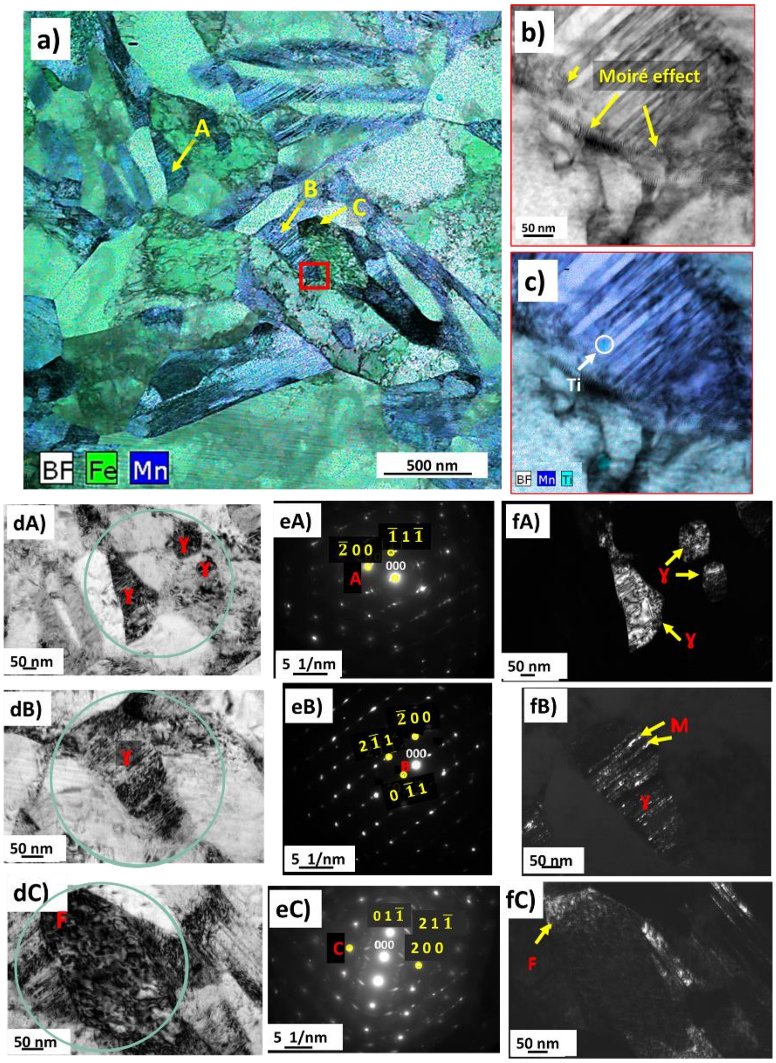

Figure A 6.1: Representative EDS map of this med-Mn in the 665°C IA condition to target Mn-enriched and -poor regions (a). Grains A-C were chosen for further analysis. High magnification BF TEM image (b) and EDS map (c) is of the red-squared region in the EDS map in(a). The BF image, SAED pattern and DF image, (dA, eA, fA), respectively is of Grain A with the indexed [0 1 1]ɣ zone axis. The BF image, SAED pattern and DF image, (dB, eB, fB), respectively is of Grain B with the indexed [0 1 1] BCT zone axis. The BF image, SAED pattern and DF image, (dC, eC, fC), respectively is of Grain C with the indexed [0 1 1] BCC zone axis.

Figure A 6.1b and c, is a high magnification STEM image and EDS map, respectively, of the red-squared-area in Figure A 6.1a. The Moire Effect present at ɣ-M/F grain boundaries in Figure A 6.1b could indicate the presence of GNDs whereas Figure A 6.1c confirms the local segregation of Mn at dissimilar phases and observed Ti precipitates. Grain A from Figure A 6.1a and dA, is Mn-enriched. The SAED pattern in Figure A 6.1eA is obtained from the encircled region in the BF image of Figure A 6.1dA, with a [0 1 1]ɣ zone axis. The DF image from spot A belongs to the ($\bar{2}$00) FCC reflection and shows block-like ɣ. Grain B from Figure A 6.1a and dB, is also Mn-enriched. The SAED pattern, in Figure A 6.1eB, is obtained from the encircled region in the BF image of Figure A 6.1dB, with a [011]BCT zone axis which represents martensite. The DF image from Spot B which belongs to the (0 $\bar{1}$ 1) BCT reflection shows a ɣ island which has very slightly transformed to martensite (i.e. bright regions pointed out in the DF image in Figure A 6.1fB. The ɣ grains, in Figure A 6.1 fA and fB, are globular with ≈95-100nm in equivalent diameter. On the other hand, Grain C pointed out in Figure A 6.1a and then again in Figure A 6.1dC is low in Mn. The SAED pattern in Figure A 6.1eC is obtained from the encircled region in the BF image of Figure A 6.1dC, with a [0 1 1] BCC zone axis. The DF image in Figure A 6.1fC from Spot C which belongs to the ($\bar{2}$ 0 0) BCC reflection illustrates that the ferrite.

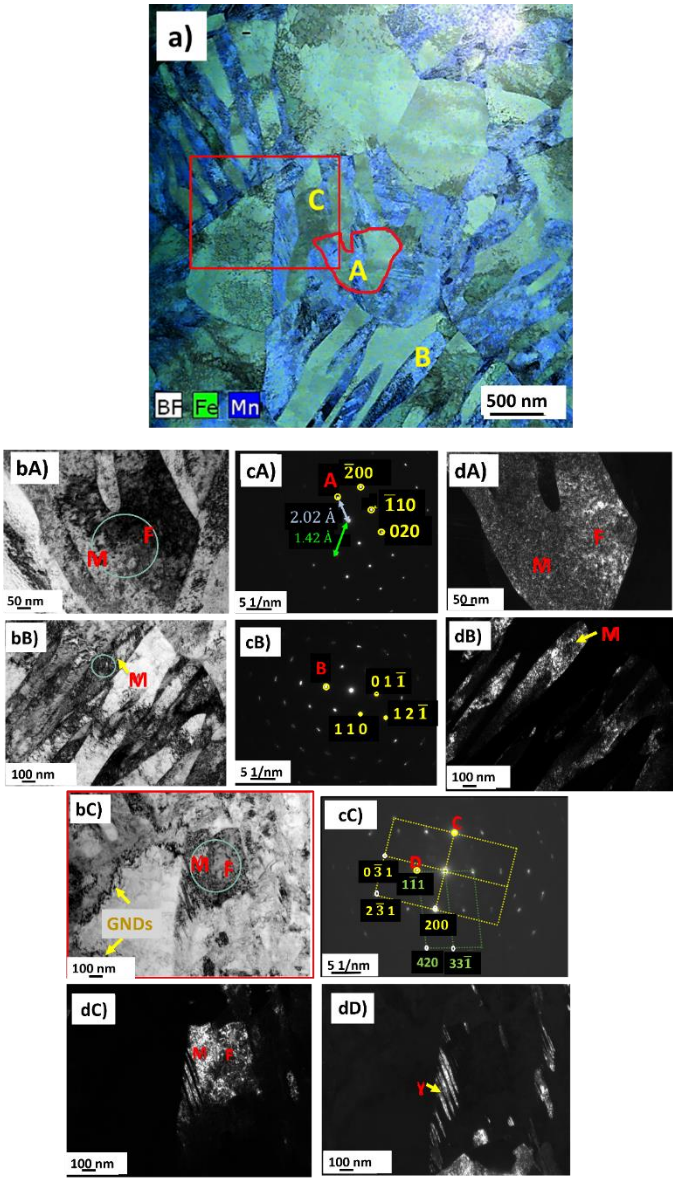

Figure A 6.2: Representative EDS map of the med-Mn in the 710°C IA condition to target Mn-enriched and -poor regions (a). Grain A, B, and red-squared region C labelled in (a) were chosen for further SAED indexing and DF imaging. The BF image, SAED pattern and DF image, (bA, cA, dA), respectively is of Grain A with indexed [0 0 1] BCC Zone axis. The BF image, SAED pattern and DF image, (bB, cB, dB), respectively is of Grain B with indexed $[\bar{1}\ 1\ 1]$ BCT Zone axis. The BF image, SAED pattern and DF images, (bC, cC, dC and dD), respectively is of the red-squared region C. Figure A 2cC shows the presence of multiple phases, identified and indexed [0 1 3] BCC (in yellow) and $[\bar{1}\ 2\ 3]$ɣ Zone axis (in green).

Figure A 6.2 refers to the TEM analysis performed on this med-Mn in the 710°C IA condition. The EDS map in Figure A 6.2a is a representative area of the 710°C IA treatment's microstructure.

Grain A, Grain B, and red-squared region C labelled in Figure A 6.2a were chosen for further SAED indexing and DF imaging. Grain A, as shown in the EDS map of Figure A 6.2a, is partially Mn-enriched. The SAED pattern in Figure A 6.2cA is obtained from the encircled region in the BF image of Figure A 6.2bA, and shows the [0 0 1] BCC zone axis. The DF image in Figure A 6.2dA is formed using the $(\bar{1}\ \bar{1}\ 0)$ BCC reflection by selecting Spot A in the SAED pattern. The section of the grain low in Mn is the ferrite while the Mn-enriched section of the grain is the ɣ which has completely transformed into martensite. This is different than the 685°C and 665°C IA conditions in which only nanoscale martensitic islands were featured at a 0.05 strain. On the other hand, Grain B, as indicated in Figure A 6.2a, is completely Mn-enriched.SAED pattern in Figure A 6.2cB, obtained from the encircled region in the BF image of Figure A 6.2bB, and shows the $[\bar{1}\ 1\ 1]$ BCT zone axis. The DF image from spot B belongs to the $(0\ \bar{1}\ 1)$BCT reflection, representing martensite, in Figure A 6.2dB. The BF image in Figure A 6.2bC is the red-squared region in Figure A 6.2a in which GNDs were observed along the boundaries of a polygonal ferrite grain. The SAED pattern in Figure A 6.2 cC from two grains encircled in green in the BF image of Figure A 6.2bC, contains multiple phases which has been identified as [0 1 3]BCC (in yellow) and $[\bar{1}\ 2\ 3]$ɣ zone axis (in green). The DF image from spot C belongs to the $(\bar{2}\ 0\ 0)$BCC reflection is illustrated in Figure A 6.2dC. Similar to what was observed in Figure A 6.2 (b-dA), the grain low in Mn is ferrite while the Mn-enriched grain is transformed martensite. In addition, sheaves of ɣ, ≈30nm in width, were observed in the DF image by using spot D, $(1\ \bar{1}\ 1)$ FCC reflection from the $[\bar{1}\ 2\ 3]$ɣ zone axis.

Ultimately, compared to the TEM analysis conducted on this med-Mn steel at its 665°C, as shown in Figure A 6.1 and its 685°C IA condition, in Figure 6.3, the presence of ɣ was less apparent. This is consistent with the Co-XRD analysis, in section 6.4.2.1, in which at a 0.15 strain, there's only ≈10% of untransformed ɣ available to be detected in this med-Mn steel when subjected to IA at 710°C. Whereas there is ≈20% and ≈40% of untransformed ɣ available to be detected in this med-Mn steel subjected to IA at 665°C and 685°C, respectively. Furthermore, it should be noted that >50% of a transformed martensite block indexed in Figure A 6.2 (b-dA) and (b-dC) were adjacent to ferrite grains which is likely due to the fact that ferrite can easily accommodate the volume expansion associated with TRIP.

6.9.2 Appendix B: HE-XRD Analysis and the Mechanical Stability of ɣ

Figure B 6.1: a shows the ɣ fraction transformed as a function of von Mises strain within the 0.5 x 0.5 mm^2 area of HE-XRD acquisition including the 95% CI error bars. Figure B 6.1: b is showing the mechanical stability of ɣ, as defined by the slope in Equation B 6.1 (i.e.; k-value). This k-value is inversely proportional to the mechanical stability of ɣ (Bai et al., 2020; Shi et al., 2010; Sugimoto et al., 1992). As described in section 6.4.2.2, this med-Mn at the 685°C IA condition (i.e. k-value of 3.7) results in the highest ɣ stability.

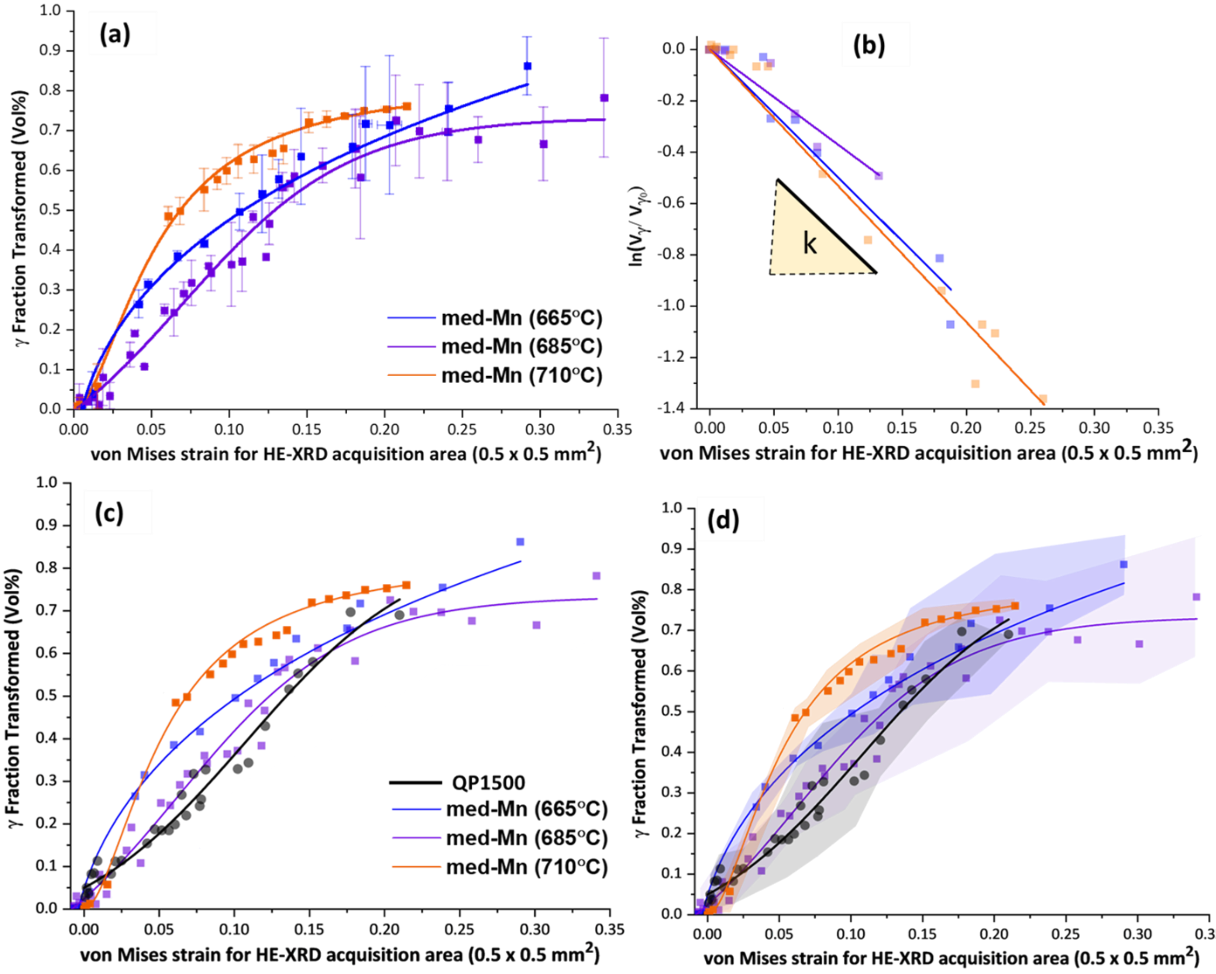

Figure B 6.1: The TRIP kinetics of this med-Mn steel subjected to IA treatments of 665°C, 685°C and 710°C held for 120s with error bars included (a). The mechanical stability of ɣ defined by the k-value/slope (b). The TRIP kinetics of the QP1500 steel is added for comparison to this med-Mn steel (c). Figure B 6.1d shows shaded regions to signify the ɣ fraction transformed within a 95% CI.

$$V_{ɣ} = V_{ɣ,0}\exp(-k\varepsilon)$$ Equation B 6.1: The Mechanical Stability of ɣ

Figure B 6.1c shows the TRIP kinetics of the QP1500 steel in relation to this med-Mn steel intercritically annealed from 665°C-710°C. Figure B 6.1d, again features the TRIP kinetics of the QP1500 steel, with the addition of shaded regions to signify the ɣ fraction transformed within a 95% CI.

6.9.3 Appendix C: Cross Sectioned Fracture Surfaces of med-Mn at the 665°C and 710°C IA conditions

EDS analysis was performed on a cross sectioned fracture surface of the med-Mn at the 665°C and 710°C IA conditions, similar to what was described in section 6.4.3.2. The Al (or combined Al,Mn,Si)-containing inclusions seen in the 685°C IA condition, as featured in Figure 6.7 bB_3 and in the 710°C IA condition in Figure C 6.1: bA_{1-3} and Figure C 6.1: bB_{1-5} are spherical in shape (i.e. have rounded edges) and the inclusion/steel interface decohesion seen does not propagate at fracture. Whereas, in the instance of the 665°C IA condition, micro-cracks are present at the corners (i.e. high local stress concentrators) of cuboid inclusions as shown in Figure C 6.1: aA_{1-5}. These cuboid inclusions were likely highly, rigid TiN particles which have formed during solidification (Hutten et al., 2021) and eliminated during polishing, with traces of Al, Mn and Si. It is possible that the voids which have nucleated because of micro-shear bands intersecting one another with increased deformation are shown in the 665°C IA condition in Figure C 6.1: aB_{1-4} and aC_{1-4}. In the 710°C IA condition, Figure C 6.1: bC_{1-4} features a centreline microcrack with embedded Al,Mn- containing particles.

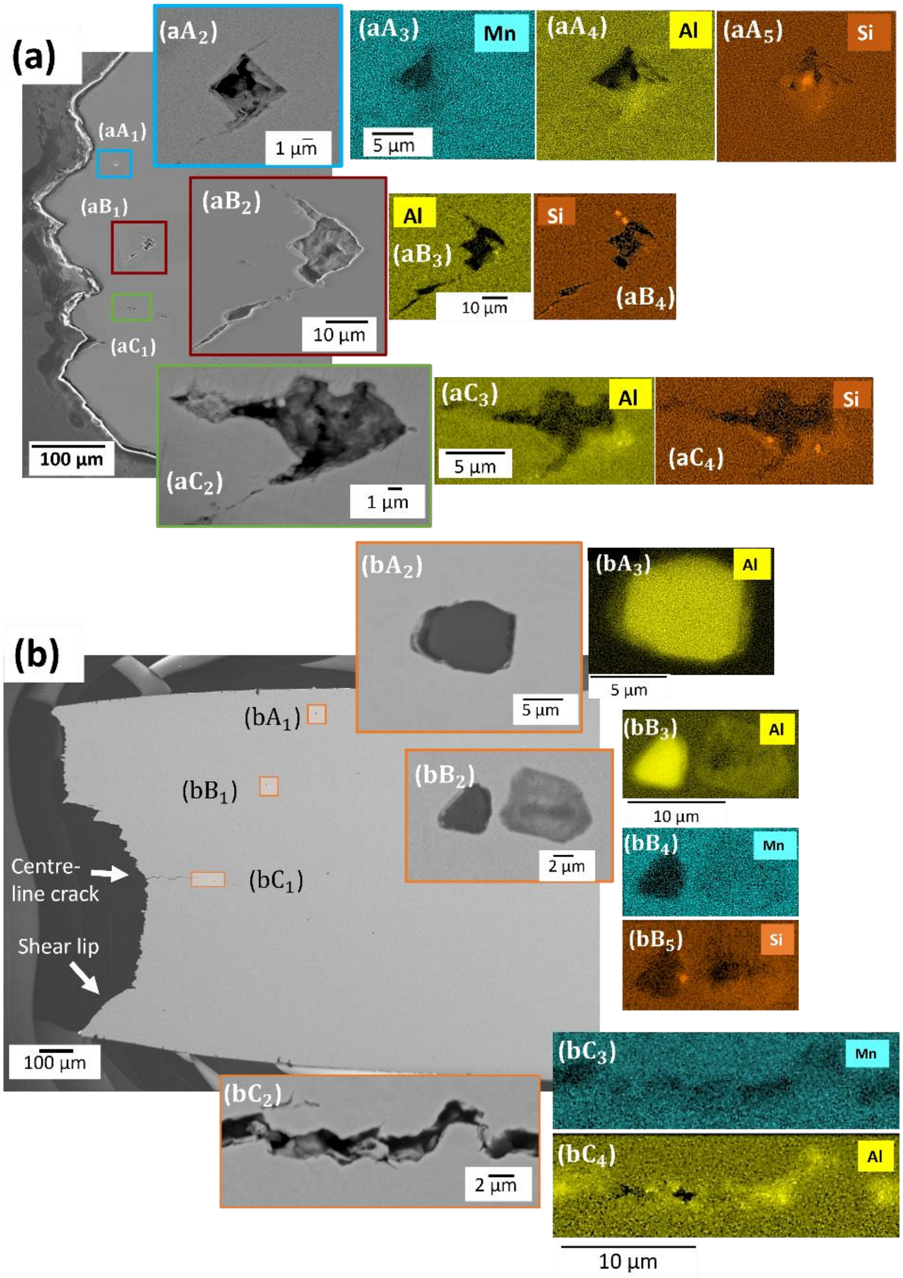

Figure C 6.1: EDS performed on cross sectioned fracture surfaces of the 665°C (a) and 710°C (b) IA conditions, respectively. Evidence of micro-cracking at cuboid inclusion corners Figure C 6.1(aA$_{1\text{-}5}$) and void formation from the intersection of micro-shear bands Figure C 6.1(aB$_{1\text{-}4}$) and (aC$_{1\text{-}4}$). An inclusion with rounded edges is featured in Figure C 6.1(bA$_{1\text{-}3}$) and (bB$_{1\text{-}5}$) whereas a centreline micro-crack with embedded particles is featured in Figure C 6.1bC$_{1\text{-}4}$.

7 Effect of Triaxiality on Microstrain Partitioning, Transformation Induced Plasticity, and the Evolution of Damage in a Third Generation Medium Mn Advanced High Strength Steel

Concetta Pelligra[1], Jidong Kang[2] and David S. Wilkinson[1]

[1]Department of Materials Science and Engineering, McMaster University, Hamilton, ON, L8S 4L7, Canada

[2]CanmetMATERIALS, Natural Resources Canada, Hamilton, Ontario L8P 0A5, Canada

7.1 Abstract

For the first time, the impact that an increased state of stress triaxiality has on Transformation Induced Plasticity (TRIP) kinetics, microstrain partitioning and damage evolution in a third generation (3G) Medium Mn (med-Mn) steel is presented. This investigation was carried out using unnotched, misaligned, shallowly and severely notched tensile geometries which enabled a range of stress triaxialities, from 0.33 to 0.89, to be tested. TRIP kinetics for these different tensile geometries was delineated with the use of High Energy X-ray Diffraction, in which the fastest and slowest transformation of austenite to martensite was experienced by the severely and misaligned notched specimens, respectively. Microscopically, the compatibility between phases and dynamic evolution of damage in two dimension was obtained through the use of quasi in-situ Scanning Electron Microscope tensile tests coupled with Electron Backscatter Diffraction (EBSD) and microscale Digital Image Correlation (μDIC). A unique electropolishing micro-speckle patterning methodology to enable the combined ability for sufficient EBSD phase indexing and μDIC is introduced through this study. Overall, the polygonal ferrite and tempered martensitic regions within the med-Mn steel microstructure were considerably more sensitive to changes in the steel's global stress-state compared to the initial austenite/eventually transformed martensitic regions. In terms of the bulk evolution of damage, a similar void area fraction just before fracture for the unnotched and notched specimens was revealed using X-ray Computed Microtomography. This is indicative of a critical void size that once reached triggers an exponential raise in coalescence and then fracture. Ultimately, this work encourages the further development of experimental and software techniques to understand the complex interplay of TRIP, microstrain partitioning, and damage evolution in 3G TRIP-assisted steels under diverse strain path conditions.

7.2 Introduction

It is well known that the introduction of lean-alloyed Advanced High Strength steels (AHSSs) in a vehicle's Body-in-White (BIW) is an effective means of reducing a vehicle's weight and improving its kinetic energy absorption in the event of a car crash (Bouaziz et al., 2013). A lesser-known fact is that the importance of producing lightweight vehicles is heightened by the increased vehicle weight in Battery Electric Vehicles (BEVs). A potential of 30-40% in weight reduction in a vehicle's BIW with the use of 3G AHSSs (i.e. with strengths that fall within the 1100-1500 MPa range) has been previously predicted (De Cooman et al., 2012). In addition, the materials which constitute BEVs must show supreme crashworthiness in protecting the battery during a crash. Yet, the stress triaxiality that is experienced by an automotive component when impacted depends on its position in the BIW and the equivalent plastic strain it experiences during the crash (Findley et al., n.d.). This cannot be explicitly characterized by an AHSS' position on the banana diagram, in which the material is characterized by its total elongation (TE) and ultimate tensile strength (UTS). For instance, the TE enables one to predict forming behavior during stretching operations but does not adequately capture its behavior during more complex forming operations that involve bending or shear. TE can vary substantially based on the specimen design, strain path, stress-state, etc. (De Moor et al., 2010; Hance, 2016; Jacques et al., 2007; Larour et al., 2017; Lian et al., 2021; Park et al., 2019).

More than this however, a lot of damage modelling to date is conventionally validated using uniaxial tensile testing, and hence, limited to predicting a material's response when subjected to concentrated loading (Brünig et al., 2008; Polatidis et al., 2020). In a traditional tensile test of a ductile metal, stress is first dominated in one direction, but once necking occurs all three principal stresses affect the metal's deformation to fracture. As a result, the stress triaxiality, defined as the ratio of the mean stress (σ_m) to the equivalent von Mises stress (σ_{vM}), not only affects the material's deformation behavior but also has a complex relationship with fracture. Bao and Wierzbicki (2004) found that for sample designs with high (0-0.4) and low (0.4-0.95) stress triaxialities, the equivalent strain to fracture increases or decreases parabolically, respectively. Notched specimens were used to understand the alloy's mode of fracture at high triaxialities. To understand fracture behavior at lower stress triaxialities, they tested misaligned-notch-type specimens with either pure shear or combined shear-tension deformation and achieved triaxialities of 0-0.15. It is worth mentioning that at these lower triaxialities, the σ_m is very small in comparison to the σ_{vM}. A plate with a circular hole was used in that study to achieve the classical uniaxial tension state with a triaxiality of 0.33. With this specimen design, Bao and Wierzbicki (2004) were able to deduce that the transition from shear dominated fracture to one dominated by void growth occurs in a triaxiality range of 0.33-0.4 but is material dependent. Wang et al. (2014) rather argue that the hole tension test is a suitable alternative to the hole expansion test (HET), allowing void evolution to be a result of the complex stress-state near the vicinity of the hole's edge. Scott (2018) was able to use a hole tension geometry to mimic stresses experienced during stretch flanging and observe damage in-plane with the use of tomography. Using Finite Element Modelling (FEM), Williams et al. (2022) determined the triaxiality at the edge of the hole during loading of a HET to be 0.33 on a Dual Phase (DP) steel of 980MPa UTS, DP980, whereas further away from the hole edge the stress triaxiality was $>$ 0.5.

To counteract this, there is also ~3% volume expansion associated with the transformation from austenite to martensite in Transformation Induced Plasticity (TRIP)-assisted steels which is said to cancel a portion of the triaxial stress, thereby reducing the local stress intensity of the material, suppressing damage evolution and inhibiting brittle type fracture (Jacques et al., 2001; Parker and Zackay, 1973; Samei et al., 2020; Withers, 2015). Moreover, multiphase microstructures along with TRIP-assistance in AHSSs has been critical being within the broadened third generation (3G) mechanical targets, 36000MPa% $\leq$UTSxTE$\geq$40000MPa% (Matlock and Speer, 2009). This is based on the United States Department of Energy's (U.S. DoE's) specific mechanical targets of 1200MPa x 30%, and 1500MPa x 25% for 3G steels. Such steels are made using the quench and partitioning technique (Speer et al., 2003), or intercritical annealing (IA) (Gibbs et al., 2011), as is the case with Medium Mn (med-Mn) steels, to stabilize austenite with a high concentration of carbon and/or manganese. Specifically, med-Mn steels, with manganese contents ranging from 4-10%, can revert a significant amount of austenite through IA (~675-700°C). In comparison to quench and partition (Q&P) steels, med-Mn steels show greater continuous galvanizing line (CGL) compatibility and can also achieve 3G mechanical targets with industrially capable short annealing times (Bhadhon et al., 2017; Pallisco et al., 2017). Furthermore, the properties of med-Mn steels are highly tunable through their starting microstructure and IA parameters.

In general, TRIP is accompanied by both a volume and distortion shape change. The volume change associated with TRIP is a function of the σ_m, whereas the distortion shape change is a function of shear stresses on habit planes. The equivalent von Mises strain is a measure of plasticity accounting for normal and shear stresses. Olson and Cohen (1975) were the first to propose a relationship between TRIP and the equivalent plastic strain using an austenitic stainless steel (AUS). Eventually their model was modified to understand the effect of strain rate (Tomita and Iwamoto, 1995) and stress triaxiality (Stringfellow et al., 1992) on phase transformations. Stringfellow et al. (1992), with data supplied by Young (1988), found that TRIP kinetics are a monotonic function of triaxiality, in which more austenite is transformed under uniaxial tension versus uniaxial compression, from a high to low triaxiality comparatively. Demania (1995) however, noted that at room temperature (20°C) the austenite transformed under uniaxial tension was similar to that under plane strain, even though the plane strain condition has a higher stress triaxiality. Beese and Mohr (2011), as well as Polatidis et al. (2020) provided evidence to show that there is not a monotonic relationship between TRIP and stress triaxiality. Instead, they argued that an influence of the Lode Parameter needs to be accounted for. On the contrary, Mansourinejad and Ketabchi (2017), note that it is possible to assess the effect of stress triaxiality on TRIP without considering the Lode parameter. This is also supported by Yang et al. (2021) in their study of a 5wt%Mn med-Mn steel subjected to different strain states. Moreover, Beese and Mohr (2011) attribute experimental differences in the TRIP-triaxiality relationship seen in the literature to experimental inconsistencies (i.e. possible buckling in compression, effect of specimen preparation on the martensite detected, specimen geometry, etc.). With that being said, another important aspect to note is that most studies to date has been focused on understanding the role triaxiality has on TRIP kinetics in AUSs (Jacques et al., 2007), which in general posses a much narrower stacking fault energy (SFE) range compared to low-alloyed TRIP-assisted AHSSs. Only a few reports have been made to understand the TRIP-triaxiality relationship of TRIP-assisted AHSSs (Polatidis et al., 2020), and even less related on 3G steels, such as med-Mn steels (Lian et al., 2021; Wu et al., 2018; Yang et al., 2021). Similar to the contradictions in the literature on the TRIP-triaxiality relationship in AUSs, Lian et al. (2021) noted that the deformation mode (i.e. uniaxial tension versus equibiaxial tension) did not impactTRIP kinetics in a 7wt%Mn med-Mn steel, whereas Wu et al. (2018) as well as Yang et al. (2021) both report that TRIP kinetics was faster under uniaxial tension then equibiaxial tension in a 10wt%Mn and 4wt%Mn med-Mn steel, respectively.

Moreover, the microscopic events (i.e. strain partitioning amongst phases, void nucleation, etc.) leading to fracture is affected by several factors. Some of these are intrinsic to the microstructure, including particle sizes (Nan and Clarke, 1996), and particle aspect ratios, while others are extrinsic to the microstructure, including specimen design-induced triaxiality (Bao and Wierzbicki, 2004; Landron et al., 2011; Toda et al., 2014). In 3G steels, another intrinsic factor governing void nucleation, growth and the overall rate at which damage evolves is TRIP kinetics (Samei et al., 2020; Sun et al., 2019). Although in-situ high-energy X-ray or neutron diffraction studies have been successful on providing an abundance of crystallographic/phase transformation data on AHSSs as they are being deformed (Abu-Farha et al., 2018; Hu et al., 2017; Jacques et al., 2007; Park et al., 2019; Polatidis et al., 2020), the ability to correlate microstrain partitioning to microstructural evolution (i.e. grain orientations, misorientations, phase transformations, estimates on the evolution of geometrically necessary dislocations (GNDs) etc.) can only be achieved with the combined use of high resolution Electron Backscatter Diffraction (EBSD) mapping, Scanning Electron Microscope (SEM) imaging and Digital Image Correlation (DIC) during in-situ testing in a defined microscopic area of interest. The ultimate challenge that arises in combining in-situ SEM tensile testing with micro-Digital Image Correlation (μDIC) and EBSD is in choosing a micro-speckle patterning technique that is compatible with both imaging/mapping modalities. A wide variation in greyscale values in SEM acquired images generally enables complete DIC mapping coverage, whereas EBSD is best performed on smooth surfaces and a narrow distribution in greyscale (Zhang et al., 2020). That being said, sophisticated micro-speckle patterning techniques has been recently ventured by several in the attempt to process SEM images using μDIC on areas previously subjected to EBSD mapping. The drop casting colloidal silica micro-speckle patterning technique, for instance, has been deemed a successful method of combining in-situ SEM tensile testing with μDIC and EBSD of 3G steel microstructures (Dutta et al., 2019; Wang et al., 2017; Yan et al., 2015). This is likely due to the fact that colloidal silica results in weak beam scattering providing the sufficient contrast needed for successful µDIC mapping and has minimal interference during EBSD mapping. Zhang et al. (2020), on the other hand, proposed a 2-step electropolishing methodology in which they electropolished their material until a smooth surface for EBSD mapping was achieved, then re-electropolished their material at high voltages to enable 'pitting decoration'. This allowed a wider variation in greyscale necessary for µDIC processing of SEM acquired images. In this paper, similar to Zhang et al. (2020), we apply an electropolishing micro-speckle patterning methodology, in which we electropolished our AHSS only once with optimal parameters such that the variation in greyscale was maximized for high resolution EBSD and sufficient for µDIC mapping. Other novel micro-speckle patterning techniques that have been attempted in order to combine µDIC on SEM and EBSD acquired areas of AHSSs include physical vapour deposition (PVD) of InSn (Hoefnagels et al., 2019) and gold remodelling (Yin et al., 2023).

It is critical to note, however, that the evolution of damage cannot be explained solely by two-dimensional (2D) examinations as is possible with in-situ SEM testing, or cross-sectioned fracture surfaces (Buffière et al., 1999; Mummery and Derby, 1994; Stiénon et al., 2009; Vijayan et al., 2020; Weck, 2007). Studies available in the literature using x-ray microcomputed tomography (µXCT) to characterize void nucleation and damage in 3D are so far limited to lower strength steels (Fabrègue et al., 2015, 2013; Landron et al., 2013; Maire et al., 2012; Toda et al., 2017, 2016), welded high strength steels (Vijayan et al., 2020), or bearing (1C-1.5Cr) steels (Stiénon et al., 2009). Furthermore, very few studies have been dedicated to characterizing damage in 3D of TRIP-assisted steels (Kumar et al., 2023; Samei et al., 2020; Schoell et al., 2022; Toda et al., 2022), with little to no work devoted to understanding damage evolution in 3G TRIP-assisted steels (Samei et al., 2020) or steels subjected to different states of stress (Kumar et al., 2023; Lorthios et al., 2010; Pelligra et al., 2022). For example, in the recent work of Kumar et al. (2023), synchrotron-based XCT studies were used to compare the evolution of damage in two, heavily strained, C-Mn sheet steel specimens with differing triaxialities - a Compact Tension (CT) and Single Edge Notched Tensile (SENT) specimen with maximum triaxialities of 2.8, and 1.8 respectively. Kumar et al. (2023) detected larger voids and a higher void volume at fracture in the

CT specimen. It was concluded that at a high stress triaxiality voids grow substantially and coalesce through impingement, whereas at a low stress triaxiality, coalescence of voids occurs through a secondary void nucleation or void sheeting (Morgeneyer et al., 2008; Tanguy et al., 2005). Furthermore, using µXCT, Samei et al. (2020) was able to show that grain refinement, TRIP and decreased mechanical heterogeneity amongst phases can all be used to suppress damage and increase the local true strain to fracture ($\varepsilon_{\mathrm{loc}}^{\mathrm{True}}$).

7.3 Material and Heat Treatment

The as-received material of study is a prototype third generation (3G) Medium Mn steel with a 1.2 mm thickness with a 0.15C-5.78Mn-0.71Si-1.77Al-0.04Cr-0.003S composition (Pelligra et al., 2024a, in draft). The thermomechanical processing route and IA treatments were conducted using McMaster's Galvanizing Simulator (MGS) as described elsewhere on comparable med-Mn steels (Mehrabi et al., 2023; Pallisco and McDermid, 2020). Specimens for testing were extracted from the uniformly heat-treated zones of the intercritically annealed material as detailed by Bellhouse (2010) and Patel (2019). The mechanical properties, determined using ASTM-E8 subsize, tensile specimens, and a thorough microstructural characterization of this med-Mn steel, has been published previously (Pelligra et al., 2024a,in draft).

In short, we have already shown that the mechanical properties of this med-Mn steel, with a martensitic (80% martensite-20% ferrite) starting microstructure, varies considerably as one modifies IA over a modest range of temperature from 665°C to 710°C with a 120s holding time (Pelligra et al., 2024a,in draft). Moreover, we have shown that an IA temperature of 685°C provides the optimal mechanical properties, by fitting within the general3G mechanical target envelope (28,809MPa%), achieving a large true strain at fracture (ε_f = 0.61) and by extending TRIP to high strains. Moreover, damage evolution studies with the use of X-ray microtomography (µXCT) conducted at the 685°C IA condition showed the largest void density, but lowest void area fraction at fracture compared to the other two IA temperatures considered. This indicates that although void nucleation is promoted at this 685°C IA condition, its subsequent growth, as a result of the local compressive stresses imposed by the continual transformation of the reverted austenite (ɣ)-

to-martensite, is effectively suppressed. As a result, this med-Mn steel and IA condition was chosen to understand the role that different stress states have on damage evolution and TRIP kinetics.

7.4 Methods

7.4.1 Tensile testing, HE-XRD, and DIC

The volumetric quantification and mechanical stability of ɣ as a function of uniaxial strain was determined through High Energy X-Ray Diffraction (HE-XRD). This technique, adapted and applied by several authors (Abu-Farha et al., 2018; Hu et al., 2017; Park et al., 2019), offers ample points to delineate a steel's TRIP kinetics. HE-XRD experiments were conducted at room temperature using a 13kN tensile load frame system at the Argonne Photon Source (APS) in beamline 11-ID-C. The synchrotron X-ray beam chamber was set at 105keV and 0.1173$\dot{A}$. These experiments were performed using wire-Electrical-Discharge Machining (wEDM)-prepared, tensile specimens customized to the APS tensile frame, as shown in Figure 7.1a. The experimental set-up and DIC post-processing parameters are presented elsewhere(Pelligra et al., 2024b). DIC post-processing was applied to define the localized strain within the 0.5x0.5 mm^2 region of HE-XRD acquisition. Any specimen slippage during tensile testing resulting in a shift of the HE-XRD 0.5 x 0.5 mm^2 acquisition window was accounted for during DIC post-processing and strain quantification.

Traditionally, tensile testing conducted at the APS 11-ID-C beamline, featuring a combined HE-XRD and DIC coupled set-up, has been performed on 'unnotched and straight gauged' specimens (Abu-Farha et al., 2018; Hu et al., 2017; Li et al., 2020; Park et al., 2019), as shown in Figure 7.1a. Limited HE-XRD studies have been conducted on TRIP steels at different stress states (Park et al., 2019; Wu et al., 2018). In this paper, we designed and varied the notch geometry within the gauge length of such customized tensile specimens to understand the impact that a variation in stress-state has on TRIP kinetics in this steel intercritically annealed at 685°C. Shallowly notched, severely notched and misaligned notches, Figure 7.1b,c and d, respectively, were wEDM machined from the conventional unnotched/straight-gauged section of these customized dog-bone tensile specimens. After fracture, these specimens were preserved for fractography, further discussed in section 7.5.3.

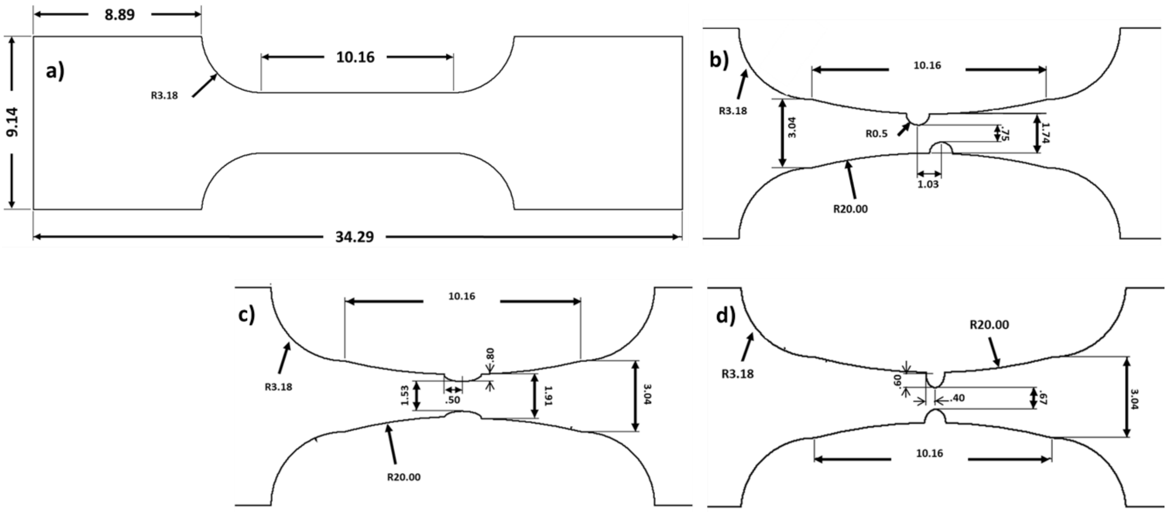

Figure 7.1:Unnotched (a), misaligned (b), shallowly (c) and severely (d) notched specimen designs used for HE-XRD experimentation at APS' 11-ID-C.

In comparing the shallowly to the severely notched specimen designs shown in Figure 7.1c and d, there is an increase in acuity in the notch such that the radius of curvature (ρ) is reduced in the severely notched specimens. Using the principles introduced by Inglis (1913), the ρ for the shallowly notched and severely notched specimens can be approximated as ~0.31 mm and ~0.26 mm, respectively. The radii of the misaligned notches specimens, shown in Figure 7.1b, were made to be semi-circular, such that, in theory, its stress concentration factor is ~3 (Fischer-Cripps, 2007). In this case, the asymmetric positioning of the notches should have a more predominant effect on this specimen's deformation.

7.4.2 Numerical Calculation of Triaxiality

ABAQUS/CAE 6.14 FEM software was used to assess the global triaxiality within the center of the notch of the tensile specimens in Figure 7.1. An implicit model was chosen for the 3D simulation and run just up to the point of fracture. This was done in order to avoid large computational costs. Isotropic hardening with elastic constants of steel, E = 210 GPa and v = 0.3, was used in our FEM analysis. The true stress-plastic strain past yielding inputs were taken from experimental uniaxial tensile testing data, presented previously (Pelligra et al., 2024a, in draft), fitted to a Voce-Linear hardening model using the Curve Fitting App in MATLAB. This was run until an R^2 value of 0.99 was achieved (Pelligra et al., 2022). Eight-node, linear brick, continuum elements (C3D8R) with reduced integration and hourglass control was used for the unnotched and notched specimen design simulations. Material Property outputs from the ABAQUS finite element simulation were extracted from the centroid of elements. Mesh sizes were set to being ~3.5x the average grain size of ferrite and ~5x the grain size of ɣ within the notched region vicinity in order to obtain a broadened ‘past grain-level’ indication of stresses, including triaxiality (i.e. global triaxiality) (Pelligra et al., 2022). The average ferrite and ɣ grain size was determined using EBSD mapping, detailed in (Pelligra et al., 2024a,in draft).

Due to symmetry, 1/4th of the unnotched, shallowly, and severely notched tensile geometries were segmented in order to determine the average stress triaxiality in the absolute centre of the specimens, as illustrated in Figure 7.2a. Due to the asymmetry of the misaligned notched tensile geometry, this FEM model was segmented through the specimen’s thickness (X-Z plane). In this instance, the average stress triaxiality was captured from the centre of the diagonal path from the apex of one notch to that of the other, as shown in Figure 7.2b. The average triaxialities obtained from the unnotched, misaligned, shallowly, and severely notched specimens are 0.33, 0.38, 0.64, and 0.88, respectively, as tabulated in Appendix A, Table A 7.1. It is important to note the misaligned notched geometry used in this paper is geared towards that of combined notched shear-tension-type deformation. As a result of the misaligned notched tensile geometry used, the average stress triaxiality was in between that of the unnotched and shallowly notched specimens. This misaligned notched design, although still providing a shear-type fracture, achieved a higher triaxiality, as shown in Figure 7.2a_1, than of that tested by Bao and Wierzbicki (2004) and Brünig et al. (2008) in which they used specimens designs whose stress triaxialities achieved 0-0.15.

For the symmetric, 1/4th segmented, unnotched, shallowly, and severely notched FEM models, a path from the specimen’s edge/notch apex to its centre was defined in order to capture the specimen’s variation in stress triaxiality, σ_m, and σ_{vM} as the specimens were strained accordingly, as shown in Figure 7.2 (c) – (e). On the other hand, the variation in stress triaxiality, σ_m, and σ_{vM} in the misaligned notched specimens, in Figure 7.2c_1, d_1 and e_1 respectively, was determined along the diagonal distance between notch apices of the model’s ½ segmentation. As a note, the diagonal distance between the notch apices in the misaligned notched specimens increases in length with increased deformation, whereas in the shallowly and severely notched specimens, the distance between notch apices decreases with increasing deformation due to necking, as shown in Figure 7.2 (c) - (e).

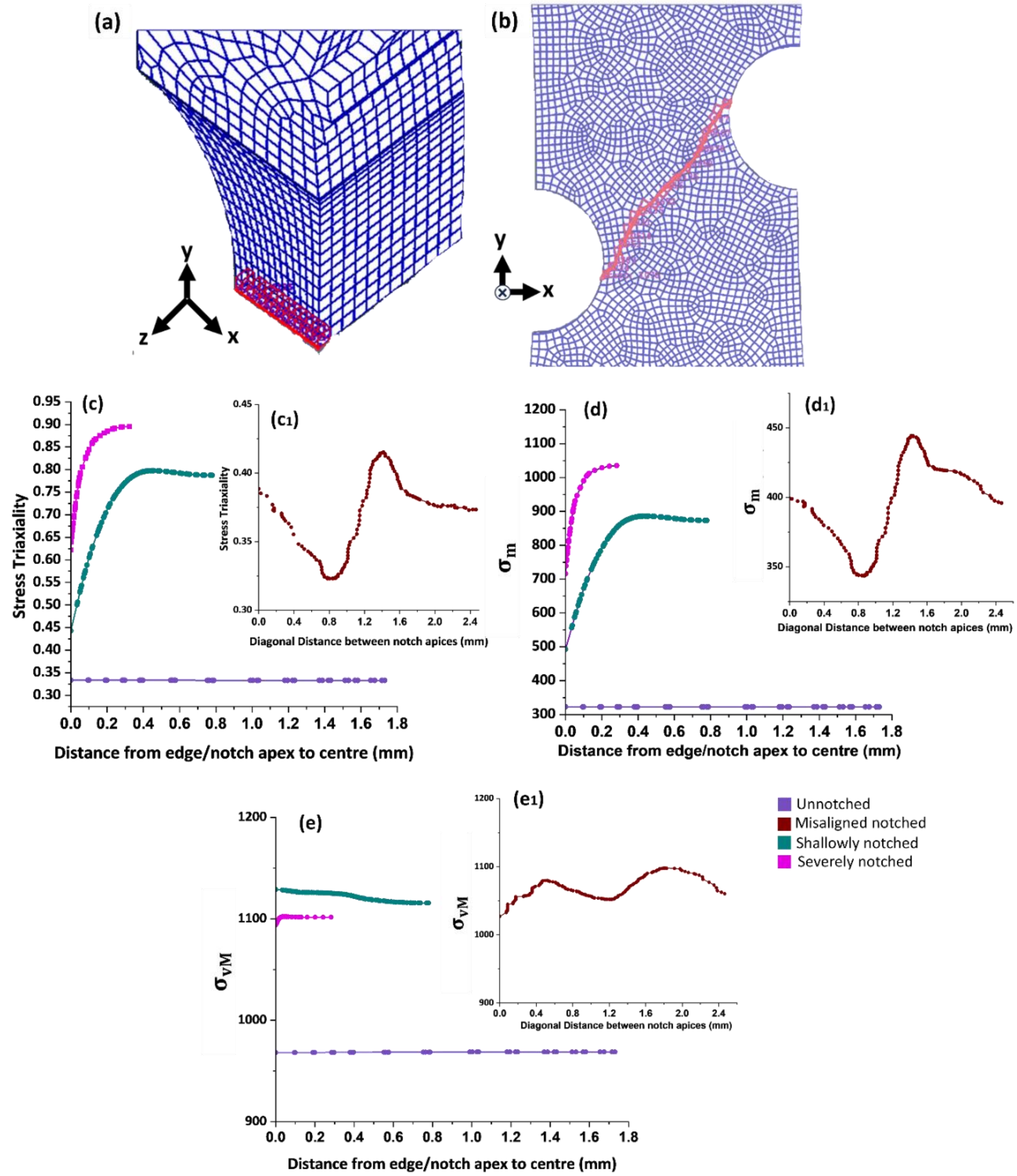

Figure 7.2: ABAQUS FEM simulations of 1/4th segmented unnotched and notched specimen geometries, with a defined path from the notch's apex to the specimen's centre (a). ABAQUS simulations of the 1/2 segmented misaligned notches specimen, with diagonal path defined between the apices of the specimen's notches (b). The variation in stress triaxiality (c) mean stress (d) and von Mises stress (e) in the defined path (as shown in Figure 2a) of the unnotched, shallowly notched and severely notched specimens. The variation in mean stress (d_1) and von Mises stress (e_1) in the diagonal defined path (as shown in Figure 2b) between the misaligned notches specimen's apices.

As can be seen in Figure 7.2d and d_1, σ_m is initially higher in the misaligned, shallowly, and severely notched tensile geometries compared the unnotched tensile specimen design. The higher initial σ_m in these geometries is due to shape effects introduced by the notches. The σ_m in the shallowly and severely notched FEM models increases towards the centre of these specimens (Figure 7.2d). The σ_{vM} slightly decreases in the shallowly notched specimen FEM model as illustrated in Figure 7.2e. On the contrary, the severely notched tensile geometry featured in Figure 7.2e shows a slight increase in σ_{vM} stress up to <0.03 mm away from the notch which eventually plateaus. The mean and von Mises stresses remain constant from the specimen's edge to centre of the straight-gauged specimen FEM model in Figure 7.2d and e, respectively. As a result, the stress triaxiality plot in Figure 7.2c shows that both the σ_m and σ_{vM} evenly contribute to the stress triaxiality of the unnotched tensile geometry, as in accordance with Patel and Cohen (1953). On the other hand, the σ_m has a more dominating effect on stress triaxiality in the other geometries. The variation in σ_{vM} from the notch apex to the specimen's centre of the shallowly notched specimens plays more of a contributing role to reducing stress triaxiality towards the centre of this tensile geometry. A minor reduction in stress triaxiality at ~0.7-0.8 mm from the notch can be observed in Figure 7.2c.

Unlike the shallowly and severely notched tensile geometries, the variation in σ_m from the apex of one notch to the other is asymmetric for the misaligned notched FEM model, as shown in Figure 7.2d_1. Some symmetry, with a difference of ~23MPa, however, in von Mises stresses across this diagonal path between notch apices can be observed, as shown in Figure 7.2e_1. In comparing Figure 7.2d_1 and e_1, an intermediate σ_m, and minimum σ_{vM} is achieved, respectively, at the centre of the diagonal path between the notch apices of the misaligned notches specimen design. Overall, it should be noted that the fluctuations in σ_m is significantly more predominant, within a span of ~500MPa (Figure 7.2d,d_1), over the σ_{vM}, within a span of ~100MPa (Figure 7.2e,e_1) from the notched specimens.

Furthermore, for in-situ SEM tensile testing coupled with µDIC experiments and µXCT studies, detailed in sections 7.5.2 and 7.5.3, respectively, notches were wEDM prepared in the gauge of traditional hourglass microtensile used elsewhere (Salehiyan et al., 2020; Samei et al., 2019; Siemens et al., 2023; Zhou, 2018). FEM simulations were also carried on such geometries in order confirm that similar average triaxialities were being tested as the notched specimens used for HE-

XRD experiments. Appendix A, Table A 7.1 compares the average stress triaxiality determined in the centre of the HE-XRD and in-situ SEM tensile testing specimens.

7.4.3 µDIC Procedure

Microstrain measurements amongst the initial ɣ- transformed martensite (ɣ-M) and ferrite-tempered martensite (F-TM) phases as well as the dynamic evolution of damage was performed using quasi in-situ SEM tensile testing. As previously noted in section 7.4.2, hourglass microtensile specimens are conventionally used to centralize deformation and damage. A manual in-house built tensile stage was utilized for in-situ SEM tensile testing to allow the working distance to be decreased (to 10 mm) for improved resolution, as shown in Figure 7.3d. SEM images were obtained using a high-resolution Field Emission Gun (FEG) SEM. These images acquired at a focused location as a function of tensile strain were coupled with DIC to obtain high-resolution microstrain maps (Kang et al., 2007, 2005). Imaging was performed within the centre of the sample, or at the centre of notches, to purposefully avoid any potential (≈25µm deep) Heat Affected Zone (HAZ) that may have developed during wEDM (Choudhary et al., 2010). It is well known that the spatial resolution and the range of local strain that can be measured with DIC is dictated by the grey scale variation arising from a particular speckle pattern. In the present paper, microtensile specimens were electropolished at 18V in a 10% perchloric-methanol solution, cooled to -20°C using liquid nitrogen before EBSD acquisition. EBSD mapping was performed on microtensile specimens to track the initial ɣ at the surface before beginning the quasi in-situ SEM tensile tests (*Step 1* in Figure 7.3a and b). After EBSD scanning, to remove the electron beam (e-beam) deposition from the area of interest as a result of long-time EBSD acquisition, the sample's surface was subjected to gentle surface milling using a ZEISS NVision 40 dual-beam gallium (Ga)-sourced Focused Ion Beam (FIB) at 30kV and 40pA (*Step 2* in Figure 7.3c). This was done to prevent subsequent SEM imaging of hydrocarbon cracking rather than microstructural deformation during in-situ SEM tensile testing. It is important to note that at low currents, Ga-ion implantation is negligible. In order to isolate the area of interest for SEM imaging during in-situ tensile testing, FIB fiducials (such as FIB perimeter milling, as shown in Figure 7.3c) a considerable distance away from the EBSD scanned area can also be applied. Once ion-milled, the area of interest shows sufficient grey scale variation on the surface for microstrain mapping at grain level resolution, as shown in *Step 3* in Figure 7.3d, similar in appearance to that of the etching technique used for µDIC (Kang et al., 2005; Pelligra et al., 2022; Tang et al., 2021). We have adapted the electropolishing method of micro-speckle patterning, modified from the work of Zhang et al. (2020), with the goal to first differentiate between Body-Centred-Cubic (BCC) and Face-Centred-Cubic (FCC) phases via EBSD on the specimen's surface (*Step 1* in Figure 7.3b) and then enable the quantification of strain partitioning between the initial ɣ and eventually transformed martensite, and F-TM phases via µDIC (*Step 3* in Figure 7.3e). However, in order to verify that microstructural damage events were unrelated to FIB milling or e-beam deposition artifacts, additional unnotched and notched hourglass specimens were 1% Nital etched for in-situ SEM tensile testing coupled with µDIC, as has been done by several authors (Kang et al., 2007, 2005; Pelligra et al., 2022; Tang et al., 2021). These results are shown in Appendix C, Figure C 7.1.

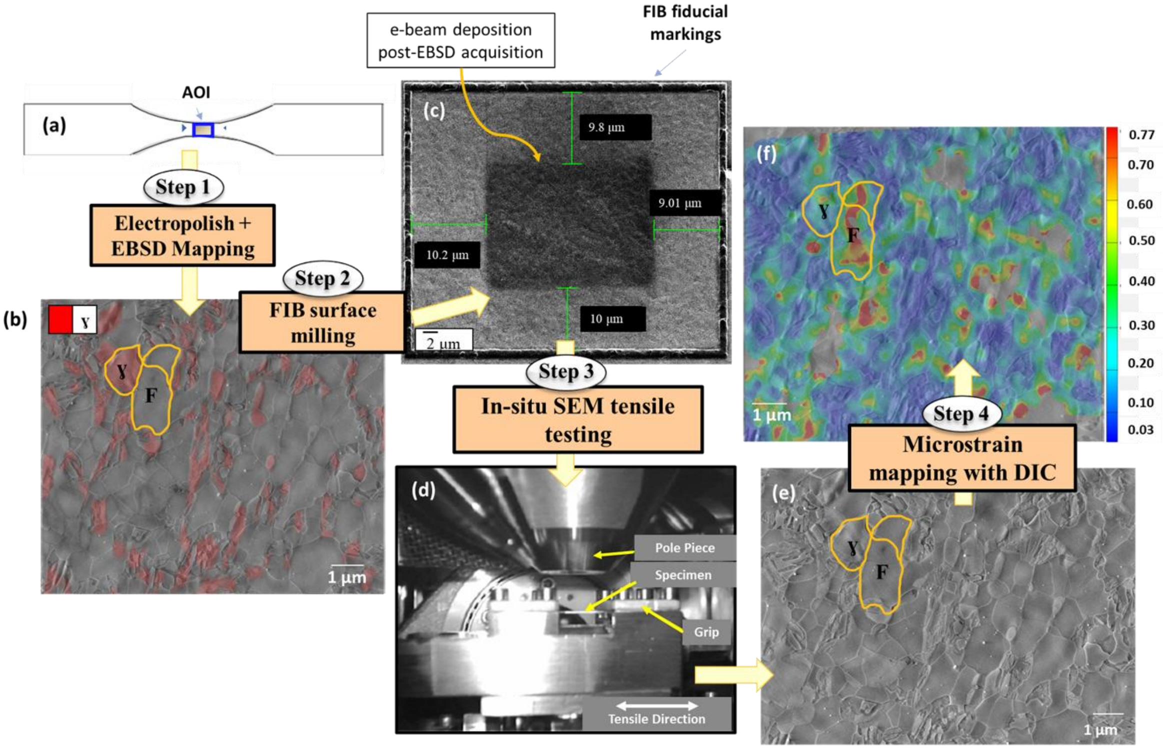

Figure 7.3: Flow diagram of the steps (from 1 to 4) used to micro-speckle pattern microtensile specimens with an electropolishing-based technique to enable EBSD acquisition and µDIC post- processing of SEM images. Figure 1.3 (d) was adapted from Zhou (2018)

Microstrain partitioning is visualized and quantified from SEM images using the commercially available ARAMIS DIC software, GOM Correlate 2018 (gom, 2016). The software assigns facets with a set of unique grayscale intensities from a reference image and tracks the displacement of the facet in the deformed states to compute strain. A facet comprising a wide variation of grey levels rather than a pixel with one grey level is used for convenient tracking in subsequent images. The facet size and point distance (distance between facet centres) were chosen to provide sufficient micro-detail and mapping coverage particularly at high strains. When the computation size is three, the virtual gauge length corresponds to two times the step size. In other words, in the local field of 3×3 facets, the strain is regarded to be uniform (Pelligra et al., 2022). The facet and step sizes used to resolve the average 'in-grain strain' for this analysis is tabulated in the Appendix B, Table B 7.1. The von Mises equivalent strain was computed with the assumption that deformation takes place at constant volume. The average von Mises strain is calculated within the imaged area during in-situ SEM tensile testing and is termed as ε_{Avg} in this paper. Details of using the ε_{Avg} from an imaged area compared to other µDIC post-processing techniques have been described elsewhere (Pelligra et al., 2022). Overall, microstrain mapping with von Mises Strain is said to directly correlate to the density of GNDs (Dutta et al., 2019).

7.4.4 µXCT Procedure

µXCT was performed on fractured unnotched, shallowly and severely notched specimens from in-situ SEM tensile tests. This was done to quantify the development of microstructural damage including void and micro-cracks during deformation in three-dimension (3D). A desktop Bruker Skyscan1172 XCT equipped with a 100kV X-ray source and an Al/Cu filter was used. Due to the fact that this desktop XCT model relies on geometric magnification, fractured specimens were placed on a rotating stage closest to the source to achieve a high resolution of 0.9µm/pixel or $0.73\mu\mathrm{m}^3$/voxel. The sample was rotated 360° with a 2D projection obtained every 0.25° rotation to collect a total of 1400 images. The commercial Skyscan 1172 software package, NRecon, CTan and CTVol, was used to reconstruct the 2D projections into a 3D model to observe and quantify internal voids and dimples (voids at the surface). The enhanced symmetry (i.e. ~1mm width, and ~1mm thickness) associated with hourglass microtensile specimens enabled efficient XCT reconstruction. To mitigate the effects µXCT artifacts can have on the quantification of damage evolution, only objects with a minimum volume of $14.6\mu\mathrm{m}^3$ were considered in the analysis.

7.5 Results and Discussion

7.5.1 TRIP Kinetics of Unnotched and Notched Specimens

The von Mises equivalent DIC strain maps of the notched specimens just before fracture are shown in Figure 7.4 (a) to (c). The white boxed areas in Figure 7.4 (a) to (c) highlight the approximate regions used for HE-XRD acquisition. Minute shifts in the 0.5 x 0.5 mm^2 HE-XRD acquisition window from specimen slippage during tensile testing, were accounted for during DIC post-processing (Pelligra et al., 2024b). The ɣ fraction transformed as a function of von Mises equivalent strain quantified via DIC within the precise location (0.5 x 0.5 mm^2) of HE-XRD data acquisition is featured in Figure 7.4d. The shaded regions in Figure 7.4 signifies the 95% confidence limits on the amount of ɣ fraction transformed were calculated from the results of three specimens of each tensile geometry. The rate of TRIP exhaustion is fastest for the severely then shallowly notched specimens, whereas the slowest rate of TRIP exhaustion is found in the misaligned notched specimens. This is in accordance with Pyshmintsev et al.'s (2002) work in which they showed that plastic deformation of the austenite via dislocation glide is favoured over TRIP during shear loading. On the other hand, by increasing the σ_m, as is the case with the shallowly and severely notched specimens, the volume expansion associated with the ɣ-to-martensite transformation is easily accommodated. It can be noted from Figure 7.4, that the greatest variability in TRIP kinetics (i.e. shaded region featured on each curve in Figure 7.4), was obtained for the misaligned notched specimens. This is likely due to dynamic variation in σ_m across the diagonal path between notch apices, as shown in Figure 7.2d_1 and e_1. Any minute shifts in the 0.5 x 0.5 mm^2 HE-XRD acquisition window during tensile testing, could have led to the significant variability in TRIP kinetics within the misaligned notched region.

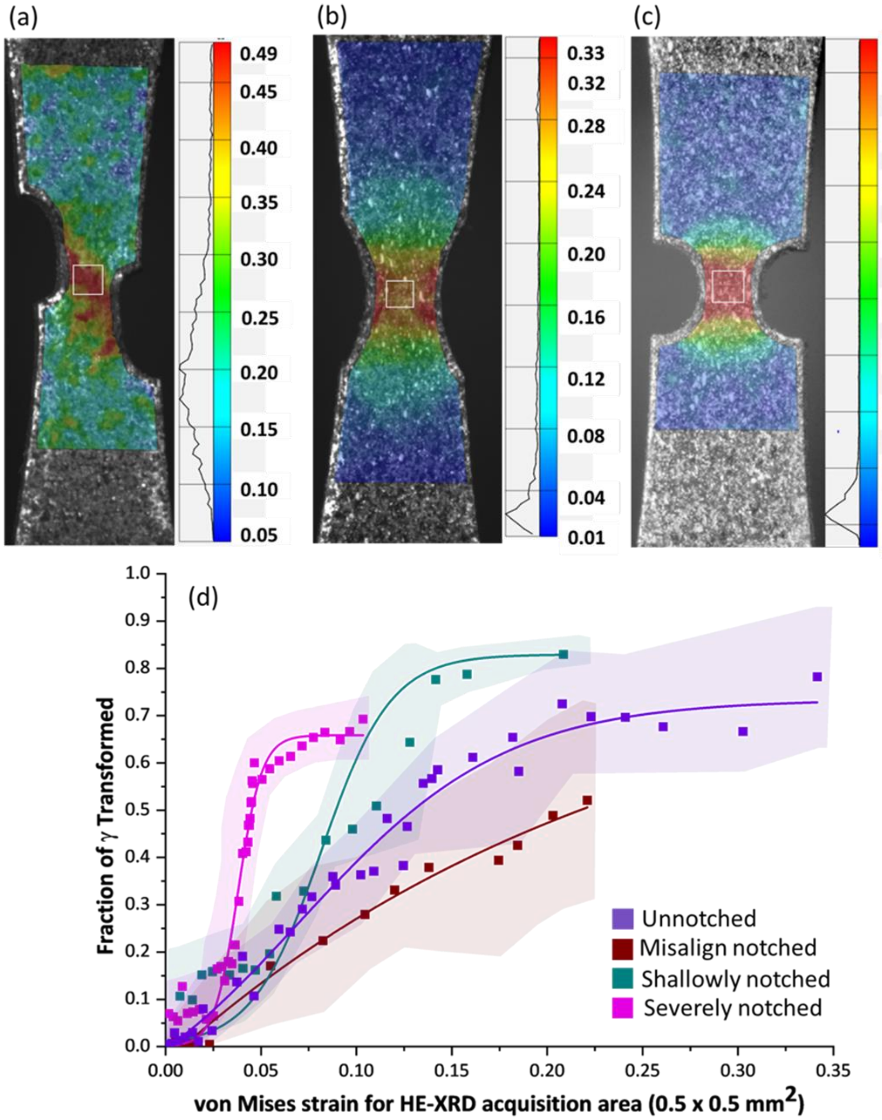

Figure 7.4: The TRIP kinetics of this med-Mn steel at different tensile stress-states – unnotched, misaligned, shallowly, and severely notched specimens. The shaded regions in Figure 7.4 show the 95% confidence interval (CI) span of ɣ fraction transformed for every tensile stress-state tested with increasing von Mises strain.

7.5.2 Microstrain Partitioning of Unnotched and Notched tensile Specimens

The microstrain partitioning of the ɣ-M and F-TM regions of the unnotched and notched specimens has been evaluated in 2D using in-situ SEM tensile testing coupled with μDIC. The electropolishing micro-speckle patterning methodology outlined in section 7.4.3 was used for this analysis, in which an EBSD map was conducted before in-situ SEM tensile testing to distinguish between FCC (ɣ) and BCC (F-TM) phases. The von Mises strain graphed in Figure 7.5i refers to the average strain computed over the entire SEM imaged area ($\varepsilon_{\mathrm{Avg}}$) whereas the average phase strain refers to the strain accommodated by the different ɣ-M and F-TM regions within the SEM imaged area. This is termed as $\varepsilon_{\gamma-\mathrm{M,phase}}$ and $\varepsilon_{\mathrm{F-TM,phase}}$ respectively.

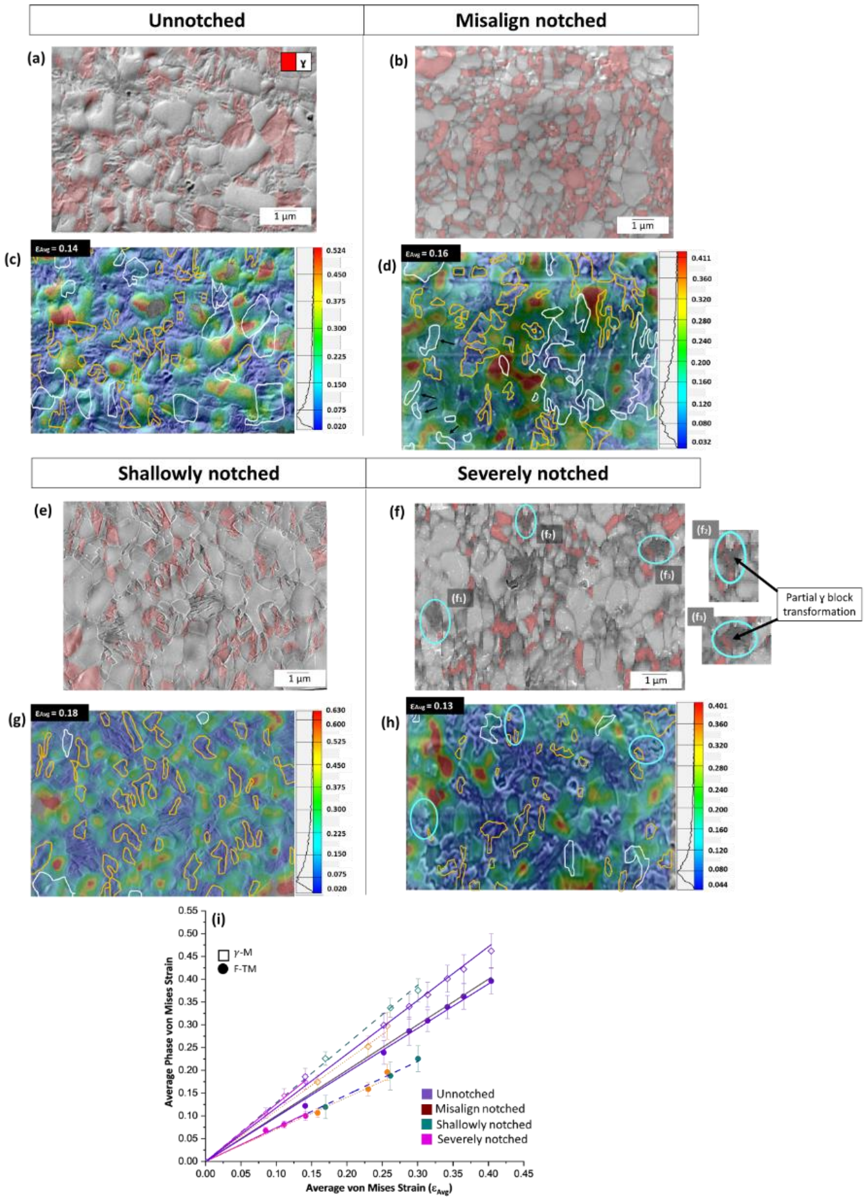

Figure 7.5: Microstrain partitioning between ɣ-M and F-TM phases of unnotched and notched specimens of this med-Mn steel at its 685°C IA condition. Figure 7.5a, d, e, and f are EBSD phase maps, with the initial ɣ coloured red, superimposed by the electropolished SEM image and Band Contrast map. Figure 7.5c, d, g, and h are µDIC maps of each tensile geometry strained to an $\varepsilon_{\mathrm{Avg}} \approx 0.15 \pm 0.02$. Outlined yellow regions in µDIC maps show the location of the initial ɣ experiencing local strains ($\varepsilon_{\mathrm{local}}$) ≤ 0.08 and outlined white regions in µDIC maps show the location of the initial ɣ experiencing $\varepsilon_{\mathrm{local}} \geq 0.15$. Figure 7.5i plots the microstrain partitioning quantified between ɣ-M and F-TM phases for each tensile geometry. 95% CI Error bars were computed from triplicate measurements for each tensile geometry tested.

The volume fraction of initial austenite captured in the unnotched, misaligned and shallowly notched specimens during in-situ SEM tensile testing is 22±4%. This is within the representative range expected from the EBSD analysis conducted on unnotched specimens at this IA condition in(Pelligra et al., 2024a, in draft), 14-26 vol%. In addition, due to the discrepancy in initial ɣ volume fraction obtained from EBSD versus X-ray Diffraction experiments, (Pelligra et al., 2024a, in draft) has speculated that ≈10-15% of the reverted ɣ is in the form of thin interlath films, not resolvable via SEM. Moreover, it is critical to note that the differentiation between ferrite and TM of this med-Mn at its 685°C IA condition is virtually impossible for the resolution used for in-situ SEM tensile testing. The area fraction of carbides within the TM is low ($2x10^{-4}$) for this IA condition, and the Ti-enriched nanoscale carbides have been previously identified with a Transmission Electron Microscope (TEM)(Pelligra et al., 2024a, in draft). The initial ɣ volume fraction changes in the severely notched specimens, achieving a volume fraction of ~9%, as shown in Figure 7.5f. It is reasonable to assume that during wEDM machining of such tight radii notches in microtensile specimens, a significant proportion of weakly Mn or C enriched ɣ would have transformed to martensite. Black, unindexed regions within the band contrast overlayed on the phase map in Figure 7.5f, shows instances of transformed martensite in the microstructure. Specifically, partial block ɣ transformations can be noted, as shown in Figure 7.5f_{1-3}. This has been reported by several others in TRIP steels (Pelligra et al., 2024b; Polatidis et al., 2020; Salehiyan et al., 2020).

The unnotched specimen with an initial triaxiality of 0.33, shows the least strain partitioning between ɣ-M and F-TM phases at all strains tested. As can be seen in Figure 7.5a and c, and graphed in Figure 7.5i. At an $\varepsilon_{Avg} \approx 0.14$, austenite grains (coloured in red in Figure 7.5a), specifically those ranging from 0.6-0.7µm in size (outlined in white in Figure 7.5c) experienced high local strains, $\varepsilon_{local} \geq 0.15$. On the other hand, austenite grains less than 0.6µm in size exhibited little to no deformation, reaching an $\varepsilon_{local} \leq 0.08$, as outlined in yellow in Figure 7.5c.

With an incremental increase in triaxiality, 0.36, achieved with misaligned notch tensile geometry, the ɣ islands that experienced the highest ε_{local} strains were not confined to those ≥0.6µm in size, as seemed to be the case with the unnotched specimens. Islands of ɣ ≤0.4µm in size experienced high ε_{local} strains (≥ 0.15) in the misaligned notched specimen, as pointed out by the black arrows in Figure 7.5b. For the shallowly notched specimen, with a ≈ 2x increase in triaxiality compared to the unnotched specimen (Appendix A, Table A 7.1),at an $\varepsilon_{Avg} \approx 0.18$, most ɣ islands showed little to no deformation, achieving a max $\varepsilon_{local} \approx 0.08$, as shown in Figure 7.5g. Lastly, most ɣ islands featured in the severely notched specimen, with an ≈ 2.5x increase in triaxiality from the unnotched specimen featured little to no deformation (max $\varepsilon_{local} \approx 0.08$), as shown in Figure 7.5h. Similar to the misaligned notched specimen in Figure 7.5d, the shallowly and severely notched specimens showed that ɣ islands which experienced the highest ε_{local} strains were not limited to those ≥0.6µm in size (Figure 7.5g and h, respectively). This indicates that neither the increased presence of shear stresses as a result of the misaligned notched tensile geometry, nor the ɣ size, whether greater or less than a diameter of 0.6µm, controls the ε_{local} strains that can be experienced by ɣ islands.

Quantitatively, as can be seen in Figure 7.5i, at an $\varepsilon_{Avg} \approx 0.25$, that there is a ∼1.7x increase in microstrain partitioning between phases in the misaligned notched compared to the unnotched specimen, whereas a ∼2.5x increase in microstrain partitioning between phases was observed in the shallowly notched compared to the unnotched specimen. Ultimately, Figure 7.5i shows that the F-TM phases is more affected by the changes in triaxiality with notched specimens, in comparison to the ɣ-M phases. For example, at a $\varepsilon_{Avg} = 0.14$, the phase strain accommodated by the ɣ-M is $\varepsilon_{\gamma-\mathrm{M,phase}} = 0.1$ whereas the phase strain accommodated by the F-TM is $\varepsilon_{\mathrm{F-TM,phase}} = 0.15$ in the severely notched specimen. As a result, from this analysis, we can report that the ability for ɣ to deform is governed by the chemical stability (i.e. degree of Mn enrichment) and the ability for its locally surrounding phases to accommodate its shape/volume changes during with increased deformation (Xiong et al., 2013) and not changes in global triaxiality. On the other hand, changes in triaxiality influences the microstrain partitioning between phases in this med-Mn steel, since F-TM phases are sensitive to these modifications.

7.5.3 µXCT of Unnotched and Notched tensile Specimens

The presence of significant plastic deformation and/or catastrophic damage events at high strains makes microstrain correlation less likely to be captured using quasi in-situ SEM tensile testing coupled with µDIC. As a result, and in addition to providing bulk measurements of damage, 2D µDIC investigations have been supplemented with 3D µXCT analyses. Scanning of fractured unnotched, shallowly and severely notched specimens using µXCT enables damage evolution to be quantified as a function of local true strain ($\varepsilon_{\mathrm{loc}}^{\mathrm{True}}$), using a reconstructed cross sectional analysis (Samei et al., 2018; Zhou, 2018). Damage evolution as a function of $\varepsilon_{\mathrm{loc}}^{\mathrm{True}}$could not be computed from a fractured misaligned notched specimen due to its slant-type fracture. Furthermore, as a result of the intensive shear fracture these misaligned notched specimens experienced, no voids were capturable via µXCT. This is consistent with the work of Lorthios et al. (2010) who documented suppressed void growth in tensile testing of a 'butterfly-gauge' specimen geometry which also produced a slant-type fracture. Furthermore, the computation of various 2D damage evolution properties, such as the void area fraction, void density and average void size has been explained elsewhere (Landron et al., 2011; Maire et al., 2008; Samei et al., 2019; Zhou, 2018). To limit the notch effect on the $\varepsilon_{\mathrm{loc}}^{\mathrm{True}}$ calculation of shallowly and severely notched specimens, only a volume of ~400 µm below the fracture surface was considered (Pelligra et al., 2022).

The effect of increased stress triaxialities on TRIP kinetics and damage was conducted using the 685°C IA condition of this med-Mn steel, not only because of it achieved prolonged TRIP kinetics in comparison to the other IA conditions tested (Pelligra et al., 2024a), but also for its damage evolution properties. Unnotched specimens at this IA condition, in comparison to the others tested previously (Pelligra et al., 2024a) showed the largest void density (i.e. significant void nucleation), but lowest void area fraction (i.e. least void coalescence/growth) just before fracture. This is consistent with the speculation made by Sun et al. (2019) in which the local compressive stresses imposed by the transformation from ɣ-to-martensite during necking opposes void growth and coalescence.

The closed void area fraction (i.e. a measure of void growth/coalescence of void just before fracture) for the unnotched, shallowly and severely notched specimens is demonstrated in Figure 7.6a. Damage evolution is fastest for the severely notched specimen, Figure 7.6a. Many nano-scaled voids remained unidentified until a $\varepsilon_{\mathrm{loc}}^{\mathrm{True}}$ of ≈0.4-0.6 due to the limited µXCT pixel resolution of 0.9µm, and this steel's fine microstructure. We have captured the presence of these nano-scaled voids, with diameters of ≈0.02-0.6µm, using quasi in-situ SEM tensile testing of unnotched specimens in (Pelligra et al., 2024a, in draft) and notched specimens in Appendix C, Figure C 7.1.

As well, it should be noted that damage indeed occurs catastrophically in this material, such that most damage events were detected within the final 10% of strain as shown in Figure 7.6. This trend in damage evolution is comparable to that presented by Landron et al. (2011) on unnotched and notched DP tensile specimens, in which they too fitted their data to exponential curves.

Interestingly, all tensile specimen geometries tested, reach a closed void area fraction of 0.07±0.01 just before fracture. This suggests that within a stress triaxiality range of 0.33-0.89, there is a critical void size within this med-Mn TRIP microstructure that once reached activates an exponential rise in void coalescence/growth and leads to fracture. This critical void size is reached earliest for the severely notched specimens. Moreover, a 0.07±0.01 void area fraction just before fracture is similar to that reached by unnotched 3G DP steel tensile specimens examined in Zhou (2018). However, in that work, due to the ultrahigh strength of their steel (≈1300MPa) and its corresponding ≈50% martensitic microstructure, thefracture strain is significantly lower (0.25-0.4) compared to this steel of study.

In addition, the void density (i.e. a measure of void nucleation) just before final fracture, featured in Figure 7.6b shows is a ≈±3σ sigmoidal trend with strain for all three tensile specimen geometries. This inflection-type increase in void density in Figure 7.6b, was also captured by Samei et al. (2019). First, the density of voids rises at an increasing rate up to an inflection point of $\varepsilon_{\mathrm{loc}}^{\mathrm{True}}$ ≈ 0.50±0.06, then continues to rise but at a decreasing rate up to fracture. Past this inflection point, the transformation from ɣ-to-martensite, or the local intensive regions of micro-shearing as shown in the Appendix C, Figure C 7.1, is likely the reason for a reduction in void nucleation rate (Jacques et al., 2001; Parker and Zackay, 1973; Samei et al., 2020). Furthermore, this corroborates well with the µDIC maps presented in Appendix C, Figure C 7.1 in which the shallowly and severely notched specimens, showed, no evidence of micro-cracking up until a $\varepsilon_{\mathrm{Avg}}$ ≈0.16. Blocky ɣ or martensite island cracking was also not observed despite the increased stress triaxiality with introduced the notches at different radii and showed little to no deformation, as shown in Appendix C, Figure C 7.1 outlined in black. This is synchronous to the observation made in section 7.5.2 in which most austenitic islands in the severely notched specimen reached only a max ε_{local}≈0.08 at high ε_{Avg} values.

From the study carried out by Landron et al. (2011) using synchrotron-based tomography, void nucleation should be accelerated with increased stress triaxiality introduced by notched specimens. Yet, in this material, the fact that there is only a ≈±3σ difference in the density of voids with increasing strain indicates that micro-shearing and rapid TRIP kinetics work together to suppress void nucleation at higher stress triaxialities.

It is important to note that although fluctuations in void density, as pointed out in Figure 7.6b with black arrows, could be the result of experimental or thresholding error involved with µXCT dataset post-processing, these minute decreases in void density could be the result of localized TRIP supressing void nucleation, growth or coalescence. Detailed, highly resolved, synchrotron-sourced tomography studies would be required to validate this theory, in which similar experiments have been performed by others (Schoell et al., 2022; Toda et al., 2022; Withers, 2015).

The average void area was computed by dividing the area fraction of voids by the number of voids per cross-sectional reconstructed slice (Samei et al., 2019; Zhou, 2018), as shown in Figure 7.6d. In turn, with the assumption that each void is circular (πR^2), the average void diameter for all voids (Figure 7.6e).

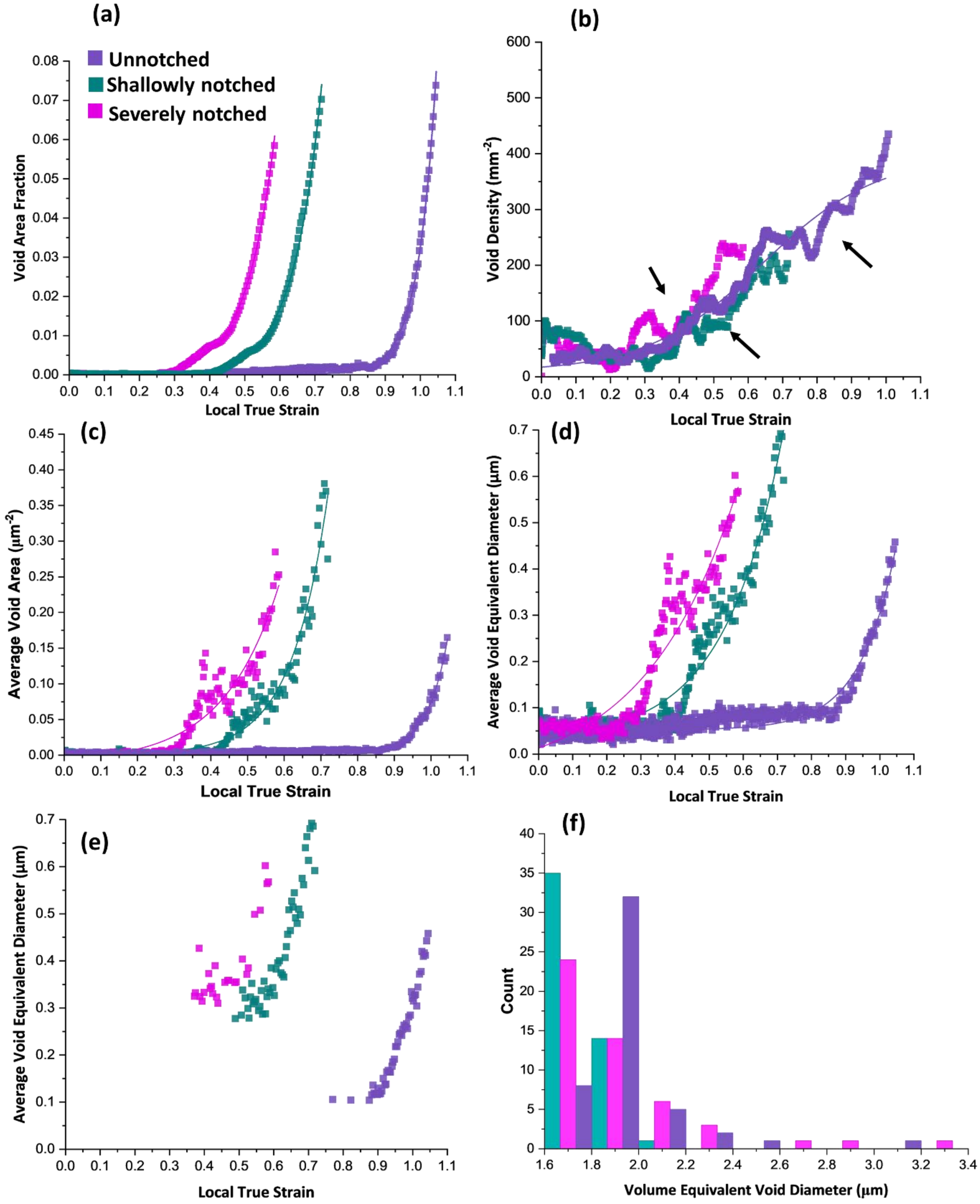

Figure 7.6: XCT analysis of the void volume fraction (a), void density (b), average void area (c) and average void size (d) as a function of ε_{loc}^{True} for fractured unnotched, shallowly and severely notched specimens. Figure 7.6d is the average void size, assuming each void is circular, and Figure 7.6e considers the 50 largest of these average void diameters as a function of ε_{loc}^{True}. Figure 7.6f is the 50 largest volume equivalent void diameters, assuming each void grows to be spherical.

Furthermore, it is helpful to examine the largest voids, such as the 50 and 100 largest voids, to negate the effect of void nucleation (Maire et al., 2012) and to determine the impact that the introduced notches have on void growth in this steel subjected to different levels of triaxiality. The 50 average largest void diameters and 50 largest void diameters per tensile geometry is shown in Figure 7.6e and f, respectively. The benefit of segregating the 50 average largest voids from the full void population, obtained through the cross-sectional analysis performed in Figure 7.6e, enables one to define the strains at which coalescence occurs. On the other hand, Figure 7.6f shows the 'outliers' within the average largest voids in Figure 7.6e which grow to contribute most to the fracture process. Presented in Figure 7.6f is a histogram of the 50 largest voids, which have volume equivalent void diameters >1.5µm. As noted in section 7.4.4, after post-processing, only objects with a minimum volume of $14.6\mu\mathrm{m}^3$ were considered in the analysis, and therefore, assuming each void grew spherically ($\frac{4}{3}\pi\mathrm{R}^3$), only voids >1.5µm in volume equivalent diameter can be accounted for. Consistent with the graph in Figure 7.6e, most voids which contribute to fracture are 1.9 µm for the unnotched specimen, and 1.8 µm for the shallowly as well as severely notched specimens. This reduction in void size computed with increased stress triaxiality using µXCT has been noted previously (Pelligra et al., 2022).

7.5.4 Damage Evolution and Fracture of Unnotched and Notched Specimens

In general, cup-cone-type ductile fracture was observed in the unnotched, shallowly and severely notched specimens. The misaligned notched specimen, rather, shows slant-type fracture. As per Bao and Wierzbicki (2004), this indicates that facture in the unnotched, shallowly and severely notched specimen occurred as a result of void formation and coalescence. On the other hand, the slant-type fracture is a result of shear stresses introduced by the misaligned notches. This slant-type fracture happened despite having a triaxiality similar to that of the unnotched specimens, as shown in Figure 7.2c, and tabulated in Appendix A, Table A 7.1. The unnotched sample showed significant necking suggesting that this med-Mn steel fractures in a ductile manner, even though quasi cleavage cracks are present throughout its fracture surface, as pointed out in Figure 7.7a, a_{1B} and a_{2B}. Dimples on the fracture surface range from ~1.5µm to ultrafine sizes, as pointed out specifically in Figure 7.7a_{2B}. Longitudinal, delamination cracks are present in the unnotched, shallowly notched and severely notched specimen, but are longest in the unnotched specimen (~1100 µm), as shown in Figure 7.7a. These delamination cracks can be arrested by densely ultra-fine dimpled regions at the centre of the fracture surface, as observed elsewhere (Liu et al., 2018). It is said that these dimpled regions can alleviate some of stress at the crack tip and slows crack propagation (Liu et al., 2018). For the unnotched specimen, however, a central delamination crack was apparent (Figure 7.7a$_{1A}$), which is not the case for the shallowly or severely notched specimens' fracture surfaces (Figure 7.8a and b, respectively). For the misaligned notched specimen's fracture surface, no delamination cracks are apparent as shown in Figure 7.7b and b$_1$. This is due to the fact that there was not enough time for these cracks to form before the brittle-slant-type fracture occurred. Elongated and structure-less dimples were also observed on fractured surfaces by Pyshmintsev et al. (2002) in which the low normal-to-shear stress (high hydrostatic pressure) results in austenite dislocation glide rather than TRIP. This can explain the large amount of necking exhibited by the despite its slant-type fracture.

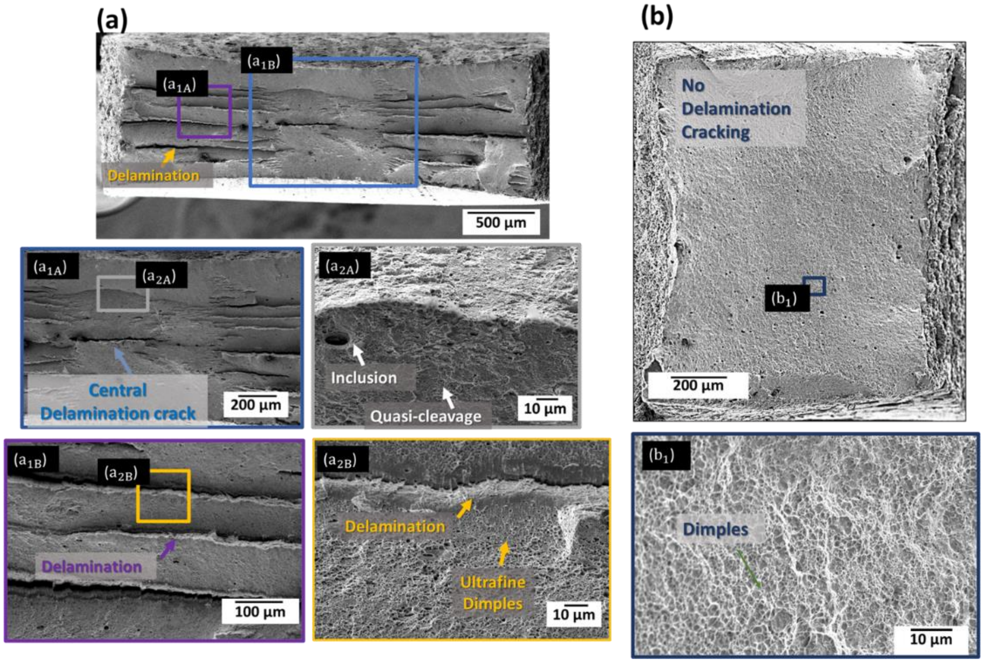

Figure 7.7: Fracture surfaces of the unnotched specimens (a) and misaligned notched specimens (b) used for HE-XRD experiments. For the unnotched specimens, Figure 7.7a$_1$ and a$_2$ points out the sides of the fracture surface with delamination cracks and central fractured region, respectively. In Figure 7.7b, and b$_1$ no delamination cracking and only dimples are apparent.

In the case of the shallowly notched specimen, deep delamination cracks, ranging ~250-500µm in length, are successfully being arrested by densely dimpled regions within the centre as shown in Figure 7.8a and a$_1$. Figure 7.8a$_2$, shows a micro-crack, likely from a cracked inclusion, which has been arrested from propagating as a result of the high density of surrounding ultrafine dimples. For both the unnotched, shallowly and severely notched specimens' fracture surfaces, regions of quasi-cleavage are present (Figure 7.8a$_1$). On the other hand, the severely notched specimens, deep delamination cracks (~200 µm in length) are less frequent, as shown in Figure 7.8b. Most micro-cracks in these specimens are shallow and visible quasi-cleavage regions of fracture are apparent (Figure 7.8b).

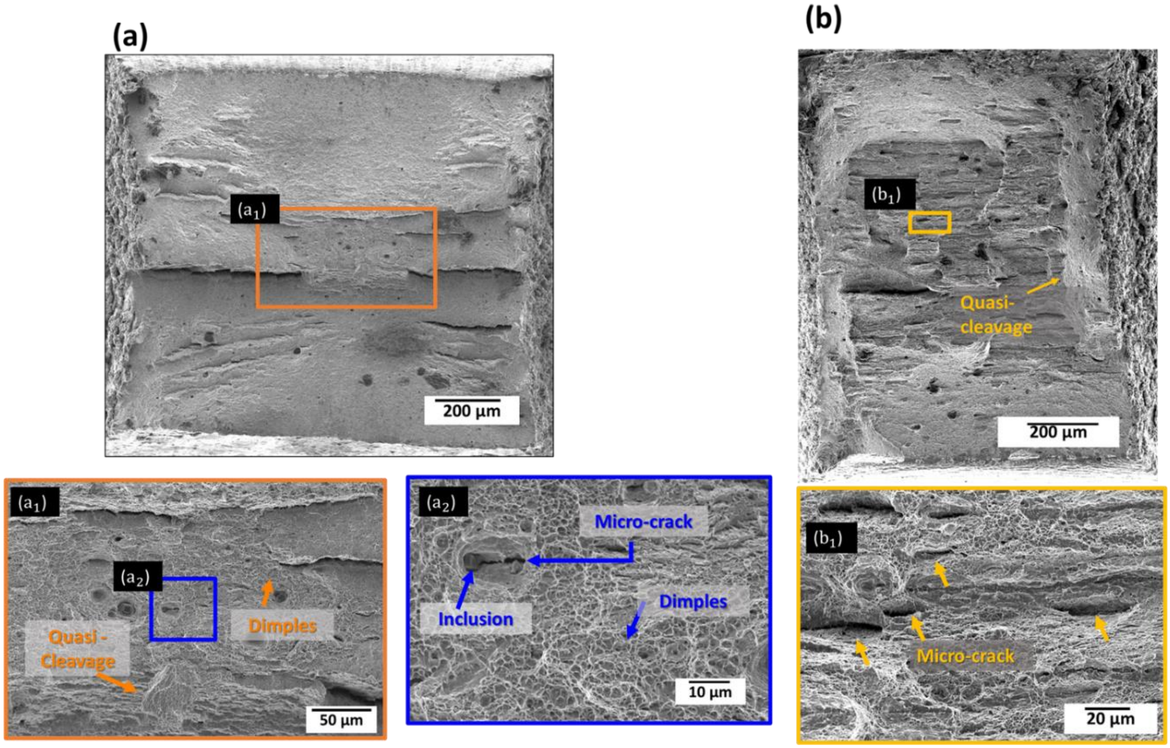

Figure 7.8: Fracture surfaces of the shallowly notched (a) and severely specimens (b) used for HE-XRD experiments. For the shallowly notched specimens, Figure 7.8a$_1$ points out regions of quasi-cleavage fracture, and dimples throughout the fracture surface. Figure 7.8b$_1$ and b$_2$ focuses on the central fractured region of the shallowly notched specimens, as fewer and shorter delamination cracks at the fracture surface's sides were present in this instance.

7.6 Summary Remarks and Future Considerations

In this paper, we extend upon the previous work conducted on unnotched samples of a med-Mn steel (Pelligra et al., 2024a, in draft), to understand the impact that variations in stress triaxiality, within the 0.33-0.89 range, has on TRIP kinetics, microstrain partitioning and damage evolution. Variations in stress triaxiality were achieved with the introduction of notches in tensile specimens. A highly resolved quantification of the ɣ as a function of strain was captured with the use of synchrotron-sourced HE-XRD in which the fastest rate of TRIP exhaustion was exhibited by the severely notched specimens while the slowest was featured by the misaligned notched specimens. This is likely the result of the increased σ_m in the severely notched specimens easily accommodating the volume expansion associated with TRIP, while the variation in σ_m within the central region of the misaligned notched tensile geometry is likely suppressing TRIP and instead encouraging plastic deformation.

Microstrain partitioning amongst phases was successfully evaluated with the use of in-situ SEM tensile testing coupled with EBSD and µDIC on electropolished micro-speckled specimens while a reliable 3D quantification of damage was obtained with the use µXCT. Our µDIC analyses on unnotched and notched specimens revealed that changes in stress triaxiality within the 0.33-0.89 range has a stronger effect on F-TM versus ɣ-M phases. This suggests that, despite the increase in global stress triaxiality, the ability for ɣ to deform/TRIP is supremely governed by its chemical stability and the ability for its locally surrounding phases to accommodate its shape/volume changes.

Furthermore, the µXCT data collected on all tensile specimen geometries showed a 0.07±0.01 closed void area fraction just before fracture. This ultimately suggests that once a void grows to a particular size, coalescence starts and proceeds at an exponential rate up until fracture. On the other hand, the void nucleation *rate*/evolution of void density is relatively similar (≈±3σ) for all tensile geometries tested. More importantly, the evolution of void density is sigmoidal in nature in which after an inflection point of strain is reached, the rate of void nucleation is reduced. The additional compressive stresses imposed by the ɣ-to-martensite transformation could be suppressing voids from nucleating even with an increased state of stress triaxiality.

To conclude, this work documents the impact a 0.33-0.98 change in stress triaxiality has on the TRIP kinetics, microstrain partitioning, and damage evolution in a med-Mn microstructure. We, however, recommend that further work be devoted to understanding the dynamic behavior of these three material characteristics under more complex/non-tensile/low stress triaxiality straining conditions (i.e. compression/rolling, intensive shear, etc.). Along with this, as noted by Pelligra et al. (2024b), the use of different specimen sizes as wellmethods of quantifying strain in the multiple experimental techniques used in the present paper makes the coupling of 2D and 3D experimental datasets non-trivial. That being said, further software/instrumental developments need to be made such that consistency in specimen design and the methods of quantifying strain between experimental techniques is applied.

7.7 Acknowledgements

The authors would like to acknowledge the financial support of NSERC (grant CRDJ522309-17) and International Zinc Association (IZA)-Galvanizing Association Partnership (GAP) members. US steel R&D is gratefully acknowledged for their in-kind fabrication of this prototype Med-Mn steel. We acknowledge the many fruitful discussions with Dr. Joseph R. McDermid concerning this project. The authors would like to acknowledge the help of Shraryar Asqardout, Abhishek Sarmah and Mahmoud Diab for their FEM ABAQUS simulation advice. The authors would also like to acknowledge beamline scientists, Dr. Andrey Andreevich Yackovenko and Dr. Tyra Chenice Douglas along with Nizia Mendes Fonseca and Cal Siemens for their technical support with HE-XRD experiments. Use of the Advanced Photon Source was supported by the U. S. Department of Energy, Office of Science, Office of Basic Energy Sciences, under Contract No. DE-AC02-06CH11357.

7.8 References

Abu-Farha, F., Hu, X., Sun, X., Ren, Y., Hector, L.G., Thomas, G., Brown, T.W., 2018. In Situ Local Measurement of Austenite Mechanical Stability and Transformation Behavior in Third-Generation Advanced High-Strength Steels. Metall Mater Trans A Phys Metall Mater Sci 49, 2583–2596. https://doi.org/10.1007/s11661-018-4660-x

Bao, Y., Wierzbicki, T., 2004. On fracture locus in the equivalent strain and stress triaxiality space. Int J Mech Sci 46, 81–98. https://doi.org/10.1016/j.ijmecsci.2004.02.006

Beese, A.M., Mohr, D., 2011. Effect of stress triaxiality and Lode angle on the kinetics of strain-induced austenite-to-martensite transformation. Acta Mater 59, 2589–2600. https://doi.org/10.1016/j.actamat.2010.12.040

Bellhouse, E.M., 2010. GALVANIZING OF AL-SI TRIP-ASSISTED STEELS. McMaster University.

Bhadhon, K.M.H., McDermid, J.R., Wang, X., McNally, E.A., Goodwin, F.E., 2017. Fine-Scale Microstructure Characterization And Mechanical Properties Of CGL-Compatible Heat Treated Medium-Mn TRIP Steel. Proceedings of Galvatech 2017 493–500.

Bouaziz, O., Zurob, H., Huang, M., 2013. Driving Force and Logic of Development of Advanced High Strength Steels for Automotive Applications. Steel Res Int 84, 937–947.

Brünig, M., Chyra, O., Albrecht, D., Driemeier, L., Alves, M., 2008. A ductile damage criterion at various stress triaxialities. Int J Plast 24, 1731–1755. https://doi.org/10.1016/j.ijplas.2007.12.001

Buffière, J.-Y., Maire, E., Cloetens, P., Lormand, G., Fougères, R., 1999. Characterization of internal damage in a MMCp using X-ray synchrotron phase contrast microtomography. Acta Mater 47, 1613–1625. https://doi.org/10.1016/S1359-6454(99)00024-5

Choudhary, R., Kumar, H., Garg, R.K., 2010. Analysis and evaluation of heat affected zones in electric discharge machining of EN-31 die steel. Indian Journal of Engineering and Materials Sciences 17, 91–98.

De Cooman, B., Kwon, O., Chin, K., 2012. State-of-the-knowledge on TWIP steel. Materials Science and Technology 28, 513–527. https://doi.org/10.1179/1743284711Y.0000000095

De Moor, E., Gibbs, P.J., Speer, J.G., Matlock, D.K., 2010. Strategies for Third-Generation Advanced High Strength Steel Development. Iron and Steel Technology 7, 133–144.

Demania, D., 1995. The influence of martensitic transformation on the formability of 304L stainless steel sheet. MIT, Cambridge.

Dutta, A., Ponge, D., Sandlöbes, S., Raabe, D., 2019. Strain partitioning and strain localization in medium manganese steels measured by in situ microscopic digital image correlation. Materialia (Oxf) 5. https://doi.org/10.1016/j.mtla.2019.100252

Fabrègue, D., Landron, C., Bouaziz, O., Maire, E., 2015. Comparison of Damage Evolution in Different Steels by Means of 3D X Ray Tomography. Steel Res Int 86, 1197–1203. https://doi.org/10.1002/srin.201500072

Fabrègue, D., Landron, C., Bouaziz, O., Maire, E., 2013. Damage evolution in TWIP and standard austenitic steel by means of 3D X ray tomography. Materials Science and Engineering: A 579, 92–98. https://doi.org/10.1016/J.MSEA.2013.05.013

Findley, K.O., Golem, L.L., Cho, L., Clarke, K.D., n.d. Evaluating crash relevant properties of advanced high strength steels.

Fischer-Cripps, A.C., 2007. Introduction to Contact Mechanics. Springer US, Boston, MA. https://doi.org/10.1007/978-0-387-68188-7

Gibbs, P.J., De Moor, E., Merwin, M.J., Clausen, B., Speer, J.G., Matlock, D.K., 2011. Austenite Stability Effects on Tensile Behavior of Manganese-Enriched-Austenite Transformation-Induced Plasticity Steel. Metallurgical and Materials Transactions A 42, 3691–3702. https://doi.org/10.1007/s11661-011-0687-y

gom, 2016. GOM Correlate. Gom.Com.

Hance, B., 2016. Advanced high strength steel: Deciphering local and global formability. International Automotive Body Congress, IABC 2016 DEARBORN - Papers.

Hoefnagels, J.P.M., van Maris, M.P.F.H.L., Vermeij, T., 2019. One-step deposition of nano-to-micron-scalable, high-quality digital image correlation patterns for high-strain in-situ multi-microscopy testing. Strain 55. https://doi.org/10.1111/str.12330

Hu, X.H., Sun, X., Hector, L.G., Ren, Y., 2017. Individual phase constitutive properties of a TRIP-assisted QP980 steel from a combined synchrotron X-ray diffraction and crystal plasticity approach. Acta Mater 132, 230–244. https://doi.org/10.1016/J.ACTAMAT.2017.04.028

Inglis, C., 1913. Stresses in a plate due to the presence of cracks and sharp corners.

Jacques, P., Furnemount, Q., Pardoen, T., Delannay, F., 2001. On the Role of Martensitic Transformation on Damage and Cracking Resistance in Trip-assisted multiphase steels. Acta Mater 49, 139–152. https://doi.org/10.1016/S1359-6454(00)00215-9

Jacques, P.J., Delannay, F., Ladrière, J., 2001. On the influence of interactions between phases on the mechanical stability of retained austenite in transformation-induced plasticity multiphase steels. Metall Mater Trans A Phys Metall Mater Sci 32, 2759–2768. https://doi.org/10.1007/s11661-001-1027-4

Jacques, P.J., Furnémont, Q., Lani, F., Pardoen, T., Delannay, F., 2007. Multiscale mechanics of TRIP-assisted multiphase steels: I. Characterization and mechanical testing. https://doi.org/10.1016/j.actamat.2007.02.029

Kang, J., Ososkov, Y., Embury, D.J., Wilkinson, D.S., 2007. Digital image correlation studies for microscopic strain distribution and damage in dual phase steels. Scr Mater 56, 999–1002. https://doi.org/10.1016/j.scriptamat.2007.01.031

Kang, J., Wilkinson, D.S., Embury, J.D., Jain, M., 2005. Microscopic Strain Mapping Using Scanning Electron Microscopy Topography Image Correlation at Large Strain. J Strain Anal Eng Des 40, 559–570. https://doi.org/10.1243/030932405X16151

Kumar, R., Besson, J., King, A., Dahl, A., Morgeneyer, T.F., 2023. X-ray microtomography investigation of damage fields ahead of cracks in CT and SENT C-Mn steel samples. Int J Fract 239, 233–254. https://doi.org/10.1007/s10704-022-00674-8

Landron, C., Bouaziz, O., Maire, E., Adrien, J., 2013. Experimental investigation of void coalescence in a dual phase steel using X-ray tomography. Acta Mater 61, 6821–6829. https://doi.org/10.1016/j.actamat.2013.07.058

Landron, C., Maire, E., Adrien, J., Bouaziz, O., 2011. Damage characterization in Dual-Phase steels using X-ray tomography, in: Proulx, T. (Ed.), Optical Measurements, Modeling, and Metrology, Volume 5. Springer New York, New York, NY, pp. 11–18.

Larour, P., Freudenthaler, J., Weissböck, T., 2017. Reduction of cross section area at fracture in tensile test: Measurement and applications for flat sheet steels. J Phys Conf Ser 896. https://doi.org/10.1088/1742-6596/896/1/012073

Li, Z., Kiran, R., Hu, J., Hector, L.G., Bower, A.F., 2020. Analysis and design of a three-phase TRIP steel microstructure for enhanced fracture resistance. Int J Fract 221, 53–85. https://doi.org/10.1007/S10704-019-00405-6/FIGURES/15

Lian, C., Zhang, H., Lin, J., Wang, L., 2021. Deformation mechanism and microstructure evolution of medium-Mn AHSS under various loading conditions. Int J Mech Sci 212. https://doi.org/10.1016/j.ijmecsci.2021.106812

Liu, C., Peng, Q., Xue, Z., Wang, S., Yang, C., 2018. Microstructure and Mechanical Properties of Hot-Rolled and Cold-Rolled Medium-Mn TRIP Steels. https://doi.org/10.3390/ma11112242

Lorthios, J., Nguyen, F., Gourgues, A.-F., Morgeneyer, T.F., Cugy, P., 2010. Damage observation in a high-manganese austenitic TWIP steel by synchrotron radiation computed tomography. Scr Mater 63, 1220–1223. https://doi.org/10.1016/j.scriptamat.2010.08.042

Maire, E., Bouaziz, O., Di Michiel, M., Verdu, C., 2008. Initiation and growth of damage in a dual-phase steel observed by X-ray microtomography. Acta Mater 56, 4954–4964. https://doi.org/10.1016/j.actamat.2008.06.015

Maire, E., Morgeneyer, T., Landron, C., Adrien, J., Helfen, L., 2012. Bulk evaluation of ductile damage development using high resolution tomography and laminography. Elsevier 328–336.

Mansourinejad, M., Ketabchi, M., 2017. Modification of Olson–Cohen model for predicting stress-state dependency of martensitic transformation. Materials Science and Technology (United Kingdom) 33, 1948–1954. https://doi.org/10.1080/02670836.2017.1342016

Matlock, D.K., Speer, J.G., 2009. Third Generation of AHSS: Microstructure Design Concepts, in: Microstructure and Texture in Steels. Springer London, London, pp. 185–205. https://doi.org/10.1007/978-1-84882-454-6_11

Mehrabi, A., McDermid, J.R., Wang, X., Zurob, H., 2023. Austenite Nucleation and Growth as a Function of Starting Microstructure for a Fe–0.15C–5.56Mn–1.1Si–1.89Al Medium-Mn Steel. Steel Res Int. https://doi.org/10.1002/srin.202200952

Morgeneyer, T.F., Starink, M.J., Sinclair, I., 2008. Evolution of voids during ductile crack propagation in an aluminium alloy sheet toughness test studied by synchrotron radiation computed tomography. Acta Mater 56, 1671–1679. https://doi.org/10.1016/j.actamat.2007.12.019

Mummery, P.M., Derby, B., 1994. In situ scanning electron microscope studies of fracture in particulate-reinforced metal-matrix composites. J Mater Sci 29, 5615–5624.

Nan, C.-W., Clarke, D.R., 1996. The Influence of Particle Size and Particle Fracture on the Elastic/Plastic Deformation of Metal Matrix Composites. Acta Mater 44, 3801–3811.

Olson, G.B., Cohen, M., 1975. Kinetics of strain-induced martensitic nucleation. Metallurgical Transactions A 6, 791–795. https://doi.org/10.1007/BF02672301

Pallisco, D.M., McDermid, J.R., 2020. Mechanical property development of a 0.15C–6Mn–2Al–1Si third-generation advanced high strength steel using continuous galvanizing heat treatments. Materials Science and Engineering A 778, 139111. https://doi.org/10.1016/j.msea.2020.139111

Pallisco, D.M., McDermid, J.R., McNally, E.A., Goodwin Frank E., 2017. Effect of Starting Microstructure and Intercritical Annealing Parameters on the Mechanical Property Development of a Medium-Mn Third-Generation Advanced High Strength Steel. Galvatech 782–789.

Park, T., Hector Jr., L.G., Hu, X., Abu-Farha, F., Fellinger, M.R., Kim, H., Esmaeilpour, R., Pourboghrat, F., 2019. Crystal plasticity modeling of 3rd generation multi-phase AHSS with martensitic transformation. International Journal of Plasticity 120, 1–46.

Parker, E.R., Zackay, V.F., 1973. ENHANCEMENT OF FRACTURE TOUGHNESS IN HIGH STRENGTH STEEL BY MICROSTRUCTURAL CONTROL. Engineering Fract Mechanics 5, 147–165.

Patel, J.R., Cohen, M., 1953. Criterion for the action of applied stress in the martensitic transformation. Acta Metallurgica 1, 531–538. https://doi.org/10.1016/0001-6160(53)90083-2

Patel, V., 2019. Microstructure and Mechanical Properties of Medium Mn steel. McMaster University.

Pelligra, C., Amirkhiz, B.S., Zafer, N., Kang, J., Wilkinson, D.S., 2024a. Microstrain Partitioning, Transformation Induced Plasticity, and Damage Evolution of a Third Generation Medium Mn Advanced High Strength Steel. Hamilton.

Pelligra, C., Samei, J., Kang, J., Wilkinson, D.S., 2022. The effect of vanadium on microstrain partitioning and localized damage during deformation of unnotched and notched DP1300 steels. Int J Plast 158. https://doi.org/10.1016/j.ijplas.2022.103435

Pelligra, C., Samei, J., Shalchi Amirkhiz, B., Hector, L.G., Wilkinson, D.S., 2024b. Microstrain partitioning, transformation induced plasticity, and the evolution of damage during deformation of an austenitic-martensitic 1.5 GPa quench and partition steel. Materials Science and Engineering: A 146181. https://doi.org/10.1016/j.msea.2024.146181

Polatidis, E., Haidemenopoulos, G.N., Krizan, D., Aravas, N., Panzner, T., Smíd, M.ˇ, Papadioti, I., Casati, N., Van Petegem, S., Van Swygenhoven, H., 2020. The effect of stress triaxiality on the phase transformation in transformation induced plasticity steels: Experimental investigation and modelling the transformation kinetics. https://doi.org/10.1016/j.msea.2020.140321

Pyshmintsev, I., Meyer, M., De Cooman, B., Savrai, R., Shveykin, V., Vermeulen, M., 2002. The influence of the stress state on the plasticity of transformation induced plasticity-aided steel. Metallurgical and Materials Transactions A 33, 1659–1667. https://doi.org/10.1007/s11661-002-0175-5

Ruggles, T., Cluff, S., Miles, M., Fullwood, D., Daniels, C., Avila, A., Chen, M., 2016. Ductility of Advanced High-Strength Steel in the Presence of a Sheared Edge. JOM 68, 1839–1849. https://doi.org/10.1007/s11837-016-1927-9

Salehiyan, D., Samei, J., Amirkhiz, B.S., Hector, L.G., Wilkinson, D.S., 2020. Microstructural Evolution During Deformation of a QP980 Steel. Metall Mater Trans A Phys Metall Mater Sci 51, 4524–4539. https://doi.org/10.1007/s11661-020-05882-2

Samei, J., Pelligra, C., Amirmaleki, M., Wilkinson, D.S., 2020. Microstructural design for damage tolerance in high strength steels. Mater Lett 269. https://doi.org/10.1016/j.matlet.2020.127664

Samei, J., Zhou, L., Kang, J., Wilkinson, D.S., 2019. Microstructural analysis of ductility and fracture in fine-grained and ultrafine-grained vanadium-added DP1300 steels. Int J Plast 117, 58–70. https://doi.org/10.1016/j.ijplas.2017.12.009

Samei, J., Zhou, L., Kang, J., Wilkinson, D.S., 2018. Microstructural analysis of ductility and fracture in fine-grained and ultrafine-grained vanadium-added DP1300 steels. Int J Plast 117, 58–70. https://doi.org/10.1016/j.ijplas.2017.12.009

Schoell, R., Xi, L., West, H., Hosemann, P., Park, J.-S., Kenesei, P., Almer, J., Shayer, Z., Kaoumi, D., 2022. Investigation of the fatigue crack behavior of 304 stainless steels using synchrotron X-ray tomography and diffraction: Influence of the martensite fraction and role of inclusions. Mater Charact 188, 111903. https://doi.org/10.1016/j.matchar.2022.111903

Scott, H., 2018. Effects of Microstructure and Particle Population on Void Damage Evolution in Complex Phase Steel.

Siemens, C., Kang, J., Wilkinson, D.S., 2023. In-situ investigation of damage mechanisms in duplex AlCoCrFeNi2.1 high entropy alloy. Materials Science and Engineering: A 884. https://doi.org/10.1016/j.msea.2023.145532

Speer, J., Matlock, D.K., De Cooman, B.C., Schroth, J.G., 2003. Carbon partitioning into austenite after martensite transformation. Acta Mater 2611–2622.

Stiénon, A., Fazekas, A., Buffière, J.-Y., Vincent, A., Daguier, P., Merchi, F., 2009. A new methodology based on X-ray micro-tomography to estimate stress concentrations around inclusions in high strength steels. Materials Science and Engineering: A 513–514, 376–383. https://doi.org/10.1016/j.msea.2009.02.008

Stringfellow, R.G., Parks, D.M., Olson, G.B., 1992. A constitutive model for transformation plasticity accompanying strain-induced martensitic transformations in metastable austenitic steels. Acta Metallurgica Et Materialia 40, 1703–1716. https://doi.org/10.1016/0956-7151(92)90114-T

Sun, B., Palanisamy, D., Ponge, D., Gault, B., Fazeli, F., Scott, C., Yue, S., Raabe, D., 2019. Revealing fracture mechanisms of medium manganese steels with and without delta-ferrite. Acta Mater 164, 683–696. https://doi.org/10.1016/J.ACTAMAT.2018.11.029

Tang, A., Liu, H., Chen, R., Liu, G., Lai, Q., Zhong, Y., Wang, L., Wang, J., Lu, Q., Shen, Y., 2021. Mesoscopic origin of damage nucleation in dual-phase steels. Int J Plast 137. https://doi.org/10.1016/j.ijplas.2020.102920

Tanguy, B., Besson, J., Piques, R., Pineau, A., 2005. Ductile to brittle transition of an A508 steel characterized by Charpy impact test: Part I: experimental results. Eng Fract Mech 72, 49–72.

Tasan, C.C., Diehl, M., Yan, D., Zambaldi, C., Shanthraj, P., Roters, F., Raabe, D., 2014. Integrated experimental–simulation analysis of stress and strain partitioning in multiphase alloys. Acta Mater 81, 386–400. https://doi.org/10.1016/J.ACTAMAT.2014.07.071

Toda, H., Hirayama, K., Okamura, K., Suzuki, T., Takeuchi, A., Uesugi, M., Fujihara, H., 2022. Multimodal assessment of mechanically induced transformation in metastable multi-phase steel using X-ray nano-tomography and pencil-beam diffraction tomography. Acta Mater 234, 117956. https://doi.org/10.1016/j.actamat.2022.117956

Toda, H., Takijiri, A., Azuma, M., Yabu, S., Hayashi, K., Seo, D., Kobayashi, M., Hirayama, K., Takeuchi, A., Uesugi, K., 2017. Damage micromechanisms in dual-phase steel investigated with combined phase- and absorption-contrast tomography. Acta Mater 126, 401–412. https://doi.org/10.1016/j.actamat.2017.01.010

Toda, H., Tomizato, F., Harasaki, R., Seo, D., Kobayashi, M., Takeuchi, A., Uesugi, K., 2016. 3D fracture behaviours in dual-phase stainless steel. ISIJ International 56, 883–892. https://doi.org/10.2355/isijinternational.ISIJINT-2015-631

Toda, H., Tsuruta, H., Horikawa, K., Uesugi, K., Takeuchi, A., Suzuki, Y., Kobayash, M., 2014. Effects of stress triaxiality on damage evolution from pre-existing hydrogen pores in aluminum alloy. Mater Trans 55, 383–386. https://doi.org/10.2320/matertrans.L-M2013841

Tomita, Y., Iwamoto, T., 1995. Constitutive modeling of trip steel and its application to the improvement of mechanical properties. Int J Mech Sci 37, 1295–1305. https://doi.org/10.1016/0020-7403(95)00039-Z

Vijayan, V., Murugan, S., Son, S.-G., Park, Y.-D., 2020. Metallography and Computed Tomography Analysis of the Shrinkage Cavity Formed in Advanced High-Strength Steel Resistance Spot Welds 9, 256–266. https://doi.org/10.1520/MPC20190257

Wang, K., Luo, M., Wierzbicki, T., 2014. Experiments and modeling of edge fracture for an AHSS sheet. Int J Fract 187, 245–268. https://doi.org/10.1007/s10704-014-9937-5

Wang, M.-M., Hell, J.-C., Tasan, C.C., 2017. Martensite size effects on damage in quenching and partitioning steels. Scr Mater 138, 1–5. https://doi.org/10.1016/j.scriptamat.2017.05.021

Weck, A.G., 2007. The Role of Coalescence on Ductile Fracture. PhD-thesis Ph.D., 291.

Williams, B., Abu-Samk, K., Xue, J., Shalchi Amirkhiz, B., Scott, C., 2022. Microstructure Modelling of the HEC Behaviour of a Novel Vanadium DP980 Cold Rolled Alloy. Minerals, Metals and Materials Series 909–920. https://doi.org/10.1007/978-3-031-06212-4_82

Withers, P.J., 2015. Fracture mechanics by three-dimensional crack-tip synchrotron X-ray microscopy. Philosophical Transactions of the Royal Society A: Mathematical, Physical and Engineering Sciences 373. https://doi.org/10.1098/RSTA.2013.0157

Wu, W., Wang, Y.-W., Makrygiannis, P., Zhu, F., Thomas, G.A., Hector, L.G., Hu, X., Sun, X., Ren, Y., 2018. Deformation mode and strain path dependence of martensite phase transformation in a medium manganese TRIP steel. Materials Science and Engineering: A 711, 611–623. https://doi.org/10.1016/J.MSEA.2017.11.008

Xiong, X.C., Chen, B., Huang, M.X., Wang, J.F., Wang, L., 2013. The effect of morphology on the stability of retained austenite in a quenched and partitioned steel. Scr Mater 68, 321–324. https://doi.org/10.1016/J.SCRIPTAMAT.2012.11.003

Yan, D., Tasan, C.C., Raabe, D., 2015. High resolution in situ mapping of microstrain and microstructure evolution reveals damage resistance criteria in dual phase steels. Acta Mater 96, 399–409. https://doi.org/10.1016/j.actamat.2015.05.038

Yang, H., Wang, H., Yang, Z., Huang, Y., Li, D., Peng, Y., Wu, P., 2021. In situ neutron diffraction and crystal plasticity analysis on Q&P1180 steel during plastic deformation. Materials Science and Engineering A 802. https://doi.org/10.1016/j.msea.2020.140425

Yang, Y., Mu, W., Sun, B., Jiang, H., Mi, Z., 2021. New insights to understand the strain-state-dependent austenite stability in a medium Mn steel: An experimental and theoretical investigation. Materials Science and Engineering: A 809. https://doi.org/10.1016/j.msea.2021.140993

Yin, W., Briffod, F., Hu, H., Yamazaki, K., Shiraiwa, T., Enoki, M., 2023. Quantitative investigation of strain partitioning and failure mechanism in ultrafine grained medium Mn steel through high resolution digital image correlation. Scr Mater 229, 115386. https://doi.org/10.1016/j.scriptamat.2023.115386

Young, C.C., 1988. Transformation toughening of phosphocarbide-strengthened austenitic stainless steel. MIT, Cambridge.

Zhang, S., Godfrey, A., Zhang, C., Liu, W., Juul Jensen, D., 2020. Surface patterning for combined digital image correlation and electron backscatter diffraction in-situ deformation experiments. Mater Charact 164. https://doi.org/10.1016/j.matchar.2020.110332

Zhou, L., 2018. Effect of Vanadium on Fracture of DP1300 Steels (Master of Science). McMaster University.

7.9 Appendices

7.9.1 Appendix A: Central Global Triaxiality of HE-XRD experiment & In-situ SEM tensile testing Specimens

Table A 7.1:Global Triaxiality within the centre of specimens used for HE-XRD and in-situ SEM tensile testing experiments

Geometry	Centre Triaxiality for APS Specimens	Centre Triaxiality for in situ Specimens
Unnotched	0.33	0.34
Misaligned Notched	0.38	0.36
Shallowly Notched	0.79	0.74
Severely Notched	0.89	0.84

7.9.2 Appendix B: Parameters used for µDIC Post-Processing

Table B 7.1: Facet X Step size used for µDIC post-processing from SEM images acquired during in-situ tensile testing of unnotched, misaligned, shallowly and severely notched specimens

	Unnotched	Misaligned Notched	Shallowly Notched	Severely Notched
Represented Area (µm^2)	12×8	22×11	23×15	23×16
Resolution (µm/pixel)	0.008	0.009	0.009	0.009
Facet × Step size (pixel)	27×9	23x7	23x7	23x7
Facet × Step size (µm×µm)	0.21×0.07	0.21×0.07	0.21×0.06	0.20×0.06

7.9.3 Appendix C: Micromechanisms of damage of Shallowly and Severely Notched Specimens

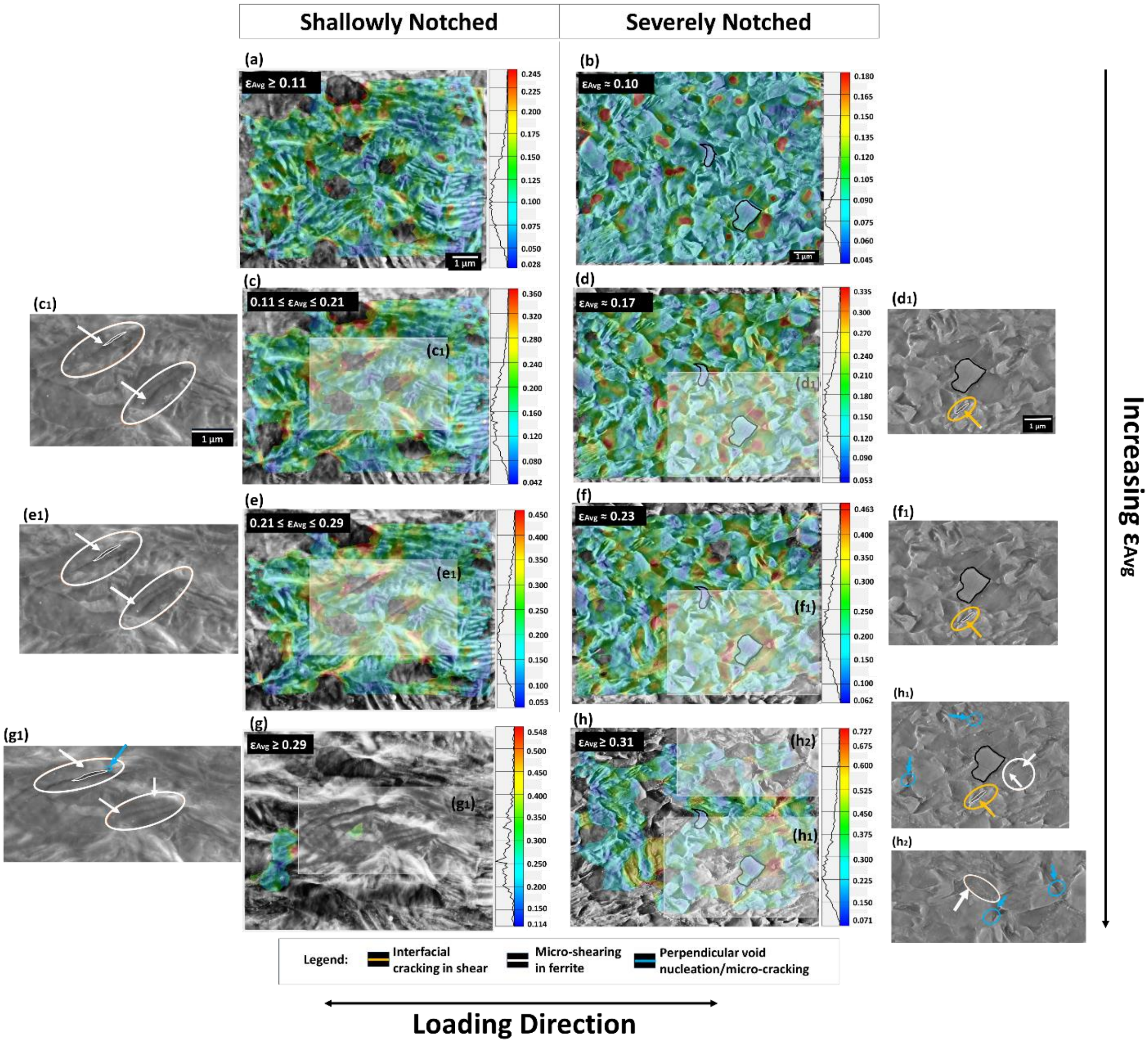

Figure C 7.1: µDIC maps from 1% nital etched surfaces of shallowly (Figure C 7.1 a,c,e,g) and severely (Figure C 7.1b,d,f,h) notched specimens. Micromechanisms of damage captured in the shallowly (Figure C 7.1c_1,e_1,g_1) and severely (Figure C 7.1d_1,f_1,h_{1-2}) notched specimens. Instances of micro-shearing in ferrite is highlighted by the white circles and arrows in Figure C 7.1(c_1,e_1,g_1, h_{1-2}). Instances of interfacial cracking engulfed by micro-shearing was featured in the severely notched specimens and highlighted by yellow circles and arrows in Figure C 7.1(d_1,f_1,h_1). Void nucleation/micro-cracking perpendicular to the loading direction is highlighted by blue circles and arrows Figure C 7.1(g_1,h_{1-2}).

As mentioned in section 7.4.3, to verify that microstructural damage events observed through 2D SEM imaging were unrelated to potential artifacts produced during FIB milling or e-beam deposition from long-time EBSD acquisition, additional unnotched and notched hourglass specimens were etched with 1% nital for in-situ SEM tensile testing coupled with µDIC. Both sites selected for µDIC processing, experiences the highest ε_{Avg} in the material just before fracture, and therefore exhibits the most severe microstrain partitioning amongst phases. As shown in Figure C 7.1: (c-g_1, h_{1-2}) (orange circles), a significant amount of micro-shearing can be seen, which suggests plastic compatibility and co-deformation of phases, as featured in other TRIP-assisted steels (Pelligra et al., 2024b; Ruggles et al., 2016).

Similar to the speculations made by Pelligra et al. (2024b) on an ultrahigh strength Q&P steel, micro-cracks, as shown outlined in white in Figure C 7.1: (c-h_1), were suppressed from further growth by intensive micro-shearing within the microstructure. The key difference between this med-Mn steel and the Q&P steel investigated by Park et al. (2019) and Pelligra et al. (2024b), despite having very similar true strains to fracture, as shown in (Pelligra et al., 2024a, in draft) is the presence of polygonal ferrite, which was introduced in the microstructure during annealing. The white circles and arrows in Figure C 7.1:c_1, e_1, g_1, h_{1-2} highlight instances of micro-shearing within the ferrite, as also captured previously in ultrahigh strength DP steels (Tasan et al., 2014)

With a 2.4-2.7x increase in stress triaxiality from the unnotched to shallowly/severely notched specimens in Figure C 7.1:, damage events were observed to accumulate in this material at a $\varepsilon_{Avg} \geq 0.17$, with very limited void growth up to a $\varepsilon_{Avg} \geq 0.29$. On the contrary, void growth was easily captured in the unnotched stress-state of this med-Mn steel at $\varepsilon_{Avg} \approx 0.45$-$0.48$, as shown in (Pelligra et al., 2024a, in draft). Ultrafine micro-cracks perpendicular to the loading direction were not observed until a $\varepsilon_{Avg} \geq 0.29$ was approached (blue circles and arrows in Figure C 7.1:g_1, h_{1-2}). Unlike the shallowly notched specimen, the severely notched specimen showed instances of interfacial cracking which initiated at $\varepsilon_{Avg} \approx 0.17$ (yellow circles and arrows in Figure C 7.1:d_1, f_1,h_1) and were suppressed from any extreme lateral growth up to a of $\varepsilon_{Avg} \approx 0.29$.

8 Global Discussion

This Chapter links the key findings from Chapters 3-7 in which I have detailed the careful investigations carried out on the microstrain partitioning, local strain gradient developments, Transformation Induced Plasticity (TRIP) kinetics and damage evolution behaviors of three Advanced High Strength Steel (AHSS) alloys. The micromechanical and TRIP kinetic studies described in Chapters 4-7, were initially motivated by the damage development study conducted using X-ray microtomography (µXCT) on a series of first generation (1G) and third generation (3G) AHSSs, described in Chapter 3. The last publication of this sandwich thesis, Chapter 7, is focused on the effect that changes in stress-state has on microstrain partitioning, TRIP kinetics, and damage development in 3G steels.

8.1 Mechanical Property Development and TRIP kinetics

8.1.1 Intercritical Annealing of a Med-Mn steel

Chapter 6 specifically focuses on the intercritical annealing (IA) of a Medium-Mn (med-Mn) steel (0.15C-5.8Mn-1.8Al-0.71Si) with a martensitic-based (80% martensite-20% ferrite) starting microstructure over a tight temperature range of 665°C to 710°C. It was seen that with only ~20-25°C interval increases in IA temperature, considerable variations in mechanical properties, work hardening, and TRIP kinetics were achieved, without significant changes made to the steel's physical microstructure. This enabled us to isolate the role that TRIP kinetics has on microstrain partitioning and damage development in this med-Mn steel. Peak properties, meeting 3G UTS x TE mechanical targets, were attained at an intermediate 685°C IA temperature (shown in Table 8.1), as also been achieved by Zhang et al. (2021).

In Chapter 6, the use of Cobalt-sourced X-ray Diffraction (Co-XRD) to acquire phase information on cross-sectioned, strain interrupted tensile specimens was used to initially estimate the trend in TRIP exhaustion of this med-Mn steel. It should be noted however, that in using this technique, x-rays only penetrate ~20µm below the steel's surface (i.e. 2% of this 1mm thick steel). We were later able to take advantage of combining the use of high energy x-rays with tensile testing to capture crystallographic information throughout the steel's 1mm thickness while also collecting ample data points to delineate the steel's TRIP kinetics. As shown in Chapters 5 and 6, in most cases, the initial austenite (ɣ) (vol%) detected in Co-XRD and High Energy X-ray Diffraction (HE-

XRD) experiments were comparable. Table 8.2 summarizes the initial ɣ content detected in both 3G TRIP-assisted steels using Co-XRD and HE-XRD. Section 6.4.2.2 of Chapter 6 states that similar initial ɣ content was detected for the 665°C, and 710°C IA conditions, 32±1, and 38±2 vol%, respectively, using Co-XRD and HE-XRD. On the other hand, the 685°C IA condition showed the most variability between the two techniques – ≈29 versus ≈36 vol%. This indicates that there is a heightened heterogeneous distribution of ɣ from the surface to throughout the thickness of the 685°C IA condition. This is important as it provides another mode of dislocation-strengthening in the steel (Zhang et al., 2021) and has assisted this steel at its 685°C IA condition to achieve peak properties.

Chapter 6 notes that there is little difference in microstructural appearance (i.e. average ɣ, martensite or ferrite grain sizes) when intercritically annealing this med-Mn from 665 to 710°C. There are and can be, however, differences between IA conditions in terms of their ɣ volume fraction and chemical heterogeneity. Insignificant changes to the steel's microstructural appearance when subjected to minor IA is to be expected since ɣ grain morphology is controlled predominately by its starting microstructure. A martensitic-based starting microstructure promotes ɣ nucleation at martensite lath boundaries (Gouné et al., 2012; Mehrabi et al., 2023). An uneven distribution of secondary phases and Mn heterogeneity has been proven to effectively suppress TRIP and improve the damage tolerance of AHSSs (Ding et al., 2023; Salehiyan et al., 2020; Yang et al., 2024). For example, this explains the ability for the 1G TRIP-assisted steel, TRIP780, discussed in Chapter 3 to contain the greatest amount of damage and achieve the highest true strain at fracture despite having a heterogeneous distribution of phases (i.e. a banded-type network of coarse ɣ as noted in Chapter 5).

Ultimately, researchers have gone to significant lengths to introduce microstructural heterogeneity to improve the strength-ductility balance of materials. Microstructural heterogeneity causes long range back stresses (Wu et al., 2015) which thereby act as additional barriers to dislocation motion. Some of the approaches that have been made to introduce heterogeneity in steel microstructures have included: using complex manufacturing techniques (i.e. severe plastic deformation (SPD), sliding friction treatments (Wang et al., 2020), torsion procedures (Wei et al., 2014)), fast heating/cooling (Liu, Dai, et al., 2020; Liu, Li, et al., 2020) and/or, in specific to med-Mn steels, heavy Al/Si alloying to promote the formation of δ-ferrite and a bimodal grain size distribution (Choi et al., 2017; Sarkar et al., 2017). Although not currently feasible for most industrial production lines, a fast-heating rate can inherit the chemical heterogeneity as a result of the 'kinetic mismatch' between the slow diffusion of Mn and rapid formation of austenite (Liu, Dai, et al., 2020; Liu, Li, et al., 2020). Furthermore, it has been proven on many materials that bimodal grain size distribution (Kang and Yoon, 2023; Nakai et al., 2023; Sabzi et al., 2016) can retain the ductility from coarser grains, and strength achieved with fine grains simultaneously. Another approach, more simplistic in nature, to introduce microstructural or chemical heterogeneity is through intercritical annealing. Gradients in Mn heterogeneity amongst phases are thought to effectively suppress TRIP (Ding et al., 2023; Yang et al., 2024) as a result of altering the local martensite start, M_s, temperatures of the ɣ. Williams et al. (2022) and Zhang et al. (2021) used intercritical annealing to encourage a heterogeneous distribution of Mn in a vanadium-microalloyed DP steel, and a med-Mn steel respectively. In effect, Williams et al. (2022) found that only a 10°C increase in IA temperature (from 800°C to 810°C) was necessary to increase the Hole Expansion Ratio (HER) performance from 27 to 37% in their vanadium-microalloyed DP steel. Furthermore, the heterogeneous distribution of Mn promoted through a 10°C increase in IA did not increase the strength of the vanadium-microalloyed DP steel, as was also demonstrated by this med-Mn steel when increasing the IA temperature from 665°C to 685°C. Zhang et al. (2021), on the other hand, who also achieved peak properties when intercritically annealing a med-Mn steel at an intermediate temperature (680°C), detected a heterogeneous distribution of Mn throughout this condition over a wide area. Recently, Yang et al. (2024) reported the ability to maintain Mn heterogeneity throughout a med-Mn microstructure through the use of slower heating rates (5°C/s). This is comparable to the heating rates applied to intercritical annealing trials conducted on this med-Mn steel (15°C/s, and 5°C/s) (Mehrabi et al., 2023; Pallisco & McDermid, 2020).

8.1.2 3G AHSSs with and without TRIP kinetics

Table 8.1 well as Chapter 6 presents a side-by-side mechanical property assessment on the three 3G AHSS steel candidates for the automotive industry presented in this thesis – an UFG DP1300 steel, an ultrahigh strength QP1500 steel and a CGL-compatible med-Mn steel at its optimal 685°C IA condition.

Table 8.1: Mechanical Properties of an UFG DP1300, a QP1500 and a med-Mn steel intercritically annealed at 685°C.

	UTS (MPa)	YS (MPa)	UE	TE	UTSxTE (MPa%)	Toughness $(\mathrm{MJ/m^3})$
med-Mn (685°C)	1067	862	0.23	0.27	28,809	893
UFG DP1300	1475	839	0.08	0.10	14,750	409
QP1500	1540	1290	0.10	0.14	21,560	1323

The mechanical properties of these steels were obtained from Chapters 3-6.

The med-Mn steel in Table 8.1 at its 685°C IA condition achieves the generalized 3G mechanical property envelope (UTS x TE ≥ 24,000 MPa%) as suggested by De Moor et al. (2010). This mostly is the result of a ≈3x increase in tensile elongation in comparison to the UFG DP1300 and QP1500 steels. Despite the vast differences in microstructures of the UFG DP1300 and QP1500 steels, both attain similar UTS and total elongation values (Table 8.1), with larger differences in their true strains at fracture, and computed toughness. On the other hand, the med-Mn steel exhibited a similar true strain at fracture to that of the QP1500 steel, yet a two-fold delay in the onset of necking. In comparison to the QP1500 steel, ductility in the med-Mn steel is not only enhanced by the contribution of ɣ islands which TRIP preferentially in the loading direction, but more so by the presence of the soft, polygonal ferrite. Moreover, it should be noted that an increase or decrease of ~20-25°C in IA temperature of this med-Mn resulted in a ~1.1-1.3x decrease in UTS x TE as shown in Table 6.2, of Chapter 6.

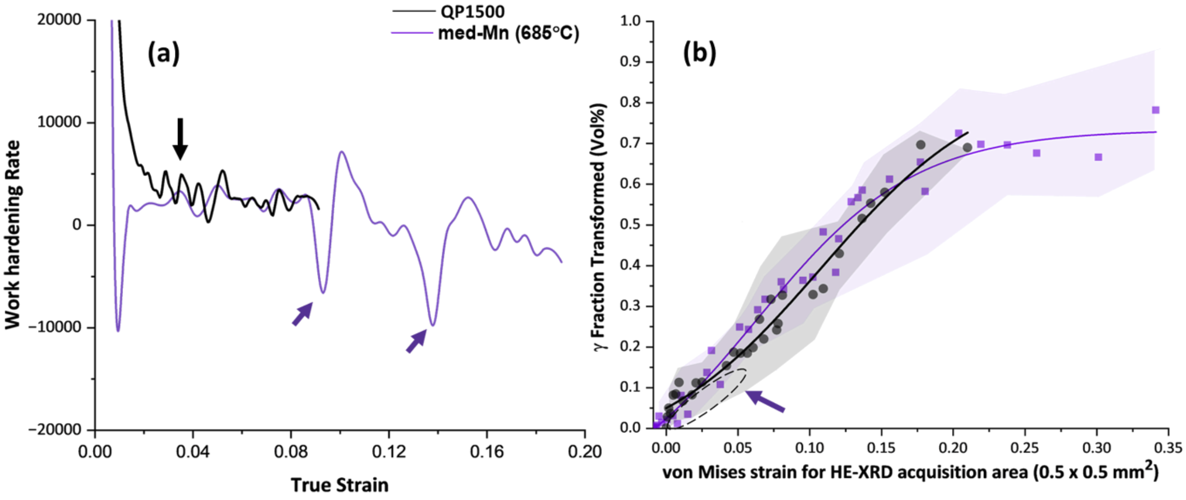

Figure 8.1: Work Hardening Curves of the med-Mn steel at its 685°C IA condition and QP1500 steel (a),TRIP kinetics captured using HE-XRD of both 3G TRIP-assisted steels of interest (b).

In the work hardening curves of Figure 8.1a, one can see dramatic fluctuations in work hardening past a strain of 0.08 in the med-Mn at its 685°C IA condition after a plateau in work hardening. This is linked to the activation of plasticity enhancing mechanisms such as TRIP and/or Twinning Induced Plasticity (TWIP) (Bhadhon et al., 2022; Pallisco and McDermid, 2020). Also pointed out in Figure 8.1 from the HE-XRD data and despite its fitted curve, TRIP is occurring initially (strain ≤0.05) faster in the QP1500 material than the med-Mn steel at its 685°C IA condition. As a note, the work hardening curves presented in Figure 8.1a have been subjected to a lower degree of smoothing than those presented in Figure 5.3 in Chapter 5 and Figure 6.1 in Chapter 6. This was purposefully done to uncover the differences in work hardening fluctuations, and hence localized occurrences of TRIP/TWIP between the med-Mn and QP1500 steel. To confirm, the same degree of smoothing using adjacent-averaging, which takes the user-defined number of data points around each point and replaces it with a new average value, was applied for comparison in the work hardening curves of Figure 8.1a. Nonetheless, at a true strain of 0.05, the initial spikes in work hardening was observed by the QP1500 steel but not seen in the med-Mn steel, corroborating well with the fact that this steel exhibits a significantly higher yield strength than the med-Mn steel (shown in Table 8.1). Microstructurally, this indicates that a martensitic matrix with retained ɣ islands saturated with carbon (0.97 wt%C) in the QP1500 steel helps to improve its yield strength, and thereby increases its anti-intrusion applicability in automotive components.

As mentioned in Chapter 2, the buckling force experienced by a vehicle's B-pillar during a crash, is strongly dependent on the materials' yield strength (Bouaziz et al., 2013). Furthermore, out of all three steels of study in this thesis, this QP1500 steel features the highest UTS and toughness, which in turn also makes this steel an ideal candidate in the construction of a vehicle's crash box (Bouaziz et al., 2013). Industrial problems arise with the manufacturing of Q&P steels, as a result of the >0.5wt% Si leading to casting and reactive wetting/galvanizing issues. On the contrary, the ability to easily customize a med-Mn steel's UTS x TE (30-70 GPa) (Hu et al., 2017; Suh and Kim, 2017; Yang et al., 2021) through IA, and tailor its thermal mechanical processing to be compatible with continuous galvanizing lines (CGLs) and continuous annealing lines (CALs) (Bhadhon et al., 2023; De Moor et al., 2011; Lee et al., 2011; Pallisco and McDermid, 2023) makes this steel attractive for commercialization.

Microscopically, there are several strengthening mechanisms at play during the deformation of the 3G AHSSs presented in this thesis. All three 3G steels have on average a fine to ultrafine grain (UFG) size $\leq$ 1μm, and as such, it can be presumed that the contribution from grain refinement has to strengthening is similar for all three steels. Interstitial carbon and precipitation strengthening are important contributors to the strength of this UFG DP1300 and QP1500 steel, as shown in the chemical composition Table 3.1 in Chapter 3. Precipitation strengthening comes from vanadium carbonitrides within the ferrite of the UFG DP1300 steel, and epsilon carbides within the tempered martensite (TM) of the QP1500 steel (Celada-Casero et al., 2022; Pushkareva et al., 2020; Scott et al., 2017). The effect of increased vanadium-microalloying on strengthening of this UFG DP1300 steel is modelled in Chapter 4, section 4.6.1. Little carbide strengthening is exhibited by this med-Mn steel because carbides quickly dissolve when subjected to IA at 685°C. As stated in Chapter 6, section 6.4.2, TEM carbide extraction replicas revealed that the area fraction of carbides decreases by $\approx$5x, from 0.001 to 0.0002, with a 20°C increase in IA temperature, from 665°C to 685°C. However, Mn in solid solution is the greatest contributor to strengthening in the med-Mn steel, whereas Si in solid solution is the greatest contributor to strengthening in the QP1500 steel.

Table 8.2: Microstructural Properties of an UFG DP1300, a QP1500 and a med-Mn steel intercritically annealed at 685°C.

	Phases	**ɣ Content – Co-XRD (vol%)**	**ɣ Content – HE-XRD (vol%)**	**Carbon in ɣ (wt%C)**	**ɣ, ɣ-M and/or M Grain Size (µm)**	**F, M and/or TM Grain Size (µm)**
med-Mn (685°C)	TM, F,ɣ, ɣ-M	29.0	36.0	0.60	~0.45	~0.67
UFG DP1300	M,F	-	-	-	-	~1.60
QP1500	TM, ɣ, ɣ-M	16.3	17.5	0.97	~0.42	~1.00

The ɣ, ɣ-M and/or M grain size of the ultrahigh strength Q&P steel in Table 8.2, is stated Chapter 5 (0.42µm). It should be noted that a different heat of this material used by Park et al. (2019) showed a 0.6µm average ɣ size. The ferrite grain size of the UFG DP1300 steel was obtained from Chapter 4. The ɣ, ɣ-M and/or M as well as tempered martensite/ferrite grain size is ~0.45µm, and ~0.67µm, respectively, as stated in Chapter 6.

As stated by Spenger et al. (2008), another form of strengthening unique to DP and TRIP steels is the generation of Geometrically Necessary Dislocations (GNDs) alongside Statistically Stored Dislocations (SSDs) to accommodate strain gradients which can simply arise frm local crystallographic misorientations between grains and the interaction of contrasting phases during deformation. As a result, the dislocation accumulation is quicker at dissimilar phase interfaces (i.e. F/M), rather than at the interface of two similarly deforming phases (Tang et al., 2021). Chapters 4-6 describe a unique post µDIC data processing technique created in this thesis to capture the local strain gradient at dissimilar phase interfaces of the subject 3G steels when subjected to uniaxial tension. This is also further discussed in section 8.2 of this Chapter.

Moreover, the production of mobile dislocations from local ɣ-to-martensite transformations (Hatem and Zikry, 2011; Sandvik and Wayman, 1983; Wang et al., 2023) provides TRIP-assisted steels with a dynamic mode of dislocation/composite-based strengthening. Interestingly, the med-Mn steel at its 710°C IA condition featured a comparable UTS x TE to the QP1500 steel, as shown in Table 6.3 (of Chapter 6) and Table 8.1 above, respectively. Chapter 6, Figure B 6.1 shows this QP1500 steel to exhibit a slower rate of TRIP exhaustion than the med-Mn steel at its 710°C IA condition. This suggests that a quick rate of TRIP exhaustion, along with Mn solid solution strengthening, plays a strong role in obtaining the ultrahigh strength (~1319MPa) in this steel's 710°C IA condition. Evidence of a >50% transformation of martensite blocks adjacent to ferritic grains was observed with Energy X-ray Dispersive Spectroscopy (EDS) mapping, coupled with

Selected Area Electron Diffraction (SAED) indexing and dark field/bright field (DF/BF) imaging shown in Chapter 6, Figure A 6.2 captured at this lightly strained 710°C IA condition.

Nonetheless, both the med-Mn steel at its 685°C IA condition and QP1500 steel show somewhat similar rates in TRIP exhaustion up to a true strain of 0.17 (i.e. during yielding, taking into account the customized dog-bone geometry mentioned in Chapter 5), shown in Figure 8.1b. A slightly slower rate of TRIP exhaustion was exhibited by the QP1500 steel. However, after a true strain of 0.17, the rate of TRIP exhaustion decreases more significantly for the med-Mn steel at its 685°C IA condition. At necking, both steels manage to retain ≈27% of their initial ɣ content. Furthermore, partial transformations within block-like ɣ islands were also observed for both steels, via EBSD in the QP1500 steel, Figure C 5.1-Figure C5.3 in Chapter 5, and via Transmission Electron Microscopy (TEM) in the med-Mn steel, Figure 6.3, Figure A 6.1 in Chapter 6. The partial transformation of block-like ɣ is in accordance with the observations of others (Salehiyan et al., 2020; Toda et al., 2022; Zhang et al., 2021) who also observed delayed TRIP kinetics.

Ultimately, the way in which a microstructure delays TRIP continues to be controversial in the literature, and this contradiction is presented with the determination of TRIP kinetics in the med-Mn steel at its 685°C IA condition, and the QP1500 steel presented here. Tirumalasetty et al. (2012) discussed that, during deformation, ɣ adjacent to a ferrite grain has the ability to rotate before transforming, whereas constrained ɣ grains with a lath-type martensitic matrix have limited rotating potential. The high local stress imposed onto an austenitic grain being constrained by its surrounding drives the martensitic transformation, whereas the more uniform stress field of a somewhat unconstrained austenitic grain, enables its rotation before a martensitic transformation. In agreement with this, Courtney (2005) notes that larger grains (as is the case with polygonal ferrite) provides a 'shielding effect' to suppress the transformation from occurring. This explains why a heterogeneous grain structure, featuring both coarse and fine grains, enables an improvement in ductility without a compromise in strength (Choi et al., 2017; Sabzi et al., 2016; Sarkar et al., 2017). Moreover, it should be considered that if the orientation of ferrite grains adjacent to an austenitic one is different, there is an increased effect of the local stress triaxiality within the austenitic region promoting its early transformation to martensite (Sidhoum et al., 2018).

On the other hand, the heavily martensitic QP1500 steel also shows an efficient 3G microstructure in delaying TRIP kinetics while attaining an ultrahigh strength and retaining a proportion of ɣ (~5 vol%) after necking. It can be argued that the lath-like retained ɣ suppresses TRIP due to the plastic constraints imposed by its martensitic surrounding (Bhadhon et al., 2022; Sarkar et al., 2004). As well, the lath-like ɣ is easily chemically stabilized due to the shorter diffusion distance that carbon and Mn have to travel from the surrounding martensite (Luo and Dong, 2015; McDermid et al., 2011). In other words, through this comparative study, it we have shown that neither a completely martensitic matrix microstructure nor a microstructure with >20 vol% of initial ɣ is necessary to suppress TRIP with the intent of attaining a high true strain a fracture (ε_f).

8.2 The Effect of TRIP on microstrain partitioning and Damage Development

In Chapter 4, conventional post µDIC data processing techniques used to quantify the microstrain partitioning between phases are compared to a novel one. These post µDIC data processing techniques were used to understand the microscopic role that vanadium-microalloying plays on the local forming properties/damage tolerance of unnotched and notched V-free and V-added DP1300 steels (Chapter 4). For all in-situ SEM tensile tests coupled with µDIC presented in Chapters 4-7, the facet and step sizes were adjusted such that a local field, of minimum 3x3 facets, reached a size to resolve the average ‘in-grain strain’ of the steel of interest. It is important to note that the micro-speckle patterning technique, and hence the variation in greyscale attained, ultimately governs the suitable facet and step sizes for µDIC processing. Furthermore, to compare the µDIC results between the three 3G steels presented in this thesis, as shown in Chapter 5 and 6, it was ensured that the facet and step sizes were tailored such that they exhibited the same sizes in microns.

Of particular interest from this work was in using µDIC to capture the microstrain gradient produced (i.e. the pile-up of GNDs), at the interface of dissimilar phases, with increased deformation. The quantification of this microstrain gradient is more critical in finer steel microstructures in which it cannot fully develop (Samei et al., 2019) and opens for opportunities in dislocation interaction modelling at the submicron scale, as done previously (Carvalho Resende et al., 2013). This technique can also enable adequate calculation of the density of GNDs at dissimilar interfaces, as presented by Bayley et al. (2006) and Li et al. (2017).

In Chapter 4, the steps to compute the microstrain gradient at dissimilar phase interfaces are described. The von Mises local strain (ε_{Local}) at a sub-micron scale was determined by performing short line scans across an abundance of dissimilar phase interfaces within an area of interest (Figure 8.2a and b). Then the slope for each short line scan was calculated (Figure 8.2c) and summarized using CDFs and PDFs (Figure 8.2d and e).

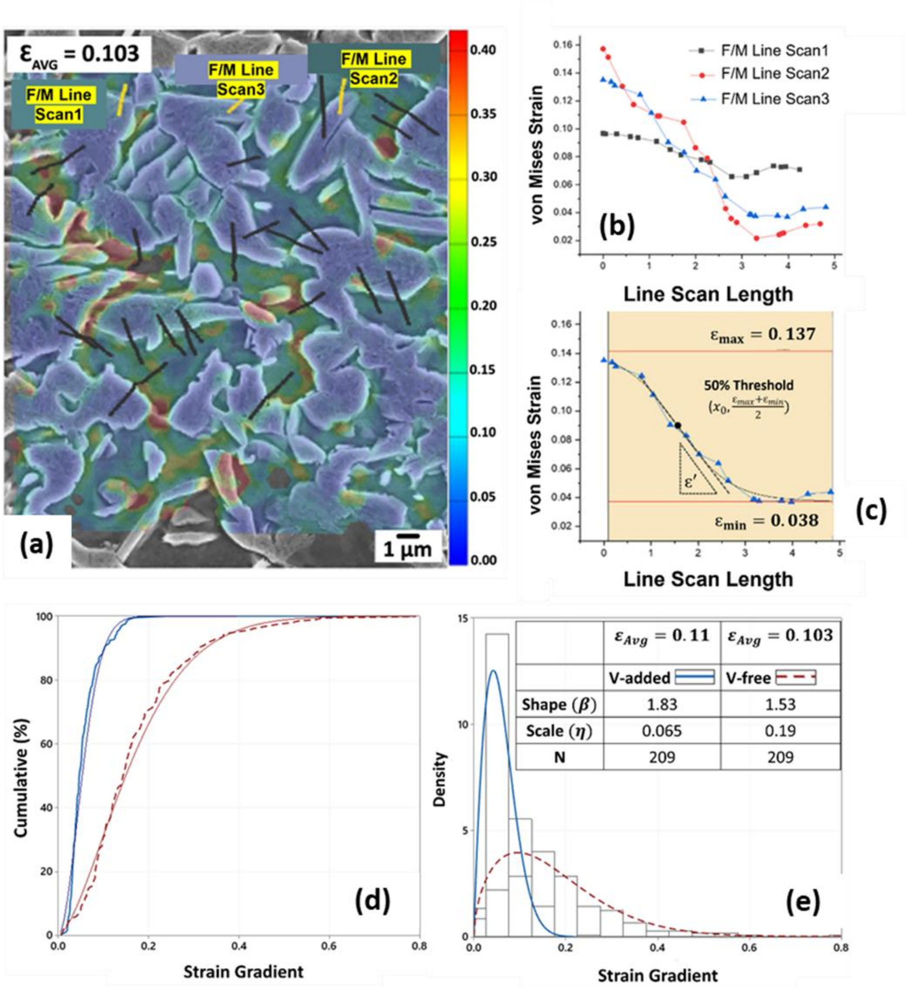

	$\varepsilon_{Avg} = 0.11$	$\varepsilon_{Avg} = 0.103$
	V-added	V-free
Shape (β)	1.83	1.53
Scale (η)	0.065	0.19
N	209	209

Figure 8.2: µDIC short line scans to determine the microstrain at dissimilar phase interfaces, Method 3 (a) (b) variation of microstrain along the 3 sample lines in (a), and (c) determination of slope/microstrain gradient. Image copied from Chapter 4, Figure 4.4 and Figure 4.8.

To some degree, this can be used as an alternative means of determining the strengths of dissimilar phases within a microstructure as is typically attempted via nanoindentation.

Nanoindentation is a surface sensitive technique in which the interfacial surface roughness between two grains/phases can obscure the correct interpretation of the data (Rodríguez and Gutierrez, 2003). This is even more critical when the material has an UFG size.

Overall, the strain gradient, μDIC post-processing technique, introduced in Chapter 4, provides a novel approach to comparing the local forming potential of fine-grained (FG) microstructures with statistical confidence. Specifically, to the UFG DP steel of study, this approach showed that vanadium-microalloying improves the microcompatibility between ferrite and martensite directly at the interface, regardless of the stress triaxiality imposed through a notched specimen design. A greater variability in the microstrain gradient across F/M interfaces in its V-free counterpart explains its earlier ε_f. This is shown in Figure 8.2d and e.

Although selective strengthening of ferrite though microalloying can be used to reduce the potency of interfacial decohesion at dissimilar phase interfaces, several authors ((Pushkareva et al. (2013), Scott et al. (2018) and Williams et al. (2022)) have stated that a more efficient means of doing so is with tempering. With that being said, the microstrain maps at an average von Mises strain (ε_{Avg}) in the UFG DP1300 steel and the two 3G steels of interest subjected to tempering - QP1500 and med-Mn steel - are compared in Figure 8.3 (a)-(c). Evidence of micro-cracking/damage (circled in yellow) was only exhibited by DP material. Overall improved microstrain partitioning behavior between dissimilar phases is seen in the QP1500 and med-Mn steel compared to the UFG DP1300 steel, Figure 8.3d. This can be quantitatively assessed using the microstrain partitioning DIC post-processing techniques that were described in Chapter 4 on 3G DP steels, later applied in Chapters 5 and 6 to the QP1500 and med-Mn steel, respectively. Furthermore, the deforming potential of initial austenite-transformed martensite (ɣ-M) constituents in the med-Mn and QP1500 steels are comparable, while the polygonal ferrite in the med-Mn steel is slightly more deformable than the TM in the QP1500 steel.

In tandem to the statement made on micromechanisms which suppress TRIP in section 8.1.1, the impact that GNDs have on local TRIP kinetics is also contradictory in the literature. Liu et al. (2017) reported that GNDs ahead of a phase interface reduce the nucleation barrier for martensite formation, thereby accommodating more of the transformation, whereas others (Hu & Luo, 2019;

Wu et al., 2016) argued that a large number of GNDs in ɣ can pin its phase boundaries, therefore reducing its potential to transform. Such studies however require the use of TEM on limited regions of interest. Only with the approach of computing the strains at targeted dissimilar phase interfaces using μDIC, it is possible to understand the local contribution of GNDs to strength and damage development at a larger scale compared to that obtainable via TEM. Figure 8.3 shows the median strain gradient ($\varepsilon'_{\mathrm{M}}$), determined by fitting the collection of strain gradients (ε') measurements to a lognormal distribution, with increasing $\varepsilon_{\mathrm{Avg}}$. The high strain gradient featured by the UFG DP1300 is explained by the severe inhibition of dislocation motion, enabling its ultrahigh strength, but also resulting in its premature damage nucleation as the high strain gradients cannot be easily maintained (Figure 8.3a). The lowest strain gradient exhibited by the QP1500 suggests that the evolution of ε' at dissimilar phases with increasing $\varepsilon_{\mathrm{Avg}}$ is much slower. The med-Mn steel rather shows an intermediate, more variable increasing trend in strain gradient which could be a cause of the greater heterogeneity in phases, texture within the microstructure, or the result of localized TRIP kinetics/work hardening.

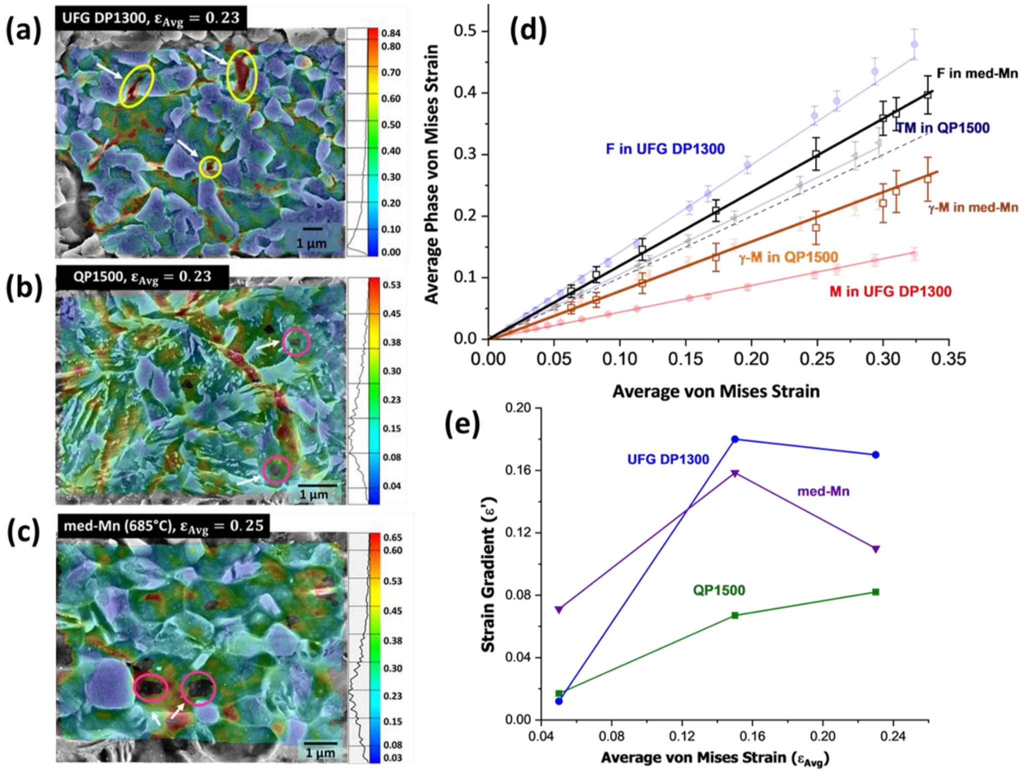

Figure 8.3: Microstrain maps of the UFG DP1300, QP1500 and med-Mn steel of study at an $\varepsilon_{Avg} \approx 0.24$ (a-c). Regions of micro-cracking are circled in yellow and regions of poor DIC correlation is circled in pink in Figure 8.3 (a-c). A comparison of the microstrain partitioning between dissimilar phases in each of the 3G steels of study is shown in Figure 8.3d. Figure 8.3e shows the median strain gradient plotted as a function of ε_{Avg}.

Damage development was characterized both in 2D with in-situ SEM tensile testing, and 3D with µXCT. Differences noticed in the amount of damage accumulated in 2D versus 3D has been speculated elsewhere (Buffière et al., 1999; Lorthios et al., 2010; Mummery and Derby, 1994; Weck, 2007). Chapter 3 shows that the UFG DP1300 steel with a finer ferritic microstructure, nucleated overall finer voids. These finer voids did not come from F/M interfacial cracking, as vanadium precipitation in the ferrite reduced the potency of interfacial decohesion. Moreover, the rate of damage evolution of the QP1500 steel compared to that of the UFG DP1300 steel is reduced, which is highly influenced by the local compressive stresses mitigating void nucleation and growth via TRIP (Sun et al., 2019). Particular focus needs to be placed on the 3G ferrite-containing QP980 steel presented in Chapter 3, Figure 3.2 which, besides the 1G TRIP-assisted steel, can tolerate a significant amount of damage before full fracture. Similar to the phase heterogeneity exhibited by the 1G TRIP-assisted steel, mentioned in section 5.9 of Chapter 5, and this med-Mn steel at its 685°C IA condition, a difference in ferrite detected at the surface versus within the bulk was also captured – 40 versus 29vol% (Salehiyan et al., 2020). Out of all 3G steels tested in Chapter 3, the presence of ferrite in the QP980 microstructure enabled the largest mean void diameter just before fracture (Figure 3.2d, Chapter 3).

It is important to note that there are key differences in the quantifying damage using µXCT on post-mortem specimens (i.e. of a ductile fractured specimens), as done in Chapters 6 and 7, versus performing interrupted uniaxial tensile tests, as done in Chapters 3 and 5. The benefit of coupling interrupted uniaxial tensile testing with µXCT is in the ability to track the void growth and coalescence of the largest voids, which is responsible for full fracture (Maire et al., 2012). For instance, the Rice and Tracey (1969) void growth model was applied in Chapter 3 to indicate early on in this thesis that TRIP-assistance suppresses void growth Figure 3.3.

8.3 The Behavior of a med-Mn steel at different stress states

Notched and unnotched specimens of this med-Mn steel at its 685°C IA condition were used to investigate the effect that an increased stress-state has on microstrain partitioning, TRIP exhaustion, and damage development behaviors. Figure 8.4a, (c) to (e) shows the severely, shallowly, misaligned and unnotched tensile specimens discussed in Chapter 7 to understand the effect an increase in stress triaxiality, from 0.33 to 0.89, has on the microstructural and damage response of a 3G TRIP-assisted steel. This study was specifically carried out on this med-Mn steel at its 685°C IA condition, not only for its prolonged TRIP kinetics compared to the other conditions tested in Chapter 6, but also for its ability to reduce the amount of void growth/coalescence before fracture (i.e. lowest void area fraction) (Figure 6.6, Chapter 6).

As noted by Patel & Cohen (1953), resolved shear stresses on a habit plane work in favour of activating the TRIP effect, whereas the mean stress (σ_m) works to support the volume expansion associated with the transformation. Finite element modelling of the severely and shallowly notched specimens showed a high σ_m in the specimen centre and therefore welcomes the volume expansion associated with TRIP. This explains the fastest TRIP kinetics exhibited by the severely and shallowly notched specimens as shown in Figure 8.4b. On the contrary, finite element modelling revealed a significant variability in σ_m within the central region of the misaligned notched specimens. As a result, the rate of TRIP exhaustion is slowest for these specimens because of the dynamic promotion-opposition of the ɣ-to-martensite transformation imposed by the σ_m variation, shown in Figure 8.4b.

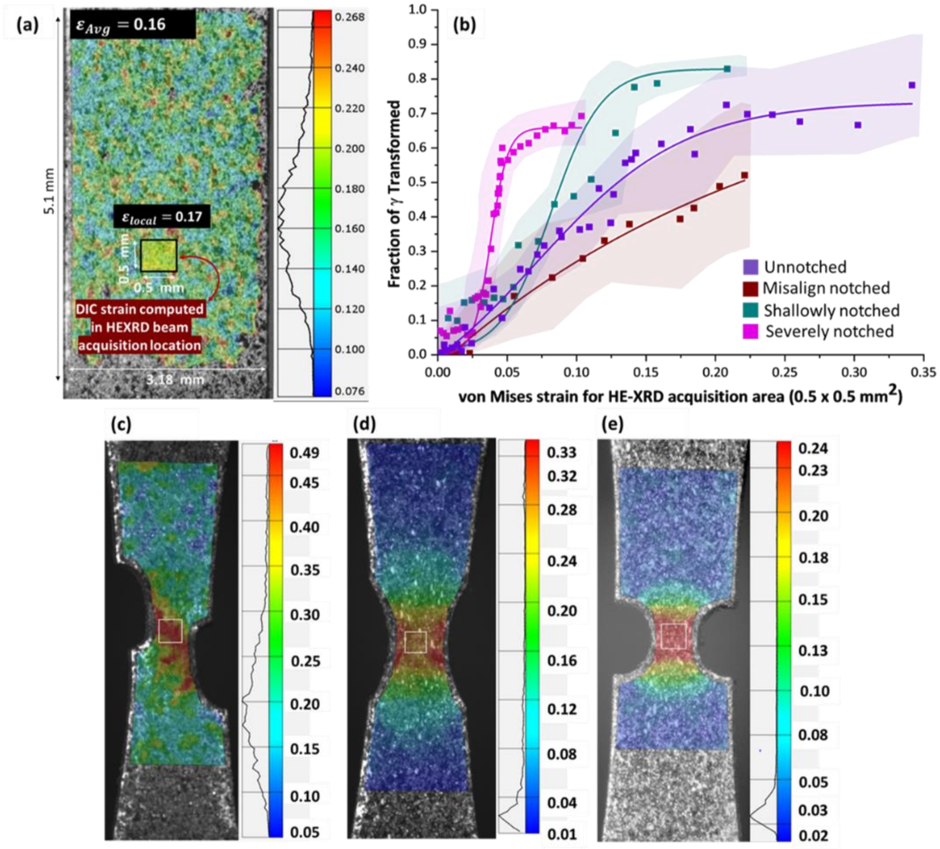

Figure 8.4: The DIC ε_{local} measurements computed within the precise region of HE-XRD acquisition compared to ε_{Avg} obtained from the larger imaged area in unnotched specimens, from Figure 5.6 in Chapter 5. The ɣ-to-martensite transformation as a function of ε_{local} for unnotched and notched specimen geometries of the med-Mn steel at its 685°C IA condition Figure 8.4b. The shaded regions in Figure 8.4b show a 95% CI span of ɣ fraction transformed for every tensile stress-state tested with increasing von Mises strain. Figure 8.4c, d, e show the strain maps and it's region of HE-XRD acquisition of misaligned, shallowly, and severely notched specimens, respectively. Figure 8.4 (b)-(e) are copied from Figure 7.4, Chapter 7.

In reference to the µDIC results gathered from these specimens presented in Chapter 7, it was seen that ferrite-tempered martensite (F-TM) phases are more sensitive to modifications in global stress triaxiality whereas ɣ-M phases are not. It is critical to note however, that the result of SEM images for µDIC processing could have impacted this result.

Some portion of this thesis was dedicated to µDIC methodology development with the introduction of a unique electropolishing micro-speckle patterning technique in Chapter 7. By optimizing the electropolishing procedure on a med-Mn steel, it was possible to obtain a variation in greyscale that was narrow enough for EBSD indexing and wide enough for average 'in-grain' µDIC computation. This micro-speckle patterning technique was inspired by the original work of Zhang et al. (2020). Using µXCT, it was seen that damage accumulation was fastest for the severely and shallowly notched specimens, however the unnotched and notched specimens showed that the same void area fraction was achieved before full fracture. This suggests that there is a critical void size in the material, that once reached, void growth and coalescence proceeds catastrophically.

Overall, this Chapter provides a detailed discussion on the findings collected from Chapters 3-7 on the microstrain partitioning, local strain gradient development, TRIP kinetics and damage evolution behaviors of 3G steels with and without TRIP-assistance. The subsequent concluding chapter will pinpoint the key developments provided through this thesis.

9 Concluding Remarks

In summary, this thesis work was motivated by the fact that the local forming capability (i.e. damage tolerance) of 3G AHSSs with and without TRIP-assistance is weakly understood. Up to now, significant strides have been made to experimentally assess the local forming capability of AHSSs, but limited studies are available in quantifying its microstrain partitioning, TRIP kinetics as well as capturing the micro-damage events which lead to fracture in 3G steels. That being said, the main objective with this Ph.D. thesis has been to determine the influence that prominent 3G microstructural features, including grain refinement and TRIP kinetics, as well as modifications in stress-state has on the microstrain partitioning behavior leading to damage in AHSSs.

The microstrain partitioning DIC post-processing techniques that were applied and introduced in Chapter 4 on 3G DP steels were then propagated into Chapters 5-7 on a TRIP-assisted 3G Q&P, and med-Mn steel, respectively. In addition, Chapters 5-7 use synchrotron-sourced HE-XRD coupled with simultaneous tensile testing and DIC acquisition to obtain highly resolved, continual information of their TRIP kinetics. This was also carried out on notched med-Mn steel specimens. Ultimately, the work featured in Chapters 5-7 is driven by the role that TRIP plays in suppressing damage development as modelled in Chapter 3. The major findings from this thesis are as follows:

1) Chapter 4 features one of the two novel developments to µDIC processing introduced in this thesis. The post µDIC data processing technique, termed as the local strain gradient in Chapter 4, was introduced to capture the microstrain gradient across dissimilar phase interfaces. This technique was first applied to show that vanadium-microalloying of DP steels improves the microcompatibility between ferrite and martensite directly at the interface and explains its improved local formability. This technique was then applied in Chapters 5 and 6 to understand the difference in GND pile up at dissimilar interfaces of two 3G TRIP-assisted steels compared to a DP steel. Ultimately, this technique provides a new approach to comparing the local forming potential (i.e. ability to maintain large strain gradients) of fine-to-ultrafine grained microstructures with statistical confidence.

2) In Chapter 6, target 3G mechanical properties and prolonged TRIP kinetics were achieved when a 0.15C-5.8Mn-1.8Al-0.71Si med-Mn steel with a martensitic starting

microstructure was intercritically annealed at 685°C. Compared to intercritical annealing of this med-Mn at 665°C or 710°C, an intermediate 685°C temperature showed the greatest potential to mitigate the growth of voids by prolonging TRIP over a large strain range. The major difference between the three IA conditions of interest, is the heightened variability in ɣ from the surface to the bulk of the 685°C IA condition. This uneven ɣ distribution combined with Mn heterogeneity throughout this 685°C IA condition suppressed TRIP kinetics and improved the steel's damage tolerance.

3) Chapter 6 compares the mechanical properties and microstrain partitioning of this med-Mn steel at its optimal 685°C IA condition to the QP1500 and UFG DP1300 steel of interest. Out of the three, only the med-Mn at its 685°C IA condition achieves 3G mechanical properties. Despite this, the QP1500 steel demonstrated the highest YS, UTS and toughness, making it a promising candidate for anti-intrusion applications as well as suitable for the crash box material in automobile construction. Microscopically, strain partitioning studies showed that the lowest strain gradients with increasing deformation was exhibited by the QP1500 steel. This suggests that the evolution of strain gradients at dissimilar phases is overall slower in 3G TRIP-assisted steels which explains their high true strain at fracture. The med-Mn steel rather showed an intermediate trend in strain gradient development which is likely a result of a greater heterogeneity in phases, texture or localized TRIP kinetics. Lastly, the UFG DP1300 steel showed the largest strain gradients which resulted in the early onset of damage nucleation.

4) Both the med-Mn and QP1500 steel exhibit efficient microstructures in delaying TRIP kinetics. The rate of TRIP exhaustion of the med-Mn steel at its 685°C IA condition and QP1500 steel is somewhat similar in its beginning stages of deformation. After a true strain of 0.17, only the med-Mn steel exhibits a reduced TRIP rate. On the one hand, the minor ferrite within the med-Mn steel allows for ample rotation of ɣ grains before its transformation, while on the other, the plastic constraints imposed by heavily martensitic QP1500 steel matrix limits ɣ rotation and suppresses the volume expansion associated with TRIP.

5) This thesis is one of the first reports which documents the impact that stress-state has on TRIP, microstrain partitioning and damage evolution in a med-Mn steel. Through this study it was found that, under tension, the severely notched specimen exhibited the fastest TRIP rate, while the misaligned notched geometry showed the slowest. This finding is in agreement with the knowledge that the increased mean stress accompanying the severely notched specimen easily accommodates the volume expansion associated with TRIP, whereas, the dramatic variation in mean stress through the misaligned notched specimen design suppresses it. In addition, the increase in mean stress exhibited by the severely and shallowly notched specimens resulted in their earlier fracture, however these specimens achieved the same void area fraction as unnotched specimen before fracture. This indicates that there is a critical void size in this steel that once reached causes exponential void growth, coalescence and then fracture.

6) Chapter 7 demonstrates the second development to µDIC processing introduced through this thesis. A novel electropolishing micro-speckle patterning technique was used on this med-Mn to enable the combined ability to perform in-situ SEM tensile testing and µDIC processing thereafter on a previously EBSD mapped area of interest. The advantage of using this electropolishing micro-speckle patterning technique is the ability to differentiate between phases, crystallographic orientations, etc. before the start of an in-situ SEM coupled with µDIC test. In Chapter 7, this micro-speckle patterning technique was used to track the strain partitioning between the initial ɣ and F-TM phases of unnotched and notched specimens.

10 References

Bayley, C.J., Brekelmans, W.A.M., Geers, M.G.D., 2006. A comparison of dislocation induced back stress formulations in strain gradient crystal plasticity. Int J Solids Struct 43, 7268–7286. https://doi.org/10.1016/j.ijsolstr.2006.05.011

Bhadhon, K.M.H., Pallisco, D.M., McDermid, J.R., 2023. Continuous Hot-Dip Galvanizing of Medium-Manganese Third-Generation Advanced High-Strength Steels. Steel Res Int. https://doi.org/10.1002/srin.202200898

Bhadhon, K.M.H., Wang, X., McNally, E.A., McDermid, J.R., 2022. Effect of Intercritical Annealing Parameters and Starting Microstructure on the Microstructural Evolution and Mechanical Properties of a Medium-Mn Third Generation Advanced High Strength Steel. Metals (Basel) 12, 356. https://doi.org/10.3390/met12020356

Bouaziz, O., Zurob, H., Huang, M., 2013. Driving Force and Logic of Development of Advanced High Strength Steels for Automotive Applications. Steel Res Int 84, 937–947.

Buffière, J.-Y., Maire, E., Cloetens, P., Lormand, G., Fougères, R., 1999. Characterization of internal damage in a MMCp using X-ray synchrotron phase contrast microtomography. Acta Mater 47, 1613–1625. https://doi.org/10.1016/S1359-6454(99)00024-5

Carvalho Resende, T., Bouvier, S., Abed-Meraim, F., Balan, T., Sablin, S.S., 2013. Dislocation-based model for the prediction of the behavior of b.c.c. materials - Grain size and strain path effects. Int J Plast 47, 29–48. https://doi.org/10.1016/j.ijplas.2013.01.003

Celada-Casero, C., Vercruysse, F., Linke, B., Smith, A., Kok, P., Sietsma, J., Santofimia, M.J., 2022. Analysis of work hardening mechanisms in Quenching and Partitioning steels combining experiments with a 3D micro-mechanical model. Materials Science and Engineering: A 846, 143301. https://doi.org/10.1016/j.msea.2022.143301

Choi, H., Lee, S., Lee, J., Barlat, F., De Cooman, B.C., 2017. Characterization of fracture in medium Mn steel. Materials Science and Engineering: A 687, 200–210. https://doi.org/10.1016/j.msea.2017.01.055

Courtney, T.H., 2005. Mechanical Behavior of Materials, 2nd ed. Waveland Press, Inc., Long Grove, Illinois.

De Moor, E., Matlock, D.K., Speer, J.G., Merwin, M.J., 2011. Austenite stabilization through manganese enrichment. Scr Mater 64, 185–188. https://doi.org/10.1016/j.scriptamat.2010.09.040

Ding, R., Zhang, Chaofan, Wang, Y., Liu, C., Yao, Y., Zhang, J., Yang, Z., Zhang, Chi, Liu, Y., Chen, H., 2023. Mechanistic role of Mn heterogeneity in austenite decomposition and stabilization in a commercial quenching and partitioning steel. Acta Mater 250. https://doi.org/10.1016/j.actamat.2023.118869

Gouné, M., Maugis, P., Drillet, J., 2012. A Criterion for the Change from Fast to Slow Regime of Cementite Dissolution in Fe–C–Mn Steels. J Mater Sci Technol 28, 728–736. https://doi.org/10.1016/S1005-0302(12)60122-4

Hatem, T.M., Zikry, M.A., 2011. A model for determining initial dislocation-densities associated with martensitic transformations. Materials Science and Technology 27, 1570–1573. https://doi.org/10.1179/1743284711Y.0000000079

Hu, B., Luo, H., 2019. A novel two-step intercritical annealing process to improve mechanical properties of medium Mn steel. Acta Mater 176, 250–263. https://doi.org/https://doi.org/10.1016/j.actamat.2019.07.014

Hu, B., Luo, H., Yang, F., Dong, H., 2017. Recent progress in medium-Mn steels made with new designing strategies, a review. J Mater Sci Technol 33, 1457–1464. https://doi.org/10.1016/j.jmst.2017.06.017

Kang, C.G., Yoon, J.W., 2023. Effect of Strain Localization on the Mechanical Properties from Nonuniform Grain Size Distribution of Ultralow Carbon Steel. Steel Res Int 94. https://doi.org/10.1002/srin.202200335

Lee, S., Lee, S.-J., De Cooman, B.C., 2011. Austenite stability of ultrafine-grained transformation-induced plasticity steel with Mn partitioning. Scr Mater 65, 225–228. https://doi.org/10.1016/j.scriptamat.2011.04.010

Li, J., Weng, G.J., Chen, S., Wu, X., 2017. On strain hardening mechanism in gradient nanostructures. Int J Plast 88, 89–107. https://doi.org/10.1016/j.ijplas.2016.10.003

Liu, G., Dai, Z., Yang, Z., Zhang, C., Li, J., Chen, H., 2020a. Kinetic transitions and Mn partitioning during austenite growth from a mixture of partitioned cementite and ferrite: Role of heating rate. J Mater Sci Technol 49, 70–80. https://doi.org/10.1016/j.jmst.2020.01.051

Liu, G., Li, T., Yang, Z., Zhang, C., Li, J., Chen, H., 2020b. On the role of chemical heterogeneity in phase transformations and mechanical behavior of flash annealed quenching & partitioning steels. Acta Mater 201, 266–277. https://doi.org/https://doi.org/10.1016/j.actamat.2020.10.007

Liu, J., Chen, C., Feng, Q., Fang, X., Wang, H., Liu, F., Lu, J., Raabe, D., 2017. Dislocation activities at the martensite phase transformation interface in metastable austenitic stainless steel: An in-situ TEM study. Materials Science and Engineering: A 703, 236–243. https://doi.org/https://doi.org/10.1016/j.msea.2017.06.107

Lorthios, J., Nguyen, F., Gourgues, A.-F., Morgeneyer, T.F., Cugy, P., 2010. Damage observation in a high-manganese austenitic TWIP steel by synchrotron radiation computed tomography. Scr Mater 63, 1220–1223. https://doi.org/10.1016/j.scriptamat.2010.08.042

Luo, H., Dong, H., 2015. New ultrahigh-strength Mn-alloyed TRIP steels with improved formability manufactured by intercritical annealing. Materials Science and Engineering: A 626, 207–212. https://doi.org/10.1016/j.msea.2014.12.049

Maire, E., Morgeneyer, T., Landron, C., Adrien, J., Helfen, L., 2012. Bulk evaluation of ductile damage development using high resolution tomography and laminography. Elsevier 328–336.

McDermid, J.R., Zurob, H.S., Bian, Y., 2011. Stability of Retained Austenite in High-Al, Low-Si TRIP-Assisted Steels Processed via Continuous Galvanizing Heat Treatments. Metallurgical and Materials Transactions A 42, 3627–3637. https://doi.org/10.1007/s11661-011-0678-z

Mehrabi, A., McDermid, J.R., Wang, X., Zurob, H., 2023. Austenite Nucleation and Growth as a Function of Starting Microstructure for a Fe–0.15C–5.56Mn–1.1Si–1.89Al Medium-Mn Steel. Steel Res Int. https://doi.org/10.1002/srin.202200952

Mummery, P.M., Derby, B., 1994. In situ scanning electron microscope studies of fracture in particulate-reinforced metal-matrix composites. J Mater Sci 29, 5615–5624.

Nakai, Y., Kikuchi, S., Shiozawa, D., Hase, T., Nakazawa, I., Fujita, K., Kawabata, M.O., Ameyama, K., 2023. Evaluation of Dislocation Density of Coarse and Fine Grains in Bimodal Harmonic Structured Steel Observed by Diffraction Contrast Tomography using Ultrabright Synchrotron Radiation. Adv Eng Mater 25. https://doi.org/10.1002/adem.202201836

Pallisco, D.M., McDermid, J.R., 2023. On the Selective Oxidation of a 0.15C-6Mn-2Al-1Si Third-Generation Advanced High Strength Steel During Two-Stage Annealing Treatments. Metall Mater Trans A Phys Metall Mater Sci. https://doi.org/10.1007/s11661-023-06985-2

Pallisco, D.M., McDermid, J.R., 2020. Mechanical property development of a 0.15C–6Mn–2Al–1Si third-generation advanced high strength steel using continuous galvanizing heat treatments. Materials Science and Engineering A 778, 139111. https://doi.org/10.1016/j.msea.2020.139111

Park, T., Hector Jr., L.G., Hu, X., Abu-Farha, F., Fellinger, M.R., Kim, H., Esmaeilpour, R., Pourboghrat, F., 2019. Crystal plasticity modeling of 3rd generation multi-phase AHSS with martensitic transformation. International Journal of Plasticity 120, 1–46.

Patel, J.R., Cohen, M., 1953. Criterion for the action of applied stress in the martensitic transformation. Acta Metallurgica 1, 531–538. https://doi.org/10.1016/0001-6160(53)90083-2

Pushkareva, I., Scott, C., Goune, M., Valle, N., 2013. Distribution of Carbon in Martensite During Quenching and Tempering Dual Phase Steels and Consequences for Damage Properties. ISIJ International 53, 1215–1223.

Pushkareva, I., Shalchi-Amirkhiz, B., Allain, S.Y.P., Geandier, G., Fazeli, F., Sztanko, M., Scott, C., 2020. The influence of vanadium additions on isothermally formed bainite microstructures in medium carbon steels containing retained austenite. Metals (Basel) 10. https://doi.org/10.3390/met10030392

Rice, J.R., Tracey, D.M., 1969. On the ductile enlargement of voids in triaxial stress fields*. J Mech Phys Solids 17, 201–217. https://doi.org/10.1016/0022-5096(69)90033-7

Rodríguez, R., Gutierrez, I., 2003. Correlation between nanoindentation and tensile properties influence of the indentation size effect. Materials Science and Engineering A 361, 377–384. https://doi.org/10.1016/S0921-5093(03)00563-X

Sabzi, H.E., Zarei Hanzaki, A., Abedi, H.R., Soltani, R., Mateo, A., Roa, J.J., 2016a. The effects of bimodal grain size distributions on the work hardening behavior of a TRansformation-TWinning induced plasticity steel. Materials Science and Engineering: A 678, 23–32. https://doi.org/10.1016/j.msea.2016.09.085

Sabzi, H.E., Zarei Hanzaki, A., Abedi, H.R., Soltani, R., Mateo, A., Roa, J.J., 2016b. The effects of bimodal grain size distributions on the work hardening behavior of a TRansformation-TWinning induced plasticity steel. Materials Science and Engineering: A 678, 23–32. https://doi.org/10.1016/j.msea.2016.09.085

Salehiyan, D., Samei, J., Amirkhiz, B.S., Hector, L.G., Wilkinson, D.S., 2020. Microstructural Evolution During Deformation of a QP980 Steel. Metall Mater Trans A Phys Metall Mater Sci 51, 4524–4539. https://doi.org/10.1007/s11661-020-05882-2

Samei, J., Zhou, L., Kang, J., Wilkinson, D.S., 2019. Microstructural analysis of ductility and fracture in fine-grained and ultrafine-grained vanadium-added DP1300 steels. Int J Plast 117, 58–70. https://doi.org/10.1016/j.ijplas.2017.12.009

Sandvik, B.P.J., Wayman, C.M., 1983. CHARACTERISTICS OF LATH MARTENSITE: PART I. CRYSTALLOGRAPHIC AND SUBSTRUCTURAL FEATURES. Metallurgical transactions. A, Physical metallurgy and materials science 14 A, 809 – 822. https://doi.org/10.1007/bf02644284

Sarkar, A., Sanyal, S., Bandyopadhyay, T.K., Mandal, S., 2017. Enhanced strength-ductility relationship in a medium Mn high Al-alloyed multicomponent steel through thermomechanical processing. Materials Science and Engineering: A 703, 205–213. https://doi.org/10.1016/j.msea.2017.07.045

Sarkar, J., Kutty, T., Wilkinson, D., Embury, J.D., Lloyd, D.J., 2004. Tensile properties and bendability of T4 treated AA6111 aluminum alloys. Materials Science and Engineering A 369, 258–266. https://doi.org/10.1016/j.msea.2003.11.022

Scott, C.P., Fazeli, F., Shalchi Amirkhiz, B., Pushkareva, I., Allain, S.Y.P., 2017. Structure-properties relationship of ultra-fine grained V-microalloyed dual phase steels. Materials Science and Engineering A 703, 293–303. https://doi.org/10.1016/j.msea.2017.07.051

Scott, C.P., Shalchi Amirkhiz, B., Pushkareva, I., Fazeli, F., Allain, S.Y.P., Azizi, H., 2018. New insights into martensite strength and the damage behaviour of dual phase steels. Acta Mater 159, 112–122. https://doi.org/10.1016/j.actamat.2018.08.010

Sidhoum, Z., Ferhoum, R., Almansba, M., Bensaada, R., Habak, M., Aberkane, M., 2018. Experimental and numerical study of the mechanical behavior and kinetics of the martensitic transformation in 304L TRIP steel: applied to folding. The International Journal of Advanced Manufacturing Technology 97, 2757–2765. https://doi.org/10.1007/s00170-018-2154-z

Spenger, F., Hebesberger, T., Pichler, A., Krempaszky, C., Werner, E.A., 2008. AHS Steel Grades: Strain Hardening and Damage as Material Design Criteria.

Suh, D.W., Kim, S.J., 2017. Medium Mn transformation-induced plasticity steels: Recent progress and challenges. Scr Mater 126, 63–67. https://doi.org/10.1016/j.scriptamat.2016.07.013

Sun, B., Palanisamy, D., Ponge, D., Gault, B., Fazeli, F., Scott, C., Yue, S., Raabe, D., 2019. Revealing fracture mechanisms of medium manganese steels with and without delta-ferrite. Acta Mater 164, 683–696. https://doi.org/10.1016/J.ACTAMAT.2018.11.029

Tang, A., Liu, H., Chen, R., Liu, G., Lai, Q., Zhong, Y., Wang, L., Wang, J., Lu, Q., Shen, Y., 2021. Mesoscopic origin of damage nucleation in dual-phase steels. Int J Plast 137. https://doi.org/10.1016/j.ijplas.2020.102920

Tirumalasetty, G.K., van Huis, M.A., Kwakernaak, C., Sietsma, J., Sloof, W.G., Zandbergen, H.W., 2012. Deformation-induced austenite grain rotation and transformation in TRIP-assisted steel. Acta Mater 60, 1311–1321. https://doi.org/10.1016/j.actamat.2011.11.026

Toda, H., Hirayama, K., Okamura, K., Suzuki, T., Takeuchi, A., Uesugi, M., Fujihara, H., 2022. Multimodal assessment of mechanically induced transformation in metastable multi-phase steel using X-ray nano-tomography and pencil-beam diffraction tomography. Acta Mater 234, 117956. https://doi.org/10.1016/j.actamat.2022.117956

Wang, L., Li, M., Tan, H., Feng, Y., Xi, Y., 2020. Enhanced Mechanical Properties of a Gradient Nanostructured Medium Manganese Steel and Its Grain Refinement Mechanism. J Mater Eng Perform 29, 3812–3823. https://doi.org/10.1007/s11665-020-04903-w

Wang, W., Liu, Y., Zhang, Z., Yang, M., Zhou, L., Wang, J., Jiang, P., Yuan, F., Wu, X., 2023. Deformation mechanisms for a new medium-Mn steel with 1.1 GPa yield strength and 50% uniform elongation. J Mater Sci Technol 132, 110–118. https://doi.org/10.1016/j.jmst.2022.05.048

Weck, A.G., 2007. The Role of Coalescence on Ductile Fracture. PhD-thesis Ph.D., 291.

Wei, Y., Li, Y., Zhu, L., Liu, Y., Lei, X., Wang, G., Wu, Y., Mi, Z., Liu, J., Wang, H., Gao, H., 2014. Evading the strength-ductility trade-off dilemma in steel through gradient hierarchical nanotwins. Nat Commun 5, 3580.

Williams, B., Abu-Samk, K., Xue, J., Shalchi Amirkhiz, B., Scott, C., 2022. Microstructure Modelling of the HEC Behaviour of a Novel Vanadium DP980 Cold Rolled Alloy. Minerals, Metals and Materials Series 909–920. https://doi.org/10.1007/978-3-031-06212-4_82

Wu, X., Yang, M., Yuan, F., Wu, G., Wei, Y., Huang, X., Zhu, Y., 2015. Heterogeneous lamella structure unites ultrafine-grain strength with coarse-grain ductility. Proceedings of the National Academy of Sciences 112, 14501–14505. https://doi.org/10.1073/pnas.1517193112

Wu, X.L., Yang, M.X., Yuan, F.P., Chen, L., Zhu, Y.T., 2016. Combining gradient structure and TRIP effect to produce austenite stainless steel with high strength and ductility. Acta Mater 112, 337–346. https://doi.org/10.1016/j.actamat.2016.04.045

Yang, D., Xiao, J., Zhang, C., Wang, Y., Xiong, Z., 2024. Mn Heterogeneity and Ductility Improvement Realized by Slow Heating Mn-Partitioned Pearlite. Metals and Materials International 30, 393–402. https://doi.org/10.1007/s12540-023-01499-3

Yang, Y., Mu, W., Sun, B., Jiang, H., Mi, Z., 2021. New insights to understand the strain-state-dependent austenite stability in a medium Mn steel: An experimental and theoretical investigation. Materials Science and Engineering: A 809. https://doi.org/10.1016/j.msea.2021.140993

Zhang, S., Godfrey, A., Zhang, C., Liu, W., Juul Jensen, D., 2020. Surface patterning for combined digital image correlation and electron backscatter diffraction in-situ deformation experiments. Mater Charact 164. https://doi.org/10.1016/j.matchar.2020.110332

Zhang, X., Yan, J., Liu, T., Liu, H., Shi, Y., Zhou, Q., Zhao, L., Lv, Z., 2021. Microstructural evolution and mechanical behavior of a novel heterogeneous medium Mn cold-rolled steel. Materials Science and Engineering: A 800, 140344. https://doi.org/10.1016/j.msea.2020.140344